LA-UR-95-1480
March 1995
Rev. 1.5

RECEIVED
AUG 13 1997
OSTI

MASTER

APT Accelerator Topical Report

PROCESSED FROM BEST AVAILABLE COPY

Submitted to: U.S. Department of Energy
Defense Programs
1000 Independence Avenue, SW
Washington, DC 20585

Submitted by: Los Alamos National Laboratory
Industrial Partnerships

PROCESSED FROM BEST AVAILABLE COPY

LA-UR-95-1480
Revision 1.5
Volume 1

LOS ALAMOS NATIONAL LABORATORY

ACCELERATOR PRODUCTION OF TRITIUM PROJECT

B&R GB0508302

ACCELERATOR TOPICAL REPORT

MASTER

HH
PROCESSED FROM BEST AVAILABLE COPY

March 1995

DISCLAIMER

This report was prepared as an account of work sponsored by an agency of the United States Government. Neither the United States Government nor any agency thereof, nor any of their employees, makes any warranty, express or implied, or assumes any legal liability or responsibility for the accuracy, completeness, or usefulness of any information, apparatus, product, or process disclosed, or represents that its use would not infringe privately owned rights. Reference herein to any specific commercial product, process, or service by trade name, trademark, manufacturer, or otherwise does not necessarily constitute or imply its endorsement, recommendation, or favoring by the United States Government or any agency thereof. The views and opinions of authors expressed herein do not necessarily state or reflect those of the United States Government or any agency thereof.

Submitted to

US Department of Energy
Office of Weapons Complex Reconfiguration, DP 40

DISTRIBUTION OF THIS DOCUMENT IS UNLIMITED

DISCLAIMER

Portions of this document may be illegible in electronic image products. Images are produced from the best available original document.

APT ACCELERATOR TOPICAL REPORT

TABLE OF CONTENTS

Page

ACRONYM LIST XX

CONTRIBUTORS XXXII

APT OVERVIEW O-1

1.0 EXECUTIVE SUMMARY 1-1
1.1 PREFACE 1-1
1.2 DESIGN OVERVIEW 1-1
1.3 ISSUES AND CONCLUSIONS 1-5

2.0 ACCELERATOR SYSTEMS DESIGN OVERVIEW 2-1
2.1 ACCELERATOR ARCHITECTURE 2-1
2.1.1 Physics and Philosophy 2-1
2.1.2 APT Linac Design 2-2
2.1.3 Engineering Considerations 2-3
2.1.3.1 New Accelerating Structures 2-3
2.1.3.2 Special Engineering Features 2-4
2.2 PHYSICS STUDIES AND SIMULATIONS 2-6
2.3 LOW-ENERGY ACCELERATOR SYSTEMS 2-9
2.3.1 Injector 2-9
2.3.2 Radio-Frequency Quadrupole (RFQ) 2-10
2.3.3 Drift-Tube Linac (DTL) 2-12
2.3.4 The Funnel 2-14
2.4 HIGH-ENERGY ACCELERATOR SYSTEMS 2-17
2.4.1 Bridge-Coupled Drift-Tube Linac (BCDTL) 2-17
2.4.2 Coupled-Cavity Linac (CCL) 2-19
2.5 HIGH-ENERGY BEAM TRANSPORT SYSTEM 2-21
2.5.1 Overview 2-21
2.5.2 Transport 2-22
2.5.3 Beam Expander 2-22
2.5.4 Performance 2-23

2.6 RF POWER SYSTEMS 2-24
2.6.1 Overview 2-24
2.6.2 Klystrons 2-25
2.6.3 Klystron Power Supply 2-25
2.6.4 Availability and Reliability 2-25
2.6.5 RF Efficiency 2-26
2.6.6 Klystron Production 2-27
2.7 ACCELERATOR SUPPORT SYSTEMS 2-27
2.7.1 Controls 2-27
2.7.2 Beam Diagnostics 2-28
2.7.2.1 Characterization Measurements 2-28
2.7.2.2 Operational Measurements 2-29
2.7.3 Vacuum System 2-29
2.7.4 Water Cooling System 2-30
2.7.5 Cavity Temperature/Resonance Control System 2-30
2.7.6 Alignment System 2-31
2.7.7 Magnet Power Supplies 2-31
2.8 INTERFACES TO ACCELERATOR 2-31
2.9 OPERATION AND SAFETY SUMMARY 2-33
2.9.1 Linac Operation 2-33
2.9.1.1 Maintenance 2-33
2.9.1.2 Startup and Tuning 2-33
2.9.1.3 Fault Recovery 2-34
2.9.2 Safety and Protection 2-34
2.9.2.1 APT Hazards and Engineered Safety 2-34
2.9.2.2 Designs for Personnel Safety, and Machine and Environmental Protection 2-35

3.0 PHYSICS AND ENGINEERING DESIGN 3-1
3.1 KEY PARAMETER SELECTION 3-1
3.1.1 Beam Current and Energy 3-1
3.1.2 Accelerating Structure Frequencies 3-1
3.1.3 Accelerating Structure Gradient 3-2
3.2 FOCUSING SYSTEM TRADEOFFS 3-2
3.3 BEAM SIMULATIONS AND ERROR STUDIES 3-4
3.3.1 End-to-End Simulation of the APT Accelerator 3-4
3.3.2 CCL Failure Mode Studies 3-8
3.3.2.1 Introduction 3-8
3.3.2.2 Effects of Quadrupole-Doublet Failure 3-8

3.3.2.3 Effects of Single RF-Module Failure 3-10
3.3.2.4 A Possible RF-Module-Failure Recovery Scheme 3-13
3.3.3 Simulations with Reduced Beam Currents 3-15
3.3.4 Tolerance Estimates for CCL Errors 3-16
3.4 LOW BEAMLOSS REQUIREMENT 3-18
3.4.1 LAMPF Reference Analysis, Activation Estimates 3-19
3.4.2 Beamloss Control Measures in APT Linac Design 3-21
3.5 ELECTRICAL EFFICIENCY CONSIDERATIONS 3-23
3.6 ACCELERATING-STRUCTURE THERMAL constraints 3-23
3.6.1 Introduction 3-23
3.6.2 Maximum Power Densities 3-24
3.6.3 Cavity Frequency Response 3-24
3.6.3.1 Ambient Temperature 3-25
3.6.3.2 RF Heating 3-25
3.6.4 Material Stresses 3-25
3.6.5 Offset Tuning and Fabrication of Accelerating Structures 3-26
3.7 SPECIAL ENGINEERING DESIGN FEATURES 3-26
3.7.1 Linac Modularity 3-26
3.7.2 Designs for Radiation Environments 3-27
3.7.2.1 Radiation Hardened EMQs 3-27
3.7.2.2 Remote Handling Capability 3-28
3.7.3 Other Features 3-29
3.7.3.1 Prototype DTL EMQ 3-29
3.7.3.2 Metal Vacuum Seals 3-29
3.7.2.3 Copper-to-Copper RF Knife Edges 3-30
3.8 MECHANICAL SUPPORT FACILITIES 3-30
3.8.1 Alignment Laboratory 3-30
3.8.2 Vacuum Laboratory 3-30
3.8.3 RF Power Laboratory 3-31
3.8.4 Mechanical Maintenance and Remote Handling 3-31
3.8.5 Machine Shop 3-31
3.8.6 Diagnostics and Magnets Laboratory 3-32

4.0 LOW-ENERGY ACCELERATOR SYSTEMS 4-1
4.1 LOW-ENERGY SYSTEMS OVERVIEW 4-1
4.2 INJECTOR 4-3
4.2.1 Ion Source 4-3
4.2.2 Low-Energy Beam Transport (LEBT) 4-6

Development 4-9
DRUPOLE (RFQ) 4-10
..... 4-10
..... 4-12
ncept 4-14
..... 4-15
..... 4-16
..... 4-16
..... 4-17
)-DTL) 4-17
..... 4-17
..... 4-19
..... 4-19
..... 4-20
..... 4-20
..... 4-20
..... 4-21
..... 4-21
..... 4-21
ters 4-21
gn 4-22
gn 4-23
..... 4-23
..... 4-25
..... 4-27
Drift Tubes 4-28
..... 4-28
s 4-29
..... 4-29
..... 4-29
..... 4-30

5.2 LAYOUT AND DESCRIPTION 5-1
5.3 DESIGN ISSUES 5-3
5.4 RF BUNCHER CAVITIES 5-4
5.4.1 Physics Description 5-4
5.4.2 Mechanical Description 5-7
5.4.2.1 Fabrication 5-7
5.4.2.2 Endwalls 5-7
5.4.2.3 Cooling 5-8
5.4.2.4 Drift Tubes 5-9
5.4.2.5 Thermal Expansion, Support, and Alignment 5-9
5.4.2.6 Vacuum 5-10
5.5 RF DEFLECTOR CAVITY 5-10
5.5.1 Physics Description 5-10
5.5.2 Thermal Design and Analysis 5-12
5.6 ADDITIONAL COMPONENTS 5-12
5.6.1 Dipoles 5-12
5.6.2 Beamtube 5-13
5.6.3 Small-Bore EMQs 5-14
5.6.4 Large-Bore EMQ 5-15
5.7 MECHANICAL SUPPORT STRUCTURE 5-15
5.8 EXPERIMENTAL STATUS 5-17
5.8.1 Los Alamos Single-Beam Experiment 5-17
5.8.2 McDonnell Douglas Two-Beam Experiment 5-18
5.9 MATCHING SECTION (FUNNEL TO BCDTL) 5-19
5.10 DIAGNOSTICS 5-20
5.11 FUNNEL RF POWER SYSTEM 5-22

6.0 HIGH-ENERGY SYSTEMS 6-1
6.1 THE BRIDGE-COUPLED DRIFT TUBE LINAC (BCDTL) 6-1
6.1.1 Introduction 6-1
6.1.2 Description 6-1
6.1.2.1 BCDTL Parameters 6-3
6.1.2.2 Physics Considerations 6-4
6.1.2.3 Modular Breakdown 6-4
6.1.3 Bridge Couplers 6-5
6.1.3.1 Function and Tuning 6-6
6.1.3.2 Construction 6-6
6.1.4 Cavity Physics 6-7
6.1.4.1 Mode Comparison 6-7
6.1.4.2 Drift Tube Shape 6-9

6.1.4.3 SUPERFISH Results 6-10
6.1.4.4 Large-Bore Effects 6-11
6.1.4.5 Complete Tank Modeling 6-12
6.1.5 Simulations 6-12
6.1.6 RF Windows and Waveguides 6-13
6.1.7 Vacuum System 6-13
6.1.8 Intertank Gaps 6-14
6.1.9 Diagnostics 6-15
6.2 TRANSITION REGION (BCDTL—CCL) 6-16
6.3 THE COUPLED-CAVITY LINAC (CCL) 6-16
6.3.1 Introduction 6-16
6.3.1.1 Improvements Over Earlier Design 6-17
6.3.1.2 Switchover at 100 MeV 6-17
6.3.2 Description 6-17
6.3.2.1 CCL Parameters 6-18
6.3.2.2 Modular Breakdown 6-19
6.3.3 Tank Description 6-20
6.3.4 Cavity Physics 6-20
6.3.5 Simulation Results 6-23
6.3.6 The Aperture Ratio 6-23
6.3.7 Cooling and Tuning 6-24
6.3.7.1 Cooling 6-24
6.3.7.2 Tuning 6-27
6.3.8 RF Windows and Waveguides 6-27
6.3.9 Intertank Gaps 6-27
6.3.10 Diagnostics 6-28
6.4 THE 700-MHz RF SYSTEM 6-29
6.4.1 RF Generator 6-29
6.4.2 RF Distribution 6-30
6.4.3 RF Layout 6-30

7.0 THE HEBT AND BEAM EXPANDER 7-1
7.1 SYSTEM OVERVIEW AND PURPOSE 7-1
7.1.1 Overview 7-1
7.1.2 Beam Expander 7-2
7.1.3 Magnetic Elements 7-2
7.1.4 Targets and Beamstop 7-2
7.1.5 Engineering 7-2

7.1.6 Diagnostics 7-3
7.2 BEAM TRANSPORT LINE 7-3
7.2.1 Physics Design 7-3
7.2.2 Initial Periodic Lattice 7-4
7.2.3 Lattice Diagnostics 7-6
7.2.4 Achromatic Bend 7-7
7.2.5 Bend Diagnostics 7-10
7.2.6 Second Periodic Lattice 7-10
7.2.7 Four-Quadrupole Matching Section 7-11
7.2.8 Matching-Section Diagnostics 7-13
7.3 BEAM EXPANDER 7-13
7.3.1 Beam-Redistribution Method 7-13
7.3.2 Physics Description 7-14
7.3.3 Engineering Description 7-19
7.3.3.1 Tuneup Beamstop 7-20
7.3.3.2 Expander Magnets 7-21
7.3.3.3 Shield Dipole 7-21
7.3.4 Beam Expander Diagnostics 7-21
7.4 ENGINEERING CONSIDERATIONS 7-22
7.4.1 HEBT Alignment System 7-22
7.4.2 Interface Requirements 7-23
7.5 HEBT PERFORMANCE 7-24
7.5.1 Beam-Expander Simulation Tools 7-24
7.5.2 Beam-Expander Performance 7-25
7.5.3 End-to-End Simulation 7-27
7.5.4 Beam-Expander Tuning and Operation 7-28
7.5.5 Effects of Fault Conditions in the Accelerator 7-29
7.5.6 Counteracting Fault Conditions 7-30

8.0 RF POWER SYSTEM 8-1
8.1 OVERVIEW AND CHOICES 8-1
8.1.1 Baseline Choices 8-2
8.1.2 APT RF Compared to Other Systems 8-4
8.2 SYSTEM DESCRIPTIONS AND LAYOUTS 8-5
8.2.1. Overview of High Voltage to RF 8-5
8.2.2 The High-Voltage System 8-5
8.2.2.1 AC-to-DC Converters 8-6
8.2.2.2 High-Voltage Distribution 8-7

8.2.2.3 High-Voltage Protection 8-8
8.2.2.4 High-Voltage Diagnostics 8-9
8.2.3 The RF Module 8-10
8.2.3.1 Module Description 8-10
8.2.3.2 Module Efficiency 8-10
8.2.3.3 Module Support Utilities 8-12
8.2.3.4 Module Control 8-12
8.2.4 High-Voltage Generation and Distribution Layout 8-13
8.2.5 Klystron Gallery Layout 8-13
8.2.6 Waveguide Layout 8-16
8.2.7 Additional RF Generators 8-17
8.3 RF SYSTEM CONTROLS 8-19
8.3.1 Control Logic 8-19
8.3.2 VXIbus Format 8-19
8.3.3 Feedback/Feedforward 8-20
8.3.4 RF System Modeling 8-21
8.4 OPERATION / MAINTENANCE / MANUFACTURE OF RF SYSTEMS 8-23
8.4.1 Operation 8-23
8.4.1.1 Initial Conditioning Operations 8-23
8.4.1.2 RF System Startup 8-24
8.4.1.3 Normal Operation 8-25
8.4.1.4 Effects on the Utility Grid 8-25
8.4.1.5 Loss-of-Beam Incidents 8-26
8.4.2 Maintenance 8-29
8.4.3 Manufacturing Issues 8-31

9.0 SUPPORT SYSTEMS 9-1
9.1 ACCELERATOR CONTROL SYSTEM 9-1
9.1.1 Overview of Functional Requirements 9-1
9.1.1.1 Hardware Interfaces 9-1
9.1.1.2 Modes of Operation 9-2
9.1.2 Control System Architecture 9-3
9.1.2.1 Input-Output Controllers (IOCs) 9-3
9.1.2.2 Software Architecture 9-5
9.1.3 Performance 9-6
9.1.3.1 EPICS Performance 9-6
9.1.4 Availability 9-7
9.2 DIAGNOSTICS 9-7
9.2.1 Overview 9-7
9.2.1.1 Characterization Measurements 9-7
9.2.1.2 Operational Measurements 9-8

9.2.2 Measurement Systems Details 9-8
9.2.3 Transverse Measurements 9-10
9.2.3.1 Transverse Beam Centroids (Beam Position) 9-10
9.2.3.2 Transverse Beam Angular Trajectory 9-12
9.2.3.3 Transverse Beam Profiles and Divergence 9-12
9.2.3.4 Transverse Emittance 9-13
9.2.4 Beamloss, Halos, and Beam Current Measurements 9-14
9.2.4.1 Beamloss 9-14
9.2.4.2 Halo Monitor (Short-Term Interception) 9-14
9.2.4.3 Transient Beam Current 9-14
9.2.4.4 CW Average Beam Current 9-14
9.2.5 Energy, Phase, and Longitudinal Measurements 9-15
9.2.5.1 Energy 9-15
9.2.5.2 Output Phase 9-16
9.2.5.3 Phase Spread or Project Phase Distribution 9-16
9.2.5.4 Longitudinal Emittance and Energy Spread 9-16
9.3 MAJOR ACCELERATOR SUPPORT SYSTEMS 9-16
9.3.1 Magnet Power Supplies 9-16
9.3.2 Vacuum System 9-17
9.3.2.1 Ion Pumps (Large and Small) 9-18
9.3.2.2 Turbomolecular Pumps (Primary) 9-18
9.3.2.3 Auxiliary Roughdown Pumps (Cart Mounted) 9-18
9.3.3 Cooling System 9-19
9.3.4 Temperature/Resonance Control 9-20
9.3.4.2 CFC Temperature Control Sensitivity 9-22
9.3.5 Alignment 9-23
9.3.5.1 Alignment Monument System 9-23
9.3.5.2 Tunnel Coordinate System 9-24
9.3.5.3 Alignment Specifications 9-24
9.3.5.4 Alignment Procedure 9-25
9.4 INTERFACES 9-25
9.4.1 RF Power Interface 9-26
9.4.3 Vacuum Interface 9-27
9.4.4 Pneumatic Interface 9-27
9.4.5 Instrumentation Interface 9-27
9.4.6 Magnet Power Interface 9-28
9.4.7 Alignment/Installation Interfaces 9-28

10.0 LINAC OPERATION AND SAFETY 10-1
10.1 AVAILABILITY AND RELIABILITY ANALYSIS 10-1
10.1.1 Availability Framework 10-1
10.1.2 Availability And Reliability in the RF System 10-3

10.1.2.1 Introduction 10-3
10.1.2.2 Availability Analysis of Klystrons 10-6
10.1.2.3 High-Voltage System Components 10-10
10.1.2.4 Availability Calculations 10-10
10.1.3 Injector Reliability 10-11
10.1.4 Supporting Subsystems Reliability 10-12
10.1.5 Summary 10-13
10.2 MAINTENANCE 10-13
10.2.1 Introduction 10-13
10.2.2 Major Maintenance Items Identified 10-14
10.2.3 Maintenance of Major Components/Modules 10-14
10.2.4 Routine On-line Maintenance 10-17
10.2.5 Remote Maintenance 10-18
10.2.5.1 Special Hardware Features 10-19
10.2.5.2 Tunnel Size 10-19
10.2.5.3 Radio-Controlled Bridge Crane 10-19
10.2.5.4 Servo-Manipulator System 10-19
10.3 STARTUP AND FAULT RECOVERY 10-21
10.3.1 Accelerator Startup 10-21
10.3.1.1 Optics Tuning Beam 10-21
10.3.1.2 RF Tuning Beam 10-22
10.3.1.3 Initiating Full Operation 10-22
10.3.2 Fault Recovery 10-22
10.4 PERSONNEL SAFETY, MACHINE, and ENVIRONMENTAL PROTECTION 10-23
10.4.1 Introduction 10-23
10.4.1.1 Hazards of the APT Accelerator 10-23
10.4.1.2 Applicable DOE Regulations 10-24
10.4.1.3 Accelerator vs. Reactor Production of Tritium 10-25
10.4.2 Preliminary Hazard Analysis 10-26
10.4.2.1 DOE Hazard-Class-Determination Guidance 10-26
10.4.2.2 Categorization of Identified Hazards 10-27
10.4.2.3 Accelerator Safety Envelope 10-28
10.4.3 Designs for Personnel Safety and Machine and Environmental Protection 10-29
10.4.3.1 Design Philosophy 10-29
10.4.3.2 Passive Safety Designs 10-29
10.4.3.3 Active Safety Designs 10-30
10.4.3.4 Administrative Controls 10-31
10.4.4 Safety and Protection Systems Descriptions 10-32

10.4.4.4 Personnel Safety System 10-36
10.4.4.5 HEBT/Target Interface 10-37
10.4.4.6 Activated Air Handling System 10-39
10.4.4.7 Activated Water Handling 10-41
10.4.5 Failure Mode and Effects Analysis (FMEA) 10-42
10.4.5.1 Overview 10-42
10.4.5.2 Summary 10-42

LIST OF FIGURES

Page

Fig. 1. Schematic of the APT System (3/8-Goal) 0-2
Fig. 2. 3/16-Goal APT Accelerator with Upgrade to 3/8-Goal 0-3

Fig. 1-1. APT accelerator concept—200 mA, 1000-MeV cw RF linac. 1-3
Fig. 1-2. High-energy beam-transport (HEBT) layout. 1-3
Fig. 1-3. APT site sketch. 1-4

Fig. 2-1. A typical BCDTL module showing tanks and quadrupole doublets. 2-5
Fig. 2-2. Phase-space distributions at the output of the CCL. 2-7
Fig. 2-3. CCL output beam distributions from the end-to-end simulation. 2-8
Fig. 2-4. Transverse and longitudinal ratios of aperture-to-rms beamsize for the CCL. 2-8
Fig. 2-5. The ECR proton source. 2-9
Fig. 2-6. A mass-analyzed LEBT with the ECR source and solenoids. 2-10
Fig. 2-7. APT four-vane, four-segment RFQ. 2-11
Fig. 2-8. Plan view of the low-energy accelerator system, including the 20-MeV funnel. 2-13
Fig. 2-9. Interlacing bunches in the 20-MeV funnel. 2-14
Fig. 2-10. APT 20-MeV funnel layout. 2-15
Fig. 2-11. An APT BCDTL module, showing two tanks and two quadrupole doublets. 2-17
Fig. 2-12. One CCL module (1000 MeV) with focusing quadrupole doublet. 2-19
Fig. 2-13. Overview of the HEBT system. 2-21
Fig. 2-14. Nonlinear beam expander and target configuration. 2-23
Fig. 2-15. Primary components of an RF module. 2-24
Fig. 2-16. RF power conversion and distribution. 2-25

Fig. 3-1. Doublet vs. singlet transverse focusing lattice. 3-2
Fig. 3-2. Aperture/beamsize ratios vs. energy for singlet/doublet BCDTL focusing lattice options. 3-3
Fig. 3-3. Aperture/beamsize ratios vs. energy for singlet/doublet CCL focusing lattice options. 3-3
Fig. 3-4. RFQ transverse, phase, and energy envelopes vs. RFQ cell number. 3-6
Fig. 3-5. DTL phase-space distributions at the end of tank 3. 3-6
Fig. 3-6. Funnel output phase-space distributions at 20 MeV. 3-7
Fig. 3-7. Transverse and longitudinal emittances vs. BCDTL cell number. 3-7
Fig. 3-8. Transverse, phase, and energy envelopes vs. CCL cell number. 3-8
Fig. 3-9. CCL output transverse emittance vs. beam energy of a failed doublet. 3-9
Fig. 3-10. Beam-profile plots for a single doublet failure (tank 51 doublet, 200 MeV) in the CCL. 3-10
Fig. 3-11. Beam-profile plots for a single failed RF module (module 51). 3-12
Fig. 3-12. Beam-profile plots for a single failed RF module (module 87). 3-12
Fig. 3-13. Loss profile for a module 87 failure. 3-13
Fig. 3-14. Profile plots for a module 6 failure with tanks 2 through 4 compensating. 3-14
Fig. 3-15. Probability distributions for random quadrupole rotation errors. 3-17
Fig. 3-16. Neutron yield vs. proton energy for copper/iron. 3-19
Fig. 3-17. Measured and simulated beamloss in the LAMPF CCL. 3-20
Fig. 3-18. LAMPF CCL activation measurements (12/15/92) beyond transition region. 3-21
Fig. 3-19. LAMPF beamloss vs. time into beam pulse. 3-22
Fig. 3-20. A typical BCDTL assembly unit or module. 3-27
Fig. 3-21. Proposed radiation-hardening fabrication procedure for EMQs. 3-28
Fig. 3-22. Prototype DTL EMQ. 3-29
Fig. 3-23. Quick flange. 3-29
Fig. 3-24. CCL vacuum and RF seal. 3-30

Fig. 4-1. Plan view of APT low-energy accelerator systems. 4-2
Fig. 4-2. Elevation view of the APT low-energy accelerator systems. 4-2
Fig. 4-3. 75-kV extraction system for the APT ion source. 4-5
Fig. 4-4. SNOW calculation for the 75-kV extraction system. 4-6

Fig. 4-5. Layout of the APT injector with a direct-injection LEBT. 4-7
Fig. 4-6. Beam envelope profiles for APT direct-injection LEBT. 4-7
Fig. 4-7. α–β tuning diagram for injector at RFQ match point. 4-8
Fig. 4-8. Beam profiles showing the effect of beam neutralization. 4-8
Fig. 4-9. Various parameters defining the RFQ design vs. position. 4-11
Fig. 4-10. RFQ thermal heat loads (W/cm^2) from SUPERFISH. 4-13
Fig. 4-11. APT RFQ cooling details. 4-14
Fig. 4-12. Electroformed RFQ cavity cross-section. 4-14
Fig. 4-13. RFQ support structure. 4-16
Fig. 4-14. Diagram of the RFQ–DTL matching section. 4-18
Fig. 4-15. RFQ–DTL matching section layout. 4-19
Fig. 4-16. Drift-tube nose shape and cell geometry. 4-23
Fig. 4-17. Shunt Impedance for the APT DTL as a function of b. 4-23
Fig. 4-18. DTL typical cross-section. 4-24
Fig. 4-19. DTL tank #3, drive loop coupled. 4-25
Fig. 4-20. APT 350-MHz DTL tank #3 exploded view. 4-26
Fig. 4-21. DTL end wall. 4-27
Fig. 4-22. DTL tank #3, waveguide/iris coupled. 4-30
Fig. 4-23. Overview of high-power 350-MHz RF system for low-energy linacs. 4-31
Fig. 4-24. LLRF controls for the 2-klystron RF system for the RFQ. 4-32
Fig. 4-25. RFQ & DTL output efficiency using GTA klystron data (normalized to CERN tube efficiency). 4-33
Fig. 4-26. RF system layout for 350-MHz systems. 4-34

Fig. 5-1. Interlacing of bunches in the funnel. 5-1
Fig. 5-2. 20-MeV funnel layout. 5-2
Fig. 5-3. Funnel buncher cavities R3 and R2. 5-4
Fig. 5-4. Funnel 2-hole buncher cavity R1. 5-5
Fig. 5-5. SUPERFISH output for untapered, two-gap, 700-MHz buncher (R3). 5-5
Fig. 5-6. SUPERFISH output for tapered, two-gap, 700-MHz buncher (R2). 5-6
Fig. 5-7. MAFIA 3D plot of one-fourth of (R1) two-hole buncher. 5-7
Fig. 5-8. Mounting and alignment scheme for buncher cavities and quadrupoles. 5-9
Fig. 5-9. 3D exploded view of the 350-MHz RF deflector cavity. 5-11
Fig. 5-10. Beam-bending dipoles for the APT funnel. 5-13

Fig. 5-11. Mechanical support structure for the APT funnel. 5-16
Fig. 5-12. Schematic of the Los Alamos single-beam funnel experiment. 5-17
Fig. 5-13. Schematic of the McDonnell Douglas two-beam funnel experiment. 5-18
Fig. 5-14. APT funnel-to-BCDTL matching section (or MEBT). 5-19
Fig. 5-15. Layout of the funnel section with location of the diagnostic elements. 5-21

Fig. 6-1. A BCDTL module, showing three tanks, two bridge couplers, and three quadrupole doublets. 6-2
Fig. 6-2. The first BCDTL tank at 20 MeV, showing part of a bridge coupler. 6-2
Fig. 6-3. BCDTL partitioned bridge coupler with five partitions. 6-5
Fig. 6-4. Transit-time factor vs. bore for 0- and π-mode structures for 100-MeV protons. 6-7
Fig. 6-5. Power density vs. bore radius for 0- and π-mode structures for 100-MeV protons (the accelerating gradient E_0T is 1.5 MV/m for all cases). 6-8
Fig. 6-6. Effective shunt impedance vs. bore for 0- and π-mode structures of Figs. 6-3 and 6-4 (the accelerating gradient E_0T is 1.5 MV/m). 6-8
Fig. 6-7. Cross section of a BCDTL 100-MeV half cell. 6-9
Fig. 6-8. Detail near the drift tube nose showing the mesh used by SUPERFISH (all cells have an inner-nose radius, r_n, of 0.1 cm and an outer-nose radius, r_{no}, of 0.3 cm 6-9
Fig. 6-9. Parameters for the low-energy section of the BCDTL (20–54 MeV), where E_0T is 1.7 MV/m and bore radius is 2.00 cm. 6-10
Fig. 6-10. Parameters for the high-energy section of the BCDTL (54–100 MeV), where E_0T is 1.5 MV/m and bore radius is 2.25 cm. 6-11
Fig. 6-11. SUPERFISH-calculated fields for an end cell at 20 MeV (the bore tube extends 4.0 cm to the left of the cell boundary). 6-12
Fig. 6-12. Intertank hardware 6-14
Fig. 6-13. Layout of the transition region between the BCDTL and CCL. 6-16
Fig. 6-14. First CCL assembly unit at 100 MeV. 6-19
Fig. 6-15. Last CCL assembly unit at 1000 MeV. 6-19
Fig. 6-16. Generic coupled-cavity geometry. 6-21
Fig. 6-17. CCL nose shape and cell geometry for a cell near 1000 MeV. 6-22
Fig. 6-18. Shunt impedance vs. β (100-1000 MeV), as determined by SUPERFISH (the calculated values have been reduced by 15% to include a correction for cavity coupling slots). 6-22
Fig. 6-19. CCL septum cooling scheme. 6-24
Fig. 6-20. Flow schematic for the 14 cells of a CCL tank. 6-25

Fig. 6-21. CCL vacuum and RF seal. 6-26
Fig. 6-22. BCDTL output efficiency using GTA klystron data (normalized to CERN tube efficiency). 6-29
Fig. 6-23. APT CCL RF power vs. module number and output energy. 6-30
Fig. 6-24. CCL output efficiency using GTA klystron data (normalized to CERN tube efficiency). 6-31
Fig. 6-25. RF system layout for 700-MHz systems. 6-31

Fig. 7-1. The HEBT system. 7-1
Fig. 7-2. RMS beam envelopes between the CCL and the beam expander. 7-4
Fig. 7-3. Initial periodic-lattice section. 7-4
Fig. 7-4. HEBT doublet mechanical support. 7-6
Fig. 7-5. The five-cell, 25°, achromatic bend. 7-7
Fig. 7-6. HEBT switching magnet area. 7-9
Fig. 7-7. Low-momentum beamstop design for switching-magnet. 7-11
Fig. 7-8. Four-quadrupole matching section. 7-12
Fig. 7-9. Beam-expander layout. 7-15
Fig. 7-10. Shielding arrangement to protect expander quads at 7.5° bend. 7-18
Fig. 7-11. Helicoflex vacuum seal used in the HEBT/target interface. 7-19
Fig. 7-12. The HEBT/target interface. 7-19
Fig. 7-13. Two-piece Helicoflex flange connector at the HEBT/target interface. 7-20
Fig. 7-14. HEBT monument alignment system. 7-22
Fig. 7-15. HEBT quadrupole translator. 7-23
Fig. 7-16. Nominal beam distribution at target for Gaussian input beam. 7-25
Fig. 7-17. Beam distribution with 0.25-rms beam jitter. 7-26
Fig. 7-18. Beam at target for code-generated input (left) and actual simulation (right). 7-27
Fig. 7-19. Beam distribution at target for a −10-MeV energy shift. 7-29
Fig. 7-20. Beam distribution at target for a +10-MeV energy shift. 7-30

Fig. 8-1. RF-system power requirements for APT. 8-1
Fig. 8-2. Primary components of an RF module. 8-2
Fig. 8-3. High-voltage-system block diagram. 8-6
Fig. 8-4. One line diagram of ac-to-dc converter. 8-7

Fig. 8-5. Five-inch aluminum tube bus. 8-8
Fig. 8-6. Layout of a typical protection unit. 8-9
Fig. 8-7. CCL output efficiency using GTA klystron data normalized to CERN tube efficiency. 8-11
Fig. 8-8. Relationship of amplitude and phase to I&Q. 8-12
Fig. 8-9. Site layout showing switchyards. 8-14
Fig. 8-10. Converter switchyard. 8-14
Fig. 8-11. Front-end klystron gallery. 8-15
Fig. 8-12. 350-MHz klystron station. 8-15
Fig. 8-13. 700-MHz klystron station. 8-16
Fig. 8-14. BCDTL & CCL klystron gallery and tunnel. 8-17
Fig. 8-15. APT multi-klystron unit with spare. 8-18
Fig. 8-16. APT multi-klystron unit with spare module in use. 8-18
Fig. 8-17. Sample control system logic for startup and shutdown. 8-19
Fig. 8-18. Typical LLRF VXIbus module. 8-20
Fig. 8-19. Block diagram of LLRF control system (with power amplifier & cavity). 8-21
Fig. 8-20. Feedback control in APT 8-22
Fig. 8-21. Response of feedback system to beam rise-time. 8-22

Fig. 9-1. Low-energy structure probe design combined with profile measurements. 9-11
Fig. 9-2. Drift distances vs. beam energy for 0.005% accuracy and 0.1% resolution. 9-15
Fig. 9-3. Primary-cooling-loop temperature/resonance control system. 9-21
Fig. 9-4. Alignment monument system. 9-23
Fig. 9-5. Principal APT linac interfaces. 9-26

Fig. 10-1. Operating time, downtime, and availability for KEK TRISTAN injector. 10-3
Fig. 10-2. Fault rate/day/klystron for TRISTAN injector klystrons. 10-4
Fig. 10-3. H^+ beam availability vs. run cycle number for LAMPF. 10-4
Fig. 10-4. Hazard rates for LAMPF and PEP klystrons vs. klystron age. 10-7
Fig. 10-5. The probability of q failures during a 168-hour operating period for 376 klystrons with 20,000-hour MTBF. 10-9
Fig. 10-6. APT drift-tube linac with drift-tube girder removed. 10-15
Fig. 10-7. BCDTL assembly unit (module) with four tanks. 10-16

Fig. 10-8. BCDTL partitioned bridge coupler with common end cells. 10-16
Fig. 10-9. Typical intertank hardware (BCDTL or CCL). 10-17
Fig. 10-10. Tunnel equipped for remote handling. 10-20
Fig. 10-11. MANTIS—CERN's remote handling system. 10-20
Fig. 10-12. Tuning beams required for APT accelerator startup. 10-21
Fig. 10-13. Risk matrix from DOE 5480.25 guidance. 10-28
Fig. 10-14. Geometry for APT linac shielding calculations. 10-32
Fig. 10-15. Annual-dose vs. shield-thickness for beamloss (maximum normal continuous operation). 10-33
Fig. 10-16. Dose vs. shield-thickness for full beamspill (along 100-meter path for 1 hour, 200 mA at 1 GeV). 10-33
Fig. 10-17. Daisy-chain-type topology for the fast-protect system. 10-34

LIST OF TABLES

Page

Table 1-1. APT Reference Accelerator Parameters 1-5

Table 2-1. APT End-to-End Simulation Summary 2-7
Table 2-2. APT RFQ Parameters 2-12
Table 2-3. APT DTL General Parameters 2-14
Table 2-4. APT Funnel Parameters 2-16
Table 2-5. APT BCDTL Parameters 2-18
Table 2-6. APT CCL Parameters 2-20
Table 2-7. RF Component Reliability Estimates 2-26
Table 2-8. RF System Efficiency 2-26

Table 3-1. Emittance Results from APT BCDTL Doublet/Singlet Simulations 3-4
Table 3-2. APT Linac End-to-End Simulation Summary 3-5
Table 3-3. Twiss Parameters at 1 GeV for Single Quadrupole-Doublet Failures in CCL 3-9
Table 3-4. Results of Single RF-Module Failures in the CCL (Computer Simulations) 3-11

Table 3-5. Power Requirements for the Compensating Tanks 3-15
Table 3-6. Output Emittances for Matched 110-, 55- and 0-mA Beams into the RFQ 3-15
Table 3-7. CCL Output at 1000 MeV for Nominal and Reduced Beam Currents 3-16
Table 3-8. Levels of Radiation and Type of Maintenance 3-18

Table 4-1. Comparison of Candidate Ion Sources for cw Injectors 4-4
Table 4-2. Definition of RFQ Parameters (used in Fig. 4-9) 4-11
Table 4-3. APT RFQ Error Study Results (Transmission >90%) 4-11
Table 4-4. Comparison of cw RFQs 4-12
Table 4-5. RFQ to DTL Matching Section Component Specifications 4-18
Table 4-6. DTL General Parameters (Each Leg) 4-22

Table 5-1. Funnel General Parameters 5-2
Table 5-2. Funnel Beam Parameters 5-3
Table 5-3. APT Funnel Cavity Parameters 5-8
Table 5-4. Deflector Cavity Power Requirements 5-12
Table 5-5. APT Funnel Dipole Specifications 5-13
Table 5-6. Funnel Dipole Specifications 5-14
Table 5-7. APT Funnel and MEBT Diagnostics 5-21

Table 6-1. APT BCDTL Parameters 6-3
Table 6-2. BCDTL Modular Breakdown 6-4
Table 6-3. APT CCL Parameters 6-18
Table 6-4. CCL Modular Breakdown 6-20
Table 6-5. Fixed Coupled-Cavity Cell Shape Geometry Parameters for the CCL 6-21

Table 7-1. Nominal HEBT Input Beam 7-4
Table 7-2. Elements of Initial periodic-lattice section 7-5
Table 7-3. Elements of the Achromatic-Bend Cell 7-8
Table 7-4. Dipole Specifications for HEBT Achromatic Bends 7-9
Table 7-5. Elements of Four-Quadrupole Matching Section in a Target Line 7-12
Table 7-6. Beam-Expander Components 7-15

Table 7-7. Nominal rms Input-Beam Parameters of Beam Expander 7-16
Table 7-8. Beam Half-Sizes x and y and "Radii" r in the Beam Expander 7-16
Table 7-9. Beam Half-Sizes x and y in the 20-Meter Drift to the Target 7-17
Table 7-10. HEBT Alignment Requirements 7-22
Table 7-11. Hot-Spot Intensities 7-28
Table 7-12. Beam Half Sizes x and y at Target after Quadrupole-Doublet Failure 7-31
Table 7-13. Beam Half Sizes x and y at Target as Function of Beam Current 7-31

Table 8-1. APT Operating Efficiency by Structure and Overall Baseline Choices 8-2
Table 8-2. RF Generator Choices and Existing cw Designs 8-3
Table 8-3. Results of Detuning and Coupling for the APT 1-GeV CCL Cavity 8-4
Table 8-4. Comparison of APT RF Parameters with Other Accelerators 8-5
Table 8-5. Klystron System Diagnostics 8-30

Table 9-1. Allocation of IOCs to Accelerator Functions 9-4
Table 9-2. APT Diagnostic Hardware Requirements 9-9
Table 9-3. Diagnostic Requirements for Beam Parameter/Measurement Type 9-10
Table 9-4. Video Profile Signal-to-Noise Estimates Based on GTA, FMIT, and ATS* 9-12
Table 9-5. APT Accelerator Doublet Alignment Requirements 9-25

Table 10-1. Failure Distribution for LAMPF for 5.7 years (2/79 to 10/84) 10-5
Table 10-2. Mean Time between Failures for Several Accelerator Klystrons 10-6
Table 10-3. Removal Causes for the LAMPF Klystrons and Modulators 10-8
Table 10-4. Failure Mechanisms for 110 SLAC Klystrons 10-8
Table 10-5. Unanticipated Outage Time Budget 10-11
Table 10-6. Preliminary Hazard Analysis for APT 10-28
Table 10-7. Isotopic Composition of APT Activated Air 10-40
Table 10-8. APT Activated Air Release Estimates 10-41
Table 10-9. Summary of APT Accelerator Failure Modes and Effects Analysis 10-43
Table 10-10. Description of Hazard Categories 10-43
Table 10-11. Description of Types of Events 10-43

ACRONYM LIST

APT	accelerator production of tritium
ASTM	American Society for Testing Materials
ATS	accelerator test stand
ATW	accelerator transmutation of waste
BCDTL	bridge-coupled drift tube linac
BEAR	beam experiment aboard a rocket
BL0	butt-line zero
BLM	beamloss monitor
BNL	Brookhaven National Laboratory (NY)
BOP	balance of plant
BPM	beam-position monitor
BPSA	beam power spectrum analyzer
CBP	capacitive beam probe
CCL	coupled-cavity linac
CCLFISH	computer code for CCL design
CCTV	closed circuit television
CERN	European Organization for Nuclear Research (Switzerland)
CFC	constant-flow cooling
CFR	code of federal regulations
CRITS	Chalk River injector test stand
CRL	Chalk River Laboratory (Canada)
CS	Courant-Snyder
CSF	Thompson CSF (a French company)
Culham	Culham Laboratory (England)
cw	continuous wave
CWBCM	continuous wave current monitor
CWDD	continuous-wave deuterium demonstrator
DBMS	database management system
dc	direct current
DCCT	dc current transducer
DF	duty factor

DOE	Department of Energy
DTL	drift tube linac
DTLFISH	a computer code
EB	electron beam weld
ECR	electron cyclotron resonance
EIA	an electrical standard
EIS	environmental impact statement
EM	electromagnet
EMI	electromagnetic interference
EMQ	electromagnet quadrupole
EPICS	experimental physics and industrial control system
ERAB	Energy Research Advisory Board
ES&H	environmental, safety, and health
FC	Faraday cup
FD	focus-defocus (focusing scheme)
FDDI	fiber-distributed data interface
FDO	focus-defocus-drift (focusing scheme)
FEA	finite element analysis
FMEA	failure mode and effects analysis
FMIT	fusion materials irradiation test
FODO	focus-drift, defocus-drift (focusing scheme)
FOFODODO	focus-drift, focus-drift, defocus-drift, defocus-drift (focusing scheme)
GTA	ground test accelerator
^{3}He	helium-3
HEBT	high-energy beam transport
HEPA	high-efficiency particulate adsorption
HEX	heat exchanger
HV	high voltage
HVAC	heating, ventilating, and air conditioning
HVPS	high-voltage power supply
I/O	input/output
I&C	instrumentation and controls
I&Q	in-phase and quadrature
IEEE	Institute of Electrical and Electronics Engineers

IMS	intermediate matching section
IOC	input/output controllers
IOT	inductive output tube
ISO	International Standards Organization
ITEP	Institute for Theoretical and Experimental Physics (Moscow)
KEK	National Laboratory for High-Energy Physics (Japan)
LAMPF	Los Alamos Meson Physics Facility
LAN	local area network
LANL	Los Alamos National Laboratory
LANSCE	Los Alamos Neutron Scattering Center
LEBT	low-energy beam transport
LEP	Large Electron Positron (collider at CERN)
linac	linear accelerator
LINDA	accelerator beam diagnostics technique for measuring beam emittance
LLNL	Lawrence Livermore National Laboratory (CA)
LLRF	low-level radio frequency
MANTIS	a remote handling machine developed at CERN
MBP	microstrip beam probe
MEBT	medium-energy beam transport
MIG	metal inert gas
MIPS	million instructions per second
MRTI	Moscow RadioTechnical Institute
MTBF	meantime between failures
MTTR	mean time to repair
NBS	National Bureau of Standards (now called NIST)
NFS	network file system
NPB	neutral particle beam
OFE	oxygen-free electronic grade
PID	proportional, integral, and differential (control)
PARMILA	an accelerator design code
PBCM	pulsed beam current monitor
PEIS	programmatic environmental impact statement
PMQ	permanent magnet quadrupole
PSM	phase spread monitor

PSR	proton storage ring
PSS	personal safety system
RF	radio frequency
RFQ	radio frequency quadrupole
RGDTL	ramped gradient drift tube linac
rms	root mean square
RPT	reactor production of tritium
SCPR	short-circuit power ratio
SDI	strategic defense initiative
SFAS	safety features actuation system
SILC	spallation-induced lithium conversion
SLAC	Stanford Linear Accelerator (CA)
SLC	Stanford Linear Collider (CA)
SNL	Sandia National Laboratories (NM)
SNOW	a computer code for injector design
SOP	standard operating procedure
SS	stainless steel
SSC	Superconducting Super Collider (TX)
SSC	systems, structures, and components
SUPERFISH	a computer code
SWM	slow wire monitor
T/B	target/blanket
TE	tritium extraction
TE_{010}	transverse electric (waveguide mode designation)
TIG	tungsten inert gas
TM	turbomolecular
TM_{010}	transverse magnetic (waveguide mode designation)
TOF	time of flight
UPS	uninterrupted power source
Vac	volts alternating current
VCR	a high-vacuum fitting
Vdc	volts direct current
VFC	variable-flow cooling
VHN	Vickers hardness number

VPM	video profile monitor
VSWR	voltage-standing wave ratio
WR	waveguide-sizing unit
ZT^2	formula for cavity shunt impedance

CONTRIBUTORS

Los Alamos National Laboratory

George Lawrence, Principle Investigator
Dan Rusthoi, Report Compiler and Editor

Jim Billen	Bob Jameson	Robert Ryne
Barbara Blind	Andy Kozubal	Darryl Sandoval
Gren Boicourt	Robert Kraus	Dale Schrage
Stuart Bowling	George Lawrence	Stan Schriber
Jean Browman	Don Liska	Robert Shafer
Nathan Bultman	Mike Lynch	Joe Sherman
Larry Carlisle	Greg McCauley	Ralph Stevens
Danny Doss	Subrata Nath	Paul Tallerico
Bob Garnett	Fillipo Neri	Tom Wangler
Doug Gilpatrick	George Neuschaefer	Dick Woods
John Graham	Amy Regan	Lloyd Young
Bob Hardekopf	Dan Rusthoi	Chris Ziomek

Grumman Aerospace (Linac Engineering)

Steve Black	Tom Ilg	John Rathke
John Erickson	Mike Kornely	Peter Smith
Steve Ellis	John Moeller	

Maxwell/Litton/ABB (Power Systems Design)

Ed Chu (Maxwell)	Donald Laycock (Litton)	Willie Wong (ABB)
	George Schofield (Maxwell)	

General Atomics (Beam Transport Engineering)

Ross Harder	Mike Heiberger	John Rawls

APT OVERVIEW

The Accelerator Production of Tritium (APT) project, sponsored by Department of Energy Defense Programs (DOE/DP), involves the preconceptual design of an accelerator system to produce tritium for the nation's stockpile of nuclear weapons. Tritium is an isotope of hydrogen used in nuclear weapons, and must be replenished because of radioactive decay (its half-life is approximately 12 years). Because the annual production requirement for tritium has greatly decreased since the end of the Cold War, an alternative approach to reactors for tritium production, based on a linear accelerator, is now being seriously considered.

The annual tritium requirement at the time this study was undertaken (1992-1993) was 3/8 that of the 1988 goal, usually stated as 3/8-Goal. Continued reduction in the number of weapons in the stockpile has led to a revised (lower) production requirement today (March, 1995). The production requirement needed to maintain the reduced stockpile, as stated in the recent Nuclear Posture Review (summer 1994) is approximately 3/16-Goal, half the previous level. The Nuclear Posture Review also requires that the production plant be designed to accomodate a production increase (surge) to 3/8-Goal capability within five years, to allow recovery from a possible extended outage of the tritium plant.

A multi-laboratory team (Los Alamos, Sandia, and Brookhaven National Laboratories), collaborating with several industrial partners (Bechtel, Babcock & Wilcox, Grumman, General Atomics, Maxwell Balboa, and Merrick), has developed a preconceptual APT design for the 3/8-Goal, operating at 75% capacity. The team has presented APT as a promising alternative to the reactor concepts proposed for Complex-21. Given the requirements of a reduced weapons stockpile, APT offers both significant safety, environmental, and production-flexibility advantages in comparison with reactor systems, and the prospect of successful development in time to meet the US defense requirements of the 21st Century.

APT was reviewed by the DOE's Energy Research Advisory Board (ERAB) in late 1989 and then by the JASONs in early 1992. Both reviews were positive about the technology, but pointed out the need for a research and development program. As a result of these reviews, DOE decided to sponsor the preconceptual 3/8-Goal APT design activity discussed in this report.

The APT tritium-supply option consists of a powerful linear accelerator that bombards a spallation target with high-energy protons. This Topical Report describes in detail the preconceptual design of the proton accelerator and beam transport system needed for a 3/8-Goal production facility. The final beam energy in the accelerator is 1000 MeV and the proton current is 200 mA, which provides the 200 MW of beam power needed for 3/8-Goal tritium production level. Beams from two 100-mA low-energy linacs are combined to produce a 200 mA current which is accelerated to the final energy in the high-energy linac. A beam transport system conveys the 1000-MeV beam to one of two identical target/blanket systems where the tritium is produced. A schematic diagram of the 3/8-Goal APT system is shown in Fig.1.

Neutrons are produced in the spallation target and are absorbed in a blanket material to produce tritium. Two spallation targets are currently under investigation: (1) a tungsten neutron-source target, and (2) a lead neutron-source target. The tungsten target is the primary system and the lead target is a backup system. In the tungsten target concept, the neutrons are

captured by gaseous ^{3}He, an isotope of helium, which is continuously circulated through the tungsten target region and the heavy-water blanket region to produce tritium via neutron capture. Because tritium beta decays to ^{3}He, a significant inventory of ^{3}He is readily available for conversion. In the lead target concept, the lead is surrounded with a lithium-aluminum blanket and the tritium is produced by neutron capture in the lithium isotope, ^{6}Li. This target is referred to as the Spallation-Induced Lithium-Conversion (SILC) target.

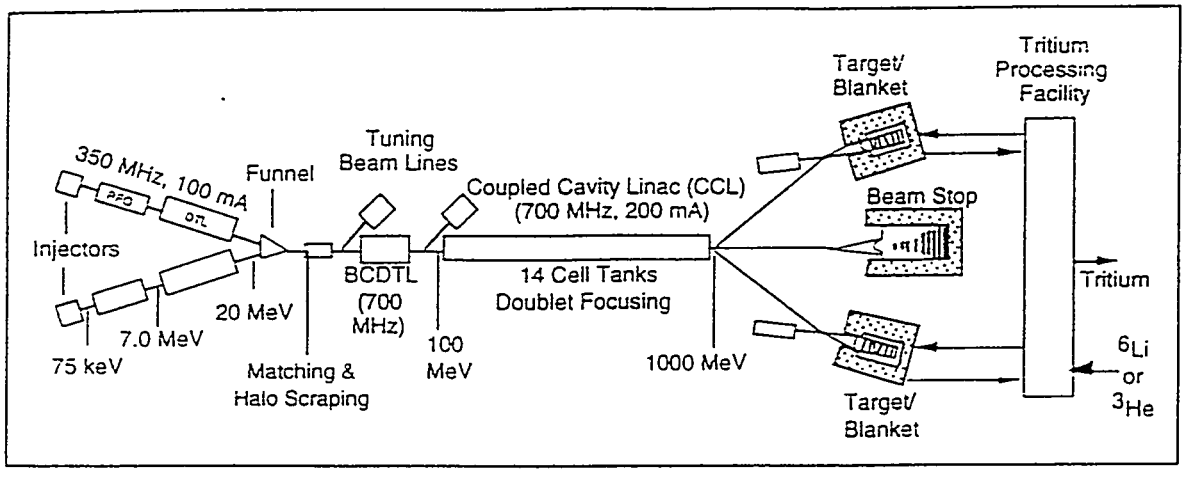


Fig. 1. Schematic of the APT System (3/8-Goal)

For the ^{3}He target, the tritium inventory is much smaller than in the SILC target because tritium is continuously extracted during operation. Also, the continuous on-line extraction process eliminates the need for fabrication and reprocessing of lithium-aluminum blanket rods; therefore, the overall waste stream and attendant environmental impact is minimized. In both target concepts, tritium is produced without the use of fissionable materials; therefore, no high-level spent fuel waste is produced, and the overall safety impacts are significantly reduced compared with reactor systems.

A significant concern for APT is the electricity requirement to power the accelerator—approximately 550 MWe for a 3/8-Goal design. However, this amount of power is available from the grid now and also in the foreseeable future at several of the potential tritium production sites. In more advanced accelerator designs, the potential exists to reduce this power requirement by 20% to 40%. Lower tritium production requirements associated with the 3/16-Goal design will also reduce the power demand significantly.

Given the new 3/16-Goal tritium requirement expressed in the Nuclear Posture Review, a revised accelerator concept has been derived from the 3/8-Goal system point design. In this 3/16-Goal (nominal) design, the beam current is reduced to 100 mA, while the beam energy remains at 1000 MeV, providing a 100-MW beam. Only a single low-energy linac is needed for this system (no beam combining). In the 3/16-Goal design, accelerating-structure frequencies are the same as in the 3/8-Goal system, and the beam-focusing magnet lattice is unchanged. Beam dynamics is identical to that of the 3/8-Goal linac because the number of

protons per bunch remains the same. RF power and ac power requirements are significantly smaller, however, because of the factor-of-two reduction in beam power. The high-energy beam transport is identical to that in the 3/8-Goal system design. The accelerator tunnel and above-ground support buildings are constructed at the full size and scale needed for a 3/8-Goal system, as are the buildings housing the target/blanket assemblies. The target/blanket design for the 3/16-Goal system is reduced in cross section from that of a 3/8-Goal target/blanket design, maintaining approximately the same beam-power density.

To provide the surge production capability implied in the Nuclear Posture Review, the 3/16-Goal linac could be upgraded to 3/8-Goal production by increasing the beam current to 200 mA. This would be accomplished by (1) adding a second 100-mA low-energy linac, (2) implementing the beam combiner, (3) adding RF power stations in the high-energy linac to supply the increased beam power, (4) replacing the target/blanket assemblies with larger-cross-section systems, and (5) adding capacity in balance-of-plant systems (power distribution, cooling, etc.). The upgrade could be accomplished within two years.

Figure 2 describes the 3/16-Goal accelerator concept, and indicates how it could be upgraded to provide twice the tritium production level (3/8-Goal), if necessary, to make up for a production hiatus of up to five years. The 3/16-Goal accelerator components are shown shaded; components that would be added to provide increased capacity are shown without shading. Beam power levels and ac power requirements of the plant are indicated in the figure for the two production levels.

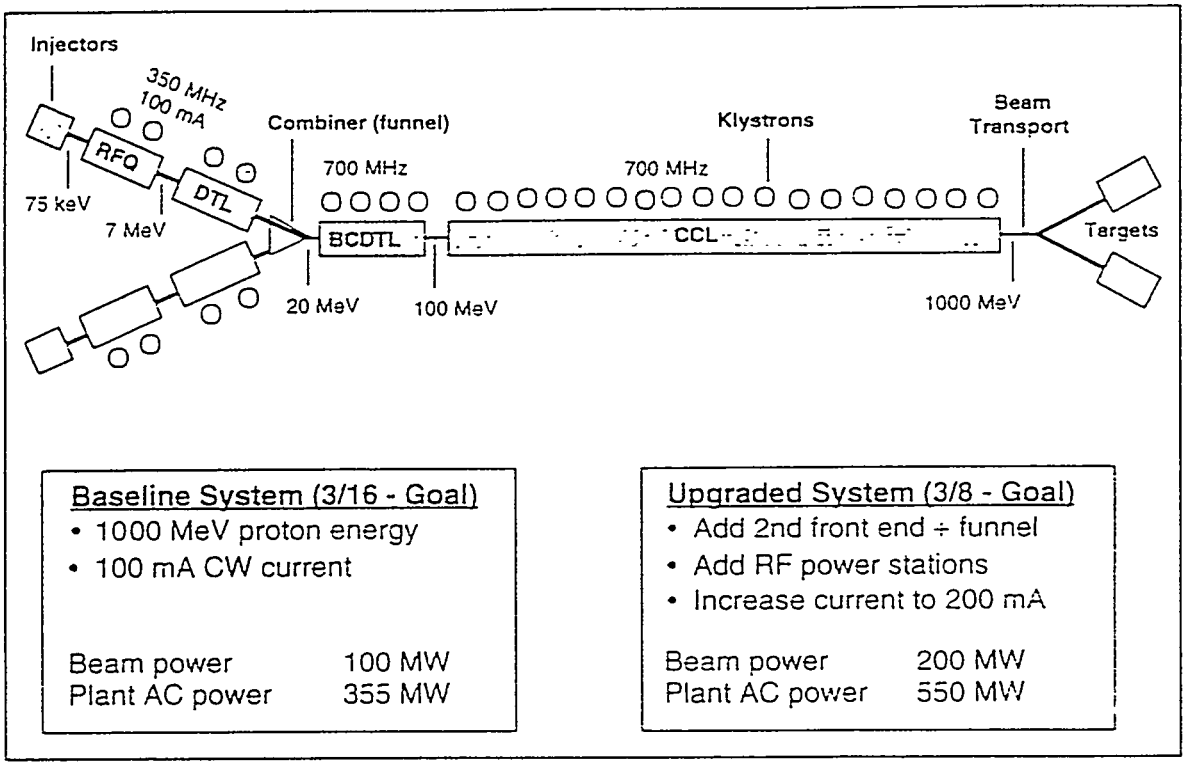


Fig. 2. 3/16-Goal APT Accelerator with Upgrade to 3/8-Goal

Scaling of a 3/16-Goal accelerator concept from the 3/8-Goal APT point design discussed in this report provides a reasonable starting point for a reduced capacity system, bounding values for ES&H impacts, and a basis for construction and operating cost estimates. However, such an approach may not generate an optimum design in terms of costs, performance, technical risk, and other factors. Trade studies are planned during the APT conceptual design phase to determine the optimum accelerator configuration to satisfy the Nuclear Posture Review requirement.

The LANL-BNL-SNL team and industrial partners believe that no technical "show stoppers" are associated with the APT technology. This position has been confirmed by several reviews that have taken place since the conclusion of the 1992-1993 3/8-Goal design study, including a very thorough and detailed assessment by a "red team" from Lawrence Livermore National Laboratory and a second review by the JASONs. The team also strongly believes that the system can be designed and constructed on a schedule to meet the future defense needs. In summary, our position is that APT is a strong contender among the competing options available to decision makers responsible for defining our nation's defense posture in the next century.

EXECUTIVE SUMMARY
CHAPTER 1

Page

1.1 PREFACE 1
1.2 DESIGN OVERVIEW 1
1.3 ISSUES AND CONCLUSIONS 5

LIST OF FIGURES

Page

Fig. 1-1. APT accelerator concept—200 mA, 1000-MeV cw RF linac. 3
Fig. 1-2. High-energy beam-transport (HEBT) layout. 3
Fig. 1-3. APT site sketch. 4

LIST OF TABLES

Page

Table 1-1. APT Reference Accelerator Parameters 5

1.0 EXECUTIVE SUMMARY

1.1 PREFACE

Los Alamos National Laboratory has completed a *preconceptual* point design of a high-power proton linac (linear accelerator) for Accelerator Production of Tritium (APT). The major criteria driving this design are *high intensity coupled with low beamloss, high electrical efficiency, and high availability*. Key parameters underlying the point design were derived from a combination of factors, including (1) consideration of target beam-energy requirements, (2) a simple cost model of the accelerator that balanced power-related and length-related elements, and (3) a limited set of comparative studies that assessed accelerating-structure-frequency alternatives and alternative focusing configurations. The APT accelerator concept is based on a conventional technology approach, within a conservative overall design framework. Performance parameters are derived from the existing technology base for room-temperature (copper) radio-frequency (RF) linacs and their components, except in terms of demonstrated high-power operation at 100% duty factor. The design of the low-energy part of the accelerator is based on the technology of high-current, high-quality ion beams recently advanced by the SDI-supported Neutral Particle Beam (NPB) program. The high-energy accelerator design rests on the well-established coupled-cavity linac technology used in the 800-MeV, 17-mA (peak current) LAMPF linac at Los Alamos. The high-power, medium-frequency RF systems needed to drive the accelerator have been developed for colliding-beam storage rings, such as the Large Electron Positron (LEP) collider at CERN.

This report is divided into 10 chapters. This first chapter provides a brief introduction to the accelerator concept. Chapter 2 gives an overview of the accelerator design and that of the high-energy beam-transport (HEBT) system. Chapter 3 discusses details of the overall engineering and physics design. Chapters 4 to 9 detail the physics and engineering of the major sections and systems of the accelerator, while Chap. 10 covers linac operation and safety issues. Chapter 11, which is not a part of this issuance (Revision 1–1.5), will be part of a subsequent issuance of this document (Revision 2) and will include discussion on the status of the technology base for high-power accelerators, as well as outstanding technical issues and recommendations for future study and development. Chapter 12, also referred to as Volume II, contains the references, appendices, supporting documentation, and design sketches. The references are also found at the end of each respective chapter.

1.2 DESIGN OVERVIEW

The APT accelerator is designed to deliver a 200-MW proton beam to one of two tritium producing targets. The output beam energy is 1000 MeV with an average beam current of 200 mA. The accelerator is an RF linac operating at 100% duty factor, or continuous wave (cw). The accelerator is made up of different accelerating structures that are optimized for accelerating protons over different velocity ranges. At the front end, there are two linacs, each delivering a 100-mA cw beam at 20 MeV. Both beams are combined at this energy in a funnel to produce a 200-mA beam, which is then accelerated in a single linac to 1000 MeV.

In each of the two low-energy (front-end) linacs, a continuous stream of protons is generated by an ion source and injected at an energy of 75 keV into a radio-frequency quadrupole (RFQ), where it is formed into bunches at a frequency of 350 MHz and accelerated to 7 MeV. The bunches are further accelerated to 20 MeV in a 350-MHz drift-

tube linac (DTL). At this point, the 100-mA bunch trains from each of the 20-MeV linacs are funneled together (combined by longitudinally interleaving bunches) to produce a 700-MHz, 200-mA beam. The combined beam is accelerated to 100 MeV in a bridge-coupled drift-tube linac (BCDTL) and then to full energy (1000 MeV) in a coupled-cavity linac (CCL). These high-energy accelerating structures are powered by 1-MW cw RF amplifiers (klystrons) and constitute the bulk of the APT accelerator. The accelerator design and architecture are sketched in Fig. 1-1.

Several power-related parameters are indicated in the box at the bottom of Fig. 1-1. The total RF power required to produce the 200-MW beam is 254 MW, counting both the 700-MHz RF needed for the BCDTL and CCL, and the 350-MHz power needed for the two RFQs and DTLs in the front end. The power at 700-MHz is 97% of the total. Because of the very high beam current in the accelerator, the RF efficiency (efficiency with which RF power is converted to beam power) of the APT linac is very high—0.79, averaging over the entire accelerator. Assuming an average efficiency of 0.59 for converting dc power to RF power in the klystrons, 0.01 losses in ac-to-dc power conversion, and 0.05 losses in RF transmission to the accelerating structures, the ac-to-beam efficiency is approximately 0.44, leading to a total ac power requirement for the accelerator of about 485 MW (including an allowance for focusing magnet power, coolant pumping power, and other miscellaneous demands).

The accelerator design incorporates some novel features that are adaptations of the established linac technology base, including a funneled front end, a high-energy RFQ, and a hybrid accelerating structure—the BCDTL—to cover the 20–100-MeV energy regime. The funnel solves the problem of obtaining a high-current, high-quality beam at low energies. The BCDTL was evolved specifically for this machine to accelerate beam in an energy region where traditional structures would be impractical or inefficient. The high-energy RFQ eliminates engineering difficulties in the first section of the DTL and also provides a nearly current-independent match to the DTL, greatly improving the ease of accelerator turn-on.

Another feature of the linac design is the *modular* concept, which breaks the accelerator into manageable lengths that can be fully assembled, aligned, and checked out for vacuum, cooling, and RF integrity in the off-line laboratory, before being transported to the accelerator tunnel and installed. The modular mechanical design has significant advantages in terms of ease and speed of maintenance, which is a high priority because of the emphasis on high machine availability. Although it is expected that activation levels will normally be low enough in the linac for hands-on maintenance, all accelerator structures and components are designed for compatibility with remote-maintenance machinery, if required.

The accelerator and HEBT have a total length of about 1.2 km. The HEBT delivers the 200-mA, 1-GeV proton beam to one of two identical target assemblies where tritium extraction takes place, or to a 0° full-power beamstop for tuning the linac. Each transport line terminates in a nonlinear beam expander that converts a small-dimension, Gaussian-like intensity profile into a large-area, rectangular, nearly-uniform profile at the face of the targets. Figure 1-2 shows the overall layout of the HEBT.

The accelerator is housed in a concrete, rectangular-section tunnel that is buried under more than 12 meters of earth for radiation shielding. Depending on site conditions and construction costs for various options, the tunnel could be placed completely below grade or could be partly above ground with an earth berm over the top. A building housing the RF amplifiers, magnet power supplies and controls, runs the length of the accelerator and is situated either over the top of the tunnel or beside the berm. This building can be occupied by operating personnel when the beam is on. A sketch of the site layout is shown in Fig. 1-3.

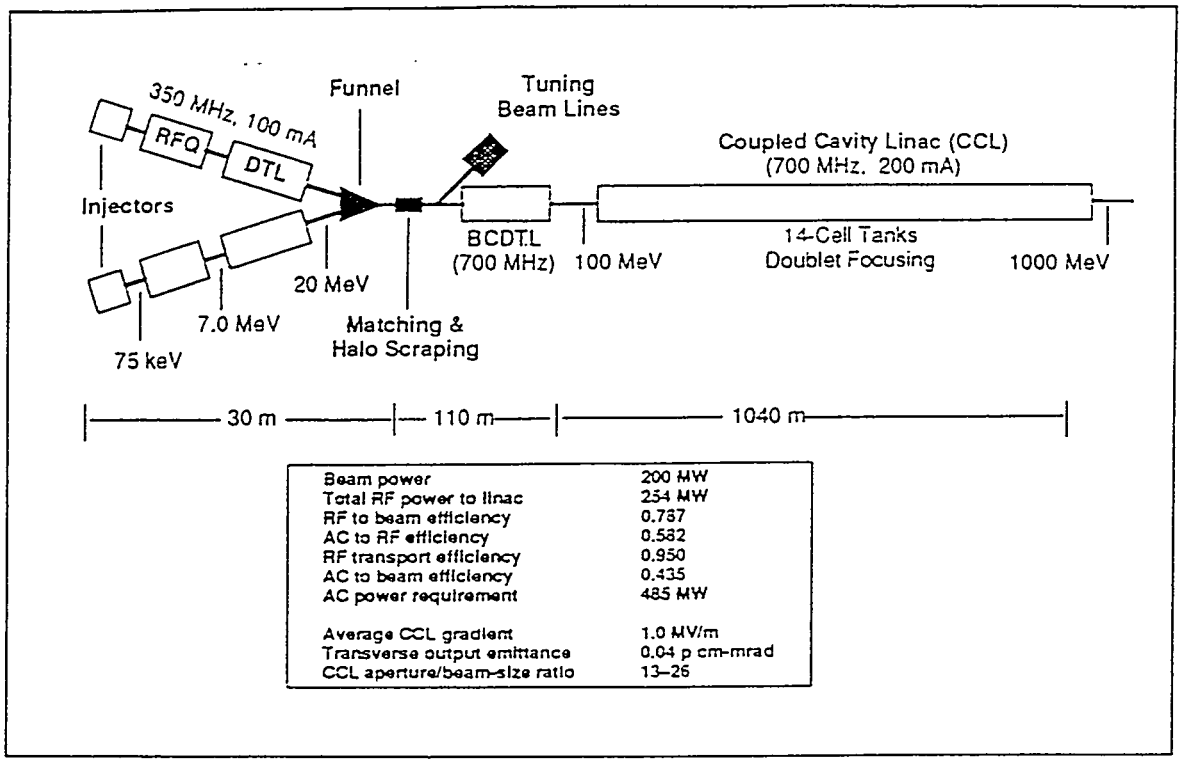


Fig. 1-1. APT accelerator concept—200 mA, 1000-MeV cw RF linac.

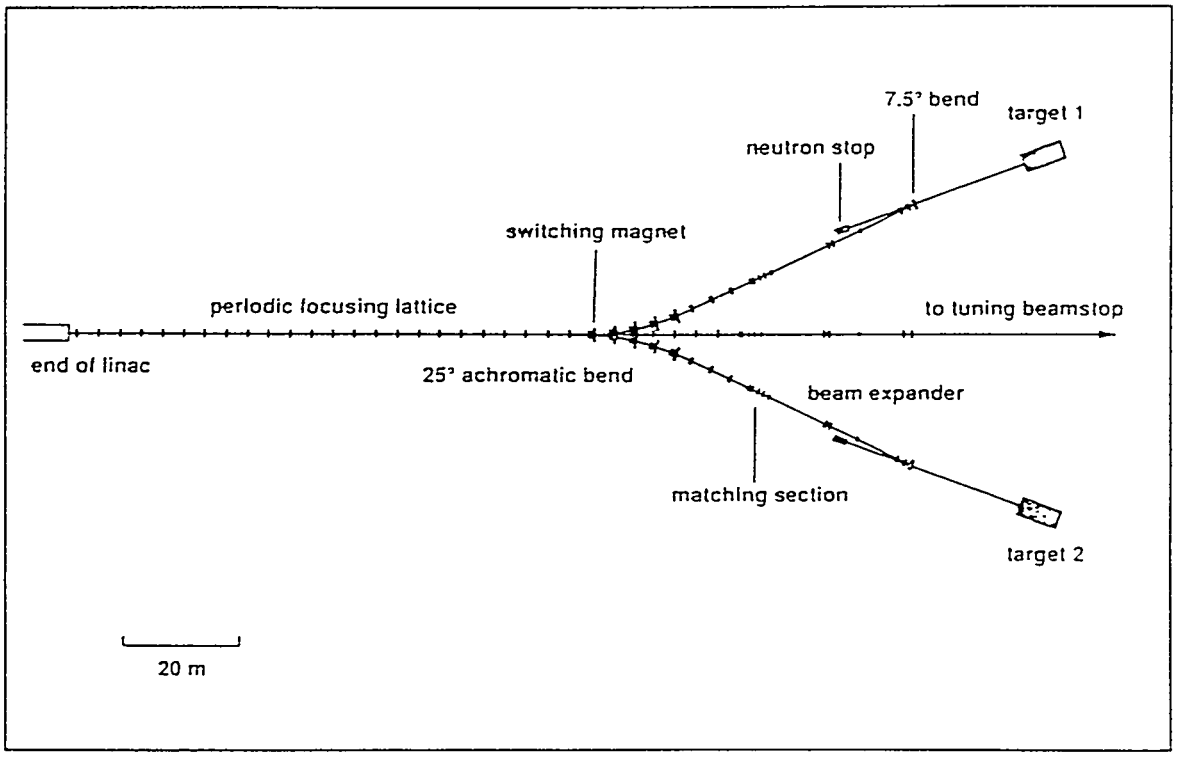


Fig. 1-2. High-energy beam-transport (HEBT) layout.

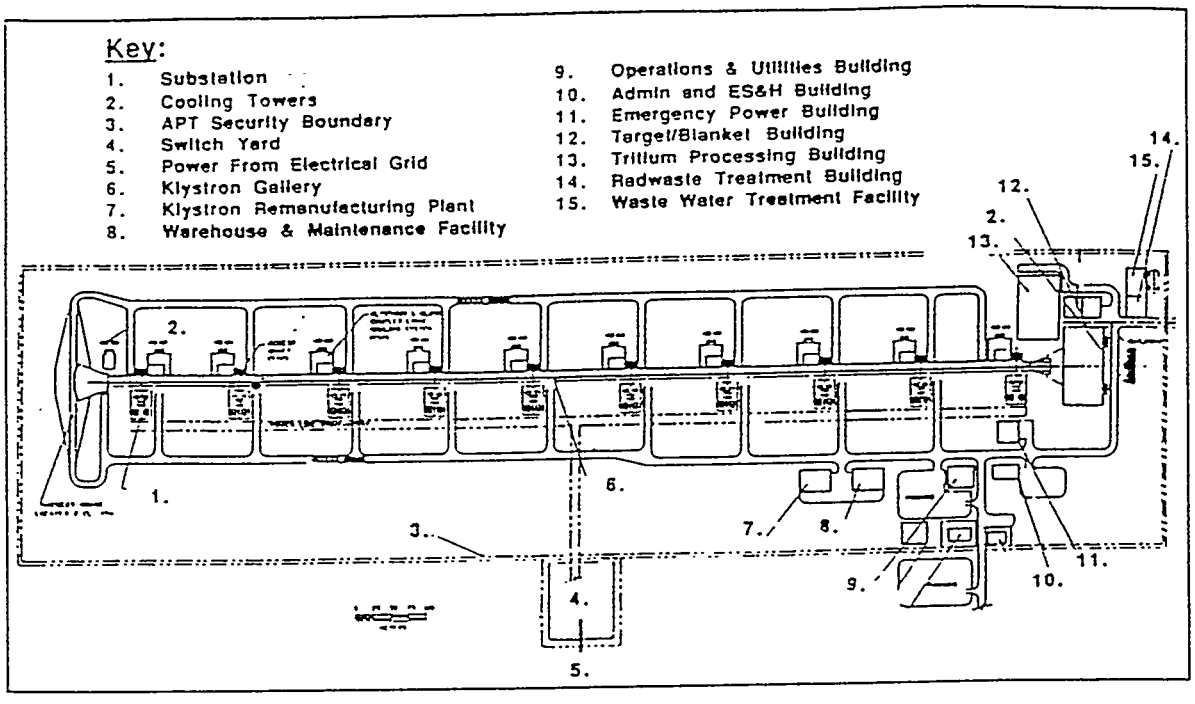


Fig. 1-3. APT site sketch.

The APT accelerator design has been guided by a conservative design philosophy and has been justified by limited trade studies. In addition to the major criteria of high intensity with low beamloss and high electrical efficiency, other general requirements that shaped the design are (1) high availability, (2) high operability, (3) minimum life-cycle costs, (4) personnel safety and machine protection, and (5) minimum environmental impact. In order to achieve an overall APT plant availability of 75%, the accelerator availability must be greater than 85%.

These general requirements, along with the basic tritium-production specification (beam power), have formed the basis for the APT accelerator design and for selecting the key parameters. The parameters for the four major accelerator sections, the RFQ, the DTL, the BCDTL, and the CCL, are summarized in Table 1-1.

Selecting the 350/700-MHz frequency combination as the frequency basis for the linac was based on a number of factors, including the availability of RF amplifiers and the need for DTL drift tubes that are large enough to house electromagnetic quadrupoles (EMQs). Permanent magnet quadrupoles (PMQs), while more compact than EMQs, were avoided wherever possible in the linac design because of their high sensitivity to radiation damage.

In the low-energy region of the accelerator (<20 MeV), the overall design emphasis is on emittance control of the high-current beam. This is addressed by (1) strong transverse focusing in the RFQs, (2) a high structure frequency (350 MHz) and strong transverse focusing in the DTLs, (3) ramped accelerating fields (strong longitudinal focusing) in the DTLs, and (4) precise matching between different accelerating structures. In addition, beam funneling at 20 MeV serves to cut the injector and RFQ current requirements in half and permits doubling the beam intensity delivered to the high-energy linac with no significant increase in emittance. At the same time, beam funneling fills all the RF cycles in the high-energy linac, reducing the charge per bunch, the beam emittance, and the beam size.

TABLE 1-1. APT Reference Accelerator Parameters

Parameter	RFQs (2)	DTLs (2)	BCDTL	CCL
Energy (MeV)	0.075–7.0	7–20	20–100	100–1000
Frequency (MHz)	350	350	700	700
Current (mA)	100	100	200	200
Structure Type	4-Vane	$1\beta\lambda$	$1\beta\lambda$	$\beta\lambda/2$
No. of Tanks or Segments	4 x 2	3 x 2	61	342
No. of RF Modules	2 x 2	3 x 2	24	342
No. of Assembly Units	—	3 x 2	24	302
No. of Cells per Tank	(433 total)	22 to 15	7	14
Length of Tanks or Segments (m)	2.03	2.44–2.50	0.615–1.281	1.29–2.62
Total Length (m)	8.10	7.98	93.66	1031.44
Radial Aperture (cm)	0.24	1.00	2.00–2.25	2.50
Aperture/Beamsize(rms) Ratio	–	4–5	8–13	13–26
Structure Gradient (MV/m)	0–1.75	1.04–2.80	1.70–1.50	1.50–1.36
Average Gradient (MV/m)	ramped	ramped	1.00	1.00
Synchronous Phase (deg)	-90 to -30	-35 to -25	-40 to -30	-30
Shunt Impedance (MΩ/m)	–	30.2–32.8	26.0–36.7	23.3–37.4
Structure Power (MW)	1.12 x 2	1.15 x 2	6.91	42.49
Beam Power (MW)	0.70 x 2	1.30 x 2	16.10	180.39
Total RF Power (MW)	1.82 x 2	2.45 x 2	23.01	223.18
Efficiency	0.385	0.530	0.711	0.806
Phase Advance/Period (deg)	30 (@ output)	80–70	80–70	70
Quadrupole Lattice	FD	FOFODODO	FDO	FDO
Quadrupole Length (cm)	–	5.7	8.2–9.5	11.0–18.0
Quadrupole Spacing (cm)	–	10.4–17.4	9.5	11.0–18.0
Quadrupole Gradient (T/m)	–	25.0–35.0	31.4–36.0	24.4–38.0
$Emit_T$, rms, norm (π-cm-mrad)	0.022	0.023	0.029	0.032
$Emit_L$, rms, norm (π-MeV-deg)	0.220*	0.216*	0.483**	0.608**

*for a 350-MHz RF cycle
**for a 700-MHz RF cycle

In the high-energy region of the accelerator (>20 MeV), a balance is struck between the need for very low fractional beamloss levels and the requirement of high RF-to-beam conversion efficiency. This has led to a design that incorporates a large ratio of accelerating-structure-aperture to rms-beamsize (10–26 in the CCL), short accelerating tanks for strong transverse focusing, smooth phase-space transitions between accelerating structures, and a relatively low accelerating gradient (1.00 MV/m averaged over accelerating structures and intertank regions). Because all the 700-MHz RF buckets are filled, and because the beam duty factor is 100%, the number of protons per bunch in the APT linac (1.78×10^9) is only 3.4 times greater than in LAMPF (0.52×10^9), even though the average current is 200 times higher. This means that the basic beam dynamics of the high-energy linac lie qualitatively within a familiar regime, rather than in an unexplored high-density regime.

1.3 ISSUES AND CONCLUSIONS

This topical report represents the results of a 1.5-year accelerator point design study conducted as part of a DOE-supported study of APT. The study was carried out by a Los Alamos core team, with support in critical areas from several industrial partners. Grumman Aerospace Corporation provided engineering support for the APT accelerator design. A Maxwell/Litton/ABB team (led by Maxwell) provided support for design of the RF power

system and for analysis of the connection to the electric power grid. General Atomics provided support for engineering of the HEBT system. The Los Alamos contributors to the accelerator design study are listed at the beginning of this report, as are the contributors from Grumman, Maxwell/Litton/ABB, and General Atomics.

The principal objective was to develop a reference design for the APT accelerator and transport system meeting the basic beam-power requirements that was sufficiently complete to address a range of performance, operations, ES&H, technical risk, and cost issues. The design that has been produced meets these requirements in a balanced way, without stressing component or system performance limits and within appropriate safety margins. Sufficient beam dynamics has been done to confirm a low-emittance-growth linac design and one that minimizes the (known) mechanisms for producing beam halos. Confidence in meeting low beamloss objectives is derived from results of the beam dynamics and from extrapolations from the LAMPF low-beamloss operation. Sufficient system integration design has been carried out to assure that packaging and spacing arrangements are realistic for all necessary components. Sufficient engineering analysis of accelerating structures has been done to confirm that they can be adequately cooled, tuned, fabricated, and maintained.

Such operational issues as failure-mode analyses, accelerator turn-on and tuning, recovery from faults, etc., have not received a complete assessment within this phase of the design study and will be addressed in more detail in following phases. The accelerator design also has not received a thorough analysis in terms of sensitivity to errors of construction, installation, and operation, although some initial work has been done and is discussed in this report.

The physics and engineering studies described in this report on the APT linac point design have turned up no *show stoppers*, nor have any fundamental flaws surfaced during the several formal design reviews. The point design is believed to be conservative, self-consistent, and capable of being implemented at the present time within the existing US industrial base. The design uses the existing technology base for room-temperature (water-cooled) copper-surfaced RF linacs as the point of reference. System and/or component performance requirements are either similar to or less stressing than those already demonstrated (in pulsed operation) or constitute reasonable extensions from and extrapolations within the technology base. The main area in which experience is lacking is in 100% duty or cw operation of integrated high-power accelerator systems, and the development of a high-power cw front-end accelerator test stand is thus a high priority for establishing an increased confidence level.

Because of the limited basis of the design study, the APT accelerator point design described in this report is just that, a design at a point, developed using a particular set of key parameters. The design is based on conventional technology and within this framework, is thought to be reasonably close to optimum. However, given the time and resource constraints of the study, there has not been an opportunity to conduct extensive trade and/or sensitivity assessments on key parameters, to examine alternative design architectures, or to investigate alternative parameter sets.

Although a funneled architecture has been selected as the best way currently to meet the APT beam intensity objective within a cost-effective framework, certain technology developments could, in the future, lead to alternative choices. For example, Russian accelerator teams at the Moscow Radio Technical Institute (MRTI) and the Institute for Theoretical and Experimental Physics (ITEP), Moscow, are investigating a new low-energy RF linac concept that has higher current limits than a comparable-frequency RFQ. If this

device could be engineered for cw operation with an acceptable output emittance, it could re-open the question of funneling.

Superconducting RF cavity technology is another area where future development could lead to design alternatives for the APT accelerator. A superconducting RF linac (fabricated from niobium cavities) could offer significant operating cost advantages in comparison with a conventional linac fabricated from copper cavities, especially in terms of reduced electric-power costs (20% lower), and could offer technical performance advantages, as well (reduced beamlosses because structure apertures can be larger). However, the superconducting RF technology base, while having made impressive advances in the past decade, is not sufficiently mature at this point to propose such a machine as the baseline choice for APT. There is no experience with acceleration of high-current proton beams, and several performance, system-design, and operational issues must be addressed.

In conclusion, the FY 1992/1993 APT study has developed a viable and detailed point design for an accelerator and beam transport system that can deliver a 200-mA, 1000-MeV high-quality beam to the tritium production targets. The design is conservative in terms of parameter choices and component selection, and rests firmly on the technology base for conventional RF linacs that has been developed over the past four decades and more recently enhanced by the NPB program. The main systems, beam physics, and engineering design issues have been addressed and have received technical review. Using the point design as a framework for further analysis, a number of operational issues need more examination. These issues are to be addressed in FY 1994.

ACCELERATOR SYSTEMS DESIGN OVERVIEW
CHAPTER 2

Page

2.1 ACCELERATOR ARCHITECTURE 1
2.1.1 Physics and Philosophy 1
2.1.2 APT Linac Design 2
2.1.3 Engineering Considerations 3
2.1.3.1 New Accelerating Structures 3
2.1.3.2 Special Engineering Features 4
2.2 PHYSICS STUDIES AND SIMULATIONS 6
2.3 LOW-ENERGY ACCELERATOR SYSTEMS 9
2.3.1 Injector 9
2.3.2 Radio-Frequency Quadrupole (RFQ) 10
2.3.3 Drift-Tube Linac (DTL) 12
2.3.4 The Funnel 14
2.4 HIGH-ENERGY ACCELERATOR SYSTEMS 17
2.4.1 Bridge-Coupled Drift-Tube Linac (BCDTL) 17
2.4.2 Coupled-Cavity Linac (CCL) 19
2.5 HIGH-ENERGY BEAM TRANSPORT SYSTEM 21
2.5.1 Overview 21
2.5.2 Transport 22
2.5.3 Beam Expander 22
2.5.4 Performance 23
2.6 RF POWER SYSTEMS 24
2.6.1 Overview 24
2.6.2 Klystrons 25
2.6.3 Klystron Power Supply 25
2.6.4 Availability and Reliability 25
2.6.5 RF Efficiency 26
2.6.6 Klystron Production 27
2.7 ACCELERATOR SUPPORT SYSTEMS 27
2.7.1 Controls 27
2.7.2 Beam Diagnostics 28
2.7.2.1 Characterization Measurements 28
2.7.2.2 Operational Measurements 29
2.7.3 Vacuum System 29
2.7.4 Water Cooling System 30

2.7.5 Cavity Temperature/Resonance Control System 30
2.7.6 Alignment System 31
2.7.7 Magnet Power Supplies 31
2.8 INTERFACES TO ACCELERATOR 31
2.9 OPERATION AND SAFETY SUMMARY 33
2.9.1 Linac Operation 33
2.9.1.1 Maintenance 33
2.9.1.2 Startup and Tuning 33
2.9.1.3 Fault Recovery 34
2.9.2 Safety and Protection 34
2.9.2.1 APT Hazards and Engineered Safety 34
2.9.2.2 Designs for Personnel Safety, and Machine and Environmental Protection 35

LIST OF FIGURES

Page

Fig. 2-1. A typical BCDTL module showing tanks and quadrupole doublets. 5
Fig. 2-2. Phase-space distributions at the output of the CCL. 7
Fig. 2-3. CCL output beam distributions from the end-to-end simulation. 8
Fig. 2-4. Transverse and longitudinal ratios of aperture-to-rms beamsize for the CCL. 8
Fig. 2-5. The ECR proton source. 9
Fig. 2-6. A mass-analyzed LEBT with the ECR source and solenoids. 10
Fig. 2-7. APT four-vane, four-segment RFQ. 11
Fig. 2-8. Plan view of the low-energy accelerator system, including the 20-MeV funnel. 13
Fig. 2-9. Interlacing bunches in the 20-MeV funnel. 14
Fig. 2-10. APT 20-MeV funnel layout. 15
Fig. 2-11. An APT BCDTL module, showing two tanks and two quadrupole doublets. 17
Fig. 2-12. One CCL module (1000 MeV) with focusing quadrupole doublet. 19
Fig. 2-13. Overview of the HEBT system. 21
Fig. 2-14. Nonlinear beam expander and target configuration. 23
Fig. 2-15. Primary components of an RF module. 24
Fig. 2-16. RF power conversion and distribution. 25

LIST OF TABLES

Page

Table 2-1. APT End-to-End Simulation Summary 7
Table 2-2. APT RFQ Parameters 12
Table 2-3. APT DTL General Parameters 14
Table 2-4. APT Funnel Parameters 16
Table 2-5. APT BCDTL Parameters 18
Table 2-6. APT CCL Parameters 20
Table 2-7. RF Component Reliability Estimates 26
Table 2-8. RF System Efficiency 26

2.0 ACCELERATOR SYSTEMS DESIGN OVERVIEW

2.1 ACCELERATOR ARCHITECTURE

2.1.1 Physics and Philosophy

The APT accelerator and beam transport system is designed to provide a 1-GeV 200-mA cw proton beam to the tritium production targets with high reliability and availability. Because of the very high beam power, key design factors include minimization of beamloss and maximization of electrical efficiency.

- Current and Energy Choices. Over a broad range of energy between 800 MeV and 2000 MeV, the beam power needed to produce the required amount of tritium is relatively constant. Choice of beam energy and current is dictated to some extent by target performance constraints, but more strongly by the need to maintain a high electrical efficiency and by overall accelerator operating economics. The electrical conversion efficiency of the accelerator is maximized (and the APT plant electrical consumption thereby minimized) by choosing the beam current to be as high as practical. The beam energy is then adjusted to provide the necessary beam power for the specified APT tritium production capability. In order to achieve the high-current performance in the low-energy portion of the accelerator, the APT linac architecture is based on a funneling scheme, in which two identical 100-mA beams are combined at 20 MeV to produce a final 200-mA beam.

- Emittance Control. An important objective of the APT linac design is to achieve very low beamloss, especially in the high-energy section of the accelerator, where even small losses would produce high activation levels. To minimize the beamloss, it is important to control the growth of the rms (and total) beam emittance (the phase-space volume occupied by the particles) and also to control the generation and growth of the beam halo (the far fringes of the transverse beam distribution) which can be intercepted by the accelerating structures. Design for good emittance control is especially critical in the low-energy portion of the accelerator, where space-charge forces are large. Low-energy system design features that assure minimum emittance growth include: (1) the use of funneling to halve the beam current, (2) relatively high accelerating frequencies to reduce the charge per bunch, (3) strong transverse focusing, (4) ramped accelerating gradients, and (5) careful matching between adjacent accelerating structures.

- Design for Low Beamloss. The APT linac is designed to reduce halo production (within the context of what is presently known about generating mechanisms), and also to minimize interception of the halo by the accelerating structures. Although the causes of beam halo formation are not completely understood, much has been learned from recent numerical simulations. In these studies it has been observed that nonlinear processes within the beam act to eject particles from the beam core into the halo. These processes are driven by time-dependent collective space-charge forces arising from mismatches of various kinds. Transitions in the accelerator phase-space acceptance (sudden changes in transverse or longitudinal focusing) also appear to drive particles into the halo. This is thought to arise from the beam heating driven by such transitions, followed by turbulent relaxation as the beam adapts to the changed environments.

There has been a strong emphasis in the APT linac design on eliminating or minimizing transitions where possible, especially at high energies. Above 20 MeV there are no significant acceptance transitions, and below this energy there has been careful attention to smooth matching between adjacent accelerating structures.

Other key features incorporated into APT linac design to assure low beamloss include: (1) very large ratios of the accelerating structure apertures to the rms beamsize, (2) large ratio of longitudinal acceptance to rms longitudinal emittance, (3) a high density of focusing elements, (4) tight RF amplitude and phase control, (5) precision transverse beam position alignment, (6) distribution of the beam among all available RF buckets in the high-energy linac, and (7) the use of a halo scraper (transverse phase space limiter) following the last significant acceptance transition (the funnel).

- **Design for High Electrical Efficiency.** High electrical efficiency in the APT linac is important to reduce the plant electric power demand, and is achieved by several factors. A key element is the emphasis on high beam current as opposed to high energy for delivering the desired beam power to the targets. This means that the RF power used for accelerating the beam is much larger than the RF power losses in the accelerating cavity walls, and the RF-to-beam power conversion efficiency is high. In the APT linac design, the RF-to-beam conversion efficiency is nearly 80%. A second element is to assure a high efficiency (high shunt impedance) cavity design for the CCL, which makes up more than 90% of the linac and therefore dominates the power equation. This is achieved by choosing a relatively high structure frequency (700 MHz), selecting a low accelerating gradient (1.0 MV/m), and by using structure apertures that are not too large. The selection of structure aperture dimension is a balanced design compromise between the larger openings needed for minimum beamloss and the smaller openings required for maximum RF efficiency. A final element in the design is the use of high-efficiency RF amplifiers (klystrons) as the baseline RF power source. High power klystrons can presently convert dc to RF power with efficiencies greater than 60%. Significant efficiency improvements are feasible in high-power RF amplifier technology in the future.

2.1.2 APT Linac Design

The physics design of the APT linac is based on the ideas outlined above in Sec. 2.1.1. The primary design objective for the low-energy portion of the accelerator (<20 MeV) is to produce a high-quality, high-intensity beam with low emittance growth and minimal halo that can then be accelerated to 1 GeV with very low beamloss. Minimizing actual beamloss in the linac front end is a secondary objective as long as activation levels are acceptable for hands-on maintenance. Since the total RF power used in this part of the linac is only 3.3% of the accelerator total, the optimization of accelerating structures in this region for high RF efficiency is a relatively low design priority. The low-energy accelerator system is essentially the "beam launcher" for the high-energy linac, and must deliver the needed high quality beam. High beam quality is achieved by: (1) providing strong transverse focusing through the use of a high accelerating-structure frequency (350 MHz), (2) ramping accelerating fields for strong longitudinal focusing, (3) precise phase-space matching between accelerating structures to minimize acceptance transitions, and (4) funneling to provide current doubling with little or no emittance penalty.

Primary design objectives for the high-energy end of the accelerator (>20 MeV) are to achieve beamloss levels low enough for hands-on maintenance and to maintain a high RF-to-beam conversion efficiency. The low beamloss objective is attained by (1) providing a large aperture-to-beamsize ratio to minimize halo interception, (2) providing a high density of focusing elements to maintain compact beamsize and minimize emittance and halo growth, and (3) eliminating major acceptance transitions that could cause beam heating and generation of halos. The ratio of aperture to beamsize (rms) is taken as a figure of merit in the design of the high-energy sections of the linac and is made as large as possible, consistent with maintaining a high RF efficiency. The aperture ratio increases with beam energy in order to assure the smallest beamlosses at high energies where the activation threat (per lost particle) is greatest. The structure apertures selected are a design tradeoff between maximizing the aperture-to-beamsize ratio and maximizing the structure RF power efficiency. Strong transverse focusing (which maintains small beam dimensions) is provided by using a quadrupole-doublet focusing lattice and short tank lengths.

2.1.3 Engineering Considerations

Important engineering considerations for the APT accelerator include: (1) development of robust and highly modularized accelerating-structure designs, (2) cavity designs that avoid high surface electric fields that could cause RF multipactoring (breakdown), (3) designs that provide high RF and vacuum seal integrity, and (4) cavity cooling-channel designs that provide adequate heat removal for the high power deposition conditions that arise in cw operation. Accelerator components that may require frequent service and/or could become activated must be designed for high accessibility, speed of maintenance, and compatibility with remote handling equipment.

2.1.3.1 New Accelerating Structures

New accelerating structure concepts have been incorporated into the APT linac point design in two areas to provide improved solutions for particular physics and engineering challenges. These new concepts are adaptations or extensions of existing structures. Based on a combination of analysis and preliminary modeling, these structures are seen as advantageous (and low-risk) departures from the conventional technology base that have important benefits for the APT linac design. The first of these new accelerating structures is a high-energy 350-MHz RFQ, which accelerates the beam in the low-energy linacs to 7 MeV. The second new structure is referred to as a BCDTL (Bridge-Coupled Drift Tube Linac); operating at 700 MHz, it provides a superior design solution for the 20–100-MeV region of the high-energy linac.

- 7-MeV RFQ. The new RFQ has a much higher output energy (7 MeV) than previous proton RFQ designs (2–3 MeV), and replaces the first tank of the 350-MHz DTL. The high-energy RFQ eliminates the difficulty (appearing in early designs) in attaining sufficient transverse focusing in the first DTL tank. At 7 MeV, this RFQ would be the longest ever built, and consists of four resonantly coupled, 2-meter-long segments joined by electroformed copper joints. Theoretical analysis and preliminary low-power RF tests with a two-section model indicate that the resonant coupling scheme should perform well. The use of high-energy RFQs in the low-energy linacs provides a nearly current-independent match between the RFQ and the DTL, which allows a more straightforward accelerator turn-on procedure.

- BCDTL. The BCDTL is a new (hybrid) accelerating structure designed specifically for the 700-MHz, 20- to 100-MeV portion of the APT accelerator. It consists of short (7-cell) drift-tube tanks, with the quadrupoles located not inside the drift tubes (as in a conventional DTL) but only in the intertank spaces. Several tanks are (RF) bridge-coupled together by side-mounted π-mode resonant cavities, and the module thus formed is powered by a single 1-MW klystron.

  The initial structure design approach for the 20- to 100-MeV region was based on a coupled-cavity linac (CCL), which would have been both impractical to build and inefficient to operate in terms of RF-to-beam power conversion. A CCL structure in this energy range would have poor shunt impedance because of the high density of cells and endwalls, and would therefore suffer high RF power dissipation for the required accelerating gradient. Major engineering and fabrication difficulties in cooling and assembling the densely packed CCL cells would also be encountered. The Alvarez DTL, which is the traditional structure solution in this (proton) velocity range is not desirable because 700-MHz drift tube dimensions are too small to contain electromagnet quadrupoles (EMQs). Compact permanent magnet quadrupoles (PMQs) are deemed too radiation-sensitive for the high-current APT application, where there is a (calculated) significant risk of field quality degradation during accelerator tuning.

  The BCDTL solves the problems of the CCL and the conventional DTL. It permits the use of EMQs between the short accelerating tanks and provides a much larger aperture than could be achieved by a conventional 700-MHz DTL. This hybrid structure also takes advantage of the (well-known) superior RF efficiency of a DTL below 100 MeV (in comparison with a CCL). A CCL structure in the 20–100-MeV energy range would have poor shunt impedance because of the high density of cells and endwalls, and would therefore suffer high RF power dissipation for the required accelerating gradient. Major engineering and fabrication difficulties in cooling and assembling the densely packed CCL cells would also be encountered. The BCDTL is much simpler and less costly to fabricate and assemble.

2.1.3.2 Special Engineering Features

Special engineering features incorporated into the APT linac design include the following:

- Modularization. The APT accelerating structures are *modularized* into assembly units, as illustrated in Fig. 2-1, which shows a typical BCDTL assembly unit. The high-energy end of the accelerator (BCDTL and CCL) is composed of 326 such units. Modularization subdivides the linac into manageable lengths for maintenance, checkout, and installation. All assembly units weigh less than two tons and do not exceed a length of five meters. The units can be preassembled in a staging area, aligned, and then checked for vacuum, cooling, and RF integrity. They are then transported to the linac tunnel, installed and aligned to adjacent units and to the tunnel reference monument grid. If any unit were to suffer a major failure, the reverse process would occur, and the unit would be returned to the maintenance building for servicing. Also seen in Fig. 2-1 is a typical quadrupole doublet mounted on precision linear rails in the intertank gap. The doublet is critically aligned relative to the linear rails. When the doublet requires servicing, it can be mounted on a similar set of rails in the lab and prealigned

before reinstallation. This procedure saves time and reduces any potential radiation exposure to personnel working in the tunnel. Modularization allows for all necessary checkouts to be done in a well-controlled laboratory environment, minimizing the time spent in the tunnel.

- Drift Tube Girders. The DTL drift tubes are designed for rapid changeout in a potential radiation environment. For ease and speed of assembly and alignment, the drift tubes in each tank are mounted on a common girder, which spans the length of the tank. The drift tubes are hard mounted and vacuum sealed into the girder. This assembly procedure is desirable to withstand the cw RF heating. If the RF or vacuum seal were to fail, the girder could be removed from the DTL as a unit and serviced in the laboratory.

- CCL Cooling Features. Careful selection of brazing alloys is necessary to avoid galvanic corrosion along the CCL structure cooling channel joints, which would negatively affect the life of the accelerator modules. Cooling water flows and volumes in the CCL are large, and the modules are precisely temperature-controlled through regulation of the cooling water flow, to maintain the correct structure resonant frequency. Design of the external manifolding of the cooling water system is important because of the potential for carrying radioactive water. To help prevent water leaks into the tunnel, high-vacuum (VCR) fittings are used for all cooling line connections.

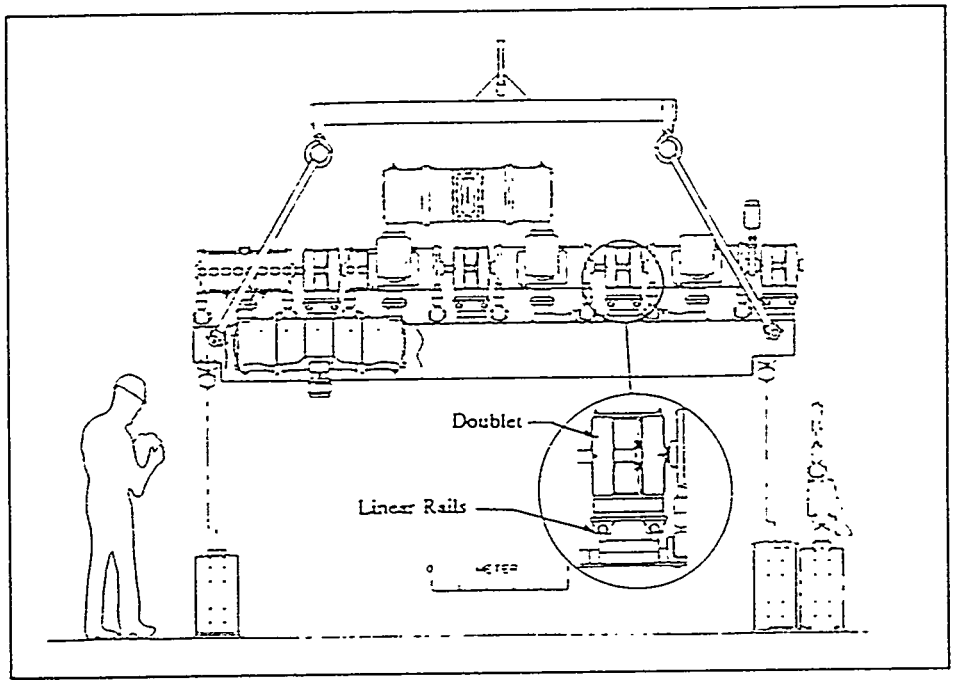


Fig. 2-1. A typical BCDTL module showing tanks and quadrupole doublets.

- Magnet Radiation Hardening. The APT linac is designed for very low beamloss during normal operation. However, because of the very high beam current, potential exists for neutron damage and activation at any point in the linac during tuning. Thus, essentially all quadrupoles are specified as EMQs with

radiation-resistant field coils. The coils windings are potted in calcium-aluminate cement, making them able to withstand orders-of-magnitude more neutron dose than conventional magnets. Additionally, the coils are fabricated in two halves for each quadrupole so that when the yoke is disassembled, the coils can be individually replaced.

- Tunnel Considerations. There are several major engineering consideration with respect to the design of the accelerator tunnel and its interfaces to the accelerator. Even though hands-on maintenance in most regions is the overall APT linac design goal, we must consider off-normal and beam-tuning operations that could temporarily produce local high-activation levels. For these reasons, it is prudent to allow (in the tunnel design) for the possibility of remote handling at any point along the accelerator. In addition, there are a small number of locations that can be identified from the beginning as requiring remote handling at all times. The most prominent example is the halo scraping system (downstream from the funnel) that will be highly activated by the nature of its function. Two major features have been incorporated into the APT tunnel design for remote handling compatibility. These are: (1) radio-controlled bridge cranes to carry surveillance booms and master-slave manipulators as adjuncts to the normal equipment handling functions, and (2) transverse dimensions that are roomy enough to allow a mobile remote maintenance master-slave servo-manipulator machine to work alongside the accelerator.

2.2 PHYSICS STUDIES AND SIMULATIONS

An end-to-end simulation of the APT accelerator, from injection (into each low-energy leg) at 75 keV to the final CCL output energy of 1 GeV, was completed using the simulation codes PARMULT/PARMTEQ, PARMILA, and FDODYN. These codes have been benchmarked against results from the LAMPF accelerator and other accelerators, and have reproduced measured rms emittances to within 10%. The simulation of the LAMPF linac also predicted observed beamlosses to within an order of magnitude (on the high side). The simulation codes model the electromagnetic design of each accelerating section, including the following: (1) the cavity fields; (2) RF-defocusing, linear and nonlinear space charge in the beam; and (3) magnetic focusing fields (using a hard-edge approximation). In the APT accelerator, each beam bunch contains approximately 2×10^9 protons at the full current of 200 mA. Exact simulation of the transport of such a large number of particles through a complex accelerator system is not practical, even with today's supercomputers. Therefore, the simulation codes use a number of approximations.

The technique of representing a real beam bunch by an equivalent bunch of *macro* particles is used to reduce the number of simultaneously followed objects to a reasonable level. A Monte-Carlo 4D waterbag input distribution of 10,000 macroparticles is generated at the RFQ input as the starting beam distribution. Each macroparticle has the same charge-to-mass ratio as an actual beam particle (proton). The charge of each macroparticle is given by the total charge in the bunch divided by the number of macroparticles. The transverse emittance of the initial beam distribution is determined by simulation of the proposed ion source. Each macroparticle is propagated through the several accelerating structures and matching sections of the linac to a final output energy of 1 GeV.

A summary of the results of such an end-to-end simulation is shown in Table 2-1. Figs. 2-2 to 2-4 show the phase space plots at the output of the CCL. The ratios of transverse

and longitudinal aperture-to-rms beamsize are also shown. This simulation is for an ideal linac with no alignment or focusing-field errors and no RF phase and amplitude errors. Results of simulations for various error and fault conditions are discussed in Chap. 3.

Table 2-1. APT End-to-End Simulation Summary

Accelerator Section	Output Emittance (rms, normalized) ε_T (π·cm−mrad)	ε_L (π·MeV−deg)	Emittance Growth (%) Transverse	Longitudinal	Aperture-to-Beamsize (rms) Ratio
Injector	0.020	±180° phase spread	n/a	n/a	n/a
RFQ	0.022	0.220*	10	n/a	n/a
DTL	0.023	0.216*	5	-2	4–5
Funnel	0.029	0.436**	26	1	5–8
BCDTL	0.029	0.483**	0	11	8–13
CCL	0.032	0.608**	10	26	13–26

*for a 350-MHz RF cycle
**for a 700-MHz RF cycle.

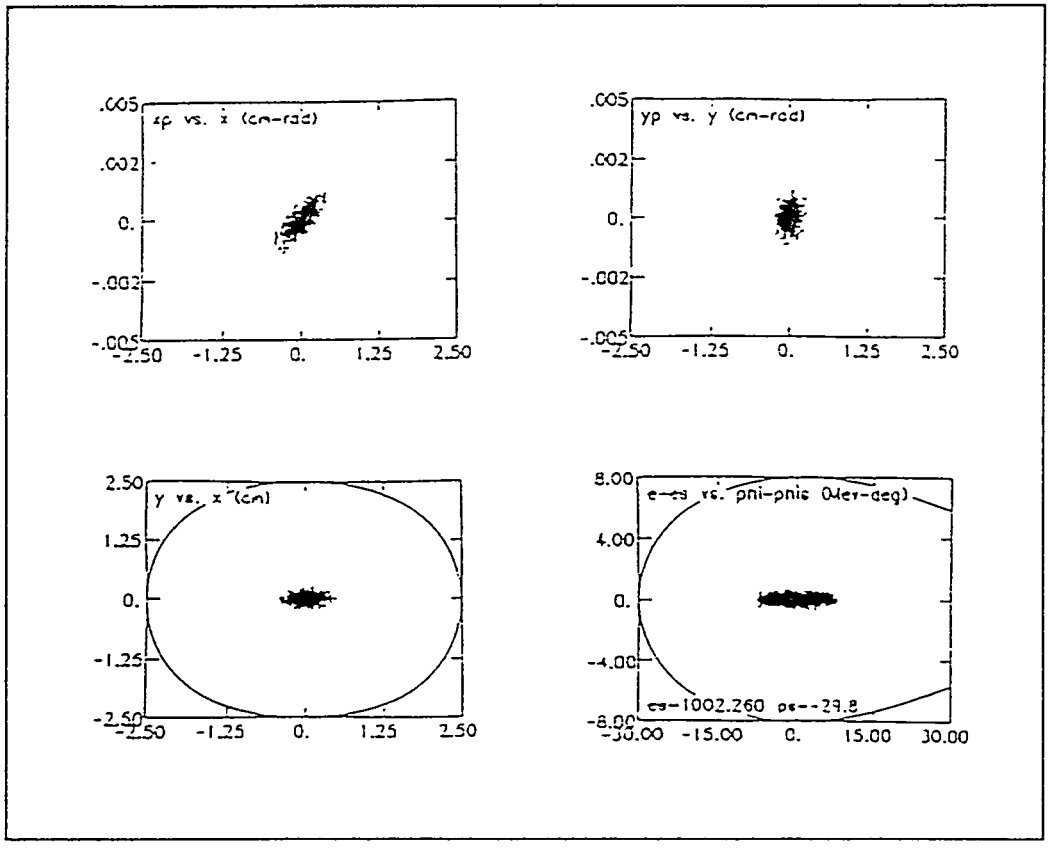


Fig. 2-2. Phase-space distributions at the output of the CCL.

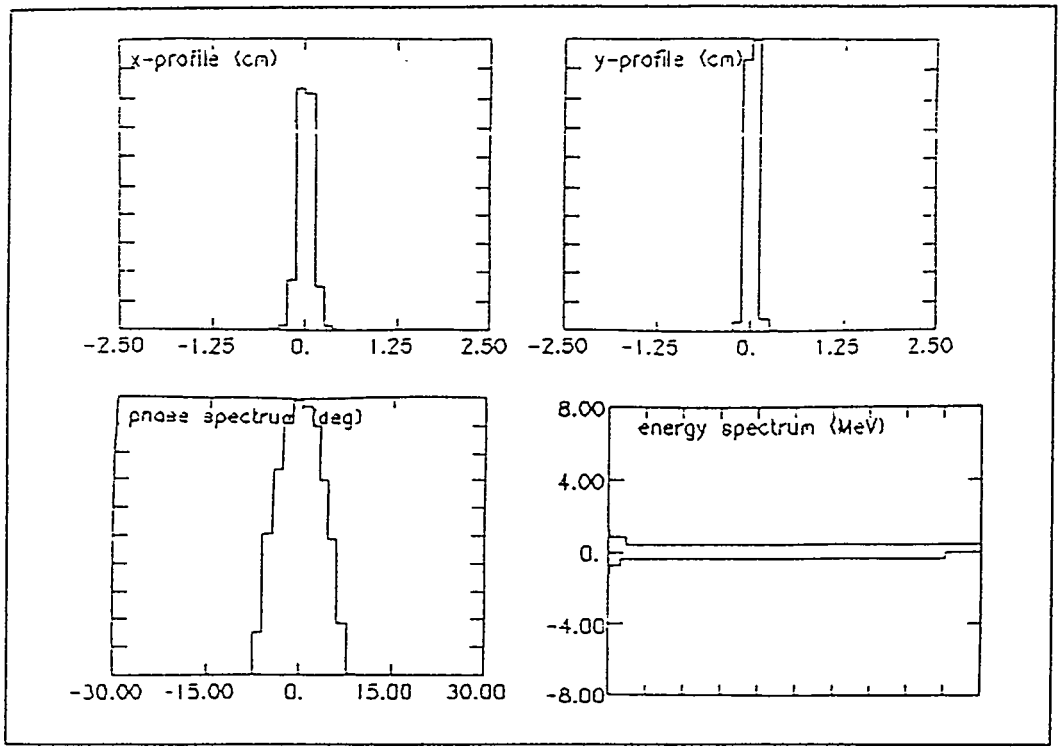


Fig. 2-3. CCL output beam distributions from the end-to-end simulation.

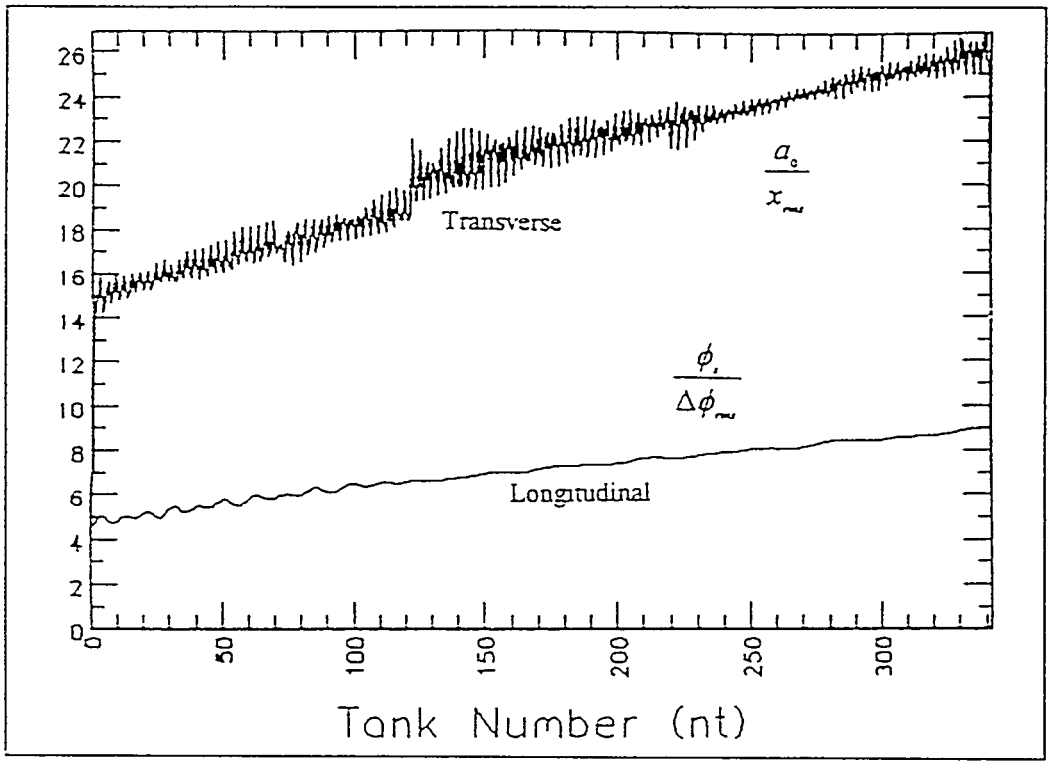


Fig. 2-4. Transverse and longitudinal ratios of aperture-to-rms beamsize for the CCL.

2.3 LOW-ENERGY ACCELERATOR SYSTEMS

2.3.1 Injector

The injector for the APT point design must meet certain stringent requirements, such as a beam availability of more than 98% during an annual operating period of 7800 hours/year (or 325 days/year). It must: (1) deliver a proton beam with a current of ≥110 mA to the input of the RFQ at 75 keV with an emittance of ≤0.02 π·cm-mrad (rms, normalized), (2) have sufficient flexibility in matching and steering to provide adequate beam adjustment at the RFQ entrance, and (3) have a lifetime of ≥328 hours; i.e., maintenance would typically be performed biweekly (with improvements in engineering on the ion source, longer periods between maintenance can be expected). Although several ion-source options have been considered, the ECR (Electron Cyclotron Resonance) source is currently the most promising, with proven and reliable continuous operation at 100% duty factor and excellent gas and power efficiency. This source has therefore been selected for the APT baseline design.

The feasibility of an ECR-based injector for APT has been demonstrated on the RFQ1 project at CRL (Chalk River Laboratory) in Canada. In this project, the ECR injector provided a record of stable operation with good beam quiescence, a gas efficiency of 60%, a proton fraction (ratio of protons to total ion species) of 70%–80%, and a proven match to the RFQ, with an output emittance of 0.012 π·cm-mrad at 125 mA and 50 keV injector energy. A diagram of this ion source is shown in Fig. 2-5.

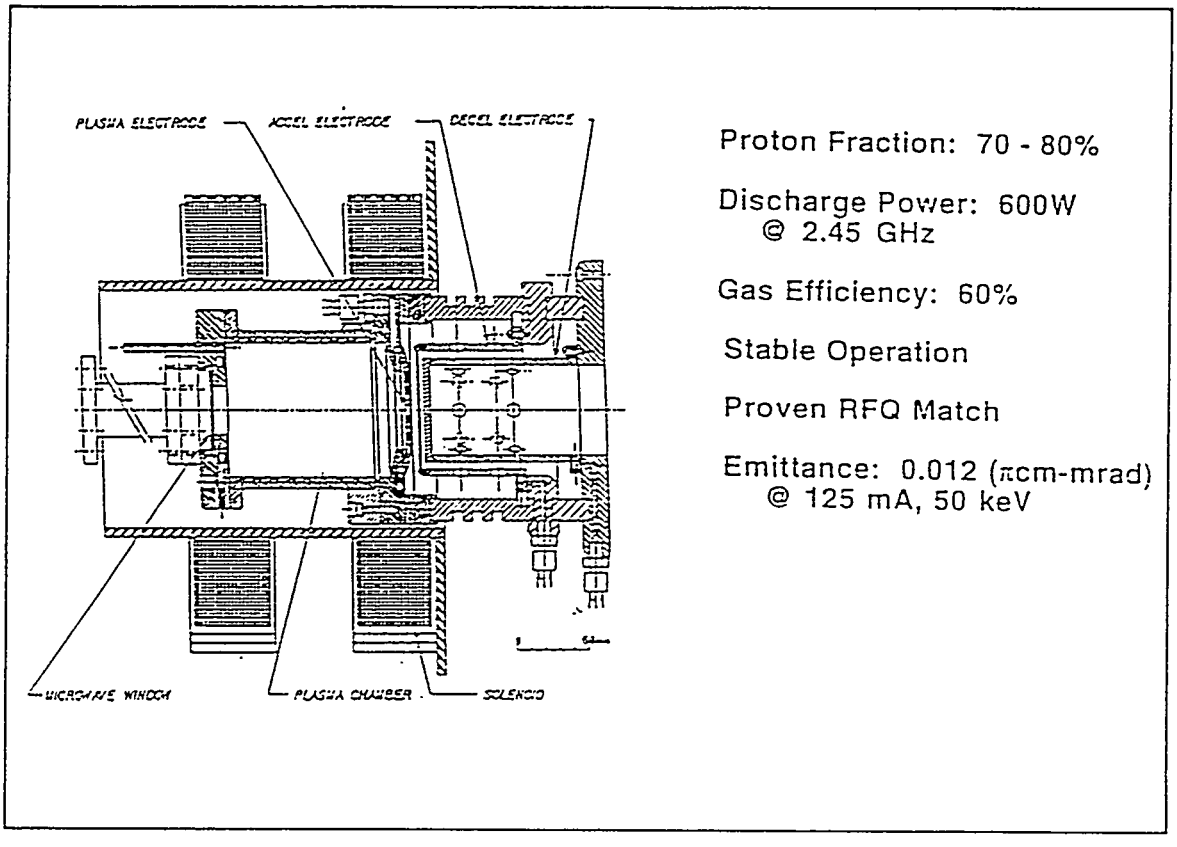


Fig. 2-5. The ECR proton source.

For the LEBT (low-energy beam transport) between the ion source and the RFQ, a two-solenoid focusing system was chosen over a quadrupole system. The use of solenoids minimizes aperture requirements and chromatic aberrations. In addition, cylindrical symmetry and space-charge compensation of the beam are maintained, and the required steering is easily implemented. To ensure a high proton fraction at the input to the RFQ, a mass analyzer is needed to filter out higher-mass ions. Figure 2-6 shows a sketch of a mass-analyzed LEBT including a 90° bend to filter out molecular ions.

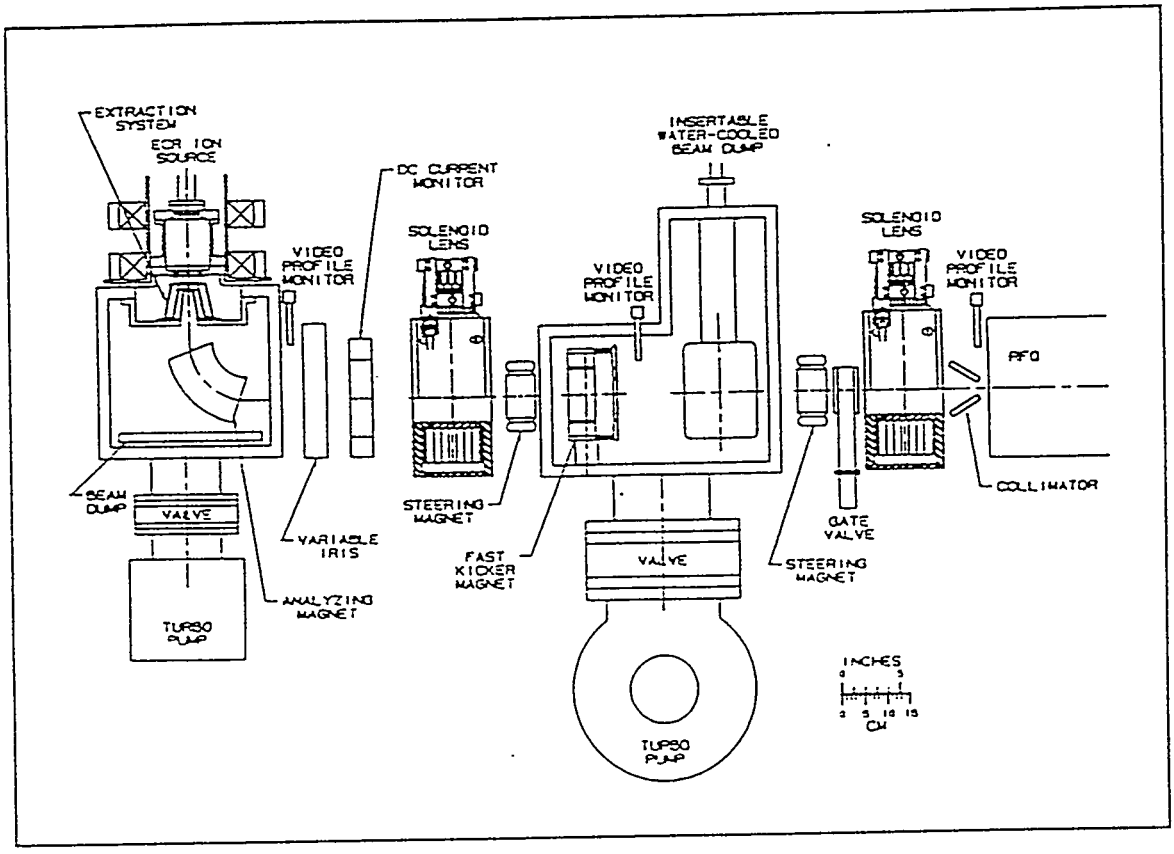


Fig. 2-6. A mass-analyzed LEBT with the ECR source and solenoids.

2.3.2 Radio-Frequency Quadrupole (RFQ)

The RFQs bunch the continuous proton beams from the injectors at 350 MHz and accelerate them to 7 MeV. Two unique features of the APT RFQs are the relatively high output energy (7 MeV) and the segmented design. The structure consists of four segments that are each approximately two meters long. They are mechanically connected but electromagnetically isolated. Because of electric-field coupling at the vanetips, the four segments of the RFQ are resonantly coupled, are driven in common phase, and function together as a single unit. The 7-MeV RFQs would be the longest ever built (over 8 meters) and require special mechanical supports.

Another feature of the RFQ design is that the relatively high output energy allows a reduction in the transverse focusing strength at the RFQ output, providing a better match to

the focusing strength at the DTL entrance. This improved match allows easier turn-on of the accelerator from low current to full beam intensity, without readjustment of focusing elements. Additionally, because the separation between the RFQ and DTL is proportional to $\beta\lambda$, more space is available for matching-section elements and diagnostics.

The 350-MHz APT RFQs were designed using the computer codes CURLI and RFQUICK. The codes give current limits and prescriptions for each section of the RFQ, including the radial matching section, and the shaper, gentle buncher, and accelerating sections. Peak surface electric fields are ≤1.8 times the Kilpatrick sparking limit. The ratio of transverse-vanetip-radius-of-curvature to average-aperture (which determines the strength of RF-field multipoles) was chosen to be 0.85, and is held constant throughout the structure. Because contributions of higher-order multipoles tend to lower the RFQ peak surface fields, the parameters chosen in this design were a tradeoff to lower the peak surface fields and still maintain the required current limit. The four-segment RFQ is shown in Fig. 2-7, and the parameters are given in Table 2-2.

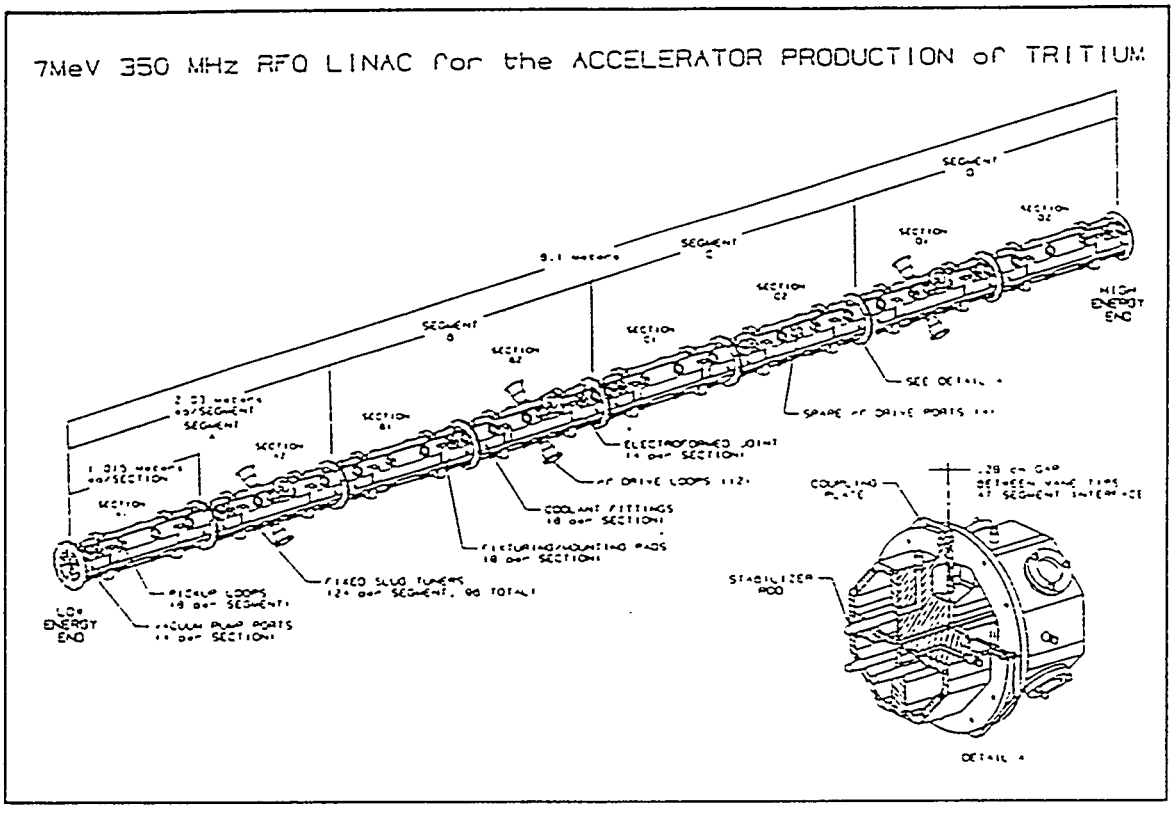


Fig. 2-7. APT four-vane, four-segment RFQ.

An RFQ-to-DTL matching section follows each RFQ. The matching section contains six EMQs (electromagnet quadrupoles) for matching the transverse phase space, and two single-gap 350-MHz RF bunchers for matching the longitudinal phase space. In the transverse planes, the phase advance per cell at the RFQ exit is 21°, whereas it is 20° at the DTL entrance, constituting a very smooth focusing transition between these two components of the accelerator. This matching section as presently designed is ~0.65 meters long.

Table 2-2. APT RFQ Parameters

Energy (MeV)	0.075–7.000
Frequency (MHz)	350
Input Beam Current (mA)	105
Transmission	95.2%
Structure Type	4-vane
No. of Segments	4
No. of RF Modules	2
No. of Cells	433
Total Length (m)	8.10 (9.45 λ)
Radial Aperture (cm)	0.235
Peak Surface Field (Kilpatrick)	≤ 1.8
Synchronous Phase (deg)	-90 to -30
Average Power Density (W/cm^2)	≤ 12
Structure Gradient (MV/m)	0–1.75
Structure Power (MW)	1.12
Beam Power (MW)	0.70
Total RF Power (MW)	1.82
Efficiency	0.385
Special Design Features:	• dipole mode suppressed • variable-radius vanetips • loop coupled
Construction Features:	• integral envelope for vacuum, RF, and structure • tellurium-copper, joined by electroforming

2.3.3 Drift-Tube Linac (DTL)

The two legs in the low-energy region of the APT accelerator each include a conventional (Alvarez type) DTL, which accelerates the beam from 7MeV to 20 MeV. Each DTL is comprised of three tanks. The angle between the two low-energy legs leading into the 20-MeV funnel is close to 45°, as illustrated in Fig. 2-8. The 350-MHz DTL frequency permits the drift tubes to be large enough to allow room for EMQs, which are much more radiation resistant than PMQs. The first DTL tank has a ramped accelerating field gradient, while the second and third tanks have constant gradients. The starting accelerating gradient in the first tank is chosen to provide nearly the same longitudinal focusing strength as at the RFQ exit, which helps to minimize current dependence in the intermediate matching section. Similarly, the final DTL gradient is adjusted to match the longitudinal focusing strength of the BCDTL (at 20 MeV). The maximum DTL accelerating gradient is limited by RF power density considerations in the structure (where the drift-tube stems join the drift tubes).

The transverse focusing strengths in the DTL are also selected so that they closely match those in the adjacent accelerating structures; that is, the phase advance per unit length at the DTL entrance and exit is the same as that in the RFQ and the BCDTL, respectively. With this focusing arrangement, the funnel and connecting matching sections (at 20 MeV) are nearly independent of beam current and provide essentially an adiabatic transport from the DTL to the BCDTL.

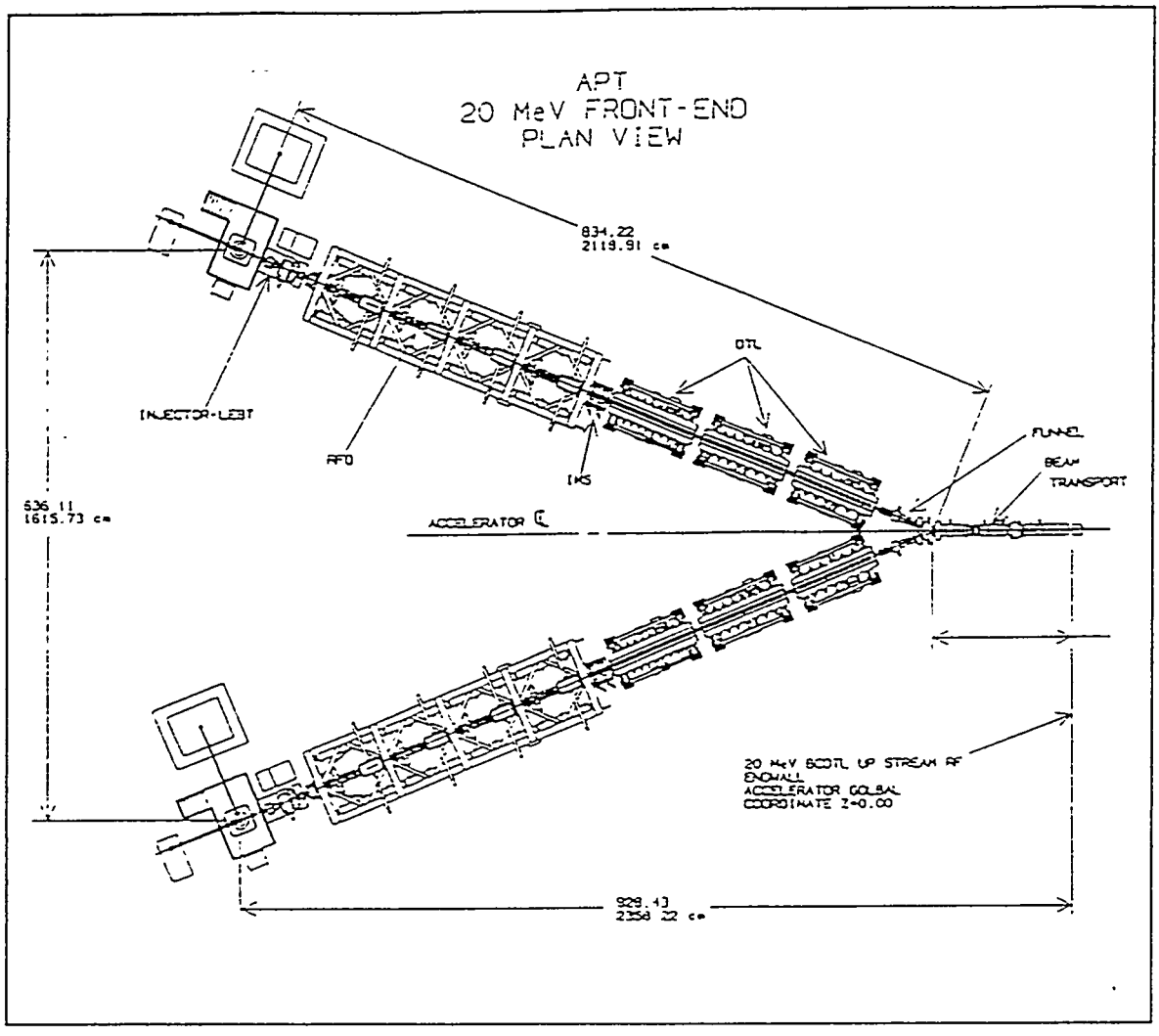


Fig. 2-8. Plan view of the low-energy accelerator system, including the 20-MeV funnel.

The DTL tanks were designed using SUPERFISH, with peak surface electric fields held below 1.0 times the Kilpatrick limit. All the drift tubes in each tank are to be mounted on a common girder; this feature greatly facilitates installation, alignment, and maintenance. Post couplers are included in each tank for stabilizing and leveling the longitudinal electric field distribution. Key parameters of the two DTLs are given in Table 2-3.

Table 2-3. APT DTL General Parameters

Energy (MeV)	7.0–20.0
Frequency (MHz)	350
Beam Current (mA)	100
No. of RF Modules	3
No. of Assembly Units	3
No. of Tanks	3
No. of Cells per Tank	Tank 1 (22), 2 (18), 3 (15)
Length of Cells	$1\beta\lambda$
Length of Tanks (m)	2.44–2.50
Total Length (m)	7.98
Intertank Spacing	$2\beta\lambda$
Radial Aperture (cm)	1.00
Aperture/Beamsize(rms) Ratio	4–5
Peak Surface Field (Kilpatrick)	<1.0
Synchronous Phase (deg)	-35 to -25
Average Power Density (W/cm^2)	~22
Structure Gradient (MW)	1.04–2.80
Shunt Impedance (MΩ/m)	30.2–32.8
Structure Power (MW)	1.153
Beam Power (MW)	1.300
Total RF Power (MW)	2.453
Efficiency	0.530
Quadrupole Lattice	FOFODODO
Quadrupole Effective Length (cm)	5.7
Quadrupole Gradients (T/m)	25.0–35.0
Quadrupole Spacing (cm)	10.4–17.4 ($1\beta\lambda$)
Quadrupole Phase Advance/Period (deg)	80–70

2.3.4 The Funnel

A feature of the APT linac design is the beam funnel. The funnel combines the 100-mA beams at 20 MeV from the two low-energy linacs each consisting of an H$^-$ injector, LEBT, and 350-MHz RFQ and DTL, as described earlier. Bunched beams exiting the DTLs are phased 180° apart at 350 MHz and are merged into a single 700-MHz bunched beam. The funnel interlaces the two beams emerging from the DTLs as shown schematically in Fig. 2-9.

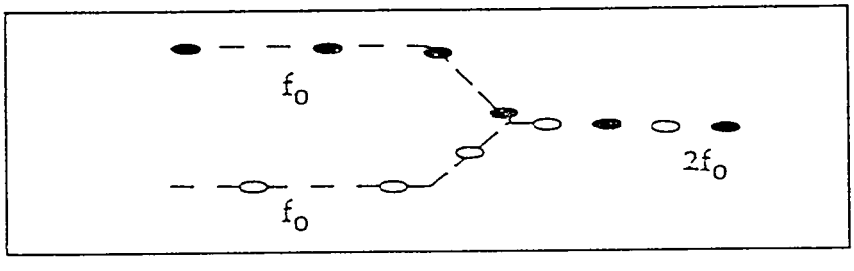


Fig. 2-9. Interlacing bunches in the 20-MeV funnel.

The two 350-MHz beams are brought close together by two transport systems that each include several RF bunching cavities to maintain longitudinal compactness of the bunches.

Final interlacing of the bunches is done in a 350-MHz deflector cavity that provides a transverse RF electric field. Bunches from each input leg of the funnel are given opposite deflections by this cavity to cancel their transverse momentum. At the cavity exit, there is a single (colinear) beam having a frequency of 700 MHz. Funneling doubles the average and peak currents of the beam, but does not increase the charge per bunch or the emittance.

The arrangement of components in the funnel is shown in Fig. 2-10. Each leg of the transport region consists of eight EMQs and two conventional, two-gap, 700-MHz bunchers. The transport regions are extensions of the DTL focusing lattice, providing the same transverse and longitudinal focusing found at the exit of the DTL. The bunchers operate at 700 MHz (second harmonic of the beam) to provide smaller cavities and save space in a fairly tight geometry. The second buncher cavity in each leg has a tapered shape to enable the close lateral packing that is required by the merging beamlines. The last quadrupoles in the individual transport legs are PMQs because of the need for compactness, while the merging quadrupole in front of the deflector cavity is a large-bore EMQ. Both beams enter this quadrupole off-axis (which is defocusing horizontally), and the resulting dipole field bends each beam close to the final combined-beam direction.

The two dipole magnets in each transport leg bend the beam 9.8° each, while the merging EMQ deflects each beam an additional ~1°. The remaining ~2° of bend required to combine the beams is accomplished by the RF deflector cavity. The transport section buncher cavities were designed using the 2-dimensional code SUPERFISH, whereas the design of the two-hole buncher (R1) in the merging section was refined using the three-dimensional code MAFIA. The initial physics design of the deflector cavity was done with the code CHARGE2D; however, to account for the cooling requirements in cw operation, the initial geometry was modified using SUPERFISH. Parameters specifying the funnel design are given in Table 2-4.

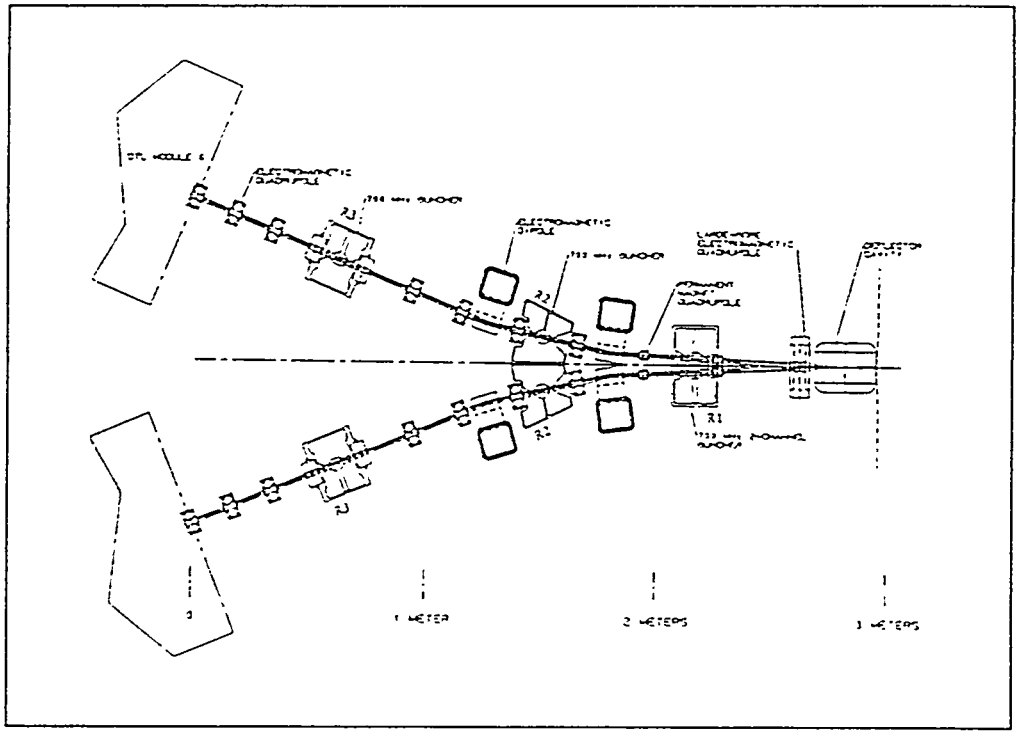


Fig. 2-10. APT 20-MeV funnel layout.

Table 2-4. APT Funnel Parameters

Energy (MeV)	20
Frequency (MHz)	350/700
Beam Current (mA)	2 x 100 (In); 200 (Out)
Length (cm)	295
No. of Quadrupoles	21
No. of Dipoles	4
No. of Bunchers	5
No. of Deflectors	1
Initial Beam Angle (deg)	22.4
Initial Beam Separation (cm)	137.8
Radial Aperture (cm)	1.0 (0.6 @deflector-bend plane)
Aperture/Beamsize(rms) Ratio (cm)	4.3 @ deflector, 5.5 @ PMQs
Quadrupole Lattice	FOFODODO
Quadrupole Length (cm)	5.7
Longitudinal Bunch Size (rms)	±5.5° @ input, ±3.3° @ deflector

Funneling is necessary in the APT linac architecture to meet the high beam-current performance specification. This technique permits the injector and RFQ to operate well below their current limits by reducing the requirement by a factor of two. Funneling also fills all RF cycles in the high-energy accelerating structures of the linac, thereby keeping the charge per bunch and thus the emittance and transverse beamsize as small as possible. This, in turn, significantly decreases the potential for beamloss in the high-energy structures of the linac.

A relatively high funneling energy of 20 MeV was chosen to reduce the impact of space-charge forces and allow enough longitudinal space for electromagnets (in most locations) as well as adequate beam diagnostics. The high funneling energy makes the deflector cavity mechanical design more challenging, but still practical.

The technology of funneling was partially demonstrated in the Los Alamos Single-Beam Funneling Experiment (1990) using a 60-mA, H^- beam at 5 MeV and 425 MHz [2-1]. This single-leg experiment, which was part of the SDI-supported Neutral Particle Beam Program, was aimed at assessing the beam-dynamics performance of a funnel. The experimental results showed 100% beam transmission through the funnel, with good steering control, essentially zero transverse emittance growth, and only a small amount of longitudinal emittance growth (~15%). These results were completely in accord with the predictions of the simulation codes. A two-beam funneling experiment was completed at McDonnell Douglas (1991) using a 25-mA, H^+ beam at 2 MeV and 425 MHz. This experiment used a two-hole buncher, which proved to be effective. Several engineering issues concerning the placement of components in the two adjacent legs were resolved.

A complete two-beam funnel has not yet been demonstrated at the high current levels (2 x100 mA) proposed for the APT system, so there are still residual concerns. A principal issue is that the time-dependent deflection produced by the RF deflector (because the bunch length is finite) may cause significant transverse spreading of the bunch tails. This effect is minimized in the APT funnel design by maintaining a very short bunch length in the deflector cavity.

The beamline downstream from the funnel, which transports the 700-MHz beam to the BCDTL, is approximately three meters long and includes a matching section with two conventional two-gap bunchers, and seven EMQs. A bend magnet is included to permit

diversion of the beam into a diagnostic beamline for tuning the low-energy accelerator systems. This diagnostic beamline and its terminating beamstop have not yet been designed.

2.4 HIGH-ENERGY ACCELERATOR SYSTEMS

2.4.1 Bridge-Coupled Drift-Tube Linac (BCDTL)

The BCDTL (bridge-coupled drift-tube linac), a module of which is shown in Fig. 2-11, is a new accelerating structure that was designed especially to meet the requirements of the 20–100-MeV energy portion of the APT point design. In an earlier study (1989), a CCL (coupled-cavity linac) structure was proposed for this energy region. After further examination, the use of a CCL in this relatively low-energy region was found to be both impractical and inefficient. A low-energy CCL structure would have considerable RF power dissipation, caused by the poor shunt impedance arising from the large bore and high density of end walls. The possibility of multipactoring was high, and the engineering and fabrication difficulties of assembling and cooling such densely packed cells were serious. The traditional Alvarez-type DTL would also have been impractical at 700 MHz because sufficient space would not be available for EMQs in the drift tubes, and the structure aperture would have been too small. The BCDTL solves these design problems by longitudinally separating the accelerating and focusing functions. The BCDTL consists of short (7-cell) 1-$\beta\lambda$ drift-tube tanks connected by RF bridges. Focusing elements (quadrupole doublets) are located between tanks, rather than inside the drift tubes themselves, which allows room for EMQs. Drift-tube apertures can be large since there are no quadrupoles in the drift-tube housings. Retention of the 2π-mode accelerating structure, with no internal cell walls provides a high shunt impedance, similar to that in a conventional DTL.

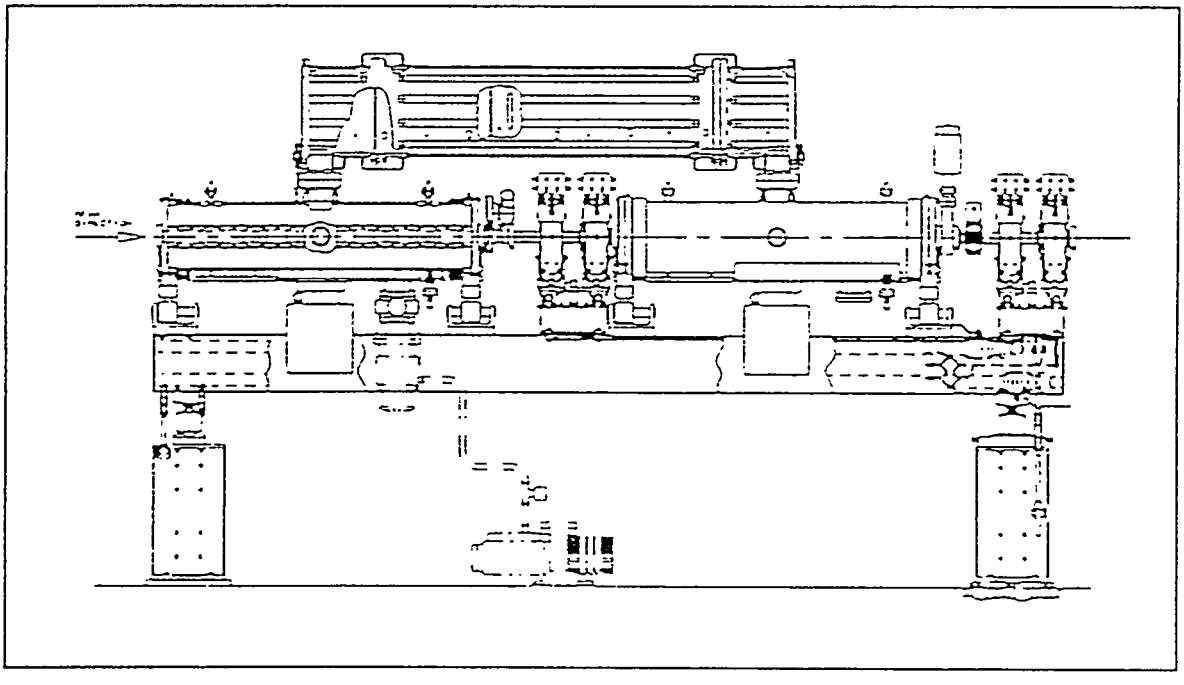


Fig. 2-11. An APT BCDTL module, showing two tanks and two quadrupole doublets.

r accelerating-structure solution for the APT frequency
gy range. It is easier to fabricate and align, will cost less,
ciency. The RF bridges, which couple energy into the
eral axially-coupled resonant cells. The APT BCDTL
re each 7βλ long. These tanks are coupled together in
ielding 24 RF modules. An example of a 2-tank BCDTL
Fig. 2-11. Also seen in Fig. 2-11 are the quadrupole
he BCDTL. Because quadrupoles are not inside the drift
of the drift tubes in the tanks is noncritical. They can
/alls for positive RF and vacuum sealing.

e listed in Table 2-5. As can be noted in the table, a
L at 52.3 MeV in tank spacing, structure aperture, and

eters

Entire Structure (20–100 MeV)	Before Transition (20–52 MeV)	After Transition (52–100 MeV)
20–100	20–52	52–100
52.29*		
700		
200		
24	9	15
24	9	15
61	28	33
7		
1 βλ		
0.615–1.281 (7 βλ)		
5 βλ–3.5 βλ	5 βλ	3.5 βλ
93.66	37.78	55.88
2.00–2.25	2.00	2.25
8–13		
1.70–1.50	1.70	1.50
1.00		
26.0–36.7	26.0–36.7	30.5–27.9
≤25		
≤1.0		
6.91		
16.10		
23.01		
0.711		
12.6λ–10.5 βλ		

quadrupole lengths at the end of RF module #9. The inter-tank spacing is 5$\beta\lambda$ upstream of the transition and 3.5$\beta\lambda$ downstream. At the same location, a change also occurs in the structure gradient. The DTL tanks operate at a structure gradient of 1.7 MV/m up to the transition energy of 52.3 MeV, and at 1.5 MV/m above this energy. These factors yield an approximate average (real estate) gradient of 1.0 MV/m throughout the BCDTL, with a slight jump at the transition.

2.4.2 Coupled-Cavity Linac (CCL)

The final APT accelerating structure, the CCL, accelerates the beam from 100 MeV to 1000 MeV. The 1000-MeV single-tank CCL module is shown in Fig. 2-12. The main physics design objectives are to assure very low beamlosses and high RF conversion efficiency. The former is achieved by maintaining a very large aperture dimension relative to the rms transverse beam dimensions, and a large longitudinal acceptance relative to the longitudinal bunch dimensions. Design features that provide this environment in the CCL include large physical apertures, a high density of transverse focusing elements, precise transverse alignment, and tight RF phase and amplitude control. High RF efficiency is achieved by a low structure gradient, the relatively high structure frequency, and structure apertures that are not excessively large. The design balance between low beamloss and high efficiency is largely controlled by the choice of aperture dimension.

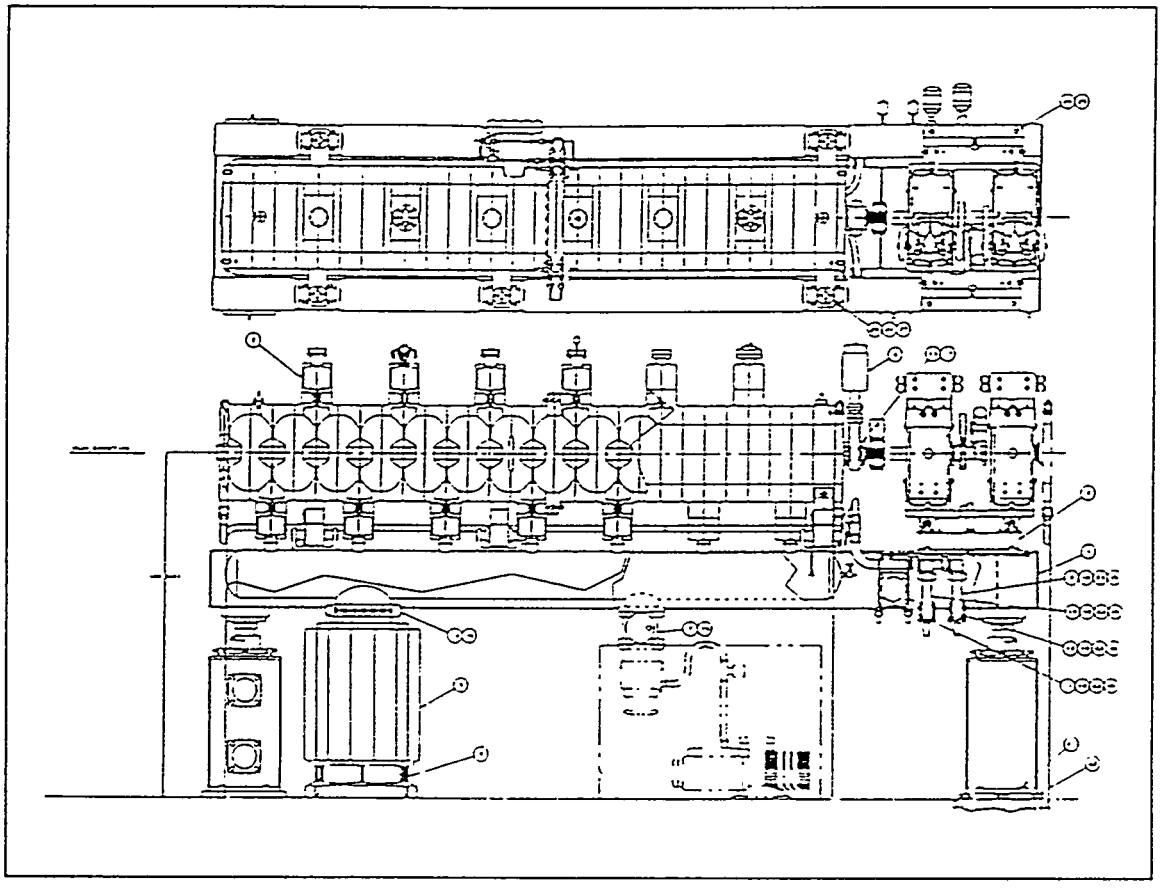


Fig. 2-12. One CCL module (1000 MeV) with focusing quadrupole doublet.

The CCL is composed of 342 tanks, with each tank supplied with RF power by its own klystron. Each tank has 14 cells and is $7\beta\lambda$ in length, spaning a range of 1.29–2.62 meters. Including the tanks and intertank spacings, the overall length of the CCL is more than 1 km (1031.4 meters). As with the BCDTL, the structure assembly is modular. The cell-to-cell coupling scheme is through unexcited (but resonant) side cells, as in LAMPF.

Key design features of the room-temperature CCL structures include not only the use of large apertures (for ultra-low beamloss), but also low electric-field variation within each tank, accelerating gradients well below the sparking limit, and wall-power densities low enough to ensure adequate cooling in cw operation. The CCL structures were designed using SUPERFISH. Table 2-6 gives a detailed list of the parameters.

Table 2-6. APT CCL Parameters

Energy (MeV)	100–1000
Frequency (MHz)	700
Beam Current (mA)	200
No. of RF Modules	342
No. of Assembly Units	302
No. of Tanks	342
No. of Cells per Tank	14
Length of Cells	$\beta\lambda/2$
Length of Tanks (m)	1.29–2.62
Total Length (m)	1031.44
Intertank Spacing	3.5 $\beta\lambda$ (100–371 MeV)
	2.5 $\beta\lambda$ (371–1000 MeV)
Radial Aperture (cm)	2.50
Aperture/Beamsize(rms) Ratio	13–26
Structure Gradient (MV/m)	1.50 (100–371 MeV)
	1.36 (371–1000 MeV)
Average Gradient (MV/m)	1.00
Shunt Impedance (MΩ/m)	23.31–37.42
Average Power Density (W/cm^2)	≤8
Peak Surface Field (Kilpatrick)	≤0.6
Structure Power (MW)	42.49
Beam Power (MW)	180.39
Total RF Power (MW)	223.18
Efficiency	0.806
Length of Focusing Period	10.5 $\beta\lambda$–9.5 $\beta\lambda$
Transit-Time Factor	0.82–0.86
Synchronous Phase (deg)	-30
Quadrupole Lattice	FDO
Quadrupole Lengths (cm)	11.0 (100–246 MeV)
and Doublet Spacing (cm)	15.0 (246–636 MeV)
	18.0 (636–1000 MeV)
Quadrupole Gradients (T/m)	29.3–38.0 (100–246 MeV)
	24.4–38.0 (246–636 MeV)
	29.3–37.4 (636–1000 MeV)
Quadrupole Pole-tip, Maximum (T)	0.950
Quadrupole Phase Advance/Period (deg)	70

Quadrupole doublets are located between CCL tanks to provide the transverse beam focusing. A comparative study of singlet (FODO) and doublet (FDO) focusing schemes showed that doublet focusing provides a 30%–40% improvement in the transverse aperture-

to-beamsize ratio. The penalty is that twice as many magnets, and higher magnet powers are needed in the doublet scheme. Three different quadrupole lengths are used to avoid exceeding safe pole-tip field levels.

The side-coupled CCL is a well-characterized and technologically mature accelerating structure and has been designed using well-established procedures. Because the CCL and BCDTL have the same focusing periodicity (quadrupole-doublet interval) at the boundary between the structures ($10.5\beta\lambda$), the transition between these segments of the linac is smooth. Simulations show that a matching section between the BCDTL and CCL is probably not needed. If limited matching adjustment is nevertheless required during tuning, the last two doublets of the BCDTL and the first two doublets of the CCL could be used for this purpose. Likewise, limited longitudinal matching could be accomplished, if necessary, by adjusting the phase and amplitude of the accelerating tanks adjacent to the transition.

2.5 HIGH-ENERGY BEAM TRANSPORT SYSTEM

2.5.1 Overview

The HEBT (high-energy beam transport) system transports the 200-mA, 1-GeV beam exiting the accelerator to either a full-power tuneup beamstop or one of two identical tritium-production targets. The HEBT (Fig. 2-13) consists of a periodic transverse focusing lattice immediately downstream from the accelerator, a dc switching magnet that directs the beam to one of the three beamlines, and the three transport beamlines to the beamstop and production targets. Following the switching magnet, each beamline includes a matching section followed by a beam expander that greatly increases the transverse beam dimensions and converts the traverse intensity distribution from a pseudo-Gaussian or parabolic distribution to a nearly uniform rectangular distribution. The beamstop line is used primarily during linac

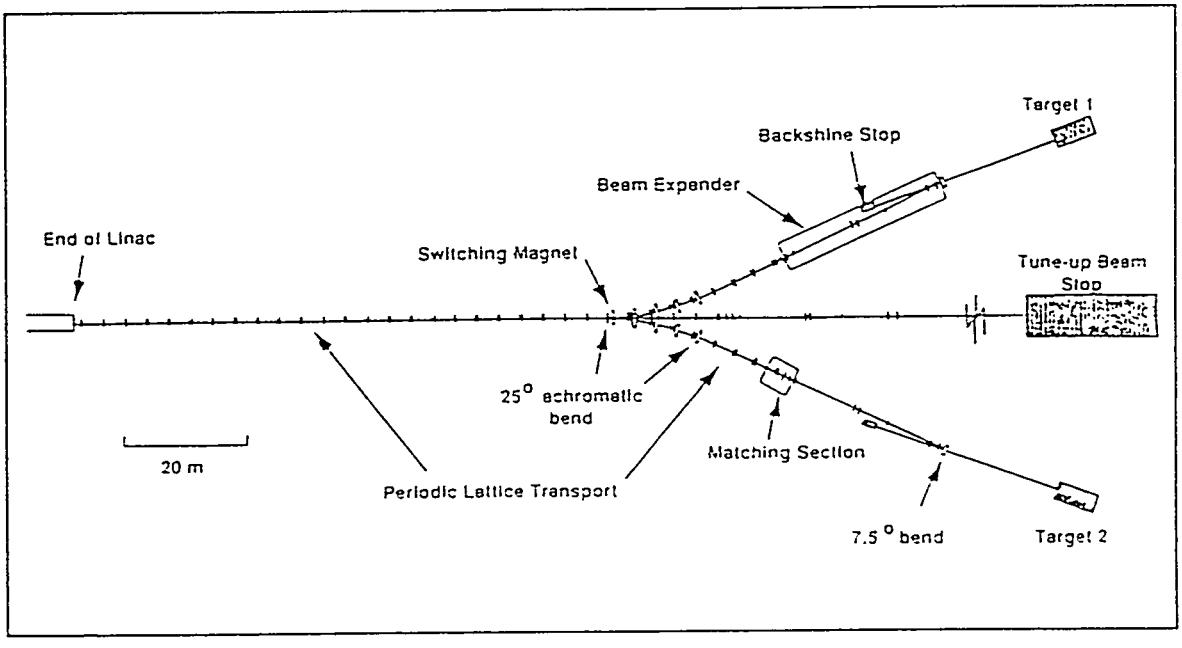


Fig. 2-13. Overview of the HEBT system.

startup and tuning, before the beam is switched to one of the targets for tritium production. The two target transport lines include large angle bends to provide the required physical (lateral) separation of the target cells. The target-cell separation distance is chosen to allow the common tritium extraction facility to be located in between. A final, small, reverse bend at the end of each target beamline enables shielding of the transport lines from neutron backshine produced by the targets. A key strategy used to design the HEBT, as with the accelerator, was to avoid any significant acceptance transitions for the beam.

2.5.2 Transport

The first section of the HEBT is a simple periodic lattice that continues the same geometry and transverse focusing as the high-energy end of CCL. This section is approximately 86 meters long. A major purpose of this first section is to allow the beam to spread longitudinally and thereby reduce space-charge forces (longitudinal focusing does not occur in the HEBT). The space-charge tune depression decreases from ~10° at the beginning of the HEBT (accelerator exit) to ~2° at the end of this section. The space-charge forces downstream from this point become relatively insignificant.

A switching magnet following the periodic lattice directs the full-energy beam to one of three transport lines. These lines are at 0°, and ±25° with respect to the linac centerline. The 0° (straight-ahead) beamline is used for tuning the accelerator and is terminated by a full-power beamstop. For each of the two target lines serving the tritium production targets, the switching magnet is the first element of a five-cell second-order achromat that bends the beam a total of 25°. Each cell of the achromat consists of a 5° bending magnet and a quadrupole doublet, retaining the geometry and closely approximating the transverse focusing pattern of the first section of the HEBT.

Following the bends, a short (~10-meter) periodic focusing lattice and a four-quadrupole matching section prepare the beam for the expander. The matching section produces a highly correlated beam (large in one transverse plane and small in the other). The periodic lattice provides additional space for diagnostics to measure and monitor beam parameters. In particular, this section can be used to detect and control (with fast steerers) transverse beam position jitter that could degrade the performance of the expander.

2.5.3 Beam Expander

The beam expansion that takes place at the end of each of the transport lines is accomplished through the use of nonlinear manipulation of the transverse phase space (x, x' and y, y'). Each expander consists of two multipole magnet elements (octupoles plus duodecapoles) and four quadrupoles, with one multipole and two quadrupoles manipulating each of the orthogonal phase planes.

The final magnetic element in the production target lines is a 7.5° (reverse) bending magnet, which is placed immediately downstream from the last expander element. Shielding is placed around this final bend to protect most of the HEBT from the flux of back-streaming neutrons originating from the target. The total distance to the target from the end of the linac, including the length of the expander itself, is ~46 meters. A sketch of the expander region, shielding, and the front face of the target cell is shown in Fig. 2-14.

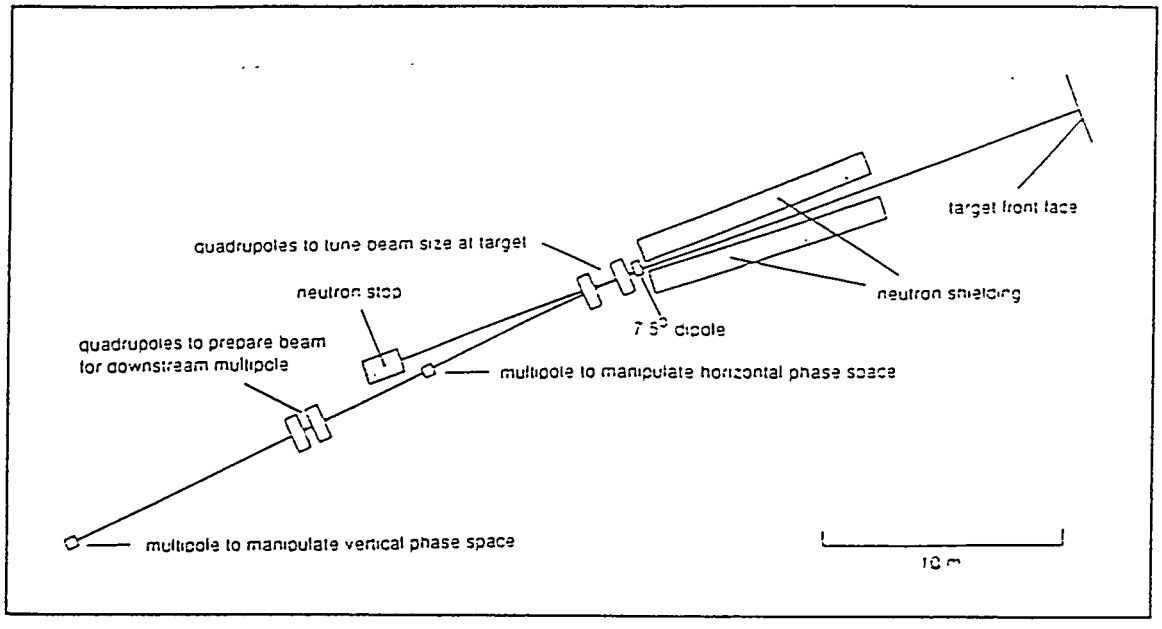


Fig. 2-14. Nonlinear beam expander and target configuration.

The expander converts the small-radius Gaussian-distributed beam exiting the linac into a large-area nearly-uniform rectangular distribution at the target. The beam fringes (the portions of the beam far from the centroid) are "folded in" towards the center of the distribution by action of the expander multipole elements, thus flattening the overall distribution. In addition to profile flattening, the expander transforms the beam from a round or elliptical distribution in (x-y) space to a rectangular one. The uniform rectangular distribution at the target minimizes the local former deposition density (eliminating a central hot spot), and also permits a uniform thermal load in the target cooling-channel array (which is aligned along one axis of the beam footprint).

2.5.4 Performance

The APT HEBT design is relatively insensitive to fluctuations in beam current and energy. Any matched beam (but with equivalent Courant-Snyder parameters) from 0–200 mA has similar x and y envelopes throughout the transport lines, with no noticeable difference in beam distribution on the targets or beamstop. Beam energy variations up to ±10 MeV have a negligible affect on the beam envelopes throughout the HEBT, but cause some skewing of the beam intensity distribution at the target.

HEBT diagnostics are largely similar to those used in the accelerator to characterize the beam and provide input for corrector elements and the beam abort systems.

The principal safety concern in the HEBT is a "loss-of-beam-expansion" event (caused by failure of one or more transport or expander magnets) that would result in an unacceptably high local power-density deposition in the target (or beamstop). The baseline protection plan consists of a redundant (multiple-layer) diagnostics-based beam abort, using the principle of defense-in-depth. The present reference design for the HEBT calls for electromagnets throughout, with only the expander magnets fabricated from permanent-magnet materials. The latter compromise is necessary to achieve the desired multipole field strengths in the

large bore sizes required to transmit beam tails out to 7σ. A fail-safe solution to the "loss-of-beam-expansion" problem would be to employ permanent magnets for all elements of the HEBT (and final sections of the CCL). However, this would require radiation-resistant permanent-magnet materials that have not yet been identified.

2.6 RF POWER SYSTEMS

2.6.1 Overview

The RF power system is the most expensive element of the APT accelerator, both in terms of capital and operating costs. For APT design parameters, about 80% of the RF power goes into the beam and the rest is deposited in the copper walls of the accelerating structures. About 376 high power cw RF amplifiers (klystrons) are required, 10 of them operating at 350 MHz and 366 of them at 700 MHz. The total RF power delivered to the accelerator is ~ 254 MW, resulting in a beam whose output power is 200 MW.

To develop a reference design, a number of baseline choices have been made for the RF system and its components. As indicated, the RF sources are klystrons, with a nominal 1.0-MW output-power capability. They contain modulation anodes to allow optimization of efficiency for a given output power level. Large cross-section waveguides (WR1500) are used to distribute power in the 700-MHz systems. A protective circulator is included in the driveline of each klystron, and accelerating-structure resonance control is accomplished via cooling-water temperature adjustment. RF amplitude and phase for each accelerating module are regulated through a feedback system based on in-phase and quadrature (I&Q) control of low-level RF (LLRF) inputs. Feedforward will be implemented in addition to feedback to provide system stability in the face of beam intensity transients. The primary components of an RF module are shown in Fig. 2-15.

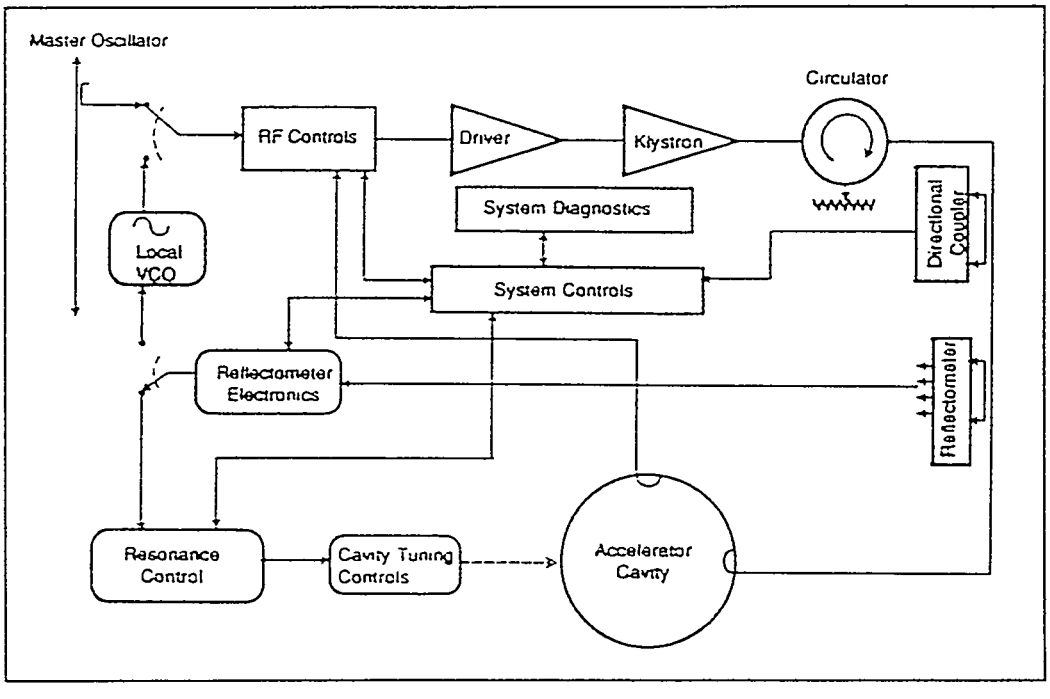


Fig. 2-15. Primary components of an RF module.

2.6.2 Klystrons

The klystron (a velocity-modulated electron-beam tube) is presently the RF generator of choice for APT frequencies and power requirements. Off-the-shelf 1.0-MW cw units are available from industry at 350 MHz, and a 1.0-MW 700-MHz tube is well within the familiar design space.

Other kinds of RF amplifiers are potential candidates for driving the APT linac, including the klystrode, multi-beam klystron, magnicon, and regotron. However, the maturity of these alternate technologies is low, making reliability projections impossible. By contrast, there is extensive experience with klystrons. All large high-frequency accelerators use klystrons, and an MTBF (mean time between failures) of 20,000 hours or better has been well demonstrated. Klystrons have long lifetimes because they have no beam-intercepting elements such as grids, and they also offer large power gain (>40 dB) which simplifies overall system design. Furthermore, when the RF input is reduced or eliminated (because of a beam fault) the electron beam power is deposited in the collector, so that no power transient is placed on the electric power grid. Most important, klystrons already exist at about the power level and within the frequency range needed for the APT linac.

2.6.3 Klystron Power Supply

The power for all the klystrons is provided by a single 500-MW dc bus, energized by two 250-MW ac-to-dc converters, as seen in Fig. 2-16. The use of a small number of large converters, rather than a large number of smaller converters provides significant advantages in terms of cost and ac-to-dc conversion efficiency. However, a resulting penalty is that isolation of single klystrons (for fault handling) becomes an important design issue. Some dc conditioning, diagnostics, and equipment protection between the klystrons and the dc bus is required. For example, the converters use 12-pulse thyristor valves for control, with extensive monitoring and alarm indication on each valve. Fast isolation switches are located upstream of each klystron, and use counter-pulse circuits to open the dc bus connection.

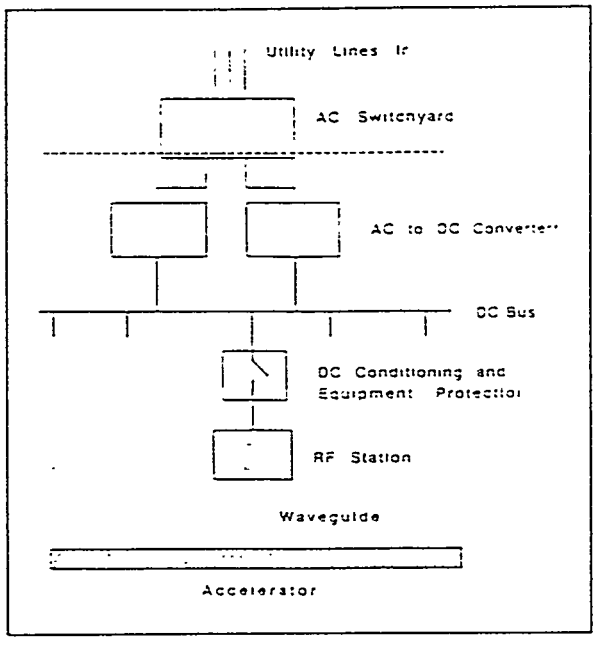


Fig. 2-16. RF power conversion and distribution.

2.6.4 Availability and Reliability

The availability of the APT RF power system is estimated to be about 97.9%, excluding the time for scheduled maintenance. The calculations were made with constant hazard rates (because true hazard rates are unknown), assuming 383 klystrons (which includes some spare

units), two ac-to-dc converters, two dc conditioners, and 48 water-cooling circuits (each cooling circuit having 8 klystrons each and a cooling-water flow rate of 450 gpm). This availability calculation applies to the RF system after the "burn-in" or initial tube conditioning phase. As a reference, the KEK linac availability from the years 1991 to 1992 was 97.7%, with 5125 hours of scheduled operation and 116.6 hours of downtime. The fault rate for their klystrons decreased from 2.5 faults per klystron-day in 1982 to 0.2 faults per klystron-day in 1991. All high-power components in the APT RF system are designed for higher-power-than-normal operation to greatly increase the reliability. Reliability estimates for the major RF components are shown in Table 2-7.

Table 2-7. RF Component Reliability Estimates

Component	MTBF (hours)
High Voltage Power System	100,000
Power Conditioning	100,000
RF Controls	100,000
Klystron	20,000
RF Transport (Waveguides)	150,000
Water-Cooling System	40,000

2.6.5 RF Efficiency

Table 2-8 summarizes the various power conversion efficiencies and total efficiency for each segment of the APT linac. The second column of data from the left indicates the average conversion efficiency of power from the grid to dc power available on the high voltage bus supplying the klystrons. The next column indicates the average conversion efficiency from dc electron beam power to RF power in the klystrons, accounting for the fact that the accelerating structures are modularized in such a way that not all tubes operate at full output ratings. The next column reflects typical waveguide losses in the RF transport from klystrons to accelerating cavities. The beam loading column shows the RF efficiency averaged over each segment of the linac. This is just (P_B/P_B+P_C) where P_B is the power imparted to the beam and P_C is the power lost in the cavity walls. Total efficiency is thus the efficiency of conversion of ac power to beam power in each part of the accelerator, and the total ac power requirement for the RF system is just 200 MW/0.435 = 459.8 MW.

Table 2-8. RF System Efficiency

Cavity	Total RF Power (MW)	ac to dc (%)	dc to RF (%)	RF Transport (%)	Beam Loading (%)	Total Efficiency (%)
RFQ	3.6	99.0	53.0	95.0	38.5	19.0
DTL	4.9	99.0	55.0	95.0	53.0	27.4
BCDTL	22.5	99.0	59.0	95.0	71.1	39.5
CCL	223.2	99.0	59.0	95.0	80.7	44.8
Overall	254.2	99.0	55.3	95.0	78.7	43.5

To attain the highest efficiency RF power distribution in the 700-MHz system, the waveguide size WR1500 was selected over WR1150. The comparative attenuation of the two waveguide sizes, assuming 30 meters of characteristic transport distances is 2.30% and 4.24%, respectively. The efficiency of WR1500 RF transport is better by almost a factor of two. In addition, if we compare estimated power densities for the two waveguide sizes (at APT power levels), we get 0.062 W/cm^2 and 0.155 W/cm^2. The lower power density for the WR1500 waveguide is easily air cooled.

2.6.6 Klystron Production

Timely production of the large number of high power cw klystrons for APT could be a concern. At present, there are three companies (all foreign) that make cw klystrons at power levels at or above 1.0 MW. These manufacturers have typically produced only 1–4 klystrons per month. A dedicated factory, however, might be able to produce up to 10 units per month. Supposing a reasonable construction schedule for the APT linac, we estimate a required production rate of about 30 klystrons per month. Thus, three such dedicated factories would be required to provide tubes for the APT power system.

2.7 ACCELERATOR SUPPORT SYSTEMS

2.7.1 Controls

Requirements for the accelerator control system include support not only for normal modes of operation, but also for tuneup, standby, commissioning, maintenance, and shutdown modes, as well as for fault handling and recovery. The control system includes a comprehensive operator interface providing timely information in a format that neither overloads the operator(s) nor requires superfluous operator actions. The control system automates digital control and sequencing algorithms, acquires, stores, and filters data on the accelerator performance; supports analysis of data, detects and predicts faults, and handles any kind of off-normal event.

Instrumentation and controls for the accelerator are integrated with a facility-wide control system, which includes controls for the target/blanket systems, tritium extraction, and balance of plant. This unified control concept ensures interoperability and clean subsystem integration, and leads to low implementation and maintenance costs. Because the accelerator places the greatest demands on the control system, we have chosen for the APT facility baseline-controls design an architecture that has worked successfully on a number of existing accelerator facilities. Operation of the accelerator is highly automated and specifically includes provisions for automatic fault detection and mitigation. A large number and variety of beam diagnostics and equipment diagnostics (that provide a continuous stream of information on the state of the beam and accelerator systems) are interfaced with the controls system.

The basic framework for the controls system is a distributed network architecture containing several IOCs (input/output controllers). An IOC consists of a fast microprocessor, such as a 68040 chip, and various I/O (input/output) modules in a VMEbus or VXIbus configuration. These IOC nodes are connected by a local area network (LAN), such as Ethernet or the FDDI. The advantages of this distributed approach are high performance, low hardware and software costs, modularity, and flexibility in location. Each IOC has direct

access to the I/O hardware and is powerful enough to perform fast, complex control algorithms and fault detection decisions. No hardware hierarchy is necessary to handle the processing load, and any required hierarchy is implemented through the software structure.

The software architecture is based on the Los Alamos EPICS (Experimental Physics and Industrial Control System) concept. This powerful system is being used successfully on several accelerator projects, including the GTA project at Los Alamos and the Advanced Proton Source at ANL. The EPICS approach allows distribution of processing power to the IOCs, yet permits efficient, system-wide sharing of data among distributed, cooperating processes. EPICS also includes applications development tools for building a fully operational, automated facility.

Operations and maintenance are conducted from operator-interface consoles that are based on modern workstations that run windowing technology on large color screens. During normal operations, the operators use multiple consoles in a central control room. During maintenance, portable (mobile) consoles with similar capabilities are used.

2.7.2 Beam Diagnostics

The goal of the APT accelerator diagnostics is to provide sufficient and necessary beam information to the accelerator commissioning staff and facility operators so that the machine can be operated safely and efficiently under normal conditions and also in expected off-normal conditions. Beam diagnostics can be divided into characterization diagnostics and operational diagnostics. Characterization diagnostics provide complete information that is only needed occasionally (such as a full measurement of the six dimensions of beam phase space), but usually at the cost of intercepting some of the beam. Operational diagnostics provide a subset of beam information (using noninterceptive or minimally-interceptive techniques) that is needed on a continuous basis. The average cw beam power density in the APT beam varies from tens to over a million kW/cm^2, and the operational diagnostics must be designed to operate throughout this range. The bulk of the beam diagnostics elements fall into the category of operational diagnostics.

2.7.2.1 Characterization Measurements

As previously indicated, characterization diagnostics measure the six dimensions of beam phase space, but intercept the beam. They are most useful in the low-energy portion of the accelerator and mainly during commissioning and machine startup after a long shut-down. With special care, beam characterization measurements can also be carried out at the high-energy end of the accelerator. These diagnostics are permanently mounted at key locations throughout the accelerator and temporarily at the end of each accelerator section during commissioning. For example, during commissioning of each of the 350 MHz DTLs, a set of characterization diagnostics is stationed downstream so that the beam phase space can be measured and the operational beam diagnostics can be calibrated. Typical beamline devices used for characterization measurements include Faraday cups, harps, slits and collectors, and segmented collimators. Faraday cups and segmented collimators are used in the injector and LEBT to measure beam current and beam position. Slit and collector hardware measures transverse emittance (under pulsed beam conditions), harps measure the expanded beam's profiles, and Faraday cups measure beam current.

Downstream from the funnel, there is a permanently installed diagnostic beamline (accessed by a energizing a bending magnet) that is used to characterize the funnel output.

This beamline incorporates interceptive transverse emittance, energy and phase-spread-measurement devices, and many of the same nonintrusive diagnostics devices used to monitor the accelerator operation during its normal operating mode(s). It may also be necessary to insert a similar diagnostic beamline at the 100-MeV point (downstream from the last BCDTL tank) so that tuning of the linac up to this point can be done without sending beam into downstream sections. These two diagnostic beamlines have not yet been designed. At 1 GeV, the 0° beamline and full beam-power beamstop will provide the necessary information for CCL tuning. This tuning line will contain mainly operational beam diagnostics and will require only a few characterization diagnostics.

2.7.2.2 Operational Measurements

Operational measurements are taken with permanent diagnostics that generally do not intercept the beam. Approximately 80% of these diagnostic devices are either microstrips or ionization chambers. Robust-designed microstrips (or striplines) are used to determine beam centroids, such as position, angle, phase, and energy. Ionization chambers positioned near the accelerator structure, but not in the beamline itself, are used to measure beamloss. About 10% of the operational diagnostics consists of video profile monitors and flying-wire profile monitors, both of which are used for measuring transverse beam profiles. When such monitors are placed in groups of three or more with the correct phase advance, transverse rms beam emittances can be measured in cw operation. Remaining operational diagnostic devices are movable graphite jaws for measuring beam halos, beam transformers (toroids) for measuring pulsed and dc-current intensity, and capacitive probes for measuring bunch phase spreads.

Microstrips and beamloss monitors are distributed throughout the entire APT linac, except for the injector, LEBT, and RFQ. A microstrip is placed between the two elements of every quadrupole doublet, and a beamloss monitor is placed adjacent to each doublet. Beam toroids are located before and after every major section of the accelerator to monitor beam transmission. Video profile monitors are used throughout the low-energy portion of the machine (to 100 MeV), followed by flying-wire scanners in the high-energy end. Beam-halo monitors (graphite jaws) are used in conjunction with ionization chambers (loss monitors) to tune the linac for minimum halo formation and beamloss.

All beam diagnostics, both characterization and operational, are designed for high reliability. All permanent operational diagnostics are designed to function at full cw beam current.

2.7.3 Vacuum System

The accelerator vacuum system is designed to evacuate and maintain a high-quality vacuum ($<10^{-7}$ torr) within more than 1.3 km of accelerator structure and beam transport lines. To maintain this vacuum, a large number of ion pumps are needed. Over 400 large (400 l/s) ion pumps are distributed along the linac for maintaining vacuum within the accelerating structures, and over 370 small (appendage) ion pumps maintain vacuum at the RF windows. Ion pumping is a mature, well-established vacuum technology, and has the advantage of ruggedness, high reliability, and long operating life; it remains the standard for most accelerator vacuum systems. Ion pumps are radiation resistant, vibration and noise free, require no oils or external cooling, have no moving parts, and have no exhaust or effluent. However, they operate only at pressures of 10^{-6} torr or below. To provide the initial evacuation of the accelerator, a small number of large turbomolecular (mechanical) pumps

are used. They bring the pressure down to $<10^{-6}$ torr, at which point the ion pumps take over. Some of these turbopumps have speeds of up to 2000 l/s. There are also a few mobile auxiliary turbopumps that are used for rapid local evacuation following the maintenance or repair of an accelerator module.

2.7.4 Water Cooling System

The quantity of cooling water that is circulated through the walls of the linac accelerating structures is about 22,500 gpm, and another 2000 gpm is circulated through the quadrupole magnet coils. These total quantities are, of course, broken down into several hundred individual modules that require no more than 50–100 gpm each. The cavity coolant is carefully temperature controlled (within 10C°) and circulates at high flow rates with relatively low pressure drops. The resonant frequency of each accelerating module is adjusted by means of the cooling water temperature, which sets the precise dimensions and volume of the individual cavities. Details of this frequency control method are discussed below. In addition, the cooling water is treated to prevent galvanic corrosion in the copper/stainless-steel joining sections. The primary loop coolant is potentially radioactive and is therefore confined to the accelerator tunnel area. Primary loop heat is exchanged to secondary and tertiary coolant loops that handle only nonradioactive water.

We can best understand the total cooling load by looking at the input and output power. The total ac power input to the accelerator and HEBT is estimated to be about 485MW. The power going into the beam is 200 MW. The remaining 285 MW is the sum of all the thermal losses in the RF cavities, klystrons, waveguides, focusing magnets, and power supplies in the accelerator, and in the bending and focusing magnets and their power supplies in the beam transport system. Most of this waste power ends up in the cooling water systems and is rejected to the atmosphere through the cooling towers. A small fraction is rejected directly to the accelerator tunnel and klystron gallery air systems. The total RF power dissipated in the walls of the accelerating cavities and waveguides is about 67 MW. The klystrons operate with dc-to-RF conversion efficiencies ranging from 53% (RFQ) to 59% (BCDTL & CCL), so approximately 188 MW of electron beam power is dissipated in the klystron collectors. The remaining 30 MW of power is lost in the ac-to-dc converters for the RF system, in the linac quadrupoles and HEBT magnets and their power supplies, and in many small loads distributed throughout the system.

2.7.5 Cavity Temperature/Resonance Control System

As mentioned above, the temperature of the primary coolant is used to control the resonant frequency of the accelerating structures. Cavity resonant frequency is linear with thermal expansion/contraction over a temperature range of about 10C°, within which a feedback control system operates. To maintain primary loop temperature, the coolant pumps drive heated water through a heat exchanger and a valve-regulated bypass line. The bypass valve receives control signals from an RF six-port analyzer that detects the RF phase of the cavity, and also from direct temperature measurements of the accelerating structure. The RF phase (relative to that of a master oscillator) indicates the amount of departure from resonance of a specific cavity or module. The temperature of the input coolant to the module is corrected to the required value by mixing the bypassed flow (hot) with the output of the heat exchanger (cooled). To maintain the accelerating structures in resonance at their specified operating frequency (within a tolerance of ±20 kHz), this coolant control system is designed to hold the average structure temperature within about ±1.7C°. A similar structure frequency control system is used in the LAMPF linac and in many other accelerators.

2.7.6 Alignment System

The system used for geometric alignment of the accelerator components is based on fixed horizontal- and vertical-reference monuments. These reference monuments are surveyed into the walls and floor of the accelerator tunnel and form a permanent grid to facilitate alignment of any module of the linac. The monuments are spaced no more than 10 meters apart and can give precision readouts to ±0.05 mm when used with alignment telescopes and optical levels, or plunging transits. The monuments themselves have tooling ball sockets that are used for making offset measurements. Alignment methods using laser-actuated or computerized spatial-locating optics can also be used with this system. Although it is assumed that the concrete and steel of the accelerator tunnel will be adequately stable, it is necessary only that the tunnel be stiff and stable within a 10-meter span. The most critical part of the monument system is the initial survey that locates the monuments themselves; this survey may have to be done several times and averaged due to thermal variations, shifting mass, etc. Once established, however, the monument system forms a reference grid to which components of the accelerator can be installed and aligned with confidence.

2.7.7 Magnet Power Supplies

Several hundred dc power supplies are needed to energize the many magnets in the accelerator and beam transport lines. More than 400 quadrupole doublets are located in the high-energy portion of the accelerator (BCDTL plus CCL), each requiring a high-current, regulated power supply. The HEBT requires another 50 power supplies to activate the doublets, dipoles, and matching quadrupoles that transport and manipulate the 1-GeV beam. At the low-energy end of the linac, more than 30 power supplies are required for the funnel, for the DTL EMQs, for the matching section EMQs, and for the solenoids in the LEBT. In addition, but needing only very small amounts of power, there are several-hundred small steering magnets distributed throughout the accelerator.

Magnet power supplies, current shunts, and power-supply controls are located in the klystron gallery building above the accelerator radiation shield. Rigid bus-bar conductors connect the power supplies with the magnet loads, and can be installed in the same tunnel penetrations as the RF waveguides. About 30 km of such conductors are needed for the linac and HEBT, assuming an average distance of 25 meters between each magnet and its associated power supply. Except for the steering elements, the power supplies typically deliver several hundred amperes (highly regulated) at modest voltages (40V dc). Applying a conservative power factor rating of 0.75 to each magnet supply (on average), the total magnet-related power demand for the linac and HEBT is estimated to be about 10 MVA.

2.8 INTERFACES TO ACCELERATOR

The seven major interfaces to the accelerator are represented by the connections to the RF power system, cooling system, vacuum system, pneumatics, instrumentation, ac power distribution for the magnet supplies, and the alignment system. These interfaces are labeled in terms of tunnel coordinates relative to a master reference point "BL0" (butt line zero), as explained in more detail in Chap. 9. A summary of the interfaces follows:

- RF Power Interface. The location of the RF power interface is defined by the particular physical structure. For example, two-, three-, and four-tank modules with one, two, or three bridge couplers are located in the BCDTL. For a module

with three bridge couplers (for example), the center one has the RF window, which defines the interface. In the CCL, each accelerator tank is driven through an iris and RF window in a centrally located cell; the iris defines the interface. In the lower-energy structures, such as the RFQ, DTL, funnel, and matching-section cavities, either waveguide or coaxial inputs define the RF power interface. All interfaces are given in tunnel coordinates.

- Cooling Systems Interface. All accelerator modules are equipped with radiation-resistant ball valves on the cooling system lines. In general, each module has two sets of such valves: one for the cooling line to the RF tanks, and one for the cooling line to the quadrupole doublets. For the RFQ, only structure cooling is required. The ball valves are the facility interfaces, defined in tunnel coordinates. Flexible hoses are attached to these valves, connecting the individual loads to the primary cooling loops.

- Vacuum Interface. Each accelerating module has four hard connections for vacuum. One connection is for the ion pump (or other pumping package in the case of the injectors and RFQ). Another connection is available for attachment of the mobile roughing pump package when required. The other two connections are for the permanently-mounted roughing pump system.

- Pneumatic Interface. Almost all accelerating modules have a hard-connect interface which receives the air supply for the electro-pneumatic beamline gate valves. The interfaces to the valves are defined by the coordinate locations of the flange surfaces. The approximately 380 gate valves are CF 63-mm (2.5-inch) aperture units. These valves have been chosen for their radiation hardness and their minimal leak rates. The air-control valve and limit-switches for each vacuum valve are attached to the main body of the valve. In case of electrical failure, the valves will automatically close, thereby protecting the vacuum integrity of the accelerator modules. Before such closure takes place, the run-permit protection system of the accelerator will shut the beam off so that no damage will occur to the valve gate. The air pressure required to actuate the valves is 70–100 psig. Since the valves are held open with air pressure, a facility air-line or lines must be provided down the length of the tunnel to which all 380 valves are connected. A backup compressor and pressurized air reservoir are provided to maintain adequate line pressure in the event of failure of the primary compressor. In case of an air line break, the valves would close, but the time delay is much greater than the time needed by the run-permit system to interrupt the beam, so again there is very little danger of beam damage to the valve gates. The use of electro-pneumatically operated valves such as described here is standard accelerator practice and unanticipated closure of beamline valves due to electrical or air failure is extremely rare (as supported by experience at LAMPF).

- Instrumentation Interfaces. A major interface is with the instrumentation. The amount of instrumentation is substantial. All equipment is interfaced on a module-by-module basis through connectors or hard-wired cables. Complete disconnection of a module or assembly unit from signal, power, and instrumentation leads at the module itself is the design basis. The instrumentation includes:

  - beam diagnostic and measurement devices,
  - beamloss monitors,
  - RF pickup loops,
  - thermocouples and thermocouple gauges,

- vacuum valve-limit switches and vacuum gauges,
- flow meters and switches,
- kinematic positioners,
- directional RF couplers and arc detectors,
- appendage pump readouts (at the vacuum side of the RF windows), and
- ion-pump high-voltage cables.

- **Magnet Power Interface.** About 1000 individual quadrupoles, dipoles, and solenoids are found in the APT design. Most quadrupoles are grouped in doublet pairs; some, such as those in the DTL, are powered as a series of singlets. Each doublet and each series of singlets requires a separate, current-regulated, remotely controllable dc power supply, which is located above the earth shielding in the klystron gallery building. The interface with the facility is defined as the 480-V, three-phase, ac input to these power supplies.

- **Alignment Interface.** An alignment interface exists between the facility monument system and the module adjusters that are mounted on the accelerator support pedestals. This interface is not a physical connection of any kind; however, it is essential that the monument system be installed before the support pedestals are put into place. This interface is schedule-driven during the final stages of construction.

2.9 OPERATION AND SAFETY SUMMARY

2.9.1 Linac Operation

2.9.1.1 Maintenance

Special maintenance considerations are required for the high-power APT linac. First, there is the potential for activation of the accelerating structures, which could require remote handling at some locations. In addition, tunnel temperatures will be high because of the high operating temperature of the cooling water. Small components of the linac that are expected to require periodic or frequent maintenance have been identified and have been made accessible for rapid service. To address the maintenance of large components, the entire machine has been modularized, or packaged, into sections not exceeding 5 meters in length. These modules or assembly units can be removed and transported to the lab, where they may be repaired or fully checked out off-line for alignment, RF tuning, vacuum, coolant integrity, and so on. If local machine activation exceeds hands-on maintenance limits, the tunnel and accelerator design includes all support capabilities that would be required as well as the necessary room for mobile remote-handling equipment.

2.9.1.2 Startup and Tuning

The accelerator startup and tuning sequence requires different kinds of beam operations for the different stages of the process. The beam needed for initial tuning of the linac and HEBT optics would be a very low-duty-factor low-peak-current beam that is threaded through the system to establish centroid corrections and focusing magnet settings. This beam is limited to a few tens of microamperes (average current) and is used principally to: (1) check the condition of steering and focusing elements, (2) establish the low-current tune

of the linac and HEBT, and (3) ascertain that all accelerator systems are ready for high power operation. Final alignment of focusing elements will be accomplished at this stage, using readouts of the position monitor system to determine the necessary corrections.

The beam needed for high-power tuning would begin as a low duty-factor, high-current pulsed beam. It will probably be preferable to start this process with low peak currents and increase the peak current in steps. Full-energy beam power would constitute tens to hundreds of kilowatts at this stage, and use of the expander and the full-power beamstop would be required. The beam macropulses would be initated with a long ramp slow enough to be followed by the RF control system, and would reach full amplitude only after about 100 μs. Final adjustment of the focusing lattice and of the RF station amplitudes and phases would take place at this point. After full peak current has been reached successfully at low duty factor, the beam pulse lengths would be gradually increased until cw conditions are achieved.

2.9.1.3 Fault Recovery

To recover from an accelerator fault, a fast magnetic deflector in the LEBT would be used to abort the beam, typically in <20 μs. A variable iris would then be inserted into the LEBT and adjusted to ramp up the current from a low value to full current. As the beam is increased, RF amplitudes in all the accelerating structures are ramped to maintain the proper energy gain. The iris adjustment would be slow enough that the linac focusing-lattice tune could be altered as the current increases, if necessary. The iris would be designed to handle beam impingement for long periods of time, so that operation at reduced cw currents can be accommodated while machine adjustments needed to reestablish low beamloss operation are carried out. Although irises have been used on pulsed sources, they have been built but not tested on cw sources. Experience on the FMIT injector, with beamstops of a similar design to that needed for this iris, has demonstrated the practicality of this device. There would probably be a long-term sputtering problem if the iris were to be used continuously to collimate the beam; however, this is not anticipated for the fault recovery scenario discussed here.

2.9.2 Safety and Protection

2.9.2.1 APT Hazards and Engineered Safety

The hazards associated with the APT accelerator are not much different in kind than those associated with existing proton linacs: but because of the high power, they are different in degree. Because of the high beam power, a significant potential exists for damaging energy deposition in accelerating structures and in beam transport lines if the beam is misdirected or misfocused even for short time periods. A significant potential also exists for activation of the accelerator structures if a very small fraction of the beam (>10^{-8}/m) is lost on a continuous basis. For this reason, special features have been included in the APT linac design that greatly reduce the potential for damaging beamspills and/or continuous low-level beamloss.

Engineered safety is an essential feature of APT. As noted elsewhere, the potential for continuous low-level loss is mitigated by the very large aperture-to-beamsize ratio in the linac structures. Distributed throughout the accelerator and beamlines are multiple, redundant sensors and diagnostics, all acting within very short time intervals (microseconds) to determine if the beam is out of acceptable limits in terms of position, angle, size, phase, energy, transmission, intensity distribution, and local loss rate. These detectors are integrated

into several layers of machine protection systems that prevent thermal damage and/or activation buildup by fast beam abort as needed. Secondary information is provided on accelerator vacuum, coolant flow and temperature, integrated beamlosses along the linac, amplitude and phase of the RF power stations, energizing currents in the focusing magnets, etc., to confirm the correct operation of the beam manipulation elements of the accelerator and transport systems. Malfunctions or out-of-tolerance values for any of these devices automatically terminates or limits operation until the situation is corrected.

The impact of hazards on safety and the environment has been evaluated. If the engineered safety systems should fail and significant beamloss should occur, the impact would be one of equipment damage rather than personnel safety or releases to the environment. There are no accelerator malfunctions that can significantly affect offsite personnel or the environment. However, the machine activation hazard is of concern because of potential exposures to accelerator personnel in maintenance operations on affected equipment.

2.9.2.2 Designs for Personnel Safety, and Machine and Environmental Protection

The design philosophy with regard to safety in the APT linac is based on standard practices and protection systems in use at existing accelerator facilities, such as LAMPF. The safety and protection design includes both passive and active elements.

Passive safety measures include the thick earth shield covering the accelerator tunnel and a complete tunnel seal to prevent significant leakage of air that may have been activated by beamloss during normal and/or off-normal operations. The tunnel shield thickness, 12 meters of compacted earth, provides a large safety margin against DOE-mandated exposure limits even for worst-case accident scenarios (full-energy spill of the entire beam for one hour).

In addition to the passive safety design, there are five active safety systems that are an integral part of the APT accelerator design. These are:

Machine Protection:	(1) Fast Protect System (2) Beam Permit System
Personnel Protection:	(3) Personnel Safety System (PSS)
Environmental Protection:	(4) Activated Air Handling System (5) Activated Cooling Water System

The fast-protect system is a hard-wired, ultra-fast-response network of distributed monitoring devices that sense status inputs from accelerator diagnostics and interrupt the beam in the LEBT in the event of a failure mode, fault, excessive beamloss, accelerator (or target) parameter exceeding preset limits, etc. The fast-protect system is intended to protect the accelerator from possible damage due to faults. Sensor response time is estimated to be about 1–5 μs, with signal transmission to the injector <4 μs and maximum transport time for beam in accelerator <7 μs. This translates to a maximum of <16 μs total response time from a sensed fault to a beam abort. We have taken 20 μs as the nominal beam-abort time.

The beam-permit system inhibits beam turn-on until all relevant accelerator, beam transport, and target conditions are fully satisfied. These conditions include inputs or instrumentation readouts to be compared to the operating setpoints for cooling-water flows and pressures, RF system parameters, vacuum pressures, magnet currents, etc. The conditions also include inputs from various beam diagnostics to ensure that beam position, transmission, and profile measurements are within acceptable ranges. An out-of-range parameter *drops* the beam permit. A key input to the beam-permit system is the personnel safety system, described below. Action of the beam-permit system is slower than the fast-protect system.

The personnel safety system (PSS) is a combined radiation-monitoring system and entry permissive interlock system (based on removable keys). The PSS keeps personnel out of the accelerator tunnel whenever the possibility of measurable radiation exposure exists, and prevents beam operation in an area that has been opened to personnel. The output of this system is connected to the beam-permit system, so that the accelerator cannot operate or deliver beam to a given area until the complete PSS chain is made up.

The impact of air activation from beamloss in the APT linac tunnel has been evaluated for the APT Programmatic Environmental Impact Statement (PEIS). Activated air is prevented from leaking to the enviroment by effectively sealing the tunnel during operation. Following beam shutdown, activated air isotopes decay rapidly (minutes to hours). The tunnel air-handling system allows purging of the tunnel air through a stack prior to the entry of service personnel, but only after activation levels have fallen below levels that would not exceed DOE-mandated dose limits to maximally exposed individuals at the site boundary.

We have also allowed for the handling of potentially-activated cooling water. Although (based on LAMPF experience) we do not anticipate the generation of significant quantities of activation products in the linac cooling water, the primary coolant loops are designed as if the water were activated. Water treatment and resin-bed filtration will be used to ensure that the cooling water will be as clean as possible. These facilities may be located at the accelerator tunnel level in shielded alcoves, or in shielded locations within surface structures adjacent to the klystron and power supply gallery. Radioactive water drains will be provided in the linac tunnel, and facilities for radioactive water storage will be provided to deal with losses of water from the primary coolant loop.

Safety of the HEBT/target interface is an important consideration. The HEBT directs a high-current, high-power beam from the linac to the target window through a beam expander to provide uniform beam-energy density on the target. A local increase of beam power density on the target (because of a loss of beam expansion) is the hazard of greatest concern, because of the potential for release of radioactive material from the target. A multilayered interlock and diagnostic system is included in the HEBT point design to defend against this potentially hazardous event. The multiple layers of defense include interlocked magnet power supplies and magnet current setpoints, beam distribution diagnostics (multiwire detector), a fusible ribbon in front of the target window, and target temperature diagnostics. The fusible ribbon concept is a promising option that could provide a high degree of passive protection against excessive power density on target, but it has not yet been designed or developed for this kind of application. The combination of the several safety systems places the possibility of damaging the target window or the HEBT/target interface region into the category of Residual Risk. In the very unlikely event that this multi-layered defense should fail and the target window indeed would be damaged or breached, sensors in the HEBT would detect loss of vacuum, trip the beam through the fast-protect system, and close the fast-acting valves (that are included in the HEBT design) before the accelerator could be damaged.

REFERENCES

2-1. K.F. Johnson et al., "A Beam Funneling Demonstration: Experiment and Simulation", *Particle Accelerators*, Vols. 37-38, pp 261-268 (1992).

PHYSICS AND ENGINEERING DESIGN
CHAPTER 3

Page

3.1 KEY PARAMETER SELECTION 1
3.1.1 Beam Current and Energy 1
3.1.2 Accelerating Structure Frequencies 1
3.1.3 Accelerating Structure Gradient 2
3.2 FOCUSING SYSTEM TRADEOFFS 2
3.3 BEAM SIMULATIONS AND ERROR STUDIES 4
3.3.1 End-to-End Simulation of the APT Accelerator 4
3.3.2 CCL Failure Mode Studies 8
3.3.2.1 Introduction 8
3.3.2.2 Effects of Quadrupole-Doublet Failure 8
3.3.2.3 Effects of Single RF-Module Failure 10
3.3.2.4 A Possible RF-Module-Failure Recovery Scheme 13
3.3.3 Simulations with Reduced Beam Currents 15
3.3.4 Tolerance Estimates for CCL Errors 16
3.4 LOW BEAMLOSS REQUIREMENT 18
3.4.1 LAMPF Reference Analysis, Activation Estimates 19
3.4.2 Beamloss Control Measures in APT Linac Design 21
3.5 ELECTRICAL EFFICIENCY CONSIDERATIONS 23
3.6 ACCELERATING-STRUCTURE THERMAL CONSTRAINTS 23
3.6.1 Introduction 23
3.6.2 Maximum Power Densities 24
3.6.3 Cavity Frequency Response 24
3.6.3.1 Ambient Temperature 25
3.6.3.2 RF Heating 25
3.6.4 Material Stresses 25
3.6.5 Offset Tuning and Fabrication of Accelerating Structures 26
3.7 SPECIAL ENGINEERING DESIGN FEATURES 26
3.7.1 Linac Modularity 26
3.7.2 Designs for Radiation Environments 27
3.7.2.1 Radiation Hardened EMQs 27
3.7.2.2 Remote Handling Capability 28
3.7.3 Other Features 29
3.7.3.1 Prototype DTL EMQ 29
3.7.3.2 Metal Vacuum Seals 29
3.7.2.3 Copper-to-Copper RF Knife Edges 30
3.8 MECHANICAL SUPPORT FACILITIES 30

3.8.1 Alignment Laboratory 30
3.8.2 Vacuum Laboratory 30
3.8.3 RF Power Laboratory 31
3.8.4 Mechanical Maintenance and Remote Handling 31
3.8.5 Machine Shop 31
3.8.6 Diagnostics and Magnets Laboratory 32

LIST OF FIGURES

Page

Fig. 3-1. Doublet vs. singlet transverse focusing lattice. 2
Fig. 3-2. Aperture/beamsize ratios vs. energy for singlet/doublet BCDTL focusing lattice options. 3
Fig. 3-3. Aperture/beamsize ratios vs. energy for singlet/doublet CCL focusing lattice options. 3
Fig. 3-4. RFQ transverse, phase, and energy envelopes vs. RFQ cell number. 6
Fig. 3-5. DTL phase-space distributions at the end of tank 3. 6
Fig. 3-6. Funnel output phase-space distributions at 20 MeV. 7
Fig. 3-7. Transverse and longitudinal emittances vs. BCDTL cell number. 7
Fig. 3-8. Transverse, phase, and energy envelopes vs. CCL cell number. 8
Fig. 3-9. CCL output transverse emittance vs. beam energy of a failed doublet. 9
Fig. 3-10. Beam-profile plots for a single doublet failure (tank 51 doublet, 200 MeV) in the CCL. 10
Fig. 3-11. Beam-profile plots for a single failed RF module (module 51). 12
Fig. 3-12. Beam-profile plots for a single failed RF module (module 87). 12
Fig. 3-13. Loss profile for a module 87 failure. 13
Fig. 3-14. Profile plots for a module 6 failure with tanks 2 through 4 compensating. 14
Fig. 3-15. Probability distributions for random quadrupole rotation errors. 17
Fig. 3-16. Neutron yield vs. proton energy for copper/iron. 19
Fig. 3-17. Measured and simulated beamloss in the LAMPF CCL. 20
Fig. 3-18. LAMPF CCL activation measurements (12/15/92) beyond transition region. 21
Fig. 3-19. LAMPF beamloss vs. time into beam pulse. 22
Fig. 3-20. A typical BCDTL assembly unit or module. 27
Fig. 3-21. Proposed radiation-hardening fabrication procedure for EMQs. 28
Fig. 3-22. Prototype DTL EMQ. 29
Fig. 3-23. Quick flange. 29
Fig. 3-24. CCL vacuum and RF seal. 30

LIST OF TABLES

Page

Table 3-1. Emittance Results from APT BCDTL Doublet/Singlet Simulations 4

Table 3-2. APT Linac End-to-End Simulation Summary 5

Table 3-3. Twiss Parameters at 1 GeV for Single Quadrupole-Doublet Failures in CCL 9

Table 3-4. Results of Single RF-Module Failures in the CCL (Computer Simulations) 11

Table 3-5. Power Requirements for the Compensating Tanks 15

Table 3-6. Output Emittances for Matched 110-, 55- and 0-mA Beams into the RFQ 15

Table 3-7. CCL Output at 1000 MeV for Nominal and Reduced Beam Currents 16

Table 3-8. Levels of Radiation and Type of Maintenance 18

3.0 PHYSICS AND ENGINEERING DESIGN

3.1 KEY PARAMETER SELECTION

In the APT linac design, the key system parameters (beam current and energy, accelerating-structure frequencies, and accelerating-structure gradients) were chosen partly on the basis of trade studies using a simple cost model, partly by beam physics constraints, and partly by reference to the existing accelerator technology base.

3.1.1 Beam Current and Energy

The energy and current balance was chosen to meet the tritium production requirement at minimum cost and with a conservative design. Over a broad range of energy between 800 MeV and 2000 MeV, the beam power needed to produce the required amount of tritium is nearly constant. The choice of beam energy and current within this constant power level is dictated to some extent by target performance constraints, but more strongly by the need to maintain a high electrical efficiency and by overall accelerator operating economics. The electrical conversion efficiency of the accelerator is maximized (and the APT plant electrical consumption thereby minimized) by choosing the beam current to be as high as practical. The beam energy is then adjusted to provide the necessary beam power for the specified APT tritium production capability.

3.1.2 Accelerating Structure Frequencies

Factors governing the choice of the APT accelerating structure frequencies include the desirability of the following: (1) minimal emittance growth in the RFQ and DTL; (2) an RFQ output current of at least 100 mA with high beam transmission; (3) DTL drift tubes with dimensions large enough to accommodate electromagnet quadrupoles; (4) RFQ and DTL structures large enough to cool in cw operation; (5) high RF-to-beam conversion efficiency in the high-energy linac; (6) off-the-shelf availability of a high power cw klystron for driving the low-energy linacs; and (7) engineering practicality of high power cw klystrons for driving the high-energy linac. These considerations have resulted in the choice of 350 MHz for the low-energy linac structures, and 700 MHz for the high-energy linac structures. Because the APT linac design has a funneled architecture, the frequency of the high-energy structures is necessarily twice that of the low-energy structures. In comparing potential advantages and disadvantages of higher or lower frequency combinations, this factor-of-two relationship continues to apply.

At considerably higher frequencies than 350/700-MHz, the current carrying capability of the RFQ and DTL is much lower than desired, unless structure designs are pushed into high risk regions of the parameter space. Also the difficulty of fitting EMQs into the DTL drift tubes increases rapidly above 350 MHz. High-energy-structure RF efficiency does not increase much because of the necessity of retaining a relatively large beam aperture.

At considerably lower frequencies than the 350/700-MHz combination, the rms beam emittance emerging from the low-energy linacs is greater, the CCL RF efficiency is reduced, and the transverse physical dimensions of the structures become larger. The first effect may not be significant in terms of beamloss because the aperture-to-beamsize ratio does not change significantly. The second effect would increase the accelerator electric power requirements. The third effect makes the structures more costly and more difficult to handle.

3.1.3 Accelerating Structure Gradient

Accelerating structure gradients in the RFQ and DTL were chosen high enough to provide good longitudinal emittance control, but low enough to avoid excessive RF thermal loads in cw operation. The BCDTL and CCL gradients were chosen low enough to yield relatively small RF losses, without causing the linac to become excessively long. These low gradients (1.0 MV/m averaged over accelerating structures and intertank regions) help to produce high RF efficiencies and lead to nonstressing thermal loads in cw operation.

3.2 FOCUSING SYSTEM TRADEOFFS

In the front-end low-energy portion of the APT linac (<20 MeV), the principal design goal is to produce and maintain a high-quality, low-emittance beam. The importance of RF efficiency is secondary in this region. Strong transverse focusing and a ramped accelerating gradient in the 350-MHz DTL will accelerate beam with relatively low emittance growth.

In the high-energy portion of the accelerator (>20 MeV), the design balances the competing objectives of low beamloss and high RF efficiency. In assessing the probability of beamloss, the ratio of transverse aperture-to-rms-beamsize is chosen as a figure of merit. To minimize beamloss and associated accelerator structure activation, it is desirable to make this ratio as large as practical. This is accomplished by (a) minimizing beamsize through a high density of focusing elements, and (b) by keeping the structure apertures relatively large. However, a practical and competing design constraint is that the structure RF efficiency is lowered significantly if the bore size becomes too large (reduced transit-time factor). Another practical limitation is that large structure apertures demand large aperture quadrupoles. The focusing strength in these magnets is limited by the maximum pole-tip fields that are attainable (pole-tip fields increase linearly with aperture dimension).

The initial choice of focusing lattice for the BCDTL and CCL sections of the linac was a singlet (FODO) scheme. This scheme was attractive at first because it minimized the number and strength of the quadrupoles. However, as the design evolved, intertank spacings were increased to allow more room for flanges, bellows, and beam diagnostics. These adjustments significantly lengthened the FODO lattice periods and reduced the transverse focusing per unit length, increasing the average beamsize. A doublet (FDO) focusing lattice was then examined to determine whether it would provide a better solution for achieving small average beamsize. Figure 3-1 shows the general structure of the singlet and doublet focusing lattices.

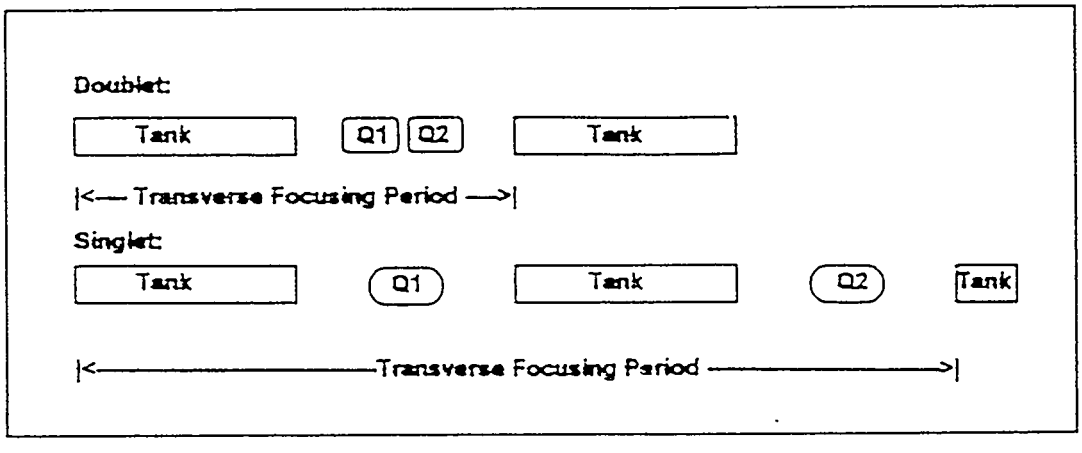


Fig. 3-1. Doublet vs. singlet transverse focusing lattice.

In the focusing comparison study, beam-dynamics simulations were run for both FODO and FDO schemes using 4000 macroparticles. Figures 3-2 and 3-3 show the results for the BCDTL and CCL, respectively. Figure 3-2 compares the singlet and doublet transverse aperture-to-rms-beamsize ratios as a function of beam energy along the BCDTL. It can be seen that the ratio is in the range of 6–8 for the singlet case and 10–15 for the doublet case.

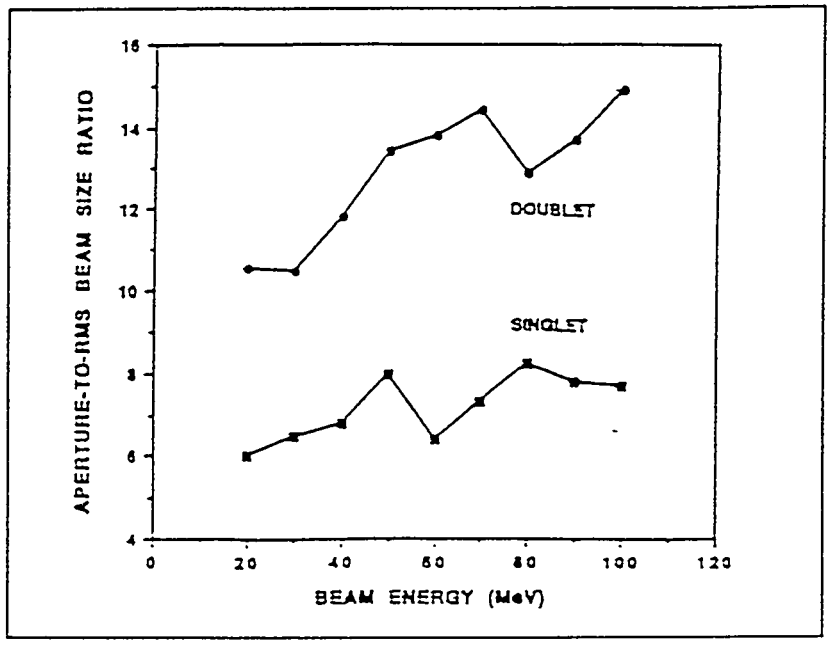


Fig. 3-2. Aperture/beamsize ratios vs. energy for singlet/doublet BCDTL focusing lattice options.

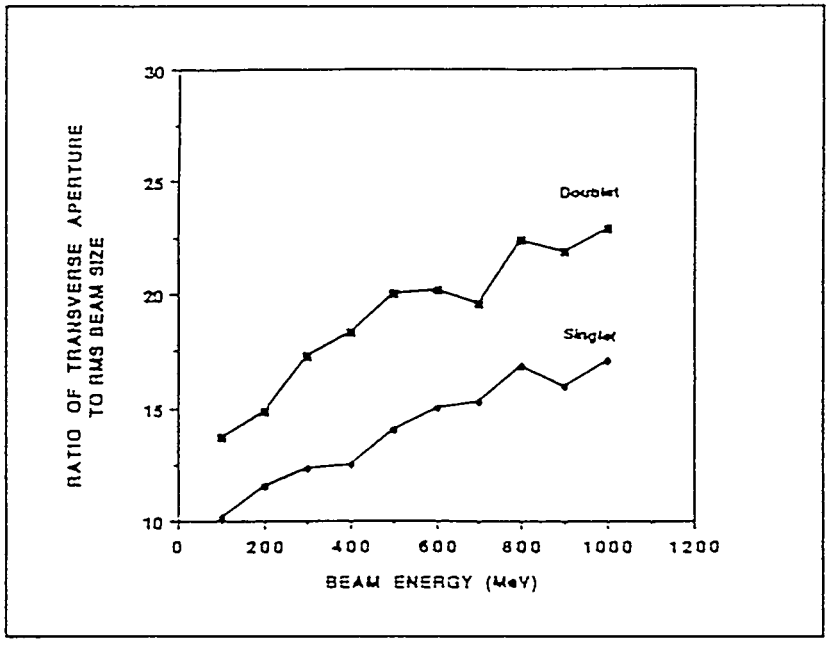


Fig. 3-3. Aperture/beamsize ratios vs. energy for singlet/doublet CCL focusing lattice options.

Table 3-1 summarizes emittance results for the BCDTL singlet/doublet simulations. The doublet scheme exhibits much less transverse emittance growth than the singlet scheme because of the stronger transverse focusing of the FDO lattice. Because of somewhat longer intertank spacing in the doublet case (two quadrupoles instead of one), increased longitudinal emittance growth is observed. Similar results are achieved for the CCL as can be seen in Fig. 3-3 and Table 3-1. There is approximately a 30% improvement in the transverse aperture-to-rms-beamsize ratio by using a doublet focusing lattice in the CCL.

Table 3-1. Emittance Results from APT BCDTL Doublet/Singlet Simulations

Emittance Plane	BCDTL with Doublets			BCDTL with Singlets		
	In	Out	$\mathcal{E}$-Growth	In	Out	$\mathcal{E}$-Growth
$Emit_X$, rms, norm (π·cm – mrad)	0.028	0.033	18%	0.028	0.041	44%
$Emit_Y$, rms, norm (π·cm – mrad)	0.028	0.033	18%	0.028	0.037	44%
$Emit_L$, 700 MHz (π·MeV – deg)	0.412	0.499	21%	0.412	0.370	–10%

From these simulations, the doublet lattice clearly provides a smaller average beamsize and less transverse emittance growth in both the BCDTL and the CCL. The doublet lattice does, however, require an additional magnet between accelerating tanks, and the field strengths are considerably higher than for the singlet scheme. There is thus a penalty to pay in terms of magnet power requirements. Also, the extra intertank space for the doublet scheme requires longer bridge couplers in the BCDTL.

3.3 BEAM SIMULATIONS AND ERROR STUDIES

3.3.1 End-to-End Simulation of the APT Accelerator

As a principal part of the design study for the APT linac, an end-to-end simulation of the complete, as-designed, ideal machine was carried out. The electromagnetic design geometry of each section of the accelerator (RFQ, DTL, Funnel, BCDTL, CCL, and matching sections) was modeled in detail in the beam-dynamics codes. The code physics incorporates the effects of RF acceleration, RF-defocusing, and both linear and nonlinear space charge effects. Magnetic focusing fields are included in a hard-edge approximation.

To initiate the simulation, a Monte Carlo distribution of 10,000 macroparticles is generated at the RFQ entrance. The macroparticles have the same charge-to-mass ratio as the protons, and the distribution is generated with a transverse emittance equal to that expected at the output of the injector. In longitudinal phase space, the input-beam distribution is launched with a 180° phase spread and no energy spread. The RFQ input current is 110 mA.

The macroparticle ensemble is transported sequentially through the various accelerating sections and associated matching sections of the linac. The parameters of each matching section are adjusted to provide an optimum match from one accelerating section to the next at

full beam current (100 mA from each leg into the funnel, and 200 mA downstream of the funnel).

Results of the end-to-end simulation are summarized in Table 3-2 and in the following plots. Figure 3-4 shows the simulation through the RFQ with a characteristic 5% beamloss following the capture section. The plot shows rms values for transverse (x-y) beam dimensions and for the bunch phase width ($\varphi - \varphi_s$) and energy width ($W - W_s$). Figure 3-5 shows phase-space plots of the beam at the exit of the DTL and Fig. 3-6 shows the phase-space at the exit of the funnel. Figure 3-7 shows the emittance through the BCDTL in all three planes. Note that there is no transverse emittance growth through this structure.

Finally, Fig. 3-8 shows the x-profile, phase, and energy spreads through the CCL. An additional 18 plots of the end-to-end simulation can be found in the Chap. 3 Appendix. It should be noted that the simulation shows zero particle losses following the RFQ. This is consistent with the design objective of very low beamloss in the CCL.

Table 3-2. APT Linac End-to-End Simulation Summary

Accelerator Section	Output Emittance (rms, normalized)		Emittance Growth (%)		Aperture-to-Beamsize (rms) Ratio
	ε_T (π·cm-mrad)	ε_L (π·MeV-deg)	Transverse	Longitudinal	
Injector	0.020	±180° phase spread	n/a	n/a	n/a
RFQ	0.022	0.220*	10	n/a	n/a
DTL	0.023	0.216*	5	-2	4–5
Funnel	0.029	0.436**	26	1	5–8
BCDTL	0.029	0.483**	0	11	8–13
CCL	0.032	0.608**	10	26	13–26

* for a 350-MHz RF cycle
** for a 700-MHz RF cycle.

It should be noted here that various types of simulations were performed on the APT linac involving different numbers of particles. The time needed for a beam simulation calculation increases rapidly with the number of macroparticles used to represent the bunch, and the precision of the results also increases with the number of particles. Thus there is a tradeoff between practical limits on computing time and desired level of detail. For the end-to-end simulation, where we are interested in developing an accurate and detailed picture of the beam evolution (emittance, beamlosses, etc.) for the accelerator reference design, it is necessary to use as large a number of particles as possible, consistent with reasonable computing time. The number 10,000 provides the desired precision, and only a single run is needed, so a long computing time is acceptable. On the other hand, to accomplish the error studies in Sections 3.3.2.2 and 3.3.2.3, it is necessary to carry out a large number of simulations reflecting different error conditions. For these calculations we are interested only in the gross features of the beam evolution, not the details. Therefore, the number of particles used per run can be reduced to a smaller number (like 500) to allow many runs to be made within a reasonable time.

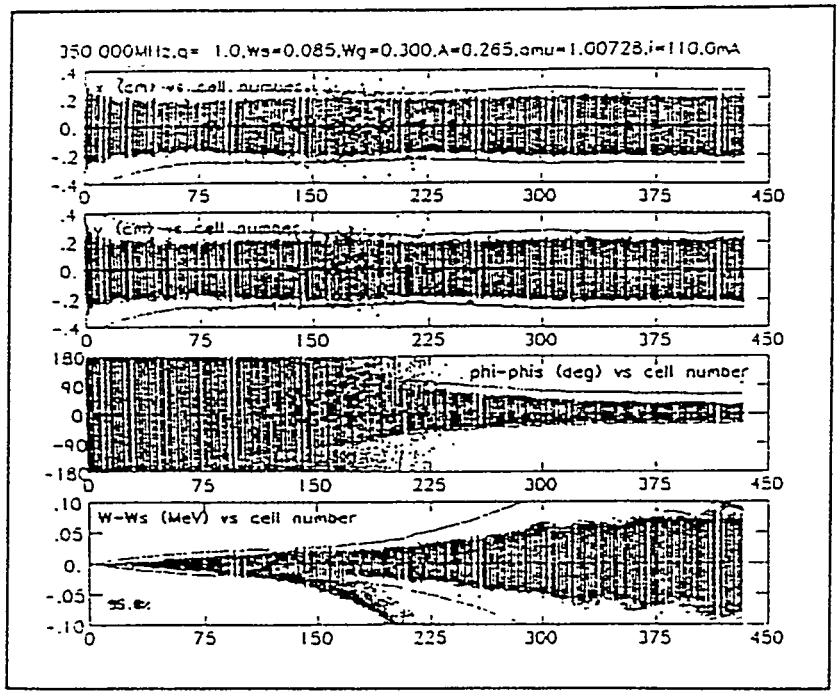


Fig. 3-4. RFQ transverse, phase, and energy envelopes vs. RFQ cell number.

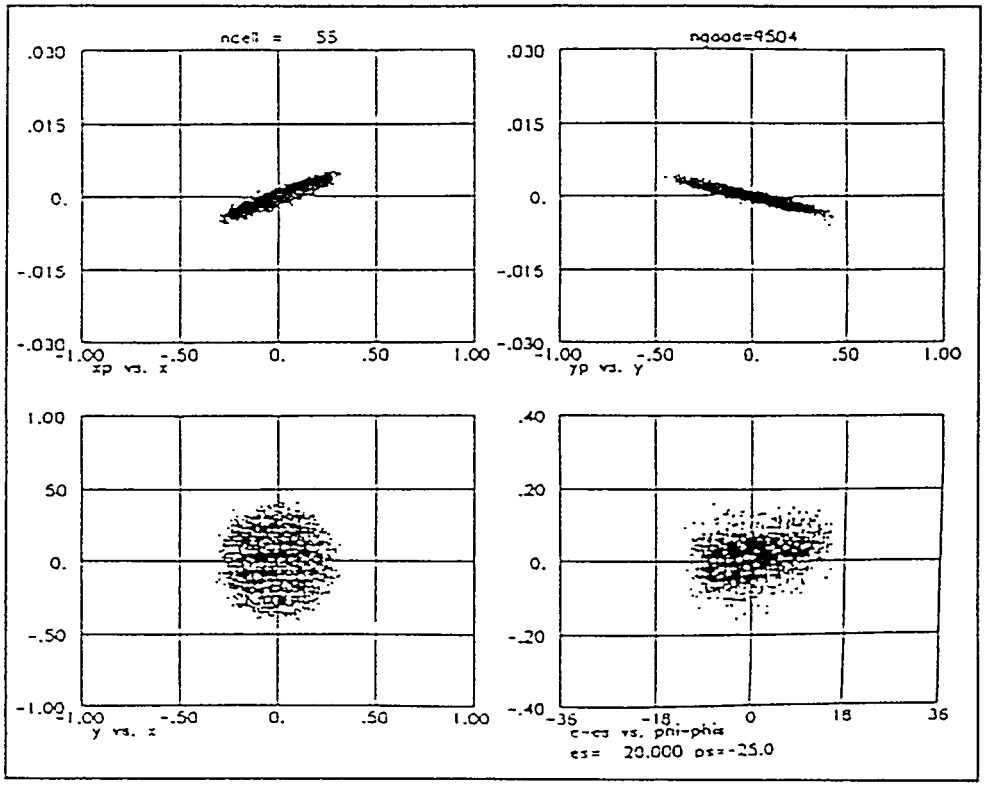


Fig. 3-5. DTL phase-space distributions at the end of tank 3.

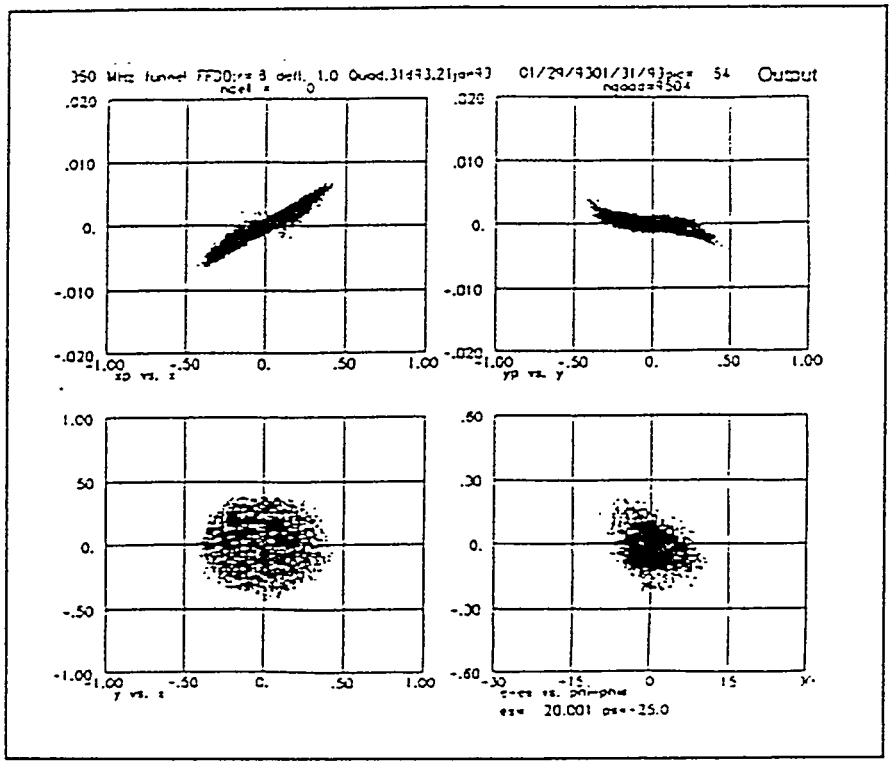


Fig. 3-6. Funnel output phase-space distributions at 20 MeV.

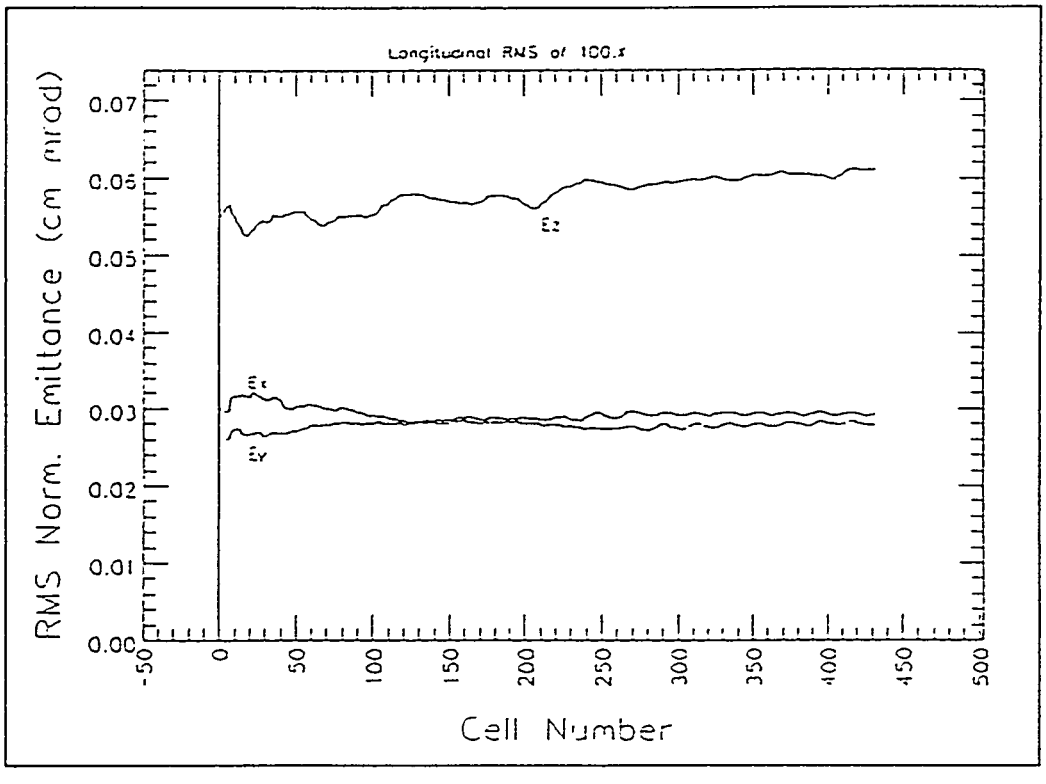


Fig. 3-7. Transverse and longitudinal emittances vs. BCDTL cell number.

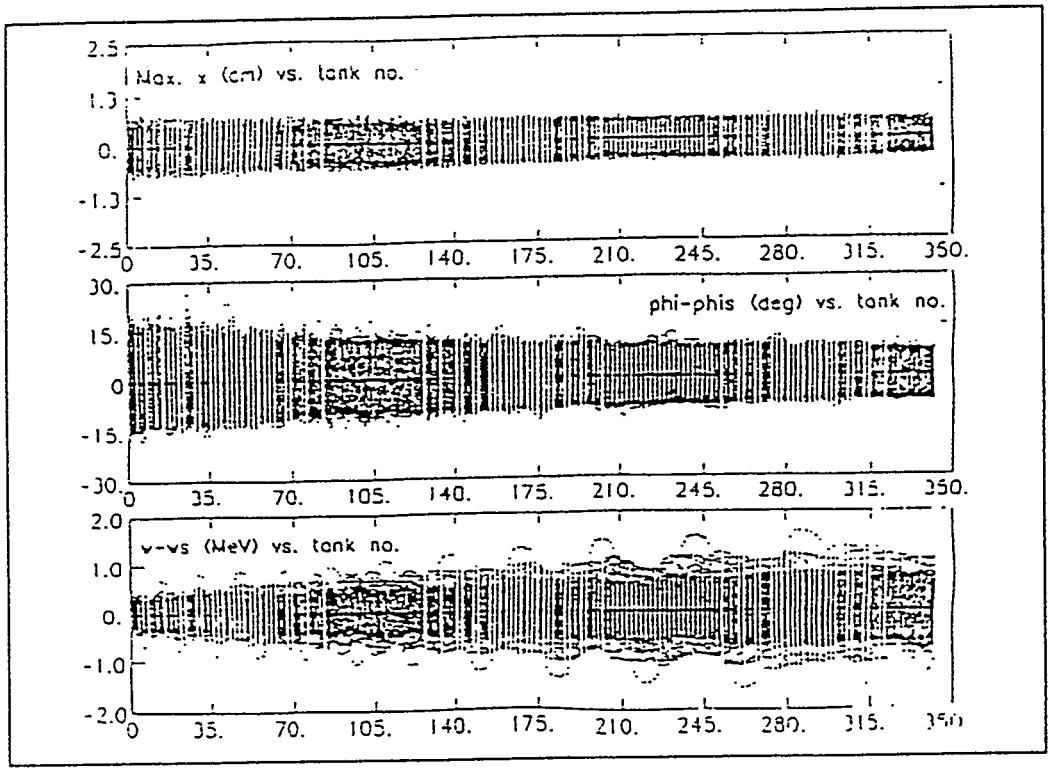


Fig. 3-8. Transverse, phase, and energy envelopes vs. CCL cell number.

3.3.2 CCL Failure Mode Studies

3.3.2.1 Introduction

Because the CCL comprises most of the APT accelerator, a study was done to evaluate the effects of a variety of potential fault conditions in this portion of the accelerator. The purpose of the assessment was to determine whether and how well the accelerator could continue to operate within a range of possible off-normal or fault conditions. The conditions investigated were quadrupole-doublet failures and RF-station failures, evaluated as a function of beam energy at the failure point. The effects of quadrupole-doublet failures on the beam were examined with particular emphasis on the response of the output (full energy) Twiss parameters. Substantial variation in the output Twiss parameters could lead to problems in matching the beam into the high-energy beam-transport system following the CCL. The effects on the beam of single RF-module failures were examined, and possible retuning procedures to compensate for this kind of fault were assessed. Results of the quadrupole-doublet and RF-station failure studies are summarized in the following sections.

3.3.2.2 Effects of Quadrupole-Doublet Failure

The effects of individual quadrupole-doublet failures in the CCL were examined. This condition was chosen as the most probable failure mode because both quadrupoles in a doublet would typically be powered from a common power supply. Simulations were run with individual doublets turned off at several locations along the linac. A matched uniform input distribution of 500 macroparticles representing a beam current of 200 mA was used in each simulation.

Output-beam Twiss parameters were tabulated for each run and are shown in Table 3-3. The first row in the table gives the beam parameters in the *no-failure* case for comparison. There is relatively little sensitivity of the output Twiss parameters to the location of the failed doublet. However, the output-beam transverse emittance is more strongly affected. The further upstream in the CCL the doublet failure occurs, the larger the transverse emittance growth, which is seen in Fig. 3-9. For example, failure of a doublet at 200 MeV results in a factor of 2.4 transverse emittance growth in the simulations. A failure at 900 MeV results in a growth factor of 1.7. The effects of the mismatch, coupled with nonlinear space charge effects, appear to be cumulative.

Table 3-3. Twiss Parameters at 1 GeV for Single Quadrupole-Doublet Failures in CCL

Energy at Failed Doublet (MeV)	α_x	β_x (cm/mrad) un-norm	ε_x (cm-mrad) norm	α_y	β_y (cm/mrad) un-norm	ε_y (cm-mrad) norm	α_L	β_L (deg/MeV)	ε_L (deg-MeV)
No Failure*	-1.25	0.521	0.038	-0.12	0.265	0.039	-0.04	8.876	1.373
102.05	-1.24	0.516	0.096	-0.18	0.246	0.100	-0.10	9.059	1.191
200.01	-1.09	0.511	0.120	-0.18	0.245	0.067	-0.07	8.780	1.220
300.14	-1.16	0.506	0.111	-0.24	0.262	0.054	-0.01	9.108	1.310
401.25	-1.22	0.504	0.110	-0.16	0.247	0.057	-0.07	9.242	1.326
500.22	-1.12	0.529	0.114	-0.15	0.219	0.061	-0.05	8.403	1.260
601.76	-1.43	0.573	0.091	-0.01	0.256	0.062	-0.02	7.987	1.411
701.64	-1.24	0.443	0.098	-0.13	0.233	0.057	-0.04	8.716	1.404
801.62	-1.48	0.463	0.103	-0.45	0.270	0.050	-0.00	7.752	1.393
901.01	-1.54	1.048	0.083	-0.27	0.331	0.048	-0.13	8.314	1.392

*The first row in the table gives the beam parameters for the no-failure case for comparison.

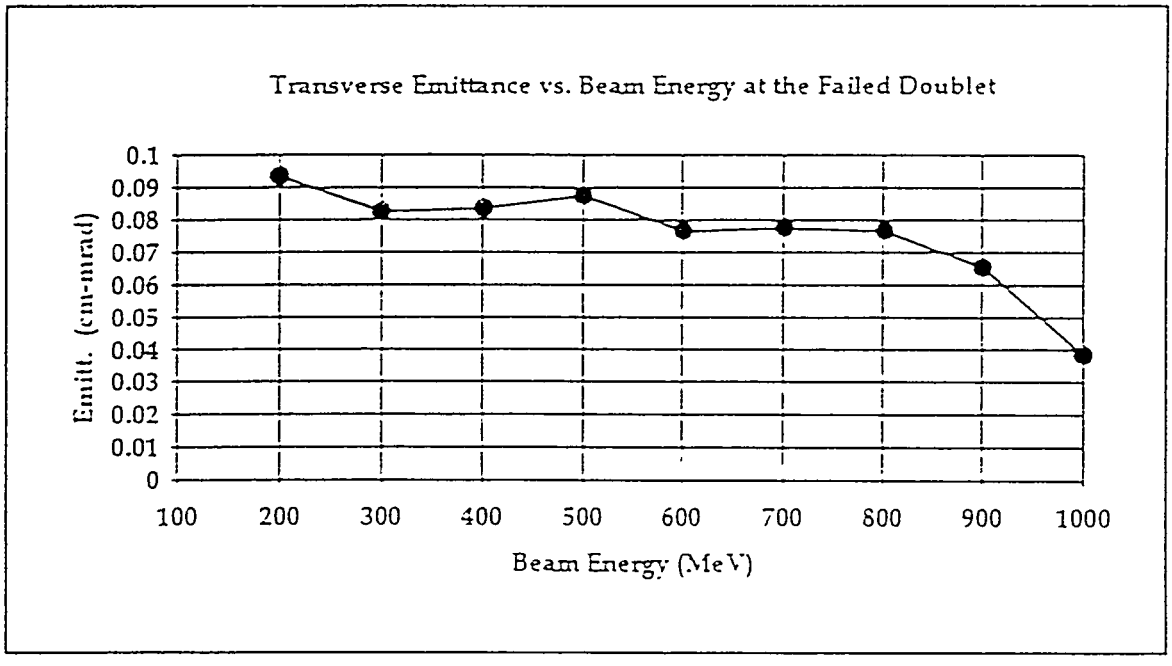
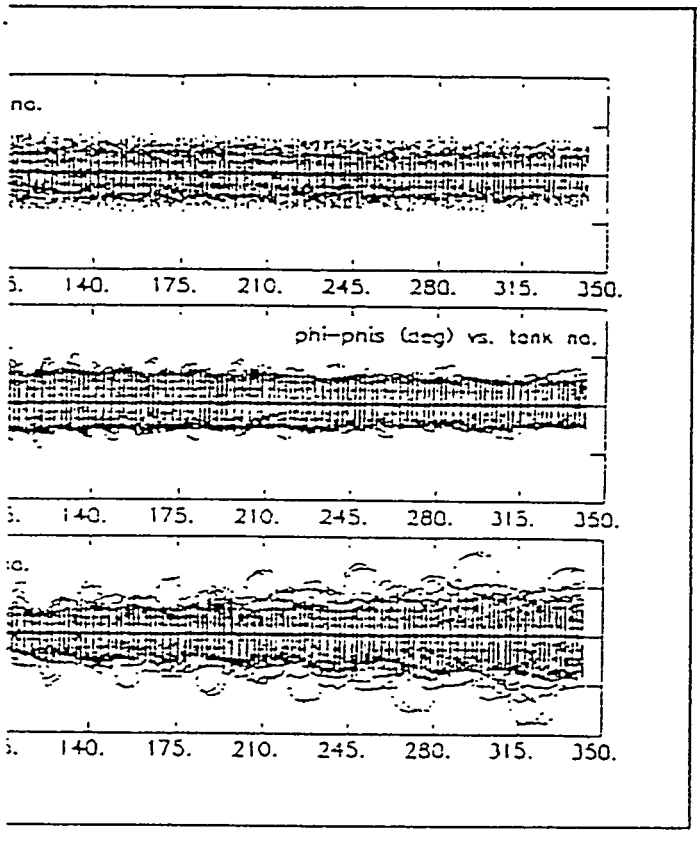


Fig. 3-9. CCL output transverse emittance vs. beam energy of a failed doublet.

/th increases the rms beamsize in the linac downstream of
)ws profile plots of the beam along the CCL for a doublet
ıe results of other doublet failure cases are given in the
ures clearly lead to a reduced ratio of aperture-to-rms-
from the failure location. This may be of concern for a
s were observed in the simulations for any failed doublet
ncluding halos) may produce particle losses significantly
terms of structure activation. However, it may not be
mmediately following a quadrupole-doublet failure since
aded enough to cause thermal damage to the accelerator.

failed doublet is probably not necessary unless beamloss
erable loss levels due to increases in beamsize. Possible
)f doublets upstream and downstream of the failed unit
.



locations and the effects on the beam dynamics were determined. Simulations using 500 macroparticles and a current of 200 mA were also used for this study. Table 3-4 summarizes the results.

Table 3-4. Results of Single RF-Module Failures in the CCL (Computer Simulations)

Failed RF Module (#)	Beam Energy (MeV)	Fraction Beam Lost (%)	Off-Energy Fraction of Output (%)	Average Energy of Off-Energy Output (MeV)
1	102.1	100.0	n/a	n/a
51	200.0	65.2	36.2	575.04*
87	285.0	8.6	37.0	427.03
88	287.5	0.0	41.0	428.54
132	401.3	0.0	0.6	598.44
170	500.2	0.0	0.0	n/a
242	701.6	0.0	0.0	n/a

*averaged for the two groups of off-energy bunches (see Fig. 3-11).

It was observed that particle losses occur downstream in the linac if a single module is lost at a beam energy less than 287.5 MeV (tank 88). For example, if the first module (tank 1, at 100 MeV) fails, all beam particles are lost by tank 101 (320.7 MeV). All such high-loss cases clearly would require the beam to be aborted immediately by the fast-protect system (<20μs) to avoid damage to the downstream accelerating structures.

Failure of a module at somewhat higher beam energy shows loss of a large fraction of the beam, but with a significant part reaching the end of the linac. For example, failure of module 51 (200 MeV) results in 65.2% (130.4 mA) of the beam being lost along the CCL. Figure 3-11 shows that part of the beam drops out of the RF bucket near tank 51, with much of it being lost transversely near tank 183. An additional portion of the beam drops out of the bucket near tank 220, but has sufficient energy to be propagated through the remainder of the CCL. A large fraction of the beam that gets through the linac is at reduced energy. For this case, 36.2% of the beam exiting the CCL is off-energy with an average output energy of 575 MeV. As before, it would be necessary to abort the beam immediately.

A failure of RF module 87 causes 8.6% (17.2 mA) of the beam to be lost downstream. Figure 3-12 shows this case. The beam is lost after tank 313, with an average energy of 913.2 MeV. Figure 3-13 shows the loss profile as a function of CCL tank number, indicating an average loss of about 1.0 mA per tank for tanks 313 through 331. The level of losses for this case is still very much higher than could be tolerated and would require an immediate beam abort.

Simulations of RF-module failures just above module 87 show no particle losses. However, a substantial fraction of the output beam is off-energy. For a failure of module 88 (287.5 MeV), 41% of the beam is well off-energy, with an average energy of 428.54 MeV. This beam would be lost immediately downstream from the first dipole in the HEBT. Again, a fast beam abort would be required to prevent damage to transport system elements. Additional figures showing the transverse dimension, phase width, and energy spread of the beam for single-module failures at and above 287.5 MeV can be found in the Chap. 3 Appendix.

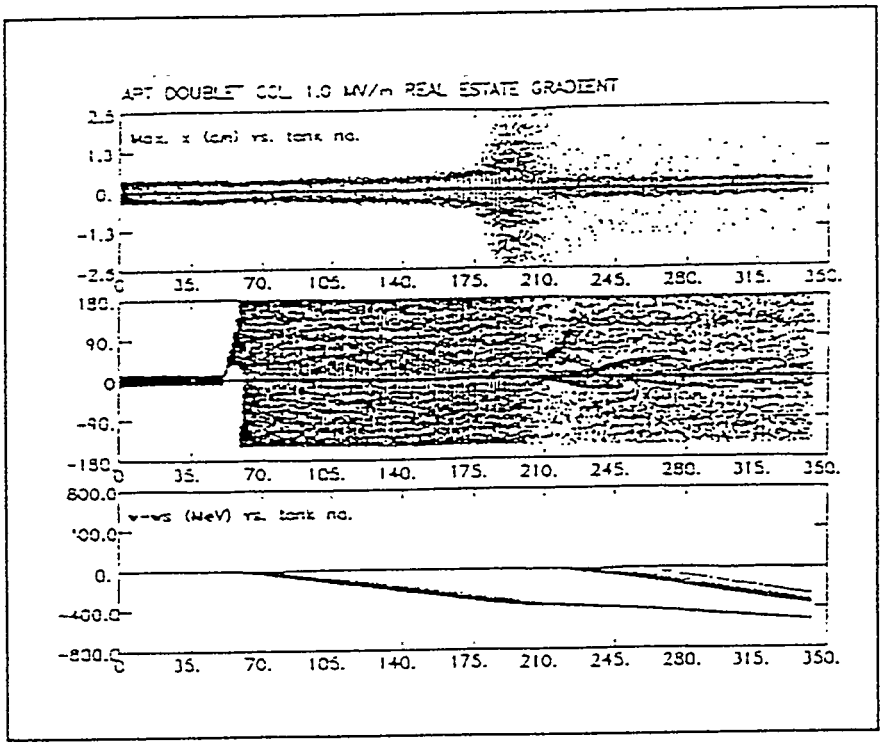


Fig. 3-11. Beam-profile plots for a single failed RF module (module 51).

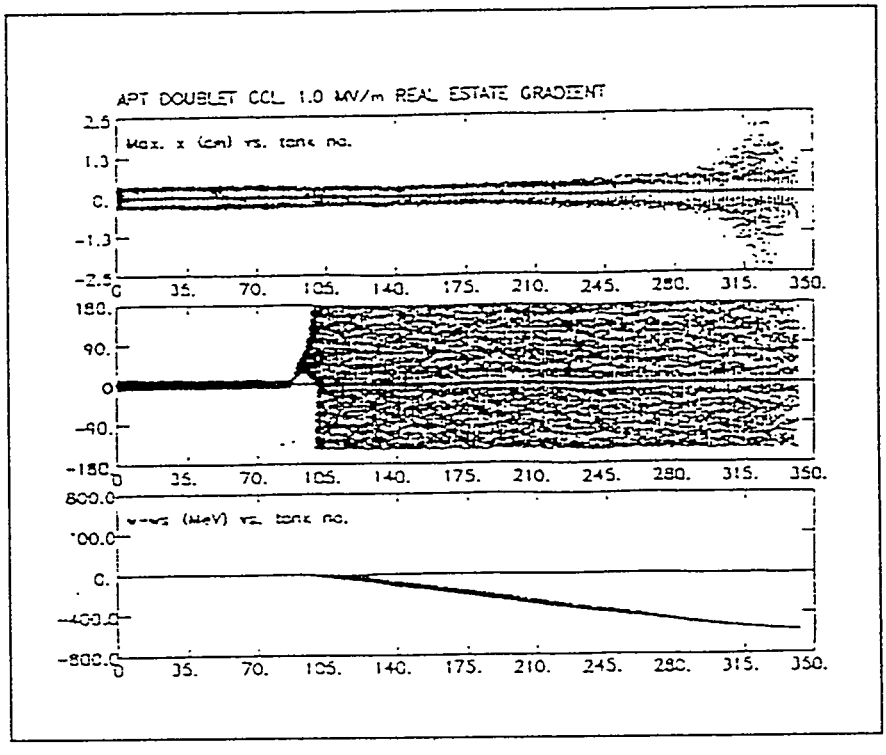


Fig. 3-12. Beam-profile plots for a single failed RF module (module 87).

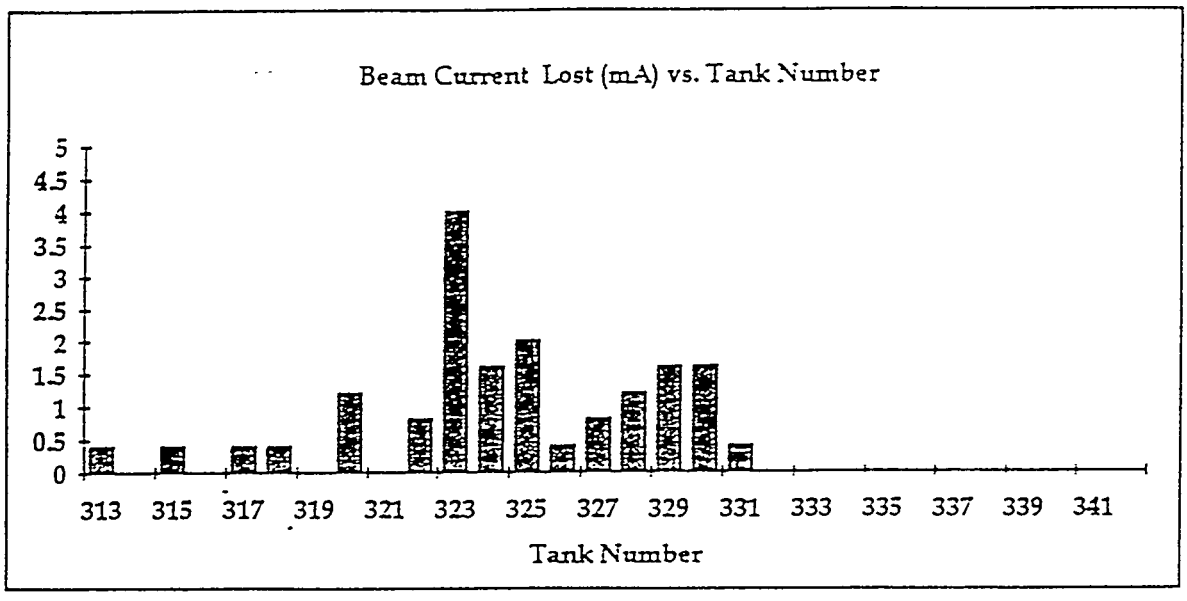


Fig. 3-13. Loss profile for a module 87 failure. Losses occur in tanks 313 through 331.

The simulations show two general trends for RF-module failures above module 88. Below about 450 MeV no beamlosses occur, but the output beam contains substantial off-energy components. The closer the failed RF module is to this "critical" energy, the smaller the energy difference between the synchronous beam and the off-energy components. If there is a substantial current in the off-energy components, a fast beam abort will be required.

Above 450 MeV, an RF-module failure results in the beam oscillating about the synchronous phase and energy, but remaining within the longitudinal acceptance of the linac (RF bucket). All of the beam (except some fraction of the halo) would be accelerated to the correct final (average) energy; but the longitudinal emittance increases significantly.

In this region of "failure space", the energy spread of the output beam is on the order of ±5 MeV or less. Since the HEBT has been designed for a ±1% momentum acceptance (corresponding to ±15 MeV), this increased energy spread should be transported successfully to the target. For these failure instances, rapid beam shutdown may not be required, and operation might continue with klystron repair or replacement being carried out on-line.

3.3.2.4 A Possible RF-Module-Failure Recovery Scheme

A possible RF-module-failure compensation scheme has been examined. This scheme is not currently part of the baseline APT point design, but indicates a possible approach for increasing overall machine availability. Control issues, which would be complex, have not been assessed. To compensate for the lost energy gain in a failed module, the operating phase and gradient (RF amplitude) of the four upstream modules were adjusted. Two cases were studied:

- a failure of module 6, using modules 2 to 5 to compensate, and
- a failure of module 88, using modules 84 to 87 to compensate.

The normal synchronous phase of the CCL tanks is –30°. For the compensating tanks, a synchronous phase of –25° is assumed. The accelerating gradient in the these tanks was increased from E_0T = 1.50 MV/m to E_0T = 1.58 MV/m to make up the lost energy gain in the failed tank. This correction allowed the beam energy to be very close to the synchronous energy for all tanks downstream. The expression,

$$(E_oT)_2 = \left[\frac{\Delta W_2}{\Delta W_1}\right]\frac{(E_oT)_1(\cos\phi_s)_1}{(\cos\phi_s)_2} \quad ,$$

gives the new gradient if the required energy gain per tank (ΔW_2) is known and the operating synchronous phase of the compensating tanks has been chosen. The tank length is a constant and, therefore, does not appear in the expression.

The phase centroid of the beam was shifted in each compensating tank and the first normal tank after the failed module so that the beam centroid was at the correct synchronous phase for the tank (–25°). This is equivalent to adjusting the phase of the RF for each individual tank such that the beam enters and exits with the correct phase. Figure 3-14 shows the results of using the compensation scheme for a failure of module 6. Tanks 2 to 4 compensate for the energy gain lost in the failed module. A small amount of coherent synchrotron motion occurs as the beam adapts to the remainder of the linac; no particle losses or off-energy particles, however, are observed in the beam.

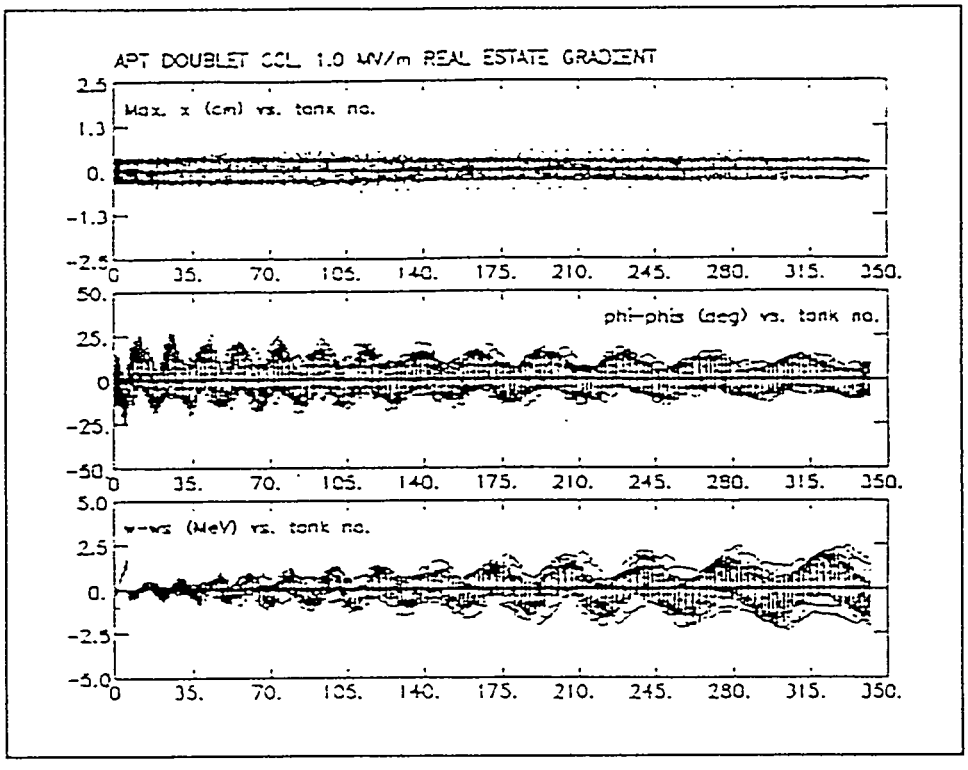


Fig. 3-14. Profile plots for a module 6 failure with tanks 2 through 4 compensating.

The RF compensating scheme appears promising. A limiting factor for application of this method is the additional RF power required in the compensating modules. An estimate

of the total power required for the two examples is given in Table 3-5. Single module failures above 500 MeV (module 170) do not produce off-energy components in the beam and will therefore require no compensation.

The RF power overhead requirements for control and retuning using the above compensation scheme need to be examined more closely. If four-module compensation requires a higher power klystron than 1 MW, this option may not be attractive. However, compensation schemes using more than four tanks could probably be employed (in principle) if the control system is sufficiently sophisticated.

Table 3-5. Power Requirements for the Compensating Tanks

Tanks	Energy Gain per Tank (MeV)	Beam Power per Tank (MW)	Structure Power per Tank (MW)	Total Power per Tank (MW)
2–5	2.140	0.428	0.178	0.606
84–87	3.125	0.625	0.191	0.816

3.3.3 Simulations with Reduced Beam Currents

To check the degree to which the APT linac design is current-independent (especially in matching sections and transitions from one accelerating structure to the next), end-to-end simulations were run at two reduced RFQ input currents (55 mA and 0 mA) and compared with the full-current results (110 mA). Input distributions of 5000 macroparticles were generated at the RFQ input and matched for each input current. The macroparticles were then transported through the entire accelerator, using the full-current (200 mA) matching conditions. RFQ beam transmission for the input currents of 110 mA, 55 mA, and 0 mA were 95.2%, 98.8%, and 99.9%, respectively. The results of the end-to-end simulations are shown in Table 3-6 and Table 3-7. No particle losses occurred downstream from the RFQ.

Table 3-6. Output Emittances for Matched 110-, 55- and 0-mA Beams into the RFQ

Current (mA)	Output Emittance (norm. rms)	RFQ (350 MHz)	DTL (350 MHz)	Funnel (700 MHz)	Funnel Matching* (700 MHz)	BCDTL (700 MHz)	CCL (700 MHz)
110	ε_T (cm-mrad)	0.0220	0.0230	0.0280	–	0.0290	0.0300
	ε_L (deg-MeV)	0.2200	0.2160	0.4360	–	0.4830	0.6080
55	ε_X (cm-mrad)	0.0214	0.0222	0.0248	0.0265	0.0296	0.0340
	ε_Y (cm-mrad)	0.0204	0.0221	0.0231	0.0234	0.0280	0.0270
	ε_L (deg-MeV)	0.2181	0.2232	0.4170	0.4224	0.4481	0.5220
0	ε_X (cm-mrad)	0.0203	0.0203	0.0244	0.0245	0.0260	0.0260
	ε_Y (cm-mrad)	0.0198	0.0198	0.0199	0.0199	0.0320	0.0350
	ε_L (deg-MeV)	0.2859	0.2891	0.2847	0.5759	1.1765	1.1580

*The current is doubled in the funnel matching section, BCDTL, and CCL.

The results shown here indicate that the APT linac design (including matching sections), is relatively current independent. The linac-output phase-space parameters are relatively unchanged even at zero current, which would allow cw operation at low beam currents for accelerator turn-on and tuneup. These lower beam current simulations demonstrate that the beam will propagate well through the entire linac, even at very low currents, without retuning the focusing lattice. Reducing the current injected into the RFQ, without rematching the RFQ, should result in a reduction of transmission through the RFQ. Table 3-7 shows the sensitivity of the CCL-output Twiss parameters to input current of the RFQ, assuming the full-current match throughout the APT accelerator. Additional simulations will be required to determine how low in current the accelerator can be operated without a significant change in output Twiss parameters. The output Twiss parameters affect the beam propagation through the beam expander in the HEBT.

Table 3-7. CCL Output at 1000 MeV for Nominal and Reduced Beam Currents

Twiss Parameter	I=200 mA	I=100 mA	I=50 mA	I=0 mA
α_X	-1.092	-1.132	-1.143	-1.201
β_X (cm/mrad, un-norm)	0.492	0.496	0.509	0.383
α_Y	-0.111	-0.159	-0.128	0.401
β_Y (cm/mrad, un-norm)	0.249	0.249	0.242	0.118
α_L	-0.052	-0.035	-0.077	-0.010
β_L (deg/MeV)	18.254	13.850	8.923	4.571

3.3.4 Tolerance Estimates for CCL Errors

Tolerance estimates for errors in the CCL were obtained by using the error simulation code, CCLTRACE. In this code, the multiparticle dynamics of the standard design codes are replaced with the beam ellipsoid dynamics of the TRACE 3-D code, which allows rapid calculation of the effects of errors on the rms beam properties throughout the linac. Probability distribution functions for various effects on the beam can be calculated.

The probability distributions are generated by the code running a large number of "traces" (beam envelope calculations) for a specified set of tolerance limits. At each element within the CCL, random values within the tolerance limits are chosen for the errors. Maximum values attained by the beam parameters are saved for each trace. Trial values are sorted, and a probability distribution is obtained. Various error conditions (such as quadrupole misalignments or rotations) can be simulated, with error types taken either singly or in combinations. For the results presented here, 100 traces were used for each run to generate probability distributions. An example is shown in Fig. 3-15.

The types of errors that can occur in the linac can be separated into two categories: (1) bench alignment errors, and (2) linac alignment and operational errors. The *bench alignment errors* are assumed to occur when quadrupole doublets are assembled as units. These include single element (singlet) rotation with respect to the doublet optical axis, single element gradient errors within the doublet, x and y displacements of the doublet elements with respect to its axis, and element tilts with respect to the axis. The doublet axis is defined to be the line passing through the magnetic centers of the focusing and defocusing elements. The tilt is the angle between the element axis and the doublet axis.

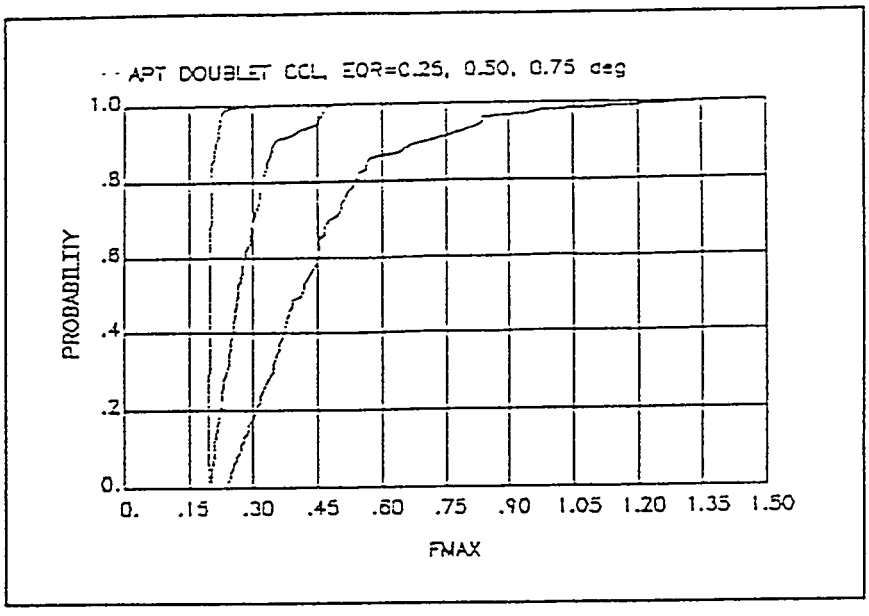


Fig. 3-15. Probability distributions for random quadrupole rotation errors.

Linac alignment errors are those involving assembly of the doublets into the accelerator, including overall machine alignment. These include displacements of the doublets with respect to the tank geometric axes, tilts of the doublet axes, and rotations of doublets about their axes. Tank displacement errors, where each end of a tank is randomly displaced in both x and y also come into play. Various linac *operational errors* must also be considered. These include quadrupole-doublet gradient errors, accelerating-tank field-amplitude errors, and accelerating-tank RF-phase errors.

A doublet focusing lattice, as chosen for the APT linac design, is generally less sensitive to displacements and rotations than a singlet lattice, but is more sensitive to tilts. Gradient errors cause the beam to become transversely mismatched and hence to oscillate in size. Rotations have the effect of mixing x and y motions and cause effective emittance growth in the transverse phase planes. Displacement and tilt errors cause the beam to oscillate about the nominal accelerator axis. The sum of all these errors cause the beam to occupy a larger part of the aperture than in the ideal error-free situation, which can result in increased particle loss.

A measure of the effect of the errors in the linac is the bore-filling factor. For a given set of random errors, the beam edge comes closest to the tank bore at some point (or points) along the CCL. The distance from the CCL optical axis to this point is denoted as r_{max}. The maximum bore-filling factor, F_{max}, is then defined to be r_{max} divided by the bore radius. For purposes of the error analysis, the total beamsize is defined to be 3 times the distribution rms value (3σ). When $F_{max}= 1$, the 3σ beam edge just scrapes the aperture. F_{max} is thus a factor which is inversely proportional to the aperture-to-rms-beamsize ratio.

Figure 3-15 shows probability distributions for F_{max}, for (bench alignment) random single quadrupole rotations of $\pm 0.25°$, $\pm 0.50°$, and $\pm 0.75°$. Several more plots of probability distributions for F_{max} for various error conditions can be found in the Chap. 3 Appendix.

Conclusions of the error study can be summarized as follows. Single quadrupole rotations of less than ±0.25° seem to have an insignificant effect on F_{max}. Gradient errors of up to 0.5% have no effect on F_{max}. Even gradient errors of 1.0% cause only 30% of the bore to be used. Displacement errors of up to 10 mils should be tolerable. Distributions for random quadrupole-singlet tilts with respect to the doublet axis were obtained for 1.0-, 5.0-, and 10.0-mrad errors. Single-quadrupole tilts of up to 5.0 mrad have little effect on F_{max}.

Random doublet-gradient errors of 2% have little effect on F_{max}. However, doublet tilt errors will need to be maintained at less than ±0.25 mrad. Doublet rotation errors of ±1.0° and doublet displacements of ±2.0 mils along the longitudinal axis of the CCL will have no effect on F_{max}. Finally, there is very little sensitivity of F_{max} for tank displacements up to 15.0 mils, which are well within present alignment capabilities.

Two accelerating-tank operational-error conditions were examined. The first was that of random accelerating-field amplitude errors. Probability distributions of F_{max}, ϕ, and W, were calculated for 0.5%, 1.0%, 2.0%, and 3.0% random RF-field errors. The results show that F_{max} is not significantly affected within this error range. Typically, the RF amplitude (and thus the cavity fields) can be controlled to within ±1.0%. Amplitude errors up to 3% can cause deviations in the average beam phase of up to 10° and deviations in average beam energy of up to 2 MeV. The second accelerating-tank operational-error condition examined was that of random phase errors. Probability distributions of F_{max}, ϕ, and W were calculated for ±0.2°, ±0.5°, ±1.0°, and ±2.0° random phase errors. Phase errors greater than ±1.0° can cause beam energy variations of up to 7.0 MeV, which significantly affects the beam trajectory in the CCL. This is indicated by the sudden increase in F_{max} when tank phase errors are greater than ±1.0°. Typically, the operating phase of modern linac RF modules is controlled to less than ±1.0°.

3.4 LOW BEAMLOSS REQUIREMENT

The necessity for very low beamloss is a major issue in the APT linac design. High beamlosses can produce heating and radiation that could damage accelerating structures and degrade accelerator performance. Even very small losses, if occurring continuously, can produce activation levels in accelerator components that hinder or prevent hands-on maintenance. The APT linac design goal is that beamlosses should be low enough to permit unconstrained maintenance operations within a short time after machine shutdown. As activation levels increase, maintenance activities on the linac become more difficult and time consuming. Table 3-8 shows how the level of machine activation affects the maintenance environment.

Table 3-8. Levels of Radiation and Type of Maintenance

Level of Radiation	Type of Maintenance
< 10 mrem/hr	Unconstrained "hands-on" maintenance
10 mrem/hr–100 mrem/hr	Hands-on maintenance; limited access time
100 mrem/hr–10 rem/hr	Hands-on maintenance, strictly controlled; very limited access time
>10 rem/hr	Remote maintenance required

3.4.1 LAMPF Reference Analysis, Activation Estimates

LAMPF operations, over the past 15 years at the 1-mA (average) current level, have provided a valuable database with respect to achievement of low beamlosses. The LAMPF CCL operates with very low (<2 x 10^{-7}/m) fractional beamloss for most of its length. This low loss baseline is a key factor (and existence proof) enabling projection of low beamlosses for the high-current APT linac.

The magnitude of beamlosses along the LAMPF CCL have been inferred from activation measurements performed following shutdown after a long production (operation) period of several months. Following such shutdowns of the LAMPF accelerator, a radiation survey is performed in which gamma dose measurements are taken 30 cm from the beampipe along the length of the machine. From these measurements, the beamloss profile for the LAMPF CCL has been estimated [3-1] using the following procedure and assumptions.

To a first approximation, the activation level, A, at a given location along the CCL is proportional to the number of neutrons produced per meter, N, (at that position) by protons striking the accelerating structures or beampipe. Thus, $A = \alpha N$, where alpha is a constant. The number of protons lost per unit length is related inversely to the number of neutrons produced, through the neutron yield, $Y(E)$, for copper and iron, shown in Fig. 3-16. Because of the rapid increase in neutron yield as a function of proton energy, it is particularly important that beamloss be minimized at the high-energy end of the accelerator. From these arguments, the number of protons lost per unit length at a specified beam energy is given by:

$$P = \frac{A}{\alpha Y(E)}$$

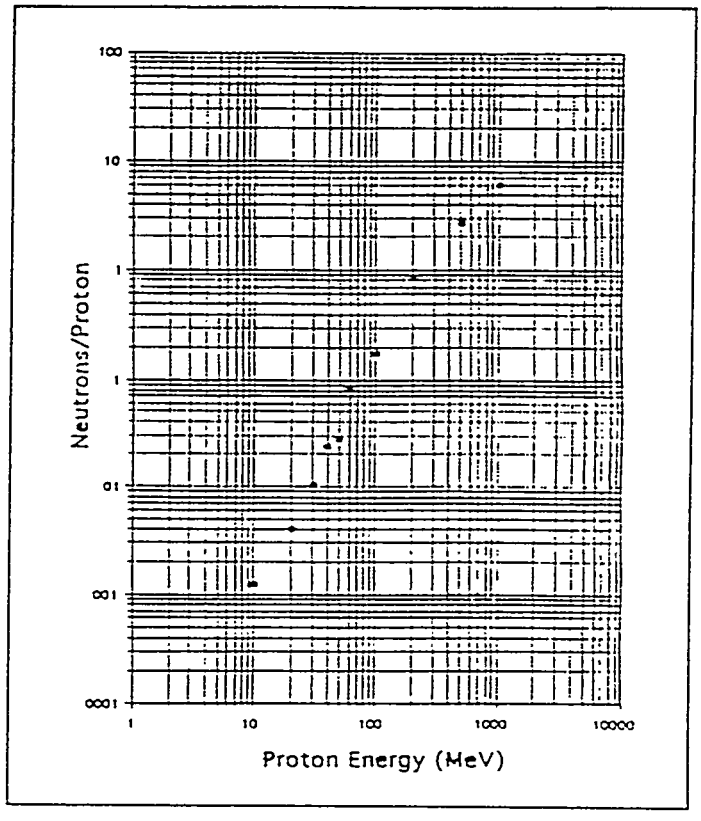


Fig. 3-16. Neutron yield vs. proton energy for copper/iron.

The sum of the losses described above is equal to the integrated beamloss from one end of the CCL to the other. At LAMPF, this quantity (typically around 400 nA) is measured continuously by comparison of precision current monitors. Using this characteristic number, an approximate value for α can be derived, and beamloss can be directly inferred at the location of each activation measurement.

After correcting for tank lengths, the approximate beamloss profile is obtained from the above procedure as a function of proton energy, and is shown in Fig. 3-17. Two high-loss regions appear (just after 100 MeV and 200 MeV), but most of the CCL operates with very low losses, below 0.2 nA/m, corresponding to a fractional loss of $<2\times10^{-7}$/m. These values are representative of typical operation; with careful tuning, the loss levels can be reduced below 0.5×10^{-7}/m. Typical activation levels in the low-loss region of the linac, two hours after shutdown from extended operations, are a few mrem/h. Thus, unrestricted hands-on maintenance is the norm in these areas.

The high-loss regions appearing in Fig. 3-17 are well understood from simulations of the "as built" accelerator [3-2]. At 100 MeV, a transition occurs between the 201.5-MHz DTL and the 805-MHz CCL, with a sudden reduction in the longitudinal acceptance. The beam is also not optimally matched in longitudinal phase space from one side of this transition region to the other. The high beamloss region just after 200 MeV is caused by a similar reduction in the transverse acceptance, resulting from a factor-of-2 increase in quadrupole-doublet spacing. These large acceptance transitions are absent in the APT linac design, as is discussed below. Figure 3-17 also shows estimates of beamloss from a computer simulation of the LAMPF linac [3-2]. The two high-loss regions are *qualitatively* predicted in the simulation. For display purposes (to show everything on one graph), the simulation results have been normalized to the losses inferred from activation measurements at 100 MeV (the first bar on the graph); consequently, the bars showing the simulation are ~5 times shorter than they would otherwise be. The simulation actually over-predicts the *magnitudes* of the beamlosses by a factor of 5 or so.

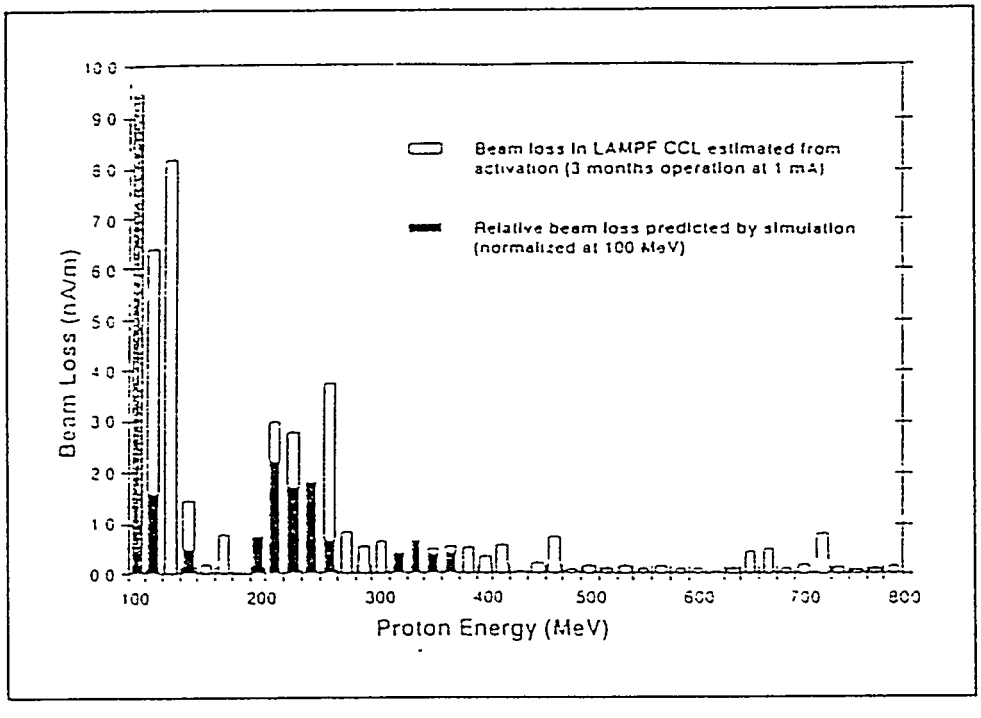


Fig. 3-17. Measured and simulated beamloss in the LAMPF CCL.

Activation readings on the LAMPF CCL made in the standard (post-shutdown) radiation survey are normally taken at the quadrupole doublets. One would expect that activation levels would be greatest at these sites because the beamsize is maximum there. A more detailed activation survey made following the 1992 operating cycle showed the pattern seen

in Fig. 3-18. This shows the activation level as a function of distance along the linac for several tanks near the high-energy end of the CCL. Activation is maximum at the quadrupole doublets, as expected, where most of the beamloss occurs.

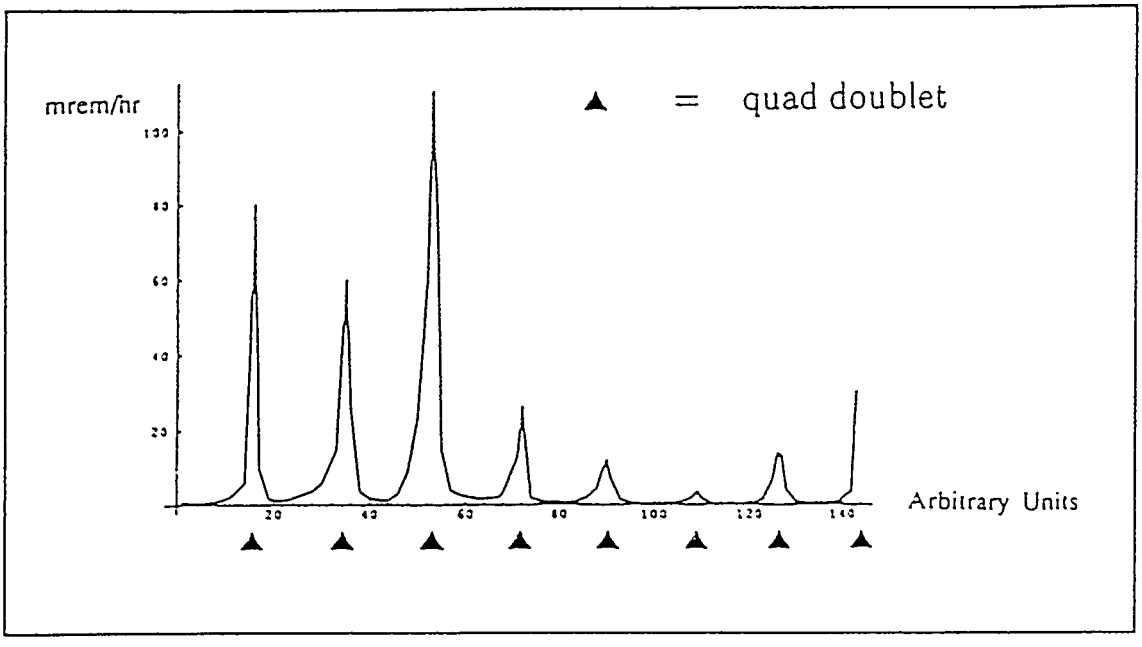


Fig. 3-18. LAMPF CCL activation measurements (12/15/92) beyond transition region.

An important piece of data from LAMPF operations is that the beamloss is very time dependent, with much of the loss occurring during the beginning of the macropulse. This is shown in Fig. 3-19. This transient beamloss is due to an incomplete match between beam current and RF power to the accelerating structures that exists during the initial 100 μs of each macropulse. Since the APT linac operates cw, there are no such transients during normal operation, and the RF drive is continuously well matched to the beam load. The transient-related beamloss seen in LAMPF will thus be absent in APT linac operation.

3.4.2 Beamloss Control Measures in APT Linac Design

The APT accelerator is designed so that beamloss at the high-energy end of the CCL is nominally less than 0.2 nA/m. Losses at this low level are associated not with the core of the beam distribution, but with particles in the outer beam halo, typically well beyond five standard deviations (5σ) from the beam axis. Much theoretical and computational effort has recently gone into understanding how the beam halo is generated [3-3 to 3-5]. A major source of beam halo is the interaction of individual particles with a bunch undergoing density and shape oscillations because of mismatches, or undergoing centroid oscillations caused by misalignments. Transitions in the accelerator phase-space acceptance (sudden changes in transverse or longitudinal focusing) also appear to drive particles into the halo. This is thought to arise from the beam heating driven by such transitions, followed by turbulent relaxation as the beam adapts to the changed environments.

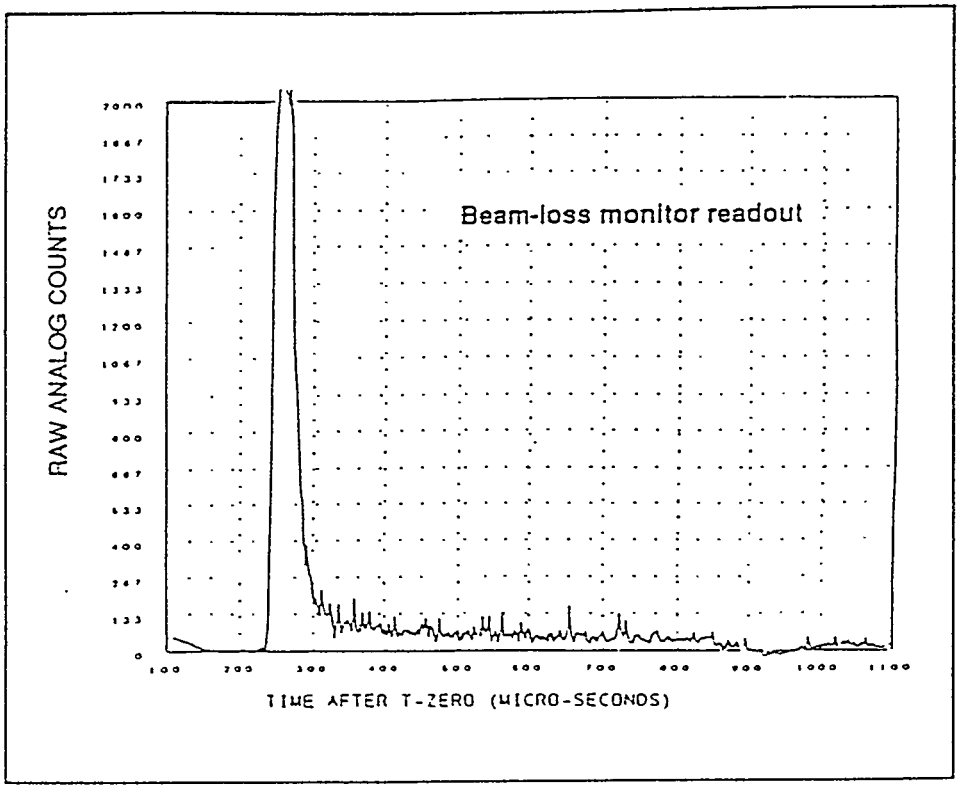


Fig. 3-19. LAMPF beamloss vs. time into beam pulse.

Thus, halo generation in the APT linac can be minimized by careful attention to beam matching, ensuring that the beamline is well aligned, and avoiding significant acceptance transitions in the design. Simulations have shown that beam halo can be minimized by strong focusing, so the high density of focusing elements in the APT linac is advantageous. A more detailed discussion of beam halo is given in the Chap. 3 Appendix.

The APT accelerator design contains many features that enable it to meet the very low beamloss requirements. These include the following:

- There is a very large aperture-to-beamsize ratio in the CCL which increases with proton energy. This ratio ranges from 13–26 for APT, as compared with 4–6.5 for LAMPF.

- There are no significant phase-space acceptance transitions at energies above 20 MeV; in contrast, LAMPF has two major acceptance transitions (at 100 MeV and at 200 MeV), which are known to be responsible for high levels of beamloss downstream.

- The beam radius is small. The APT linac design incorporates strong transverse focusing, a key factor in maintaining a large aperture/beamsize ratio. Strong focusing also reduces the effects of nonlinearities present in the outer regions of the focusing elements which can be responsible for ejecting large amplitude particles from the transverse acceptance.

- There is a high density of position-sensing diagnostics and correctors to enable precise beam alignment, minimizing aperture reductions and halo generation.
- There are no beam transients in normal operation, and thus no transient beamloss associated with an imperfect match between the RF drive and the beam load.
- The linac design includes a halo scraper just downstream from the last major transition (the funnel). This system consists of a series of beam-scraping stations containing remotely-adjustable blades that remove all particles in x–x' and y–y' phase space beyond a specified number of standard deviations, say 5σ.

3.5 ELECTRICAL EFFICIENCY CONSIDERATIONS

High electrical efficiency in the APT linac is important to reduce the plant electric-power demand, and is achieved by several factors. A key element is the emphasis on high beam current, as opposed to high energy, for delivering the desired beam power to the targets. This means that the RF power used for accelerating the beam is much larger than the RF power losses in the accelerating cavity walls, and the RF-to-beam power conversion efficiency is high. In the APT linac design, the RF-to-beam conversion efficiency is nearly 80%. A second element is to assure a high efficiency (high shunt impedance) cavity design for the CCL, which makes up more than 90% of the linac and therefore dominates the power equation. This is achieved by choosing a relatively high structure frequency (700 MHz), selecting a low accelerating gradient (1.0 MV/m), and by using structure apertures that are not too large. The selection of structure aperture dimension is a balanced design compromise between the larger openings needed for minimum beamloss and the smaller openings required for maximum RF efficiency. A final element in the design is the use of high-efficiency RF amplifiers (klystrons) as the baseline RF power source. High power klystrons can presently convert dc to RF power with efficiencies greater than 60%. Significant efficiency improvements are feasible in high-power RF-amplifier technology in the future.

3.6 ACCELERATING-STRUCTURE THERMAL CONSTRAINTS

3.6.1 Introduction

The large amounts of thermal energy dissipated in the APT accelerating structures by cw RF-power losses establish the overall performance and capacity requirements for the linac water-cooling systems, in terms of flow rates, volumes, and temperature differentials. In addition to transferring this heat load to the environment, the cooling system also has the critical function of establishing and maintaining all the accelerating structures at the correct resonant frequency during operation. The following general considerations apply:

- There is a limit to the local power densities that can be tolerated with achievable film coefficients in water-cooled channels.
- The structure resonant frequency changes in response to ambient (input coolant) temperature changes and also as a result of the internal (differential) response to RF heating. The combination of these mechanisms sets the resonant frequency.

- Material stresses arise when RF power is dissipated in the accelerating structure due to differential heating, because RF losses are deposited on the cavity inner surfaces rather than uniformly through the cavity walls.

Although similar thermal constraints on power density apply generally to all sections of the accelerator, the frequency-tuning function of the coolant is most critical in the CCL. This is because the other structures (RFQ, DTL, BCDTL) incorporate mechanical tuning devices that adjust the cavity internal volumes with removable machinable components. The CCL, on the other hand, is a brazed structure that is tuned entirely by thermal adjustment of the cavity dimensions through control of the coolant. Because the CCL dominates the APT linac in both physical and cost terms, the following discussion of offset tuning is addressed to this part of the machine.

Details of the thermal analyses for each portion of the APT accelerator are given in other parts of this report. The power dissipation, the detuning due to thermally-induced changes in cell profile, as well as the Von Mises thermal stresses, have been analyzed for all the hot spots (highest power dissipation regions) of the design. This information is included in Appendix 12.5, Thermal and Vibration Analyses.

3.6.2 Maximum Power Densities

In the thermal-management design of the accelerating structures, a power dissipation of 25 W/cm^2 is the highest average-power density that is conventionally acceptable. This criterion has been successfully applied in the APT structure designs. Some localized exceptions occur, however. For example, within the BCDTL, the power density at the junction of the last drift-tube body and stem in the 100-MeV tank is 60 W/cm^2. In the DTL, a power density of 45 W/cm^2 exists at the base of the highest-energy drift-tube stem. Despite the existence of such hot spots, the cooling is adequate because the high-power deposition regions are very small and localized.

The deflector cavity in the funnel is another element that carries high power densities in small localized areas. While the deflector cavity as a whole is designed for <25 W/cm^2, localized power densities are as high as 66 W/cm^2.

The CCL cavity power densities are moderate everywhere, with the maximum power hot spots ranging from 6–8 W/cm^2. The CCL cavities could operate at higher fields (from a thermal-management point of view) if reduced accelerator length were a more important consideration than high RF efficiency.

3.6.3 Cavity Frequency Response

Cavity frequency changes and cavity material stresses result from thermally-induced changes in cell shapes. Power deposition and cooling-system constraints are imposed in the accelerating-structure and cooling-system design to minimize these effects. There are two main considerations:

- The bulk operating temperature in the structures (determined by the coolant) must be high enough to control the resonant frequency in worst-case ambient-air conditions (e.g., summertime in high-humidity regions). This temperature rise produces uniform change in cavity dimensions, but does not induce stresses in the materials.

- There is a differential temperature increase in the structures due to RF heating of the interior copper surfaces. The RF heating produces both a frequency change and thermal stresses in the materials because of the differential heat deposition.

3.6.3.1 Ambient Temperature

To address the ambient temperature rise under worst-case cooling conditions, the APT CCL cooling system has been designed to supply cooled water to the cavities at 36°C under the highest (wet-bulb) temperature conditions for the cooling towers, assuming the hottest of the potential APT plant sites. The maximum RF-induced calorimetric temperature rise is specified to be 10C° for the bulk coolant. The outlet temperature during operation would thus be 46°C, and the average temperature of the structure would be 41°C. By general accelerator standards, this is a high-temperature operating condition. The tuning change due to the increase in temperature from the cavity fabrication environment (taken as 20°C) is significant. This frequency shift is

$$\Delta f / f_o = 1.66 \times 10^{-5} \times \Delta T$$

For f_o = 700 MHz and ΔT = (36°C − 20°C) = 16°C, Δf = 186 kHz. This frequency shift is accounted for by predictive analysis in specifying the nominal machining dimensions of the CCL cells. When the cells are tuned in the laboratory (at 20°C) the frequency will be (nominally) 186 kHz high.

3.6.3.2 RF Heating

In addition to this ambient temperature detuning due to the elevated cooling-water temperature, an additional tuning shift occurs when the cells are carrying full power cw RF fields. As indicated above, the ΔT (inlet to outlet temperature differential) in the cooling water due to RF heating is 10C°, giving an average structure temperature gain of 5C°. The actual frequency shifts caused by RF power, however, are slightly greater than those predicted by the simple bulk-expansion formula. This is because there is internal distortion of the cavity which is due to differential heating. The additional frequency shift is derived from a SUPERFISH analysis of the detailed changes in cavity shape. The cell is more sensitive to dimensional changes in the nose area than in the outer regions. The 100-MeV cell gives the largest RF-induced frequency shift in the CCL, about 204 kHz. This frequency shift is the amount that the local oscillator must accommodate if a klystron trips off and the accelerating module cools down. The sum of ambient and RF-induced frequency shifts in the worst case is 186 kHz + 204 kHz = 390 kHz. This excursion is defined as an *upper thermal constraint* on the accelerator.

3.6.4 Material Stresses

Because of the magnitude of the Von Mises stress from differential heating in the structure, the coolant temperature rise must be limited to 10C° at full cw RF power. In the worst cases, these thermal stresses reach almost 4000 psi, which have been specified in the structure design as the maximum allowable stress for fully annealed copper cavities. A maximum 10C° temperature rise during RF heating turns out to be a reasonable specification for the linac point design.

3.6.5 Offset Tuning and Fabrication of Accelerating Structures

Tuning of the CCL structures involves a number of processes where tight tolerances must be held, and will constitute a significant part of the accelerator construction effort. The cavities are initially mounted in clusters in a press with brazing foils inserted between cells, and are then joined by firing in a hydrogen furnace. The frequency of the cavity assembly after brazing must be high by the amount prescribed by the combined thermal offsets that will be experienced in operation. Thus, the cavities must be machined (before brazing) to dimensions that will establish the required offset frequency, allowing for shrinkage of the braze joints. In the final tuning adjustment, the cavity walls are dimpled to raise the frequency to the final desired offset value. It is desirable to tune the cavities so that the nominal operating frequency is achieved at temperatures slightly *above* the average operating point (41°C), providing additional control margin to the resonance controller. The cavities would thus be tuned to an offset temperature of 46°C, which would accommodate the maximum thermal rise and give adequate control margin.

A rough estimate of the magnitude of the CCL-cavity machining offset can be made as follows. As before, the worst case CCL cavity (at 100 MeV) is taken as the example. We add the offset caused by shrinkage of the brazing foils (0.04 mm) to the dimensional offset to account for the 390 kHz total frequency offset. Assuming that the dimensional sensitivity of the cavity nose is 800 kHz/mm and that all offset machining is accomplished by tailoring the nose alone, the room-temperature machining offset would be $390/800 \div 0.04 = 0.53$ mm. That is, the nose of each CCL half-cell would be trimmed back by $0.53/2 = 0.265$ mm.

3.7 SPECIAL ENGINEERING DESIGN FEATURES

3.7.1 Linac Modularity

The high-energy portion of the APT accelerator (BCDTL and CCL) is *modularized* into assembly units, as illustrated in Fig 3-20, which shows a typical BCDTL assembly unit. There are 326 such units, taking into account both the BCDTL and the CCL. Modularization breaks the linac into manageable lengths for maintenance, checkout, and installation. All units weigh less than two tons each and do not exceed a length of five meters. The units can be preassembled in the laboratory, aligned, and then checked out for vacuum, cooling, and RF integrity before they are transported to the accelerator tunnel. Each unit is then installed in its proper location and aligned to the adjacent units and to the tunnel monument-reference grid. If any unit were to suffer a major structure failure, the process would be reversed and the unit would be returned to the laboratory for servicing. Modularization allows for all necessary checkout to be done in a well-controlled laboratory environment, with minimal in-tunnel radiation exposure.

In addition to the large, modular assembly units, there are intertank subassemblies. These are also modular and easily removed for maintenance, alignment, or check-out in the laboratory. Typical hardware making up the intertank subassemblies are the beamtube, diagnostic devices, vacuum bellows and disconnect flanges. These are all mounted on a removable platform that is itself mounted on two linear tracks using sets of precision linear bearings. The overall modular design of the linac will generally facilitate rapid installation, alignment, maintenance, and repair.

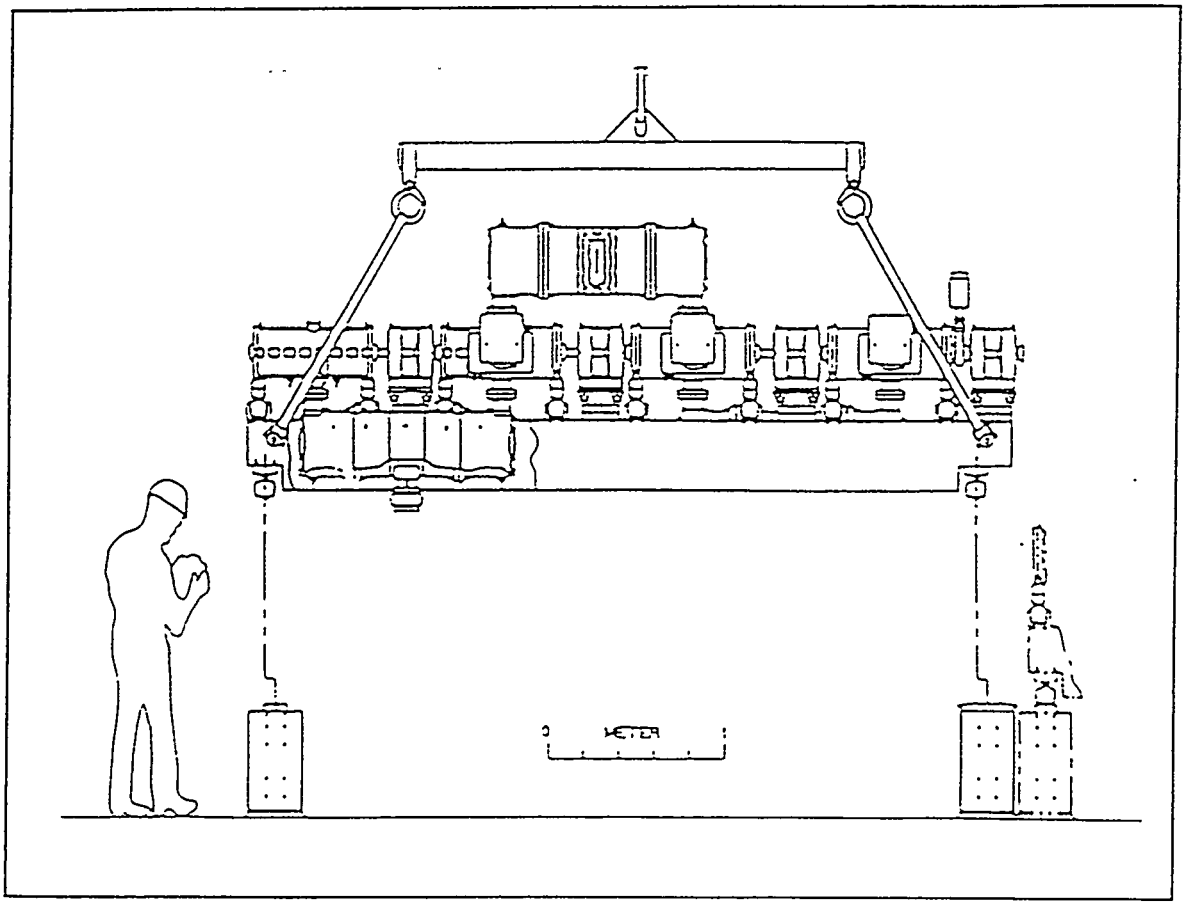


Fig. 3-20. A typical BCDTL assembly unit or module.

3.7.2 Designs for Radiation Environments

3.7.2.1 Radiation Hardened EMQs

Because of the potential for radiation-induced damage to materials arising from beamlosses during linac tuning or high-loss, off-normal operating conditions, essentially all the quadrupoles in the APT point design are electromagnets, with radiation-resistant field coils. The hardening technique is illustrated in Fig. 3-21. In a multi-step process, the coils are coated with a high-integrity continuous glass insulation layer, and then potted in calcium-aluminate cement to fit in the magnet yokes. Radiation-hardened magnet coils can withstand several orders-of-magnitude more neutron and gamma dose than standard epoxy-potted coils. All the APT accelerating-structure quadrupoles, (including the small units designed to fit into the 350-MHz DTL drift tubes) can be fabricated in this way. The rad-hard coils would be potted in two halves, so that when the (demountable) yoke is disassembled, the coils can be individually replaced. In most instances, this would be a practical maintenance task to perform on line.

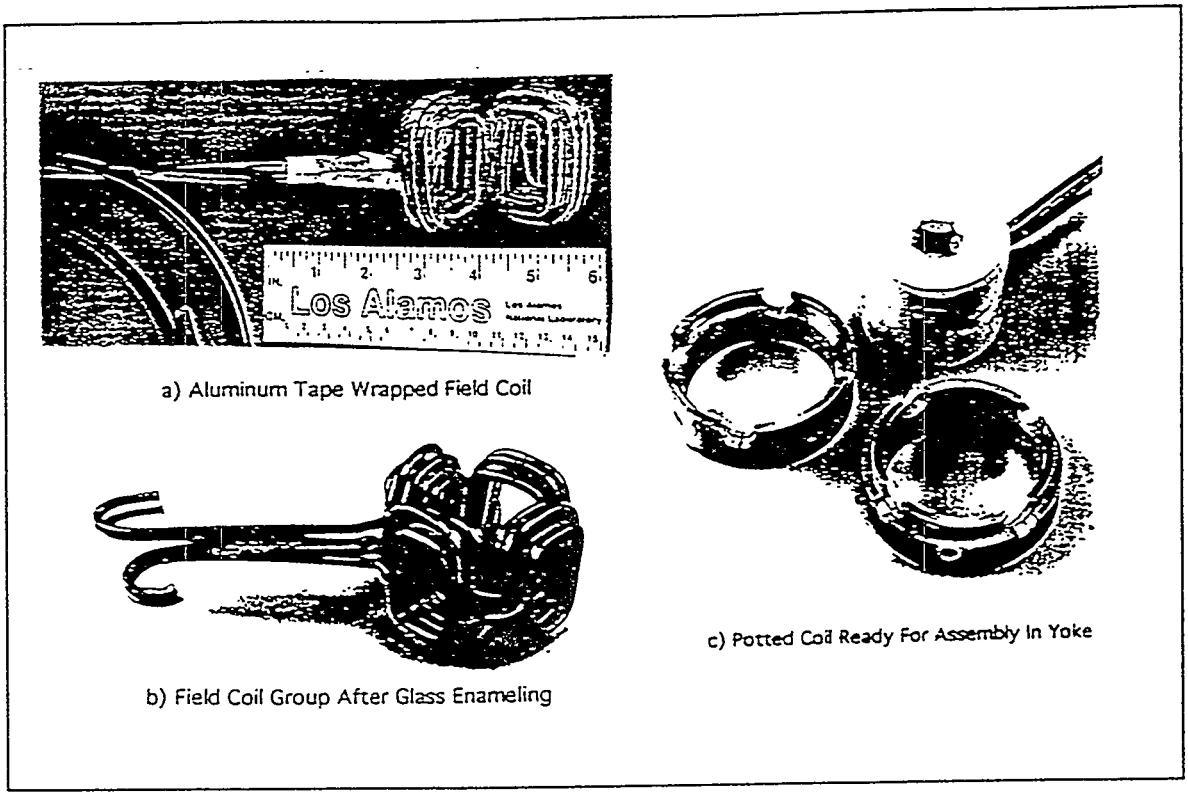


Fig. 3-21. Proposed radiation-hardening fabrication procedure for EMQs.

3.7.2.2 Remote Handling Capability

Special hardware features such as quick flanges, self-aligning linear rails, and easy removal and modularization of components have been included in the linac mechanical design to allow for ease of maintenance under nonideal conditions such as high temperature or potential radioactive environments. The facility design also allows for remote maintenance capability, if needed. The tunnel transverse dimensions are sized to allow working room alongside the linac for a mobile master-slave servo-manipulator machine that can perform remote maintenance on any part of the accelerator.

3.7.3 Other Features

3.7.3.1 Prototype DTL EMQ

Special compact radiation-resistant EMQs are needed in the 350-MHz DTL drift tubes, in the matching sections following the DTLs, and in the funnel. A prototype of a DTL EMQ is shown in Fig. 3-22. The DTLs require 104 of these units, and the matching sections and funnel require an additional 35 units. The envelope of this EMQ is very restricted because of the limitations imposed by the size of the 350-MHz drift tubes. The quadrupole coils carry current densities of over 4000 A/cm^2 to achieve the required *GL* product of 20 kG. The prototype that is shown in Fig. 3-22 was constructed to confirm the demountable design concept and to confirm that the coils could be wound with sufficient turns.

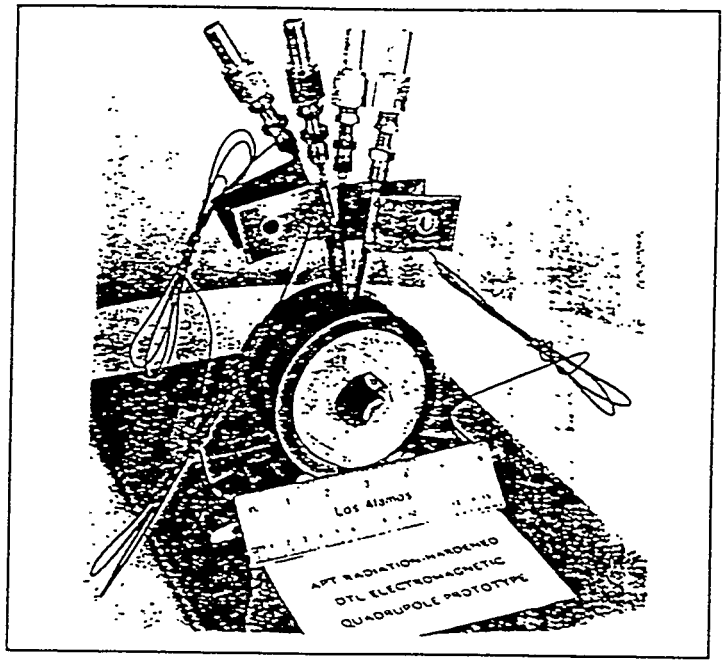


Fig. 3-22. Prototype DTL EMQ.

3.7.3.2 Metal Vacuum Seals

Another major feature of the linac mechanical design is the use of flexible metal seals (Helicoflex type) for all accelerator and beamline vacuum closures. Most Helicoflex vacuum seals are used in conjunction with Helicoflex quick flanges that can be released and re-sealed from the aisle side of the machine with a single air-driven screw. The quick flanges cost about twice as much as an equivalent Conflat flange pair (the conventional standard for high vacuum connectors), but can be released or tightened in seconds, a big plus in a potentially radioactive or thermally hot area. An illustration of the Helicoflex quick flange is shown in Fig. 3-23.

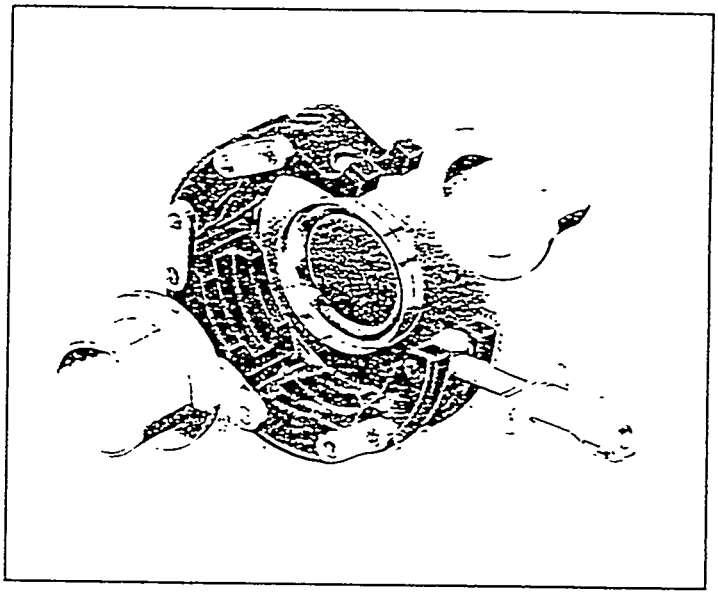


Fig. 3-23. Quick flange.

3.7.2.3 Copper-to-Copper RF Knife Edges

To assure high RF integrity, the RF joints throughout the machine are knife edges, backed up by an independent hard-vacuum Helicoflex seal enclosed between the same flange pair. This concept is illustrated in Fig. 3-24, which shows a typical vacuum and RF seal in the CCL. Knife edges have proven their reliability in cw applications and in high duty factor pulsed linacs (LAMPF). They are used on the RF joints in the APT point design. In all cases, the RF joint is made by two copper-plated steel knife edges pressed ~0.1 mm into both faces of an annealed copper gasket. The gasket is slitted at azimuthal intervals to provide vacuum relief behind the RF joint, and the vacuum seal is made with either a Conflat seal into the same gasket or by means of a separate Wireseal or Helicoflex seal.

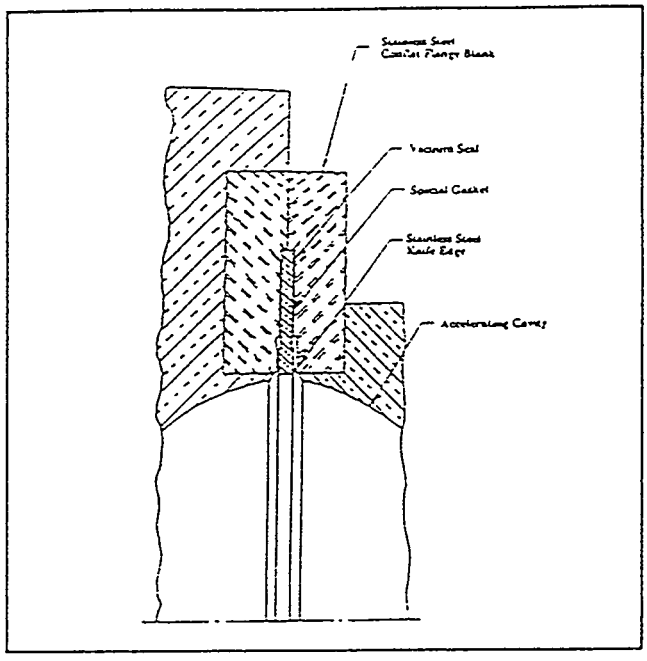


Fig. 3-24. CCL vacuum and RF seal.

3.8 MECHANICAL SUPPORT FACILITIES

The mechanical support facilities that will be required for accelerator alignment, installation, and maintenance consist of a number of well-equipped laboratories. These labs would likely be centrally located, but could be split into smaller installations along the length of the machine. They would be located at grade and well away from the linac tunnel, since they should be permanent occupation zones during accelerator operations.

3.8.1 Alignment Laboratory

The alignment laboratory would contain precision alignment equipment. Key items would be a 1.5-m-thick isolated concrete slab for vibration-free calibration of the equipment and precision-ground stone tables. Both optical and laser alignment equipment would be stored here. This laboratory would be temperature controlled.

3.8.2 Vacuum Laboratory

The vacuum laboratory would contain the equipment necessary to maintain and repair the vacuum pumps. Because the pumps in the APT linac are primarily ion pumps, this laboratory would carry replacement titanium getter elements for these pumps, as well as controllers, cables, power supplies, ion gauges, piping, hosing, and roughdown equipment. The bulk of the spare components (about 40 pumps and ancillary equipment) would be housed in an adjacent warehouse. The vacuum laboratory would require a clean environment

for assembling vacuum components and facilities for cleaning solvent use during assembly and servicing. Several helium mass-spectrometer leak testers will be required to service the linac.

Numerous vacuum valves of various sizes are used in the APT linac. Leak testing the valves and rigging them for on-line installation is a significant part of the vacuum laboratory work. Special trucks and in-tunnel handling equipment are required to move the pumps into position for installation, and to transfer them to tunnel access shafts for repair or rebuilding. Storage in or near the tunnel for the mobile roughdown stations will also be needed.

3.8.3 RF Power Laboratory

A considerable amount of RF power conditioning will be done in the linac accelerating structures after installation and checkout. RF windows may fail occasionally and require replacement. Replacement windows must be coated with titanium nitride to suppress multipactoring. Certain other components of the RF chain, such as the DTL coupling loops, will also require titanium nitriding. The facilities for this treatment should be available on site within the RF lab. The linac carries a great deal of RF instrumentation in the form of monitoring loops, directional couplers, RF diodes, etc., which must be periodically calibrated. During accelerating-structure installation, machine tools are needed to tune the coupling irises. The RF laboratory would contain instrumentation such as directional couplers, RF amplifiers, spectrum analyzers, oscilloscopes, slotted lines, and a variety of other equipment for testing and tuning accelerating structures, and components of the RF distribution network.

3.8.4 Mechanical Maintenance and Remote Handling

To carry out mechanical maintenance on the machine, special handling and lifting equipment is required, such as trucks and "cherry picker" mobile hoists, for the removal and transport of vacuum pumps, quadrupole-doublet assemblies, and other heavy components. This equipment would come from the maintenance laboratory, which plays a major role in the initial machine installation and a supporting role thereafter. If any component or portion of the machine becomes significantly activated, this laboratory would provide special handling or (in extreme cases) the necessary remote handling equipment and expertise. All the tools required to maintain the mechanical equipment will be available in this laboratory, including air-driven tools and special long-handled tools to reduce any possible radiation exposure during maintenance work on potentially activated portions of the accelerator. The laboratory will contain a hot cell with master-slave manipulators for performing off-line service (if needed) on activated components.

3.8.5 Machine Shop

A fully-equipped machine shop that includes welding and brazing capability will be required for maintenance support of the linac. A key processing facility is a large-volume hydrogen brazing furnace, which must be available on site to deal with repair and re-assembly of the oxygen-free copper accelerating structures. The furnace should have sufficient capacity to handle the longest CCL module. A welding shop capable of TIG, MIG, arc, and electron-beam welding will be required. A broad range of machine tools of standard configuration, as well as numerically-programmable milling machines, will also be required.

3.8.6 Diagnostics and Magnets Laboratory

Because of the large number of diagnostic elements and electromagnets in the APT accelerator, a laboratory dedicated to servicing this equipment is necessary. Because most of the diagnostic hardware is exposed to high vacuum when on line, a clean area similar to the vacuum lab is desirable for storage and servicing. A significant amount of electronic equipment is needed for calibrating the diagnostics.

Magnet test and repair requires the availability of high pressure, chilled cooling water of moderate-flow volumes (a few gpm, up to 150 psi). High-current and moderate-current power supplies will also be required. Magnetic-field measuring and mapping equipment in the form of gauss meters, Hall probes, and search coils will be required, along with the normal computer-based, data analysis and readout terminals. Since the APT quadrupoles are mounted as doublets, precision optical equipment and jigs will be needed to align the quads in their mounts. Finally, a taut wire apparatus (described in Chap. 9) must be available to check the magnetic centers of the quadrupoles being serviced.

REFERENCES

3-1. G. Lawrence, "A Los Alamos Concept for Accelerator Transmutation of Waste and Energy Production (ATW)", External Review of ATW Concept, December 10-12, 1990, Los Alamos National Laboratory report LA-UR-90-4432 (1992).

3-2. R. Garnett, R. Mills and T. Wangler, "Beam Dynamics Simulation of the LAMPF Linear Accelerator," Proceedings of the 1990 Linear Accelerator Conference, Albuquerque, NM (1990).

3-3. P. Channell, "Mechanisms and Estimates of Halo Formation," Los Alamos National Laboratory, Private Communications (1993).

3-4. P. Channell, "Estimates of Halo Growth Due to Beam Offset in the Presence of Space Charge," Los Alamos National Laboratory, Private Communications (1993).

3-5. R. Jameson, "Beam Halo from Collective Core/Single-Particle Interactions," Los Alamos National Laboratory report LA-UR-93–1209 (1993).

LOW-ENERGY ACCELERATOR SYSTEMS
CHAPTER 4

Page

4.1 LOW-ENERGY SYSTEMS OVERVIEW 1
4.2 INJECTOR 3
4.2.1 Ion Source 3
4.2.2 Low-Energy Beam Transport (LEBT) 6
4.2.3 Recommendations for Development 9
4.3 RADIO-FREQUENCY QUADRUPOLE (RFQ) 10
4.3.1 Physics 10
4.3.2 Engineering Analysis 12
4.3.3 Mechanical Design Concept 14
4.3.4 Support Structure 15
4.3.5 Vacuum System 16
4.3.6 Diagnostics 16
4.3.7 Recommendations 17
4.4 MATCHING SECTION (RFQ-DTL) 17
4.4.1 Introduction 17
4.4.2 Description of IMS 19
4.4.3 Buncher Cavities 19
4.4.4 Quadrupoles 20
4.4.5 Support Structure 20
4.4.6 Diagnostics 20
4.5 DRIFT-TUBE LINAC 21
4.5.1 Introduction 21
4.5.2 Description 21
4.5.2.1 DTL Parameters 21
4.5.2.2 Physics Design 22
4.5.3 DTL Component Design 23
4.5.3.1 Tanks 23
4.5.3.2 Endwalls 25
4.5.3.3 Girder 27
4.5.3.4 EMQs and Drift Tubes 28
4.5.3.5 Tuners 28
4.5.3.6 Post Couplers 29
4.5.4 Interfaces 29
4.5.4.1 RF Couplers 29
4.5.4.2 Vacuum 30

4.5.5 Diagnostics 31
4.6 THE 350-MHZ RF POWER SYSTEM 31
4.6.1 RF Generator 32
4.6.2 RF Distribution 33
4.6.3 RF Layout 34

LIST OF FIGURES

Page

Fig. 4-1. Plan view of APT low-energy accelerator systems. 2
Fig. 4-2. Elevation view of the APT low-energy accelerator systems. 2
Fig. 4-3. 75-kV extraction system for the APT ion source. 5
Fig. 4-4. SNOW calculation for the 75-kV extraction system. 6
Fig. 4-5. Layout of the APT injector with a direct-injection LEBT. 7
Fig. 4-6. Beam envelope profiles for APT direct-injection LEBT. 7
Fig. 4-7. α–β tuning diagram for injector at RFQ match point. 8
Fig. 4-8. Beam profiles showing the effect of beam neutralization. 8
Fig. 4-9. Various parameters defining the RFQ design vs. position. 11
Fig. 4-10. RFQ thermal heat loads (W/cm^2) from SUPERFISH. 13
Fig. 4-11. APT RFQ cooling details. 14
Fig. 4-12. Electroformed RFQ cavity cross-section. 14
Fig. 4-13. RFQ support structure. 16
Fig. 4-14. Diagram of the RFQ–DTL matching section. 18
Fig. 4-15. RFQ–DTL matching section layout. 19
Fig. 4-16. Drift-tube nose shape and cell geometry. 23
Fig. 4-17. Shunt Impedance for the APT DTL as a function of b. 23
Fig. 4-18. DTL typical cross-section. 24
Fig. 4-19. DTL tank #3, drive loop coupled. 25
Fig. 4-20. APT 350-MHz DTL tank #3 exploded view. 26
Fig. 4-21. DTL end wall. 27
Fig. 4-22. DTL tank #3, waveguide/iris coupled. 30
Fig. 4-23. Overview of high-power 350-MHz RF system for low-energy linacs. 31
Fig. 4-24. LLRF controls for the 2-klystron RF system for the RFQ. 32
Fig. 4-25. RFQ & DTL output efficiency using GTA klystron data (normalized to CERN tube efficiency). 33
Fig. 4-26. RF system layout for 350-MHz systems. 34

LIST OF TABLES

Page

Table 4-1. Comparison of Candidate Ion Sources for cw Injectors 4
Table 4-2. Definition of RFQ Parameters (used in Fig. 4-9) 11
Table 4-3. APT RFQ Error Study Results (Transmission >90%) 11
Table 4-4. Comparison of cw RFQs 12
Table 4-5. RFQ to DTL Matching Section Component Specifications 18
Table 4-6. DTL General Parameters (Each Leg) 22

4.0 LOW-ENERGY ACCELERATOR SYSTEMS

4.1 LOW-ENERGY SYSTEMS OVERVIEW

As illustrated in Fig. 4-1, the low-energy systems of the APT accelerator comprise the following major subsystems, which are assembled in two identical 20-MeV linacs and a beam-combining funnel, in a Y-configuration:

- Two H^+ injectors, each supplying a 110-mA continuous proton beam at 75 keV; each injector includes an ECR ion source, associated RF and dc power supplies, safety cages, and access platforms.
- Two low-energy beam transport (LEBT) sections, including focusing solenoids, collimator interfaces with the RFQs, and large turbomolecular vacuum pumps.
- Two 350-MHz, 8.1-meter-long RFQs enclosed in support cages; each RFQ is powered by two 1-MW klystrons and accelerates a 100-mA beam to 7.0 MeV.
- Two intermediate matching sections (IMSs), consisting of quadrupole lenses and 350-MHz buncher cavities; these elements match the RFQ beams into the DTLs.
- Two 350-MHz DTLs, each consisting of three tanks; each DTL tank is powered by one 1-MW klystron. The DTL accelerates a 100-mA beam to 20 MeV.
- A beam-combining funnel, which consists of two converging transport lines to direct the twin 100 mA, 20-MeV beams into a 350-MHz RF deflector cavity where they are combined into a 200 mA beam.
- A medium-energy beam transport (MEBT) section, which matches the combined beam from the funnel into the BCDTL and provides beam diagnostics and energy measuring equipment.

The Y-configuration illustrated in Fig. 4-1 has an angle between the two legs of 44.8°. Because of the multiple bends in the funnel, the actual beam-convergence point is located downstream from the theoretical convergence point by about 1.1 meters. The length of the accelerator from the ECR ion source to the theoretical convergence point is 21.2 meters. The spacing between the two legs at the ion sources is ~16.2 meters. The total distance (projected along the axis of the Y) from injector to the entrance of the BCDTL, is 23.6 meters.

An elevation view of one leg of the low-energy accelerator system is shown in Fig. 4-2. The figure indicates a hinge pin located at the downstream end of the RFQ support cage that is used during vertical assembly of the eight 1-meter-long RFQ sections.

The low-energy system beamline height (above the floor) is 58 inches (1.47 meters), which has been used throughout the APT linac design. All components, even the large, underslung ion pumps used in the CCL, fit under this height as do the 350-MHz RF couplers used on the DTL tanks. The beamline height was chosen for convenient access to machine components by maintenance personnel. Keeping the accelerator as low to the tunnel floor as practical also serves to stiffen the support structures and raise their mechanical vibration frequencies above the frequencies of normally occurring facility disturbances.

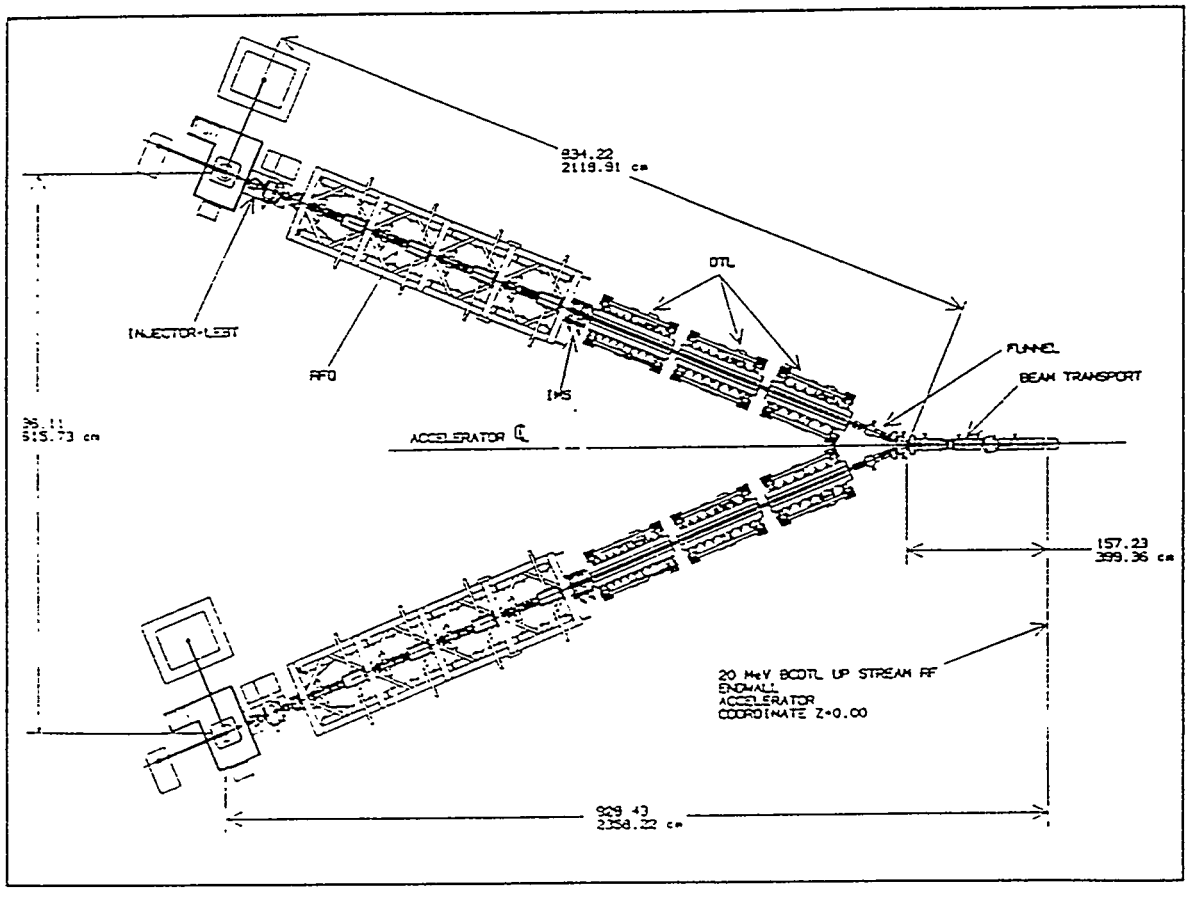


Fig. 4-1. Plan view of APT low-energy accelerator systems.

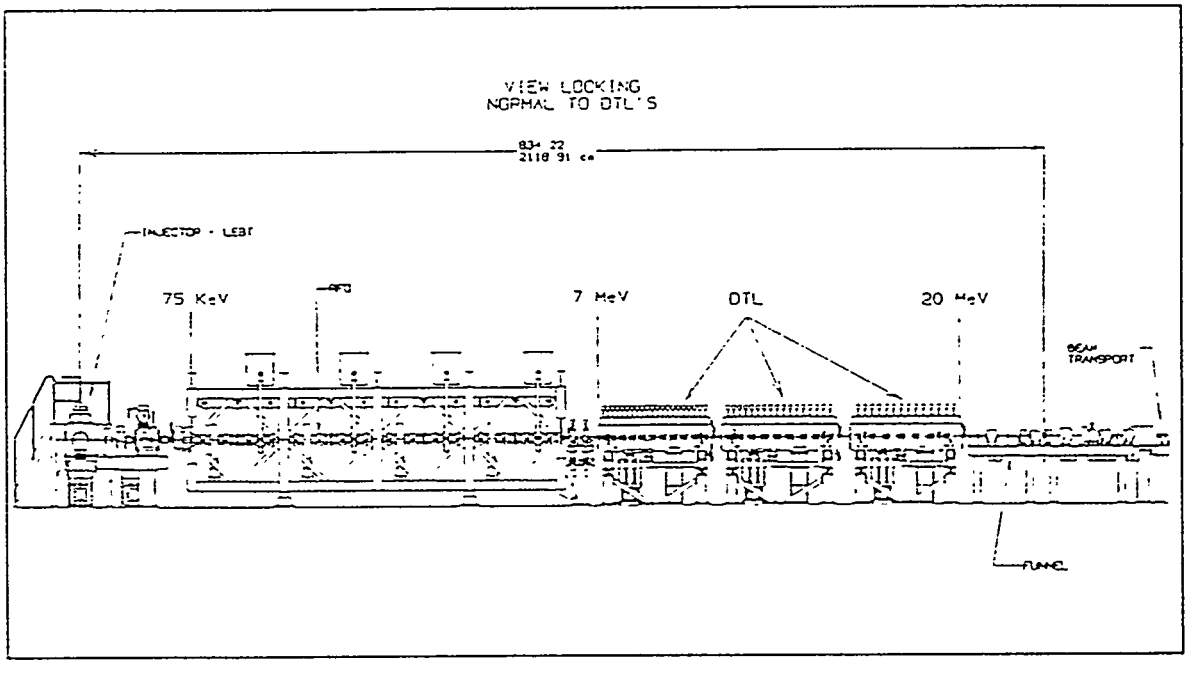


Fig. 4-2. Elevation view of the APT low-energy accelerator systems.

The 20-MeV front end of APT is complex and densely packaged, consisting of several major accelerating structures, all of which require resonance control by means of cooling-water temperature adjustment. There are several different kinds of magnets (7 dipoles, 4 solenoids, 140 EMQs, 20 PMQs), and several individual RF cavities (12 bunchers, one deflector). The 7-MeV RFQ is a much higher-energy design than has been previously considered, and is operated as four resonantly coupled 2-meter-long sections. This high-energy RFQ replaces a difficult-to-build low-energy DTL tank and permits an improved (nearly current-independent) match to the DTL. The latter feature represents a major asset during accelerator turn-on and tuning.

4.2 INJECTOR

4.2.1 Ion Source

The H^+ injectors for the APT accelerator must provide stable high-intensity proton beams with high availability. Thus, these injectors must be designed for a long operational lifetime and for low fault rates.

For the APT application, the accelerator is expected to be on-line for 7800 hours per year, with an overall availability of 85%. This translates to full (100%) availability for 75% of the calendar year. To achieve this total accelerator availability, it is anticipated that the injector availability will have to approach 98% during the scheduled on-time. Routine ion-source maintenance may be done once per week during a scheduled 8-hour maintenance period; thus, the meantime between ion-source failures must exceed this time. The injector fault rate (primarily high-voltage sparking) must be limited to less than once per hour. Automated fault recovery must be provided in the injector to reestablish the beam in the linac quickly, with minimal perturbation and beam spill. The LEBT system must provide proper matching and centroid control at the RFQ entrance and must pump the effluent gases from the ion source. Noninterceptive beam diagnostics are needed in the LEBT to ensure proper tuning and on-line monitoring of the injector beam.

The choice of an electron-cyclotron-resonance (ECR) ion source for the APT accelerator has been made on the basis of proven performance in 100% duty-factor operation, for long-term availability and operational stability, as well as specific beam intensity and emittance requirements.

Gas and discharge efficiencies are important criteria for 100% duty-factor ion sources. The ion-source gas efficiency, η, is defined as

$$\eta = 6.95 i_{H^+} \div Q_{H_2} \ ,$$

where the proton current, i, is expressed in amperes (A) and the hydrogen flow, Q, is given in standard cm^3 per minute (sccm). The discharge power efficiency, ζ, is given by

$$\zeta = j_{H^+} \div P_d \ ,$$

where j_{H^+} is the proton current density in mA/cm^2 at extraction, and P_d is the discharge power in kW.

Other important operating parameters are the proton current, proton fraction, beam emittance, and source lifetime. Table 4-1 summarizes the demonstrated performance of several candidate ion sources for the APT injector application. These are the multicusp source with filament drive, the multicusp source with 2.0-MHz RF drive, the monocusp ion source, and the 2.45-GHz ECR ion source. Emitter radii, r_e, are given immediately below the source description in the first column. The extraction voltage, V_{ext}, is given in the second column and the total extracted beam current, i, (with proton current in parentheses) is given in the third column. A high proton fraction (ratio of proton current to total ion current) is desirable to limit beam perveance and to eliminate the need for mass analysis. The discharge power, P_d, is presented in the fourth column, and the discharge power efficiency, ζ, is shown in the fifth column. The duty factor (DF) employed for the data presented is shown in the sixth column, and the gas efficiency, η, is shown in the seventh column. Finally, the measured normalized emittance at 95% beam fraction is shown in the last column. A Gaussian phase space distribution has been assumed to contain the 95%-beam-fraction emittance values.

Table 4-1. Comparison of Candidate Ion Sources for cw Injectors

Type Source	V_{ext} (kV)	i (mA)	P_d (kW)	ζ (mA/cm²kW)	DF (%)	η	ε @95% (π · mm-mrad)
Multicusp (filament) r_e = 0.4 cm	60	56 (45) H^+	7.1	13	100	0.07	0.59
Multicusp (2.0-MHz RF) r_e = 0.32 cm	35	82 (70) H^+	18.0	12	0.3	0.02	0.60
Monocusp (filament) r_e = 0.65 cm	200	200 (120) D^+	1.5	60	100	0.14	-
ECR proton (2.45 GHz) r_e = 0.35 cm	42	96 (67) H^+	0.6	290	100	0.31	0.60

The ECR ion source that was recently developed at the Chalk River Laboratory (CRL) in Canada is the most promising candidate for APT, as evidenced by its proven cw performance and high gas and discharge efficiencies (η, ζ). The basic ECR confinement geometry has been modified to optimize the production of protons by eliminating the axial confinement geometry (mirror fields). Operation at 2.45-GHz microwave frequency is sufficiently low that the required axial magnetic field of 875 Gauss for ECR resonance produces minimal growth in the beam emittance after extraction. Current densities up to 500 mA/cm² at 90% proton fraction have been achieved. Operation in an off-resonance mode improves beam stability at some expense in beam current. This ion source has been used for several years with the RFQ1 experiment at Chalk River and has demonstrated sufficient lifetime and stability at the 90-mA total-current level to support extended operation of their cw RFQs.

Another promising candidate ion source for APT is the RF-driven, multicusp, volume ion source. A 2.0-MHz version of this source has been tested at low duty factor and has demonstrated 85% proton fraction with currents close to that needed. A low gas efficiency was observed in these low duty factor tests; this efficiency, however, is expected to increase for 100% duty-factor operation. The observed beam emittance was essentially the same as that of the ECR source. A low-current (30 mA) version of this source is now being tested for

on-line operation on the injector at the Paul Scherrer Institute in Switzerland; therefore, data on its long term performance will soon be available. Further testing of the various candidate ion sources is needed at 100% duty-factor before a final choice can be made.

A single-gap extractor operating at 75 kV has been selected based on previous operating experience (at 100% duty factor) with the FMIT (Fusion Materials Irradiation Test facility) injector. A layout of the ion extractor now being considered is shown in Fig. 4-3.

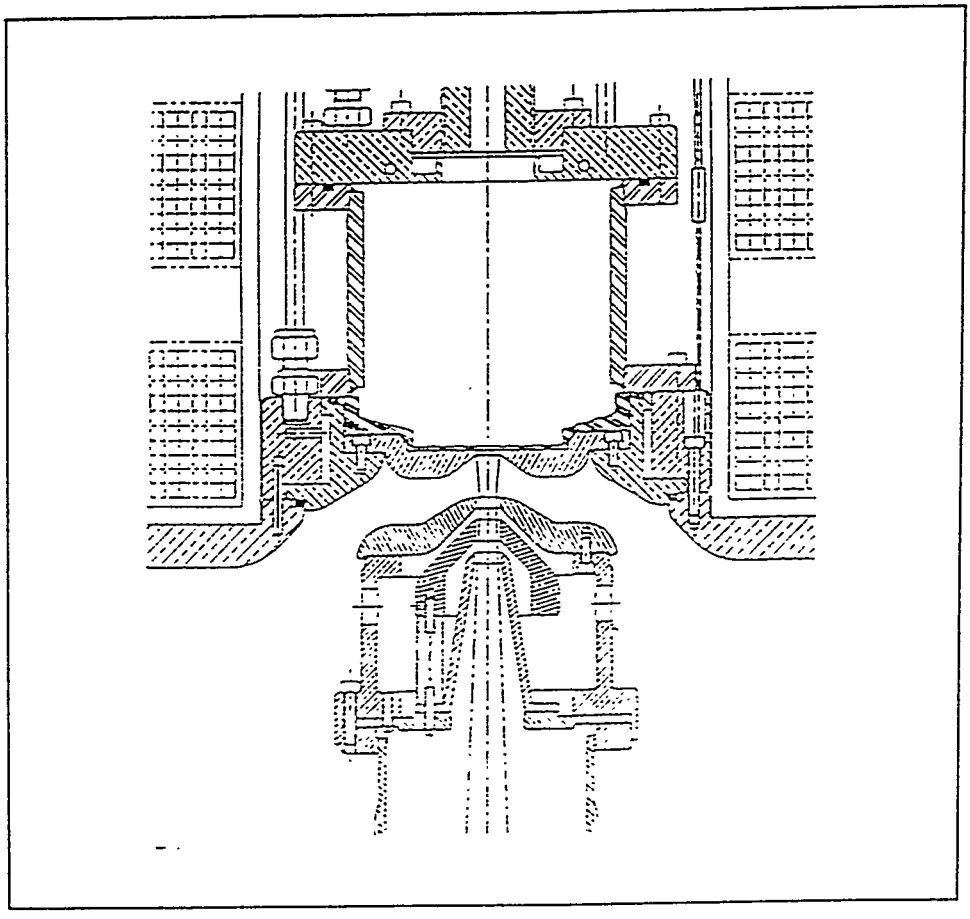


Fig. 4-3. 75-kV extraction system for the APT ion source.

This extraction system has been designed to produce 110 mA of protons, assuming a proton fraction of 85%, with H_2^+ and H_3^+ fractions of 7.5% each. Thus, this design entails a total extracted ion current of 130 mA. The extracted current density was chosen to be 235 mA/cm^2 with an emitter radius of 0.42 cm. This extractor design was carried out using the SNOW code. Ion trajectories and equipotentials from the SNOW code simulations are shown in Fig. 4-4.

The electron trap is a proven design used in the FMIT injector. Calculations have been carried out for a range of extracted currents. The geometry shown in Fig. 4-4 has a minimum emittance at the design current of 130 mA. The minimum divergence occurs at a lower current density and thus the design is not optimal in terms of beam divergence.

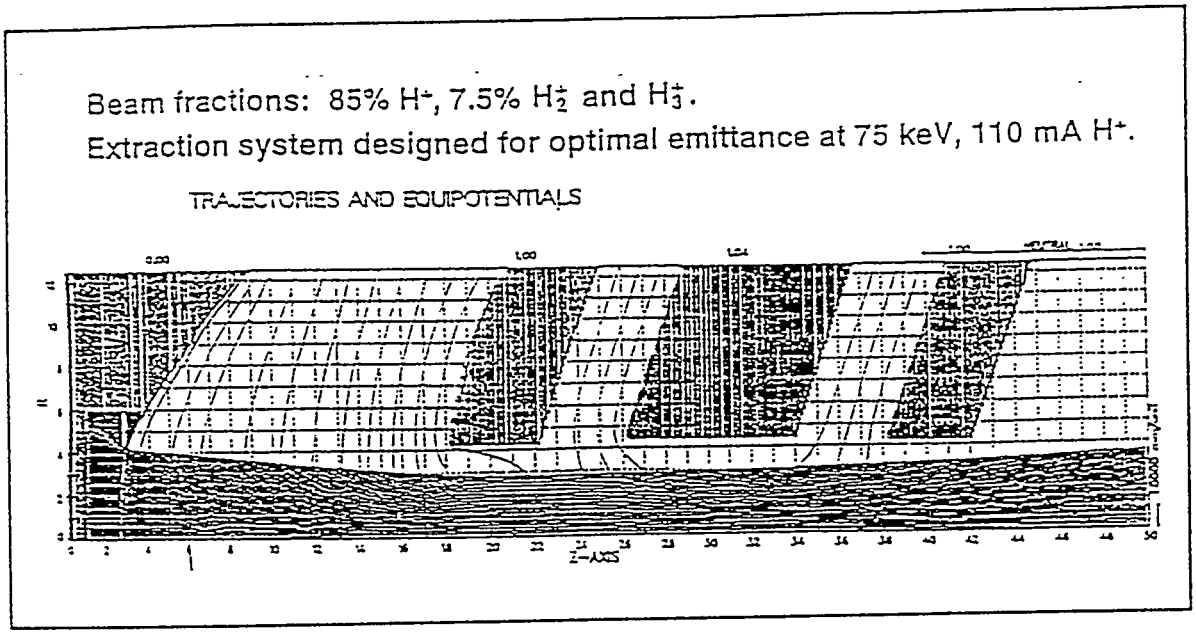


Fig. 4-4. SNOW calculation for the 75-kV extraction system.

4.2.2 Low-Energy Beam Transport (LEBT)

The LEBT system transports and matches the beam extracted from the ion source to the RFQ linac. The optimal-emittance design beam predicted from the SNOW simulations for this application has an envelope radius of 0.43 cm and an envelope divergence of 46 mrad, while the input beam required for proper match to the RFQ has an envelope radius of 0.29 cm and an envelope convergence of 53 mrad. The function of the LEBT is to transport and match this diverging beam to the converging acceptance of the RFQ.

Two basic approaches can be used for such a LEBT system, depending upon whether electric or magnetic optics are used. Electrostatic transport systems have been used to transport 100-mA, 100-keV H- beams, and could be also be used in this high-current proton beam application. This option entails the transport of unneutralized beams and is less sensitive to beam noise and beam instabilities. However, it is limited by space-charge effects for high perveance beams and has relatively large chromatic aberrations. A magnetic-element LEBT, which is the baseline choice made for APT, uses gas neutralization to reduce the focusing requirements, and has other advantages. A two-solenoid magnetic-lens system preserves the cylindrical beam symmetry and is extremely versatile in beam matching to the RFQ. For the APT application with a 130-mA beam at 75 keV, the beam is expected to be over 95% space-charge neutralized and thus, space-charge effects will be minimal. Fig. 4-5 shows the ion source and a two-solenoid-lens direct-injected LEBT.

Fig. 4-6 shows the expected beam profiles in this design for all three ion species. Assuming 85% proton fraction, these simulations show that less than 0.5 mA of H_2^+ and H_3^+ contaminant ions enter the RFQ input aperture for this design. These currents are much less than the expected proton losses in the RFQ, and thus should not pose an operating problem.

In addition to the solenoid focusing lenses, steering elements are needed in the LEBT to correct for minor ion source and magnet alignment errors. Two steering pairs placed

between the solenoid lenses can provide these corrections. Steering algorithms have been developed to provide independent control of both centroid position and angle in both transverse planes. Beam centroid position is the more important parameter to be controlled because the RFQ is relatively insensitive to centroid angle errors.

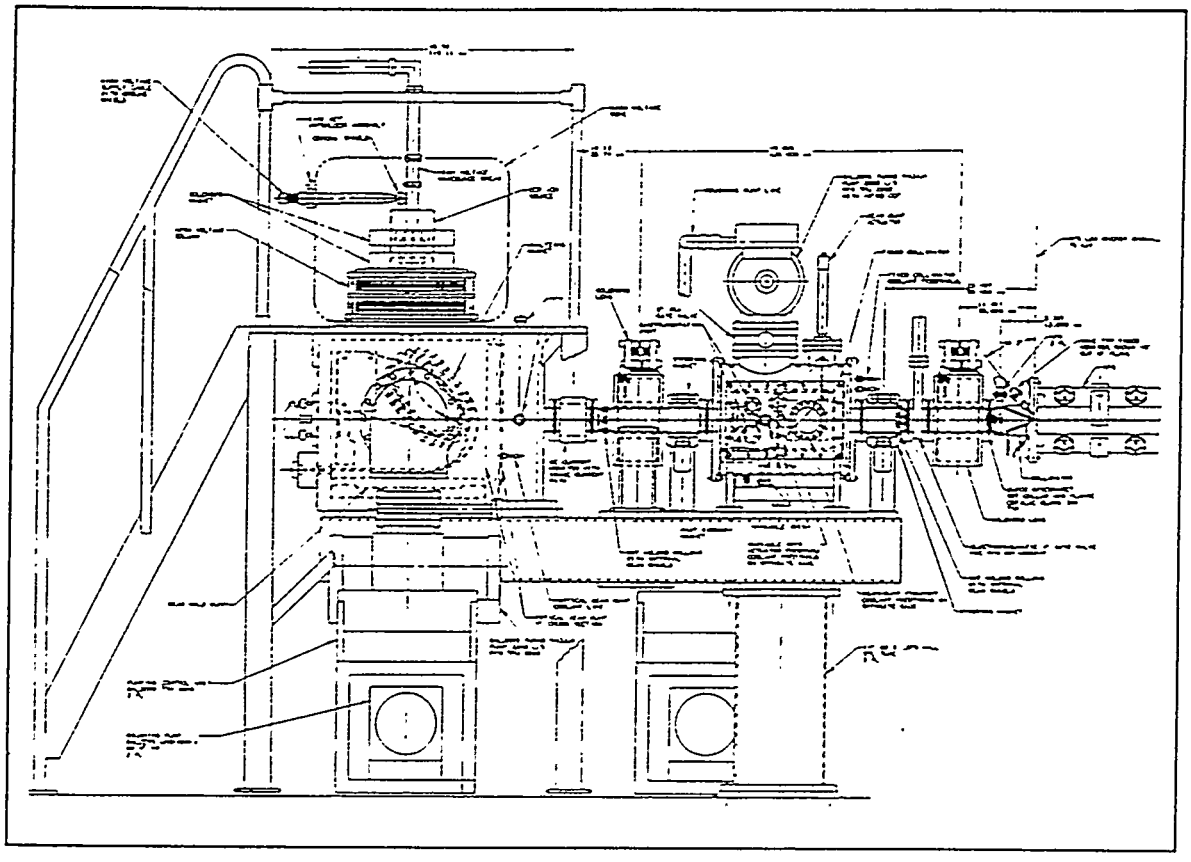


Fig. 4-5. Layout of the APT injector with a direct-injection LEBT.

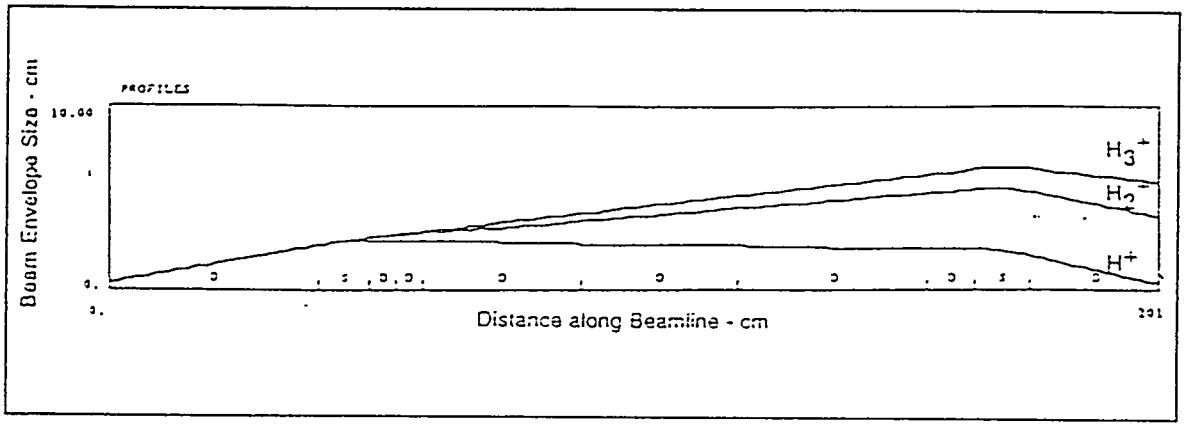


Fig. 4-6. Beam envelope profiles for APT direct-injection LEBT.

The injector design presented is for a nominal current density of 235 mA/cm^2, but designs have also been carried out for a range of current densities from 200 mA/cm^2 to 500 mA/cm^2. The 235 mA/cm^2 refers to the nominal current density at the ion source exit (the 8.4-mm ion-source aperture diameter gives the desired 110 mA at the RFQ input with ample margin). The two-solenoid-lens LEBT has a tuning range that is sufficient to match any of these beams to the RFQ accelerator. Figure 4-7 shows the α–β tuning diagram for the nominal current-density design of 235 mA/cm^2.

This diagram is a plot of the beam Twiss parameters α and β at the RFQ match point. The contours show the loci of the Twiss parameters that are obtained at the RFQ entrance for a specified excitation of the first LEBT solenoid while the strength of the second solenoid is adjusted. The allowed errors for tuning the RFQ can be displayed by calculating the contour in this tuning space of the beam mismatch factor between the off-tune beam and the desired RFQ beam. A mismatch contour for a 0.3 mismatch factor, a conservative error limit, is shown in the tuning diagram. All beams within this contour have an acceptable transmission loss in the RFQ. Using two solenoids provides an adequate tuning range in α-β space to accommodate variations in the input proton beams or to provide different match conditions to the RFQ, if needed. In these simulations, the input beam was assumed to be fully neutralized. Beam profiles for the 100% and 95% neutralized cases are shown in Fig. 4-8.

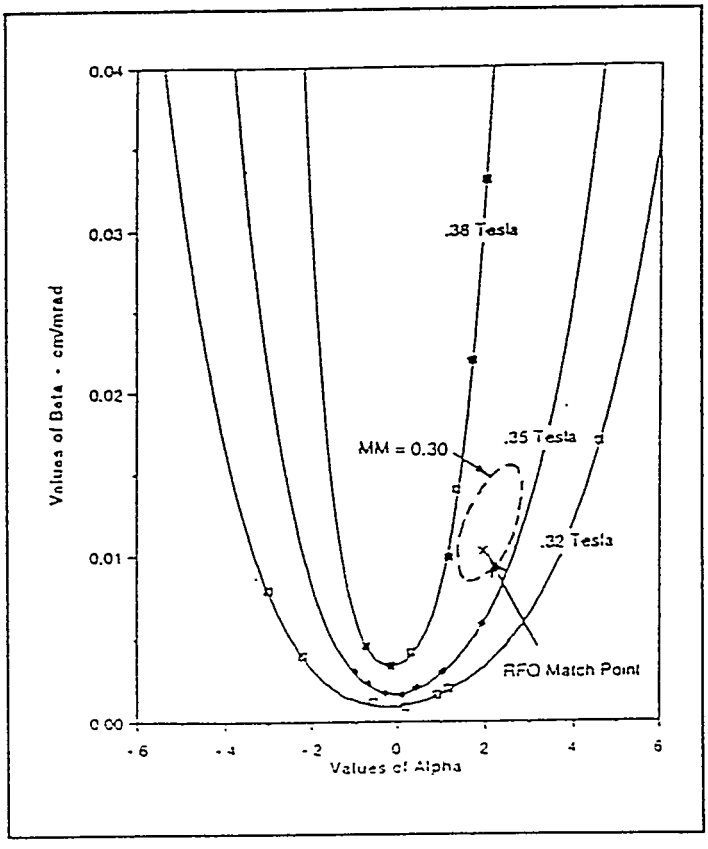


Fig. 4-7. α–β tuning diagram for injector at RFQ match point.

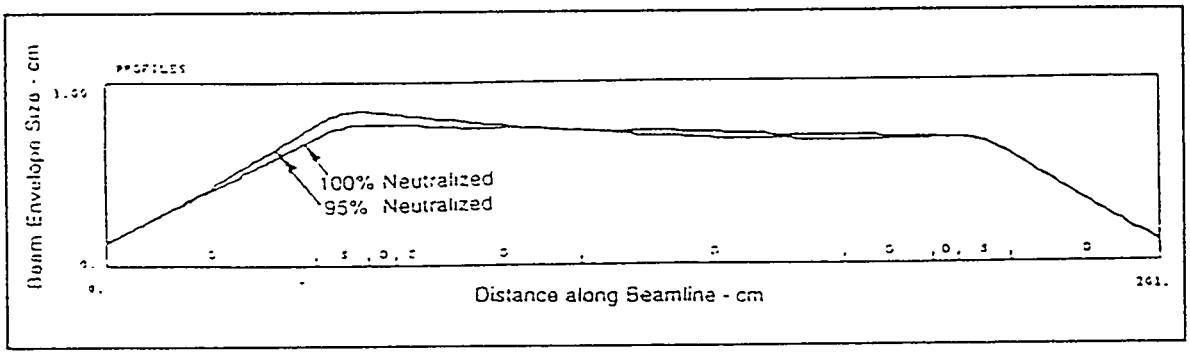


Fig. 4-8. Beam profiles showing the effect of beam neutralization.

The transport tune was adjusted for the two cases shown in Fig. 4-8 to provide the same match at the RFQ entrance. The example shows that a two-solenoid LEBT design has sufficient flexibility to account for changes in the beam neutralization. The calculations were done for a phase-space area corresponding to six times the specified emittance. This emittance choice corresponds to a 100% beam fraction for a uniform waterbag distribution, and to ~95% beam fraction for a Gaussian distribution. Similar tuning diagrams were found for beams with 95% neutralization, and for input beams obtained with ±15% current variation from the nominal 130 mA design beam .

Error studies indicate that beam-centroid positioning must be controlled within ±0.50 mm and ±10 mrad at the RFQ match point. Optical aberrations are limited by conservative design of the solenoid lenses, with the beam filling less than half the magnet bore, and by optimization of the extractor system. The use of adequate pressure in the transport line (1×10^{-5} torr of a suitable background gas) ensures that beam neutralization limits the nonlinear space-charge-induced emittance growth in the LEBT.

Additional hardware in the LEBT includes a fast-kicker magnet that provides a means to rapidly abort the proton beam (in <20 μs) if a fault occurs anywhere in the accelerator or target systems, dumping the beam into collimators. Provision is also made to insert a variable iris at the midpoint of the LEBT. The variable iris can adjust the beam-current level injected into the RFQ to facilitate cw turn-on of the accelerator. It provides a means to ramp the current in the accelerator from zero to design value over several seconds. Because the accelerator focusing lattice is relatively insensitive to beam current, this transverse-aperturing scheme can be used to vary the current smoothly during initial machine turn-on or while recovering from fault conditions without inducing excessive beamloss.

Noninterceptive beam-diagnostic sensors are included in both the injector and the LEBT to facilitate beam tuning and to diagnose operating problems. Optical profile monitors provide continuous, on-line beam-profile and centroid monitoring. Tomographic techniques can be used to deduce the beam emittance. Proper setting of ion-source parameters can be achieved by tuning for optimal profile shape. The tune of the focusing and steering elements can also be monitored on-line by these profile monitors with a positional accuracy of ±0.2 mm. A dc transductor provides continuous monitoring of the LEBT beam current. An insertable beam dump is provided in the LEBT downstream from the beam-abort kicker for limited beam-off periods when it is necessary to remove the beam from the accelerator without turning off the ion source. The beam-abort kicker and collimators are only employed for very brief beam interruptions. Water-cooled collimators and apertures are used throughout the transport line to intercept any errant beam. The H_2^+ and H_3^+ molecular ion beams are mostly intercepted on collimators at the entrance of the RFQ and at the midpoint of the LEBT.

4.2.3 Recommendations for Development

The basic design for the injector required for the APT accelerator has been described above. With the advent of the RFQ linac, required injector energies can be much lower than was previously the case, greatly enhancing reliability and operability. An ECR ion source operating with a standard high-voltage column, and feeding a magnetic-transport line using solenoid lenses presently appears to be the most suitable design solution for the APT injector. Further development and testing of this system is needed to confirm that the required long-term operation can be achieved.

4.3 RADIO-FREQUENCY QUADRUPOLE (RFQ)

The RFQ proposed for APT is a 100% duty-factor (cw) linac that produces a 100-mA beam of protons with an output energy of 7 MeV. The RFQ concept was shown previously in Fig. 2-7, with the general specifications given in Table 2-2. This design is described in complete detail in Ref. [4-1]. The present RFQ concept is an extension of the robust design that operated successfully on BEAR (Beam Experiment Aboard Rocket) in 1988 [4-2]. The same concept was also used for the CWDD (Continuous Wave Deuterium Demonstrator) and for the injector linac in the SSC (Superconducting Supercollider) [4-3]. BEAR and CWDD are accelerator experiments within the SDI-supported NPB (Neutral Particle Beam) Program. The APT RFQ is an 8-meter-long structure consisting of four 2-meter-long segments that are resonantly coupled together. Each segment is a resonant structure assembled from two 1-meter sections. In an early version of the APT linac design, the RFQ had a conventional output energy (2.5 MeV). The present 7-MeV RFQ is an advanced design representing an extension of the technology that solves difficulties in the previous linac design (in the DTL lowest-energy accelerating tank and the RFQ-to-DTL match). While computer modeling and preliminary low-power RF tests provide confidence that such a high-energy RFQ will perform satisfactorily, additional development and testing is needed for confirmation. If unforeseen problems crop up, the earlier 2.5-MeV RFQ design (coupled with a low-energy DTL tank) provides a backup solution, although a less-satisfactory one.

4.3.1 Physics

The RFQ design uses recently improved beam-dynamics codes [4-4] that include multipole field effects, and these codes have been benchmarked successfully against operating RFQs. The APT RFQ system design incorporates a current-independent match to the RFQ/DTL matching section. The overall physics design is conservative, with a transverse current limit greater than 240 mA throughout the length of the structure. The longitudinal current limit exceeds 150 mA beyond the 1-MeV point.

The details of the beam-dynamics parameters are plotted in Fig. 4-9 as a function of distance along the RFQ. The parameters on these curves are defined in Table 4-2 below.

The peak surface field along the length of the vane tips does not exceed 1.8 times the Kilpatrick sparking limit. This criterion for the safe working electric-field level was selected on the basis of experience with the CRL RFQ [4-5, 4-6] which was designed at 1.75 times Kilpatrick and has been operated at up to 2.1 times the Kilpatrick limit.

A major concern in the RFQ physics design is the dependence of beam transmission on a variety of possible errors and parameter variations. Error studies have been carried out and the results are summarized in Table 4-3. The conclusion is that the proposed RFQ design will transmit more than 90% of the input beam with reasonable alignment tolerances and operating parameter variations.

It has been the practice in RFQ design to use longitudinal variation of the ratio of the vane-tip (transverse) radius of curvature (ρ) to the vane-tip displacement (r_0) to maintain a longitudinally-uniform local resonant frequency while the aperture varies. For the APT RFQ, the value of ρ/r_0 is held constant at 0.85, which is a compromise between minimum peak surface fields ($\rho/r_0 = 0.75$) and minimum multipole effects ($\rho/r_0 \sim 1.00$). The resonant frequency is held constant while r_0 varies with the cavity cross-section (inductance) by modulating the width of the vane base. This also maintains a low capacitance, which reduces the structure power.

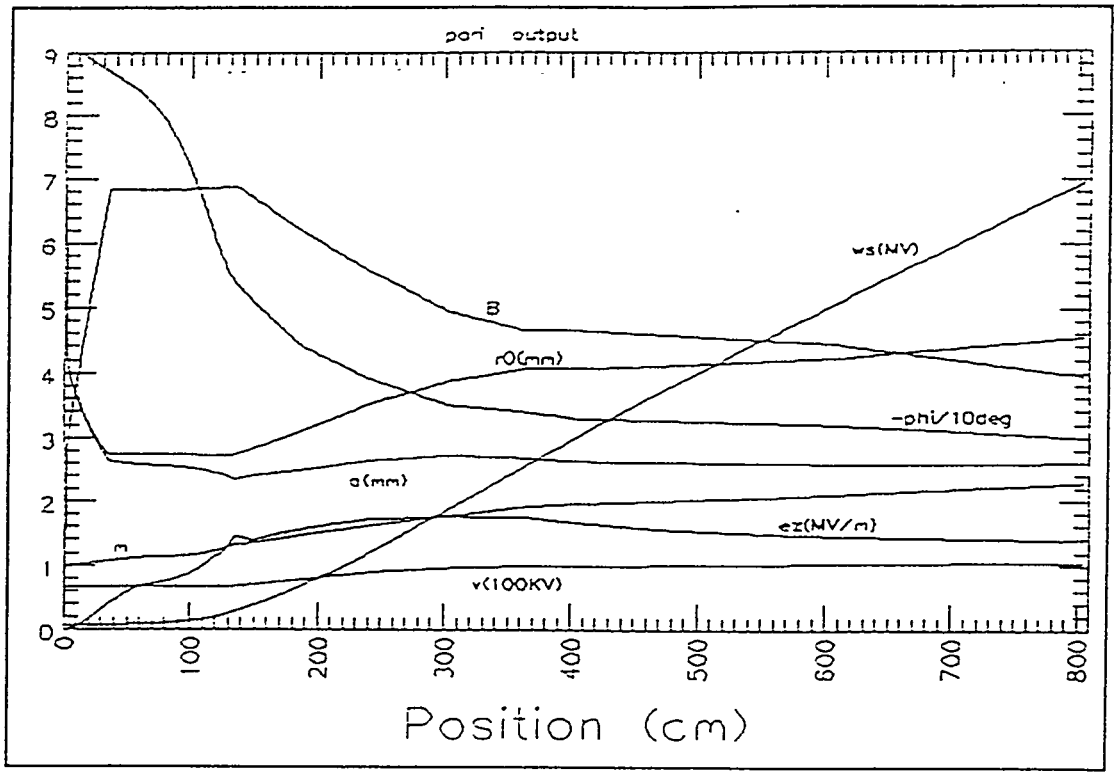


Fig. 4-9. Various parameters defining the RFQ design vs. position.

Table 4-2. Definition of RFQ Parameters (used in Fig. 4-9)

B	Focusing Strength (dimensionless)
r_o	Average Vane-tip Displacement (mm)
a	Half-aperture (mm)
m	Modulation Parameters (dimensionless)
e^z	Accelerating Gradient
-phi/10 deg	Synchronous Phase (divided by 10)
v	Intervane Voltage (100 kV)
ws	Proton Energy (MeV)

Table 4-3. APT RFQ Error Study Results (Transmission >90%)

Allowable Input Beam Displacement (mm)	1.0
Allowable Input Beam Angle (mrad)	23.0
Allowable Vane Voltage Range	0.95 <V/V *design* <1.25
Allowable Input Energy Range (keV)	±2
Allowable Input Beam Emittance (π·cm-mrad)	0.025
Allowable Input Beam Current (mA)	<120
Allowable Field Tilt (%/m)	5

Producing an output beam of 7 MeV while maintaining peak surface fields below 1.8 times the Kilpatrick limit leads to a long RF structure. The proposed APT RFQ will have an electrical length of 9.45 wavelengths. The CWDD RFQ, at 4.6 wavelengths, is the longest one built to date. It was tuned as a single cavity using procedures that resulted in field tilt and dipole errors <5% of the specified quadrupole fields [4-7].

For the longer APT RFQ, a coupled-cavity structure is planned [4-8]. Use of a coupled-cavity structure for the APT RFQ was verified by preliminary low-power RF experiments conducted at Los Alamos [4-9]. These "cold-model" tests demonstrated that resonantly coupling 2-meter-long segments together to form an 8-meter-long structure is feasible.

A comparison of cw RFQs is given in Table 4-4. The state of the art with respect to maximum output energy for 4-vane RFQs in the APT frequency range is presently 2.5 MeV (the SSC injector linac). There is limited experience in the operation of cw RFQs. Most of the experience that exists was gained in a recently terminated development program at CRL (0.6-MeV and 1.2-MeV RFQs). The equipment from this program has recently been moved to LANL, where a follow-on study to gain additional operational experience with cw systems is being pursued. A higher-energy (cryogenic) cw RFQ (2 MeV, D^-) has been designed and fabricated for the CWDD project, but has not yet been operated. The FMIT [4-10] RFQ (2 MeV, H_2^+) operated briefly. The proposed APT RFQ will have an output energy of 7.0 MeV, much higher than previous designs. Theoretical analysis and preliminary low-power RF measurements indicate that the high energy poses no special performance challenges.

Table 4-4. Comparison of cw RFQs

Parameters	FMIT	CRL1	CRL2	CULHAM	CWDD	APT
Particle	H_2^+	H^-	H^-	H^-	D^-	H^+
Frequency (MHz)	80	267	267	352	352	350
Injection Energy (keV)	70	50	50	100	200	75
Final Energy (MeV)	2.0	0.6	1.27	2.0	2.0	7.0
Output Current (mA)	100	75	75	101	80	105
Length (m)	4.00	1.47	1.47	2.52	3.97	8.10
Gradient (MeV/m)	0.48	0.37	0.83	0.75	0.45	0.87
No. of Wavelengths	1.00	1.31	1.31	3.00	4.66	9.48
Peak Surface Field (Kilpatrick)	1.00	1.50	1.75	1.80	1.80	1.80
Structure Power (kW)	407	83	95	210	160	1200
Beam Power (kW)	193	50	105	200	144	963
Total Power (kW)	600	133	200	410	304	1923
Power/Length (kW/m)	100	56	65	84	40	150
Power/Area (kW/m^2)	4	24	28	63	30	114
Maximum Surface Power (W/cm^2)	-	8.67	10.00	9.88	2.70	12.00
Maximum SF* End Power (W/cm^2)	-	-	60.00	-	-	65.00

* SUPERFISH

4.3.2 Engineering Analysis

Most engineering problems associated with cw operation result from the RF thermal loads on the cavity surfaces and are independent of output energy or electrical length. A cross-section of the RFQ and the associated RF thermal loads from a SUPERFISH analysis are shown in Fig. 4-10.

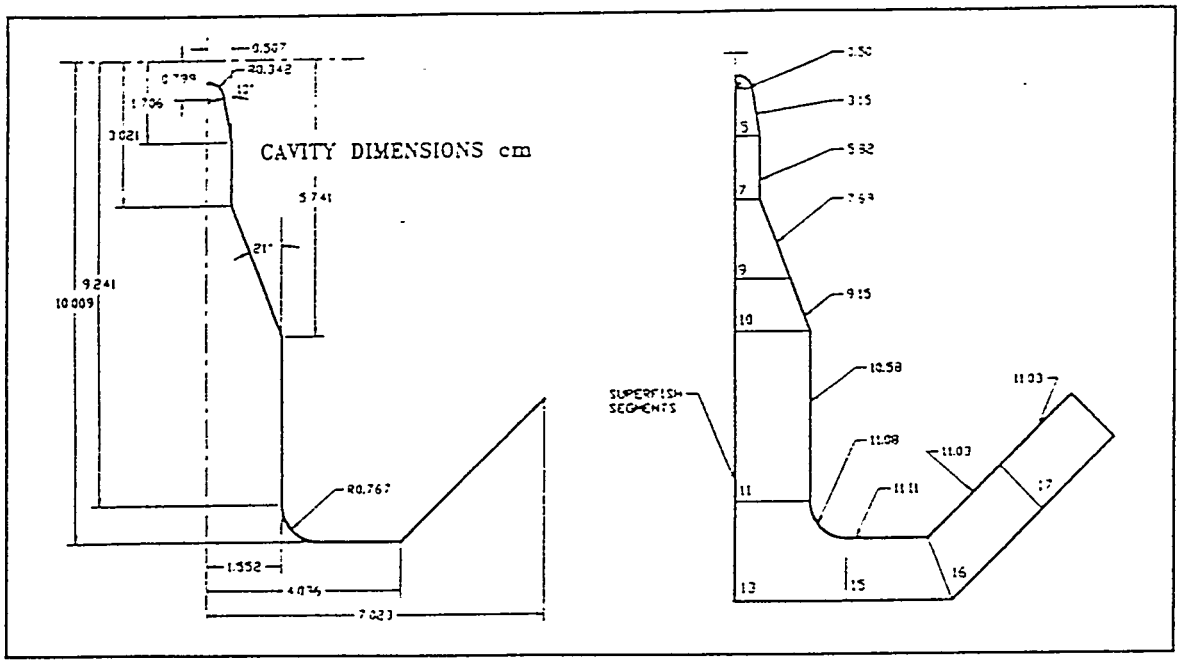


Fig. 4-10. RFQ thermal heat loads (W/cm^2) from SUPERFISH.

It is instructive to compare the RF heat loads in the APT RFQ with those in CRL2 (shown in Table 4-4). Although the peak heat flux on the cavity surface and in the end region of the APT RFQ is not significantly greater than that for the CRL2 RFQ, the design of the cavity is different because of the higher beam current and brightness. This results in the average power per unit length being significantly higher for APT (150 kW/m vs. 65 kW/m). Furthermore, with the higher frequency (smaller surface area) of the APT RFQ, the average power per unit area is a factor-of-four higher for APT (114 kW/m^2 vs. 28 kW/m^2).

To accommodate the high heat loads, there are a total of 20 longitudinal coolant passages, one near each vane tip, two in the skirt of each vane, and two in the wall of each cavity. These are shown on Fig. 4-11. The end region coolant paths will be designed as shown in Fig. 4-11 to assure good cooling in the end region where thermal loads are highest.

To minimize the longitudinal frequency shifts resulting from heating of the coolant, the coolant passages run one-half the length of the structure. With a bulk velocity of 15 fps in each of the 20 passages, the longitudinal frequency shift over the 0.5-m length of the coolant passages is 25 kHz, an acceptable value. The total coolant flow is 1040 gpm for each of the two RFQs. The coolant pumping power requirement is approximately 50 hp per RFQ.

Cavity frequency is controlled by varying the inlet temperatures of the base and wall coolant passages. Given that the RF power deposited along the structure varies along its length, the inlet temperatures of each of the base and wall coolant passages will vary as is necessary to maintain a zero frequency shift locally.

Further engineering information on the APT RFQ can be found in "Conceptual Design of a 7-MeV RFQ Linac for the Accelerator Production of Tritium" [4-1]. The details and the results of several engineering studies, including finite element, thermal and structural analyses, a 3D thermal analysis, and a 3D structural analysis, are described in this reference. The results were found to be satisfactory.

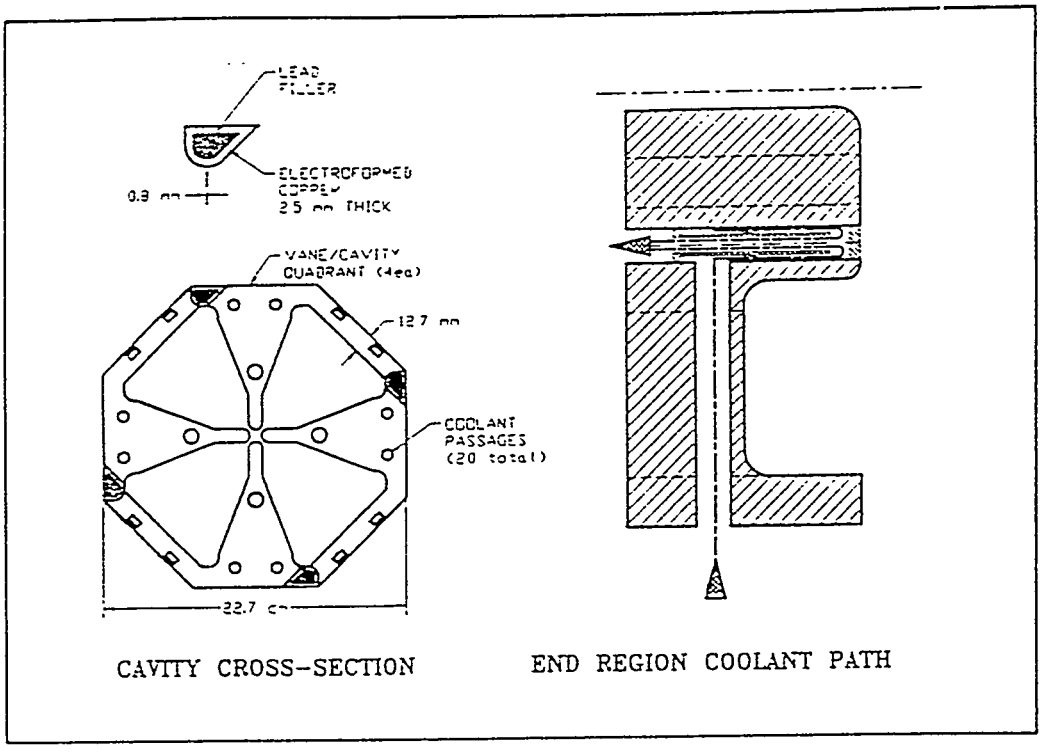


Fig. 4-11. APT RFQ cooling details.

4.3.3 Mechanical Design Concept

The mechanical design of the APT RFQ—an extension of the mechanical design concept that was developed for the RFQ on the BEAR project and later used for the CWDD and SSC RFQ projects—incorporates four individual vane-cavity quadrants that are joined by electroforming to produce monolithic 1-meter-long sections. A cross-section of the cavity and electroformed joints are shown in Fig. 4-12. Before the joints are electroformed, the vane-cavity quadrants are mounted in a rigid frame. Temporary RF seals are installed in the electroformed joint volumes and cavity frequency and RF field distribution measurements are performed before commencing the electroforming process.

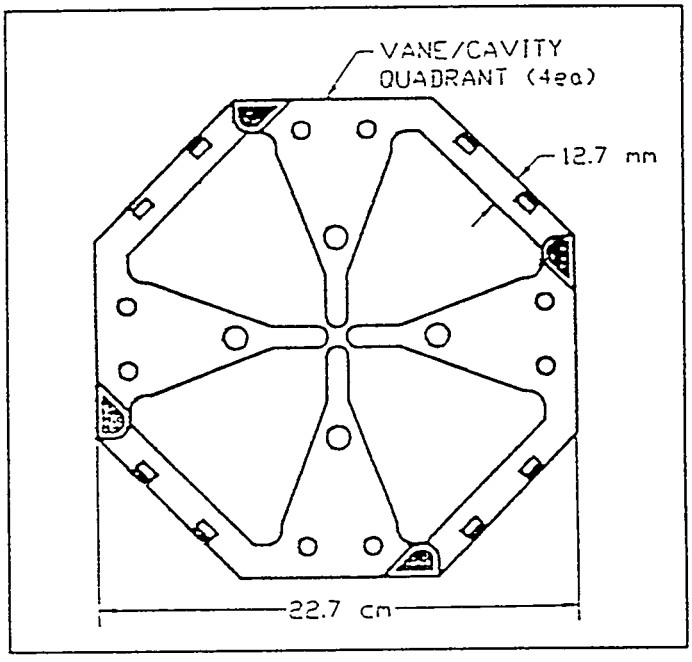


Fig. 4-12. Electroformed RFQ cavity cross-section.

The mechanical design concept described here was selected for the APT RFQ because it offers the following advantages:

- **Integral Vacuum Vessel.** The cavity walls form the vacuum vessel, thus minimizing the number of vacuum seals and allowing easy access to tuners, RF probes, drive loops, and coolant fittings.
- **No RF Joints.** There are no longitudinal mechanical RF joints, which minimizes concerns about cavity Q degradation caused by corrosion of RF seals and surfaces. In other cw RFQ applications, high power dissipation that has resulted in high temperatures in such joints has been a problem.
- **RF Tuning Stability.** The vanes are integral parts of a monolithic structure. There is no stored energy (produced by thermal cycling or other sources) to be released that could cause changes in the mechanical alignment or RF tuning.
- **High Structural Efficiency.** The completed monolithic structure, with the exception of the tuners, drive loops, and pickup loops, is entirely load-carrying. This serves to mitigate the cost and complexity of the mechanical support system.

4.3.4 Support Structure

A major consideration in the design of the APT RFQ is its length. The longest physical length of a 4-vane RFQ is currently the 7-meter-long 100-MHz heavy ion RFQ *TALL* for the TARN II synchrotron [4-11]. At 100 MHz, the cavity bore diameter is 58 cm, giving a length-to-diameter ratio of 12—a moderately stiff structure. The APT RFQ has a length-to-diameter ratio of 35. The bending stiffness of such a structure varies roughly as the cube of the length-to-diameter ratio. Mechanical support of the long slender APT RFQ structure is thus a matter of concern. This also affects the choice of RFQ cavity material.

The engineering analysis and design concept of the APT RFQ and its support system were carried out assuming OFE copper as the cavity material. There are, however, two other choices: tellurium copper and GLIDCOP™, an alumina dispersion-strengthened copper that has high yield strength. A comparison of materials which have been used for RFQs is given in the Chap. 4 Appendix (Table 12.2.4-1). Aluminum and steel are eliminated because of their lower thermal conductivity. Zirconium-copper is not a suitable substrate for the electroforming joining process.

The support system for the APT RFQ, shown in Fig. 4-13, is a statically indeterminate arrangement. The statically indeterminate support was necessary because of the slenderness of the RFQ structure and to accommodate applied loads from the RF-power feeds, coolant lines, vacuum supply, etc. There are vertical and horizontal displacement constraints at five axial locations: the end plus each interface between the resonant segments. In addition, there is a rotational and an axial constraint at the low-energy end. Under the 8.8-lb/in load of the RFQ, plus applied loads averaging 1 lb/in, the maximum static transverse deflection of the RFQ will be <0.001 inch with a maximum Von Mises stress of <200 lb/in^2. A 100-lb transverse (or vertical) load applied at the mid-point between supports would produce a deflection of 0.0005 inch.

The support frame is a box structure that is fabricated as a weldment of commercial structural steel shapes. It is designed to be tilted to a vertical position to allow the RFQ

sections to be installed. The assembly would then be rotated to the horizontal orientation for installation on the beamline. The assembly will be kinematically mounted to the floor so that the position of the RFQ can be adjusted without adjustment of the RFQ supports.

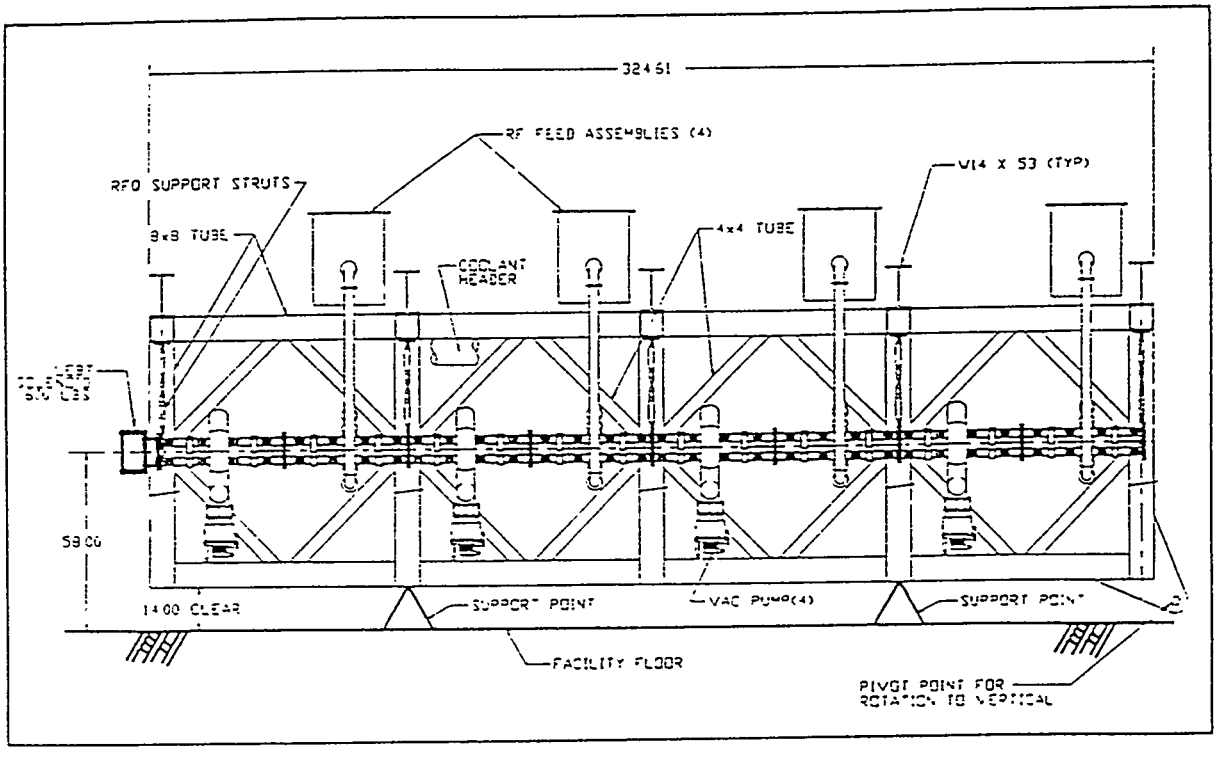


Fig. 4-13. RFQ support structure.

4.3.5 Vacuum System

While the basic operational vacuum requirements of the RFQ are no different than for similar devices, the necessity of handling a full internal loss of the beam without exceeding 5×10^{-5} torr is a unique requirement. With 90% transmission, the normal beamloss is 12 mA, corresponding to 2×10^{-3} torr-l/s of H−. The current preconceptual design incorporates four pumping stations along the length of the RFQ, one in each 2-meter-long segment. There is a pumping port in each quadrant for each segment. Each set of four ports is manifolded to a turbopump with 570 l/s pumping speed for hydrogen. The predicted vacuum level is 9×10^{-7} torr during normal operation and 9×10^{-6} torr with 100% beamspill. In a situation where one pumping station is disabled, the predicted resulting pressure is 3×10^{-6} torr under normal operating conditions and 3×10^{-5} torr with 100% beamspill.

4.3.6 Diagnostics

The same set of diagnostics is duplicated on each low-energy leg of the APT accelerator. The main diagnostics for the RFQ consist of operational (permanent) measurement devices for measuring beam profiles, position, and current. There are some characterization diagnostics for measuring transverse phase-space parameters, longitudinal beam centroids, and beam energy; however, these devices will only be available and used during

commissioning, and will be off-line during normal operations. These off-line diagnostics will probably be interceptive emittance measuring devices of the slit-and-collector variety.

Position information is measured both with a VPM (video position monitor) and a BPM (beam position monitor). A BPM is a radially symmetric, four-quadrant microstrip probe with the beam passing (ideally) through the center of the probe. The signal amplitude detected in each quadrant is a function of beam-centroid location within the beampipe. Both VPM and BPM systems can be integrated into a single component called a VPM/BPM unit.

An ac current transformer (toroid), located very near the output of the RFQ, is used to monitor the current and current fluctuations of the RFQ. The RFQ beam transmission is measured by comparing the current measured by the toroids located in the two endwalls of the RFQ (at the entrance and exit).

4.3.7 Recommendations

The general conclusion is that the APT RFQ, as specified, can be fabricated with reasonably predictable cost, schedule, and performance. While there are a few issues of concern, there are none that cannot be resolved by careful design work and prototype testing. There are, however, several areas of further work that should be carried out to improve the robustness of the design. These are as follows:

- **Cold Model.** A full-scale low-power test structure should be built to allow the full exploration of RF field perturbations in a resonantly-coupled 8-m-long structure. This device would also be used to develop RF field distribution measurement techniques for an 8-m-long structure and for tests of an iris-coupled waveguide to be used in lieu of the drive loops.

- **Thermal Stability.** Understanding details of the thermal behavior of the cavity is important. For the design work done to date, a 1/8-length FEA model of the high-energy section was used. For the final engineering design, a full section of the RFQ should be analyzed. A laboratory demonstration of full power cw operation of such a section should be completed prior to final design.

- **Material Selection.** Some investigation of a material with higher-yield strength and better machining properties than OFE copper should be carried out.

- **Alternate Structural Concepts.** The electroformed-joint design used for the BEAR, CWDD, and SSC RFQs and proposed for the APT RFQ has the disadvantage of being very time consuming in manufacture. Investigations of alternative designs and joining processes would be warranted if fabrication times could be significantly reduced.

4.4 MATCHING SECTION (RFQ-DTL)

4.4.1 Introduction

Located between the RFQ and the DTL in each leg of the low-energy system is an intermediate matching section or IMS. A preliminary design of this section which matches the output beam from the RFQ into the DTL has been completed, but further work is required

to resolve minor discrepancies between the element spacings in the beam simulation and the spacings required by realistic engineering constraints. The IMS design requires six electromagnetic quadrupoles and two single-gap RF bunchers. A schematic diagram of the IMS and a proposed arrangement of the individual elements is shown in Fig. 4-14. Four EMQs are required to match the beam in transverse phase space, and two buncher cavities are required to match in longitudinal phase space. Table 4-5 gives the performance requirements of the individual elements for a full-current match between RFQ and DTL for the simulated beam. The required inter-element drift spaces are specified along with quadrupole and buncher settings determined for an rms match of the beam at the desired rms emittances. The total IMS length specified in the simulation is 64.8 cm from the inner RF surface of the RFQ to the edge of the DTL-endwall focusing quadrupole. However, an initial engineering analysis shows that a more realistic beamline-element-packaging scheme will require an additional length of 18 cm. Therefore, the layout described in the next section differs slightly from the one shown here. A second beam-dynamics iteration is needed to determine the small corrections to beam behavior that will result from this change.

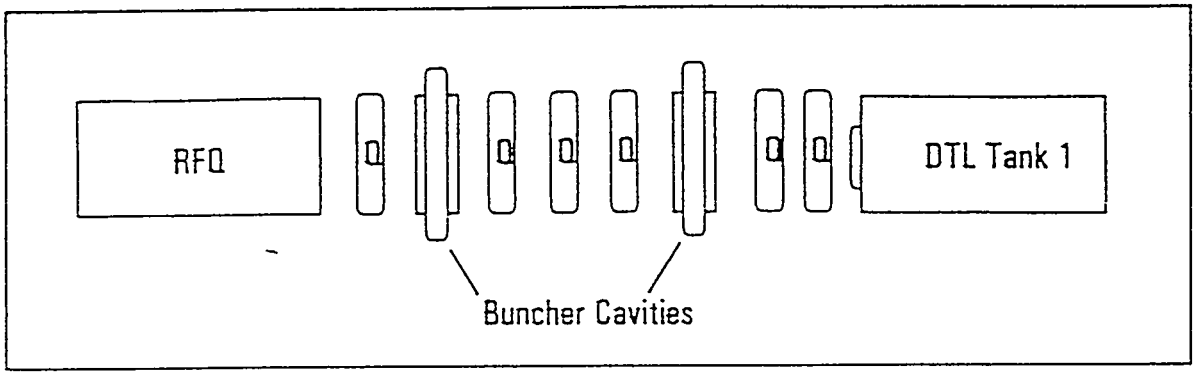


Fig. 4-14. Diagram of the RFQ–DTL matching section.

Table 4-5. RFQ to DTL Matching Section Component Specifications

Element Type	Length (cm)	Field Gradient (T/m)
Drift	2.35	—
EMQ	5.70	-35.00
Drift	2.35	—
RF Buncher Cavity	Uses drift space	$E_oTl = 0.0309$ MV ($\phi_s = -90°$)
Drift	2.35	—
EMQ	5.70	-39.97
Drift	4.70	—
EMQ	5.70	37.42
Drift	4.70	—
EMQ	5.70	41.19
Drift	2.35	—
RF Buncher Cavity	Uses drift space	$E_oTl = 0.0314$ MV ($\phi_s = -90°$)
Drift	2.35	—
EMQ	5.70	-39.93
Drift	4.70	—
EMQ	5.7	-34.57
Drift	4.70	—

4.4.2 Description of IMS

The preliminary mechanical layout for the RFQ-DTL intermediate matching section is shown in Fig. 4-15. As noted above, more work needs to be done on this section to determine a final configuration. The IMS includes two high-power buncher cavities, six EMQs, eight quick-disconnect vacuum flange pairs and clamps, three vacuum bellows, an in-line electropneumatic vacuum valve, a beam current monitor, and a combined VPM/BPM beam-diagnostic unit. In addition, it is necessary to accommodate support and alignment hardware for these components, RF coupling loops and drive lines for the bunchers, cooling water manifolding for the buncher cavities and magnets, power-bus terminals for the EMQs, vacuum pumps, and the support structure itself.

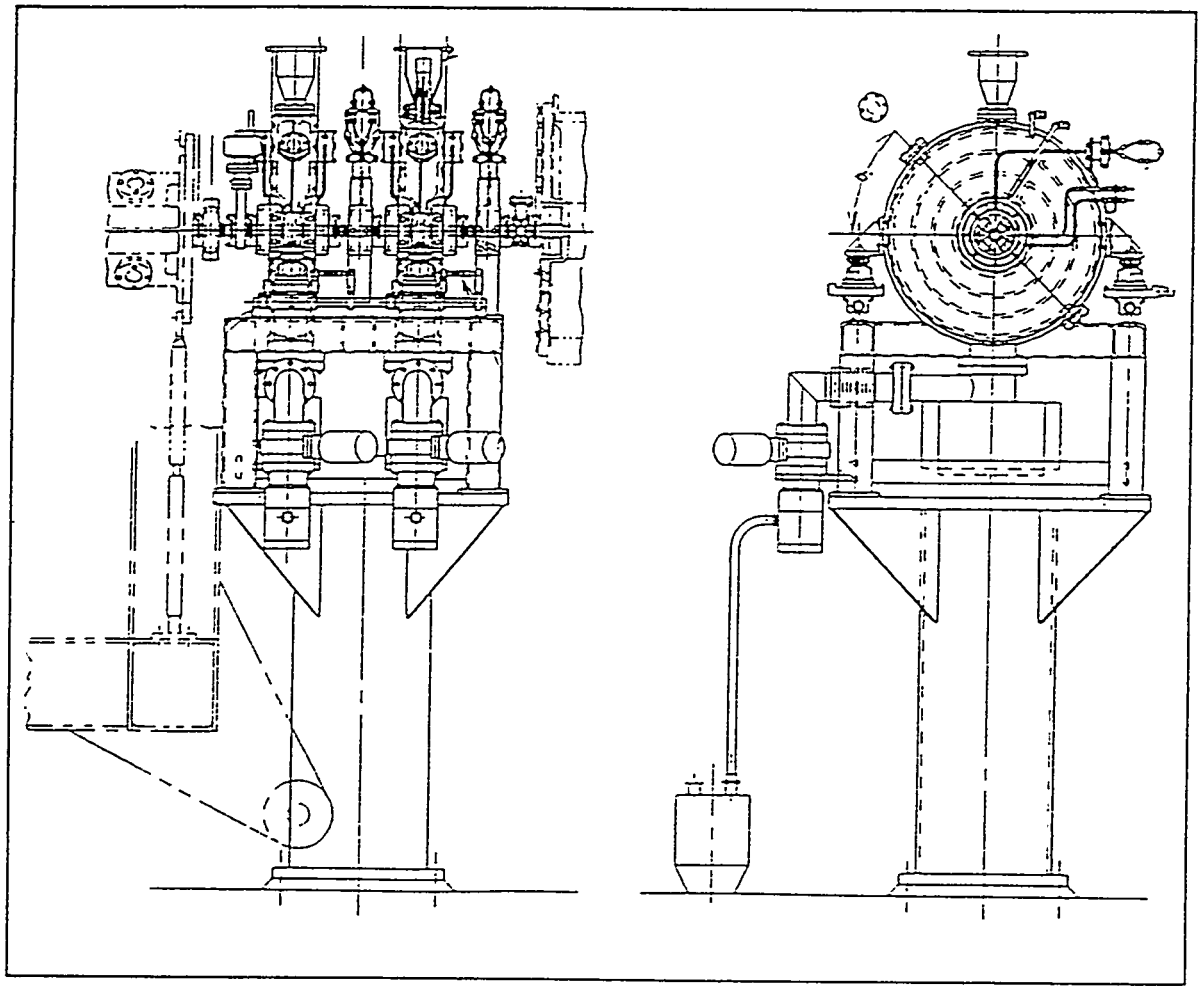


Fig. 4-15. RFQ–DTL matching section layout.

4.4.3 Buncher Cavities

The two buncher cavities each dissipate about 1 kW of RF power and generate RF electric-fields of about 3 MV/m. The Kilpatrick limit at 350 MHz is 18 MV/m, so the cavities are not heavily stressed electrically. The cavities are easily cooled to maintain a

maximum temperature rise of only 9C° in the copper. This relatively small ΔT gives rise to Von Mises stresses of only about 1/3 the yield strength of annealed copper. Detailed thermal and structural analyses of the buncher cavities are given in the Appendix. The vacuum pumping for each cavity is done through longitudinal slots in the cavity wall to a 60 l/s ion pump.

The cavities are equipped with two fixed slug tuners, each of which are iteratively tuned to provide the proper offset frequency for the cavities. The cavities reach resonant frequency with water temperature at about 46°C. Resonance control is as described for similar accelerating cavity systems in Chap. 9 of this report. The design of the coupling loops that provide RF power to the cavities is based on the configuration developed for the SSC RFQ, with the modification of improved cooling to handle the APT cw power rating. More information on the bunchers and the coupling loops is given in the Chap. 4 Appendix.

4.4.4 Quadrupoles

All the EMQs in the IMS are identical to those in the DTL and the funnel. The EMQs for the IMS would thus be taken from production lots of the same units designed to fit into the 350-MHz drift tubes of the DTL tanks. They are glass and calcium-aluminate-insulated magnets that use 0.1443-inch, square, directly water-cooled, field-coil conductors. The conductors and associated ceramic water breaks are terminated, either as is done at the top of the drift tube stems in the DTL design or as a specially designed termination mounted on the side of the buncher cavities.

Six EMQs are needed in total for the IMS. The physical spacing between the EMQs is close to the simulated preconceptual design (within 20%); however, more space is needed on each end of the IMS to accommodate the rest of the hardware.

4.4.5 Support Structure

The support structure for the IMS is a single pedestal with stiffening gussets. The pedestal is grouted to the facility floor and the gussetted platform supports a box beam cagement which in turn supports the IMS beamline components. The two buncher cavities and the four EMQs connected to these cavities are mounted on linear bearings and screw jacks. The remaining two EMQs are also mounted on screw jacks. The adjustment range of the EMQs and cavities is ±6.5 mm which relieves the pedestal from critical tolerances during installation.

4.4.6 Diagnostics

As with the RFQ, permanent diagnostics measure beam current, beam position, and beam profiles. A toroid is located in this section at the exit of the RFQ. Depending on available space, up to three VPM/BPM units can be installed, one at the output of the RFQ immediately after the toroid, another between the two matching section buncher cavities, and the third immediately upstream of the DTL. These units give beam position, profile, energy, and phase information.

4.5 DRIFT-TUBE LINAC

4.5.1 Introduction

The DTL design for the APT accelerator is a composite of many designs for similar linacs implemented over a 25-year period at Los Alamos. The 201.25-MHz DTL at LAMPF was the first to introduce longitudinal RF field stabilizers in the form of post couplers. The 80-MHz FMIT linac included the first cw DTL to use the CERN concept of girder-mounted drift tubes. It was also the first to develop instrumented drift tubes and 600 kW cw RF coupling loops (at 80 MHz).

As part of the SDI-supported NPB program, uniform-gradient and ramped-gradient 425-MHz low-duty DTLs were developed and tested, and were the first such machines to use permanent magnet quadrupoles (PMQs) at Los Alamos. The ramped gradient DTL (RGDTL) introduced rotary tuners, instrumented drift tubes, bent-stem post couplers, and the taut-wire alignment technique, and used copper-plated extruded aluminum for the tank barrels. The 850-MHz DTL for the GTA linac is an all-copper cryogenic machine designed to operate cw at 20°K with liquid hydrogen as a coolant. It introduced intertank beam-steering PMQs, and coaxial socket post couplers, and achieved high duty-factor Q-enhancement through cryogenic cooling.

The APT DTL has been designed out of the rich experience and technology base from various programs over the past 25 years.

4.5.2 Description

Each of the two legs in the low-energy region of the accelerator includes a DTL that accelerates the beam (exiting each IMS) from 7 MeV to 20 MeV. Each DTL is made up of three accelerating tanks. The 350-MHz DTL frequency permits the drift tubes to be large enough to allow room for EMQs, which are much more radiation-resistant than PMQs. The first of the DTL tanks has a ramped accelerating gradient (1.04–2.80 MV/m), while the second and third tanks have constant gradients.

The tanks were designed electromagnetically using SUPERFISH, with peak surface electric fields held below the Kilpatrick limit at 350 MHz. The drift tubes in each tank are mounted on a common girder, which greatly facilitates installation, alignment, and maintenance. The tanks include post-couplers for stabilizing and leveling the longitudinal field distribution. Inter-tank quadrupoles are PMQs mounted on x-y positioners to provide beam steering adjustments. In addition to these PMQs, the intertank gaps contain beam diagnostic instrumentation, bellows, and pneumatic in-line vacuum valves to isolate the tanks.

4.5.2.1 DTL Parameters

Key parameters of the DTLs are given in Table 4-6. The DTL tanks are 1$\beta\lambda$-type accelerating structures with a FOFODODO focusing lattice. The intertank spacing is 2$\beta\lambda$ to minimize emittance growth and prevent quadrupole end-cell shifts. Each tank is about 2.5-meters long. There are 55 accelerating cells in total for the three tanks. The drift-tube quadrupoles are EMQs, each 5.7 cm in length. Required gradients range from 25–35 T/m.

Table 4-6. DTL General Parameters (Each Leg)

Energy (MeV)	7.0–20.0
Frequency (MHz)	350
Beam Current (mA)	100
No. of RF Modules	3
No. of Assembly Units	3
No. of Tanks	3
No. of Cells per Tank	Tank#1–22, #2–18, #3–15
Length of Cells	$1\beta\lambda$
Length of Tanks (m)	2.44–2.50
Total Length (m)	7.98
Intertank Spacing	$2\beta\lambda$
Radial Aperture (cm)	1.00
Aperture/Beamsize(rms) Ratio	4–5
Peak Surface Field (Kilpatrick)	<1.0
Synchronous Phase (deg)	-35 to -25
Average Power Density (W/cm^3)	~22
Structure Gradient (MW)	1.04–2.80
Shunt Impedance (MΩ/m)	30.2–32.8
Structure Power (MW)	1.153
Beam Power (MW)	1.300
Total RF Power (MW)	2.453
Total Cooling, both legs (gpm)	505
Efficiency	0.530
Length of Focusing Period	$1\beta\lambda$
Quadrupole Types	EMQs (drift tubes), PMQs (end walls)
Quadrupole Lattice	FOFODODO
Quadrupole Effective Length (cm)	5.7
Quadrupole Gradients (T/m)	25.0–35.0
Quadrupole Spacing (cm)	10.4–17.4 ($1\beta\lambda$)
Phase Advance/Period (deg)	80–70

4.5.2.2 Physics Design

The starting accelerating gradient in the first tank is chosen to provide similar longitudinal focusing strength to the beam as it exits the RFQ and enters the DTL. This helps to minimize beam current dependence in the IMS. After the gradient is ramped in the first DTL tank, it is then adjusted in the final tanks to match the longitudinal focusing strength of the first tank of the BCDTL (at 20 MeV).

The DTL is also designed so that transverse focusing strengths closely match the adjacent structures: i.e., the phase advance per unit length at the DTL entrance and exit is the same as that of the RFQ and the BCDTL, respectively.

Both FODO and FOFODODO focusing lattices were compared for the DTL with beam simulations; the FOFODODO lattice produced less transverse emittance growth. A comparison of intertank spacings was also carried out to determine a reasonable tradeoff between beam emittance growth and intertank equipment packaging. A minimum intertank spacing of $2\beta\lambda$ was selected, which provides enough space for vacuum valves, beam diagnostics, and two focusing/steering quadrupoles.

The bore radius of the DTL is set at 1.0 cm. SUPERFISH cavity data were obtained and optimized for this aperture. Fig. 4-16 shows the drift-tube nose shape and cell geometry. Only the accelerating-gap-to-cell-length ratio was varied throughout the DTL. The same drift-tube nose shape was used throughout. After a prototype EMQ that can fit into the DTL drift-tubes has been built and tested, it may be possible to increase the DTL bore radius. The cavity shunt-impedance as a function of β (7–20 MeV) is shown in Fig. 4-17. A very preliminary study of error tolerances was carried out for the DTL design. It was found that the beam centroid moves 0.071 mm transversely for random drift-tube offsets (vibrations) of 0.0001 inch.

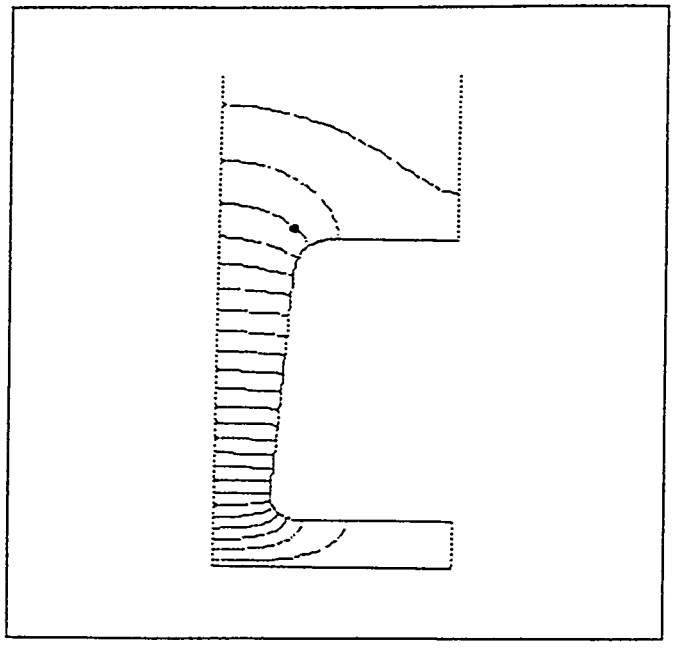


Fig. 4-16. Drift-tube nose shape and cell geometry.

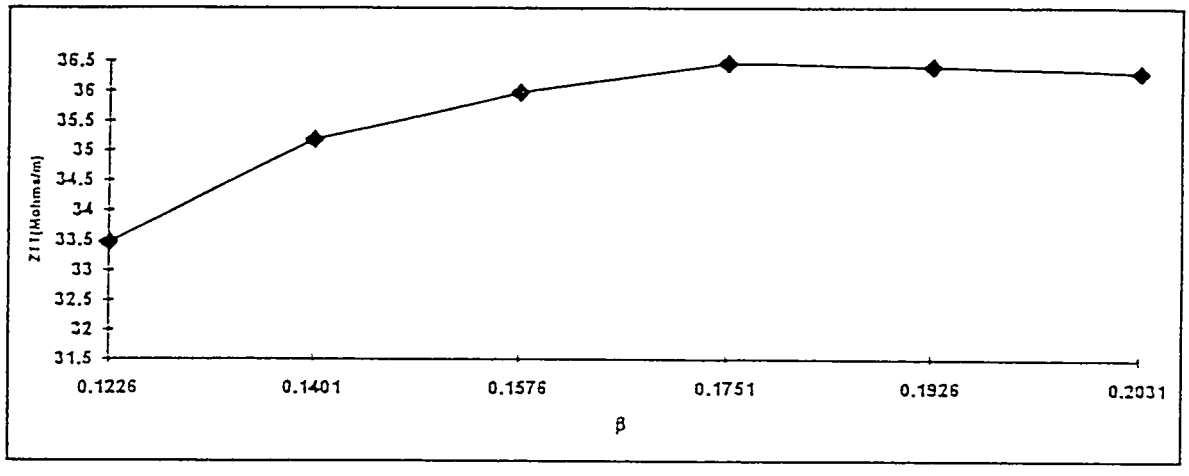


Fig. 4-17. Shunt Impedance for the APT DTL as a function of β.

4.5.3 DTL Component Design

4.5.3.1 Tanks

A sketch of the DTL layout is shown in Figs. 4-18 and 4-19. An exploded view is shown in Fig. 4-20 for clarity in describing the major components of the system. The tanks

are fabricated from 2219-T8511 extrusions. This is one of the hardest of the extrudable aluminum alloys with a Vickers hardness number (VHN) of 130. This hardness is required to withstand the pressure of the Helicoflex vacuum seals which are used widely in the DTL mechanical design. The longest tank is 2.50 meters which is within the capacity of the aluminum-extruding process. The barrels are 60 cm in outer diameter with 6-cm-thick walls. They weigh about 700 kg each.

Along the top of the barrels, a 16-cm-wide slot is cut that extends almost the entire length of the barrel. This is the girder slot through which the drift tubes extend. The ends of the tanks are closed with endwall covers that have half drift-tubes machined into them and are sealed against the tank barrel with knife-edged copper-to-copper RF seals and Helicoflex vacuum seals. The post couplers alternate along either side of the tanks, one for each drift tube. Along the bottom of the tanks are the vacuum grills and RF couplers. Two fixed tuning slugs are located in the upper quadrant if twin RF loop couplers are used, or along the bottom if a single waveguide and iris coupler are used. Along either side of the girder slot are tuning bars. The tuning slugs and tuning bars, both iteratively machined during tuning, are the means by which the offset operating frequency of the DTL is set in the test lab. The tank barrels and endwalls are copper plated to a depth of 0.06 mm, which is almost twenty skin depths at 350 MHz. The copper is well adhered to the aluminum by means of a nickel strike under zinc to which the copper is then electroplated. The copper reduces power dissipation by raising the cavity quality factor (Q).

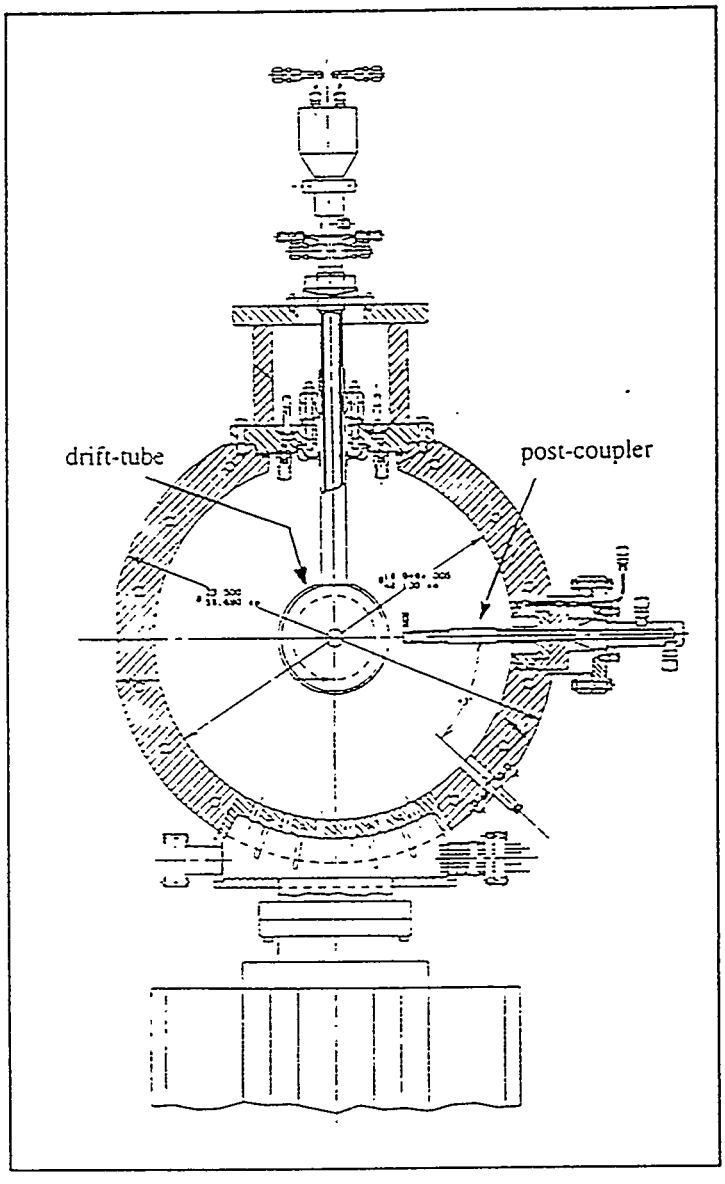


Fig. 4-18. DTL typical cross-section.

The DTL tanks are cooled by numerous longitudinal gun-drilled 1.27-cm-diameter cooling channels. These channels are fed from manifolds on either end of the barrels so that alternate channels counterflow. The principle applied here is that of mass-balanced counterflow cooling, which gives the best thermal uniformity to the structure. The maximum temperature excursion in the aluminum walls is 14C°. Details of the thermal analyses and cooling requirements are given in the Appendix.

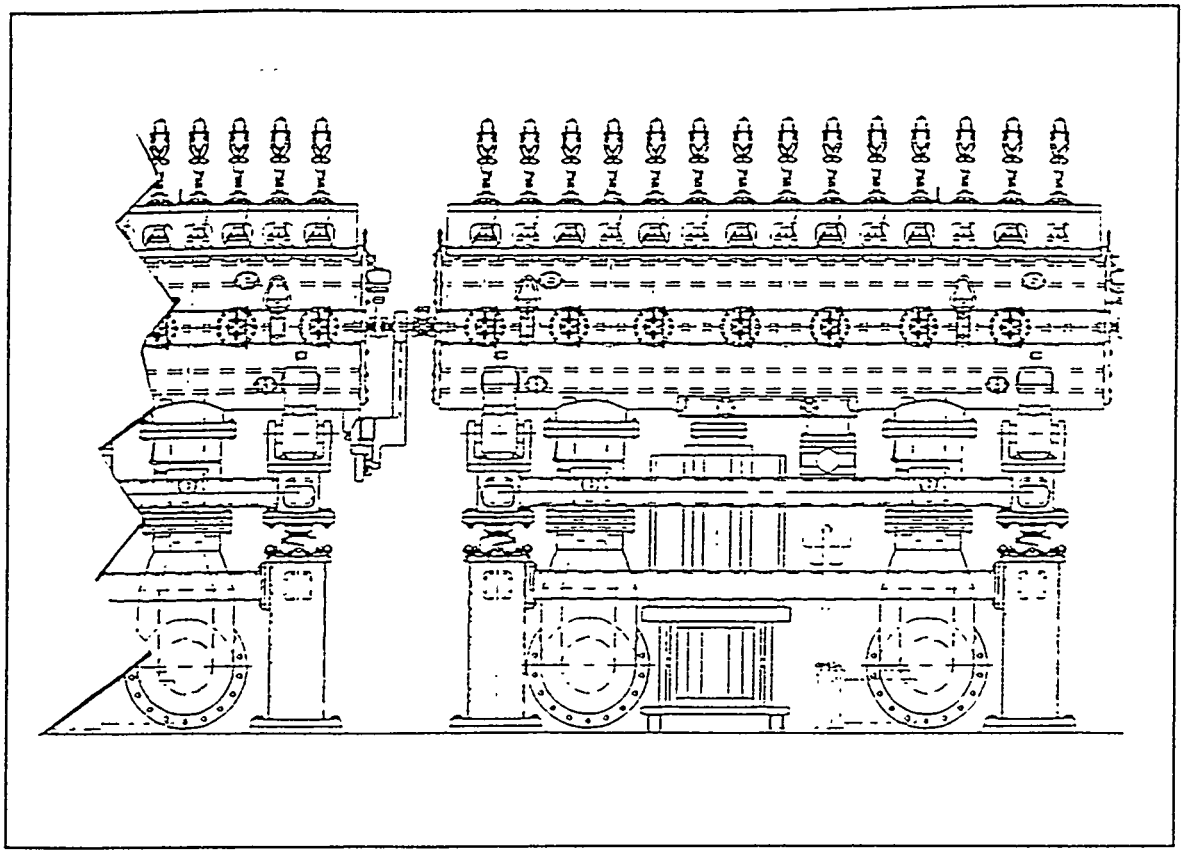


Fig. 4-19. DTL tank #3, drive loop coupled.

The tank barrels are supported on four linear bearings that allow for the longitudinal motion of the tanks that results from thermal expansion during operation. The bearing mounts are adjustable to provide for alignment of the magnetic centerlines of the tanks relative to the pedestal support adjusters. The linear-rail-support mounts are bolted to a structural framework (box beam carriage) that supports the tank assembly (in a fashion similar to the box beam carriages on all of the BCDTL and CCL modules). The carriage is, in turn, bolted to the pedestal support adjusters. When final alignment is done, these adjusters are manipulated to bring the tank into critical alignment with the facility monument system. The pedestal support adjusters have a ±13-mm adjustment range, which means that the linear bearing adjusters have only to align the tank within this range.

4.5.3.2 Endwalls

The aluminum endwalls, shown in Fig. 4-21, are bolted to the tank barrels and in the process, two copper-plated steel-knife edges are pressed into an annealed copper gasket to form a high integrity RF joint. The steel-knife-edge inserts are press-fitted into the end walls and tank barrels after they are copper plated and form an integral part of the tank and endwall assembly. Alignment pins are inserted into the tank-side knife-edge insert to hold and align the RF gasket, and the endwalls are located with tapered pins to the tank for accurate positioning.

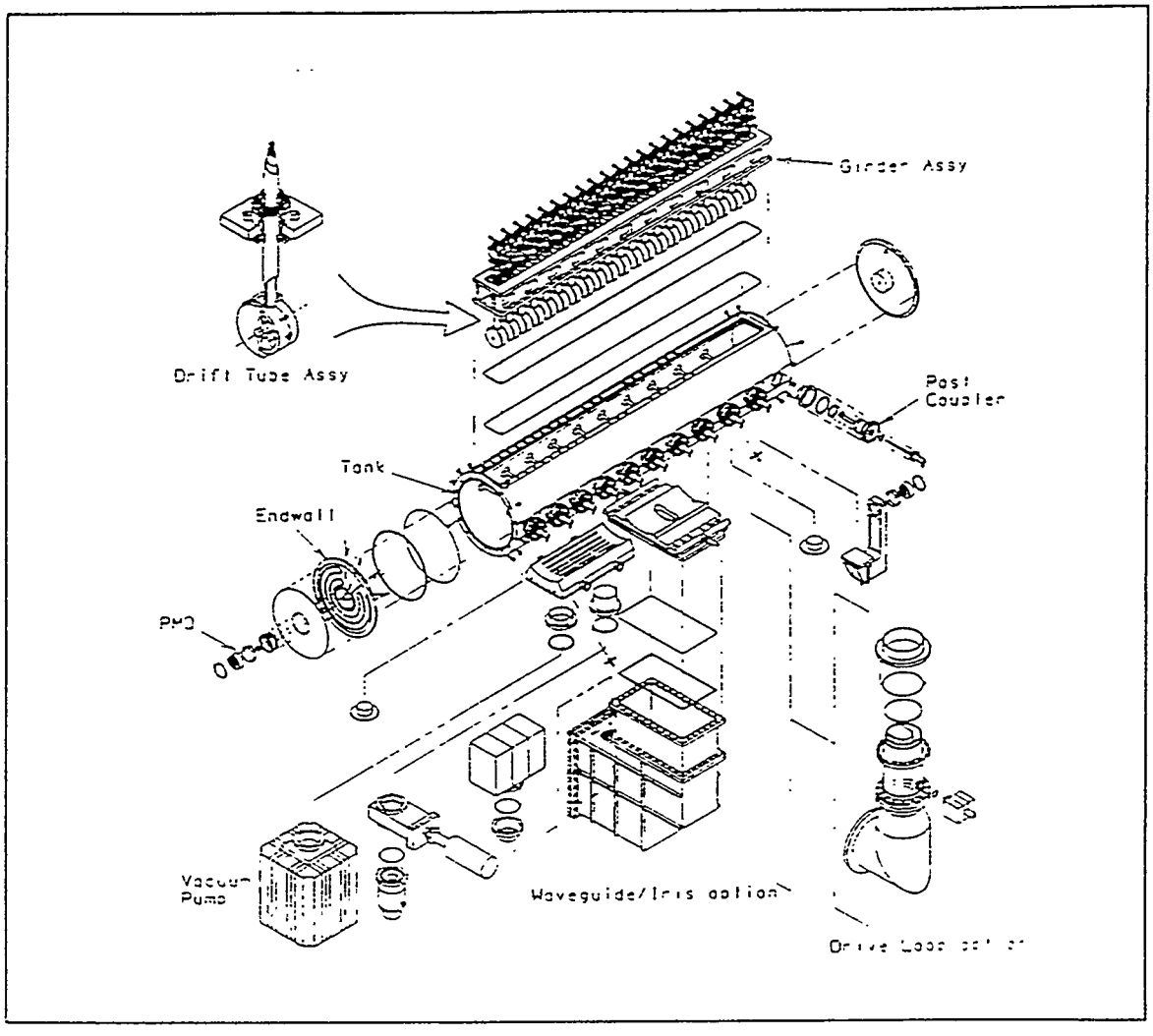


Fig. 4-20. APT 350-MHz DTL tank #3 exploded view.

Backing the RF gasket is a silver-plated Helicoflex vacuum seal with vacuum relief slots cutting radially across the knife edge and into the gap between the seals. The endwalls consist of a 2219-T87 aluminum plate into which the cooling channels are machined. The channels are then covered on the air side with a plate that is EB-welded around the channels for water-to-air sealing as well as channel-to-channel sealing. The drift tube half-bodies are machined into the interior surface of the endwalls. On the air side, a socket is provided for the PMQ. This socket is machined with recesses for tolerance rings that permit accurate transverse location and anchoring of the PMQ. The tolerance ring technique to hold and locate PMQs in drift tubes was developed for the GTA DTL and was applied successfully to all the cryogenic drift tubes over very large temperature excursions. The endwall boretube is machined into an aluminum alloy insert that is EB-welded vacuum tight into the endwall drift tube body. An ISO flange, modified to fit the Helicoflex Quick-Flange profile, is then welded onto the boretube. After all welding is complete, the RF surfaces of the endwall are copper-plated.

The endwall PMQs can be changed out from the air side without disturbing the endwall or its alignment. To assure success with this method, it is necessary that the PMQs be

manufactured to tight tolerances so that the magnetic center of any given PMQ relative to its outside diameter will not differ from any other PMQ in the stockpile by more than ±0.13 mm. The magnetic centers of the endwall PMQs on either end of the DTL tank determine the beam axis of that tank. Therefore, the PMQ magnetic centers are measured and referenced directly to tooling balls mounted on the x- and y-axes of the endwall. These tooling balls determine the position of the beam axis of a given tank relative to the facility monument system, as well as to the other DTL tanks. The internal alignment of all the drift tubes of a tank are also referenced to the endwall magnetic centers.

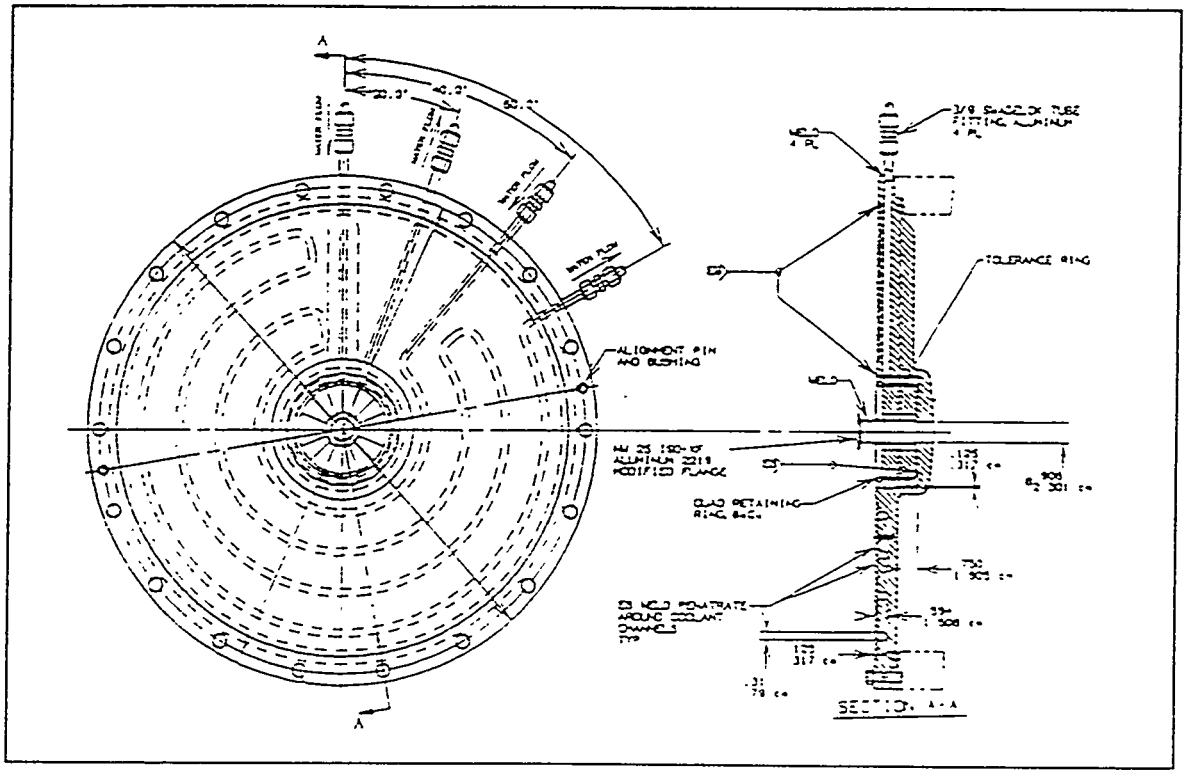


Fig. 4-21. DTL end wall.

4.5.3.3 Girder

The drift-tube support girders are fabricated from 3–4-cm-thick aluminum alloy plate that matches the thermal expansion of the tanks closely. The girder is bolted and sealed to the tank in the same way as the endwalls: namely, a copper-plated, steel, knife-edged insert is pressed into both the tank and adjoining girder surfaces, and an RF gasket is dropped onto locating pins on the tank-side insert. The vacuum seal is made with a Helicoflex ring, shaped into a rectangle. Slots are machined across the knife edge at several places to vacuum-relieve the area between the two seals. The mating surfaces of the girder and tank are *match-lapped* to a precision fit after the tank and girder are annealed (but before copper plating). It is essential that a matched fit be made at this junction, because the repeatability of the drift tube alignment precision depends on the stress-free mating of the girder and tank when they are bolted together. It is also essential that the alignment remain within close tolerances following girder removals and reinstallations. To assure repeatability, tapered alignment pins are pressed into steel inserts mounted in the tank barrel which mate with steel bushings

pressed into the girder. One bushing is slotted longitudinally to allow the girder and tank barrel to expand and contract freely. The girder is heated by conduction from the tank wall as well as from RF dissipation along the surfaces exposed in the slot. The junction between the tank and the girder are in intimate contact and are consequently in thermal equilibrium; therefore, no differential expansion occurs between the two bodies and no warpage results.

The girder is a stiff beam, but the tank is stiffer. Any minor discrepancies in the mating surfaces will be dictated by the tank. The girder is machined with access ports on both sides to allow work to be done on the drift tube mounting bolts and alignment cams. When the girder is installed, it forms a structural bridge across the slot and carries the vacuum load that would otherwise distort the slot. On the top of the girder, large ports are machined through which the drift tube stems protrude. The stems are anchored here by adjustable rocker clamps after the drift tubes have been aligned. On the topside of each girder, there are four lifting eyelets which are used to transport, install, and remove the girder.

On the RF underside of the girder, there are the drift-tube sealing sockets and the tuning bars. The 1-cm-deep sealing sockets are machined with 10° tapers all around that serves as a choke joint to attenuate the fields near the RF seal and reduce heating. The sealing sockets use knife-edged inserts as described above for the tanks and girders, with silver-plated Helicoflex vacuum seals backing up the RF seals. The tuning bars are solid copper and are sealed against the girder to form a cw-rated RF joint.

The girder receives its primary cooling from longitudinal channels running the length of the base plate (which is bolted to the tank slot). It receives secondary cooling from intimate contact with the tank barrel, and thirdly from the drift-tube sockets which are cooled by the flex-membrane cooling tube.

4.5.3.4 EMQs and Drift Tubes

The DTL drift tubes are equipped with EMQs rather than PMQs because: (1) they are much more radiation-resistant, and (2) can be adjusted to optimize the aperture-beamsize ratio for minimum beamloss during operation. Thus, the combination of radiation resistance and adjustability are important advantages of EMQs for the APT DTL. The Chap. 4 Appendix describes the fabrication and assembly of the EMQs and drift tubes.

4.5.3.5 Tuners

The DTL is passively tuned using cooling water temperature (described in Chap. 9). Basically, a constant coolant flow is directed through the DTL tanks and drift tubes. The inlet temperature of this water is adjusted by means of a servo-controlled bypass loop which carries preheated or recirculated water. This permits the ΔT of the coolant to remain constant while varying the inlet temperature and thus prevent mechanical stressing. Detuning effects of the tank and drift tubes from RF heating are different, so the amount of total flow through each part of the manifold system will be controlled by orifice plates, giving the greatest tuning effect per degree of temperature change in the inlet flow (highest tuning sensitivity). The sizing of these orifice plates requires a complex thermal analysis and hardware tests.

Because the tank is initially tuned at room temperature (20°C) but operated at 46°C, with a coolant inlet temperature that varies from 36°–46°C, all RF dimensions of the DTL

components must be *undersized* by 0.6 mils per inch and tuned almost 210 kHz *higher* in frequency at 20°C. Besides the predictive dimensioning for room temperature compensation, precise offset tuning is accomplished by means of the tuning bars described for the girder, as well as fixed water-cooled tuning slugs mounted at two positions in the upper quadrants of each tank. These slugs are iteratively shortened during the tuning operation and act as adjuncts to the tuning bars.

4.5.3.6 Post Couplers

The post couplers serve as RF field stabilizers. They give longitudinal stability to the tank fields by providing a transverse electric field that resonates with the drift tube body. This transverse E-field interacts with the azimuthal magnetic field to provide a power flow vector (Poynting Vector) which is longitudinal, thereby stabilizing the field over the entire length of the tank. The post couplers carry significant RF currents, especially in the first DTL tank of each leg because of the field ramp in this tank. The other two tanks in each leg have constant fields, so the load on the post couplers in these tanks is less.

Because of RF dissipation, the post couplers must be water cooled. Internal construction of the cooling passages is shown in Fig. 4-18. The eccentric tip is also cooled, and the post coupler is provided with a Conflat flange that rotates and a high vacuum copper gasket to allow rotation of the tip to any position. Rotation is necessary to allow tuning of the gap-to-gap fields between drift tubes. The post couplers are seated against a knife-edged RF seal in a manner similar to that described previously for other parts of the DTL system. Once the couplers are set, there is no need to change the settings; because tuning is done at room temperature, however, some effort must be taken to assure that the couplers stay in tune at the elevated operating temperatures.

4.5.4 Interfaces

4.5.4.1 RF Couplers

One of two methods for coupling RF power into the DTL tanks will be used: either coaxial-loop coupling, or iris-and-waveguide coupling. The preferred coupler is the coaxial loop coupler. The impedance of the coaxial line is 35 ohms, offering the greatest power carrying capacity for a coaxial transmission system. The RF window is made from high purity alumina (AD995), with a thin titanium nitride layer sputtered on the vacuum side to reduce multipactoring. The position of the window is set slightly less than 1/2 wavelength back from the loop strap so that RF faults at the loop cause a voltage minimum at the window. To aid in monitoring activity at the window and maintaining good vacuum quality, an appendage pump vacuum port is provided on the vacuum side. The loop strap and coax walls will be well cooled, and the transmission line on the air-side of the window will taper up to match the 14-inch diameter of the transmission line. This tapered section may have to be pressurized to sustain the high RF fields near the window. If this method is inadequate, it might be necessary to taper the coax to 14 inches on the vacuum side and provide an even larger diameter RF window. Because of cw-power transmission limitations, two RF feeds rated at 500 kW (cw) each will be designed for each tank, as shown in Fig. 4-19.

The kind of coaxial coupling loop described here was built and tested (for 80 MHz service) on FMIT at 600 kW cw into high Q loads. The higher APT frequency reduces the power transmission capability of the coaxial line to about 500 kW cw.

An iris-and-waveguide approach is the other posibility for RF coupling into the DTL, as shown in Fig. 4-22. Because of the 350 MHz frequency, WR2100 waveguide must be used. This waveguide has such a large power transmission capability that electric fields in the waveguide even at full tank power demand of 1 MW would be quite low. The iris will also be relatively large and easily cooled. The iris is built into an insert which is cooled independently of the tank cooling and welded into the tank barrel. The vacuum waveguide that is attached to the iris insert contains an H-plane bend and a port for an appendage vacuum pump to be placed close to the RF window. At present, however, no windows exist that are rated for 1 MW cw in this application. There are 1 MW windows on the 350-MHz Thompson CSF klystrons, but in these applications they are protected by circulators. In the DTL drive application, the window would occasionally be exposed to high VSWRs caused by RF faults in the tank or beam failures. Therefore, while an iris/window combination appears capable of high-power delivery, the window itself must be developed. For this reason, the coaxial loop coupler is currently the preferred choice for the APT DTL design.

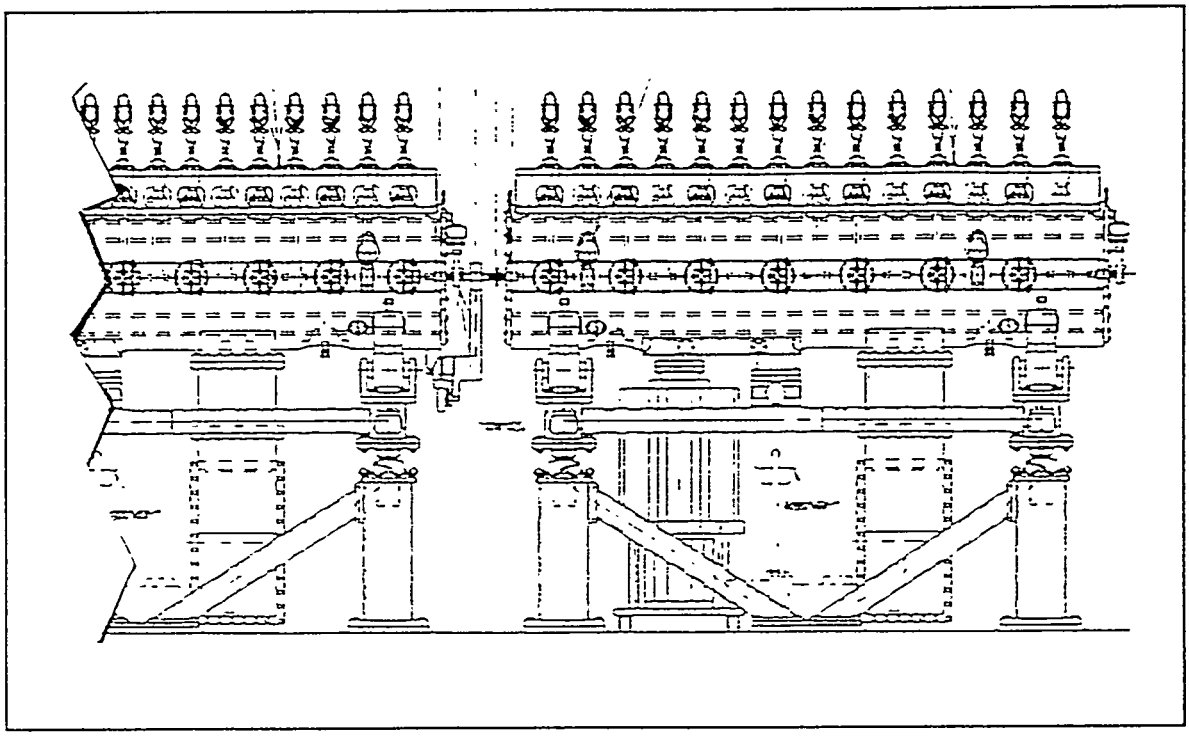


Fig. 4-22. DTL tank #3, waveguide/iris coupled.

4.5.4.2 Vacuum

The vacuum grill is shown as another tank insert in Fig. 4-20. The grill is cut with 18 1.3 x 16 cm rectangular slots. The wall thickness is cut to 2.5 cm, which gives the grill a total conductance of 3360 l/s, more than enough to support a large ion pump. Between each slot is a 0.95-cm-diameter cooling channel. The entire grill assembly is EB-welded into the tank barrel and equipped with a vacuum box to which is attached a 20.3-cm-diameter nipple with a Conflat flange for a floor supported 900 l/s ion pump. The cooling-channel tubing is welded through the vacuum box endwalls and manifolded externally as an independent cooling circuit. The vacuum box carries ports for ion and thermocouple gauges as well as spare instrumentation ports. In addition, the vacuum box has a second 20.3-cm port and

manual all-metal valve to which a 300-l/s turbomolecular (TM) pump can be attached during roughdown.

4.5.5 Diagnostics

The DTL permanent diagnostics include devices which measure beam current, beam position, and beam profiles. Position information at the output of the DTL will be measured with VPM/BPM units. These units will give beam position, profile, energy, and phase information. Toroids located at each of the outputs of the three DTL tanks will be used to monitor the current and current fluctuations. The DTL transmission will be measured by comparing the current measured by a toroid located at the input to the DTL and one located at the output.

An ion-chamber beamloss monitor will be placed near each of the DTL structures. If there is excessive beamspill, these loss monitors provide a signal to the accelerator fast-protect system that can be used for rapid beam abort.

There will be off-line diagnostics to measure transverse phase-space parameters, longitudinal beam centroids, and beam energy during commissioning. An interceptive slit-and-collector device will probably be used for transverse emittance measurements.

4.6 THE 350-MHZ RF POWER SYSTEM

Two high-power 350-MHz RF systems are required for each RFQ to accelerate the 100-mA beam to 7 MeV. Three more high-power 350-MHz RF systems are needed for each DTL to accelerate the beam to 20 MeV. Two low-power 350-MHz RF systems are required for the buncher cavities in each IMS. Altogether there are 14 of the 350-MHz RF systems in the low-energy APT linacs, 10 of which are high-power units and based on the 1-MW class klystrons. An overview of the 350-MHz high-power RF system is shown in Fig. 4-23.

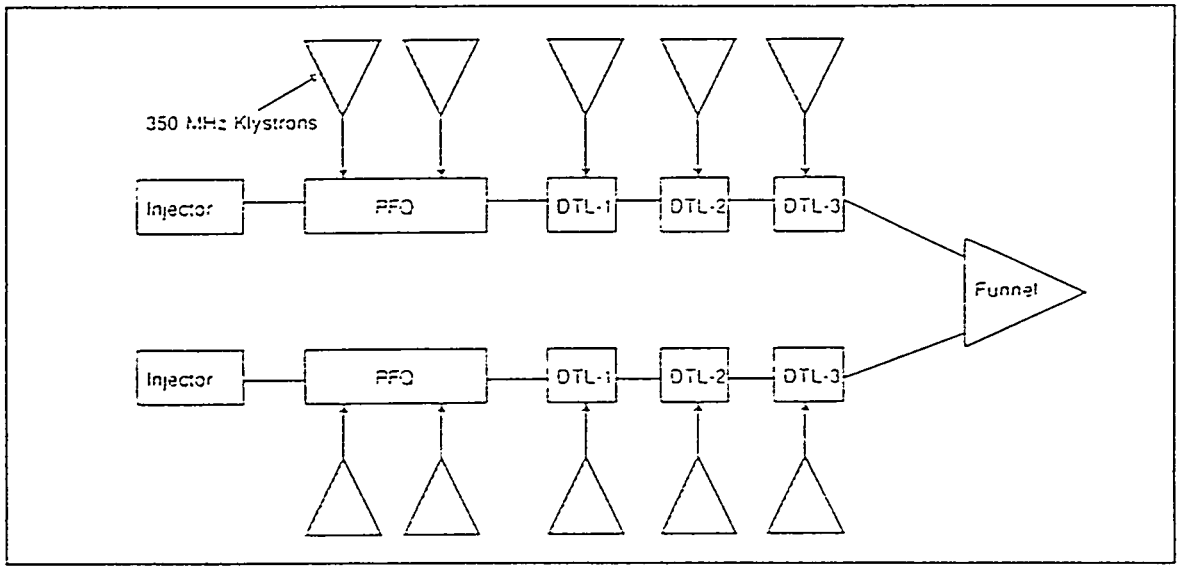


Fig. 4-23. Overview of high-power 350-MHz RF system for low-energy linacs.

From a HV power supply and interlock viewpoint, all 10 high-power RF systems are identical. Each klystron has an independent connection to the HV bus and a set of interlocks to protect the equipment and personnel. However, from a cavity-field-control point of view, the ten systems look somewhat different. Each RFQ is an assembly of coupled tanks and therefore requires only one cavity-field control system, as depicted in Fig. 4-24. The RFQ acts as a combiner for the two RF systems.

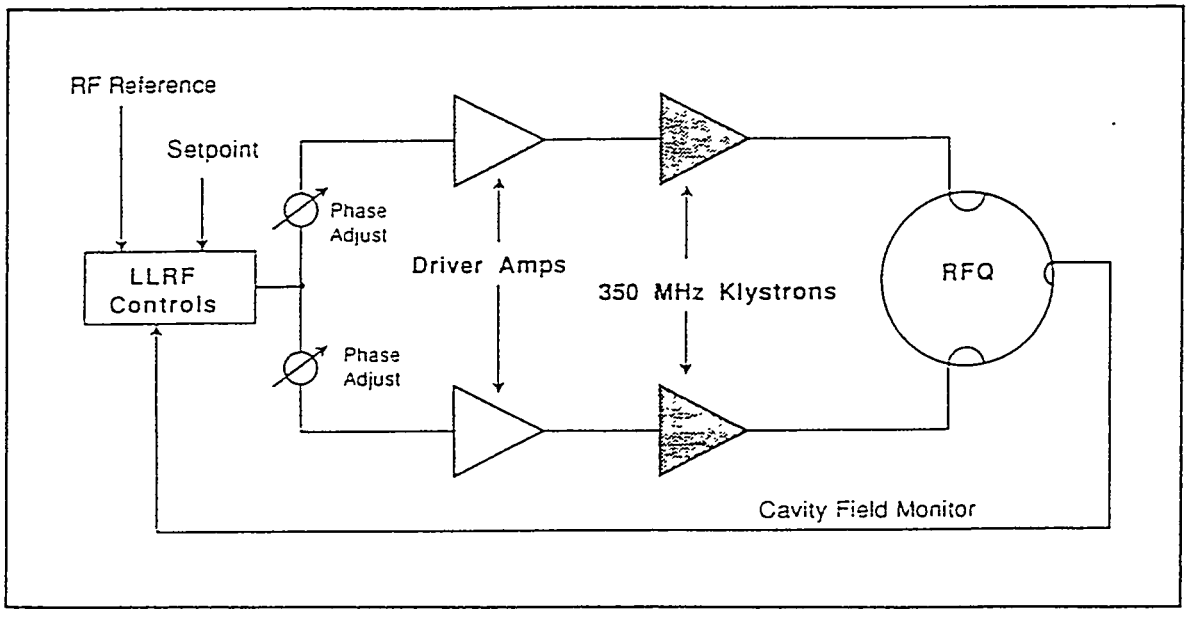


Fig. 4-24. LLRF controls for the 2-klystron RF system for the RFQ.

The RFQ power delivery arrangement, therefore, requires that each RF system be properly phased with respect to the other to combine power efficiently. Any misphasing results in each amplifier seeing significant reflected power, requiring more drive to appropriately power the RFQ. This can be seen in the following analysis, which adds two RF waves of the same frequency, but a small phase difference (<20°):

$$R = A\sin(\omega t) + B\sin(\omega t + \phi)$$

$$R \equiv \sqrt{A^2 + B^2 + 2AB\cos\phi}\cdot\sin(\omega t + \frac{B}{A+B}\phi) \ .$$

If $\phi=0$, the output amplitude is just $(A+B)$ at a frequency of ω. For any $\phi\neq0$, the amplitude is reduced, and the RF wave is shifted in phase. As an example, for $A=B$ and $\phi=10°$, the output amplitude is reduced by about 0.4% and the output phase is changed by 5°. This power combining method was used for the BEAR RFQ and worked quite well. Because the effect is small for small phase angles, it can be implemented with *set-and-forget* manual phase shifters.

4.6.1 RF Generator

The range of power required from the 350-MHz RF systems for the RFQ and DTL is 0.62–1.05 MW, including 10% excess power for control margin and disturbance rejection.

The RF generator for the 350-MHz systems is based on the proven Thompson-CSF 352-MHz klystron which has seen extensive service in the CERN Large Electron Positron (LEP) collider. This klystron is available in 1.1-MW and 1.3-MW cw versions. The higher power unit requires a slightly higher voltage (93 kV versus 85 kV). Based on the APT linac power requirements, the lower power tube (85 kV) is adequate. This klystron has a modulating anode which allows control of the electron beam current level, and hence the maximum output power. The mod anode is used to optimize the amplifier operating efficiency (efficiency of dc to RF conversion). If the mod anode is used for this kind of optimization (refer to Chap. 8, Sec. 8.2), the efficiencies shown in Fig. 4-25 are achievable in the RFQ and DTL.

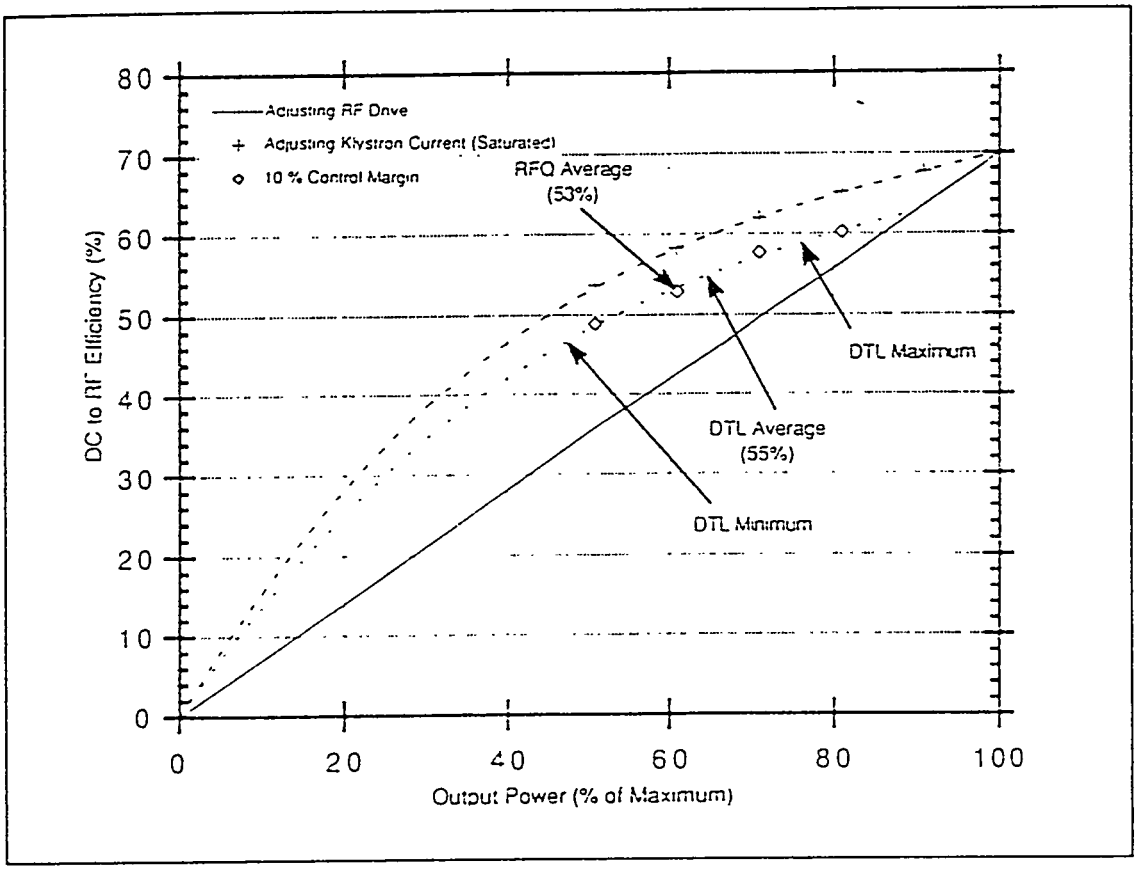


Fig. 4-25. RFQ & DTL output efficiency using GTA klystron data (normalized to CERN tube efficiency).

4.6.2 RF Distribution

The RF power from the 350-MHz klystrons is distributed with air-cooled WR2100 waveguide. Each waveguide line includes a circulator and directional couplers at the klystron and the cavity ends. The waveguide is slightly pressurized with dry air so that pressure interlocks can be used to indicate waveguide integrity. The pressurized air has a small flow rate through the waveguide to enhance cooling.

4.6.3 RF Layout

The layout of the 350-MHz systems is shown in Fig. 4-26. Each klystron requires three electronics racks—one for the klystron preamplifiers, one for interlocks, and one for system controls and interface—as well as a small oil tank around the cathode and high-voltage input connections. The RFQ needs slightly less rack space because there is only one LLRF (low-level RF) control system for the RFQ. Every other klystron system for APT requires its own LLRF system.

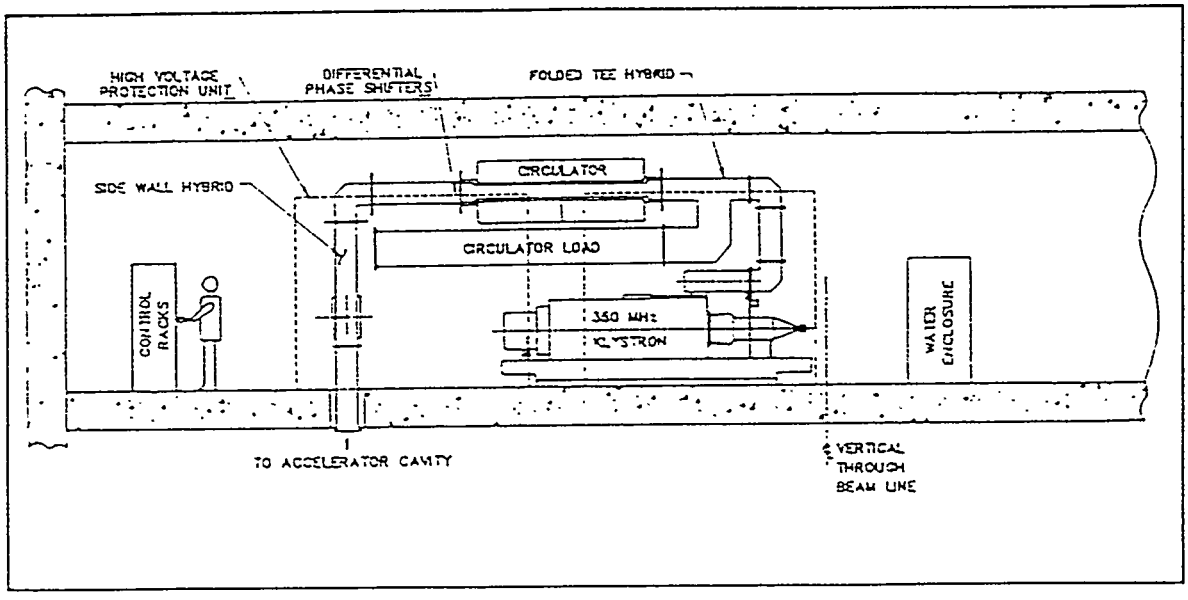


Fig. 4-26. RF system layout for 350-MHz systems.

CHAPTER 4 REFERENCES

4-1. D. Schrage et al., "Conceptual Design of a 7 MeV RFQ Linac for the Accelerator Production of Tritium," Los Alamos National Laboratory report LA-UR-93-1790 (1993).

4-2. D. Schrage et al., "A Flight-Qualified RFQ for the BEAR Project," Proceedings of the 1988 Linear Accelerator Conference, Williamsburg, VA (1988).

4-3. D. Schrage et al., "Radio Frequency Quadrupole Linac for the Superconducting Super Collider," Proceedings of the 12th Conference on the Application of Accelerators in Research & Industry, Denton, TX (1992).

4-4 T. Bhatia et al., "Beam Dynamics Design of an RFQ for the SSC Laboratory," Proceedings of the 1991 IEEE Particle Accelerator Conference, San Francisco, CA (1991), IEEE Conf. Record 91CH3083-7, 3, 1884-1886 (1991).

4-5. G. Arbique et al., "Beam Parameter Measurements on the CW RFQ1-1250 Accelerator," Proceedings of the 1992 Linear Accelerator Conference, Ottawa, ON (1992).

4-6. J. Y. Sheikh and R. J. Burton, "Tuning and Conditioning of RFQ1-1250 Cavity," Proceedings of the 1992 Linear Accelerator Conference, Ottawa, ON (1992).

4-7. L. Young, "Tuning and Stabilization of RFQ's," Proceedings of the 1990 Linear Accelerator Conference, Albuquerque, NM (1990).

4-8. M. Browman and L. Young, "Coupled Radio Frequency Quadruples as Compensated Structures," Proceedings of the 1990 Linear Accelerator Conference, Albuquerque, NM (1990).

4-9. L. Young, "Segmented Resonantly Coupled Radio-Frequency Quadrupole (RFQ)," Proceedings of the 1993 IEEE Particle Accelerator Conference, Washington, DC (1993).

4-10. W. Cornelius, "CW Operation of the FMIT RFQ Accelerator," Proceedings of the 1985 Particle Accelerator Conference, Vancouver, BC (1985).

4-11. N. Ueda et al., "Construction of the RFQ 'TALL'," Proceedings of the 1985 Particle Accelerator Conference, Vancouver, BC (1985).

THE FUNNEL
CHAPTER 5

Page

5.1 SYSTEM OVERVIEW AND PURPOSE 1
5.2 LAYOUT AND DESCRIPTION 1
5.3 DESIGN ISSUES 3
5.4 RF BUNCHER CAVITIES 4
5.4.1 Physics Description 4
5.4.2 Mechanical Description 7
5.4.2.1 Fabrication 7
5.4.2.2 Endwalls 7
5.4.2.3 Cooling 8
5.4.2.4 Drift Tubes 9
5.4.2.5 Thermal Expansion, Support, and Alignment 9
5.4.2.6 Vacuum 10
5.5 RF DEFLECTOR CAVITY 10
5.5.1 Physics Description 10
5.5.2 Thermal Design and Analysis 12
5.6 ADDITIONAL COMPONENTS 12
5.6.1 Dipoles 12
5.6.2 Beamtube 13
5.6.3 Small-Bore EMQs 14
5.6.4 Large-Bore EMQ 15
5.7 MECHANICAL SUPPORT STRUCTURE 15
5.8 EXPERIMENTAL STATUS 17
5.8.1 Los Alamos Single-Beam Experiment 17
5.8.2 McDonnell Douglas Two-Beam Experiment 18
5.9 MATCHING SECTION (FUNNEL TO BCDTL) 19
5.10 DIAGNOSTICS 20
5.11 FUNNEL RF POWER SYSTEM 22

LIST OF FIGURES

Page

Fig. 5-1. Interlacing of bunches in the funnel. 1
Fig. 5-2. 20-MeV funnel layout. 2
Fig. 5-3. Funnel buncher cavities R3 and R2. 4
Fig. 5-4. Funnel 2-hole buncher cavity R1. 5

Fig. 5-5. SUPERFISH output for untapered, two-gap, 700-MHz buncher (R3). 5
Fig. 5-6. SUPERFISH output for tapered, two-gap, 700-MHz buncher (R2). 6
Fig. 5-7. MAFIA 3D plot of one-fourth of (R1) two-hole buncher. 7
Fig. 5-8. Mounting and alignment scheme for buncher cavities and quadrupoles. 9
Fig. 5-9. 3D exploded view of the 350-MHz RF deflector cavity. 11
Fig. 5-10. Beam-bending dipoles for the APT funnel. 13
Fig. 5-11. Mechanical support structure for the APT funnel. 16
Fig. 5-12. Schematic of the Los Alamos single-beam funnel experiment. 17
Fig. 5-13. Schematic of the McDonnell Douglas two-beam funnel experiment. 18
Fig. 5-14. APT funnel-to-BCDTL matching section (or MEBT). 19
Fig. 5-15. Layout of the funnel section with location of the diagnostic elements. 21

LIST OF TABLES

Page

Table 5-1. Funnel General Parameters 2
Table 5-2. Funnel Beam Parameters 3
Table 5-3. APT Funnel Cavity Parameters 8
Table 5-4. Deflector Cavity Power Requirements 12
Table 5-5. APT Funnel Dipole Specifications 13
Table 5-6. Funnel Dipole Specifications 14
Table 5-7. APT Funnel and MEBT Diagnostics 21

5.0 THE FUNNEL

5.1 SYSTEM OVERVIEW AND PURPOSE

In the funnel section, two beams from two separate low-energy legs, each consisting of one ion source, LEBT, RFQ, and DTL, are combined together to form a single collinear beam. The two legs carry bunched beams that are phased 180° apart of frequency f_0; these two beams are then merged, forming a single beam of frequency $2f_0$. The beams are interlaced as shown in Fig. 5-1. The interlacing is done in a deflector cavity by alternating RF transverse deflecting fields operating at frequency f_0 to form a single collinear beam with a frequency $2f_0$. It should be noted that funneling doubles the effective current of the beam but does not increase the charge per bunch.

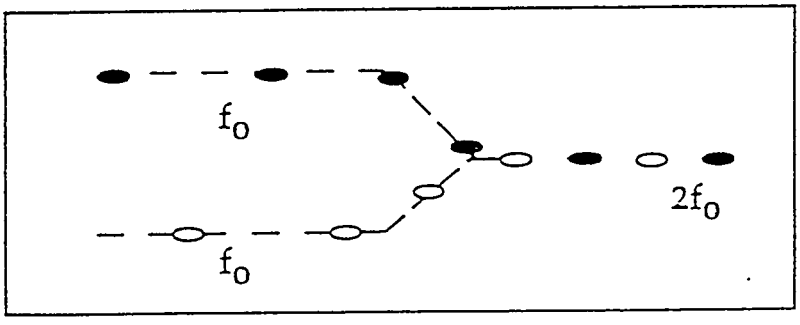


Fig. 5-1. Interlacing of bunches in the funnel.

Funneling is necessary to meet the basic design criteria for APT. Since all ion sources and low-energy sections of the linac have beam current limits, we avoid these limits by cutting our injector and RFQ current requirements in half and funneling at an appropriate stage. It allows us to fill all the RF cycles in the high-energy portion of the linac and thereby increase the efficiency of the machine. The emittance, the beamsize, as well as the charge per bunch are also much smaller, compared with an unfunneled beam of the same effective current. This provides the potential for lower beam losses at the high-energy end of the linac.

The energy of funneling was chosen to be 20 MeV for this design. The choice of energy is a compromise between several conflicting requirements. This energy was chosen (over a lesser energy) to keep space charge forces relatively small and to have high enough velocity so that the 700-MHz linac would accept the funneled beam. Also, a relatively high energy was necessary to maintain interquad distances that were large enough to meet engineering and diagnostic constraints. The 20-MeV energy is still low enough to result in a beam that is not too rigid for deflection in the RF deflector.

5.2 LAYOUT AND DESCRIPTION

The arrangement of components in the 20-MeV funnel is shown in Fig. 5-2. Each leg of the transport region consists of eight EMQs and two conventional two-gap 700-MHz bunchers (R3 and R2). These elements transport the beam with about the same transverse and longitudinal focusing strengths as that at the exit of the DTL. The funnel legs are designed with 700-MHz bunchers operating at the second harmonic of the beam, resulting in

smaller cavities and savings of power and space in a fairly tight configuration. The second of the two buncher cavities (R2) in each leg has a special tapered geometry to enable the bunchers in the two adjacent legs to fit together. The last two quadrupoles in each leg that flank the R1 buncher cavity are made of permanent magnet material for compactness, while the final quadrupole in the "merge" section in front of the deflector cavity is a large-bore EMQ with both beams entering off-axis. The dipoles in each leg of the funnel each bend the beam 9.77°, while the common large-bore EMQ (where the beams enter off-axis) deflects the beam an additional ~1°. The remaining ~2° of bend to merge the beams on-axis is done in the RF deflector cavity. The parameters that specify the APT funnel are given in Tables 5-1 and 5-2 below.

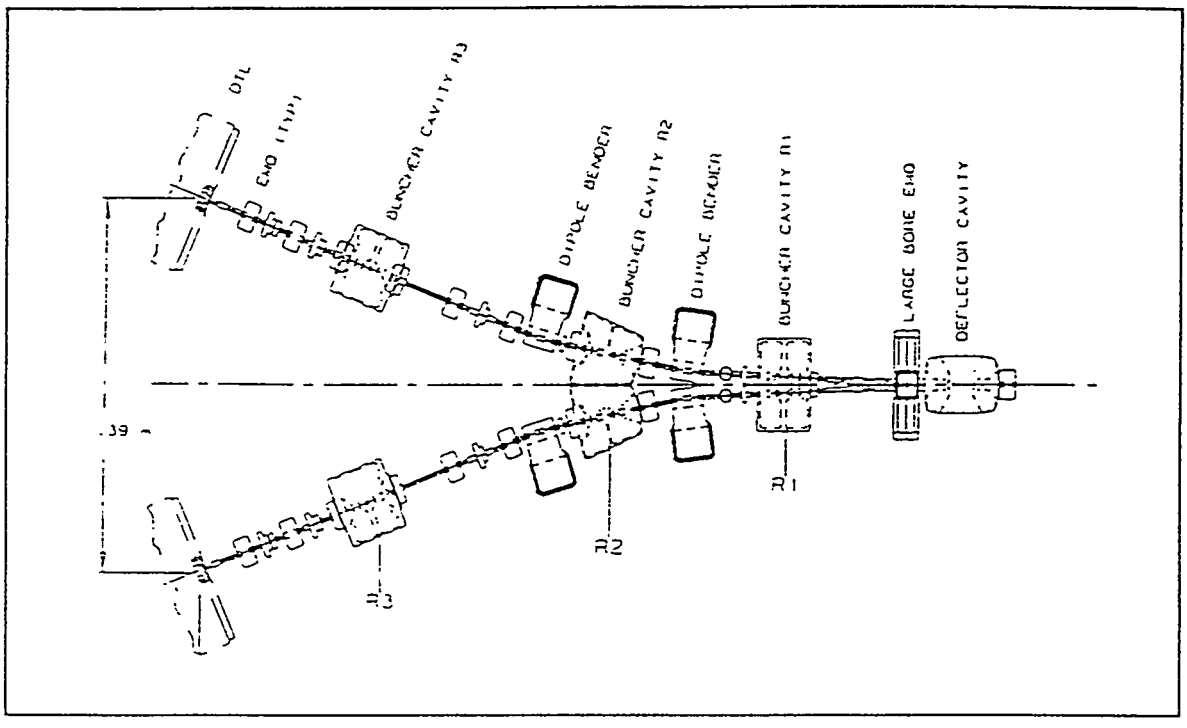


Fig. 5-2. 20-MeV funnel layout.

Table 5-1. Funnel General Parameters

Energy (MeV)	20.0
Frequency (MHz)	350/700
Length (cm)	295.0
No. of EMQs	2X8+1 = 17
No. of PMQs	2X2 = 4
Total No. of Quadrupoles	2X10+1 = 21
No. of Dipoles	2X2 = 4
No. of Bunchers	2X2+1 = 5
No. of Deflectors	1
Initial Beam Approach Angle (deg)	22.4
Initial Separation of Beams (cm)	137.8
Quadrupole Lattice	FOFODODO
Quadrupole Lengths (cm)	5.7

Table 5-2. Funnel Beam Parameters

Beam Current, In (mA)	2 x 100
Beam Current, Out (mA)	200
Radial Aperture (cm)	1.00 (0.6 between deflector plates in bend plane)
Aperture/Beamsize (rms) Ratio	4.3 @ deflector, 5.5 @ PMQs
Transverse Emittance, rms*, In (π·cm-mrad)	0.023
Transverse Emittance, rms*, Out (π·cm-mrad)	0.026
Longitudinal Emittance, rms, In (π·MeV–deg)	0.216 @ 350 MHz
Longitudinal Emittance, rms, Out (π·MeV–deg)	0.219 @ 350 MHz
Longitudinal Beam Bunch Size, rms (deg)	±5.5 @ input, ±3.3 @ deflector

*normalized

5.3 DESIGN ISSUES

In designing a complete configuration for the funnel, i.e., the layout of the components, the quadrupole focusing lattice, component strengths, etc., we had to strike a compromise between a number of physics and engineering requirements. Some of the important physics issues that have shaped the design of the funnel are as follows:

- The final deflection at the RF deflector is time dependent, which creates transverse beam spreading. This demands a small longitudinal bunch width at the deflector.
- The beam suffers momentum dispersion at the site of the bending magnets and bunchers. This requires that the bending and bunching be done in small steps and should be as evenly distributed as possible along the length of the funnel.
- The phase advance per transverse focusing period has to be kept below 90° to avoid beam instability. This limits the inter-element spacing at the merging end of the funnel section.
- The gap between the deflector plates in the bend plane is limited by the electric field needed and the cooling requirement. This forces the transverse beamsize in the bend plane to be as small as possible.

The important engineering issues that have shaped the design of the funnel are mainly concerned with having adequate space for components, such as the following:

- quadrupoles and dipole bending magnets (PMQs were chosen for the merging end because of their smaller size);
- other components at the merging end of the funnel;
- the RF deflector at the output end of the funnel; and,
- diagnostics throughout the length of the funnel;

These are the main physics and engineering issues that have driven the funnel design.

5.4 RF BUNCHER CAVITIES

5.4.1 Physics Description

The buncher cavities used on the APT funnel are two-gap, drift-tube linacs. The bunch frequency of the beam on each leg of the funnel is 350 MHz; however, the bunchers operate at 700 MHz. The higher frequency allows for a smaller structure that fits into the drift space between the quadrupole focusing magnets and where the two legs of the funnel get quite close together. This constraint eliminates consideration of a single-gap, 350-MHz buncher in all but one location of the funnel. Note that there is no difference in the beam dynamics between a 350-MHz and a 700-MHz buncher. Therefore, in the present design, we have used only 700-MHz bunchers.

Three distinct RF buncher cavity designs are incorporated into the funnel and into the matching section between the funnel and the BCDTL. Figure 5-2 depicts the locations of the three cavity designs, R1, R2, and R3. Sketches of all three geometries are shown in Figs. 5-3 and 5-4.

Figure 5-5 shows a SUPERFISH calculation of the R3 buncher, and Fig. 5-6 shows the same for the tapered R2 buncher. The SUPERFISH output, listing the RF properties of these structures, can be found in the Chap. 5 Appendix. Although the code indicates that the maximum power dissipation per unit area for the bunchers occur on the walls of the drift tube, in the actual structure, the maximum power dissipation will occur at the joint of the drift tube and its support stem (not included in the SUPERFISH calculation). The peak power dissipation at this joint, averaged around the stem, will be approximately double the maximum value indicated at the boundary, or 52 W/cm² for the R3 buncher.

The R2 buncher is used where the two legs of the funnel are so close together that the R3 geometry will not fit. Because the two legs of the funnel are mirror images of each other, no element may extend past the centerline—hence the need for the tapered R2 buncher geometry.

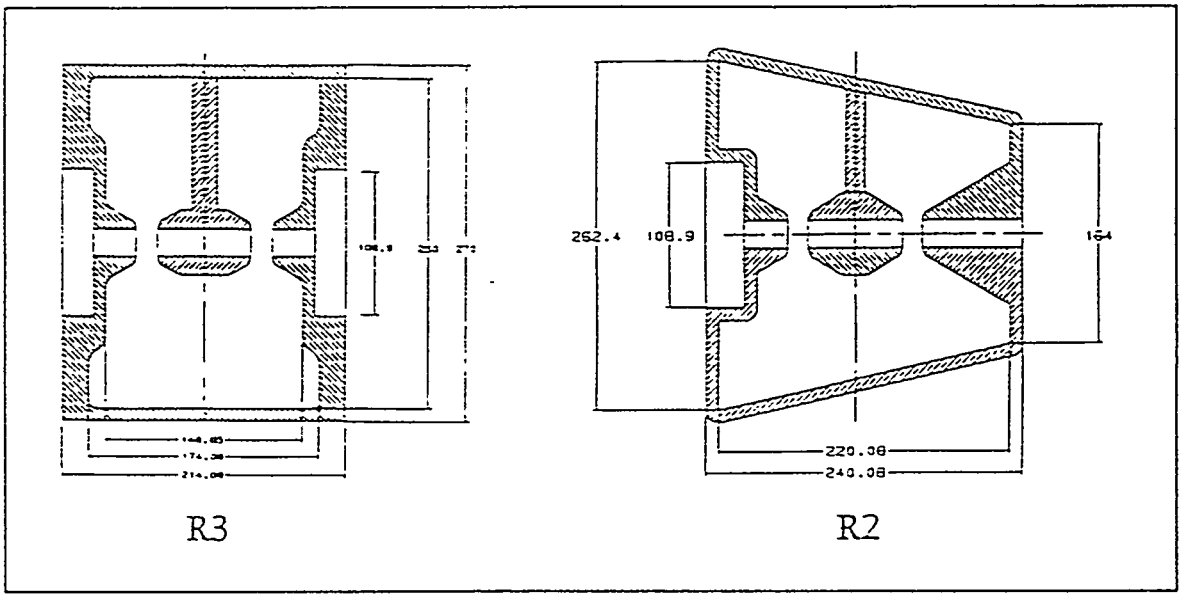


Fig. 5-3. Funnel buncher cavities R3 and R2.

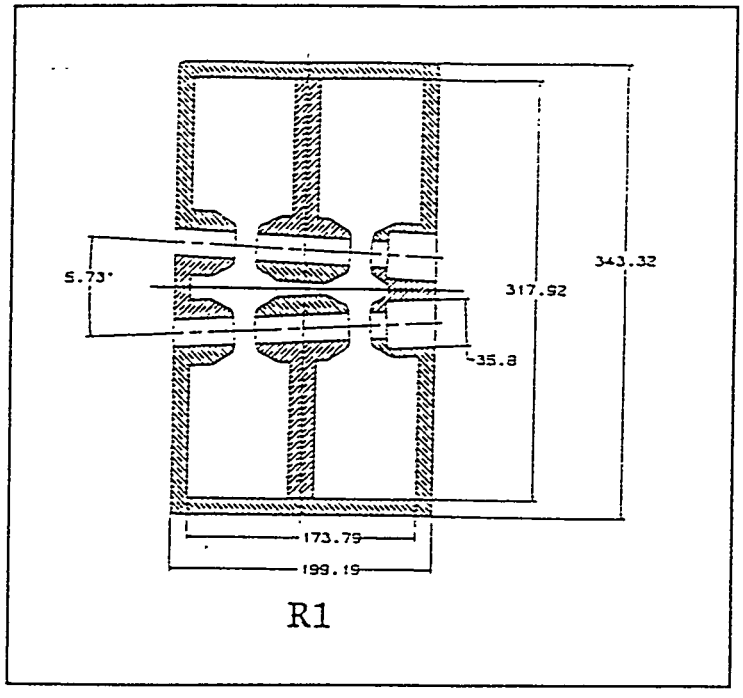


Fig. 5-4. Funnel 2-hole buncher cavity R1.

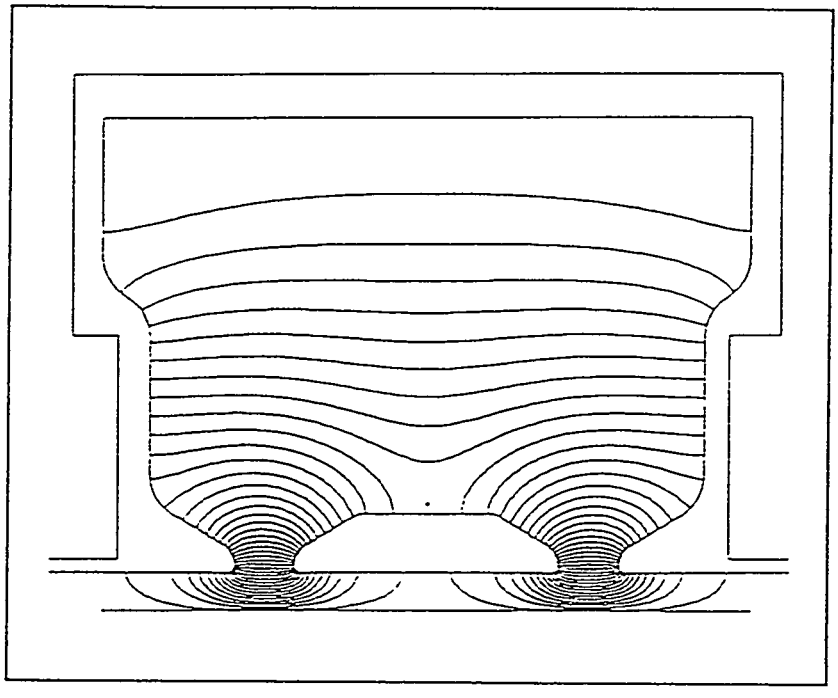


Fig. 5-5. SUPERFISH output for untapered, two-gap, 700-MHz buncher (R3).

Both Figs. 5-5 and 5-6 show the cross section of cylindrically symmetric cavities. The axis of rotation is at the bottom of the figures. The SUPERFISH output (Chap. 5 Appendix)

indicates that the power consumption and peak power dissipation for the R2 (tapered) buncher is approximately double that of the R3 (untapered) buncher. The reason the power is higher is that the gap voltage required for this buncher is higher.

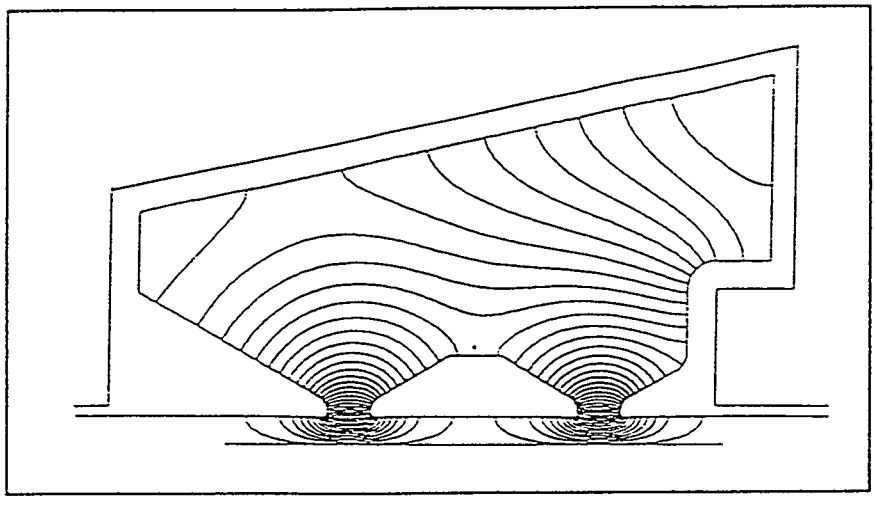


Fig. 5-6. SUPERFISH output for tapered, two-gap, 700-MHz buncher (R2).

The final buncher, R1, shown in Fig. 5-4, is located where the two legs of the funnel are very close together. In this case, a common cavity is used as the buncher on both legs. This buncher cavity has two beamlines through it. It may be best described as a drift tube linac with two beamlines. Since this cavity is not cylindrically symmetric, SUPERFISH cannot calculate its exact properties. Using SUPERFISH on an equivalent cavity that has cylindrical symmetry, however, we can calculate some properties. The equivalent cavity is one that has the same capacitance as the two-beamline cavity. It also has the same cross-sectional area of the drift tubes. The SUPERFISH output (Chap. 5 Appendix) lists the properties of the equivalent cavity, which can be compared with the 3D MAFIA code calculation. The output indicates that the peak power dissipation on the drift tubes is ~67 W/cm^2. The RF power dissipation at the joint between the drift tube and the stem, averaged around the stem, will be approximately double, or ~134 W/cm^2; if not averaged around the stem, it is ~268 W/cm^2.

The power loss densities were also calculated using MAFIA (3D). The buncher geometry as modeled in MAFIA is shown in Fig. 5-7. For this (power) analysis, the cavity is aligned with the grid, and the drift tubes are tilted from their actual orientation so that each drift tube also aligns with the grid.

The results of this analysis should be reasonably good for estimating power densities in the areas where they are expected to be highest. Electric fields near the beamline, however, are not expected to be accurate, with the approximations made here. Further analysis of this structure needs to be performed using a different set of approximations that will give better accuracy near the beamline. Due to symmetry, only one-fourth of the structure was modeled. Figure 5-7 is a 3D plot of the model, with the gridlines shown on the surfaces. Additional MAFIA calculations and plots can be found in the Chap. 5 Appendix, including a plot of an x-y cross section, a y-z cross section, and the electric field line patterns in the bend plane of the buncher. The peak power densities, calculated from tiny localized "hot spots", range from 115–390 W/cm^2. The list of the highest 150 values for peak power densities at different grid points, sorted in decreasing order of magnitude, can be found in the Chap. 5 Appendix.

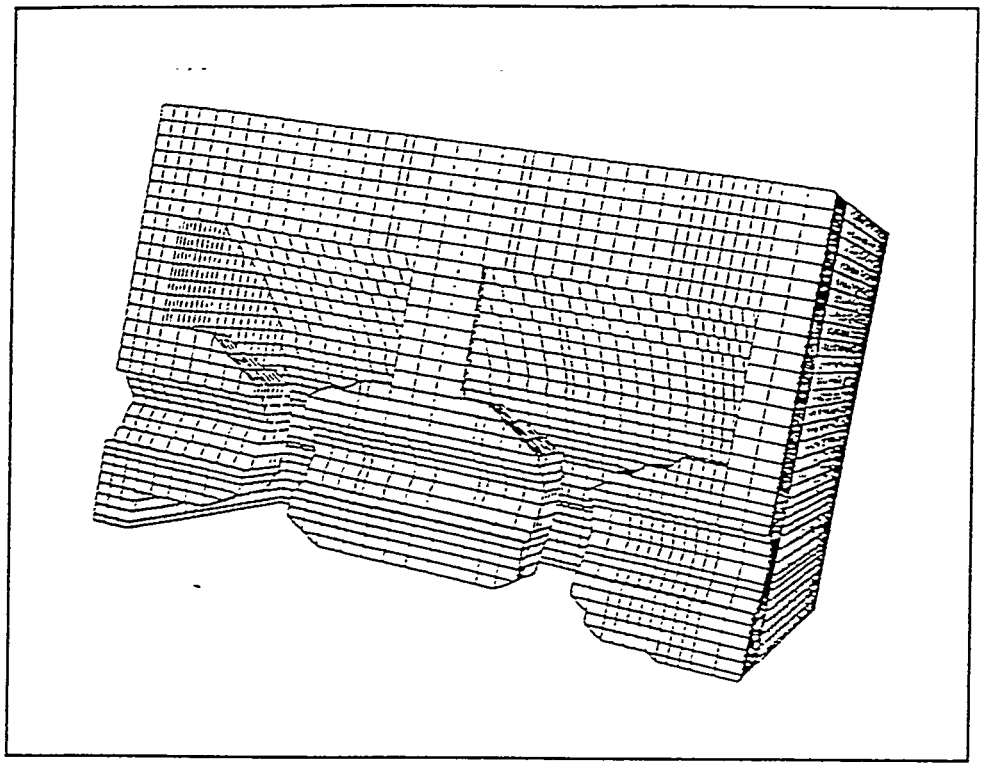


Fig. 5-7. MAFIA 3D plot of one-fourth of (R1) two-hole buncher.

5.4.2 Mechanical Description

The three buncher-cavity designs in the funnel section are depicted in Figs. 5-3 and 5-4. Cavity R3 is the simplest of the three buncher designs. It is completely symmetric. The R1 cavity is the most complicated; although the cavity body is cylindrical, a two-channel drift tube is required due to the relative proximity of each funnel leg at this location. The tapered shape of the R2 cavity is necessary due to the close proximity of the two funnel beamlines.

5.4.2.1 Fabrication

Each cavity will be manufactured of copper, specifically OFE grade, fully annealed class 2 copper. Oxygen-free copper is required to prevent blistering during brazing operations in which hydrogen is used. Each cavity body will be machined from a roll-formed forging. The tapered (R2) buncher body will also be manufactured from a roll-formed forging. Each endwall will be machined from plate stock. The drift tube noses attached to each endwall will be machined separately and subsequently brazed or EB-welded in place. Each nose is a multipart assembly due to internal cooling channels.

5.4.2.2 Endwalls

The forward endwalls of the R3 and R2 buncher cavities incorporate a recess and necessary mounting features (threaded inserts) for a small-bore EMQ. The aft endwall is removable to accommodate drift tube installation and replacement. The removable endwall

will be fastened to the cavity body with a mechanical RF and vacuum joint. The joint will incorporate separate metallic RF and vacuum seals. Heavy wall flanging is required to accommodate the high compressive load required to *plastically deform* the metallic vacuum seal (plastic deformation of the seal implies strain of the material beyond the knee of the stress-strain curve for copper, i.e., beyond the strain range where Hooke's law for purely elastic materials applies). The other endwall will be brazed directly to the cavity body.

5.4.2.3 Cooling

The wall of each cavity is cooled with twelve equally spaced axial passages. Where the RF-drive loop or the drift-tube mount interferes with a passage, the passage is plugged on either side, and a section of tubing is used to externally connect the passages together to form a continuous cooling run. The coolant flow in each passage is opposite in direction to the flow in the two adjoining passages, called counterflow cooling. This type of flow logic provides for a more symmetric, less distorted cavity shape after thermal deformation.

Endwall cooling is accomplished via a serpentine channel cut into the exterior surface with an endmill. A thin cover is brazed or EB-welded over the endwall exterior to seal the cooling channels. Two loops are incorporated into each endwall; the primary purpose of one loop is to supply coolant to the nose passages at the endwall center. A pair of circumferential external manifolds will be brazed at the forward and aft edges of each cavity body. Two manifolds are required: one for the supply and the other for the return in the counterflow cooling scheme. Before the brazing operation, passages will be drilled into the cavity wall connecting each axial wall-coolant passage to either the supply or return manifold.

Spring-loaded thermocouples will be installed with bayonet mounts in the drift tubes, endwall noses, and bodies of each buncher. This type of thermocouple allows for rapid replacement, either manually or remotely. By monitoring the thermocouples, any malfunction of the cooling system will be immediately detected.

The total thermal load, maximum and average surface-heat fluxes and the required coolant flow can be found in Table 5-3 for the R2 and R3 cavities. Additional analyses have yet to be done to arrive at values for these parameter for the more complicated R1 cavity. The required coolant flows are based on operating the cavities with a maximum coolant temperature rise of 10C°. This relatively small temperature rise is chosen to limit the stresses induced in the cavity walls by RF power dissipation. It should be noted that the R3 and R2 buncher cavities carry 2 MW of cw beam power.

Table 5-3. APT Funnel Cavity Parameters

Parameter	Cavity R1	Cavity R2	Cavity R3
Frequency (MHz)	700	700	700
Length (cm)	19.9	24.0	21.4
Structure (Single Drift Tube)	2-gap, 0-mode	2-gap, 0-mode	2-gap, 0-mode
Peak Surface Field (Kilpatrick)	<1.4	<1.4	<1.4
Average Surface Heat Flux (W/cm^2)	—	~16.8	~6.8
Maximum Surface Heat Flux (W/cm^2)	—	40.0	25.0
Thermal Load (kW)	60.0	44.0	19.0
Coolant Flow (gpm)	—	17.1	7.0

5.4.2.4 Drift Tubes

The drift tubes used in each buncher will be very similar in detail to the drift tubes used in the BCDTL. They will not contain quadrupole magnets. This results in a less complicated design and allows a more generous positional tolerance. Each drift tube body is EB-welded together from four individually machined detail parts. A coaxial stem design is utilized. The coolant enters through the inner tube and returns through the annulus between the inner and outer tubes. The drift tube for cavity R1 is of a somewhat more complicated geometry due to the asymmetry of the cavity. The drift tube stem mount at the cavity wall will be identical to the scheme used for the BCDTL, namely a conical *hard socket*, which provides alignment through machining precision alone and also assures high-integrity RF and hard-vacuum sealing. The transition from the coaxial stem coolant passages to the separate supply and return fittings will also be done as in the BCDTL.

5.4.2.5 Thermal Expansion, Support, and Alignment

Each cavity is subjected to a substantial degree of thermal growth because of the internal surface-heat flux caused by eddy-current power dissipation. This flux is nonuniformly distributed, as are the RF fields in the cavity. An important requirement concerning beam quality is maintaining very precise alignment of the cavities. Precision alignment is also required for the quadrupole magnets mounted on each cavity. An interesting problem is the design of a support method that maintains alignment of the cavities as they grow thermally but does not induce excessive structural loading on the annealed copper. Such a concept was developed that meets both design requirements and is depicted in Fig. 5-8.

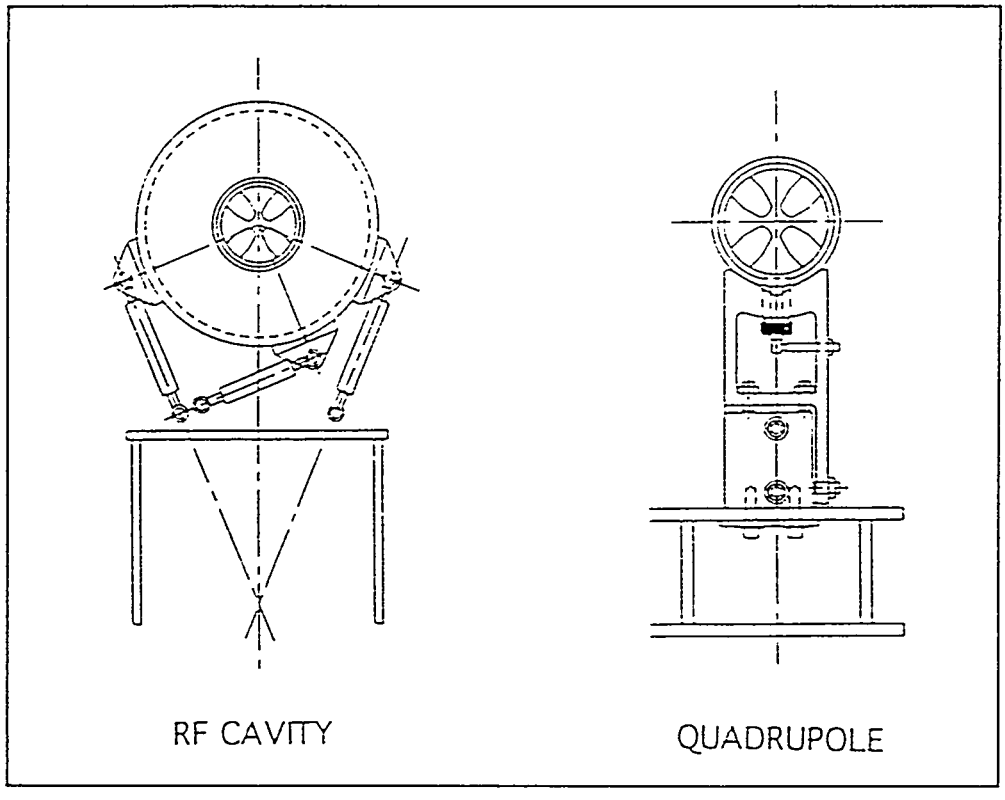


Fig. 5-8. Mounting and alignment scheme for buncher cavities and quadrupoles.

Since each cavity has basic geometric axial symmetry (the exception to this symmetry is the drift tube), the surface heating and cooling schemes are symmetrical about the beam axis. This combination of geometric and thermal symmetry leads to cavity thermal displacements that are almost purely radial and axial. The mechanical mounting scheme developed uses this feature by permitting radial growth of the cavity but maintaining axial alignment as the cavity grows. The scheme includes five support links fastened via external fittings on each cavity (only three links can be seen in Fig. 5-8). Each link consists of two spherical-rod-end bearings threaded on to each end of a hexagonal strut. Precision rod-end bearings are used to provide enhanced vibrational stability. One end of the strut is threaded with left-hand thread, while the other end has conventional right-hand thread. Rotation of the strut extends or contracts the strut.

Alignment of the cavity is performed by adjusting each of the five links. The alignment of a cavity would proceed as follows:

- The cavity would be installed with all adjoining hardware, and each link would be set to its nominal length.
- The global position of the cavity would be determined optically.
- These data and the theoretical cavity global position data would be used as input into a personal computer. A simple code, written to calculate the necessary movements for each link, considering the actual and desired positions, would be used. The specified adjustments to each link would then be made.
- The alignment procedure would then be verified by remeasuring cavity position using standard alignment equipment.

This alignment scheme, in conjunction with the semikinematic support scheme, provides a very fast and efficient means for cavity installation and replacement. The iterative procedure typically required for alignment using conventional support schemes is not required here.

5.4.2.6 Vacuum

Because of limited space along the beamline for vacuum pumpout manifolds, as well as conductance limitations imposed by the small-diameter beamtube, all pumping is performed through slots in the RF cavity walls. A vacuum manifold is mounted beneath each cavity. These manifolds are brazed to the cavities at the time of manufacture. An RF attenuation grill, similar to the one incorporated in the DTL is used to provide a high-conductance pumpout port to the manifold where it interfaces with the cavity. Each vacuum manifold will have Conflat flange ports for ion gauges, thermocouple gauges, etc. A 120-l/s ion pump will be mounted directly below each manifold.

5.5 RF DEFLECTOR CAVITY

5.5.1 Physics Description

The deflector is one of the most important components in the funnel section. Figure 5-9 shows a 3D exploded view of the deflector geometry. As summarized elsewhere, an

alternating RF electric field is established between two electrodes that are part of the cavity. The two beam pulses from the two separate legs enter the deflector gap at 180° out of phase and hence suffer deflection in the opposite directions. The deflections suffered by two successive beam pulses from separate legs, in principle, are equal and opposite, resulting in a merged beam collinear with the symmetry axis.

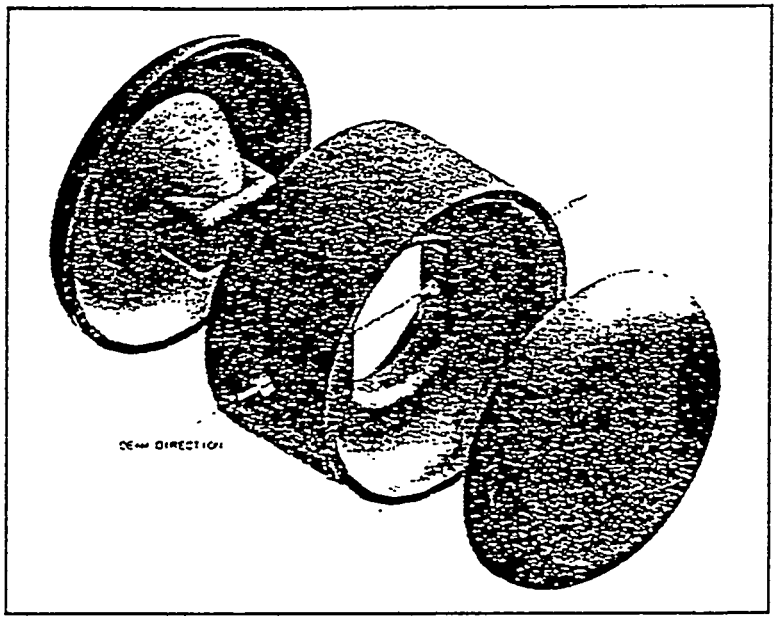


Fig. 5-9. 3D exploded view of the 350-MHz RF deflector cavity.

The equations of motion of a particle in the deflector are given in the Chap. 5 Appendix. As pointed out in the Appendix, the head and tail of the particle bunch will be deflected less, compared with the synchronous particle. The effect will be particularly pronounced the larger the phase spread from the synchronous particle. This effect immediately dictates that the longitudinal width of the beam bunch should be kept as small as possible.

The maximum deflection obtainable for a particle in a bunch, is directly proportional to the amplitude of the alternating field between the electrodes. A desired deflection, then, dictates the electric field in the gap which, for a robust design, should be kept within a conservative Kilpatrick limit. Moreover, the engineering constraint of thermal cooling is directly related to the current in the electrode structure, which in turn is directly coupled to the geometry and the voltage across the gap. This issue is critically important for cw operation.

The other important design issue is the gap-to-beamsize ratio. For a given peak voltage across the plates, the electric field is inversely proportional to the gap distance. This constrains the beamsize in the bend plane, within the deflector, to be made as small as possible. This usually comes at the cost of increased beamsize in the vertical plane (normal to the bend plane). The challenge there is to secure as uniform a field as possible for as large a distance as possible in the vertical plane.

Another important issue is the physical size of the deflector. The distance between the quadrupoles bracketing the deflector assembly has to meet the engineering constraint on the length imposed by the cooling capabilities. To maintain adequate transverse focusing for

increased lengths, this calls for increased quadrupole strengths. However, this directly contradicts the requirement of keeping the zero-current transverse phase advance below 90° to avoid beam instability.

In the present design, the deflector cavity is azimuthally symmetric around the axis perpendicular to the beamline and parallel to the direction of deflection. Therefore, the preliminary design can be modeled with SUPERFISH. The SUPERFISH output can be found in the Chap. 5 Appendix.

5.5.2 Thermal Design and Analysis

To produce the desired electric fields in the deflector cavity, the required RF power is high compared with the regular-shaped (R3) cavities. The deflector cavity power requirements are given in Table 5-4. The deflector cavity, therefore, will require special attention in the area of thermal design. Nominally, water-cooled room-temperature RF structures made of copper are designed for average power densities of less than 25 W/cm^2, and it can be seen from Table 5-4 that while the average power density is under 24 W/cm^2, surface heat fluxes reach 66 W/cm^2 at certain locations within the cavity. For comparison, certain high power areas on the DTL and BCDTL, namely the drift tubes and stems, reach 45 W/cm^2 and 89 W/cm^2, respectively. Over small enough areas, such extremely high power densities are tolerable. The 66 W/cm^2 in the deflector is certainly within this range, assuming the affected area is small enough. The funnel deflector cavity is one of the more crucial cavities in the APT linac because it is responsible for bending through precise angles. Cavity deformation and alignment under RF thermal loading, therefore, must be carefully controlled.

Table 5-4. Deflector Cavity Power Requirements

Total RF Power Required (kW)	72.4
Average Surface Heat Flux (W/cm^2)	23.8
Maximum Surface Heat Flux (W/cm^2)	66.1

The first step in the deflector cavity thermal design is to incorporate as many coolant channels as possible. This is done to reduce the net heat flux per coolant-channel area to manageable levels. For this preconceptual design phase, a 3D geometry of the cavity was simplified for the purpose of finite-element analysis. A 2D axisymmetric model was then built that is representative of the deflector (except in the area of the nose). The details of the structural analysis (thermal and thermally induced) are given in Appendix 12.5, Thermal and Structural Analyses. The analysis shows that the cavity operates within design stress levels.

5.6 ADDITIONAL COMPONENTS

5.6.1 Dipoles

Each funnel leg contains two dipole electromagnets for bending the beam. Each dipole bends the beam by ~9.774°. The dipoles are conventional "C"-type yoke designs, having a pole width of 11.6 cm, which gives a wide region of uniform field. The dipole specifications are given in Table 5-5.

The basic dipole geometry is depicted in Fig. 5-10. The field coil consists of 30 turns of 0.2576-inch, square, hollow-core conductor. Each dipole will be mounted on two support assemblies. These assemblies permit vertical adjustment. Lateral adjustment is obtained with translation on the strongback deck. A spherical fitting at the top of each support at the magnet interface permits roll. An alignment fixture will be used for prompt magnet installation. After all of the vertical, translational, and roll adjustments have been made, through-bolts from below the strongback deck permanently fix the magnets in position.

Table 5-5. APT Funnel Dipole Specifications

Number of Dipoles	4
Yoke Design	"C"-type
Gap (cm)	2.0
Pole-tip Field (T)	0.93
Weight (kg)	63.5
Power Consumption (kW)	4.8
Coolant Flow* (gpm)	0.61

*based on operation with 30°C coolant temperature rise

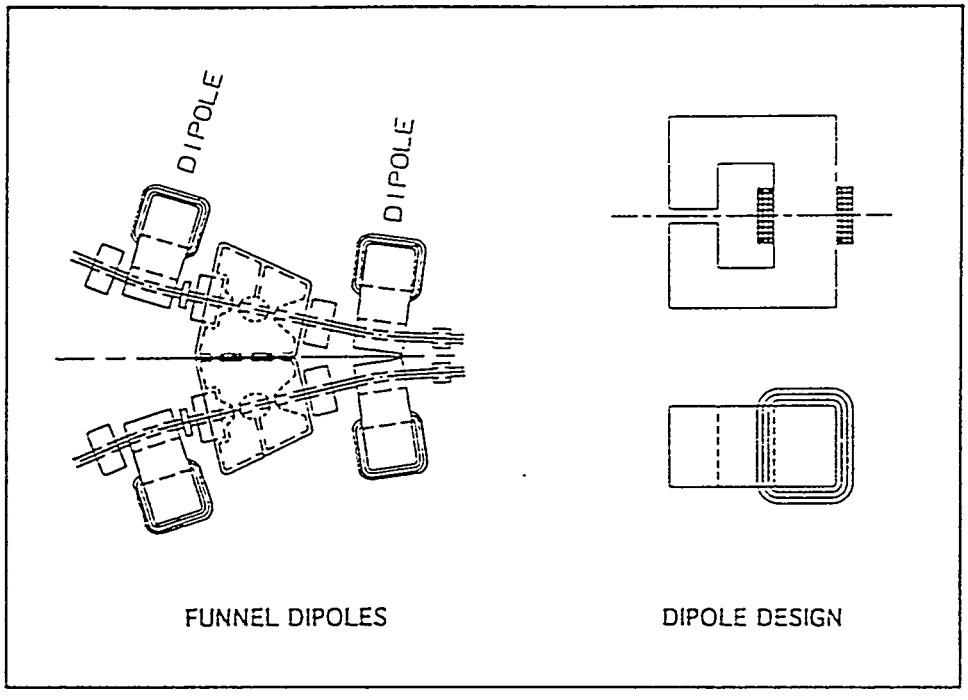


Fig. 5-10. Beam-bending dipoles for the APT funnel.

5.6.2 Beamtube

A stainless steel beamtube, type 304L, will be used throughout the medium-energy beam transport or "MEBT," also referred to as the funnel-to-BCDTL matching section. Tubing of 0.75-inch o.d. and 0.020-inch wall thickness has been chosen. The 0.020-inch wall beamtube

is basically thin-walled tubing, but provides a margin of four (4X) over buckling when exposed to one atmosphere of external pressure (the maximum exposure for the beamtube). Additionally, a minimum wall thickness maximizes the beamtube clear aperture and is beneficial in minimizing activation due to beamloss.

A small amount of compliance (springiness) in the beamtube is required to compensate for inherent manufacturing tolerances. This is accomplished with welded bellows installed in the beamline. Single convolution bellows will be used only where beamline space is very limited. These bellows will be formed of 304L stainless steel, as in the beamtube itself, and will be TIG welded into the beamtube.

Limited space along the beamline and the small clear apertures available in the beamline hardware prohibit the use of conventional flanging to join beamtube segments. An alternative method is to TIG-weld the segments together. This is quickly and reliably accomplished with an automated orbital-tube welding system, providing very high-quality welds. Tube segments are automatically aligned axially and butted together prior to welding. Remote performance of this operation is not only possible but quite common. Since beamtube flanges are not required, the tube segments may be easily inserted through the small-bore EMQs. Stainless beamtube stub sections will be brazed into the entrance and exit ports of each RF cavity during fabrication of the cavity. The diagnostic modules will also incorporate short tube-stub sections. During assembly of the beamline, the beamtube sections and the bellows will be welded to these stubs.

Disassembly of the beamline will necessitate sawing through the welds. Reassembly will require rewelding. Before rewelding, the sawed tube edge is dressed and finished using conventional tooling techniques. Also, one slightly longer beamtube segment would need to be used.

5.6.3 Small-Bore EMQs

Twenty-three small-bore EMQs are used in the funnel and MEBT—sixteen in the funnel and seven in the MEBT. The EMQs used are the magnets developed for the APT DTL. The magnetic performance requirements and the physical geometry limitations are similar, and the DTL magnet design has proven suitable for all funnel focusing needs. The specifications for the small-bore EMQs are listed in Table 5-6.

Table 5-6. Funnel Dipole Specifications

Parameter	Small Bore	Large Bore
Number of EMQs	23	1
Quadrupole Length (cm)	5.70	5.70
Outer Diameter (cm)	10.96	31.50
Maximum Operating Field Gradient (kg/cm)	2.5	3.0
Maximum (DTL) Design Field Gradient (kg/cm)	3.5	—
Clear Aperture (cm)	2.30	6.00
Power Consumption (kW)	1.0	7.2
Coolant Flow* (gpm)	0.13	0.91

*based on operation with 30°C coolant temperature rise

The small-bore EMQs will be mounted on a unique support stand. Due to limited space, six EMQs will be mounted directly on the endwalls of the buncher cavities. An interface

housing is mounted on the top of the magnet yoke, and conductor leads are routed through the yoke into the housing. The dc electrical interface, coolant interface, and thermocouple electrical interface are similar to the scheme used for the DTL EMQs. The EMQ power supplies are the same as those used in the DTL.

An alignment tool design has been developed to aid in aligning the EMQs. This device will be accurately located on the strongback by means of tooling pins that mate with predrilled precision holes in the strongback deck. Each EMQ will have its own set of precision holes. The alignment device incorporates a system of micrometer heads that will be used to quickly and accurately locate the EMQ with respect to the strongback. Two tooling holes will be drilled in the upper deck of the strongback on each side of the EMQ. These holes will be very accurately located. A removable alignment fixture will be placed on the strongback and located with pins that fit into deck holes.

Temperature monitoring of the conductor will be performed to detect failure of the magnet cooling system. One pair of thermocouples (two for redundancy) will be installed on one lead of each conductor pair. The thermocouples will be placed outside the magnet body in the interface housing, providing easy thermocouple access. A plugged or partially plugged cooling passage or a system leak would immediately affect flow. Any reduction in flow corresponds to an immediate conductor temperature rise. Thus, a cooling system failure is immediately detected. This scheme is simpler, more reliable, and less expensive than a system that monitors coolant flow (such as a flow meter).

5.6.4 Large-Bore EMQ

Only one large-bore EMQ is required in the funnel, and specifications for this EMQ are given in Table 5-6. This magnet is located just upstream of the deflector cavity. Final steering of each beam before entry into the deflector cavity is done in this quadrupole as the beam from each funnel leg enters the large-bore EMQ off-axis.

The mounting scheme will be identical to the scheme developed for the BCDTL and CCL EMQs. This scheme provides full alignment capability, rapid magnet replacement, and commonality with all other large-bore EMQ mounts. The dc electrical interface, coolant interface, and thermocouple electrical interface will also be identical to those in the BCDTL and CCL, and the cooling system failure detection scheme will be the same as that described for the small-bore EMQs.

5.7 MECHANICAL SUPPORT STRUCTURE

The primary supporting structure for the APT funnel is depicted in Fig. 5-11. The structure consists of a strongback on which each beamline component is mounted. Each strongback section is mounted on two legs that are anchored to the tunnel floor.

Each strongback is a weldment that will be made of 3/8-inch-thick ASTM A36 structural-quality carbon steel plate. The top surface of the strongback is 9 inches below the beam centerline. The strongback width is 11.5 inches, and the height is 8 inches. The large section of relatively thin plate provides a stiff structure at minimum cost. The design allows the ion vacuum pumps, which are mounted below each RF cavity, to fit into the hollow region below the strongback. Cutouts at each pump are required to permit passage of a manifold connecting the cavity and pump. The open bottom allows ample access to

fasteners, wiring, and plumbing. Lateral stiffeners are welded periodically along each strongback, joining the top deck and the two sides. This feature is required to enhance the torsional stiffness. The supporting legs are also weldments, made of 8-inch-diameter, 3/8-inch-wall steel pipe, with ends made of 1/2-inch steel plate.

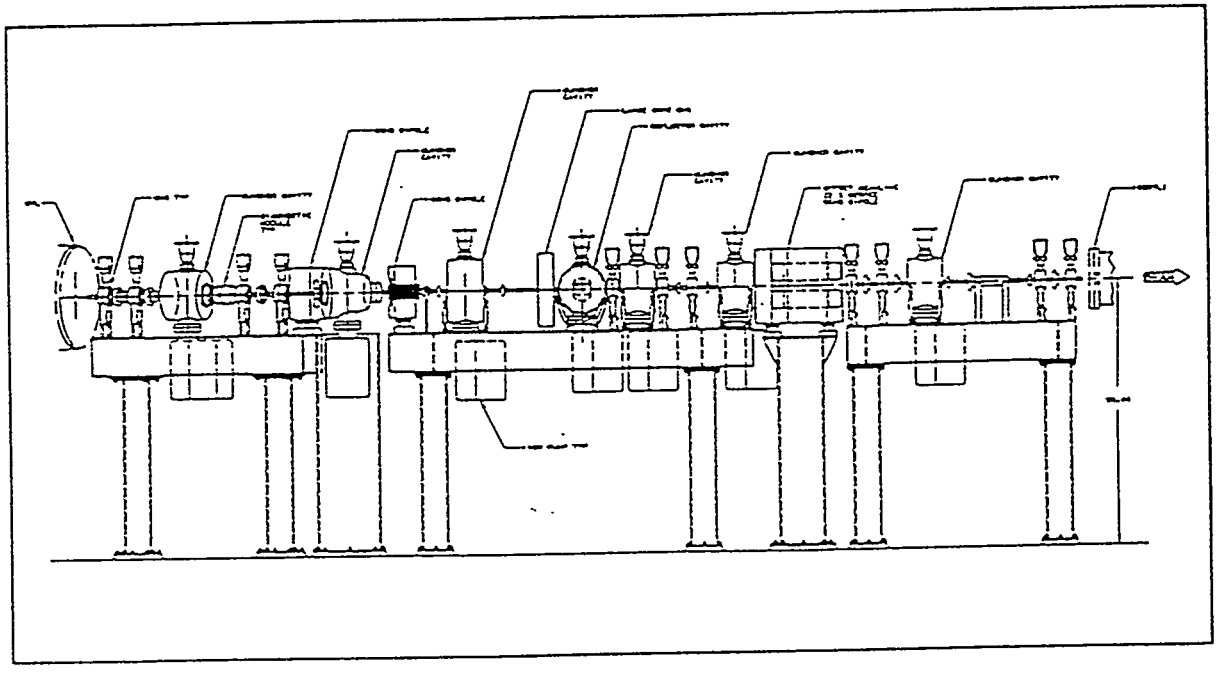


Fig. 5-11. Mechanical support structure for the APT funnel.

The strongback and leg assemblies are bolted together. The bottom of the strongback section is closed and stiffened at the location where a leg is attached. Alignment of the supporting structure is accomplished only at the base of each leg. A conventional scheme utilizing jackscrews and studs has been incorporated.

Each leg will be mounted on cement anchor studs mounted in the floor or studs threaded into a mounting plate grouted into the floor when the concrete is poured. The fastener holes in the lower plate of each leg are oversized, which allows some tolerance for lateral alignment. Height adjustment is accomplished with jacking bolts located in the lower flanges of each leg. Once the proper height is attained, the leg is permanently secured by fastening the lower leg flange to the threaded studs with nuts above and below.

The basic structural requirements of the supporting structure for the funnel and the following matching section or MEBT are dynamic stability, static load-carrying capability, and seismic-loading capability. The funnel and MEBT beamline components are of relatively low mass compared with an average accelerator module in the APT linac, permitting a smaller and simpler support structure. The support structure design was driven primarily by stiffness requirements imposed by dynamic-stability requirements. Element sizing required for the stiffness criterion far surpassed that required for the static and seismic loading requirements, i.e., an adequately stiff structure was also an extremely strong structure.

In considering background-vibratory-input spectra for typical accelerator facilities of the type required for APT, we find that most of the vibratory input occurs at low frequencies. If

structures are designed with mechanical resonances that are high, compared with the tunnel frequencies, amplification of the large, low-frequency input motion is greatly reduced. With these concepts in mind, the approach used was to design hardware systems with a minimum natural mechanical frequency of 30 Hz where possible. For initial layout and design, this is a prudent design method. Vibration analyses for the funnel and supporting structures can be found in Appendix 12.5

5.8 EXPERIMENTAL STATUS

5.8.1 Los Alamos Single-Beam Experiment

An experimental demonstration confirming the beam dynamics of funneling was recently completed on the ATS at Los Alamos National Laboratory [5-1]. The experiment used a single-leg layout. The funnel input beam was from the ATS H-, 425-MHz, 5-MeV DTL. The funnel beamline is shown schematically in Fig. 5-12.

The beamline elements included four permanent-magnet dipoles (PMDs), four offset PMQs, four movable PMQs for steering, and one RF deflector. Transverse and longitudinal emittance control was obtained with 15 PMQs and four RF bunchers (two 425-MHz and two 850-MHz). A large cylindrical vacuum vessel contained the transport elements that were mounted on four separate plates to allow for staged installation. The 850-MHz bunchers and magnet mounts extend into space that would be occupied by the second beamline in a two-beam funnel.

The experimental results showed ~100% beam transmission through this single-leg funnel, with good steering control. Transverse and longitudinal emittance growth were controlled. Within experimental precision, no transverse emittance growth was observed. Non-optimum operation of the RF bunchers also failed to produce any measurable transverse emittance growth. The observed longitudinal emittance growth was ~15% with an uncertainty of ±5%. This observed level of longitudinal emittance growth had no effect on the funnel's performance. The results with non-optimum buncher operations were basically the same.

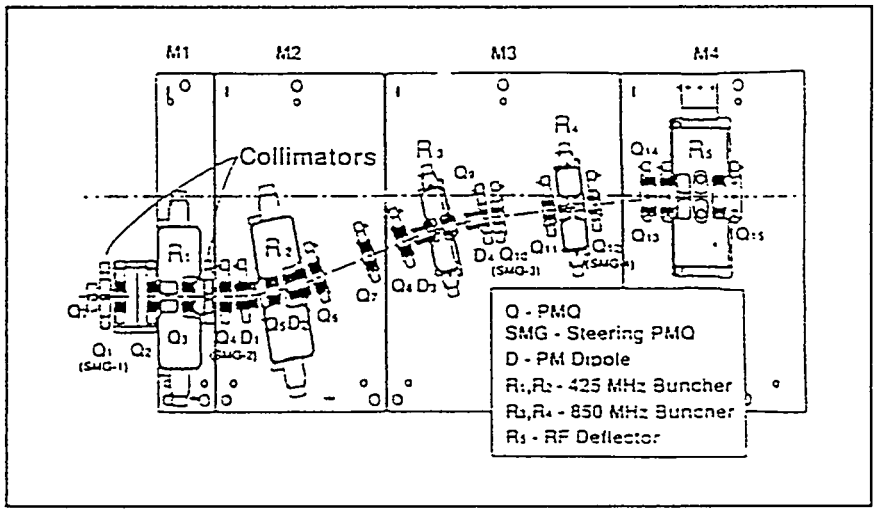


Fig. 5-12. Schematic of the Los Alamos single-beam funnel experiment.

5.8.2 McDonnell Douglas Two-Beam Experiment

A two-beam funnel experiment was successfully performed at the McDonnell Douglas site in 1991. The purpose of this two-beam experiment was to resolve funnel issues not addressed in the earlier ATS experiment at Los Alamos. One of the most important questions was the simultaneous control of two independent beams in the same system. This experiment also required, as envisioned, an RF buncher that could effectively rebunch both beams in the same RF cavity.

A schematic of the experiment is shown in Fig. 5-13. The experiment used two beams from two separate linacs, each providing 2 MeV of H^+, with a nominal current of 25 mA at 425 MHz. The funnel beamline was optically similar to the ATS beamline, except that the input beams entered the funnel at 20° from the output axis rather than parallel to it. The APT funnel design has the same feature, i.e., the beam enters at an angle of 22.4° rather than parallel to the symmetry axis. The purpose of this is to reduce the number of beamline components and simplify the system. In particular, with the use of the two-hole rebuncher accepting two beams in the same cavity, only four RF bunchers were required for the complete system.

The experiment demonstrated that a two-hole rebuncher can be successfully used to control two independent beams. It also resolved some of the engineering issues concerning the placement of components in adjacent legs.

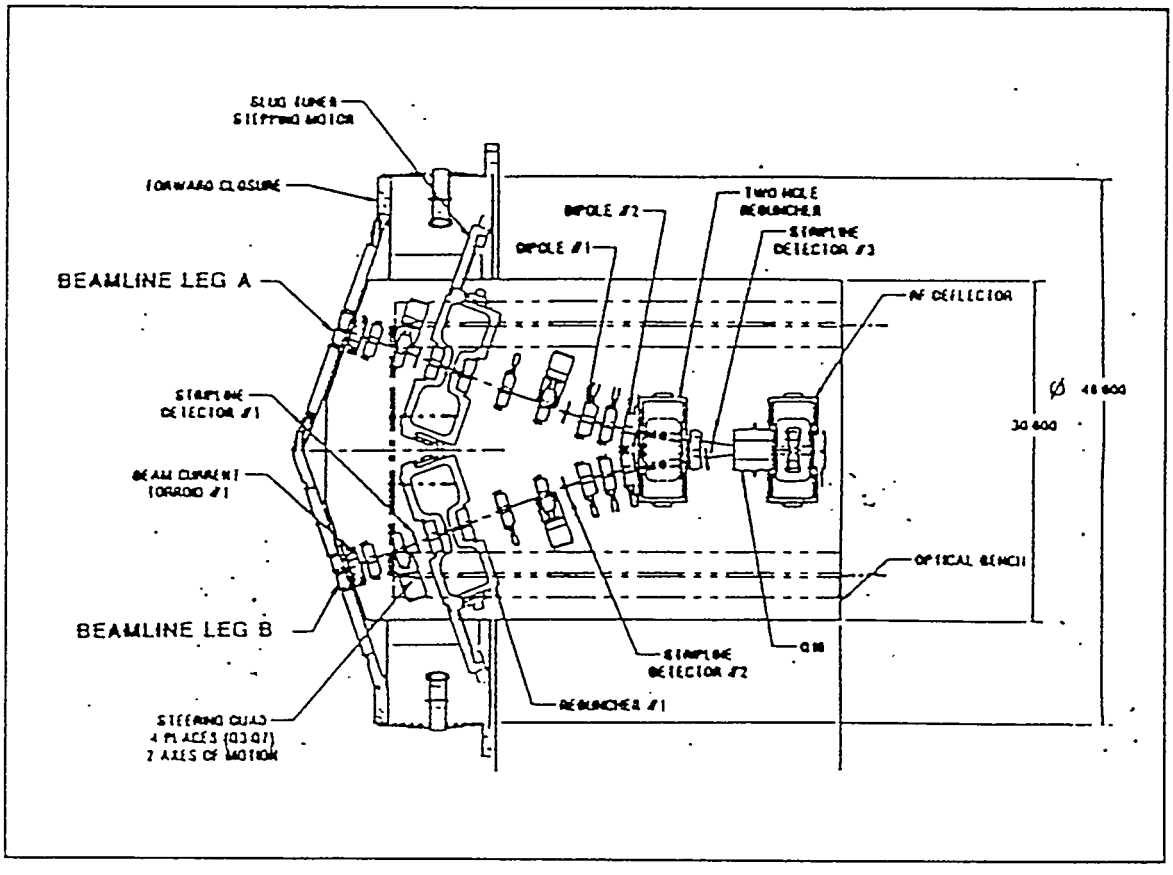


Fig. 5-13. Schematic of the McDonnell Douglas two-beam funnel experiment.

5.9 MATCHING SECTION (FUNNEL TO BCDTL)

A preliminary design of a matching section that matches the merged output beam at 700 MHz from the funnel into the BCDTL (also called the MEBT) has been completed. It is approximately 3 meters long and includes two standard geometry bunchers, 7 EMQs, and a bending magnet that can be energized to bend the beam into a dedicated diagnostic beamline. The bunchers in this section are essentially the same as the R3 bunchers shown in the funnel (Fig. 5-2). A diagram of the matching section is shown in Fig. 5-14.

This matching section is intended to serve two objectives. First, this makes the transition between the FOFODODO lattice, used by the DTL and the funnel, and the FDOFDO (doublet) lattice, used by the BCDTL and the CCL that follow. Second, it will provide enough room away from the funnel section for placement of a complete set of diagnostics, enabling direct characterization of each beam, as well as the merged beam through the funnel.

Vacuum isolation of the funnel and MEBT as a subsystem to the rest of the linac is accomplished with electropneumatic, all-metal gate valves. One such valve is installed at the exit of each DTL leg and also at the entrance to the BCDTL. A fourth valve will be installed at the beginning of the offset diagnostic beamline.

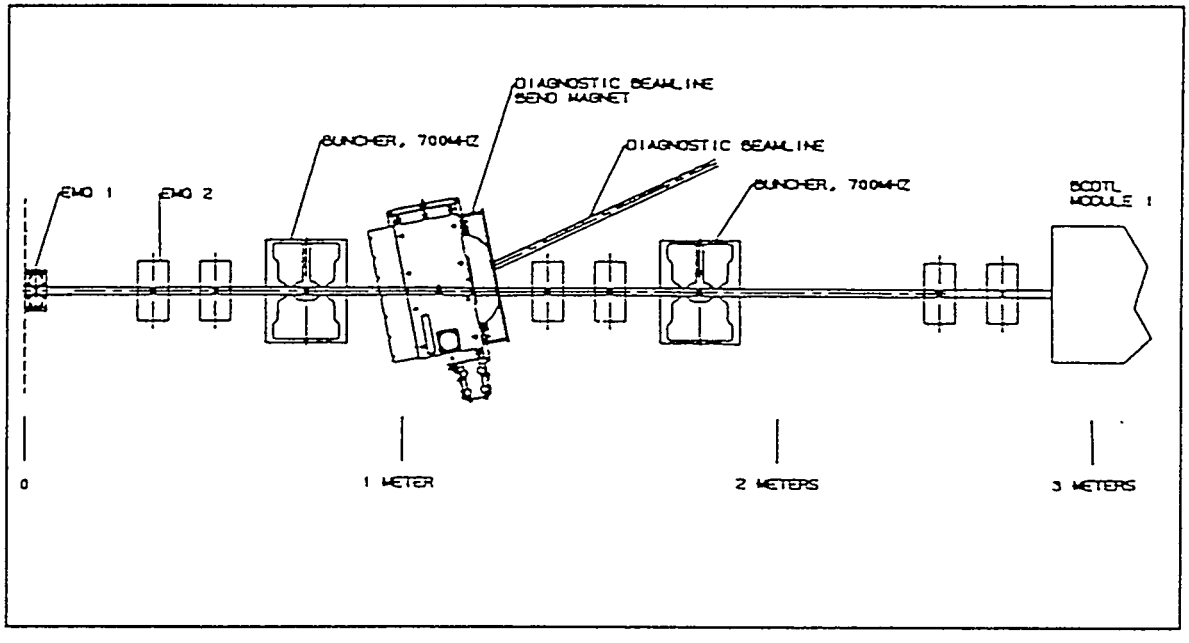


Fig. 5-14. APT funnel-to-BCDTL matching section (or MEBT).

The MEBT design includes a diagnostic beamline that is inclined 22.5° from the accelerator beamline. The same dipole design from the GTA offset beamline will be used for the bending electromagnet in the MEBT except for a 17% down-scaling in field strength and total power due to the lower APT MEBT beam energy of 20 MeV. The 22.5°-bending dipole is positioned just after the second MEBT buncher cavity. Space limitations may require some modification to the beam transport plenum within the dipole. The dipole is mounted on a single pedestal. Alignment is accomplished with four jacking devices.

5.10 DIAGNOSTICS

The funnel is a very specialized area of this accelerator in terms of its requirements for beam diagnostics. It has many controllable parameters that must be measured and verified by the beam diagnostics during both normal and off-normal beam conditions for various transverse and longitudinal beam parameters. Both types of measurements, viz., permanent and characterization beam diagnostics, will be required in the funnel area. The characterization beam diagnostics are located in the offset beamline, whose sole purpose is to characterize the 20-MeV, 200-mA beam. This means that a well-shielded, high average-power beamstop at the end of the offset beamline is necessary. This beamline will contain sufficient diagnostics to completely understand both the transverse and longitudinal phase space and will include both distribution and centroid information. For the centroid measurements, the microstrip or capacitive beam position measurements will be used. The transverse profile and emittance measurements will be accomplished by using slow wire scanners and slit-and-collector-type measurements. Both of these measurements, require that the beam be pulsed at low duty factors (e.g., <0.25%). By placing these profile measurements in dispersive regions of the offset beamline, beam energy or momentum-spread information may be acquired. The slit and collector may be operated under low duty-factor conditions at full beam current, allowing emittance data to be acquired under full space-charge conditions. The pulsed beam will be intercepted at the input and output legs of the funnel with an intercepting Faraday cup to facilitate beam tuning without allowing the beam to enter the higher-energy portions of the accelerator. Finally, a similar offset beamline may be required at the 100-MeV point in the accelerator in order to tune the BCDTL. However, this second offset beamline needs further study.

The permanent diagnostics must operate under cw beam conditions. These diagnostics will primarily measure the transverse and longitudinal beam centroids, beam current, and transverse- and longitudinal-beam profiles. Again, the microstrip or capacitive beam-position measurements will be used for the transverse and longitudinal centroids. The transverse-profile information will be acquired by video-profile monitors, and the longitudinal profiles will be acquired by a phase-spread monitor. The pulsed-beam and cw-beam currents will be monitored with two different types of toroidal transformers. A very special beam diagnostic measurement will be required to verify that the bunches have the correct longitudinal spacing and velocity. This monitor is the beam-power spectrum analyzer and is placed either upstream or downstream of each cavity or deflector in the funnel. All permanent-diagnostics measurements will be used to maintain the tune of the two input legs of the funnel with respect to each other.

A key goal for the funnel beam diagnostics is the sensing of off-normal conditions for the funnel; e.g., a difference in transverse-beam centroids or charge-density functions between the input funnel legs. This condition will tend to change either the beam position or the trajectory angle after the two beams are merged, and may increase the emittance of the beam and produce losses further downstream from the BCDTL entrance. Another off-normal condition would be if the beam energy or phase were not properly set for the two beams entering the funnel. If this condition were severe enough, it would result in longitudinal emittance growth after the beams are combined, and beamloss further downstream. Both examples are correctable with the existing funnel components, given sufficient and adequate diagnostics.

Fig. 5-15 shows the placement of the diagnostic elements in the funnel layout. The abbreviations used in the figure are explained in Table 5-7. The table lists all beam diagnostics incorporated into the funnel and the MEBT. This list, however, does not include diagnostics for the offset beamline.

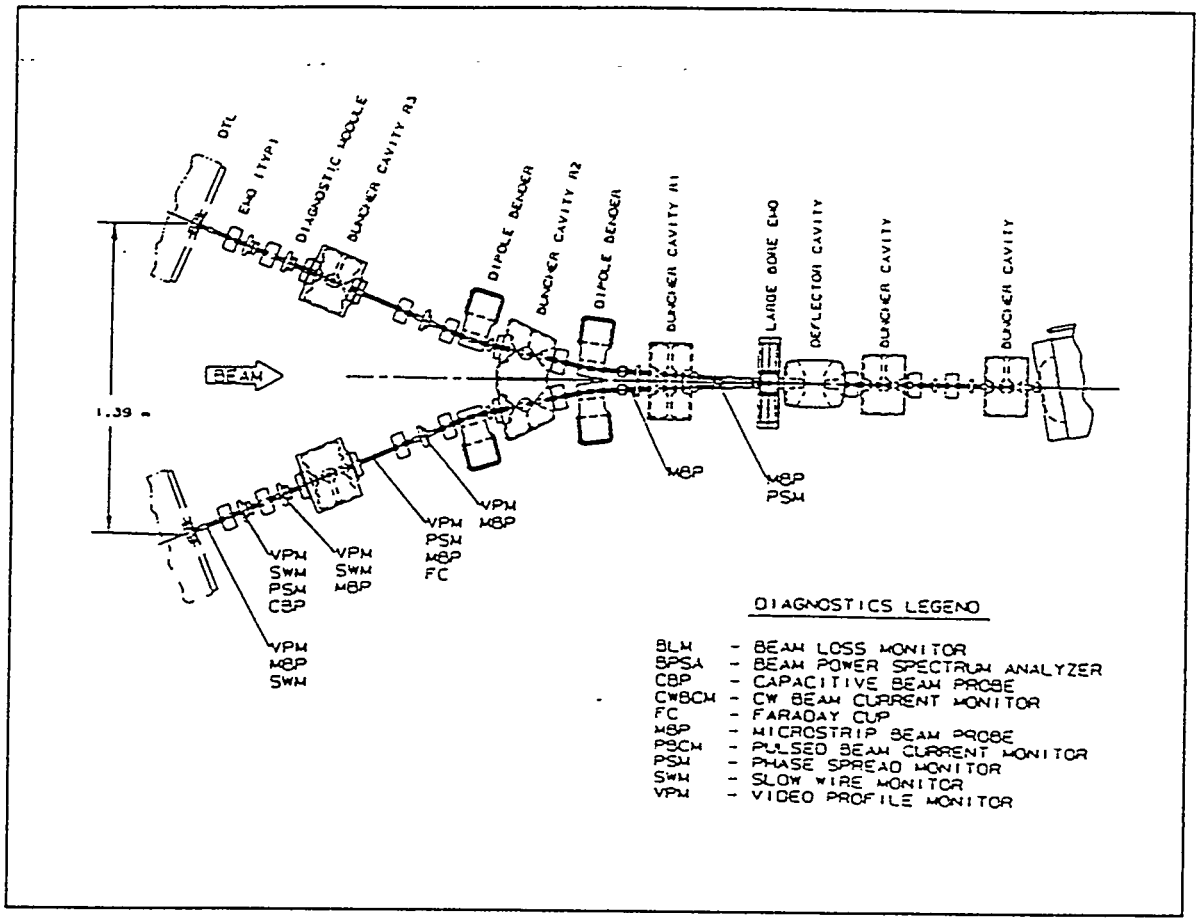


Fig. 5-15. Layout of the funnel section with location of the diagnostic elements.

Table 5-7. APT Funnel and MEBT Diagnostics

Device	Measurement	Symbol
Beamloss Monitor	Radiation Due to Beamloss	BLM
Beam Power Spectrum Analyzer	Bunched Beam Power Spectrum	BPSA
Capacitive Beam Probe	Position and Intensity	CBP
cw Beam Current Monitor	Average cw Beam Current	CWBCM
Faraday Cup	Beam Current	FC
Microstrip Beam Probe	Position, Intensity, Output Phase, and Energy	MBP
Pulsed Beam Current Monitor	Average Macropulse Beam Current	PBCM
Phase Spread Monitor	RMS Bunch Length	PSM
Slow Wire Monitor	Transverse Profiles for Pulsed Low-Current Beams	SWM
Video Profile Monitor	Transverse Profiles, Position Angles for cw Beams	VPM

5.11 FUNNEL RF POWER SYSTEM

The funnel and MEBT RF-power system consists of a total of 8 low-power RF systems, 7 of which deliver 19–60 kW of cw output power at 700 MHz, and the eighth (for the deflector cavity) delivering 40 kW at 350 MHz. These values include the 10% control margin required for cw systems and are similar to the power required for UHF television transmitters. Each funnel RF system will consist of either two IOT amplifiers in series, or a single klystron, depending on economics. Both amplifier chains would be driven by a solid-state amplifier. The optimum power levels for each stage will be determined by the relative costs of solid-state and the high-power amplifiers at the 700-MHz operating frequency. The design of the amplifiers also depends on the precise output power required for each stage, and this has not been accurately calculated. At present, most of the buncher cavities are two-gap, drift-tube bunchers, and these require 19 kW. Whenever space permits, the R1 regular geometry cavity (lowest cavity) will be used. Once the beamlines are close together, the tapered R2 bunchers are used, requiring 44 kW each. Finally, the R1 buncher (right before the deflector), which has two beamlines within a single vacuum envelope, will require 60 kW. The deflector cavity itself will require 40 kW. The beam loading in the bunchers will be zero (ideally), and the beam loading in the deflector is negligible, compared with the power loss in the walls.

Commercial television transmitters are manufactured at 700 MHz at powers up to 100 kW, and the modern solutions are either the IOT (including the klystrode) or a multiple-stage, depressed-collector klystron. Both of these solutions result in a system that is more expensive than the lower-technology, simple klystron solution, but they have the advantages of lower operating costs due to higher efficiency, and the efficiency stays high over a fairly large range of output power. Another significant advantage of the IOT is that it is a class B device, which means that the required dc power follows the RF power required (to first order). This helps operating efficiency when power levels less than maximum capability are needed or when operating in a pulsed mode (such as during startup and conditioning). This not only saves energy, but also allows more peak power to be produced during the pulsed operation.

In the funnel, there is only one RF system not covered by standard commercial television transmitters. This is the system powering the deflector cavity (40 kW at 350 MHz). At least three options exist for the deflector cavity driver. The first is to have a specially built IOT made for 350 MHz, and use a standard television-transmitter mainframe (HV power supplies, racks, interlocks, cooling) which has been modified for the IOT. This would be a relatively inexpensive approach. The second option is to develop a klystron transmitter for 350-MHz and 50-kW (maximum output power); although in this case, a special klystron would have to be developed. The third option is to develop a tetrode transmitter for this application. All three approaches are technically feasible. It is likely that the tetrode transmitter would cost the least. If the cost penalty is small, it would seem better to have all medium-power transmitters with IOTs or klystrons to limit the types of RF technology present in the APT machine. This would be an operating cost and maintenance advantage.

CHAPTER 5 REFERENCES

5-1. K.F. Johnson et al., "A Beam Funneling Demonstration: Experiment and Simulation", *Particle Accelerators,* Vols. 37-38, pp 261-268 (1992).

HIGH-ENERGY SYSTEMS
CHAPTER 6

Page

6.1 THE BRIDGE-COUPLED DRIFT TUBE LINAC (BCDTL) 1
6.1.1 Introduction 1
6.1.2 Description 1
6.1.2.1 BCDTL Parameters 3
6.1.2.2 Physics Considerations 4
6.1.2.3 Modular Breakdown 4
6.1.3 Bridge Couplers 5
6.1.3.1 Function and Tuning 6
6.1.3.2 Construction 6
6.1.4 Cavity Physics 7
6.1.4.1 Mode Comparison 7
6.1.4.2 Drift Tube Shape 9
6.1.4.3 SUPERFISH Results 10
6.1.4.4 Large-Bore Effects 11
6.1.4.5 Complete Tank Modeling 12
6.1.5 Simulations 12
6.1.6 RF Windows and Waveguides 13
6.1.7 Vacuum System 13
6.1.8 Intertank Gaps 14
6.1.9 Diagnostics 15
6.2 TRANSITION REGION (BCDTL—CCL) 16
6.3 THE COUPLED-CAVITY LINAC (CCL) 16
6.3.1 Introduction 16
6.3.1.1 Improvements Over Earlier Design 17
6.3.1.2 Switchover at 100 MeV 17
6.3.2 Description 17
6.3.2.1 CCL Parameters 18
6.3.2.2 Modular Breakdown 19
6.3.3 Tank Description 20
6.3.4 Cavity Physics 20
6.3.5 Simulation Results 23
6.3.6 The Aperture Ratio 23
6.3.7 Cooling and Tuning 24
6.3.7.1 Cooling 24
6.3.7.2 Tuning 27
6.3.8 RF Windows and Waveguides 27
6.3.9 Intertank Gaps 27

6.3.10 Diagnostics 28
6.4 THE 700-MHz RF SYSTEM 29
6.4.1 RF Generator 29
6.4.2 RF Distribution 30
6.4.3 RF Layout 30

LIST OF FIGURES

Fig. 6-1. A BCDTL module, showing three tanks, two bridge couplers, and three quadrupole doublets. 2
Fig. 6-2. The first BCDTL tank at 20 MeV, showing part of a bridge coupler. 2
Fig. 6-3. BCDTL partitioned bridge coupler with five partitions. 5
Fig. 6-4. Transit-time factor vs. bore for 0- and π-mode structures for 100-MeV protons. 7
Fig. 6-5. Power density vs. bore radius for 0- and π-mode structures for 100-MeV protons (the accelerating gradient E_0T is 1.5 MV/m for all cases). 8
Fig. 6-6. Effective shunt impedance vs. bore for 0- and π-mode structures of Figs. 6-3 and 6-4 (the accelerating gradient E_0T is 1.5 MV/m). 8
Fig. 6-7. Cross section of a BCDTL 100-MeV half cell. 9
Fig. 6-8. Detail near the drift tube nose showing the mesh used by SUPERFISH (all cells have an inner-nose radius, r_{ni}, of 0.1 cm and an outer-nose radius, r_{no}, of 0.3 cm 9
Fig. 6-9. Parameters for the low-energy section of the BCDTL (20–54 MeV), where E_0T is 1.7 MV/m and bore radius is 2.00 cm. 10
Fig. 6-10. Parameters for the high-energy section of the BCDTL (54–100 MeV), where E_0T is 1.5 MV/m and bore radius is 2.25 cm. 11
Fig. 6-11. SUPERFISH-calculated fields for an end cell at 20 MeV (the bore tube extends 4.0 cm to the left of the cell boundary). 12
Fig. 6-12. Intertank hardware 14
Fig. 6-13. Layout of the transition region between the BCDTL and CCL. 16
Fig. 6-14. First CCL assembly unit at 100 MeV. 19
Fig. 6-15. Last CCL assembly unit at 1000 MeV. 19
Fig. 6-16. Generic coupled-cavity geometry. 21
Fig. 6-17. CCL nose shape and cell geometry for a cell near 1000 MeV. 22
Fig. 6-18. Shunt impedance vs. β (100-1000 MeV), as determined by SUPERFISH (the calculated values have been reduced by 15% to include a correction for cavity coupling slots). 22
Fig. 6-19. CCL septum cooling scheme. 24

Fig. 6-20. Flow schematic for the 14 cells of a CCL tank. 25
Fig. 6-21. CCL vacuum and RF seal. 26
Fig. 6-22. BCDTL output efficiency using GTA klystron data (normalized to CERN tube efficiency). 29
Fig. 6-23. APT CCL RF power vs. module number and output energy. 30
Fig. 6-24. CCL output efficiency using GTA klystron data (normalized to CERN tube efficiency). 31
Fig. 6-25. RF system layout for 700-MHz systems. 31

LIST OF TABLES

Table 6-1. APT BCDTL Parameters 3
Table 6-2. BCDTL Modular Breakdown 4
Table 6-3. APT CCL Parameters 18
Table 6-4. CCL Modular Breakdown 20
Table 6-5. Fixed Coupled-Cavity Cell Shape Geometry Parameters for the CCL 21

6.0 HIGH-ENERGY SYSTEMS

6.1 THE BRIDGE-COUPLED DRIFT TUBE LINAC (BCDTL)

6.1.1 Introduction

A hybrid accelerating structure, the BCDTL, was chosen to accelerate the beam in the 20–100-MeV range. In our 1989 design study, we looked at a CCL structure for this energy region. After careful examination of the mechanical engineering aspects of such a CCL, we determined that it would be difficult to construct this structure at such a low energy. Therefore, we examined alternative structures because of the difficulties of: (1) assembling densely packed cells, (2) power dissipation, (3) the increased possibility of multipactoring for short cells, and (4) poor shunt impedance in this energy range for a CCL with such a large bore. We also looked at a traditional Alvarez DTL, but rejected it for reasons of inadequate bore size and the need to use PMQs because of space restrictions in the small drift tubes (PMQs are not as resistant to radiation effects). It was at this point that the BCDTL was conceived of and designed by Don Liska of AT Division.

The advantages of a BCDTL over a CCL at low energies include not only a higher shunt impedance for a given aperture size, but fewer high-power operational difficulties and simpler, cheaper, more reliable fabrication. In addition, by applying the DTL concept to a lattice-type focusing scheme (i.e., drift tubes without quadrupoles—EMQs are located only between the tanks), two other significant advantages are realized: the aperture size of the drift tubes is largely unrestricted, and the need for critical alignment of the drift tubes is almost eliminated.

6.1.2 Description

The BCDTL consists of 61 short, seven-cell drift-tube tanks. The 61 tanks are "bridge coupled" together in modules of two, three, or four tanks for a total of 24 modules and 37 bridge couplers. A three-tank module (or assembly unit) with two bridge couplers and three quadrupole doublets (one between each tank) can be seen in Fig. 6-1.

A more detailed sketch, showing the first BCDTL tank at 20 MeV, can be seen in Fig. 6-2. Below the tank, part of one bridge coupler is shown. The structure is really quite simple. The tank is a right circular cylinder with drift tubes that have no quadrupoles inside. At 20 MeV, the BCDTL shunt impedance is 26 MΩ/m (compared to 4 MΩ/m for a CCL). The BCDTL is considerably more power efficient at low energies, although this advantage diminishes as the energy increases and vanishes when the energy reaches 100 MeV. The tanks range in length from ~0.6 to 1.3 meters and require only six drift tubes. Two half drift-tubes are also built into the end walls, which are simply bolted to the tank barrel with all-metal RF and vacuum seals. The axis of the tank is defined as the geometric centerline described by the bore centers of the end-wall drift tubes. Postcouplers are not needed for longitudinal field stability because the tanks are so short. Initial tuning of the tank is accomplished by means of fixed tuning bars and tuning slugs.

A significant feature of the BCDTL is the drift tube. As mentioned, there are no quadrupoles required in the drift tubes because transverse beam focusing is achieved via the quadrupole doublets located in the intertank spaces. This means that the drift tubes can be made thin walled and configured for good RF efficiency because only cooling is required. Also, alignment of the drift tubes is not critical. Alignment precision of ±0.5–1.0 mm is adequate. Alignment precision at this level can easily be achieved with simple tapered

sockets machined into the tank walls. The drift tubes are simply hard-point socketed against metal RF and vacuum seals. No adjustability for alignment purposes is required.

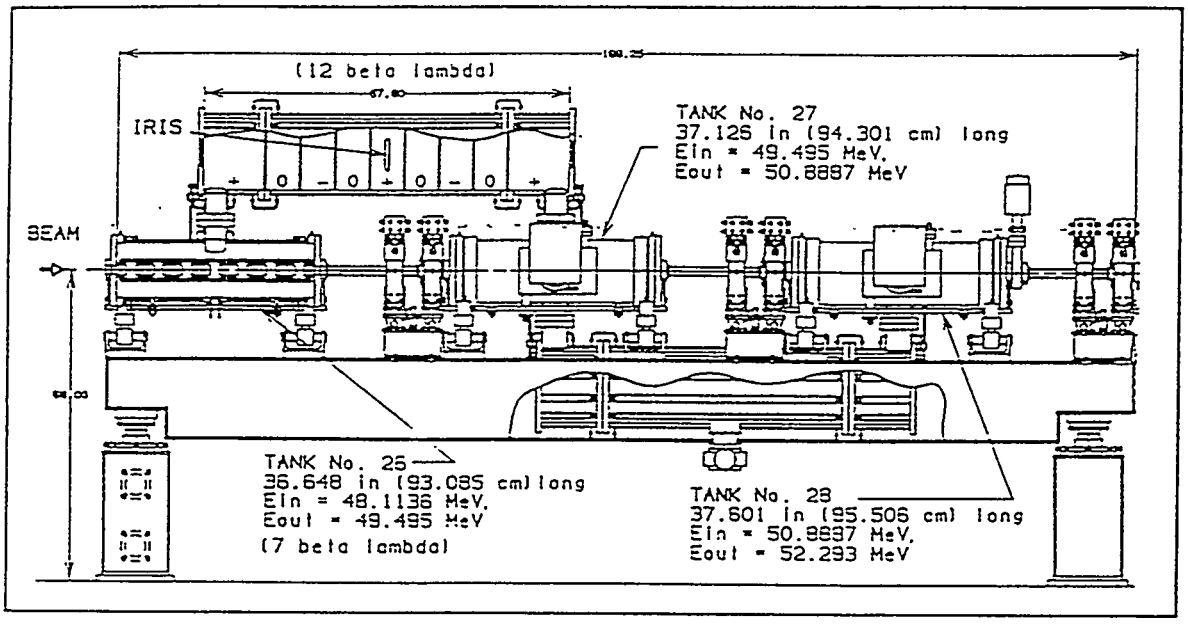


Fig. 6-1. A BCDTL module, showing three tanks, two bridge couplers, and three quadrupole doublets.

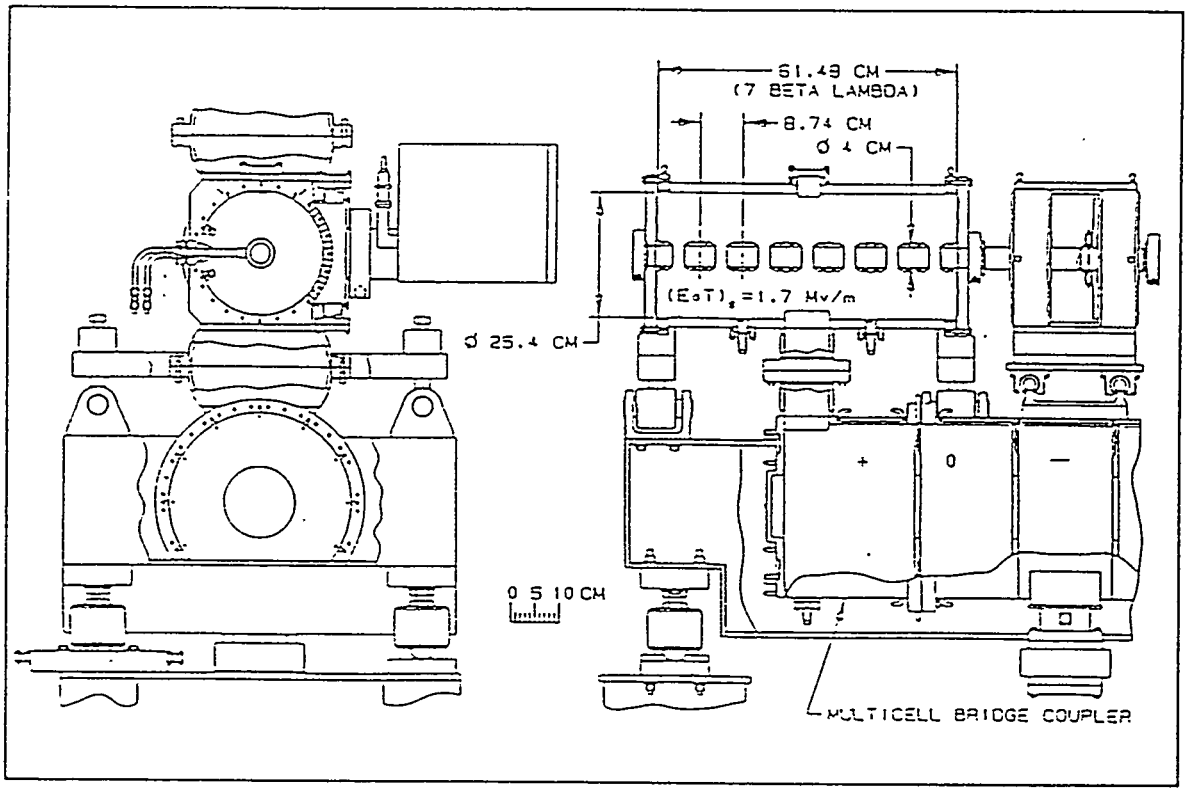


Fig. 6-2. The first BCDTL tank at 20 MeV, showing part of a bridge coupler.

6.1.2.1 BCDTL Parameters

Each of the 61 seven-cell drift-tube tanks is 7βλ long. The tanks operate at a structure gradient (E_0T) of 1.7 MV/m up to a transition energy of 52.3 MeV, and at 1.5 MV/m from the transition energy to 100 MeV. These values of structure gradient lead to a constant real estate gradient of 1 MV/m throughout the BCDTL given the intertank spacings chosen. The intertank spacing is 5βλ up to 52.3 MeV and is then reduced to 3.5βλ. Table 6-1 gives a detailed list of parameters for the BCDTL.

Table 6-1. APT BCDTL Parameters

Parameter	Entire Structure (20–100 MeV)	Before Transition (20–52 MeV)	After Transition (52–100 MeV)
Energy (MeV)	20–100	20–52	52–100
Transition Energy (MeV)	52.29*		
Frequency (MHz)	700		
Beam Current (mA)	200		
No. of RF Modules	24	9	15
No. of Assembly Units	24	9	15
No. of Tanks	61	28	33
No. of Cells per Tank	7		
Length of Cells	1 βλ		
Length of Tanks (m)	0.615–1.281 (7 βλ)		
Intertank Spacing	5 βλ–3.5 βλ	5 βλ	3.5 βλ
Total Length (m)	93.66	37.78	55.88
Radial Aperture (cm)	2.00–2.25	2.00	2.25
Aperture/Beamsize(rms) Ratio	8–13		
Structure Gradient (MV/m)	1.70–1.50	1.70	1.50
Average Gradient (MV/m)	1.00		
Shunt Impedance (MΩ/m)	26.0–36.7	26.0–36.7	30.5–27.9
Average Power Density (W/cm^2)	≤25		
Peak Surface Field (Kilpatrick)	≤1.0		
Structure Power (MW)	6.91		
Beam Power (MW)	16.10		
Total RF Power (MW)	23.01		
Efficiency	0.711		
Length of Focusing Period	12 βλ –10.5 βλ		
Transit-Time Factor	0.57–0.67	0.57–0.67	0.63–0.61
Synchronous Phase (deg)	-40 to -30 (20-37.6 MeV) -30 (37.6-100 MeV)		
Quadrupole Lattice	FDO		
Quadrupole Length (cm)	8.2–9.5	8.2	9.5
Quadrupole Doublet Spacing (cm)	9.5		
Quadrupole Gradients (T/m)	31.4–36.0	32.4–34.6	31.4–36.0
Quadrupole Pole-tip, Maximum (T)	0.810	0.690	0.810
Quadrupole Phase Advance/Period (deg)	80 to 70 (20-37.6 MeV) 70 (37.6-100 MeV)		

*end of RF module #9

The constant "real estate" or average gradient of 1 MV/m over the length of the accelerator was chosen after careful cost modeling. This value of the average gradient falls within a rather broad cost minimum when the overall accelerator cost is plotted against the accelerating gradient.

6.1.2.2 Physics Considerations

The ratio of transverse aperture to rms beamsize has been used as a figure of merit in determining the design parameters for the BCDTL. We have attempted to make this ratio as large as is practical for a 700-MHz structure, reasoning that the larger this ratio, the lower the activation of the accelerator structure due to beamloss. Both singlet and doublet transverse-focusing lattices were examined. On the basis of the ratio of aperture to rms beamsize for the tank lengths we have chosen, a doublet-focusing scheme gives us superior beam-dynamics performance.

The synchronous phase is ramped in the BCDTL. The initial synchronous phase of –40° was chosen to provide adequate longitudinal acceptance of the funneled input beam. The phase is then ramped linearly with β, to –30° to provide more efficient beam acceleration.

In the design presented here, the quadrupole gradients are ramped such that the zero-current transverse phase advance per period is ramped from 80° to 70° in the first 17.6 MeV of acceleration. The phase advance per period is then held constant at 70° throughout the remainder of the BCDTL. This ramping was done to match the transverse focusing strengths at each end of the BCDTL with those of the adjacent structures: matched at the input from the DTL/funnel and matched at the output to the CCL. We have found from past experience that this should lead to a nearly current-independent match between the different structures. However, since all the quadrupoles of the BCDTL will be of the electromagnetic type, different matching/tuning schemes will be possible.

6.1.2.3 Modular Breakdown

The BCDTL is broken down into 24 modules (or assembly units) that range from 3.20–4.86 meters in length. These lengths are convenient for assembly and checkout in the test lab and for transport and installation in the beamline. Each module has at least two tanks and the intertank hardware, including the quadrupole doublets, diagnostics, valves, steering dipoles, bellows, and quick-disconnect flanges. The 61 tanks are divided between the modules (assembly units) as shown in the breakdown in Table 6-2.

Table 6-2. BCDTL Modular Breakdown

Assembly Unit Nos.	No. of Assembly Units*	No. of Tanks per Assembly Unit	Intertank Spacing	Radial Aperture (cm)
1	1	4	5.0 $\beta\lambda$	2.00
2-9	8	3	5.0 $\beta\lambda$	2.00
10-12	3	3	3.5 $\beta\lambda$	2.25
13-24	12	2	3.5 $\beta\lambda$	2.25

* There is one RF module for every assembly unit.

Each assembly unit is designed to use one 1.25-MW, cw, 700-MHz power amplifier. In the present BCDTL modularization, 1.25-MW klystrons are required in a few places. However, further design refinements may lead to module sizes requiring only 1.0-MW klystrons. In any event, there is no concern about the feasibility of building 700-MHz klystrons with 25% more power than the nominal 1.0-MW systems used in the CCL (if they are needed). The modules range in total RF-power consumption from 0.76–1.13 MW. This

is the power consumed by the accelerating tanks only. The excess drive available between these power levels and the output rating of the power amplifier (1.25 MW) represents the overdrive capability used to provide for additional losses in the waveguides, bridge couplers, coupling cells, and control margin. As a percentage, the overdrive capability ranges from 11%–64%. A breakdown that gives detailed information on each module can be found in the Chap. 6 Appendix.

6.1.3 Bridge Couplers

Bridge couplers couple the TM_{010}* accelerating mode into individual tanks. The tanks will be coupled from center to center to avoid excessive field droop within individual tanks (coupling at the tank ends would require postcouplers for field stabilization). The bridge couplers are expected to consume 5%–10% of the total structure power.

A portion of a bridge coupler that joins two of the tanks together was shown in Fig. 6-2. A complete bridge coupler for 20 MeV is shown in Fig. 6-3. The coupling cells that connect the tanks to the bridge couplers are located on the longitudinal centers of the tanks.

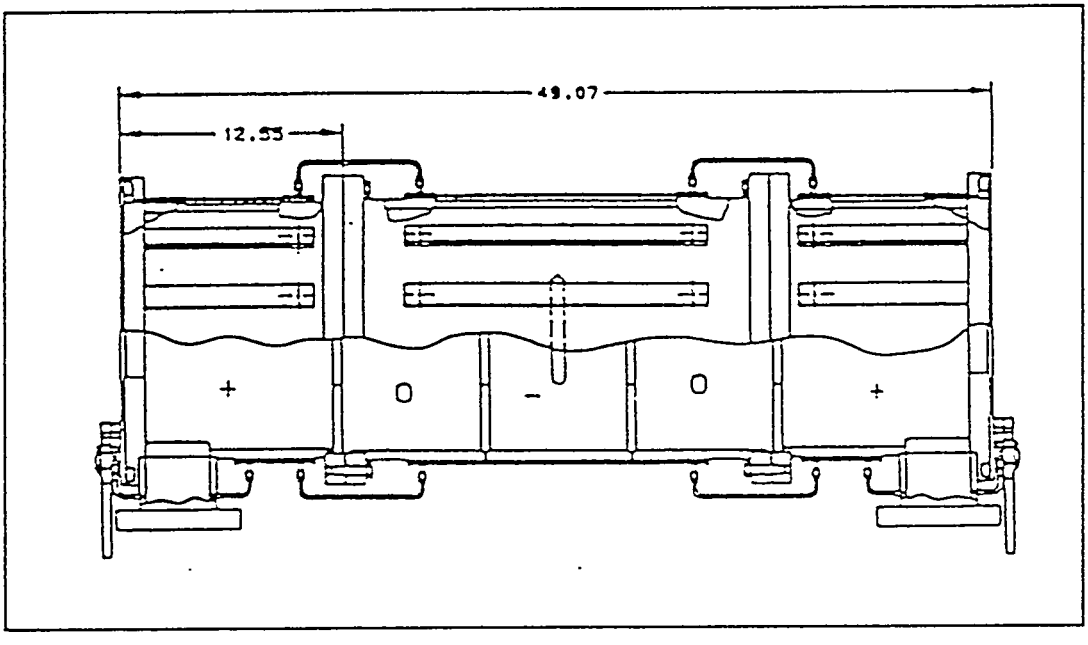


Fig. 6-3. BCDTL partitioned bridge coupler with five partitions.

* The term TM_{010} is RF cavity nomenclature describing the standing-wave electromagnetic field configuration (mode) that is excited within the bridge couplers (or any cylindrical accelerating cavity). TM stands for "transverse magnetic" which means that the RF magnetic field oscillates in paths encircling and *transverse* to the cavity cylindrical axis, while the RF electric (accelerating) field oscillates parallel to the axis. The numerical subscript gives the number of RF half-wavelengths in the azimuthal, radial, and axial directions, respectively, for the excited mode; 010 thus indicates that there is zero field amplitude variation in the azimuthal and axial directions, while in the radial direction the field amplitude goes through one-half cycle, from minimum (at the wall) to maximum (on the axis) to minimum again (at the opposite wall).

The bridge couplers are standing-wave structures that lock the phase of the tanks at either 0° or 180° relative to each other, corresponding to the length of the intertank gap. The phase shift is determined by the number of internal partitions in the barrel of the bridge coupler. If the gap is an integer number of $\beta\lambda$ lengths, the phase shift between tanks will be zero. If the gap is a half-integer number, the phase shift will be 180°. Every second cell in the bridge coupler is an empty cell; that is, it carries virtually no power. In the 20-MeV module, the intertank gap is $5\beta\lambda$ and the number of internal cells in the connecting bridge couplers is five, with two zero-power cells. At 100 MeV, the number of internal cells is 11, the intertank gap is $3.5\beta\lambda$, and the bridge coupler has five zero-power cells. The choice of the number of internal cells is determined by several factors, including (1) the phase shift required, (2) the fact that the end (coupling) cells and the iris (drive) cell must be fully powered cells, and (3) the length of the cells chosen to avoid higher-order mode coupling.

The major component parts of the bridge couplers are the end cells, the coupling-cell halves that mate to opposite halves on the adjoining accelerating tanks, and the central portion, which consists of several internal partitions to produce the desired phase shift. The central portion varies for each BCDTL module with respect to the number of partitions and the length of the cells. We have designed the end cells of all the bridge couplers to be identical. Thus, all 37 bridge couplers in the BCDTL have the same end cells.

The only drawback of the bridge couplers is their physical length. The longest bridge coupler is in the last module (~2 meters long). However, the advantages of bridge couplers as standing-wave, phase-locked devices make them preferable to other coupling means.

6.1.3.1 Function and Tuning

The bridge couplers function by means of magnetic coupling to the coupling cells. The bridge-coupler cells operate as TM_{010} cavities, which are capacitively coupled together by means of the large apertures in the internal diaphragms separating the cells. Because these apertures are so large, the associated field levels are low, as is the total power consumption of the bridge coupler. Typical power dissipated in the couplers is below 10 kW. They can be cooled with simple, externally mounted cooling channels (Fig. 6-3). The central cells in the bridge couplers respond like TM_{010} right-circular cylinders, with a small decrease in capacitance caused by the irises. For example, at 700 MHz, a short right-circular cylinder has a diameter of 32.82 cm. The BCDTL bridge-coupler diameter is 33.98 cm, indicating that the decrease in capacitance must be offset by a corresponding increase in inductance, i.e., a small increase in cell diameter.

The only cells that must be critically tuned are the end cells. This is done by providing a predictive recess in the end walls to compensate for the iris (see Fig. 6-3) and to adjust the size of the coupling-cell slot. Both of these adjustments can be predicted based on cold-model measurements of trends produced by iterative tuning.

6.1.3.2 Construction

The mechanical structure of the bridge couplers consists of both end cells bolted to the central barrel by means of Conflat- or Wireseal-style flanges that provide both RF and vacuum seals. The RF joints in both cases are positioned in the zero-power cells which always exist adjacent to the end cells (which are powered cells). This relieves the seals of essentially all RF current and imparts high reliability to these joints. Each of the central barrels of a given module is identical from an RF standpoint but differs in detail. One barrel

in a module must be equipped with the iris and tapered waveguide; another may carry the port for the roughdown vacuum valve; a third may have none of these, only the partitions, etc. All of these considerations are determined by the modular breakdown.

6.1.4 Cavity Physics

The details of the RF cavity physics design for the BCDTL are described here. The parameters provided the basis for the engineering design work. Details of the drift-tube shapes and SUPERFISH-calculation results are discussed in this section.

6.1.4.1 Mode Comparison

It is useful to distinguish between 0-mode vs. π-mode structures. The BCDTL cavities, like DTL cavities, are 0-mode structures. "Zero mode" signifies that the accelerating field points in the same direction in all cells at a given instant of time. The cell-to-cell phase shift is zero. A π-mode structure has a phase shift of 180° or π radians from cell to cell. In other words, in a π-mode structure, the fields point in opposite directions in adjacent cells.

The DTL (a 0-mode structure) is often the structure of choice for proton energies below about 100 MeV. It is usually more efficient than π-mode structures, such as the CCL. At higher energies, the CCL becomes more efficient than the 0-mode DTL. For APT, however, the choice was not obvious because of the need for very large bore radii. Figure 6-4 shows the reason for a cautious approach to the choice of an accelerating structure with a large bore radius in the energy range of 20–100 MeV. We used DTL and CCL cells with similarly shaped drift-tube noses for these calculations. Computer programs DTLFISH and CCLFISH varied the drift-tube gap to tune the cells to 700 MHz.

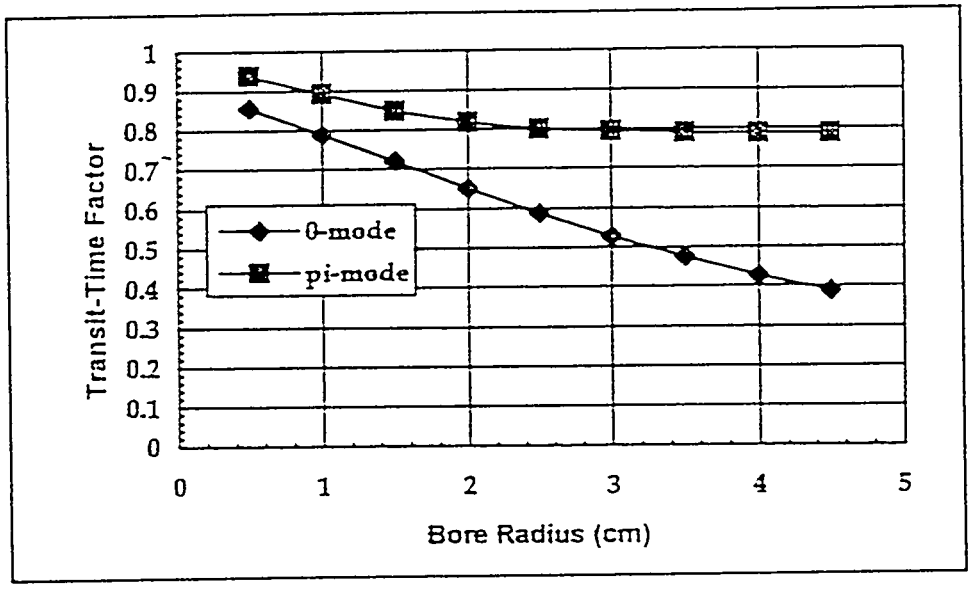


Fig. 6-4. Transit-time factor vs. bore for 0- and π-mode structures for 100-MeV protons.

For 0-mode structures, the transit-time factor T falls rapidly as the bore radius increases. To maintain a desired accelerating gradient E_0T, where E_0 is the average axial electric field, the designer must increase E_0 to compensate for the loss in T, resulting in higher power

losses. The consequences of the higher fields are shown in Fig. 6-5. Note that power density figures for the π-mode structure have been multiplied by 10. The power density on the drift tube stem is over thirteen times higher than the power density on the walls of a CCL cell. Nevertheless, as shown in Fig. 6-6, the effective shunt impedance of the 0-mode BCDTL is slightly higher than that of a π-mode structure for the bore radii of interest (2 cm). Therefore, provided one can cool the high power-density regions of the cavity, the BCDTL is a good choice. The calculations for Fig. 6-6 neglect the tank end walls of the BCDTL; for seven-cell tanks, this effect will lower ZT^2 (the shunt impedence) by a few percent for the 0-mode curve.

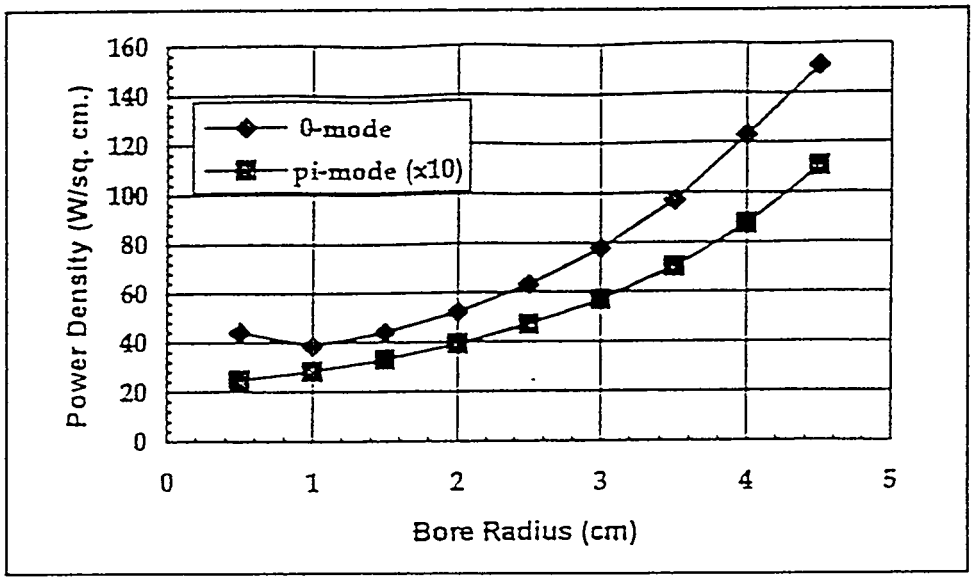


Fig. 6-5. Power density vs. bore radius for 0- and π-mode structures for 100-MeV protons (the accelerating gradient E_0T is 1.5 MV/m for all cases).

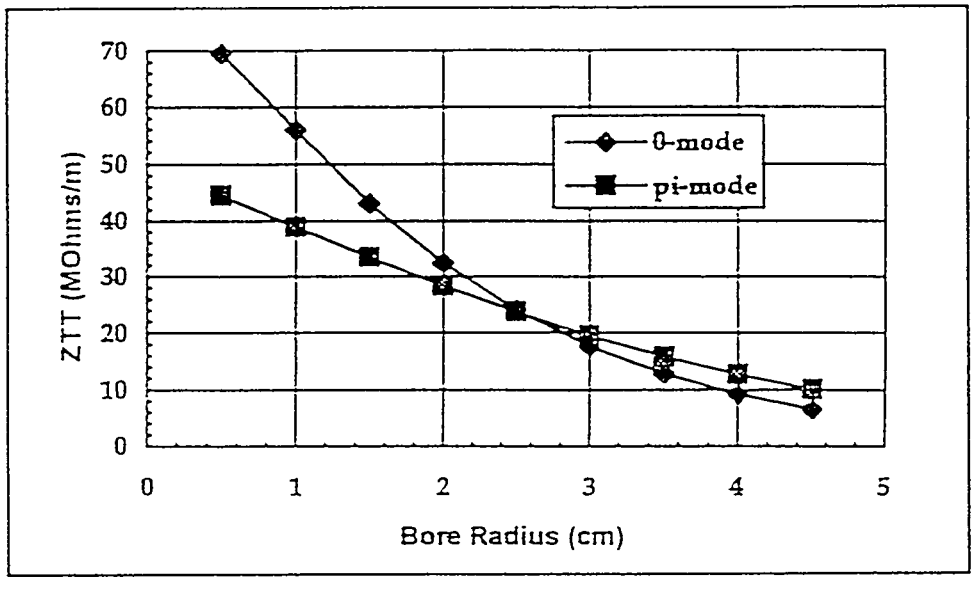


Fig. 6-6. Effective shunt impedance vs. bore for 0- and π-mode structures of Figs. 6-3 and 6-4 (the accelerating gradient E_0T is 1.5 MV/m).

6.1.4.2 Drift Tube Shape

Two properties of the BCDTL allow considerable flexibility in the choice of a drift-tube shape. First, there are no magnets inside the drift tubes because EMQs between tanks focus the beam. Second, the tanks are short, which makes postcoupler stabilization unnecessary. Without postcouplers, there is no constraint on the distance between the drift tubes and the tank wall. Figure 6-7 shows a cross section of a half cell from a SUPERFISH run (the bottom of the figure is the beam axis and the left-hand edge is a symmetry plane). Figure 6-8 is a detail near the drift tube nose. The drift tube has a steep face angle that extends from a sharp nose almost to the drift-tube center.

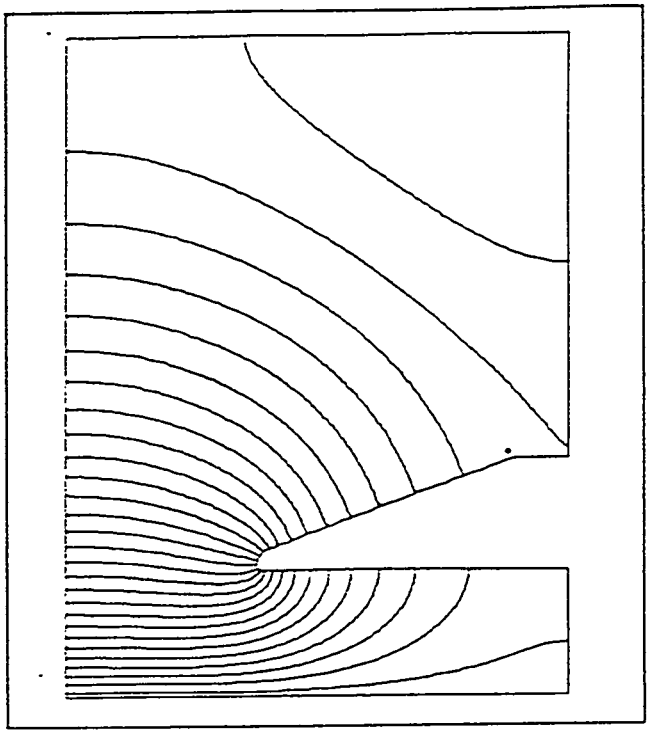


Fig. 6-7. Cross section of a BCDTL 100-MeV half cell.

Compared to more traditional shapes, the design has several advantages in this application: (1) low capacitance

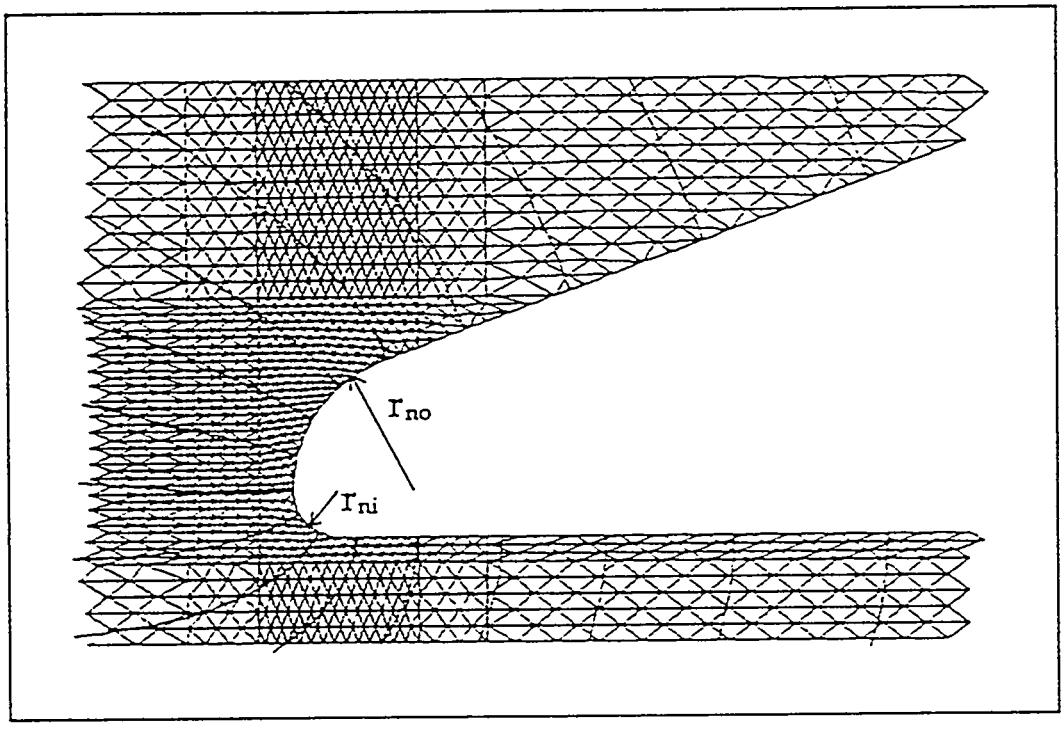


Fig. 6-8. Detail near the drift tube nose showing the mesh used by SUPERFISH (all cells have an inner-nose radius, r_{ni}, of 0.1 cm and an outer-nose radius, r_{no}, of 0.3 cm; this shows the same field lines as in Fig. 6-7).

between drift-tube noses, reducing total power; (2) a smaller gap between the noses, increasing the transit-time factor; and (3) lower peak-power density near the stem connection.

The shape is reminiscent of a coupled-cavity-cell nose, except that it attaches to a stem instead of the cell wall. At the longitudinal position of the stem, the magnetic field increases inversely with radius between the drift tube and the tank wall. The magnetic field drops off toward the drift-tube nose. Making the drift-tube diameter large near the stem adds some total power to the cell (because of the additional surface area) but dramatically reduces power density on the drift tube. The Chap. 6 Appendix contains details and results of SUPERFISH runs on representative cells throughout the energy range of the BCDTL.

6.1.4.3 SUPERFISH Results

Figures 6-9 and 6-10 show selected RF-cavity parameters from data included in the Chap. 6 Appendix. Program DTLFISH varied the gap between drift-tube noses to tune the cells to 700 MHz. The two plots correspond to different accelerating gradients and bore radii. In the current design, the bore radius increases from 2.00 cm to 2.25 cm at a beam energy of 52.29 MeV. The accelerating gradient E_0T is 1.7 MV/m up to an energy of 40 MeV, where it changes to 1.5 MV/m. Figure 6-9 shows parameters for E_0T= 1.7 MV/m all the way to 52.29 MeV. The values of E_{max} and H_{max} will actually be lower than shown for the points above β= 0.28.

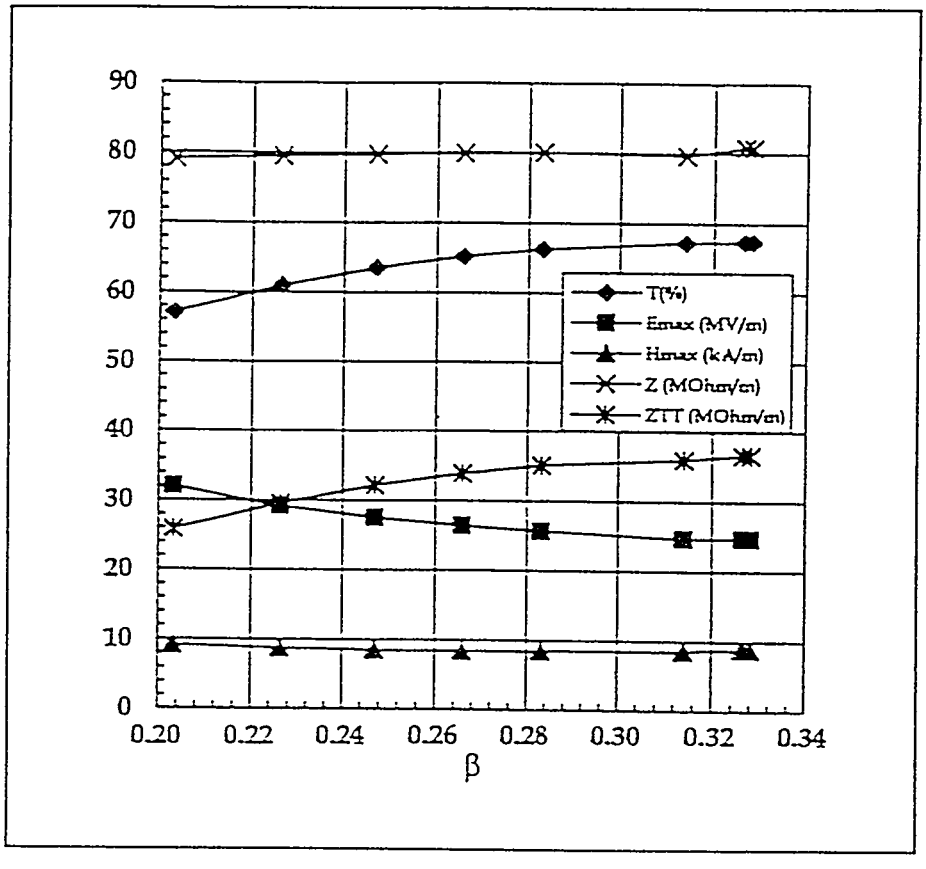


Fig. 6-9. Parameters for the low-energy section of the BCDTL (20–54 MeV), where E_0T is 1.7 MV/m and bore radius is 2.00 cm.

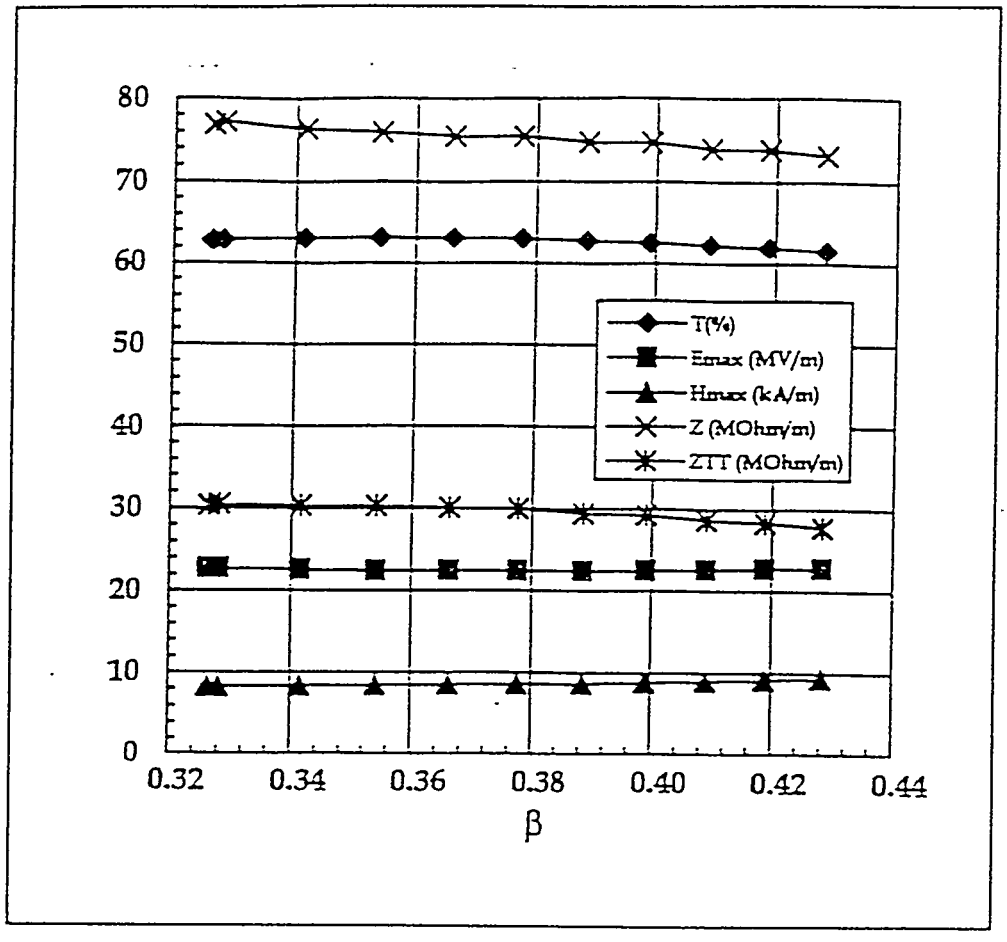


Fig. 6-10. Parameters for the high-energy section of the BCDTL (54–100 MeV), where E_0T is 1.5 MV/m and bore radius is 2.25 cm.

6.1.4.4 Large-Bore Effects

The large-bore radius may affect the symmetry of the field distribution in the end cells of the BCDTL tanks. The bore is large enough that a significant amount of field "leaks into" the bore. Figure 6-7 illustrates the problem. Note the electric field line that terminates on the right-hand side of the cell inside the bore (the lowest field line). For internal cells, the Neumann boundary condition (perpendicular electric field lines) is the correct choice. Neither Dirichlet nor Neumann boundary conditions are appropriate for an end cell. The field penetrates beyond the end of the tank to terminate perpendicular to the walls of the bore tube.

A 20-MeV cell was examined, where the effects are most pronounced. In Fig. 6-11, we can the see electric field lines in a full-cell SUPERFISH geometry whose length corresponds to 1$\beta\lambda$ for 20-MeV protons. To improve the simulation of the BCDTL cell and check for large-bore effects, the bore tube was extended by 4 cm on the left side of the cell to allow the field in the bore to penetrate beyond the cell edge (more closely depicting the actual field distribution).

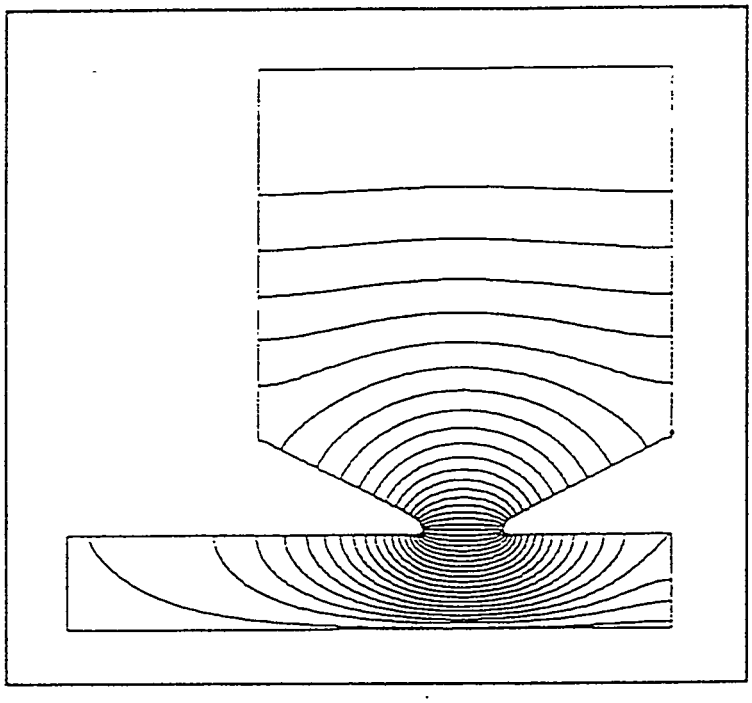


Fig. 6-11. SUPERFISH-calculated fields for an end cell at 20 MeV (the bore tube extends 4.0 cm to the left of the cell boundary).

6.1.4.5 Complete Tank Modeling

Some preliminary work modeling an entire BCDTL tank using SUPERFISH was done. One advantage of a full-tank model is that it provides information about the sensitivity of the cavity to manufacturing errors. In one test using the 100-MeV, seven-cell tank, the second, full drift tube was displaced longitudinally by about 0.25 mm. This change reduced the size of gap #2, lowering the resonant frequency of cell #2. Simultaneously, it increased gap #3, raising the frequency of cell #3. The result was a small (1%) step in the accelerating gradient in nearby cells. When we get closer to building these tanks, more calculations of this type may be useful for setting manufacturing tolerances.

6.1.5 Simulations

Because the BCDTL design requires a rather large bore, there was some concern as to whether the fields leaking into the beampipe at the end cells of an accelerating tank would affect the beam. In particular, we were worried that the effect might be large enough that the cell generation in PARMILA would not be correct because PARMILA only uses transit-time factors and not the actual field distributions.

A PARMELA simulation using the fields generated by SUPERFISH for our cell geometry was run for the first end-cell (at 20 MeV) of the BCDTL. Figure 6-11, shown previously, shows how the electric field lines extend beyond the end wall and into the beampipe. A single synchronous particle was injected into the cell at the correct phase (corrected for the drift) and allowed to propagate through the cell. The energy of the particle at the output of the cell was compared with the output energy as generated in PARMILA. A

0.0011-MeV (0.0055%) difference in output energy was found, indicating that the effect was indeed small and that the PARMILA cell generation was correct.

6.1.6 RF Windows and Waveguides

The coupling iris of the bridge coupler is located as close to the center of the structure as possible and in a powered cell. The window is cut through the wall of the cell and opens into a tapered-waveguide section. The tapered-waveguide section is water cooled, as is the iris itself. The flange is sized for standard EIA WR1150 waveguide. A window can be placed at the flange location and protected from overvoltage in the event of a fault at the iris (it may prove preferable to include a vacuum spacer of any multiple number of half-guide wavelengths attached to the flange because this would place the window farther away from the iris to avoid potential X-ray and electron bombardment of the window). The transmission line from the klystrons is WR1500, larger than the WR1150 size. The WR1500 was chosen because of reduced power attenuation and heating, requiring a WR1150 to WR1500 transition, either in the form of a taper or a matched step.

The coupling window has not been designed in detail. Windows of this power capability require considerable development. The window must be able to transmit up to 1.131 MW in the BCDTL and up to 750 kW in the CCL, as well as stand up to large VSWRs due to beam fluctuations. When beam is lost, the iris is no longer matched to the load, and the tank moves off resonance. The result is large reflections at the iris that backdrive through the window. The klystrons are protected from reflected power by circulators, but the linac window must be able to withstand such abuse. We have at present a choice for such a window, namely the LAMPF CCL beryllium-oxide window, redesigned to operate at 700 MHz rather than 805 MHz. The LAMPF window is designed to transmit 1.25 MW into a relatively low VSWR with 2-ms pulses at 12% duty factor. This long pulse capability, as well as the high duty factor of the LAMPF window, are promising for application to APT. The reduced power demand and frequency of the APT CCL are positive factors, while the high VSWR and duty factor are negative factors. Testing a LAMPF-style window in a cw test stand is a high-priority prototype program for the APT BCDTL/CCL.

6.1.7 Vacuum System

Each of the 61 BCDTL tanks is equipped with a 230-l/s ion pump with a nonevaporable getter for extra pumping margin. The pumps are sideslung in the case of the four-tank and three-tank modules and underslung in the case of the two-tank modules. The tanks are equipped with welded-steel vacuum boxes brazed to the tank walls. Pumping is done through grills of 18 longitudinal slots, which give a total conductance of 1600 l/s to each vacuum box. The RF attenuation of the slots in the TE_{010} mode is 4.5 dB at 700 MHz, over twice the attenuation of the LAMPF DTL grills at 201.25 MHz. The pumps are attached to the vacuum boxes by means of 203-mm Helicoflex Quick-Flanges to allow for easy changeout. The pumps weigh 84 kg and will require special handling equipment in the form of crane slings or trucks during installation and maintenance.

The modules (or assembly units) are also equipped with 100-mm manual gate valves to which the turbomolecular pumping packages can be attached for roughdown of the module. In the four-tank and three-tank modules, which all have underslung bridge couplers, these pumpdown ports are attached to one bridge coupler in the module. For the two-tank modules, the pumpout port is attached directly to one tank, and pumping is done through a

vacuum grill. Instrumentation (such as ion gauges and thermocouple gauges) is provided on the tanks in all cases.

6.1.8 Intertank Gaps

The intertank gaps are located between the accelerating tanks. The length of these intertank gaps are $5\beta\lambda$ in the energy range of 20–52.3 MeV and $3.5\beta\lambda$ in the energy range of 52.3–100 MeV. The first gap (between modules #1 and #2) determined the need for a $5\beta\lambda$ spacing at the low-energy end of the BCDTL; and to limit the number of transitions seen by the beam, the $5\beta\lambda$ gap was continued to module #10 (up to an energy of 52.3 MeV) before shortening the gap to $3.5\beta\lambda$ for the rest of the BCDTL.

The physical hardware that is installed in the intertank gap is shown in Fig. 6-12. It consists of a platform on which are mounted two sets of precision linear bearings. The quadrupoles are aligned in the lab relative to the centerlines of the linear shafts on which these bearings ride, as is described in Sec. 9.3.5 (Chap. 9). The intertank module also contains the beamtube, any diagnostic devices, bellows, and disconnect flanges. The in-line valve, not shown here, is considered an integral part of the tank or module to which it is attached. As a subassembly, the intertank module can be completely checked out and aligned in the lab before installation. This technique is intended to facilitate maintenance and repair.

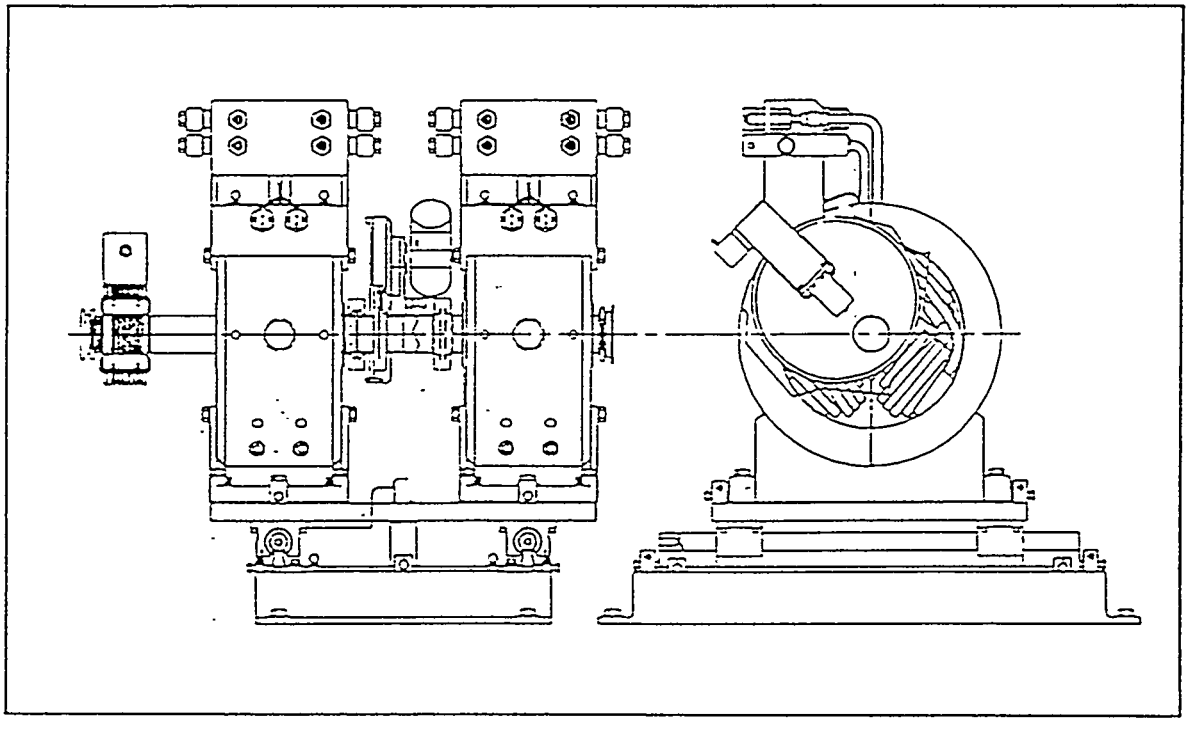


Fig. 6-12. Intertank hardware: quadrupole doublet, beampipe, diagnostics, and bellows.

The tank assemblies are equipped with brazed Helicoflex quick-disconnect high-vacuum flanges on both ends. These flanges accept a silver-plated metal vacuum seal and a hinged collar clamp, which can be tightened to form a high-vacuum seal with a single drive screw, accessible from the aisle side of the machine.

6.1.9 Diagnostics

To minimize beamloss, the BCDTL will require permanent beam diagnostics throughout its length to adequately measure the transverse and longitudinal phase-space characteristics of the beam. The measurements must verify the phase-space centroids, the amount of beamloss, and the transverse phase-space match between beam emittance and structure acceptance as the beam traverses the BCDTL. This allows operators to minimize beamloss.

To carry out these goals, a microstrip or stripline probe will measure the *transverse beam centroids* (horizontal and vertical position) and the *longitudinal beam centroids* (energy and output phase) between each of the EMQ doublets in the BCDTL intertank spaces. This probe placement equates to a total of 61 beam-centroid measurement systems in the BCDTL. The phases and amplitudes of the fields in the BCDTL cavities are verified using these same microstrip probes (and a cavity field sensor) by measuring the longitudinal beam centroids. Also, the peak beam current is measured with the microstrip probes to understand relative changes in beam current. Each of these measurements will be capable of operating under either pulsed- or cw-beam conditions and with a large dynamic range from only a few milliamperes to full beam current so that any off-normal conditions may be quantified.

Another frequently installed beam-diagnostic measurement is the beamloss monitor (BLM). While not consuming any direct beamline space, this device will be placed slightly downstream from each of the 61 quadrupole doublets and offset from the beamline center. If there is any beamspill, the BLMs will sense the resultant ionizing radiation from the split beam interaction with beamline structures. These devices are generally very sensitive to the ionizing radiation but are not accurate in terms of sensing the quantity or location of the lost beam. In accelerator tuning, BLMs serve as a minimization-measurement-type diagnostic.

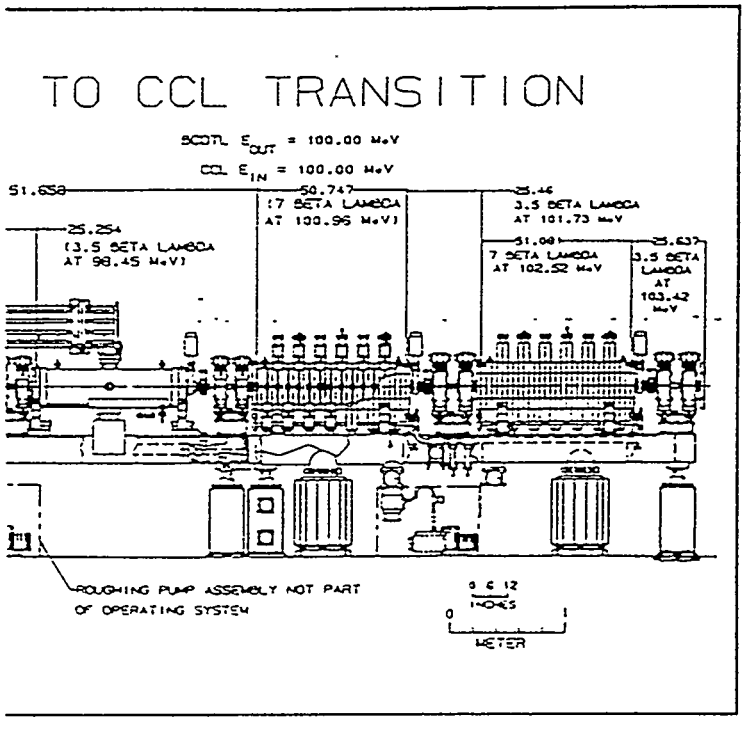
In locations where perturbed beam is possible, such as near the 52.3-MeV transition point where intertank spaces change in length from $5\beta\lambda$ to $3.5\beta\lambda$, beam profiles will be taken in five contiguous intertank spaces. For beam energies up to ~100 MeV, the beam profiles will be acquired by sensing the fluorescent light resulting from the beam interaction with the residual nitrogen in the region. The beam emittance constructed from multiple profiles acquired along the transport provide an understanding of tuning parameters and allows operators to correct any errors.

Pulsed and cw beam-current-measurement devices will be installed at or near the end of the BCDTL to monitor any off-normal conditions. These measurements can accurately sense a few tenths of a percent of the full-scale beam current, and will be able to sense a few hundred microamperes of beamloss over the length of the BCDTL. Under normal conditions, the expected beamloss will be much lower than the resolution of the measurements. Using both the funnel and the BCDTL output-current measurements, off-normal lost beam and low BCDTL transmission-efficiency conditions will be sensed.

Finally, in the locations where perturbed beam is possible and at every tenth doublet, beam-halo detectors will be installed. These devices will provide information regarding halo distributions outside the core of the beam (i.e., 2–8 standard deviations of the beam profiles). A total of 11 halo detectors will be installed in the BCDTL, including the 5 detectors installed directly downstream from the transition area. Each detector will use existing BLMs and will have some minimally interceptive device (e.g., graphite paddles) that intercept the outer edges of the transverse beam distribution. As each of these devices intercepts the beam edges, the resulting ionizing radiation (e.g., γ-radiation) is sensed by the nearby BLMs. Beam profile measurements capable of sensing the more intense portions of the halo (i.e., 2–3 standard deviations) will provide an on-line calibration of the halo measurements.

(BCDTL—CCL)

of the CCL is just an extension of the BCDTL focusing transverse phase advance per period of 70°. Therefore, output beam from the BCDTL to the input of the CCL iditional matching section between the two structures. beam does remain both transversely and longitudinally If additional transverse matching should be required, the id the first two doublets of the CCL could be used. Also, ne by adjusting the phases and amplitudes of two tanks ws a layout of the transition region.



transition region between the BCDTL and CCL.

TL to the CCL at 100 MeV is smooth and uninterrupted, sturbances. The lattice structure length is equal to $10.5\beta\lambda$ nodule and first 100-MeV CCL module, and the structure

higher energies, this is achieved by keeping the beam away from the transverse apertures and longitudinal bucket limits through the use of large apertures, large buckets, good alignment, good phase control, and low accelerating gradients. Although our reference design of 1989 was adequate, many improvements and simplifications have been incorporated into this design.

6.3.1.1 Improvements Over Earlier Design

The 1989 APT design required a CCL that ranged 20–1600 MeV. Since that time, both the beam energy and beam current requirements changed, and we replaced the 20–100-MeV section of the linac with a BCDTL structure (described above) that is more electrically efficient in this regime. The 1989 APT CCL design incorporated tanks ranging from 4 cells/tank at 100 MeV up to 10 cells/tank at 1000 MeV, and the intertank spacing increased as a function of β with $1 \times \beta\lambda$ lengths between tanks. However, upon reexamination of this design, it was determined that the construction of very short tanks would be rather difficult. It was also determined that a larger intertank spacing would be more practical to allow for focusing quadrupoles and beam diagnostics.

We determined from beam-dynamics simulations of our earlier design that our choice of CCL geometry led to discontinuous jumps in both emittance growth and rms beamsize. This was found to occur due to abrupt changes in the transverse and longitudinal focusing strength per unit length from one section to the next, where the number of cells/tank was increasing. Even though the beam was rms-matched at the input to the CCL, the transitions were nonadiabatic enough to cause both emittance and beamsize growth. In the 1989 design, to reduce the effects of the nonadiabatic transitions, we found we had to match the beam from section to section both transversely and longitudinally. The features of this design would have required the accelerator to be tuned and operated in a rather complex manner. The improvements to the 1989 design that have been incorporated into our new reference design help meet the desired beamloss requirements, allow for easier structure manufacturing and assembly, and reduce or eliminate the strong sensitivity to matching between sections.

6.3.1.2 Switchover at 100 MeV

One reason we chose 100 MeV as the crossover energy to switch from the BCDTL to the CCL is that the shunt impedance of the CCL becomes greater than the BCDTL at about 100 MeV, so the CCL is the more efficient structure to use beyond 100 MeV. The other reason is the precedent set by LAMPF. LAMPF is a higher-frequency machine (805 MHz) and is therefore about 15% physically smaller than the APT CCL. LAMPF makes the transition from a DTL to the CCL at 100 MeV and provides an excellent precedent for any fabrication problems that might be associated with a CCL-type structure at 100 MeV.

6.3.2 Description

The CCL consists of 342 tanks that range in length between 1.29–2.62 meters. The total length of the CCL is longer than 1 km. Each tank contains 14 cells, each cell $\beta\lambda/2$ in length, operating at a frequency of 700 MHz. EMQ doublets are located between the tanks to provide transverse focusing of the beam. A previous comparison between singlet and doublet focusing schemes showed that for the tank lengths we have chosen, doublet focusing provides a 30%–40% improvement in the transverse aperture-to-rms-beamsize ratio. The transverse zero-current phase advance per period is held constant at 70°. Three different

magnet lengths are used to avoid exceeding the pole-tip field maximum allowable for electromagnets. The doublet spacing has been chosen to be equal to a single quadrupole length.

6.3.2.1 CCL Parameters

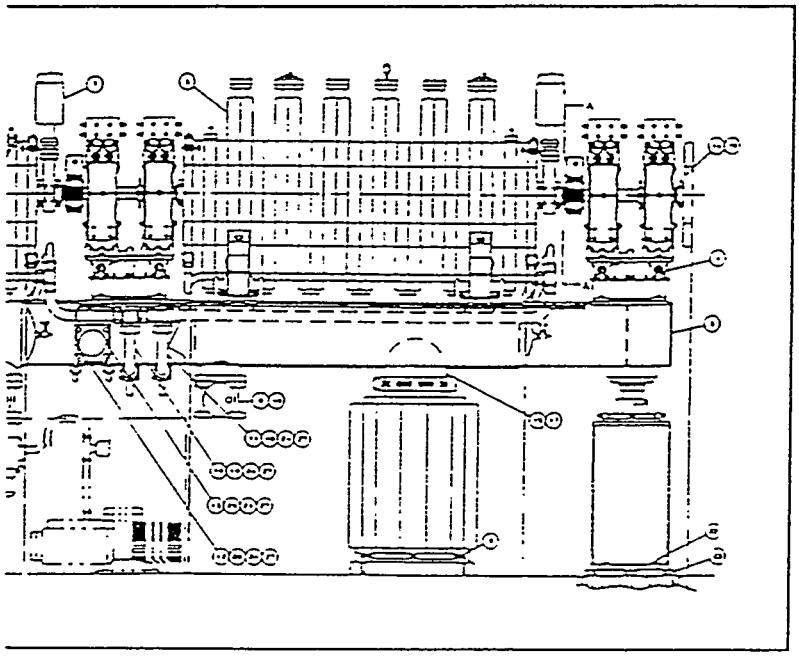
Table 6-3 gives a detailed list of parameters for the CCL. The accelerating gradients were chosen to give a real estate (average) gradient of 1 MV/m over the entire length of the accelerator. The tanks are designed to operate at a structure gradient of 1.5 MV/m up to 371 MeV and at 1.36 MV/m between 371–1000 MeV. The intertank spacing is $3.5\beta\lambda$ up to 371 MeV and is then reduced to $2.5\beta\lambda$. Each tank will be powered by a 1-MW klystron.

Table 6-3. APT CCL Parameters

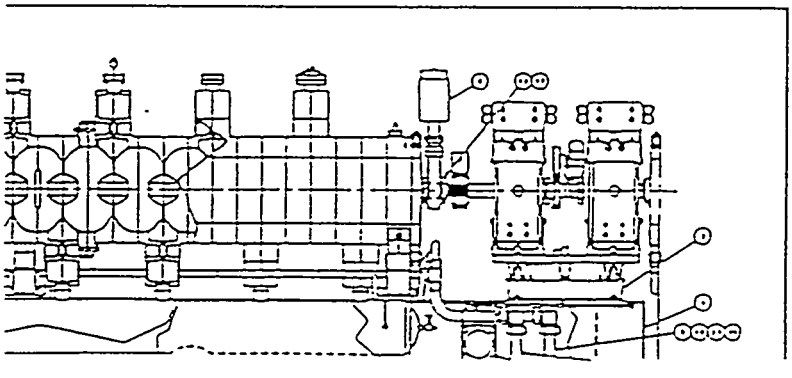
Energy (MeV)	100–1000
Frequency (MHz)	700
Beam Current (mA)	200
No. of RF Modules	342
No. of Assembly Units	322
No. of Tanks	342
No. of Cells per Tank	14
Length of Cells	$\beta\lambda/2$
Length of Tanks (m)	1.29–2.62
Total Length (m)	1031.44
Intertank Spacing	$3.5\ \beta\lambda$ (100-371 MeV)
	$2.5\ \beta\lambda$ (371-1000 MeV)
Vacuum/Tank (l/s)	900
Cooling/Tank (gpm)	50–112
Total Cooling (gpm)	18,730
Radial Aperture (cm)	2.50
Aperture/Beamsize(rms) Ratio	13–26
Structure Gradient (MV/m)	1.50 (100-371 MeV)
	1.36 (371-1000 MeV)
Average Gradient (MV/m)	1.00
Shunt Impedance (MΩ/m)	23.31–37.42
Average Power Density (W/cm^2)	≤8
Peak Surface Field (Kilpatrick)	≤0.6
Structure Power (MW)	42.49
Beam Power (MW)	180.39
Total RF Power (MW)	223.18
Efficiency	0.806
Length of Focusing Period	$10.5\ \beta\lambda$–$9.5\ \beta\lambda$
Transit-Time Factor	0.82–0.86
Synchronous Phase (deg)	-30
Quadrupole Lattice	FDO
Quadrupole Lengths (cm)	11.0 (100-246 MeV)
and Doublet Spacing (cm)	15.0 (246-636 MeV)
	18.0 (636-1000 MeV)
Quadrupole Gradients (T/m)	29.3–38.0 (100-246 MeV)
	24.4–38.0 (246-636 MeV)
	29.3–37.4 (636-1000 MeV)
Quadrupole Pole-tip, Maximum (T)	0.950
Quadrupole Phase Advance/Period (deg)	70

cdown

layouts of the 100-MeV and 1000-MeV CCL structures. Each .ong, as were the tanks in the BCDTL, with the intertank gaps and switching to $2.5\beta\lambda$ at 371.3 MeV. The lattice length is ı from BCDTL to CCL.



·14. First CCL assembly unit at 100 MeV.



Each of the 342 individual CCL tanks requires one klystron, for a total of 342 klystrons or 342 RF modules. The physical breakdown of the CCL is given in Table 6-4. Two-tank assembly units are designed at the low-energy end of the CCL, as shown in Fig. 6-14, because the tanks are short. Doubling up results in assembly units that are more or less uniform in length throughout the APT point design. Each tank requires a waveguide so that the first 20 two-tank assembly units each have twin waveguides supplying them. All the rest of the assembly units have single waveguide feeds.

Table 6-4. CCL Modular Breakdown

Assembly Unit Nos.	No. of Assembly Units	No. of Tanks* per Assembly Unit	Intertank Spacing	Radial Aperture (cm)
1-20	20	2	$3.5\,\beta\lambda$	2.50
21-322	302	1	$2.5\,\beta\lambda$	2.50

* There is one RF module for every tank.

6.3.3 Tank Description

The CCL accelerator tanks are hydrogen-furnace-brazed assemblies. The cells are coupled through slots that connect to the side-coupling cells. The CCL structure, also called a side-coupled linac, has side-coupling cells that serve electrically as zero-power cells and mechanically as vacuum-pumpout ports for the main cells. The coupling cells on the bottom of the tank connect to a large vacuum manifold, which in turn is connected to a 900-l/s ion pump. The manifold is equipped with a roughdown port and a valve to which a roughing package can be attached when needed. The upper coupling cells also provide convenient locations for vacuum instrumentation, such as ion and thermocouple gauges.

The tank assemblies are also equipped with brazed Helicoflex, quick-disconnect, high-vacuum flanges on either end as in the BCDTL. These flanges accept a silver-plated metal vacuum seal and a hinged collar clamp, which can be tightened to form a high-vacuum seal with a single drive screw, accessible from the aisle side of the machine. On the downstream flange of each tank is the in-line vacuum valve, which is considered an integral part of the tank assembly. The opposite flange of the valve is also a quick-disconnect unit to which the rest of the intertank doublet module assembly is attached.

6.3.4 Cavity Physics

SUPERFISH code runs were done to determine reasonable cell geometry parameters for the CCL. Transit-time factors and shunt impedances were calculated to make power estimates for the CCL. The shunt impedance values are used by the design code to calculate the structure power. Figure 6-16 shows a generic coupled-cavity geometry. Table 6-5 gives the fixed geometry parameters for a cell.

An optimized-cell geometry for the low-energy part of the CCL was found. This cell geometry was fixed and the gap-to-cell-length ratio held constant at 0.436 throughout the CCL. The tank diameter was allowed to vary to tune the tanks to the correct resonant frequency of 700 MHz. Figure 6-17 shows the cell shape and nose geometry near

1000 MeV. Figure 6-18 shows the variation of shunt impedance, corrected for coupling slots, with relativistic β, as determined by SUPERFISH.

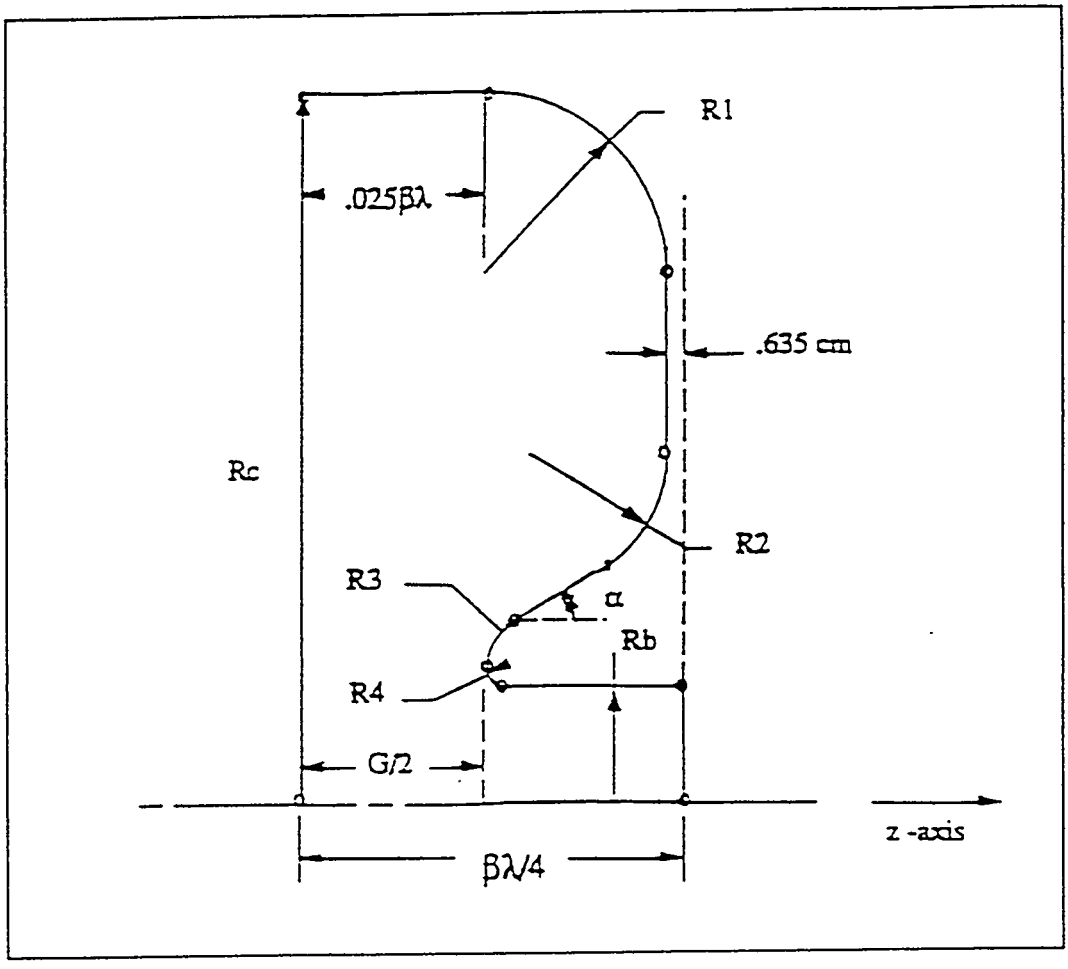


Fig. 6-16. Generic coupled-cavity geometry.

Table 6-5. Fixed Coupled-Cavity Cell Shape Geometry Parameters for the CCL

Cell Length, $\beta\lambda/2$ (cm)	9.17–18.74
Cavity Radius, R_c (cm)	30.55–26.83 (100–1000 MeV)
Radial Aperture, R_b (cm)	2.5
Cavity Side Radius, R1 (cm)	1.433
Side Nose Radius, R2 (cm)	0.257
Nose Tip Radius, R3 (cm)	0.257
Nose Bore Radius, R4 (cm)	0.0857
Nose Face Angle, α (deg)	30
Gap, G/2 (cm)	4.0–8.2

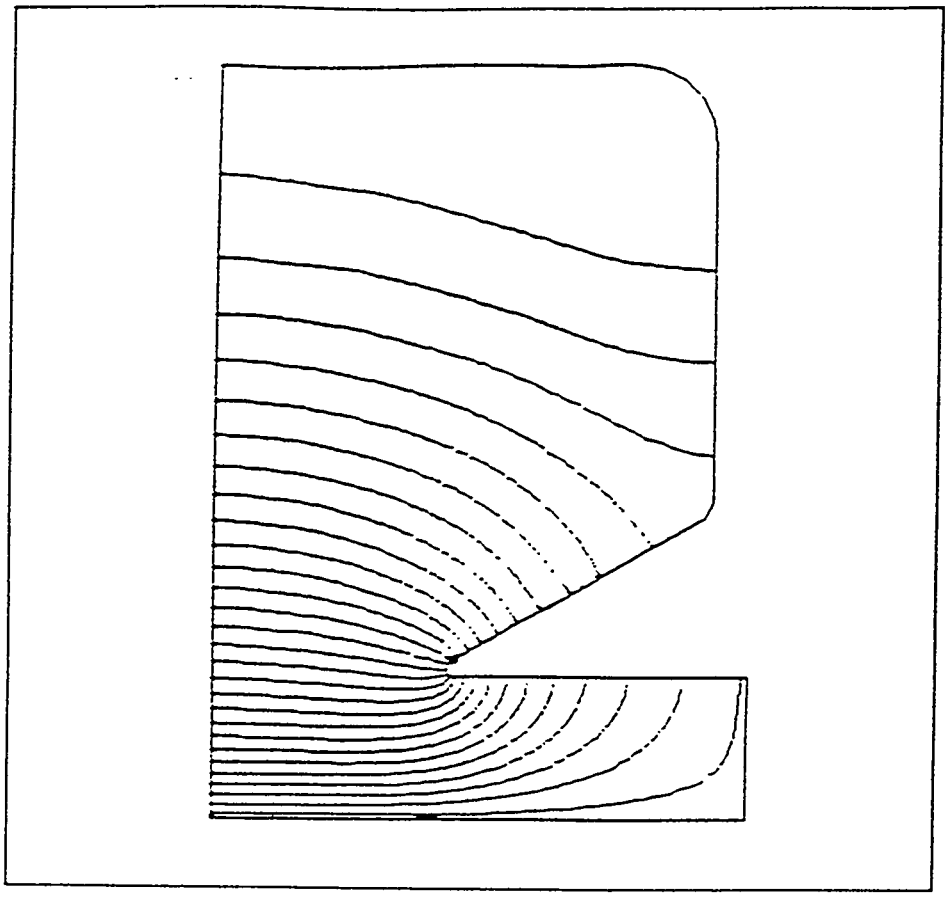


Fig. 6-17. CCL nose shape and cell geometry for a cell near 1000 MeV.

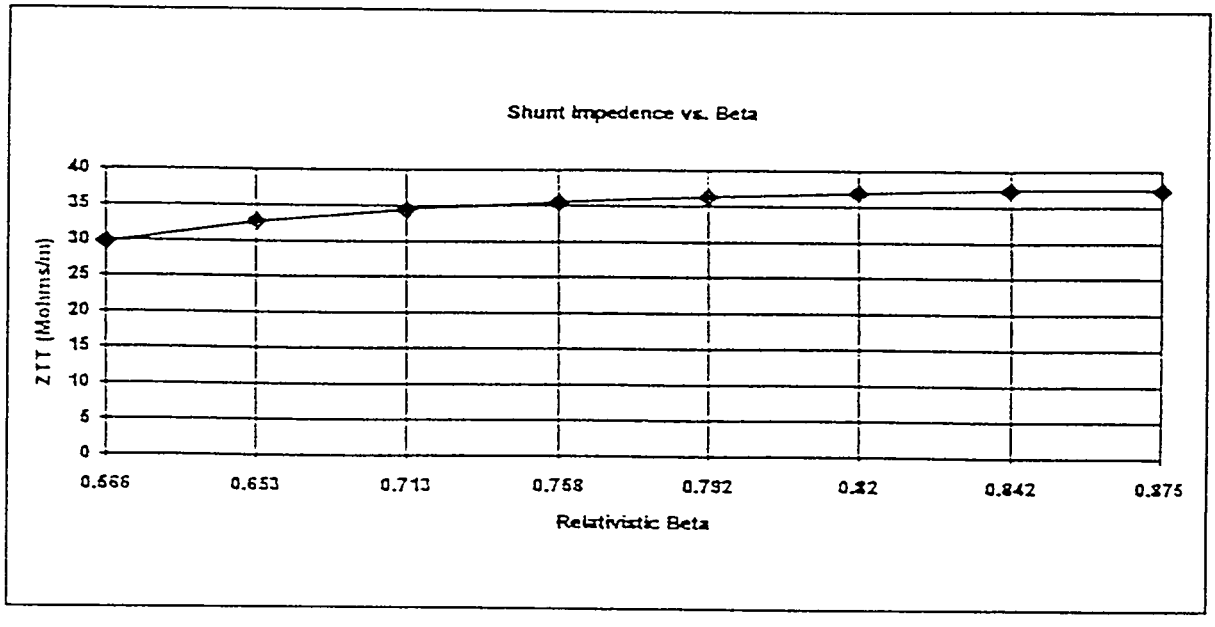


Fig. 6-18. Shunt impedance vs. β (100-1000 MeV), as determined by SUPERFISH (the calculated values have been reduced by 15% to include a correction for cavity coupling slots).

6.3.5 Simulation Results

The beam-dynamics simulations completed so far indicate that the coupled-cavity linac design presented in this report will meet the accelerator requirements for the Accelerator Production of Tritium. It has been found that allowing only adiabatic transitions in the CCL, namely, varying tank lengths and focusing periods linearly with β, leads to improved performance. Because abrupt transitions have been eliminated, the requirement to match between sections no longer exists. Strong transverse focusing helps to reduce transverse emittance growth and maintain a large transverse aperture ratio.

6.3.6 The Aperture Ratio

In beam-dynamics simulations carried out to check the design parameters chosen, it was noticed that the transverse-aperture-to-rms-beamsize ratio was increasing as a function of energy in the CCL, even though the bore size was fixed. This meant the transverse beamsize was decreasing as the beam gained energy in the CCL, even though both the transverse and longitudinal emittances were growing. This reduction in beamsize can be understood from some simple scaling arguments.

The expressions shown below were derived using the envelope equations in the smooth approximation. For an emittance-dominated beam, which would be the worst-case scenario, the transverse rms beamsize is given by

$$X_{rms} = \sqrt{\frac{\varepsilon_n L}{\beta\gamma\sigma_0}} \quad ,$$

where L is the length of the transverse focusing period and σ_0 is the zero-current phase advance per period. Because L is proportional to $\beta\lambda$, the rms beamsize scales as the normalized emittance divided by the relativistic γ. Ignoring the effect of γ, which reduces the beamsize, the emittance would need to increase by a factor of four to double the beamsize (square root effect). Because the emittance growth observed in the simulations is very small, the rms beamsize decreases.

For a space-charge-dominated beam, the situation is even better. Here, the rms beamsize is given by

$$X_{rms} = \frac{L}{2\sigma_0}\sqrt{\frac{qI}{2\pi\varepsilon_0 mc^3\beta^3\gamma^3}} \quad .$$

If the phase advance per period is constant, as in our design, the focusing length is still proportional to $\beta\lambda$, and the rms beamsize will decrease as

$$\frac{1}{\sqrt{\beta\gamma^3}} \quad .$$

The decrease in beamsize is therefore a beneficial kinematic effect that can be taken advantage of in high-current designs.

6.3.7 Cooling and Tuning

6.3.7.1 Cooling

One of the more innovative developments in the APT point design studies is the cooling system for the CCL. The individual cells are fabricated from OFE copper forgings, each of which consists of a half main cell and a half coupling cell. Two such pieces brazed together make up a complete main cell and two half-coupling cells, or a complete coupling cell and two half-main cells, depending on which side the braze is made. Brazing together 26 such forgings along with two half-cells makes up the 14-cell ($7\beta\lambda$) tank assembly. This technique for building CCL cavities was developed by Lloyd Young of AT Division and will be used throughout the APT CCL. This system of assembly provides natural split lines along the central planes of both the main-cell septums and the coupling cells. These surfaces can be used to machine the cooling channel patterns before brazing. A typical septum cooling-channel pattern is illustrated in Fig. 6-19. It consists of four parallel cooling paths numerically machined into the face of a septum split plane. The cooling channels are fed by a single pair of inlet and outlet ports. These supply and return ports are 180° apart. All the septums in the tank are fed in the same way, but the ports are "clocked" by one step for every second septum. Note that there are 14 supply and return ports shown in Fig. 6-19. This is sufficient to supply coolant to seven septums.

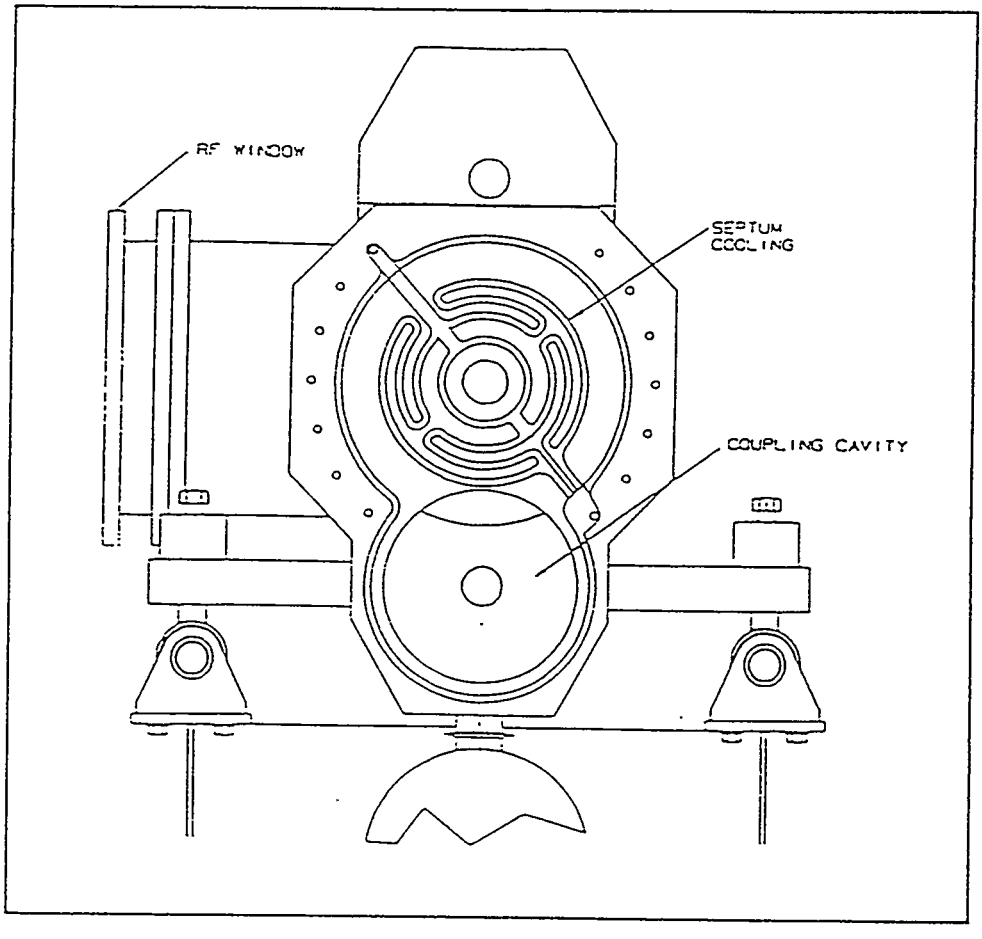


Fig. 6-19. CCL septum cooling scheme.

Because a tank consists of 13 septums and 2 endwalls, a total of 30 ports are required to cool the entire tank assembly. The flow schematic by which this is accomplished is shown in Fig. 6-20.

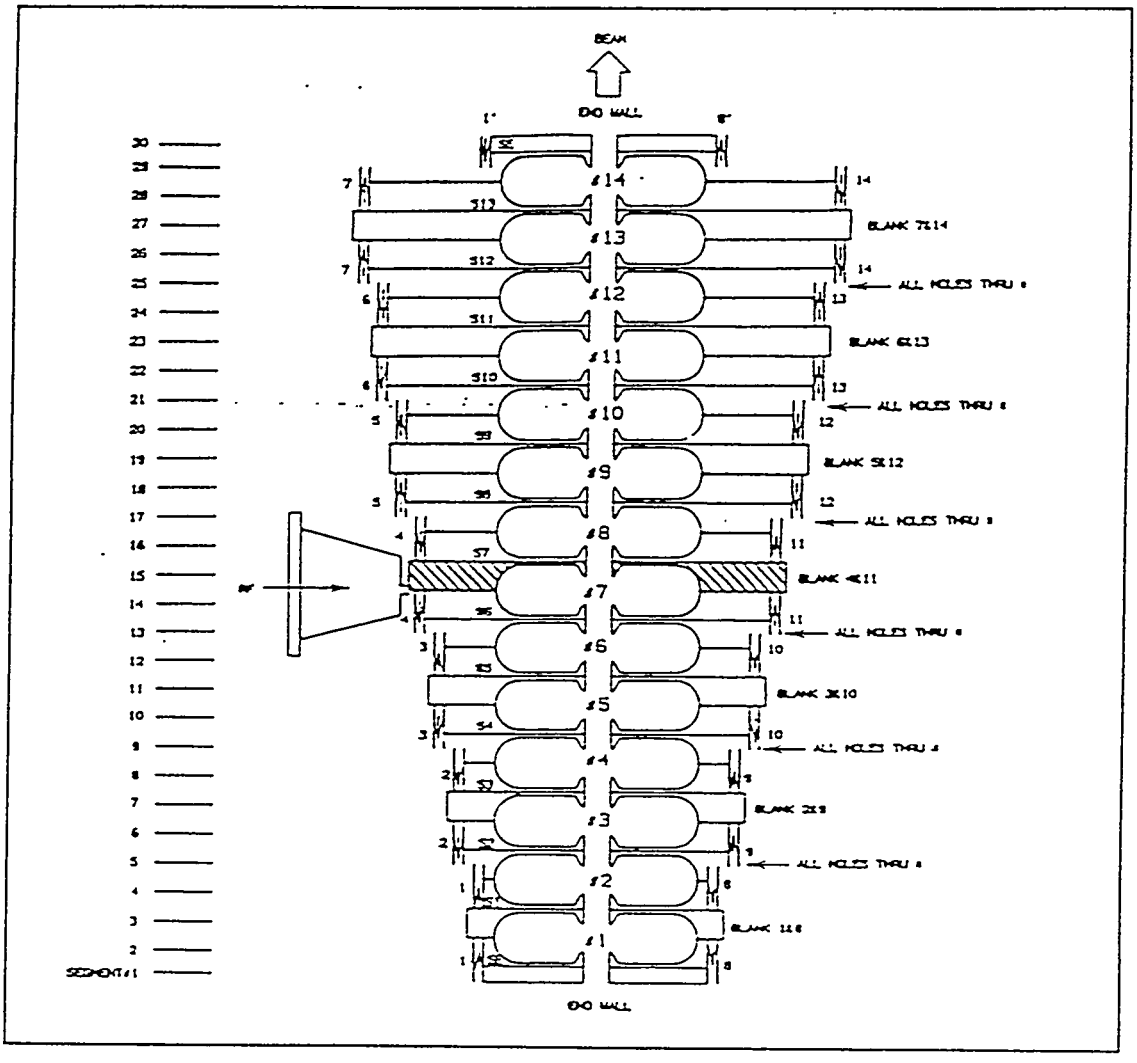


Fig. 6-20. Flow schematic for the 14 cells of a CCL tank.

The coolant for one end wall and every second septum for six septums is delivered from the upstream end of the tank; the coolant for the opposite end wall and the intermediate seven septums is delivered from the downstream end of the tank. This produces two advantageous effects in terms of controlling the uniformity by which RF power heats the tank: (1) the gun-drilled supply and return ports around the periphery of the tank carry mass-balanced, counterflow coolant for uniform *peripheral* temperature control, and (2) the flow through the septums is also mass-balanced, with counterflow coolant for uniform *transverse* temperature control.

Therefore, the CCL tanks are symmetrically cooled in both the longitudinal and transverse dimensions. This tends to control the thermal expansions in the copper as closely as possible to those that would result from a true ambient temperature change despite the fact that the thermal energy is being deposited internally by skin-depth RF heating, which is very

nonisotropic. The amount of coolant per CCL tank is quite large, requiring about 26 gpm/m of structure. The individual tanks require as much as 60 gpm or almost 4 gpm per septum.

In addition to septum cooling, which accounts for the bulk of the flow in the tank, we have also provided a cooling channel around the seam of each cell at the cell centerline and another channel around the periphery of the coupling cell. These auxiliary cooling channels account for only about 15% of the total flow. Even though the coupling cells are ostensibly zero-power cells, they carry power during transients and, as a result, experience small heating effects. Maintaining a constant temperature in the coupling cells by increasing their thermal mass through additional cooling helps keep the cavity system safe from a runaway field-tilt phenomenon, as was seen during the early checkout stages of the CCL at LAMPF.

The cooling system described above cannot be used to cool an entire $7\beta\lambda$-long tank above a certain energy, because the CCL tanks eventually become too long for normal and reliable brazing. At about 200 MeV, the tanks reach about 1.7 meters in length. At this point, a flange is introduced as close as possible to the center of the tank, and two tank sections are bolted together to make up a $7\beta\lambda$-long assembly. About 290 of the tanks are two-piece assemblies of this sort. Even though the 1000-MeV CCL module is the longest assembly unit, the longest single-tank section is around 200 MeV. The flanges that join the tanks are of two possible types. We have considered both Conflat and Wireseal styles. The Conflat flanges would have to be manufactured from scratch, whereas the Wireseal flanges are commercially available in the sizes required. Both types would then be modified to provide the RF knife edge. The RF seal cuts into a disc of copper. The vacuum seal is either a standard Conflat, a Helicoflex seal, or a wire.

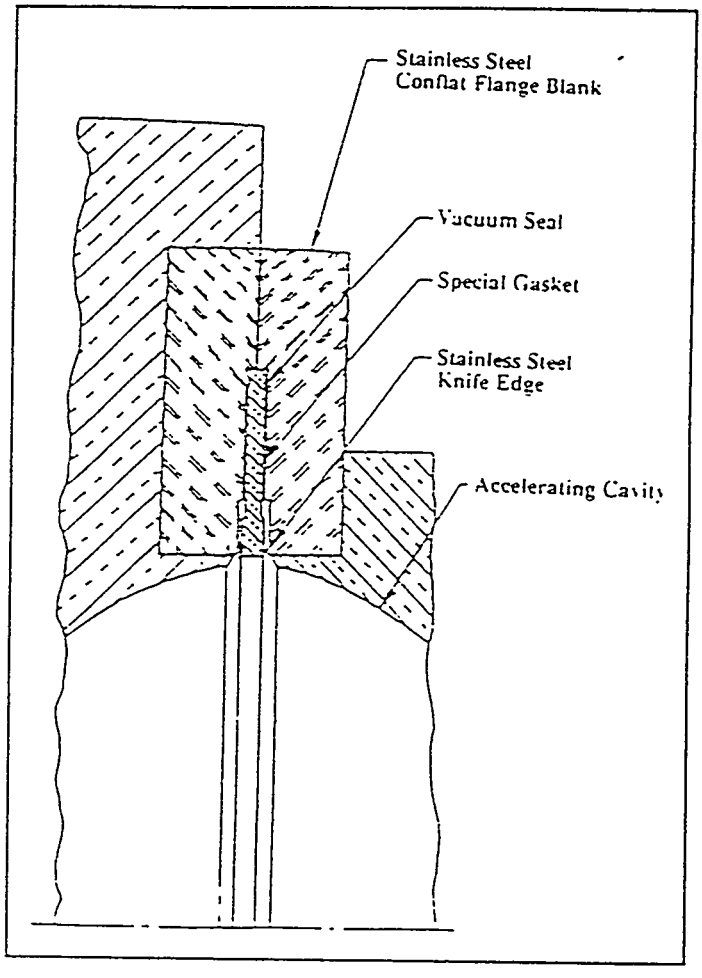


Fig. 6-21. CCL vacuum and RF seal.

Both the RF and vacuum seals are made simultaneously by the same flange-tightening process. A typical seal of this type showing the Conflat concept with a knife-edge RF joint and a standard vacuum seal is shown in Fig. 6-21. This was shown previously in Chap. 3 as a special engineering feature of APT.

The tank-mating flanges naturally interrupt the cooling passages around the periphery of the tank. Therefore, the flanges must be further modified to include ports so that jumpers can be installed once the flanges have been bolted together. Normally, the flanges are made up only one time, and for the life of the machine they should never have to be taken apart. The use of the high-integrity RF and vacuum joints described above assures this will be so. This method of

joining tank sections has been used at LAMPF with complete success. The main difference between APT and LAMPF is that the APT flanges use independent copper gaskets with copper-plated steel knife edges on either side for the RF joint. LAMPF used copper-plated steel knife edges directly into the cavity copper.

6.3.7.2 Tuning

The coupling slots, which connect the accelerating cells to the side cells, are precision machined and critically tuned. Differential distortion of these slots will result in a field tilt occurring across those cells. It is essential in tuning these tank assemblies that the septums not be distorted because this will cause the coupling coefficients for the two adjacent main cells to differ slightly. The resulting field tilt arises from the following relationship:

$$E_1 k_1 = E_2 k_2 \quad ,$$

where E_1 and E_2 are the field levels in adjacent cells and k_1 and k_2 the coupling coefficients linking these cells through the side coupler. If k_1 and k_2 differ, then E_1 and E_2 must also differ. If the cells are tuned with a septum-bending technique, as was done in the early tuning of LAMPF, it is possible that accumulative errors resulting from coupling-slot distortions will lead to a field tilt in the tank. A technique better than septum bending is to use depression tuning of the outside walls of the cavities to reduce inductance and raise frequency. It must be remembered that tuning will be done at room temperature (about 20°C), whereas ambient operating temperatures for the CCL will be about 46°C; so several hundred kHz of offset tuning will have to be anticipated. This is discussed in more detail in Chap. 9.

6.3.8 RF Windows and Waveguides

The considerations for the CCL iris, window, and waveguide transmission line are similar to those described previously for the BCDTL. The coupling iris, which is in the most central cell of the tank assembly, is cut through the wall of the cell and opens into the tapered waveguide section. The taper allows the iris to be cut narrower, which is a necessary feature in the 100-MeV cells. These cells are only about 9.2 cm long, with about 7.9 cm of physical space to squeeze in the iris. The irises in the CCL do not carry as much power as in the BCDTL but must still deliver about 460 kW at 100 MeV and up to 750 kW at 1000 MeV. The tapered waveguide section is heavily water cooled, as is the iris itself, and the section is cut to about a half-guide wavelength in length. The flange is a standard EIA WR1150, as in the BCDTL. The same considerations apply regarding the window development. The transmission waveguide between the CCL and the klystrons is WR1500 for reduced transmission losses.

6.3.9 Intertank Gaps

The hardware that was described for the BCDTL intertank spaces is also used in the CCL system and in the same manner. The only differences are in the quadrupoles, which have higher fields and are more widely spaced in the CCL, and in the mix of diagnostics. Above 100 MeV, it is possible to use rapid interception of the penetrating beam, so several "flying wire" diagnostic devices are installed between 100 and 1000 MeV. The bore of the beamtube in the intertank modules has an i.d. of 5.0 cm (the same as the bore of the tanks), so the quadrupoles have to be built considerably larger, more powerful and heavier than in the

BCDTL. The same technique of checkout, alignment, installation, and maintenance as was described for the BCDTL is used in the CCL assembly units.

6.3.10 Diagnostics

In terms of the beam diagnostics, the CCL is a direct continuation of the BCDTL. The CCL will require the same permanent beam diagnostics throughout its length to adequately measure the transverse and longitudinal phase-space characteristics so that beamloss is minimized. The measurements must verify the transverse and longitudinal phase-space beam centroids, the amount of beamloss, and the transverse phase-space match between the beam emittance and the structure acceptance as the beam traverses the CCL. As in other parts of the accelerator, the beam diagnostics in the CCL must be able to make measurements for both the cw beam present during normal operation and for various pulsed-beam formats that will be present during startup and tuning. For most kinds of measurements, the same hardware is used for both cw and pulsed beams, but in some cases (current monitors, for example) different devices are needed to satisfy the different requirements of the two situations.

A total of 283 beam-centroid-measurement systems will be required in the CCL. As in the BCDTL, the beam-position measurements will be used to steer the beam through the CCL for minimum beamloss. The phases and amplitudes of the fields of the CCL cavities are verified using these same microstrip probes (and a cavity-field sensor) by measuring the longitudinal beam centroids. Also, the peak beam current is measured with the microstrip probes to understand relative changes in beam current.

Beamloss monitors will also be placed slightly downstream from each of the 283 quadrupole doublets and offset from the beamline center. Both pulsed and cw beam-current measurement devices will be installed at or near the end of the CCL to sense any off-normal conditions; as mentioned above, different hardware is needed for handling the two kinds of current measurements. Using both the BCDTL and the CCL output-current measurements, lost beam and low CCL-transmission efficiency will be sensed.

In locations where perturbed beam is possible, such as the area near the 371 MeV transition point in the CCL where the intertank spaces change in length from $3.5\beta\lambda$ to $2.5\beta\lambda$, beam profiles will be taken in five succeeding CCL intertank spaces. At energies above 100 MeV, the flying-wire scanning technique (e.g., wire speeds of >20 m/s) will be used to acquire the beam profiles. The transverse beam-profile and emittance measurements will allow for corrections to be made due to mismatched beam from perturbations or misalignments.

Finally, in the same locations where perturbed beam is possible, beam-halo detectors will be installed. A total of 33 halo detectors will be installed in the CCL, including the 5 detectors installed directly downstream from the 371-MeV area. Each detector will use existing BLMs and will have a minimally interceptive device that will intercept only the outer edges of the transverse beam distribution. As each of these devices intercepts the beam edges, the resulting ionizing radiation is sensed by the nearby BLMs.

There is consideration of another offset beamline (not shown in the overall design) that would serve as a beam characterization station for the beams near 100 MeV. It is not clear that this offset beamline could be installed at the beginning of the CCL without perturbing the periodic lattice. Therefore, the inclusion of this particular offset beamline is still being considered

6.4 THE 700-MHZ RF SYSTEM

There are a total of 24 RF systems required for the BCDTL that serve to accelerate the beam from 20–100 MeV. The CCL uses 342 RF systems to accelerate the beam to the final energy of 1000 MeV. Each klystron has its own LLRF system, an independent connection to the high-voltage bus, and has a set of interlocks to protect the equipment and personnel.

6.4.1 RF Generator

The power required for the 700-MHz systems ranges from 0.52–1.25 MW, including 10% excess power for control margin and disturbance rejection. There are a total of 366 700-MHz RF systems, all identical in layout, but with differently sized klystrons to maximize efficiency. The BCDTL uses 1.25-MW klystrons (24 each), and the CCL uses a mixture of 0.9-MW klystrons (232 each) and 0.75-MW klystrons (110 each). The RF generator for the 700-MHz systems is based on the CERN 352-MHz klystron, and because of the difference in frequency, the generator will need a development effort, although only an incremental change in the existing state of the art, as it is not a high risk or major change in technology. This klystron also has a modulating anode that allows control of the current in the klystron (and hence the maximum output power). As in the 350-MHz systems, the mod anode is used to optimize the operating efficiency. The BCDTL uses 24 1.25-MW klystrons. By adjusting the mod anode to maintain the maximum output power of the klystron at 10% above the operating point, the average operating efficiency for the BCDTL is 59%, as seen in Fig. 6-22.

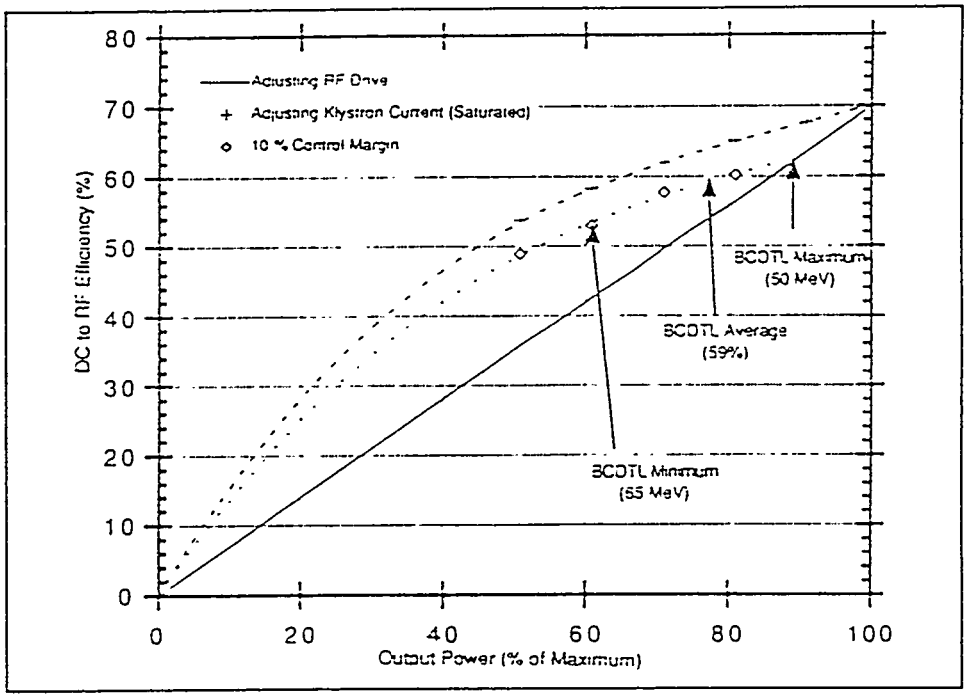


Fig. 6-22. BCDTL output efficiency using GTA klystron data (normalized to CERN tube efficiency).

In the CCL, the required RF-generator-power operating range is large (475–770 kW), as shown in Fig. 6-23. The step in power required at 371 MeV (module 120) is due to changing the accelerating gradient from 1.50 MV/m to 1.36 MV/m.

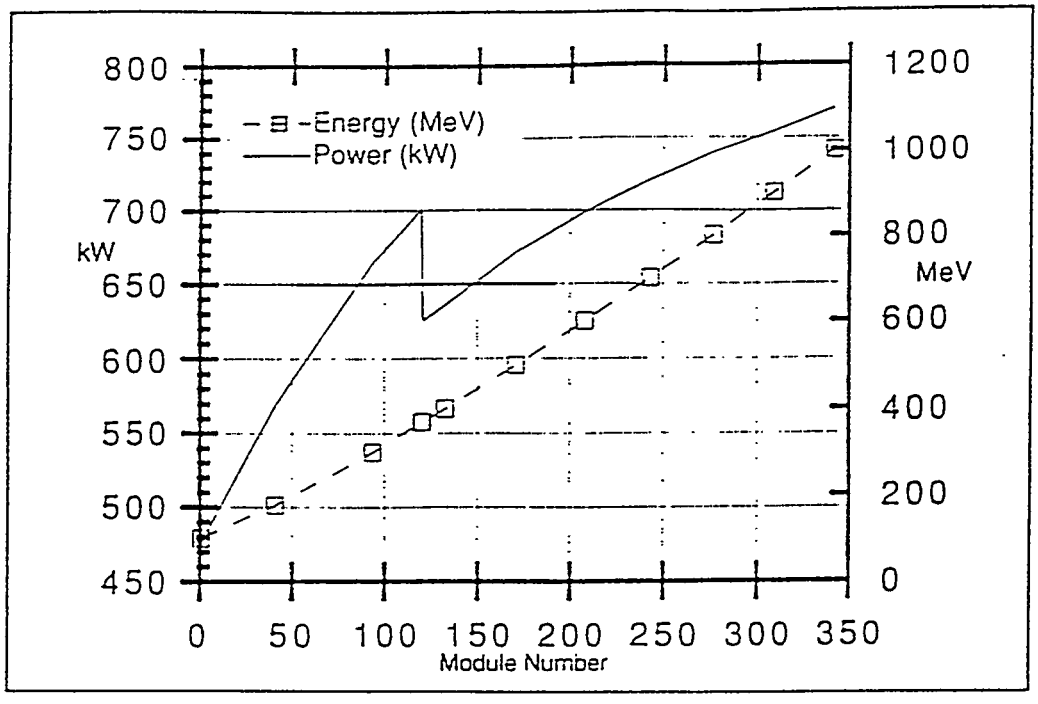


Fig. 6-23. APT CCL RF power vs. module number and output energy.

Adjusting the mod anode setting alone would produce an operating efficiency of approximately 50% (assuming 1.25-MW klystrons such as those needed for the BCDTL). However, this efficiency can be improved by specifying two additional sizes of klystrons for the CCL. A reasonably good compromise is achieved by selecting 0.75-MW and 0.9-MW klystrons, a large number of which are needed at both power levels (110 at 0.75 MW and 232 at 0.9 MW). Operating efficiency in this mode for the CCL is 59% as shown in Fig. 6-24.

6.4.2 RF Distribution

The RF power from the 700-MHz klystrons will be distributed with air-cooled, WR1500 waveguide. Each waveguide line includes a circulator and directional couplers at the klystron and the cavity ends. The waveguide will be slightly pressurized with dry air so that pressure interlocks can be used to indicate waveguide integrity. The pressurized air will have a small flow rate through the waveguide to enhance the cooling. Smaller waveguide (WR1150) can transport 700 MHz, but there is a penalty in losses. Assuming a one-way length of 100 ft, WR1500 has 0.1 dB of loss compared to 0.19 for WR1150 (at 700 MHz). For 250 MW of total RF power, this represents a savings of almost 5 MW. Therefore, the larger waveguide offers more efficient operation, as well as reduced cooling requirements.

6.4.3 RF Layout

The layout of the 700-MHz systems is shown in Fig. 6-25. Each klystron requires three electronic racks—one for the klystron preamps, one for interlocks, and one for system controls and interface—as well as a small oil tank around the cathode and high-voltage input connections. Each klystron system also requires its own LLRF system. Cooling is provided via a water manifold, which distributes water for approximately 40 klystrons.

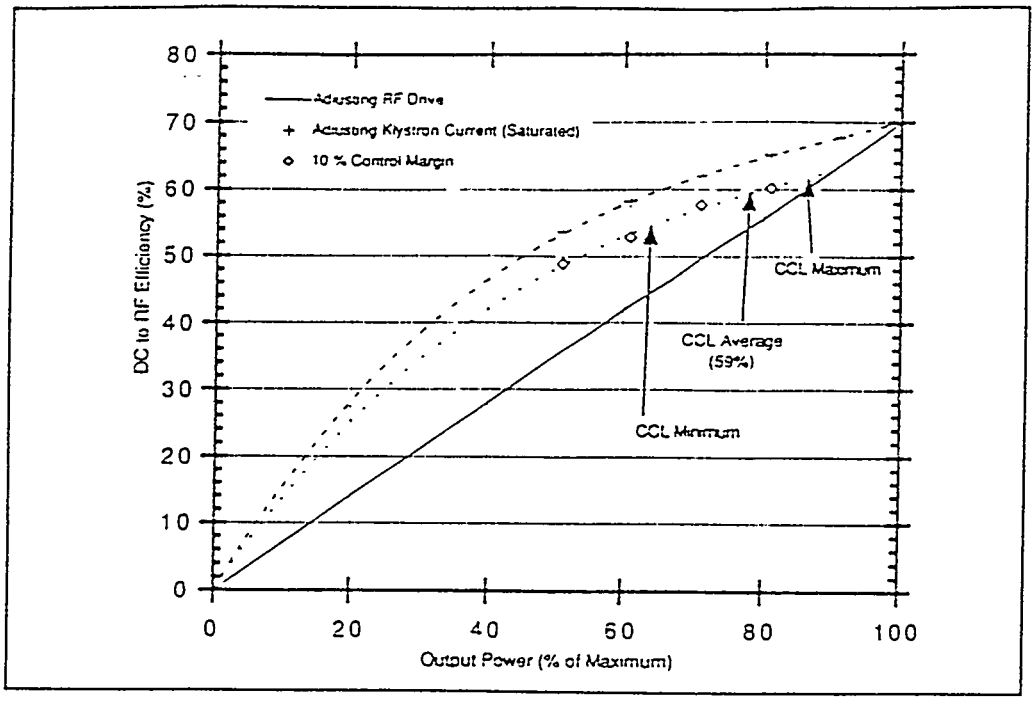


Fig. 6-24. CCL output efficiency using GTA klystron data (normalized to CERN tube efficiency).

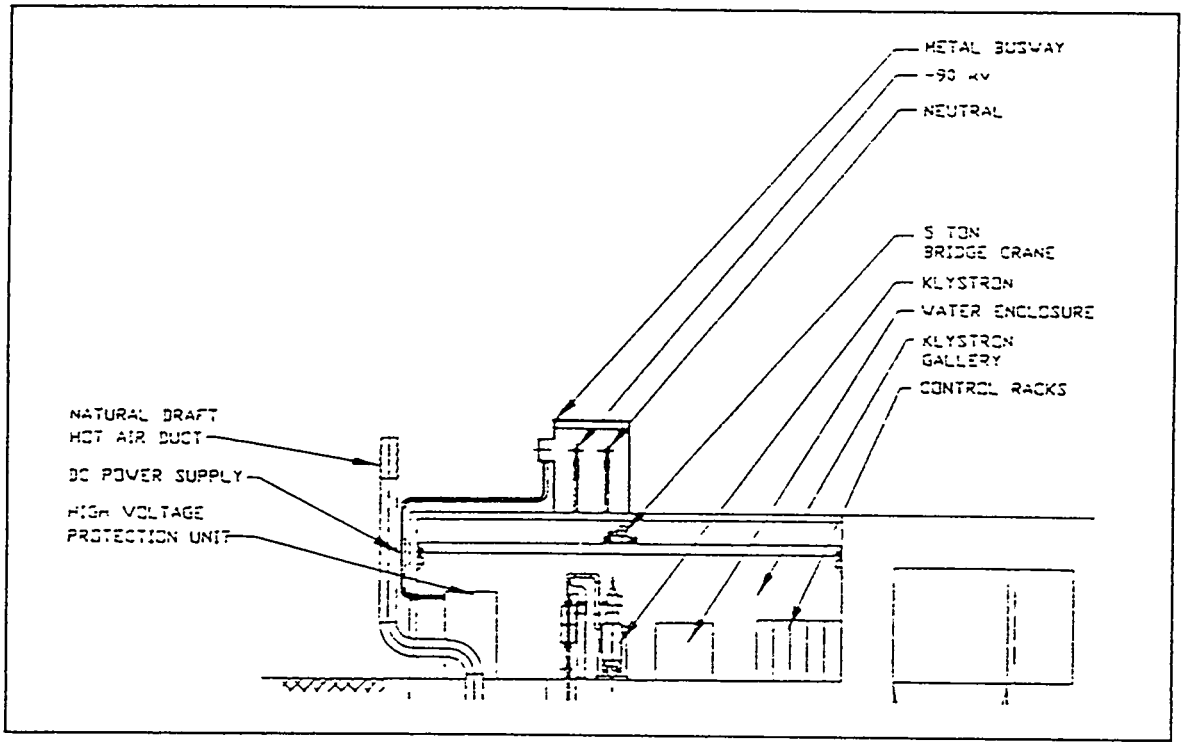


Fig. 6-25. RF system layout for 700-MHz systems.

THE HEBT AND BEAM EXPANDER
CHAPTER 7

Page

7.1 SYSTEM OVERVIEW AND PURPOSE 1
7.1.1 Overview 1
7.1.2 Beam Expander 2
7.1.3 Magnetic Elements 2
7.1.4 Targets and Beamstop 2
7.1.5 Engineering 2
7.1.6 Diagnostics 3
7.2 BEAM TRANSPORT LINE 3
7.2.1 Physics Design 3
7.2.2 Initial Periodic Lattice 4
7.2.3 Lattice Diagnostics 6
7.2.4 Achromatic Bend 7
7.2.5 Bend Diagnostics 10
7.2.6 Second Periodic Lattice 10
7.2.7 Four-Quadrupole Matching Section 11
7.2.8 Matching-Section Diagnostics 13
7.3 BEAM EXPANDER 13
7.3.1 Beam-Redistribution Method 13
7.3.2 Physics Description 14
7.3.3 Engineering Description 19
7.3.3.1 Tuneup Beamstop 20
7.3.3.2 Expander Magnets 21
7.3.3.3 Shield Dipole 21
7.3.4 Beam Expander Diagnostics 21
7.4 ENGINEERING CONSIDERATIONS 22
7.4.1 HEBT Alignment System 22
7.4.2 Interface Requirements 23
7.5 HEBT PERFORMANCE 24
7.5.1 Beam-Expander Simulation Tools 24
7.5.2 Beam-Expander Performance 25
7.5.3 End-to-End Simulation 27
7.5.4 Beam-Expander Tuning and Operation 28
7.5.5 Effects of Fault Conditions in the Accelerator 29
7.5.6 Counteracting Fault Conditions 30

LIST OF FIGURES

Page

Fig. 7-1. The HEBT system. 1
Fig. 7-2. RMS beam envelopes between the CCL and the beam expander. 4
Fig. 7-3. Initial periodic-lattice section. 4
Fig. 7-4. HEBT doublet mechanical support. 6
Fig. 7-5. The five-cell, 25°, achromatic bend. 7
Fig. 7-6. HEBT switching magnet area. 9
Fig. 7-7. Low-momentum beamstop design for switching-magnet. 11
Fig. 7-8. Four-quadrupole matching section. 12
Fig. 7-9. Beam-expander layout. 15
Fig. 7-10. Shielding arrangement to protect expander quads at 7.5° bend. 18
Fig. 7-11. Helicoflex vacuum seal used in the HEBT/target interface. 19
Fig. 7-12. The HEBT/target interface. 19
Fig. 7-13. Two-piece Helicoflex flange connector at the HEBT/target interface. 20
Fig. 7-14. HEBT monument alignment system. 22
Fig. 7-15. HEBT quadrupole translator. 23
Fig. 7-16. Nominal beam distribution at target for Gaussian input beam. 25
Fig. 7-17. Beam distribution with 0.25-rms beam jitter. 26
Fig. 7-18. Beam at target for code-generated input (left) and actual simulation (right). 27
Fig. 7-19. Beam distribution at target for a −10-MeV energy shift. 29
Fig. 7-20. Beam distribution at target for a +10-MeV energy shift. 30

LIST OF TABLES

Page

Table 7-1. Nominal HEBT Input Beam 4
Table 7-2. Elements of Initial periodic-lattice section 5
Table 7-3. Elements of the Achromatic-Bend Cell 8
Table 7-4. Dipole Specifications for HEBT Achromatic Bends 9
Table 7-5. Elements of Four-Quadrupole Matching Section in a Target Line 12
Table 7-6. Beam-Expander Components 15
Table 7-7. Nominal rms Input-Beam Parameters of Beam Expander 16

Table 7-8. Beam Half-Sizes x and y and "Radii" r in the Beam Expander 16
Table 7-9. Beam Half-Sizes x and y in the 20-Meter Drift to the Target 17
Table 7-10. HEBT Alignment Requirements 22
Table 7-11. Hot-Spot Intensities 28
Table 7-12. Beam Half Sizes x and y at Target after Quadrupole-Doublet Failure 31
Table 7-13. Beam Half Sizes x and y at Target as Function of Beam Current 31

7.0 THE HEBT AND BEAM EXPANDER

7.1 SYSTEM OVERVIEW AND PURPOSE

7.1.1 Overview

The purpose of the high-energy beam transport (HEBT) and expander, shown in Fig. 7-1, is to transport the 200-mA, 1-GeV beam from the accelerator to either a tuneup beamstop or one of two tritium-producing targets while expanding the beam to a large, rectangular geometry with uniformly distributed intensity. The beam is expanded, reducing the power density to prevent any damage to target or beamstop components. A uniform intensity distribution is required to efficiently use the entire target cell volume for tritium extraction.

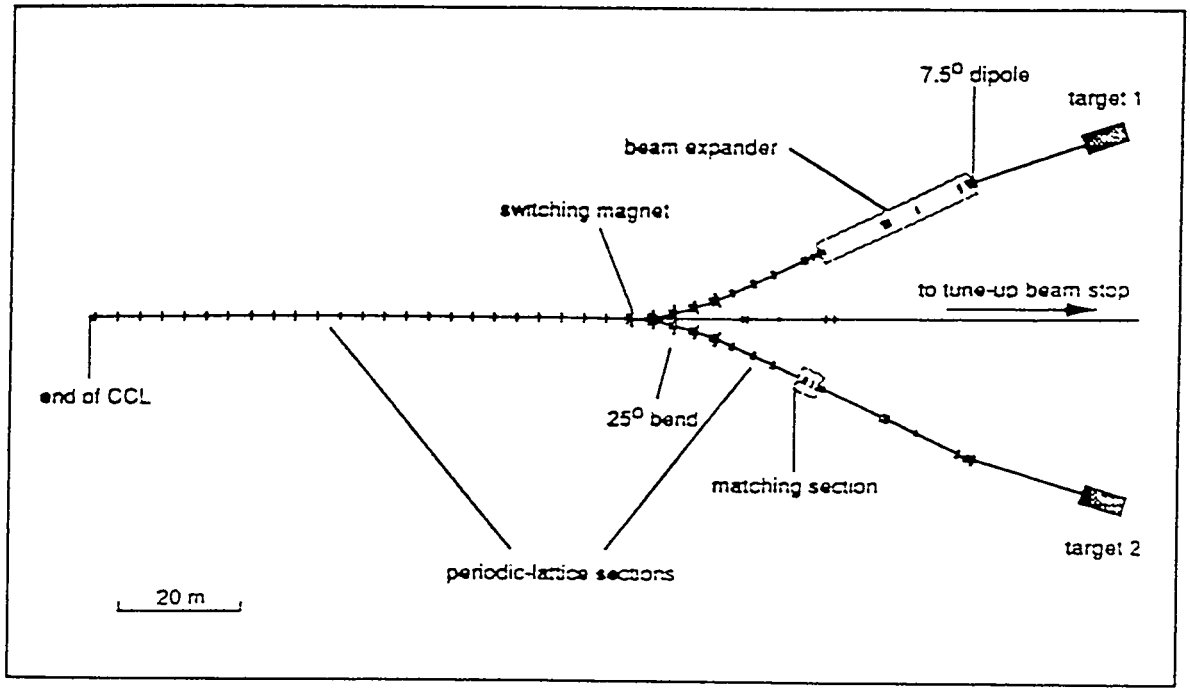


Fig. 7-1. The HEBT system.

The design is modular, consisting of an initial periodic-lattice section common to all beamlines, a dc switching magnet that directs the beam to one of the three transport beamlines, and the transport beamlines from the switching magnet to the beamstop or targets. The two transport beamlines leading to the targets after the switching magnet include each an achromatic bend (the switching magnet is the first element of the achromatic bend), while all three beamlines include a second periodic lattice section, a matching section, and a beam expander. The initial periodic-lattice section continues the CCL lattice and allows longitudinal expansion of the beam. The beam is bent by the achromatic bends in a fashion that is independent of small energy differences in the beam. The matching section properly matches the beam for the expander, which then both increases the transverse dimensions of the beam and flattens the transverse beam intensity distribution from a Gaussian-like distribution to a nearly uniform distribution. The final 7.5° shield dipole bends the beam

slightly before the target to help shield the beamline elements upstream of the magnet from backstreaming neutrons and photons from the target (backshine). The modularity of the design makes it possible to alter individual sections without affecting the rest of the system. The strategy used to design the HEBT, as with the accelerator, was to avoid any significant transitions for the beam that could lead to beamloss.

7.1.2 Beam Expander

The beam expander section is the most important part of the HEBT, expanding the beam to the size of the target window while redistributing the intensity from a small, elliptical, and peaked (Gaussian or parabolic) beam-intensity distribution—typical for accelerators—to a very large rectangular, nearly-uniform beam-intensity distribution. The beam redistribution is required to optimize tritium extraction in the target while protecting the target and target window from damage that would result from a peaked beam-intensity distribution. Beam redistribution is accomplished with a combination of nonlinear elements (octupoles with a duodecapole component) and linear elements (drifts and quadrupoles). The beam expander delivers virtually all beam particles to the target, reducing activation and avoiding damage to areas outside the target. The four quadrupoles of the matching section optimize the beam-intensity distribution at the target by delivering a properly focused beam to the nonlinear expander elements. The last two quadrupoles in the beam expander adjust the size of the irradiation area at the target.

7.1.3 Magnetic Elements

The baseline design for magnetic elements throughout the HEBT calls for using electromagnetic devices, with the exception of the nonlinear expander elements (octupole and duodecapole). The electromagnet baseline has been chosen primarily because of the need for variability and the uncertainty of the radiation resistance of permanent-magnet materials at the current time. Preliminary magnetic designs for the nonlinear elements of the beam expander indicate significant difficulty in fabricating a combined-function electromagnetic octupole-duodecapole with the required operational parameters. Using permanent-magnet materials would greatly simplify these devices.

7.1.4 Targets and Beamstop

The beamstop line is used during linac startup and tuning of both the linac and the HEBT before switching the beam to one of the targets for *production* operation. The two transport beamlines leading to the targets include bends that separate the two targets. The target separation distance is chosen to incorporate a single processing facility located between the targets. A final inward bend of 7.5° in each transport beamline helps to shield the upstream portion of each transport line from neutron backshine.

7.1.5 Engineering

The engineering design goal for the HEBT is to maximize the reliability and maintainability while minimizing cost for the overall system. The design uses many of the same components that are used in the accelerator. For example, the quadrupole doublets of the periodic lattices consist of the same 18-cm-long quadrupoles as those used in the CCL intertank spaces. The mechanical design of the HEBT has developed preliminary designs or

workable concepts for all beamline sections, as shown in Fig. 7-1. Specific details for component designs, alignment, and interface requirements and general engineering considerations applicable to the HEBT as a whole are discussed in Sec. 7.4.

7.1.6 Diagnostics

The design goal for the beam diagnostics in the HEBT is to minimize beamloss and off-nominal beams while maximizing the reliability of the overall system. Sufficient beam-diagnostic instrumentation and beam-correction elements are required to determine the necessary beam parameters and correct any off-nominal beams. Beam expanders, for example, are sensitive to magnet misalignment and beam-centroid jitter, therefore position measurements must be made in each cell. Both dc steerers and fast steerers are needed to correct off-nominal conditions.

Three basic types of beam diagnostics and instrumentation are provided: (1) characterization, (2) operational, and (3) protection. *Characterization* diagnostics more fully measure the six dimensions of beam phase space; however, these measurements require intercepting the beam. *Operational* diagnostics provide a subset of beam information using noninterceptive or minimally interceptive techniques. The average cw beam-power density will vary from tens to approximately a million kW per cm^2 because of the beam expansion near the target. Operational diagnostics will be designed to operate throughout this range. The bulk of the diagnostic devices will be of the operational type. The bulk of the characterization diagnostics used for beam tuneup will reside in the beamstop line of the HEBT. *Protection* diagnostics are used to detect beamloss or severely off-nominal beam conditions, and to interrupt the beam delivery to the HEBT, either through the fast-protect system or through other slower methods, depending on the severity of the given condition. Further descriptions of the diagnostic instrumentation and measurement systems are discussed in other sections of this chapter.

7.2 BEAM TRANSPORT LINE

7.2.1 Physics Design

The HEBT was designed using the code TRACE 3-D [7-1]. The nominal input-beam Twiss or Courant-Snyder (CS) parameters and emittances used for the HEBT were generated by running a 10,000-particle end-to-end simulation of the accelerator. The parameters and emittances are given in Table 7-1. The transverse emittances are laboratory emittances representing an average of the quoted horizontal and vertical emittances of the accelerator output-beam distribution. In Fig. 7-2, the transverse-rms-beam envelope is plotted as a function of distance along the beam transport line from the CCL to the start of the beam expander.

A long periodic-lattice section immediately following the CCL is part of a very conservative HEBT design. This design allows the beam to expand longitudinally through the periodic lattice, resulting in beam bunches with insignificant space-charge forces at the end of the lattice (beginning of the achromatic bend). Furthermore, major lattice transitions upstream of the matching section are avoided, thereby contributing to the insensitivity of the design to the off-nominal HEBT input beams that may result from fault conditions in the accelerator. Finally, the long periodic lattice provides ample space for diagnostics for beam characterization and corrector elements for correcting off-nominal beam conditions.

Table 7-1. Nominal HEBT Input Beam

Horizontal	Vertical	Longitudinal
$\alpha_x = -1.0918$	$\alpha_y = -0.1112$	$\alpha_L = -0.0517$
$\beta_x = 0.4925$ cm/mrad	$\beta_y = 0.2485$ cm/mrad	$\beta_L = 18.254$ deg/MeV
$\varepsilon_x = 0.018$ π-cm-mrad	$\varepsilon_y = 0.018$ π-cm-mrad	$\varepsilon_L = 0.608$ deg-MeV

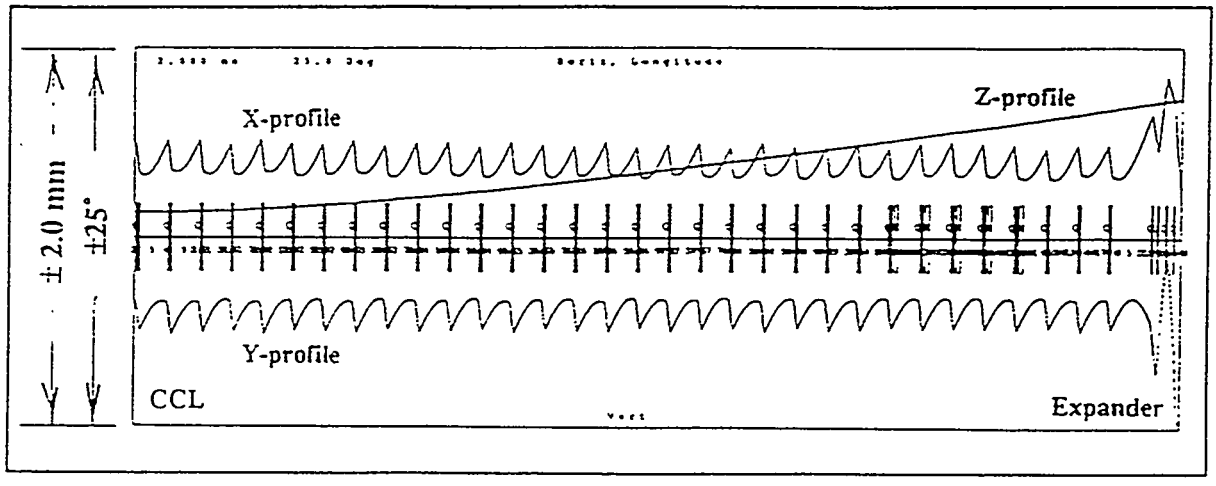


Fig. 7-2. RMS beam envelopes between the CCL and the beam expander.

7.2.2 Initial Periodic Lattice

A schematic of the initial periodic-lattice section, located immediately downstream of the CCL, is shown in Fig. 7-3. Diagnostic instrumentation in this section serves to study the CCL output beam, to characterize the beam, and to correct for beam jitter before going into the matching sections of either the tuneup or the target beamlines.

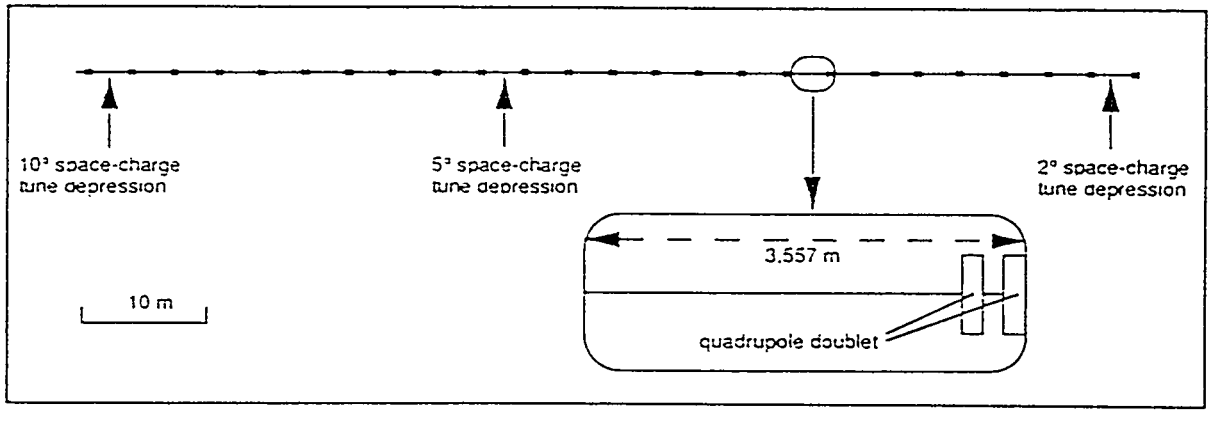


Fig. 7-3. Initial periodic-lattice section.

The periodic-lattice cells have the same magnetic components as those of the high-energy portion of the CCL, both to avoid a major lattice transition and to simplify engineering considerations. The total length of each cell is 355.7 cm, equivalent to the $9.5\beta\lambda$ cell length in the CCL. Transverse focusing is provided by quadrupole doublets. Each quadrupole is 18 cm long, with an 18-cm drift separating the two magnets of the doublet. The transverse focusing is tuned for zero-current phase advance per cell of 70°, as in the CCL. Because there are no bunching cavities in the HEBT, the beam spreads longitudinally, causing a decrease of the space-charge forces along the line. The 10° space-charge tune depression at the exit of the CCL is reduced to 2° after 24 cells, immediately before the achromatic bend. Physics requirements for the beamline elements of the periodic-lattice cell are listed in Table 7-2.

Table 7-2. Elements of Initial periodic-lattice section

Element Type	Length (m)	Strength (T/m)
drift	3.017	
quadrupole	0.180	37.244
drift	0.180	
quadrupole	0.180	–37.244

The first cell of this periodic-lattice section, however, is different because it functions as a bridge between the end of the CCL, at the exit of the $7\beta\lambda$ tank, and the beginning of the first complete cell, as shown in Table 7-2. To maintain the linac periodicity, the initial drift of this first cell is only 19.8 cm (instead of 3.017 meters).

The quadrupole doublets are engineered into the same modular units with nearly identical linear-rail mounts as in the CCL intertank spaces. The magnets have aperture radii of 2.75 cm, providing the same aperture-to-beamsize ratio for the nominal beam as that in the high-energy end of the CCL. The preliminary magnetic design for these quadrupoles will provide a maximum G·L of 7.5 T, a substantial 12% margin over the required integrated strength. The linear-rail mounting system will use fewer vacuum valves and different diagnostic and beam correction devices than those used in the CCL. There are 25 vacuum valves in the initial periodic lattice to provide isolation at various points for leak testing and fault analysis, and also to allow flexibility for inserting additional diagnostics during beamline development and commissioning. The valves are electropneumatic and are held open by air pressure in the 70–100 psig range. The same Helicoflex Quick Flanges and all-metal high-vacuum seals used in the accelerator will be used in the HEBT. The diagnostics and beam-correction devices required in each rail-mounted quadrupole-doublet unit will be incorporated as an integral part of each module, which are identical to those designed for the CCL linac. A total of 78 such units are required in the HEBT. The magnets use glass-coated, 0.2576-inch, square, directly-cooled field coil conductors potted in calcium aluminate cement for high radiation resistance.

Twenty-five quadrupole-doublet units (24 complete cells plus one bridging cell) are present in the 89-meter-long initial periodic-lattice section leading to the switching magnet. As can be seen in Fig. 7-4, the units are spaced 355.7 cm apart and are supported on individual stands. Each module includes a pair of 18-cm-long quadrupoles, a 5-cm vacuum valve, and a low-power steering-correction magnet for both the horizontal and vertical planes. Not shown in the figure are the beam diagnostics that would be mounted between the quadrupole magnets (including a beam-position monitor and other devices), the bellows, and

the quick-disconnect flanges with all-metal vacuum seals (see Chap. 3). The doublet modules are supported on rack-out alignment stands consisting of the same linear-rail system that is used in the linac (see Chap. 9). The rails are mounted transverse to the support stand, continuing the same module maintenance and removal scheme as in the linac, namely from the aisle side of the beamline.

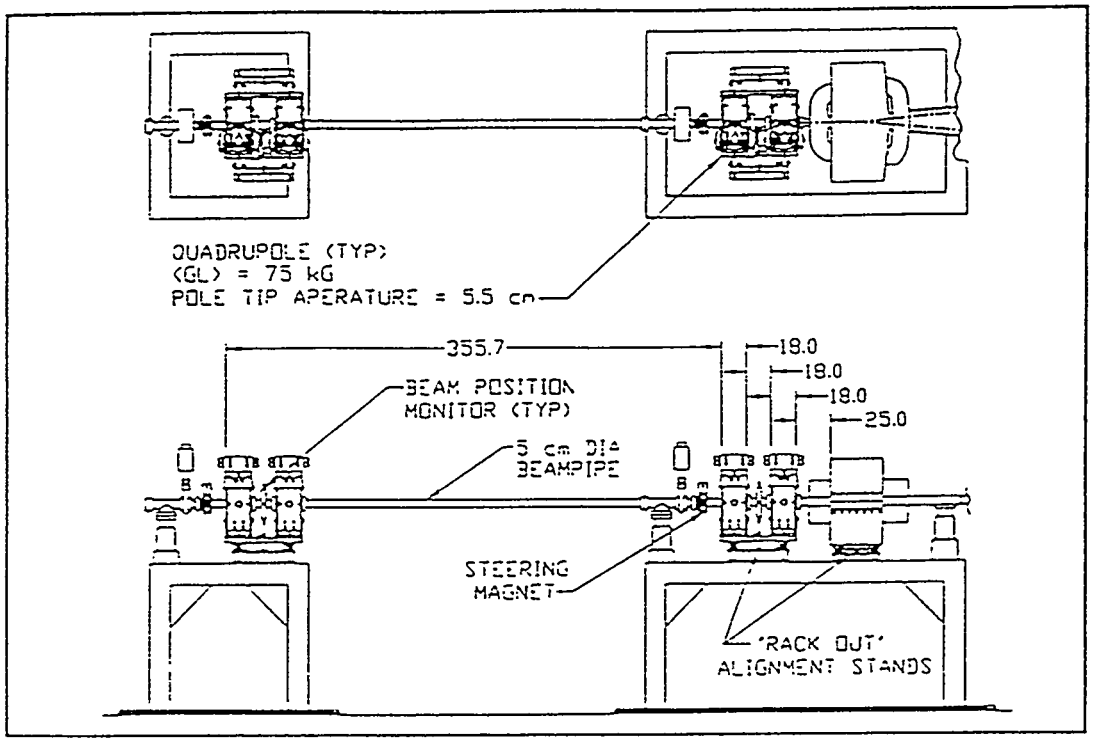


Fig. 7-4. HEBT doublet mechanical support.

Vacuum calculations show that ion pumps with a several hundred l/s capacity will be needed periodically along the transport line to maintain the beamline at $<10^{-6}$ torr. The out-gassing rate of the beamline under anticipated beamloss conditions will determine the final size and distribution of the ion pumps. Ample pumpout ports have been designed into the HEBT to provide for a large range of anticipated out-gassing rates.

7.2.3 Lattice Diagnostics

A beam-centroid-measurement system will be required between each magnet of the quadrupole doublets to measure beam position, as in the CCL and the BCDTL. The beam position data will be used to control beam-steering elements, placed along with the diagnostics, to minimize beamloss throughout the HEBT. Longitudinal beam centroids will not be measured throughout the HEBT (except for the measurements associated with energy and phase control of the final few CCL cavities) because there are no longitudinal bunching cavities in the HEBT. However, peak beam currents or intensities will be measured with the same microstrip probes to track relative changes in beam current.

The HEBT input beam (from the accelerator) will be characterized by several flying-wire beam-profile measurement systems. Five to seven systems are combined into a group to

provide horizontal and vertical beam information necessary to calculate the Twiss (or CS) parameters and emittances of the HEBT input beam. The beam-profile information will be used to tune the HEBT input beam, if possible, and the beam exiting the matching section upstream of the beam expander.

Pulsed and cw beam-current measurements will be installed near the beginning and end of the straight HEBT beamline. Current fluctuations will indicate off-normal accelerator conditions. Pulsed-beam current measurements will also provide high-frequency beam-current jitter information that impacts accelerator operation but will in general not impact HEBT operation. The current measurements made at the CCL output and in the HEBT will be used to calculate integrated beamloss in the HEBT, providing a second layer to the beamloss protection. Severe beamloss will cause a fast-protect event, whereas small but off-nominal beamloss in the HEBT will indicate the need for retuning or maintenance.

BLMs will be placed slightly downstream of each of the quadrupole doublets and offset from the beamline center. Errant protons or beam bunches are most likely to impinge on the beampipe in these regions, producing the largest signals in the BLMs. The BLM output signal will be hardwired into the accelerator fast-protect system to enable rapid shutdown of beam in the event of a fault outside preset limits. The BLM signal will also be input to the computer control system to detect patterns of lower-level beamloss indicative of potential problems that can be resolved by maintenance or improved tuning of the accelerator or HEBT.

7.2.4 Achromatic Bend

The five-cell, 25°, achromatic bend for one of the target lines is shown in Fig. 7-5. The two target lines, which have the 25° achromatic bends, serve to physically separate the targets from one another and from the tuneup beamstop. The first dipole is the switching magnet which is used to direct the beam toward either of the two targets or the tuneup beamstop.

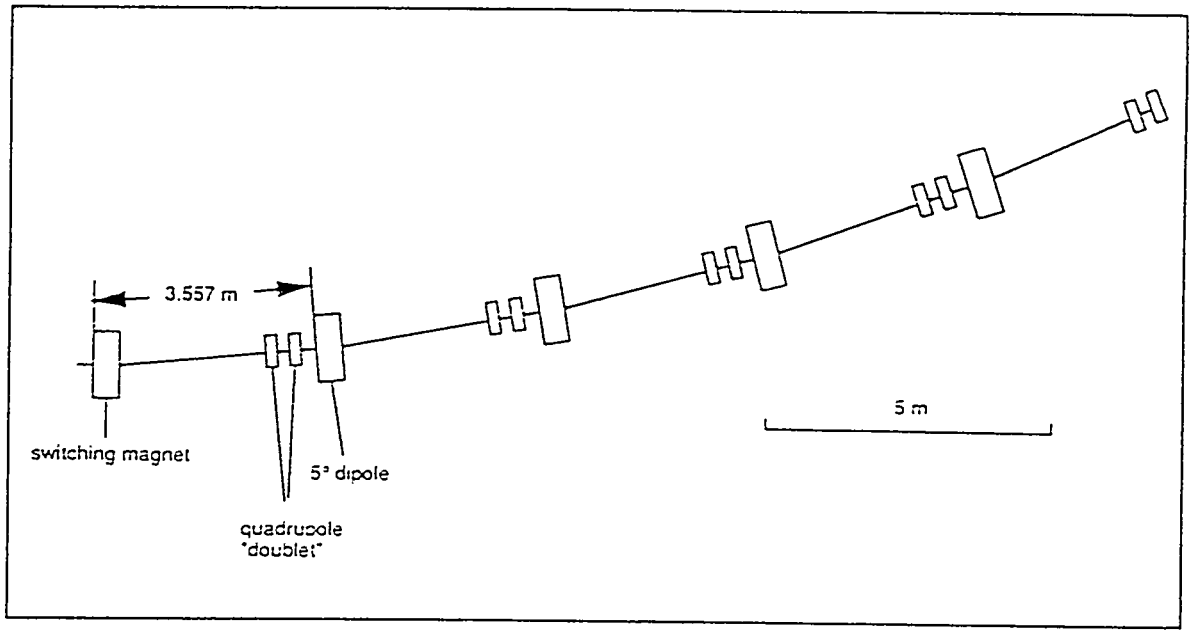


Fig. 7-5. The five-cell, 25°, achromatic bend.

Care must be taken when bending beams in the presence of space charge. A zero-current achromatic bend was chosen over a nominal-current design. This can be stated as choosing the terms of the first-order transfer matrix, R, as $R_{16} = R_{26} = 0$ for $I = 0$ rather than setting $R_{15} = R_{25} = R_{16} = R_{26} = 0$ for $I = I_{nominal}$, as required for the nominal-current design. The zero-current design is easy to tune and is insensitive to beam-energy jitter. With the nominal-current design, the bend would be extremely difficult to tune, and beam jitter with energy fluctuations would be a problem.

Our simulations indicate that no significant emittance growth will result from the zero-current achromatic bend. This is because the initial periodic-lattice section dramatically reduces the space-charge tune depression from that at the accelerator output. Calculations show that after five cells of the initial periodic lattice, the space-charge forces are sufficiently reduced, causing extremely small emittance growth. The number of cells needed in the initial periodic lattice may depend less on space-charge forces and more on how far the targets and tuneup beamstop should be separated from the accelerator.

The achromat is designed with five cells, resulting in a phase advance of 72° per cell, which very nearly matches the 70° per cell phase advance in the initial periodic-lattice section, avoiding a major lattice transition. The achromat cells are simply a continuation of the initial periodic-lattice cells with a 5° dipole inserted into the 3.017-meter drift. The dipoles are placed as far upstream in the cell as possible to avoid mechanical interference with components of the target and tuneup beamstop lines. The elements in each cell of the achromatic bend are listed in Table 7-3. Since the beam in the HEBT is very nearly the matched beam for the achromat, the baseline design for APT is chosen to be a first-order achromat (without sextupoles). The Twiss or Courant-Snyder (CS) parameters (α_x, β_x, α_y, β_y) for a beam that is matched to a first-order achromatic bend will have no linear dependence on particle momentum [7-2], and the beam will stay elliptical.

Table 7-3. Elements of the Achromatic-Bend Cell

Element Type	Length (m)	Strength (T/m)
drift	0.250	
dipole	0.415	1.190
drift	2.352	
quadrupole	0.180	37.901
drift	0.180	
quadrupole	0.180	−37.647

The inherent benefits in the modular design of the HEBT have already been demonstrated with the achromatic bend. Originally, 7.5° dipoles were chosen to avoid component interference. However, the (five-dipole) 37.5° bend resulted in an excessive separation between targets. To reduce the distance between targets, the 7.5° dipoles were replaced by 5.0° dipoles to get a 25.0° total bend. This was accomplished without consequence to the rest of the system, except for insignificant changes in the settings of the target-line matching-section quadrupoles.

To achieve achromaticity, the elements of all five cells of the achromatic bend are the same. Thus, all dipoles (with the exception of the switching magnet) and all quadrupoles are constructed identically. The dipoles have parallel pole faces and 5.0-cm gaps; the quadrupoles have aperture radii of 2.75 cm. The maximum dispersion in the achromatic bend is 0.463 cm per percent δ p/p, assuring transmission of a beam to 25 rms and with ±1% δp/p

(±15-MeV energy shifts). If the transverse extent of the beam is smaller, for instance 20 rms, then the momentum acceptance would increase to ±2% δp/p.

The region around the HEBT switching magnet, shown in Fig. 7-6, consists of the switching magnet (the first dipole in the achromatic bend) and three beamlines. The two outboard legs, which include the ±25° achromatic bends, lead to the targets, and the straight-through leg leads to the tuneup (graphite) beamstop. The beamstop line is used for tuning up the accelerator and the HEBT, and is capable of absorbing the full 200-MW cw beam on a series of graphite plates indefinitely (the beamstop is expected to last the lifetime of the facility given the anticipated operating schedule and tuning needs of the accelerator). Figure 7-6 shows the switching magnet and the next three 5° bending magnets in each target leg following the split in the beamlines. All quadrupole doublets in the achromatic bend are the same design as those in the initial periodic-lattice section. The placement of the dipole magnets at the far upstream end of each cell provides sufficient space to use the standard EMQ doublets in all three beamlines.

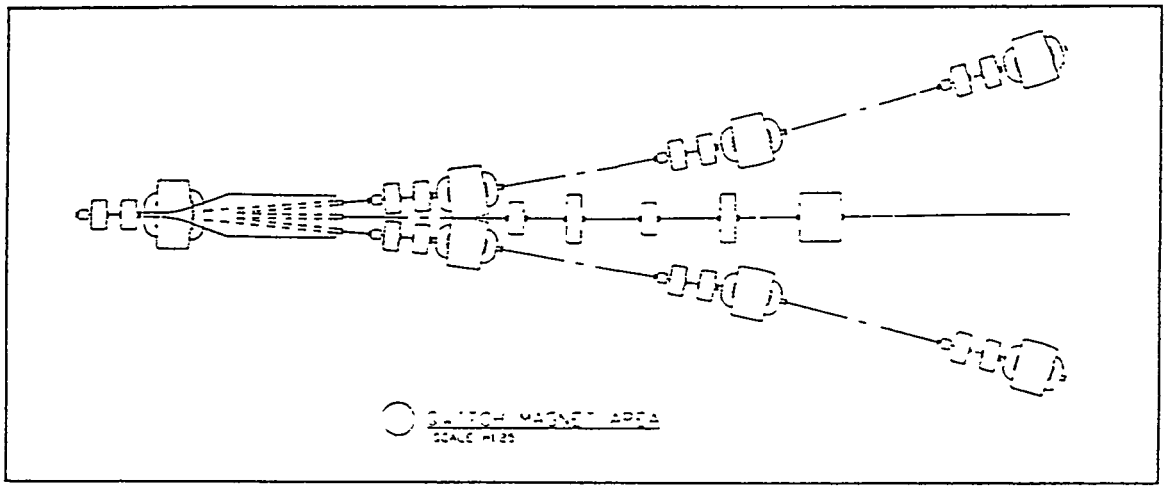


Fig. 7-6. HEBT switching magnet area.

The bending magnets in the achromatic bend are designed with a pole-tip width 3 times the gap for good field uniformity over the size of the beam (the switching magnet is 5 times the gap to accommodate the switching angles and off-momentum beamstops). Specifications for the HEBT dipoles in the achromatic bends are given in Table 7-4.

Table 7-4. Dipole Specifications for HEBT Achromatic Bends

Number of Dipoles	9 (8 + 1 switching magnet)
Bend Angle of Dipoles (deg)	5
Structure	"H" type (solid or laminated)
Minimum Aperture (cm)	6.03
Pole-tip Field (T)	1.19
Number of Amp-Turns	63,300
Conductor	mineral insulated, 0.75-inch, square, directly cooled
Weight (kg)	930 (1625 kg for switching magnet)
Power Supply (kW)	~35

7.2.5 Bend Diagnostics

A beam-centroid-measurement system will be required between each magnet of the quadrupole doublets, as was described for the initial periodic-lattice section. Steering correctors will be provided in the achromatic bend for small beam-centroid adjustments. The impact of typical steering corrections (caused by breaking the symmetry between the cells) will have an insignificant effect on the achromaticity of the bend.

Diagnostics provided in the last cells of the CCL and the initial periodic-lattice section will measure the beam energy and momentum spread. Simulations of the APT accelerator show that the nominal momentum spread anticipated, resulting from random fluctuations in phase and amplitude control, will be less than 0.4%, which is significantly less than and well within the acceptance of the bend. The first line of defense against significant momentum spread or slightly off-momentum beams (that would result in beamloss) will be the beamloss monitors (discussed below). A second line of defense will be tracking trends of increasing momentum spread or energy drift and correcting these trends by tuning the accelerator before the parameters drift out of the nominal operating ranges.

Under certain fault conditions in the accelerator (such as beam bunches falling out of accelerating buckets), there will be some very low-momentum components to the beam. Analysis of beam bunches falling out of RF buckets in the accelerator show that a distribution of low-momentum components is possible from 200–650 MeV (particles that are accelerated to less than 200 MeV are lost in the accelerator). The low-momentum beam bunches will be bent sharply in the first dipole, requiring an off-momentum beamstop (or collimator) inside and downstream of the switching magnet. A preliminary design for this low-momentum beamstop is shown in Fig. 7-7. The low-momentum beamstop in the switching magnet will be sufficiently thick to stop all low-momentum beam components and will be electrically isolated to measure the beam current deposited. These data will be monitored by the diagnostic system, providing information on accelerator performance and faults.

BLMs will be placed slightly downstream and offset from the beamline center from each of the quadrupole doublets, as described in the initial periodic-lattice section. BLMs will also be placed around the low-momentum beamstop to provide a second layer of beamloss monitoring of this region (the first layer of protection is provided by current monitors on the low-momentum beamstops and toroidal current monitors on the beamline itself).

7.2.6 Second Periodic Lattice

The second periodic-lattice section, located downstream of the achromatic bend, serves to characterize the beam and to counteract any remaining beam-centroid jitter before the beam moves into the four-quadrupole matching section. Two cells in this section are the same as those in the initial periodic-lattice section, described in Table 7-2, again avoiding a major lattice transition. The engineering considerations are identical to those in the initial periodic-lattice section.

The beam emittance is measured in this and the following beamline section with five flying-wire beam-profile monitors. In cases where the error in a beamsize measurement is proportional to beamsize, that is, where $\Delta x = bx$ or $\Delta y = by$, the optimum phase advance between profile monitors is π/N, where N is the number of profile monitors. These monitors must cover a total phase advance of $((N-1)/N)\cdot\pi < \pi$. The error in emittance is:

$$\Delta\varepsilon = \left(2b/\sqrt{N}\right)\varepsilon.$$

For example, for $N = 4$ and $b = 0.1$, one finds $\Delta\varepsilon = 0.1\,\varepsilon$. Because the phase advance per cell is 70°, two cells and their adjacent drifts are adequate to perform an emittance measurement. Data from the two flying-wire beam-profile monitors in the second periodic-lattice section, placed between each magnet of the quadrupole doublets, along with the beam-profile monitors in the following matching section, are used to fully characterize the transverse emittances and CS parameters.

The remaining diagnostic design in this lattice (beam-position monitors and beamloss monitors) is identical to that in the initial periodic-lattice section. The initial monitoring and correction of the beam position (both slow drift and fast jitter of the centroid) is performed in the initial periodic lattice. Because the beam expander is extremely sensitive to beam centroid offset, however, and because the large aperture of the HEBT could transmit beams that are unacceptable to the beam expander, the beam position monitors and correction elements in this section of the HEBT will be critical for determining the beam centroid position and correcting any remaining slow position drift or fast position jitter.

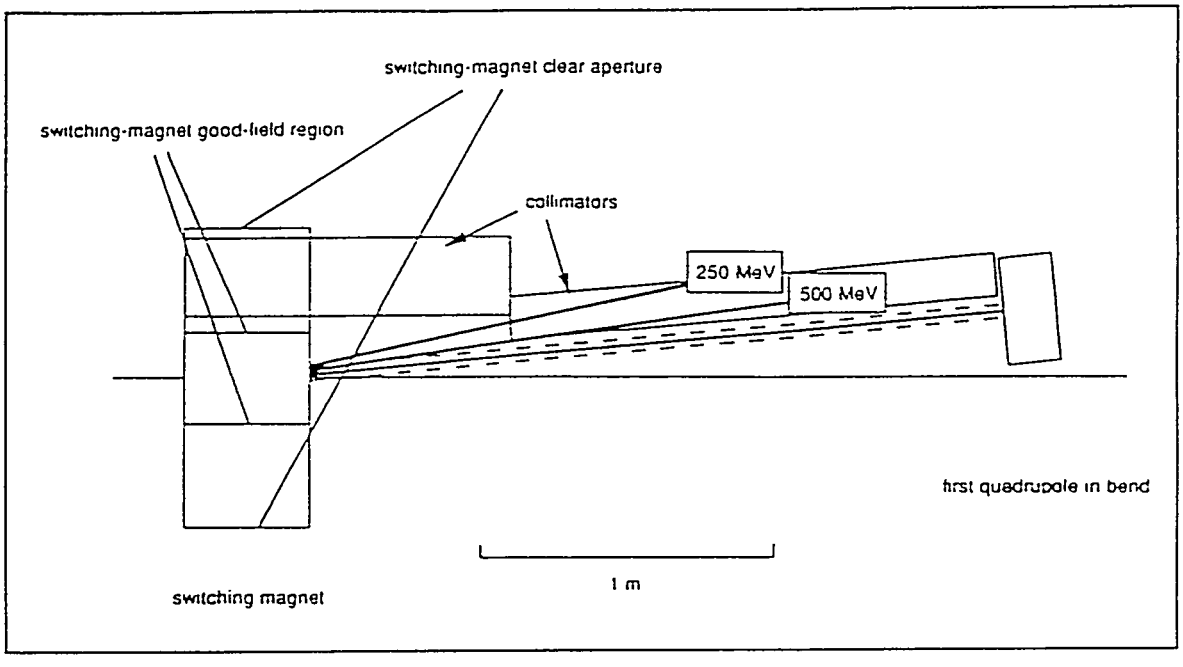


Fig. 7-7. Low-momentum beamstop design for switching-magnet.

7.2.7 Four-Quadrupole Matching Section

The HEBT matching section is schematically shown in Fig. 7-8. Four independently tunable quadrupoles make up the matching section. The matching section transforms a beam of approximately round cross-section into one of large aspect ratio required at the first beam-expander element and thus represents the first major lattice transition for the beam in the HEBT.

The matching-section elements for one of the two target lines are listed in Table 7-5. Small differences in the matching-section quadrupole strengths exist between the one tuneup and the two target beamlines. The differences in the tunes (quadrupole strengths) of the two matching sections result from a different periodicity in the target and tuneup beamlines and the presence of space charge. The space-charge tune shift (or defocusing) decreases as a function of distance from the accelerator because no longitudinal bunching occurs in the HEBT. The strengths of the matching-section quadrupoles in the target beamlines compared with the tuneup beamline differ by up to 2.2% because of the periodicity difference and the difference in distance from the CCL to the respective matching sections. Except for these differences, the matching sections are very similar. The matching sections are kept as similar as possible to facilitate transferring the beamline tune for the tuneup beamline to the target lines. This is accomplished by using identical geometries for each four-quadrupole matching section (there is one matching section in each HEBT transport line). Independently tunable matching-section quadrupoles are essential to correct for off-nominal conditions (discussed in Sec. 7.3). The matching-section quadupoles can be adjusted separately with either (1) independent power supplies or (2) a common power supply with tunable shunts.

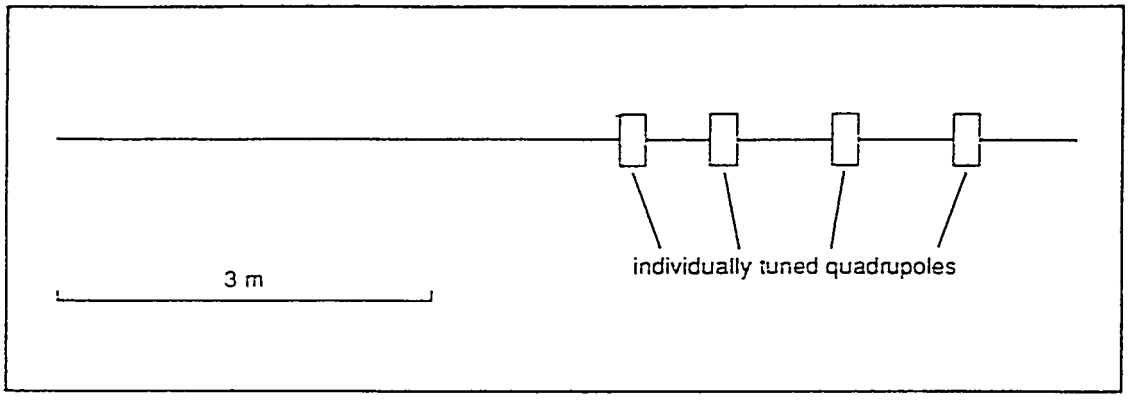


Fig. 7-8. Four-quadrupole matching section.

Table 7-5. Elements of Four-Quadrupole Matching Section in a Target Line

Element Type	Length (m)	Strength (T/m)
drift	4.500	
quadrupole	0.210	18.332
drift	0.500	
quadrupole	0.210	−41.600
drift	0.750	
quadrupole	0.210	18.889
drift	0.750	
quadrupole	0.210	19.071
drift	0.750	

shielding (not yet designed) in this region. This allows using the same quadrupole-magnet engineering design as employed in the CCL and the periodic lattice sections of the HEBT. Scraping to 7 rms in this region allows controlled and localized deposition of beam particles that would otherwise be lost in the expander. Preliminary magnetic designs show that the second quadrupole of the matching section would require a higher-current power supply and that the coil has sufficient cooling to dissipate the increased power.

7.2.8 Matching-Section Diagnostics

Five flying-wire beam-profile-measurement systems for both transverse planes will be installed in the matching section, one before the first quadrupole and one after each of the four quadrupole magnets. As noted above, the data from these devices will be combined with the data from the BPMs in the second periodic lattice to fully describe the transverse beam entering the beam expander. This information will be used to tune the matching section for the beam required by the expander.

Halo detectors and scrapers located in the matching section, or immediately thereafter, will monitor the beam halo and scrape sufficient beam to prevent irradiation of beamline elements in the beam expander. The halo detectors will sample the beam down to 7 rms, with minimal interception, to determine the quantity of beam that will be lost in the beam-expansion region (beam that does not impinge the target window). Growth in beam halo will indicate the need to retune the accelerator and/or the HEBT.

BLMs will be placed after each quadrupole of the matching section. The signals will be used as described previously to protect against faults and to alert operators to slowly increasing beamloss that may require retuning of the accelerator and HEBT.

For most "out-of-tolerance" situations, where the accelerator or HEBT parameters have changed only incrementally from the normal configuration, this kind of retuning would be carried out on-line, with no interruption of operation. For more consequential faults and/or sudden large increases in beamloss, production would be halted, and the beam would be switched to the high-energy beamstop and reduced in intensity as appropriate. The accelerator would then be retuned by the operators to return it to the standard parameter configuration, after which it would be switched back to the target to resume production. This procedure might take anywhere from a few minutes to several hours, depending on the problem, but would not generally require shutdown of the accelerator.

7.3 BEAM EXPANDER

7.3.1 Beam-Redistribution Method

Transverse particle-beam phase space can be manipulated, one plane at a time, by nonlinear, even-multipolarity elements such that during subsequent transport through linear elements, the beam fringes are folded into the core of the beam [7-3, 7-4]. A system of two nonlinear elements combined with the appropriate linear transport can be designed to transform the peaked intensity-distribution (Gaussian or parabolic) of a typical input beam into a nearly uniform distribution for both transverse phase-space planes. The result, for the APT application, is to transform the beam distribution at the exit of the accelerator to a rectangular, nearly uniform-intensity distribution with the required dimensions at the target.

For high-rigidity beams, such as 1-GeV protons, building nonlinear beamline elements that are sufficiently strong to fold the inner-beam fringes with an aperture large enough to prevent scraping of the outer-beam fringes is difficult. Using the lowest-order, nonlinear element of even-multipolarity (the octupole, N = 4) to accomplish the beam redistribution while maximizing the aperture within the physical and magnetic constraints of the element is the best compromise. The degree of uniformity in the intensity distribution that is achievable with a beamline consisting of quadrupoles for a proper first-order focus and octupoles for beam redistribution depends on the input-beam distribution. One can produce a final intensity distribution that is essentially uniform with an initially parabolic intensity distribution; this is not possible, however, using only octupoles with the more realistic Gaussian input-beam distribution. Octupole magnets with the required strength to redistribute the inner-beam fringe cause an excessive folding of the outer fringe, resulting in excessive beamloss downstream of the octupoles. Adding a component of the next-higher even-multipolarity order, the duodecapole, counteracts this effect of the octupole at the outer-beam fringe. Such a solution is required where the loss of even a minute fraction of the outer-beam fringe cannot be tolerated. An APT beam-redistribution system consisting of octupoles exclusively will transmit 4.5 rms of the beam to the target, whereas the addition of the duodecapole component will transmit 7 rms. Particles that may be in the outermost, extreme beam fringe—between 14–25 rms (transmitted through the accelerator and HEBT up to this point)—will be scraped in a controlled region before arriving in the beam-expander region, preventing random losses along extended regions of the beamline.

The complete beam expander consists of five parts: (1) the matching section (previously described) that prepares the beam for the first nonlinear beamline element; (2) the first nonlinear element that manipulates the beam in one transverse phase plane; (3) the linear elements that follow and cause folding in that transverse plane and prepare the beam for the second nonlinear element; (4) a second nonlinear element that manipulates the beam in the other transverse phase plane; and (5) the linear elements that cause folding in the other transverse plane and expand the beam to the desired irradiation area at the target. While nonlinear beamline elements initiate the process of beam redistribution, sections containing linear elements, including long drifts, are necessary for the beam to evolve. A long drift downstream of the last two quadrupoles avoids excessively large gradients for these magnets and unnecessarily large beam divergence at the target. The maximum divergence for the APT system is 17 mrad in the x-plane (horizontal) and 30 mrad in the y-plane (vertical).

7.3.2 Physics Description

A schematic of the beam expander is shown in Fig. 7-9, and a list of the beam-expander components is given in Table 7-6. The four-quadrupole matching section provides the proper input beam into the first nonlinear element (first octupole with duodecapole component) that initiates beam redistribution in vertical (y) phase space. The first two quadrupoles of the beam expander, located between the nonlinear elements, assures the proper beam focus into the second nonlinear element that initiates beam redistribution in horizontal (x) phase space. The last two quadrupoles of the beam expander allow tuning the irradiation area at the target to the nominal horizontal half-width of 25 cm and vertical half-height of 50 cm. Both nonlinear elements are combined-function octupole and duodecapole devices.

The last two quadrupoles in the expander can be used to tune the beam to a large range of different sizes limited only by the strength of the magnets and the length of the drift to the target. Earlier beam-expander designs, with only two quadrupoles, were not tunable in this way. The last two quadrupoles are also tuned to provide both a vertical and horizontal waist (minimum beam dimension) in the final 20-meter drift to facilitate shielding of beamline

components from backstreaming neutrons from the target. Further, a 7.5° *shield dipole* (discussed below) was recently added downstream of the last two quadrupoles, necessitating a minor change in the tune of the final two quadrupoles over previous designs to produce the required beamsize at the target. Dispersion in the shield dipole slightly increases the horizontal size of the beam at the target. Energy jitter in the beam resulting from nominal operation will not substantially increase the beamsize on target but will have the beneficial side-effect of slightly smoothing out any nonuniformity in the beam-intensity distribution.

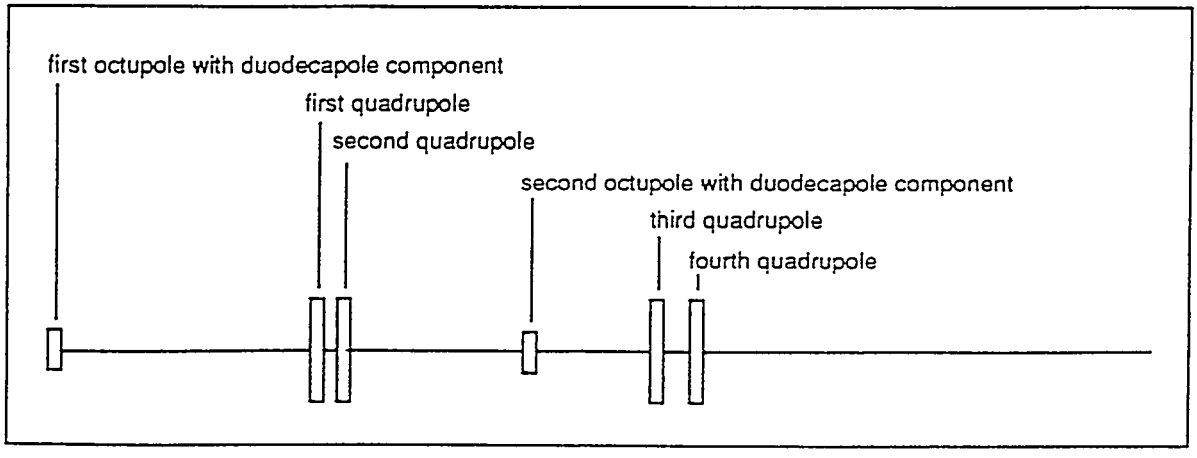


Fig. 7-9. Beam-expander layout.

Table 7-6. Beam-Expander Components

Element Type	Length (m)	Strength
octupole (with duodecapole)	0.500	7.55×10^{4} T/m^3 (1.30×10^{8} T/m^5)
drift	10.000	
quadrupole	0.500	7.224 T/m
drift	0.500	
quadrupole	0.500	−7.502 T/m
drift	4.546	
octupole (with duodecapole)	0.500	2.30×10^{4} T/m^3 (-1.50×10^{6} T/m^5)
drift	7.000	
quadrupole	0.500	−7.252 T/m
drift	1.000	
quadrupole	0.500	6.905 T/m
drift	20.000	

The rms parameters, in TRANSPORT notation [7-5], of the (Gaussian) nominal-input beam into the expander are given in Table 7-7 for a beam with transverse rms emittances of 0.018 π-cm-mrad. This beam was generated by a 10,000-particle end-to-end simulation of the APT accelerator and transported to the expander with TRANSPORT. The matching section can be retuned for other emittances to produce the same vertical and horizontal rms spot sizes and divergence into the first and second nonlinear beamline elements. The procedure to retune these quadrupoles would be to keep x', y, and y' of Table 7-7 constant, to choose x to produce a horizontal waist in the middle of the first nonlinear element

(to minimize x-y coupling), and to calculate r_{12} and r_{34} for the new emittances. Input beams that are not Gaussian have parameters that are slightly different from those of Table 7-7. In all cases, the rms beam must have the same ratio of vertical-divergence to spot-size into the first nonlinear beamline element and the same ratio of horizontal-divergence to spot-size into the second nonlinear beamline element as the input beam of Table 7-7.

Table 7-7. Nominal rms Input-Beam Parameters of Beam Expander

Horizontal Parameters	Vertical Parameters
x = 0.03506 cm	y = 0.25714 cm
x' = 1.2857 mrad	y' = 1.8857 mrad
r_{12} = −0.9168	r_{34} = +0.9993

To quickly determine the beamsize at an arbitrary point in the beam expander, we wrote a program that follows ellipses in one transverse plane through beamlines consisting of drifts, quadrupoles, and octupoles with duodecapole component, neglecting x-y coupling because the program treats only one phase-space plane at a time. Table 7-8 lists half-widths, x, and half-heights, y, of the 7-rms ellipses (or their equivalent shapes) of a beam with emittances of 0.036 π·cm-mrad in the specified positions in the beam expander. Once the fringe of the beam is folded into the core for a phase-space plane, the concept of a beam "rms" no longer implies a Gaussian tail for that plane, but rather expresses a given fraction of the beam contained within the beam extent. Table 7-8, therefore, lists the beam extent or size that contains the fraction of the beam that is represented by the 7-rms beam ellipse in a normal distribution.

Beam footprints are rectangular everywhere except in the first nonlinear element, thus making it useful to think in terms of a beam radius r—half the length of the diagonal of the rectangle. Dimensions necessary for the beam-expander magnet apertures can be calculated from the x and y values in Table 7-8. The beam sizes can also be used for tuning the beam expander with the help of beam-profile diagnostics.

Table 7-8. Beam Half-Sizes x and y and "Radii" r in the Beam Expander

Position in the Beam Expander	x (cm)	y (cm)	r (cm)
first octupole• (entrance)	0.3 –	1.8 –	
first octupole• (exit)	0.3 –	2.0 •••	
first quadrupole (entrance)	9.3 –	4.0	10.1
first quadrupole (exit)	8.3 –	4.7	9.5
second quadrupole (entrance)	5.8 –	6.4	8.6
second quadrupole (exit)	4.3 –	6.8	8.0
second octupole • (entrance)	2.9 –	1.0	3.1
second octupole • (exit)	3.2 •••	0.5	3.2
third quadrupole (entrance)	3.5	10.0	10.6
third quadrupole (exit)	4.4	9.2	10.2
fourth quadrupole (entrance)	7.0	4.2	8.2
fourth quadrupole (exit)	7.3	2.3	7.7

•Octupole with duodecapole component
– Beam is not folded in this plane at this position.
•••Beam is folded, but intensity distribution is not uniform.

Table 7-9 lists half-widths, x, and half-heights, y, of the beam envelope along the last 20-meter drift of the beam expander containing the 7-rms beam with transverse emittances of 0.036 π·cm-mrad. Again, beam footprints are rectangular through the entire 20-meter drift. The beam has a vertical waist near z = 0.75 m and a horizontal waist near z = 4.50 m. The beam has nonuniform distributions at positions marked by *. The beamsize changes linearly with position only where the beam is tightly folded. Shielding upstream of the target and shielding for backstreaming from the target is designed using the data in Table 7-9.

Whereas the 7-rms ellipses at the target (z = 20 m) have a half-width of 27.18 cm and a half-height of 57.37 cm, the 3.5-rms ellipses have dimensions of 24.59 cm and 50.81 cm, respectively. The vertical edge is more gradual than the horizontal edge. Two reasons for this are: (1) the vertical beamsize at the target is larger than the horizontal one, and edge dimensions are proportional to this beamsize; and (2) the vertical beamsize and divergence are smaller through the first nonlinear element than the horizontal beamsize and divergence through the second nonlinear element. Because of this, beam emittance is more important vertically, making that edge more gradual than the horizontal edge. As pointed out, the numbers were established for a beam with rms emittances of 0.036 π·cm-mrad. For the smaller emittances of 0.018 π·cm-mrad now considered nominal, the edges will be less gradual than for emittances of 0.036 π·cm-mrad.

Table 7-9. Beam Half-Sizes x and y in the 20-Meter Drift to the Target

z (m)	x (cm)	y (cm)
0.00	7.30	2.24
0.25	6.87	1.62
0.50	6.44	0.98
0.75	6.01	0.35*
1.00	5.57	0.74
1.50	4.71	2.23
2.00	4.02	3.71
2.50	3.37	5.20
3.00	2.71	6.75
4.00	1.40	9.67
4.25	1.08*	10.42
4.50	0.87*	11.16
4.75	0.94	11.91
5.00	1.35	12.65
10.00	9.94	27.56
20.00	27.18	57.37

*Beam has a nonuniform distribution.

The tuneup beamline also includes an expander section that delivers a beam with intensity uniformly distributed over a large beamstop. The design of the tuneup beamline includes a drift to the beamstop that is nearly three times as long as the 20-meter drift to the targets to allow using the same tune in the expander as that used in the target lines. This provides a one-to-one correlation between the tune of the matching sections and expanders in the beam tuneup line and the target lines. The final size of the beam at the beamstop is 1.5 meters (x) by 3 meters (y).

The various magnetic elements in these downstream sections have not yet been designed in detail. Although the baseline design for magnetic elements throughout the HEBT calls for electromagnets, the nonlinear expander elements (octupole and duodecapole) will be

permanent-magnet devices. The radiation resistance of permanent-magnet materials at the current time is uncertain. Recent experiments have shown that modern samarium-cobalt (Sm-Co) materials show no degradation in performance to at least 5×10^{15} neutrons/cm^2 fluence [7-6]. Because obtaining neutron fluences above this level is difficult, experiments are continuing slowly. Preliminary magnetic designs indicate potentially insurmountable difficulties in fabricating an electromagnetic combined-function octupole-duodecapole element with the required operational parameters. Feasible designs have been developed for these nonlinear combined-function elements of the beam expander using permanent-magnet materials. Using permanent-magnet materials in these magnets will also enhance the fault protection against overfocusing the beamspot on the target window caused by a power supply failure. Additional shielding against backstreaming radiation from the target and designing a simple remote-handling change-out scheme for the nonlinear elements may be necessary if the permanent-magnet material is not found to be resistant to neutron fluences in excess of 10^{16} neutrons/cm^2.

The last magnetic element in the beamline before the target is the 7.5° shield dipole that bends the beam back toward the accelerator axis. The purpose of this bend is to protect the upstream HEBT components from radiation (particularly neutrons) backstreaming from the target. The dipole is the last element in each target leg. The shielding is arranged around the beamline as close to the beam as feasible, optimizing the attenuation of radiation by placing the shielding primarily at the beam waists. The shielding arrangement is shown in Fig. 7-10, illustrating the placement both upstream and downstream of the dipole. A backstreaming radiation *stop* is also located in a line-of-sight position upstream of the dipole (not shown).

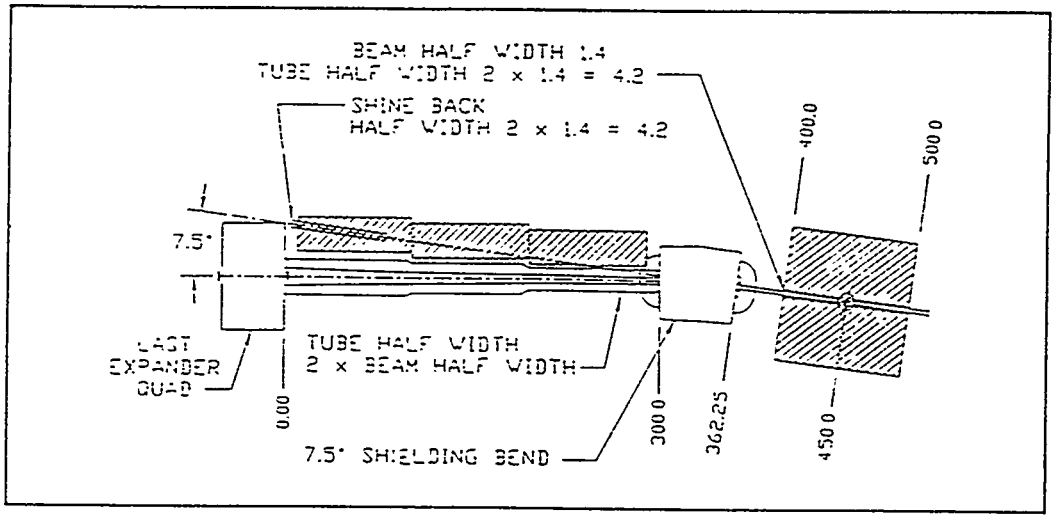


Fig. 7-10. Shielding arrangement to protect expander quads at 7.5° bend.

At the output of the expander section, the beam enters an evacuated and expanding beampipe through which the beam travels to the target window with a final rectangular spot size of 0.5 x 1.0 meters. A longer and larger chamber is required for the drift between the final beamline element and the beamstop of the tuneup beamline. The expander beampipe in the target line is an evacuated vessel, 20 meters long, in which the internal diameter is stepped up at several locations to accommodate the growth of the folded beam. Because the beam is folded, there is no halo to accommodate, and the beampipe diameters can closely fit the beamsize (see Table 7-9), with allowances for beam jitter and steering errors. The

beampipe has a diameter of about 10 cm at the beam waist in the center of the shield block just downstream of the shield dipole and expands to a diameter of 150 cm at the target interface flange. This diameter will comfortably accommodate the rectangular beam at the target, which has a diagonal width (radius) of 112 cm.

7.3.3 Engineering Description

The HEBT/target interface arrangement is shown in Figs. 7-11 to 7-13. The interface consists of two 200-cm-diameter flexible-roller-chain clamp flanges. The roller chains are remotely removable, and the flanges use all-metal Helicoflex double-vacuum seals that are compressed by the flexible chains acting against the tapered surfaces of the flanges. The double-vacuum seal, as shown in Fig. 7-11 has a pumpout test port between the sealing rings.

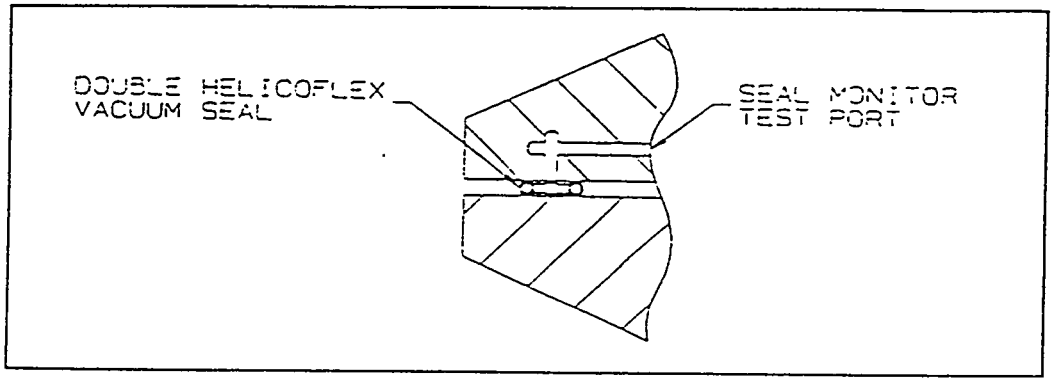


Fig. 7-11. Helicoflex vacuum seal used in the HEBT/target interface.

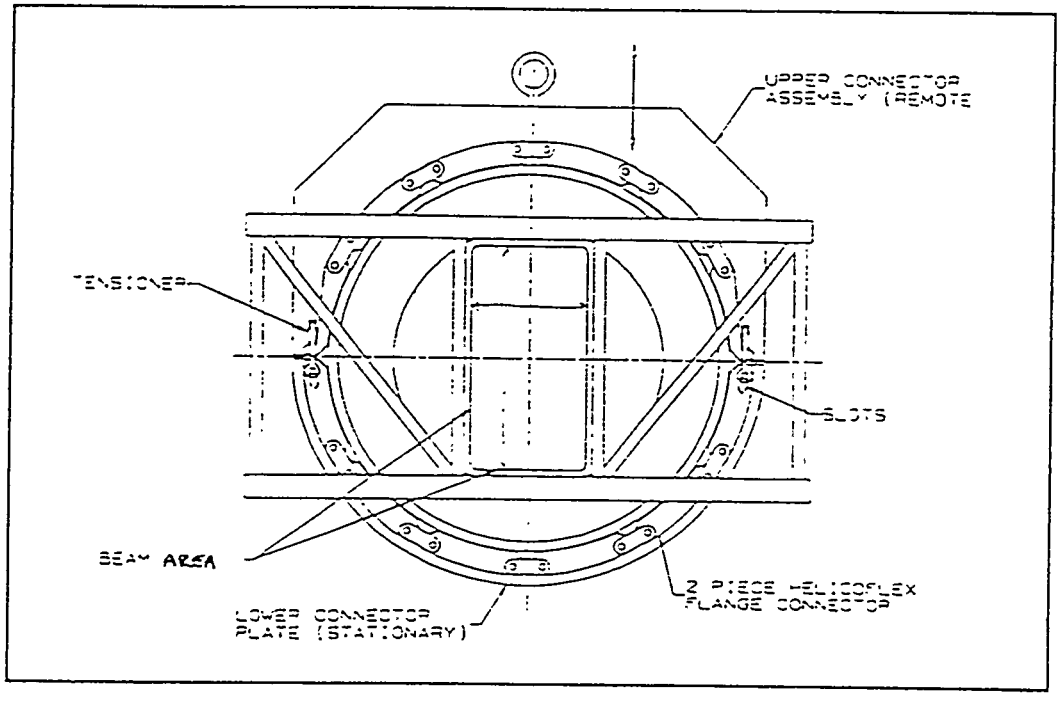


Fig. 7-12. The HEBT/target interface.

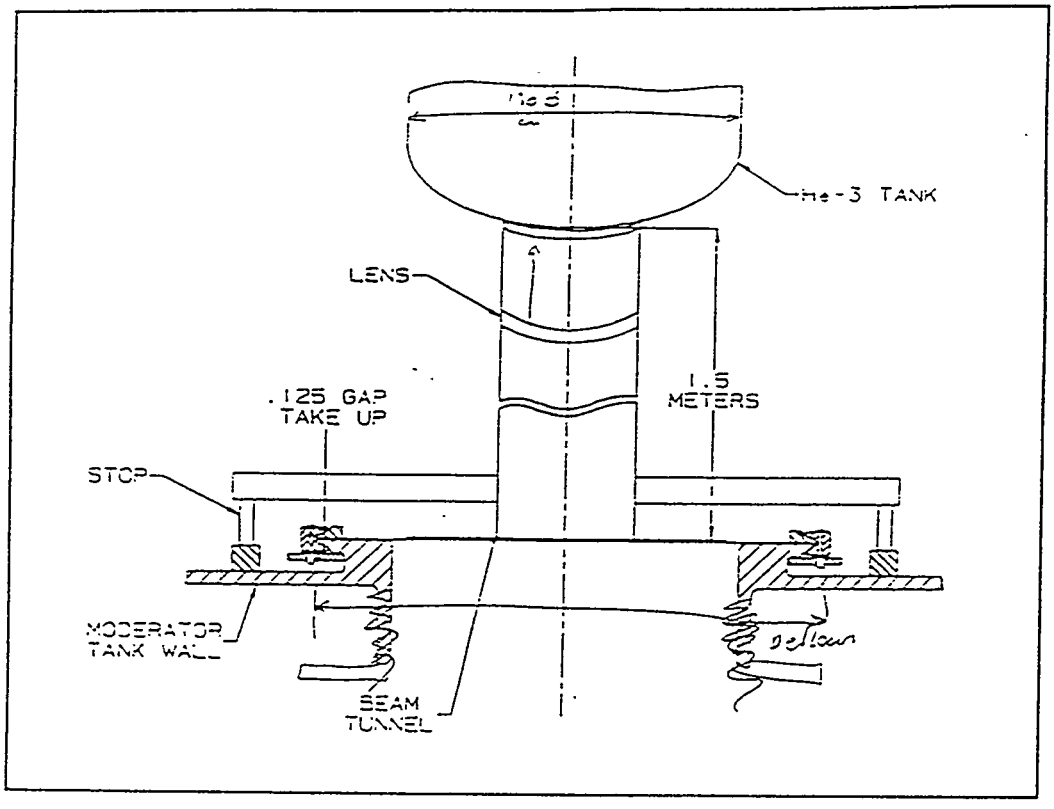


Fig. 7-13. Two-piece Helicoflex flange connector at the HEBT/target interface.

In the event that one seal should develop a leak, a soft vacuum could be pumped between the seals to maintain hard-vacuum integrity on the beampipe side. The two sets of flanges are located upstream and downstream of the heavy-gauge-steel moderator-tank wall. The upstream flange serves to disconnect the expander beampipe from the moderator, and the downstream flange allows the ^{3}He tank to be disconnected from the moderator-tank wall. A bellows of several convolutions is placed between the two flanges, allowing for slight misalignments and for the beampipe to be slightly compressed for removal and replacement of the vacuum seal. The bellows is blocked during evacuation of the beampipe. The primary HEBT interface is the upstream flange. Tightening the roller chains can be accomplished remotely. This remote maintenance concept is the same as that used in the linac intertank beampipes and on the ion pumps, but is much larger in scale and requires special considerations regarding support and accessibility.

7.3.3.1 Tuneup Beamstop

The tuneup beamstop is capable of absorbing the full 200-MW cw beam power during tuneup in a series of large graphite plates which we expect to last the lifetime of the facility. The beam is folded and expanded in the same manner as in the target beamlines. A 4.5-meter drift places the first quad of the matching section downstream of the switching magnet to allow adequate room for the magnet between the diverging achromatic-bend sections. The tuneup beam is expanded to the tuneup beamstop in a 60-meter-long stepped-expander beampipe similar to the target-expansion beampipes. The diameter of the interface flange of

the beampipe at the beamstop is 400 cm to accommodate a rectangular beam with a 335-cm diagonal cord. The interface flange is a roller-chain-type clamp system backed by a multiconvolution bellows on the beamstop side. This is a scaled-up version of the concept used for the target interfaces. The same special considerations required for the final engineering design of the target interface region also apply to the beamstop line.

7.3.3.2 Expander Magnets

Magnets in the expander section require apertures up to 22 cm. These apertures vary with position in the section, and cost studies have not yet been performed to determine the tradeoffs between duplicating as many magnets as possible and minimizing the aperture for the application (and reducing power consumption). Electromagnets in the expander region of the HEBT are designed with the same techniques as described in previous sections. Coils will be mineral-insulated core-cooled copper. Poles and yokes will be fabricated from standard magnet iron (i.e., C-1006). Construction of the iron will be either solid or laminated, depending on cost. Conceptual designs of the nonlinear combined-function permanent-magnet elements incorporate a 10% variability around the nominal value for each multipole. These designs require extensive engineering to reach a preliminary design stage.

7.3.3.3 Shield Dipole

The 7.5° shield dipole bending magnet in front of the target cell will receive large radiation doses, potentially requiring a *super rad-hard* design. The mineral-insulated conductor is directly cooled with an internal channel. This design for a magnet-coil package can be used to the point where the neutron fluxes are high enough to disassociate the water and release free oxygen. At that point, corrosion of the copper would require a solid-core mineral-insulated coil design cooled indirectly by stainless steel channels imbedded in a potting matrix of lead. Coil designs of this type have been developed for the quadrupoles that were to be operated near the target in the FMIT project at Los Alamos. A study for the APT target region must be completed to determine if the flux of backstreaming neutrons would justify the indirectly cooled design approach. The entire subject of backstreaming radiation from the target and associated shielding has significant engineering implications that have not yet been examined in detail.

7.3.4 Beam Expander Diagnostics

BLMs will be placed periodically throughout the expansion region of the HEBT. Specifically, BLMs will be positioned after each quadrupole doublet and nonlinear element of the expander, offset from the beamline center as described in preceding sections. BLMs will also be placed around the 7.5° dipole to monitor qualitative changes in the flux of backstreaming radiation from the target and possible beamspill in the magnet.

Two pairs of flying-wire beam-profile monitors will be installed into the expander region. The first will be placed immediately after each nonlinear element and the second at the downstream end of the drift following the multipole magnet. These devices will measure divergence angles and beam profiles that determine the performance of the expander in each phase-space plane. Measurement of the expanded-beam profile near the target area will require a more precise harp-profile-measurement system. This is the final diagnostic for the beam before impinging the target window. The harp system will be a removable system with wire spacing of 2.5 x 5 cm (5% of the beamsize at the target). Special attention to designing a

device with sufficient radiation tolerance will be required for this diagnostic. The harp data will verify the beam-intensity distribution and current density required at the target. The harp data can be used as a relatively fast target-protection diagnostic, providing one of the several layers of defense against an overfocus event that may damage the target window or the target itself.

7.4 ENGINEERING CONSIDERATIONS

7.4.1 HEBT Alignment System

The overall HEBT alignment requirements for all magnets, shown in Table 7-10, are the same as for the quadrupole magnets in the linac. Standard optical surveying methods will meet the requirements shown in Table 7-10. Installation of the overall monument system in the HEBT tunnel, shown in Fig. 7-14, will allow for the installation of the HEBT components

Table 7-10. HEBT Alignment Requirements

x	±0.13 mm
y	±0.13 mm
z	±0.50 mm
Roll	±0.25 deg
Pitch	±0.25 deg
Yaw	±1.00 deg

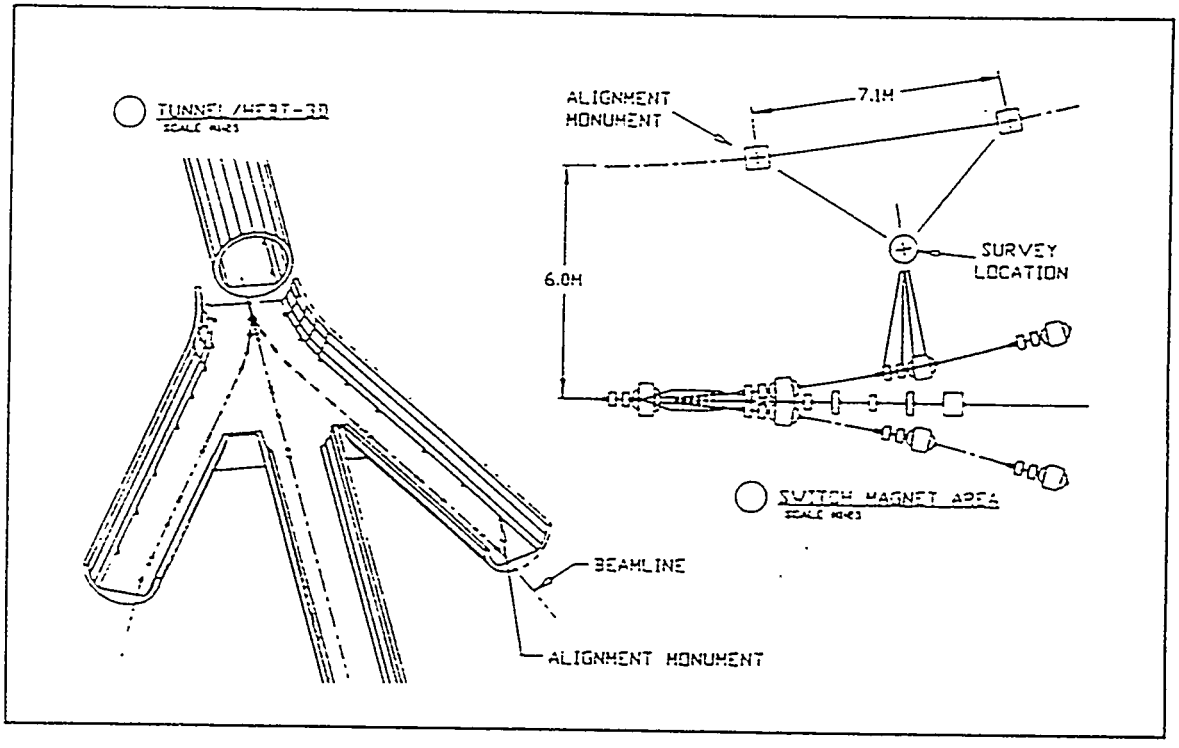


Fig. 7-14. HEBT monument alignment system.

to these specifications. The monuments are located about 6 meters from the beamlines and spaced 7.1 meters apart. The alignment optics are positioned between the monument system and the element being aligned so that the lines of sight do not exceed about 4 meters, which simplifies achieving the specified precision.

Figure 7-15 shows a typical quadrupole doublet mounted on a translator. The alignment references (tooling balls, fiducials, levels) are shown attached to the quadrupole magnets. The translator is mounted on the linear rail system, which provides the rack-out features of the maintenance and alignment system. The translator is manually adjusted and, in keeping with the general design philosophy of the APT quadrupoles, the split-yoke design allows for ease of assembly and replacement of the beampipe and field coils without removing the entire magnet.

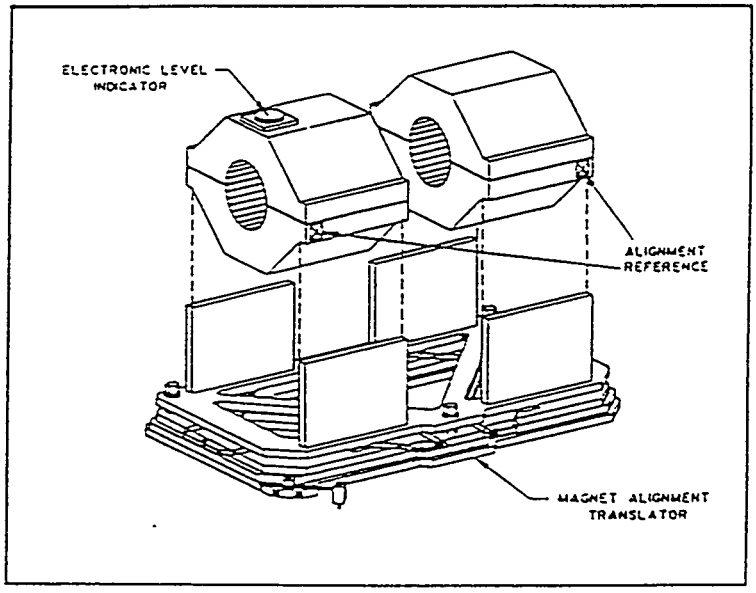


Fig. 7-15. HEBT quadrupole translator.

7.4.2 Interface Requirements

General facility interface requirements in the HEBT include power, cooling, and vacuum as well as maintenance for such components as permanent magnets. Details of the interface requirements for the power, cooling, and vacuum sections are given in the appendices.

A total of 119 magnets are present in the HEBT. The designs for these elements allow a cooling-water temperature rise in the field coils of 25C° and require a 200-psi water pressure system. The total HEBT thermal load for magnets is estimated to be 2.46 MW, with the power supplies dissipating another 100 kW. No estimate for the beamstop or collimator cooling is included in these estimates. There are six combined-function permanent-magnet elements in the HEBT. No cooling of these elements is required; however, power is required for motors to vary the fields and control signals. Accessibility to the magnets should be assured in the event that more frequent servicing and maintenance of these elements is required because of possible radiation damage.

The maximum allowable pressure in the HEBT beamlines during operation is 1×10^{-6} torr. A conservative estimate for the out-gassing rate in stainless steel under beam-on conditions (assuming nominal beam losses and temperatures) is 1×10^{-8} torr-l/s-cm^2. The structure of the HEBT, consisting of long sections of relatively small-bore beamtube, results in a conductance-limited vacuum system. The spacing of the pumps in such a system is generally more critical than their capacity, assuming sufficient capacity is available. Estimates of the capacity required for ion pumps in this system vary from 400–1000 l/s. While the pump spacing will also vary in parts of the HEBT, the spacing in the periodic-lattice sections (the greatest length fraction of the HEBT) will be a constant 355.7 cm. These

sections of the HEBT also contain the smallest beampipe—5-cm internal diameter. Analysis of the vacuum system has shown that, despite the conductance limitations of such a beam transport line, the pump spacing of 355.7 cm is adequate to hold the internal vacuum quality of the beamline to better than 1×10^{-6} torr—the worst out-gassing conditions during operation.

7.5 HEBT PERFORMANCE

7.5.1 Beam-Expander Simulation Tools

Beam-expander performance has been studied with previously available tools, as well as with those developed specifically for this application. Ideally, the simulation code used to study APT HEBT performance would include the following features: particle-tracking capability, accurate treatment of space charge (including beams with large aspect ratios), magnet fringe fields, high-order magnetic fields (i.e., octupoles and duodecapoles), and combined-function magnetic fields. Further, the simulation code should be capable of efficiently tracking input-beam distributions with very large numbers of particles, obtained from an accelerator end-to-end run. To study the effects of numerous parameters on the final output beam, studies of the APT accelerator design were typically run end-to-end with 500 macroparticles. The statistics that would result from tracking this ensemble through the HEBT, however, would not be useful. Instead, a significantly larger simulation consisting of 10,000 macroparticles was generated; even these results, however, provided rather poor statistics for the final beam distributed over the 50x100-cm^2 irradiation area at the target.

Theoretical input-beam distributions, usually Gaussian, were generated for most HEBT beam simulations. Two particle-tracking codes were used to characterize the beam-intensity distribution at the target, assuming the theoretical input-beam distributions. The beam-optics code PATH [7-7], incorporates space-charge effects and octupole fields, but does not account for duodecapole components or quadrupole fringe fields. Output-beam distributions calculated by PATH can be plotted as contour plots or 1-D projections.

PATH has been used to generate plots that convey a visual impression of the final beam-intensity distribution at the target and as such, the absence of duodecapole components does not greatly impact the results. The duodecapole only redistributes the far beam halo, a tiny fraction of the beam, which is not contained in any code-generated input-beam distribution of a size that can feasibly be treated by an optics simulation code such as PATH. Pure octupole magnets fold the beam slightly more tightly than octupoles with duodecapole components, resulting in a slightly reduced beamsize at the target and higher-intensity spikes at the edges. The dimensions of the 3.5-rms beam ellipses at the target (with rms emittances of 0.036 π-cm-mrad) produced by an expander with pure octupoles (no duodecapoles) are x = 24.16 cm, y = 49.15 cm, compared with x = 24.59 cm and y = 50.81 cm for a beam expander using octupoles with duodecapole components. The effect of quadrupole fringe fields was estimated by other means to be small, and again affects only the particles that cannot be feasibly treated by PATH with code-generated input-beam distributions. The specific expanded beam dimensions mentioned here are those produced for the Los Alamos ^{3}He target/blanket concept. However, with very minor retuning, the beam expander is capable of providing the correct beam dimensions for the BNL SILC target concept.

A simulation code, written specifically to analyze the APT beam expander, can track particles through beamlines containing drifts, quadrupoles without fringe fields, and octupoles with duodecapole components. The code does not treat space charge because the space-charge tune depression in the expander is insignificant. A probability-weighted input-beam distribution enables the user to track particles with arbitrarily large rms values. The

particle distribution is generated by randomly choosing particle coordinates, then assigning a probability based on these coordinates and on the desired beam distribution, usually Gaussian. Particles that populate beam ellipses out to arbitrary probability—7 rms, for instance—can be studied without generating unreasonably large particle ensembles, such as those required by PATH. The output-beam distributions generated by this code were analyzed by binning the particles based on final position, summing the probability in each bin, and analyzing, both numerically and graphically, the final probability distributions. Effects such as space charge and quadrupole fringe fields will smear out the edges of the distributions generated by this simulation code.

7.5.2 Beam-Expander Performance

PATH was used to track 5,000 particles through an expander, both with and without space charge, to assess the importance of space charge. No visible differences in the final beam-intensity distributions at the target were observed. Subsequently, the code was always run with 100,000 particles to maximize statistics at the target window, but without space charge to reduce the computer CPU time required for each simulation. The nominal output-beam distribution from the beam expander (with pure octupoles and a 10-meter final drift) for a Gaussian-distributed input beam with emittances of 0.018 π·cm-mrad and an rms momentum spread of 0.081% is shown in Fig. 7-16. Additional distributions on target characterized by bins of normalized probabilities can be found in the Chap. 7 Appendix.

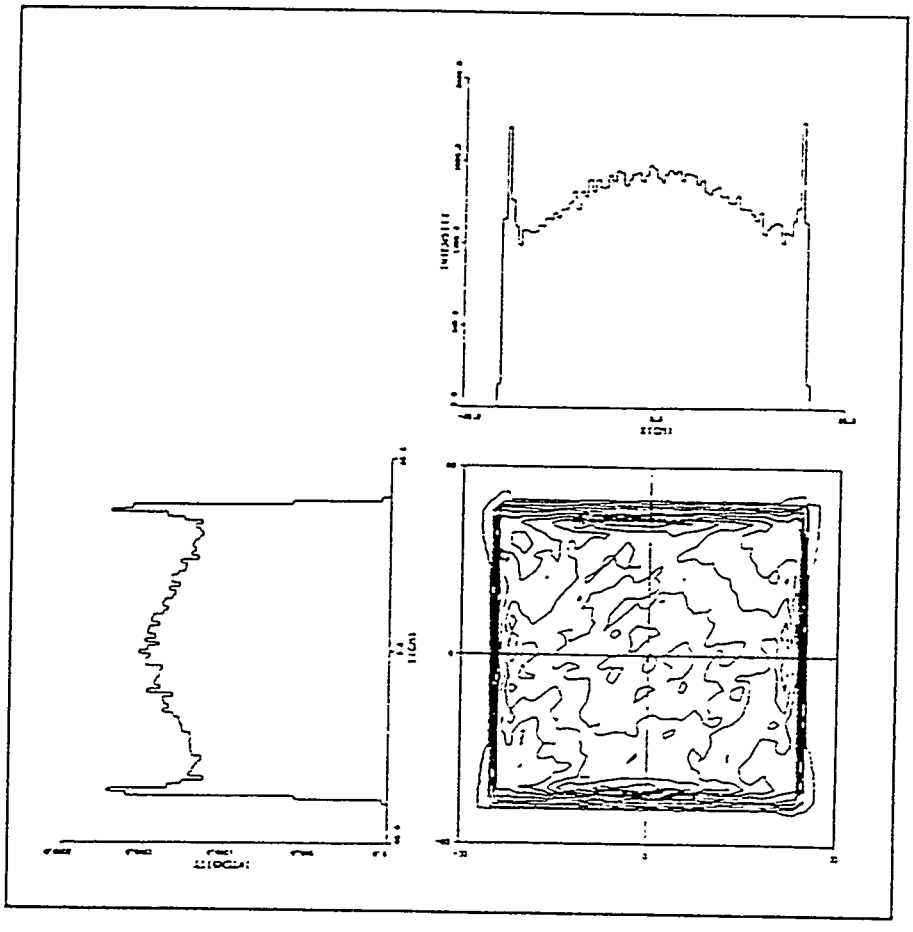


Fig. 7-16. Nominal beam distribution at target for Gaussian input beam.

Beam expanders are sensitive to beam-centroid jitter. Figure 7-17 illustrates the effect of a 0.25-rms beam-centroid shift of the beam shown in Fig. 7-16 after going through the expander. Although the edges of the beam distribution remain fixed, the beam-intensity distribution becomes skewed within the irradiation area (see Chap. 7 Appendix for detailed explanation).

Techniques that were developed for the GTA program at LANL will be used to control beam-centroid jitter to 0.1 rms, using position monitors and fast steerers. Characterization of the beam-intensity distribution as a function of jitter can be found in the appendix.

Precise alignment of all HEBT magnets, especially those in the expander, will be required to avoid static beam-centroid offsets. DC steering magnets will ensure correction of any latent effects. Details of the nominal beam-intensity distributions and the operational variability expected was also studied with the specialized particle-tracking code discussed above; however, the analysis was performed with an earlier version of the expander [7-8]. This expander had the same set of magnetic components but a slightly different input beam and was tuned for a nominal beam size at the target of 25 cm by 100 cm. A Gaussian-distributed input beam with emittances of 0.036 π·cm-mrad and a uniform distribution with a particle-momentum deviation between -0.444% and +0.444% was used for most of this work. A second beam consisting of 4,000 particles and with emittances of about 0.018 π·cm-mrad was also studied.

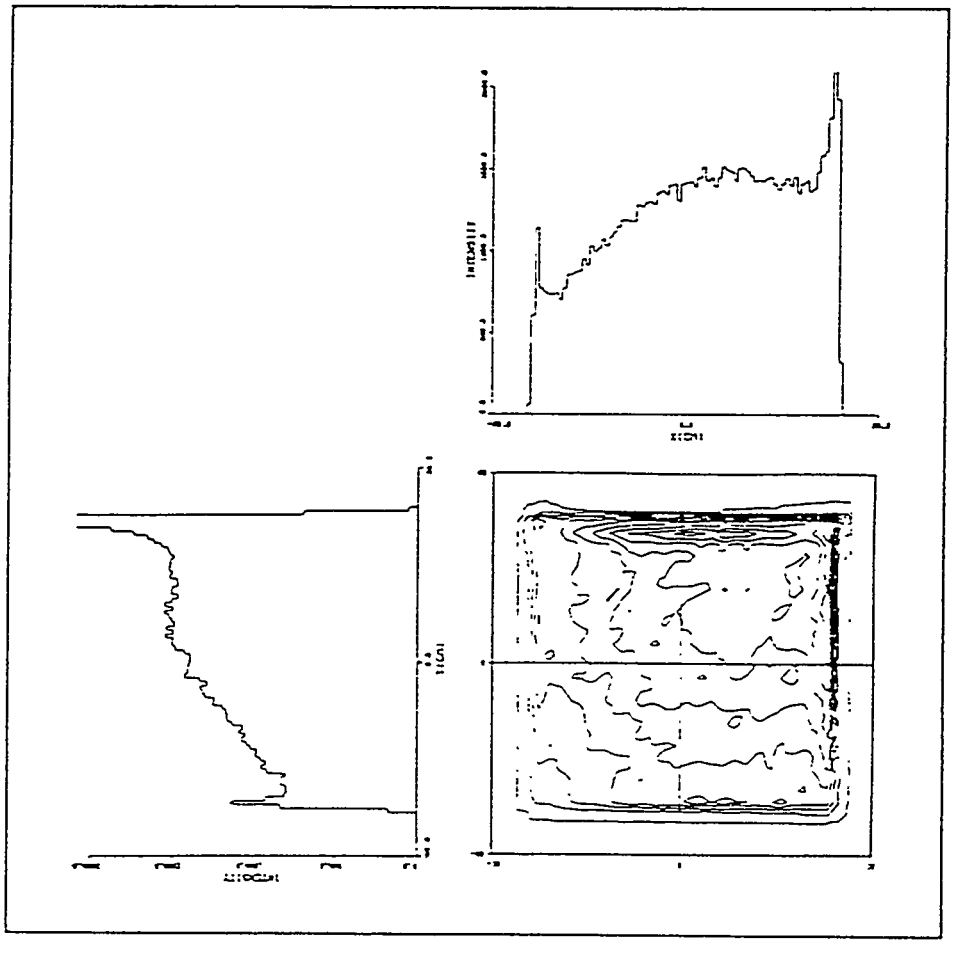


Fig. 7-17. Beam distribution with 0.25-rms beam jitter.

In conclusion, the *ideal* beam-intensity distribution cannot be obtained with the constraints of (1) extremely high intensity, (2) a limited number of multipole elements, (3) realistic multipole field strength, and (4) ruling out beam scraping. The tradeoff for a realistic beam expander is between an intensity distribution with a more peaked central region and smaller spikes at the edges and one with a flatter center and larger spikes at the edges. Results from simulations using a more realistic accelerator output-beam as input to the HEBT suggest that the expected intensity distribution at the target is more uniform than that from a Gaussian-distributed input beam.

7.5.3 End-to-End Simulation

An end-to-end simulation of the APT accelerator tracked a 10,000-particle ensemble to the output of the CCL. This beam ensemble was used as the input-beam and tracked through the HEBT [7-9] using a modified version of PARMILA [7-10]. This simulation code is capable of treating octupoles with duodecapole components and will calculate the effects of space charge, but does not incorporate the effects of quadrupole fringe fields. As a comparison, a PARMILA-generated nominal input-beam distribution, uniform in x-y-z, was also tracked through the HEBT. The beam scatter plots at the target are shown in Fig. 7-18 for the code-generated input beam (left) and for the 10,000-particle ensemble end-to-end simulation (right).

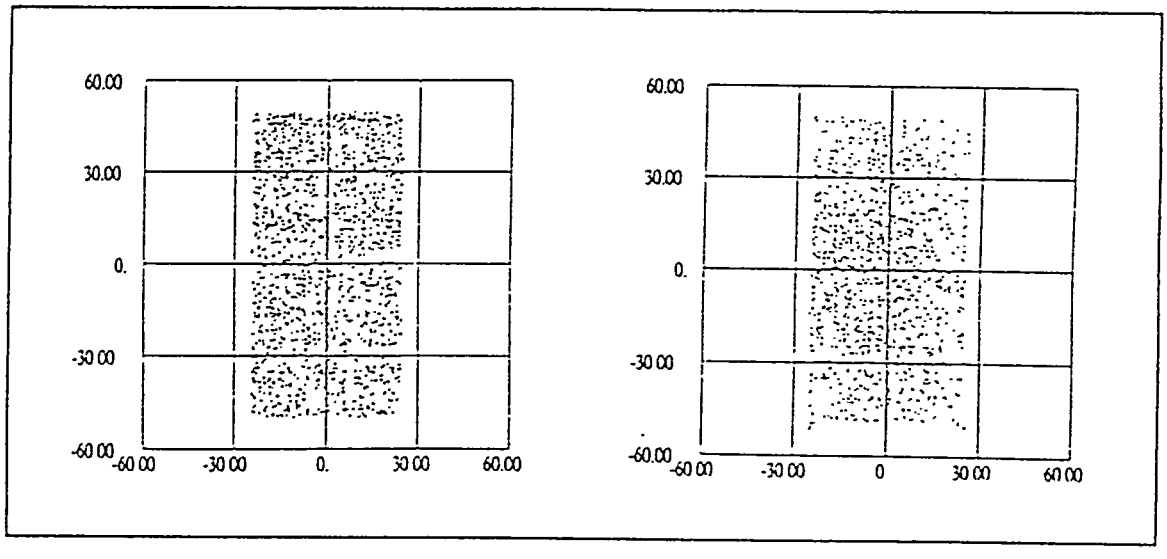


Fig. 7-18. Beam at target for code-generated input (left) and actual simulation (right).

To analyze the uniformity of the beam at the target, mirror symmetry in both horizontal and vertical planes was assumed. A 10 x0 grid of bins, each 2.5 cm horizontally by 5.0 cm vertically, was constructed to describe one 25 x50-cm^2 quadrant of the 50x100-cm^2 target distribution. A perfectly uniform distribution would have 100 particles in each bin. A 10,000-particle beam ensemble, assuming the particles are randomly distributed, would populate each bin with an average of 100 particles and a standard deviation of 10 particles.

The hot-spot intensity (largest bin population), relative to the average intensity, that was obtained from the PARMILA-generated, 10,000-particle, accelerator simulations is shown in Table 7-11.

Table 7-11. Hot-Spot Intensities

Case	Relative Maximum Intensity
code-generated input beam	1.29
end-to-end actual simulation	1.52

The worst hot spot for the PARMILA-generated input-beam distribution is 29% above the mean. A statistical fluctuation of this magnitude can be expected to occur once every five simulations (once in every 500 bins). This result can be considered consistent with a nearly uniform distribution, given the limited statistics for this calculation. The 10,000-particle end-to-end actual simulation has a hot spot in the output distribution 52% above the mean. Statistically, this should occur only once every 100,000 cases for a uniform beam. Both of these calculated hot spots are not of serious concern because of their very limited extent (a single bin). A possibility exists that the space-charge computation of PARMILA may be enhancing statistical fluctuations, which would require further investigation. The most enlightening course of future action, however, would be to increase the statistical ensemble significantly over the 10,000 particles used in the above analysis.

It is also important to note that a perfectly uniform beam-intensity distribution is neither expected nor required for the APT target. Severe hot spots over large regions (as would result from severe position jitter) would be a cause for concern.

7.5.4 Beam-Expander Tuning and Operation

Diagnostics in the matching section will be used to characterize the CS parameters and emittance of the beam. The tune of the matching section must be verified in order to produce the required input beam for the expander, as tabulated in Table 7-7. Finally, the beam-expander elements must be set to achieve the nominal beam at the target (Table 7-8 should be useful for this purpose). Space-charge effects are expected to be insignificant. The matching and beam-expander sections were designed assuming no space-charge forces. A slight (1%–2%) increase in magnetic fields may be necessary to compensate for the real space-charge effects. The beamsize at the target can be fine-tuned with the third and fourth quadrupole in the beam expander. The change in full width of the irradiation area in x, Δx, y, Δy, can be calculated from the expander quadrupole gradients (for the expander of Table 7-6) as follows:

$$\Delta x = -2.74\ \Delta g_3 + 23.08\ \Delta g_4 , \quad \text{and}$$

$$\Delta y = 58.89\ \Delta g_3 - 10.36\ \Delta g_4 ,$$

where Δg_3 and Δg_4 are the gradients of the third and fourth quadrupole, respectively. Here, Δx and Δy are in units of cm, and Δg_3 and Δg_4 are in units of T/m. Once the expander is properly tuned and is producing the desired beam at the target, no further adjustment is needed to dimension the beamspot.

Details of the beam distribution can be tuned using the quadrupoles in the expander. If, for instance, a beam that is too peaked in the central region is detected, the beamsize and divergence at the entrance to the octupoles can be increased slightly to reduce the central intensity, but at the expense of increasing the edge intensity slightly. Similarly, if the intensity at the edges is too great, the beamsize and divergence should be decreased at the octupoles.

7.5.5 Effects of Fault Conditions in the Accelerator

A preliminary study for a 1.6-GeV accelerator with a FODO lattice, very similar to the APT design, indicated that an accelerator-quadrupole failure results in a doubling of the output-beam transverse emittance, without changes in the CS parameters. Such a failure increases the rms spot size and divergence of the expander input beam by 41%, resulting in the types of effects discussed above—depletion in the center of the distribution and large spikes at the edges.

The same study also indicated that RF-module failure does not affect the transverse parameters but could result in energy shifts by up to 10 MeV. To assess the impact of a ±10-MeV energy shift, the matched beam for the last cell of the accelerator was calculated using nominal focusing-element settings, but a particle energy of 990 MeV and of 1010 MeV. Transverse beam emittances of 0.018 π·cm-mrad and an rms momentum spread of 0.081% were assumed. These beams were transported through the HEBT (using the original 37.5° achromatic bend) with all magnets at their nominal settings. Gaussian-distributed input beams at the first nonlinear element (with the parameters obtained using this procedure) formed the input beams for PATH. These distributions were tracked through the expander (with pure octupoles and a 10-m final drift). Figure 7-19 shows the 990-MeV beam at the target, and Fig. 7-20 shows the 1010-MeV beam.

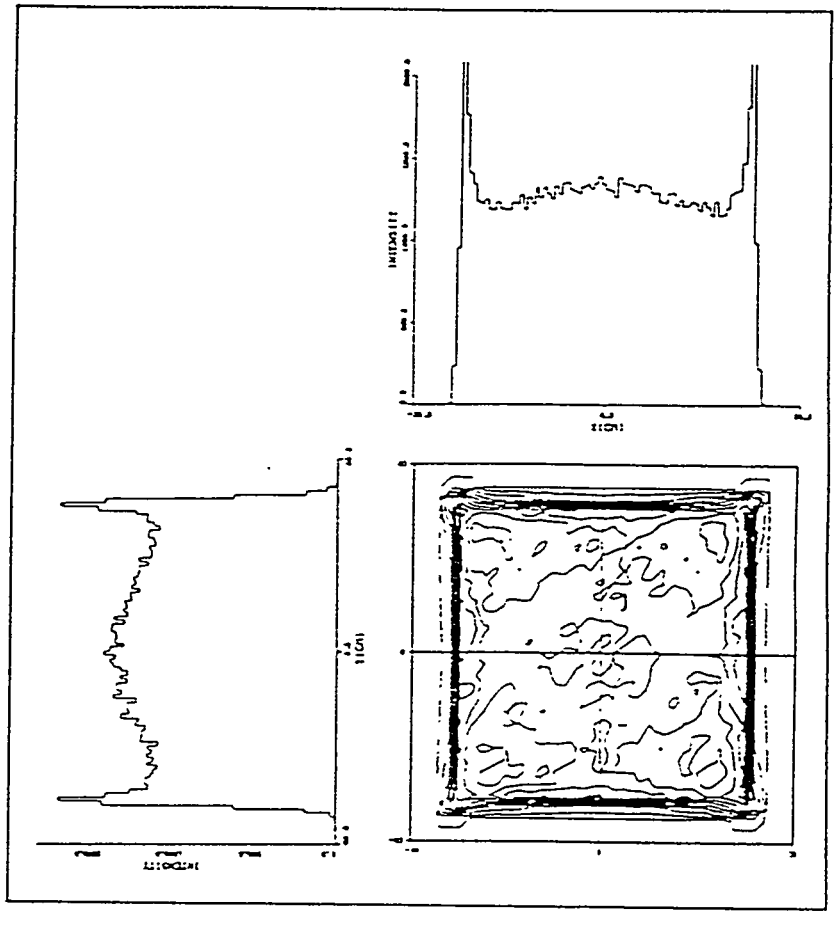


Fig. 7-19. Beam distribution at target for a –10-MeV energy shift.

The 10,000-particle distribution resulting from the APT accelerator end-to-end simulation was used to tune the HEBT for the required CS parameters and

beam emittances (0.018 π-cm-mrad) tabulated in Table 7-7. A set of 500-particle simulations of quadrupole-doublet failures at different positions in the accelerator were performed [7-11] and provided accelerator output beams for determining the impact of such failures on the HEBT performance. Generally, the CS parameters were unaffected by such events, but emittances, however, were up to 3.7 times the nominal value. The increased emittance causes a near doubling of the nominal beamsizes and divergence at the nonlinear elements. The 3.5-rms ellipses were transported through the expander, and the resulting half-sizes at the target are given in Table 7-12.

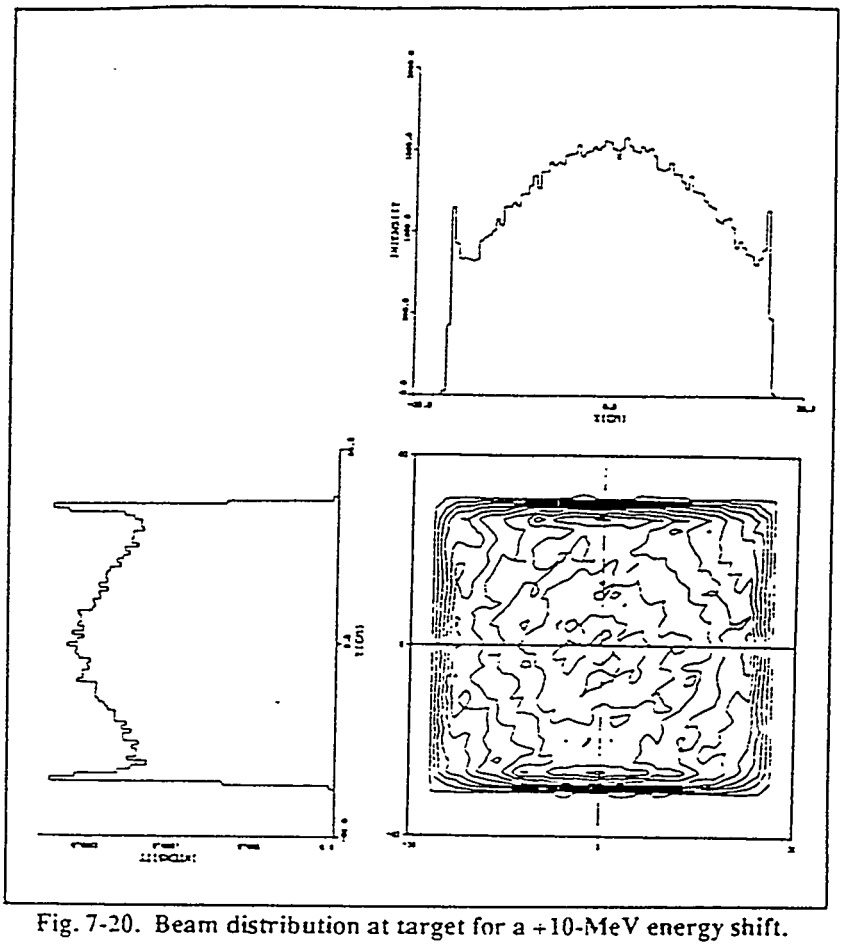


Fig. 7-20. Beam distribution at target for a +10-MeV energy shift.

In all of the cases where accelerator focusing-element failure did occur, insignificant changes in the irradiation area were observed. Although the ellipse tracking method does not give particle distributions, changes in distribution can be predicted by inspecting the effect of the nonlinear elements on the phase-space ellipses. The changes to the degree of folding are observed, resulting in significant (defined as nontolerable from the perspective of target operation) spikes at the edges of the distribution. The procedure was repeated to assess the effect of running at half current or zero current with the nominal-current settings for the accelerator and HEBT elements. The results are given below in Table 7-13.

The irradiation area for all cases does not change significantly, but for the zero-current case, vertical phase space is folded such as to result in a beam with pronounced spikes at the horizontal edges. This will do no harm because of the low current.

7.5.6 Counteracting Fault Conditions

One may wish to continue operating the APT facility after the failure of an accelerator RF module that results in a shift in beam energy. The best strategy would be to determine the new nominal beam energy and to change all HEBT and beam-expander magnets by the ratio of the beam rigidities to reproduce the nominal beam-transport conditions. This scenario points strongly to the need for some degree of magnet tunability, be it an electromagnet or permanent-magnet device.

Table 7-12. Beam Half Sizes x and y at Target after Quadrupole-Doublet Failure

Energy at Failed Doublet (MeV)	x(cm)	y (cm)
No-Failure Case*	25.1	48.6
102.05	25.6	50.8
200.01	25.8	49.9
300.14	25.7	49.3
401.25	25.7	49.5
500.22	25.8	49.9
601.76	25.5	49.9
701.64	25.5	49.5
801.62	25.4	48.7
901.01	26.3	49.2

*The No-Failure Case is included for comparison purposes.

Table 7-13. Beam Half Sizes x and y at Target as Function of Beam Current

I (mA)	x (cm)	y (cm)
200	25.02	48.47
100	25.03	48.18
0	24.69	48.53

The 7.5° shield dipole in the last 20-meter drift of the beam expander will cause a horizontal shift of the beam spot at the target for a shift in beam energy. The calculated dispersion is approximately 2.2 cm per percent $\delta p/p$. A 10-MeV energy shift (as large as any calculated for accelerator fault conditions) corresponds to a 0.673% $\delta p/p$, which shifts the beamspot at the target by 1.5 cm. Failure of the dipole is far more problematic and would be detected by the layered diagnostic system installed in the HEBT.

Following failure of an accelerator quadrupole doublet, beamspill will be increased because of increased transverse emittances. A change will also take place in the beam-intensity distribution at the target. For a failure where emittances increase by a factor of 3.7, the HEBT will transmit 13 rms instead of the nominal 25 rms, and the beam expander will clear 3.6 rms instead of 7 rms. The spikes at the edges of the distribution double in intensity. The increased beamspill would again be detected immediately by the layered diagnostic system; however, one may wish to continue operation with a failed quadrupole doublet. The best strategy would be to determine the new transverse emittances and to tune the four quadrupoles in the matching section to recover acceptable beam-intensity distributions at the target. After this adjustment, the HEBT will continue to clear 13 rms, but the expander will again clear 7 rms. This strategy would require retuning quadrupoles in the matching section by up to 16% to recover a desirable beam-intensity distribution at the target. Quadrupole-doublet failures beyond some point in the accelerator do not simply lead to beam redistribution in the accelerator with increased emittance, but also to a severely mismatched output beam. Such failures somewhere between the 900-MeV and 1000-MeV points in the CCL would require accelerator shutdown and repair.

CHAPTER 7 REFERENCES

7-1. K.R. Crandall, D.P. Rusthoi, *TRACE 3-D Documentation,* Los Alamos National Laboratory document LA-UR-90-4146 (1990).

7-2. B. Blind, "Injection Lines for PILAC -- Comparison Between a Line Containing a Modified Second-Order Achromat and a Line Containing a True Second-Order Achromat," Los Alamos National Laboratory report LA-UR-91-683 (1991).

7-3. B. Blind, "Production of Uniform and Well-Confined Beams by Nonlinear Optics," Nuclear Instruments and Methods, **B56**, 57 (1991).

7-4. A.J. Jason, B. Blind, and E.M. Svaton, "Uniform Ribbon-Beam Generation for Accelerator Production of Tritium," Proceedings of the 1988 Linear Accelerator Conference, Williamsburg, VA (1988), CEBAF Report 89-001, p 192 (1989).

7-5. K.L. Brown, R. Rothaker, K.C. Carey, Ch. Iselin, "TRANSPORT: A Computer Program for Designing Charged Particle Beam Transport Systems," SLAC 91 (rev 1977), NAL91 and CERN 80-04.

7-6. R.H. Kraus, Jr., "Permanent-Magnet Material Applications in Particle Accelerators," *Permanent Magnet Devices,* S.G. Sankar, ed., (1994), Los Alamos National Laboratory report LA-UR-92-365 (rev 1993).

7-7. J.A. Farrell, D.P. Rusthoi, "PATH - A Lumped-Element Beam-Transport Simulation Program with Space Charge," Los Alamos National Laboratory report LA-UR-84-1766 (1984).

7-8. B. Blind, "Beam-Intensity Distributions at the APT Target," Los Alamos National Laboratory memorandum AT-3:92-336 (1992).

7-9. W.P. Lysenko, "APT End-to-End Simulations", Los Alamos National Laboratory memorandum AT-3:93-204 (1993).

7-10. G. Boicourt, J. Merson, *PARMILA USERS AND REFERENCE MANUAL*, Los Alamos National Laboratory document, LA-UR-90-127 (1992).

7-11. R. W. Garnett, "Effects of Doublet and RF Module Failures in the APT CCL," Los Alamos National Laboratory memorandum AT-1:93-037 (1993).

RF POWER SYSTEM
CHAPTER 8

Page

8.1 OVERVIEW AND CHOICES 1
8.1.1 Baseline Choices 2
8.1.2 APT RF Compared to Other Systems 4
8.2 SYSTEM DESCRIPTIONS AND LAYOUTS 5
8.2.1. Overview of High Voltage to RF 5
8.2.2 The High-Voltage System 5
8.2.2.1 AC-to-DC Converters 6
8.2.2.2 High-Voltage Distribution 7
8.2.2.3 High-Voltage Protection 8
8.2.2.4 High-Voltage Diagnostics 9
8.2.3 The RF Module 10
8.2.3.1 Module Description 10
8.2.3.2 Module Efficiency 10
8.2.3.3 Module Support Utilities 12
8.2.3.4 Module Control 12
8.2.4 High-Voltage Generation and Distribution Layout 13
8.2.5 Klystron Gallery Layout 13
8.2.6 Waveguide Layout 16
8.2.7 Additional RF Generators 17
8.3 RF SYSTEM CONTROLS 19
8.3.1 Control Logic 19
8.3.2 VXIbus Format 19
8.3.3 Feedback/Feedforward 20
8.3.4 RF System Modeling 21
8.4 OPERATION / MAINTENANCE / MANUFACTURE OF RF SYSTEMS 23
8.4.1 Operation 23
8.4.1.1 Initial Conditioning Operations 23
8.4.1.2 RF System Startup 24
8.4.1.3 Normal Operation 25
8.4.1.4 Effects on the Utility Grid 25
8.4.1.5 Loss-of-Beam Incidents 26
8.4.2 Maintenance 29
8.4.3 Manufacturing Issues 31

LIST OF FIGURES

Page

Fig. 8-1. RF-system power requirements for APT. 1
Fig. 8-2. Primary components of an RF module. 2
Fig. 8-3. High-voltage-system block diagram. 6
Fig. 8-4. One line diagram of ac-to-dc converter. 7
Fig. 8-5. Five-inch aluminum tube bus. 8
Fig. 8-6. Layout of a typical protection unit. 9
Fig. 8-7. CCL output efficiency using GTA klystron data normalized to CERN tube efficiency. 11
Fig. 8-8. Relationship of amplitude and phase to I&Q. 12
Fig. 8-9. Site layout showing switchyards. 14
Fig. 8-10. Converter switchyard. 14
Fig. 8-11. Front-end klystron gallery. 15
Fig. 8-12. 350-MHz klystron station. 15
Fig. 8-13. 700-MHz klystron station. 16
Fig. 8-14. BCDTL & CCL klystron gallery and tunnel. 17
Fig. 8-15. APT multi-klystron unit with spare. 18
Fig. 8-16. APT multi-klystron unit with spare module in use. 18
Fig. 8-17. Sample control system logic for startup and shutdown. 19
Fig. 8-18. Typical LLRF VXIbus module. 20
Fig. 8-19. Block diagram of LLRF control system (with power amplifier & cavity). 21
Fig. 8-20. Feedback control in APT 22
Fig. 8-21. Response of feedback system to beam rise-time. 22

LIST OF TABLES

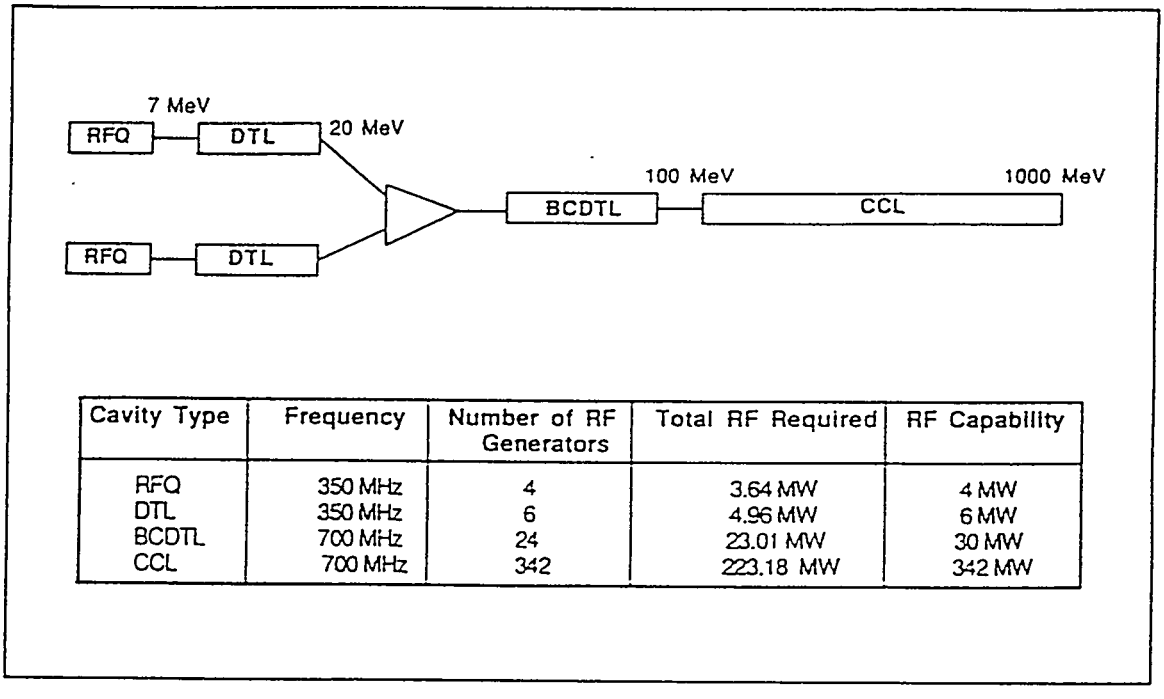
Page

Table 8-1. APT Operating Efficiency by Structure and Overall Baseline Choices 2
Table 8-2. RF Generator Choices and Existing cw Designs 3
Table 8-3. Results of Detuning and Coupling for the APT 1-GeV CCL Cavity 4
Table 8-4. Comparison of APT RF Parameters with Other Accelerators 5
Table 8-5. Klystron System Diagnostics 30

8.0 RF POWER SYSTEM

8.1 OVERVIEW AND CHOICES

The RF-system power requirements for APT are shown in Fig. 8-1. Ten 350-MHz stations are needed for the 2 RFQs and the low-frequency DTLs before the funnel. The vast majority of the RF power is needed for the BCDTL and the CCL that require a total of 366 700-MHz RF stations. The BCDTL uses 24 stations, and the CCL uses 342 stations. Overall, approximately 255 MW of continuous RF power is needed. In addition, approximately 10 low-power (<100 kW each) RF stations are needed for matching and bunching between sections and for the funneling (these do not require much floor space). Some bunching cavities will need only a few kW; each RF system, however, will require a complete set of system hardware, including interlocks, computer interfaces, LLRF controls, and operator interfaces.



Cavity Type	Frequency	Number of RF Generators	Total RF Required	RF Capability
RFQ	350 MHz	4	3.64 MW	4 MW
DTL	350 MHz	6	4.96 MW	6 MW
BCDTL	700 MHz	24	23.01 MW	30 MW
CCL	700 MHz	342	223.18 MW	342 MW

Fig. 8-1. RF-system power requirements for APT.

A diagram of a typical RF module is shown in Fig. 8-2. The principal components include the controls (LLRF, system, and resonance), the RF generator (including the driver amps), the RF transport, the diagnostics, the master oscillator distribution, and the accelerator or buncher cavity.

The entire accelerating system operates with an efficiency of somewhat less than 50% (beam power out vs. ac power in). Table 8-1 shows a derivation of the system efficiency. The total ac power required for the high-power RF generation, excluding support equipment, is about 485 MW.

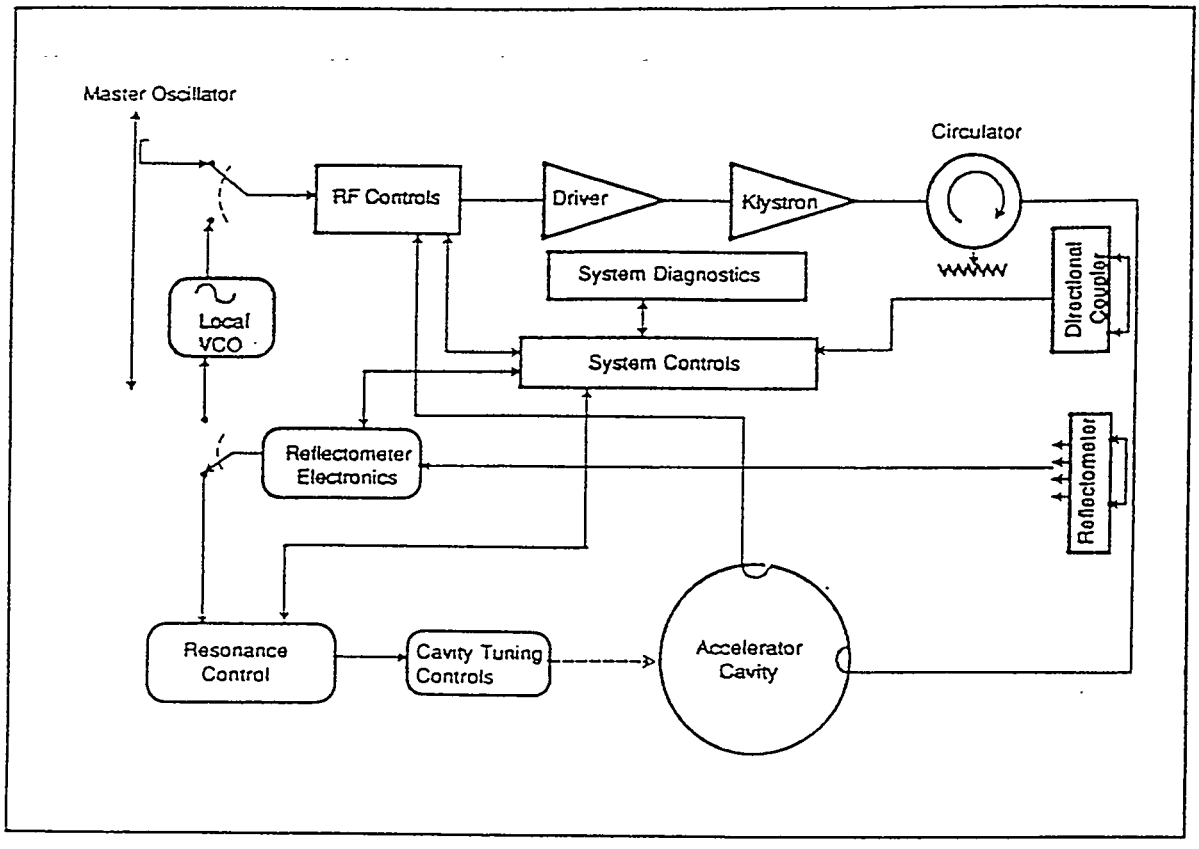


Fig. 8-2. Primary components of an RF module.

Table 8-1. APT Operating Efficiency by Structure and Overall Baseline Choices

Cavity	Total RF Power (MW)	ac to dc (%)	dc to RF (%)	Transport RF (%)	Beam Loading (%)	Efficiency, Total (%)
RFQ	3.64	99.0	53.0	95.0	38.5	19.2
DTL	4.96	99.0	55.0	95.0	53.0	27.4
BCDTL	23.01	99.0	59.0	95.0	71.1	39.5
CCL	223.18	99.0	59.0	95.0	80.6	44.7
Overall	254.79	99.0	58.8	95.0	78.5	43.4

8.1.1 Baseline Choices

To proceed with the early design, a set of baseline choices has been made for the RF system. Further investigation and development is needed, however, to ensure that the system design is optimal. The baseline design is discussed in the paragraphs that follow.

- **Generator Type.** The klystron is the generator type. All modern particle accelerators are based primarily on the use of the klystron. The klystron performance characteristics are well suited to accelerator use and are well

understood; however, there are other promising new types of generators that should be investigated in parallel. As a point of reference, LAMPF designers purchased prototypes of three generators (klystron, amplitron, and a coaxial triode) before deciding on the klystron. A list of potential RF generators is shown in Table 8-2.

Table 8-2. RF Generator Choices and Existing cw Designs

Type	Frequency (MHz)	cw Power (MW)	Efficiency (%)	Maturity
Klystron	352	1.30	67	Very High
Klystrode	267	0.25	75	Medium
Klystron (dc)*	476	1.20	70	Low
Magnicon	700	>2.00	80	Very Low
Regotron	991	5.00	70	Very Low

*Depressed Collector.

- **Generator Size.** The nominal generator size is 1.0 MW. This number is meant to be conservative because of the high availability requirement for APT. This level (or higher) has been demonstrated at two frequencies, viz., 352 MHz and 508 MHz.

- **Modulation Anode.** The klystron will have a modulation or "mod" anode. In a graded-β accelerator designed to optimize beam transmission such as APT, each RF module needs a different amount of power. The variation can approach 100% over the length of the accelerator. In addition, APT requires a very large amount of power. The mod anode on the klystron allows the operation of each RF module to be optimized for best efficiency. Refer to the figures in Secs. 4.5 and 6.3, RF System (350 MHz) and RF System (700 MHz), respectively.

- **Waveguide.** Large waveguide (WR1500) will be used for the 700-MHz systems. This waveguide will reduce the losses by approximately 5 MW when compared with the use of the smaller WR1150. In addition, the larger waveguide will ease the cooling requirements because of its larger surface area. Higher-order modes do propagate further in the larger waveguide, and could be a problem if the waveguide layout is not done properly. Discontinuities, such as mitered bends, tees, and flexible sections, must be located so that the higher-order modes will damp out before reaching critical components, such as other discontinuities, the coupling iris, or directional couplers. Harmonic absorption filters will be used in each high-power waveguide to eliminate the propagation of higher harmonics from the RF generator.

- **Circulator.** A circulator will be used in each transport line between the generator and the cavity. To optimize the klystron efficiency, designers must make the tube less robust to variations in output impedance. An accelerator, particularly one with very heavy beamloading such as APT, can demonstrate very large impedance swings, depending on the variations in current. The circulator will make the klystron very robust and thus help maintain a high level of availability. Table 8-3 shows the effect of shutting off the beam when the accelerator is operating at full power. The reflected power can exceed 50% of the incident (generated) power (column 3).

Table 8-3. Results of Detuning and Coupling for the APT 1-GeV CCL Cavity

Parameter	Coupling* Matched for Full-Beam Current (@700MHz, -30°)		
	Optimal Detuning	Tuned to Drive Freq.	Detuning for Full Beam
Current (mA)	200	200	0
Cavity Power (W)	149,772	149,772	149,772
Beam Power (W)	617,996	617,996	0
Generated Power (W)	767,768	809,221	315,586
Reflected Power (W)	0	41,453	165,814
VSWR	1.00	1.59	6.27
Percent Reflected	0.00%	5.12%	52.54%

*Coupling coefficient is matched for full beam current.

- **Resonance Control.** Resonance control will be used on each cavity. This is an operating efficiency issue. If the cavity is maintained at the proper resonant frequency, the reflected power from the cavity can be kept to a minimum. Table 8-3 shows that without detuning, more than 5% of the power is reflected which directly impacts the operating efficiency.

- **Feedback Control.** Inphase and quadrature (I&Q) control will be used in the feedback system. This choice allows us to make full use of the feedback hardware developed for the GTA program. In addition, the use of I&Q implies that all controlling hardware is identical. In an amplitude/phase system, totally different hardware must be developed for the amplitude and the phase systems.

- **Feedforward.** Feedforward will be implemented in addition to feedback, allowing the use of precontrol signals whenever a known or repetitive disturbance exists. The disturbance rejection can be greatly improved in these instances when compared to the use of feedback alone.

- **Control Margin.** A control margin of 10% for the feedback system will be used. This is done strictly to maximize efficiency. In this way, less power is dissipated in the klystron collectors. The drawback is slower response of the control system. With feedforward and slow turn-on of the beam, we feel that this control margin will be adequate.

8.1.2 APT RF Compared to Other Systems

Several accelerator systems around the world are worth comparing with the proposed APT system. Table 8-4 lists several such accelerators and the pertinent points of comparison. As can be seen from the table, the power required for APT is an order of magnitude more than that needed for any cw accelerator built to date. A very large number of RF stations is needed even when compared to large pulsed machines such as SLAC.

When combined together, certain features about APT make it particularly challenging. APT accelerates protons rather than electrons and uses a graded-β structure rather than a fixed β. In fixed-β (electron) machines, particle velocity is constant and therefore does not depend on acceleration to maintain synchronism. In a graded-β machine, the particles must see acceleration to maintain synchronism with the structure.

Table 8-4. Comparison of APT RF Parameters with Other Accelerators

Machine	Location	Freq. (MHz)	No. Stations	Peak MW	Duty Factor	First Beam
LAMPF	LANL	805	44	55	12%	1972
LEP	CERN	352	28*	32	cw	1989
TRISTAN	KEK	508	34	38	cw	1986
SLAC	SLAC	2856	247	16000	0.03%	1966
INR-MMFL	Moscow	991	28	130	1%	1990
APT		350/700	376	382	cw	

*by end of 1994.

The effect of lost RF stations down the length of the accelerator has been studied (reported in Chap. 3). In summary, below 286 MeV, a lost RF station leads to a significant loss of the beam. Below 500 MeV, a lost RF station leads to a significant portion of the beam coming out at the wrong energy. Above 500 MeV, if an RF module is lost, no beam is lost, and the beam comes out at the correct energy (but with increased emittance). Therefore, one could consider an operating scenario in which a failed module above 500 MeV (CCL module 170) allows operation to continue, perhaps with some retuning of adjacent modules. This mode is not in our baseline plan, but it is something that warrants further consideration.

8.2 SYSTEM DESCRIPTIONS AND LAYOUTS

8.2.1. Overview of High Voltage to RF

The RF-power system requires a dc power supply. Power converters using thyristors will be used to convert (rectify) ac power from a utility ac network to dc power. The preliminary requirements for the dc power supply are as follows:

- total dc power: ~500 MW;
- nominal dc voltage: 100 kV;
- dc voltage operating range: 65–100 kV;
- maximum dc voltage ripple: 1% peak-to-peak; and
- dc voltage regulation: 1%.

8.2.2 The High-Voltage System

The high-voltage system consists of the converter switchyard, two 250-MW ac-to-dc converters, one 15-MW ac-to-dc converter, a short dc bus feeding the front end, a long dc bus feeding the remainder of the accelerator klystrons, and high-voltage protection units and diagnostics. The incoming transmission lines connect to the converters through breakers located in the switchyard. In addition to the converters and breakers, the switchyard contains disconnect switches, ac harmonic filters, dc smoothing reactors, the dc bus capacitor, and station arresters. During normal operation, the 15-MW converter would power the front-end klystrons, and the two large converters would power the remainder of the accelerator klystrons. The 15-MW converter may also power both busses simultaneously with the two

large converters turned off. This is accomplished by a bus switch that can switch power from either of the converters to the long bus. Such an arrangement is required because the large converters cannot supply continuous current below about 5% of their full load, and small numbers of klystrons anywhere along the accelerator may need to be energized during checkout. A block diagram of the high-voltage system is shown in Fig. 8-3.

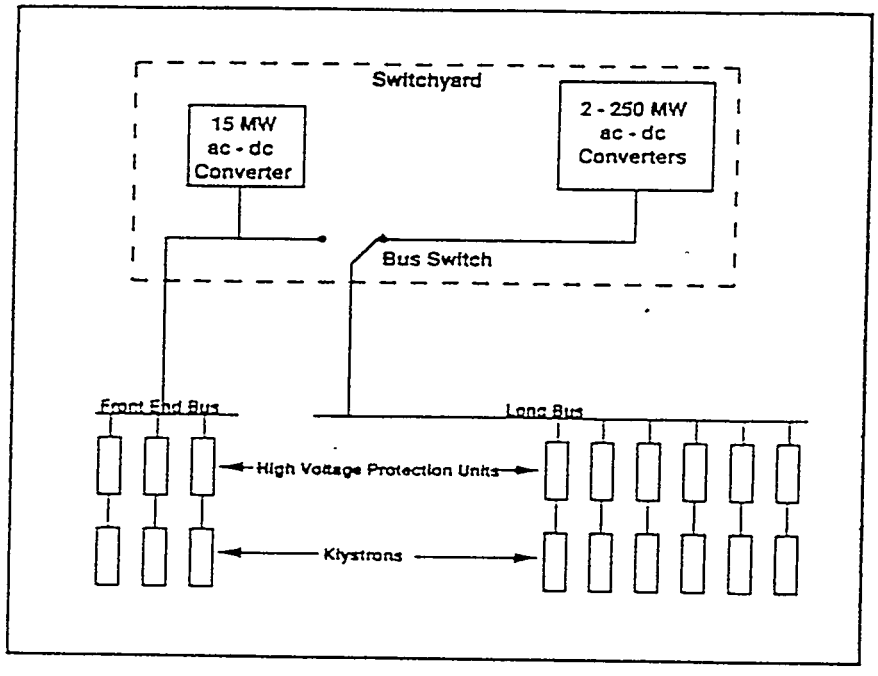


Fig. 8-3. High-voltage-system block diagram.

8.2.2.1 AC-to-DC Converters

Two converters, each rated at 250 MW and 100 kV, will be connected to the ac system via converter transformers. Figure 8-4 shows a one-line diagram of the converter station. Each converter consists of two 6-pulse thyristors to give 12-pulse operation. The thyristors provide the conversion from ac to dc, and the transformers provide a suitable voltage ratio to achieve the desired dc voltage and galvanic separation of the ac and dc systems. A smoothing reactor in the dc circuit for each converter reduces the harmonic currents on the dc side and limits transient currents. A large dc capacitor provides fast dc-voltage regulation during a klystron fault and before isolating the faulted klystron. If necessary, the dc capacitor can be divided and tuned as dc filters.

Filters in the ac switchyard absorb the harmonic currents generated by the conversion process. As the converters are operated in a 12-pulse mode, only 11th and 13th harmonic and high-pass filters are required. The filters produce a large part or all of the reactive power that is necessary to compensate the reactive consumption by the converters. Additional compensating reactance (measured in vars), if required, may be supplied by shunt capacitors, or in some cases, by the connecting ac system. A microprocessor-based control system provides the desired operation performance. The two converters will be housed in the converter building. The converter building will be designed and constructed to support the satisfactory operation of the converters. The inside of the building will be environmentally

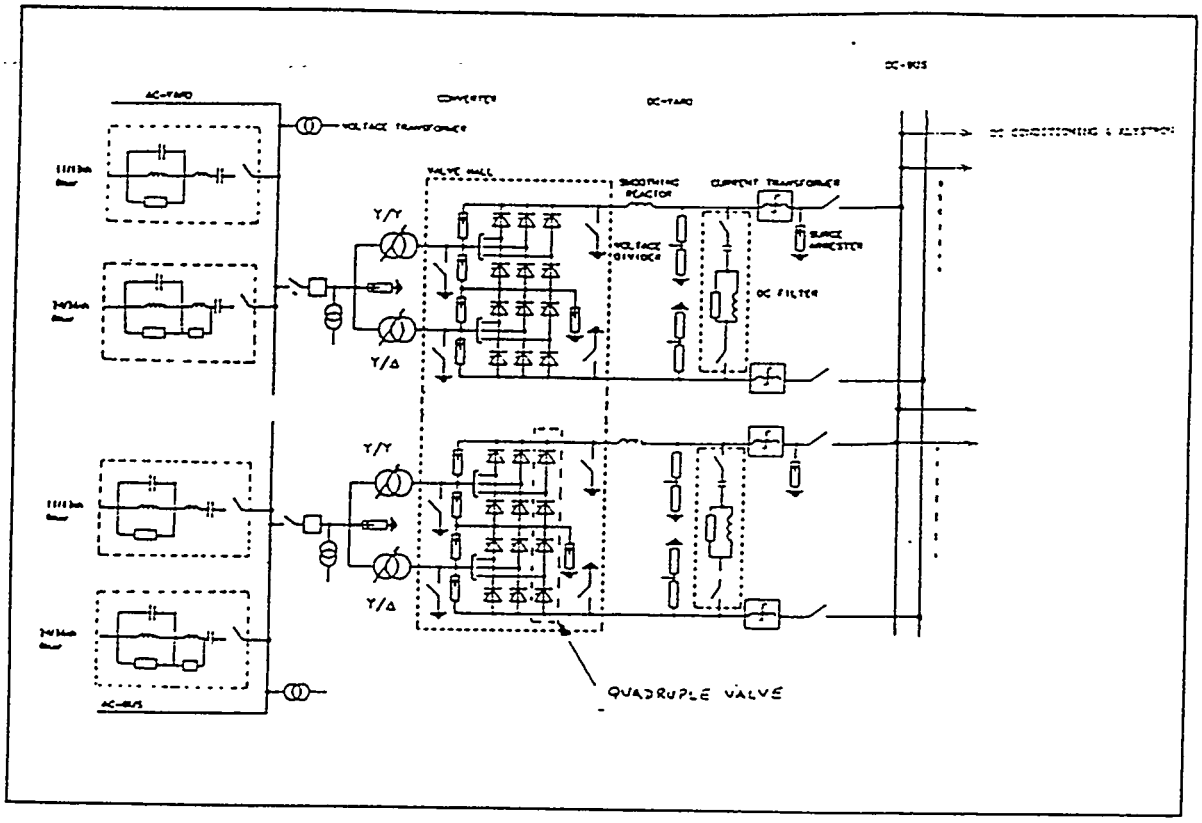


Fig. 8-4. One line diagram of ac-to-dc converter.

controlled. The building will also act as a screen or shield to limit RF interference that may be caused by the converters. For seismic design reasons, the thyristor valves structures (three quadruple valves) will be suspended from the roof of the building.

A compact design is achieved by setting up the converter transformers next to the converter building with feedthrough bushings passing through the wall. Similarly, the smoothing reactor is placed close to the wall on the opposite side of the converter building with one of its bushings passing through the wall. With this arrangement, the size of the interconnecting bus structures is minimized, and the busbars are kept in a controlled environment, thereby reducing their exposure to ground faults. In addition to the thyristors, the converter building contains surge arresters for overvoltage protection.

The thyristor valves are cooled with water. Water is pumped to circulate around the valves and back to a heat exchanger. A part of the water passes through a water processing unit. The water in the secondary circuit is cooled in an outdoor cooling tower.

8.2.2.2 High-Voltage Distribution

The dc power is delivered to the klystrons from the converters via the two high-voltage busses, as described earlier in the high-voltage system description section. A cross section of the buswork is shown in Fig. 8-5. The busses are 5-inch diameter, schedule 40, aluminum tubing that is held in place by insulators on steel supports, 15 meters on centers. Aluminum is the standard choice for such a power transmission system, because it is lighter and not as

expensive as copper. The bus is housed in a metal busway for personal safety and protection from lightning. The busway is located on the roof of the front end of the klystron gallery, distributing power the length of the accelerator.

8.2.2.3 High-Voltage Protection

For the converters and associated equipment, the protections that have been successfully applied in modern high-voltage dc systems will be used. The protections for the ac-side equipment are conventional transformer protections for the converter transformers and specially designed filter and capacitor-bank protections for ac filters and shunt capacitors. Most dc-side protections will be based on those designed for high-voltage dc systems. One major requirement for APT is the fast isolation of a faulted klystron without adverse affect on the converters or other klystrons. This is the purpose of the high-voltage protection unit.

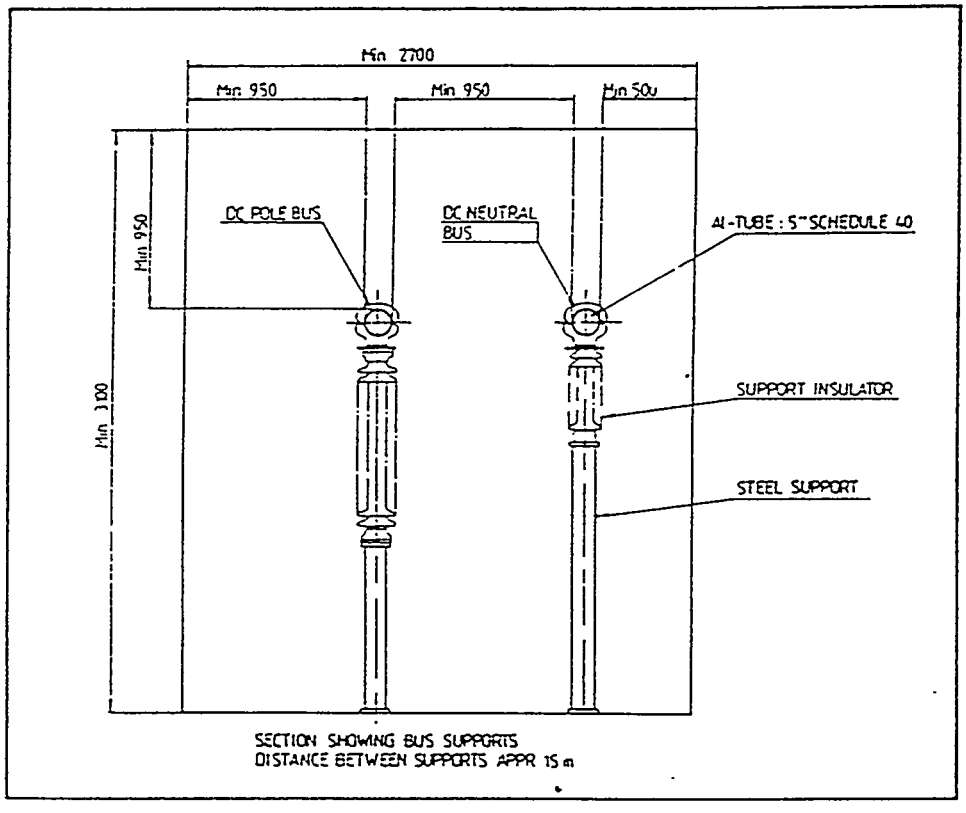


Fig. 8-5. Five-inch aluminum tube bus.

The high-voltage protection unit is used to disconnect klystrons from the bus and to clear klystron arcs. Each unit accepts power from the dc bus and distributes it to approximately eight klystrons. Therefore, about 50 units would be required. If we took advantage of the ability to operate above 500 MeV with a failed klystron, each klystron above that energy would need its own protection unit. In this case, approximately 210 high-voltage protection units would be required for the whole accelerator.

A high-voltage protection unit contains a mechanical-disconnect switch, a fast current-limiting fuse, a remotely-operable electronic dc switch (capable of both opening and closing

operations), an electronic crowbar, current-limiting reactors, a voltage and current monitor, input and output bushings, and various transient-protection circuits. These components would be air insulated inside the high-voltage protection unit's metal enclosure.

The dc switch allows fast connect and disconnect operations from the dc bus. It would provide remote sequenced turn-on of the accelerator klystrons at startup and quick disconnect and subsequent reconnection in case of a klystron arc. The crowbar would be used during a klystron arc to prevent the buildup of excessive current through the klystron while the electronic switch is opening. The fuse would provide backup in case of a failed electronic switch. The electronic switch could take the form of a vacuum tube or a series string of gate turn-off thyristors. An electronic opening switch of this size will require development.

Size estimates have been made for the protection unit, based on existing designs at similar voltage levels. The estimated dimensions are 6 x2x10 ft high. Figure 8-6 shows a typical layout for a protection unit. This particular unit contains a switch tube and ignitron crowbar and is one of the regulator/protection unit designs for the Ground Based Free-Electron Laser Program. The APT protection unit would be similar in layout.

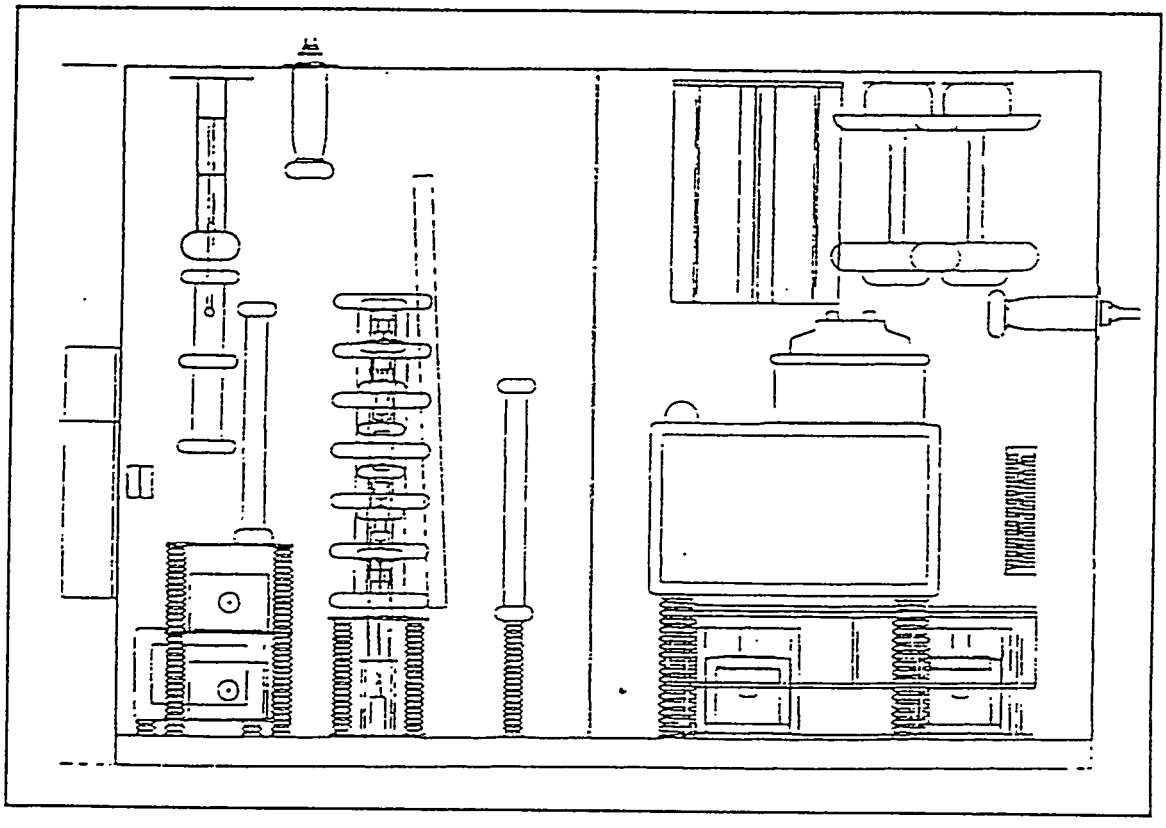


Fig. 8-6. Layout of a typical protection unit.

8.2.2.4 High-Voltage Diagnostics

The protection circuits for the converter equipment will selectively indicate faults to facilitate troubleshooting. A thyristor monitoring function is located in the valve control cubicle. This monitoring function gives an alarm if the number of faulty thyristors within any valve exceeds a preset level. It will also de-energize the converter transformers by

tripping the ac-side circuit breakers if the number of faulty thyristors in any valve are above a preset level when the converter is energized. A pulse train, with one pulse for each thyristor, is compared with a second pulse train. Each pulse in the second pulse train represents a thyristor that has taken up voltage. If a pulse is missing in the second pulse train, the corresponding thyristor is detected as faulty. The number of faulty thyristors and their positions will be printed out at operator request. If a protection orders a trip, the positions of the faulty thyristors are stored until they have been printed out, even if the converter has been re-energized. The thyristor valve monitoring system is a self-supervising computerized system. Internal faults are indicated, and therefore, no backup monitoring system is required.

Diagnostics for the high-voltage protection unit incorporates (1) a dc voltage monitor on the klystron-side of the dc switch, (2) a dc current monitor for measuring klystron cathode current, (3) a blown-fuse monitor, and (4) fiber-optic monitors for dc switch and crowbar internal integrity. The voltage monitor provides direct evidence of the open or closed state of the dc switch. The current monitor will provide fault information that will be used to control the dc switch and crowbar triggers.

For the solid-state switch and crowbar, the trigger status and individual device-blocking capability would be performed continuously. More individual devices would make up the switch or crowbar than are actually needed to hold off the voltage so that if one or two should fail, they need not be replaced until a scheduled maintenance period arrives. This is made possible by the fact that the devices invariably fail in a shorted condition. The trigger circuits are designed such that if a device fails to receive a trigger, it will be triggered by the subsequent overvoltage. This overvoltage is controlled by a breakover diode, and such triggering is not harmful to the device. As in the case of a failed device, the trigger malfunction is detected and repaired during the next scheduled maintenance period.

If an impending failure is detected for any of the major components in the high-voltage protection unit, immediate action will be taken to prevent the possible destruction of a klystron (equipment protection). In the event of an incipient crowbar malfunction, the dc switch and mechanical disconnect switch are opened (in that order). In the event of an incipient dc-switch malfunction, the converters would be shut down momentarily to interrupt the dc current so that the mechanical disconnect switch could then be opened. To monitor the state of the insulation and the conductor surfaces within the high-voltage protection units, corona detectors will be used. Increasing corona levels will require that the unit be serviced at the next periodic maintenance interval.

8.2.3 The RF Module

8.2.3.1 Module Description

An RF module consists of the high-power RF generator, its associated prime power and diagnostics, the preamp, the RF transport, the fast feedback/feedforward controls, the slower system controls and diagnostics, the system interface, and the personnel and equipment protection, some of which was seen in Fig. 8-2.

8.2.3.2 Module Efficiency

The efficiency of operation depends principally on the beamloading and on the RF generator operating efficiency (see Table 8-1). Beamloading in the CCL is over 80%, which leaves very little room for improvement there. The estimated RF generator efficiency for the CCL is 59%. This is based on several assumptions. The first assumption is that the klystrons

have a saturated efficiency of 70% at any design power level. This is the efficiency that the CERN LEP klystron is currently achieving. For APT, however, three different design power levels are needed, viz., 1.25 MW, 0.9 MW, and 0.75 MW. The second assumption is that the mod anode voltages of the klystrons can be used to adjust the klystron current and thereby keep the operating point just 10% below the saturated power level. As the mod anode is adjusted, however, there is a penalty in saturated efficiency.

If we look once more at the graph of CCL output efficiency (from Sec. 6.3, shown again in Fig. 8-7), we see three curves. The first curve (straight line) shows the generator operating efficiency when the klystron current is held at its design level, and the RF output is adjusted with the RF drive to the klystron only. At an output level of 60% compared with the full saturated level, the efficiency has dropped to just over 40%. The second curve (+) shows the operating efficiency as the klystron is kept saturated, but is adjusted. At the 60% output power point, the operating efficiency is just under 60%. The third curve takes into account that a 10% margin is needed to allow for control of the accelerator fields. In this case, the klystron current is adjusted so that the saturated output is 10% above the operating power level, and the operating power level is achieved by adjusting the RF drive to the klystron. In this case, the operating efficiency at the 60% output power point is just over 50%. One can see that if the klystron operating point must cover too much of this curve, the average efficiency suffers. For this reason, three different design power levels for the 700-MHz klystrons are used. It allows the operating points to remain around the 60% dc-to-RF efficiency in all cases.

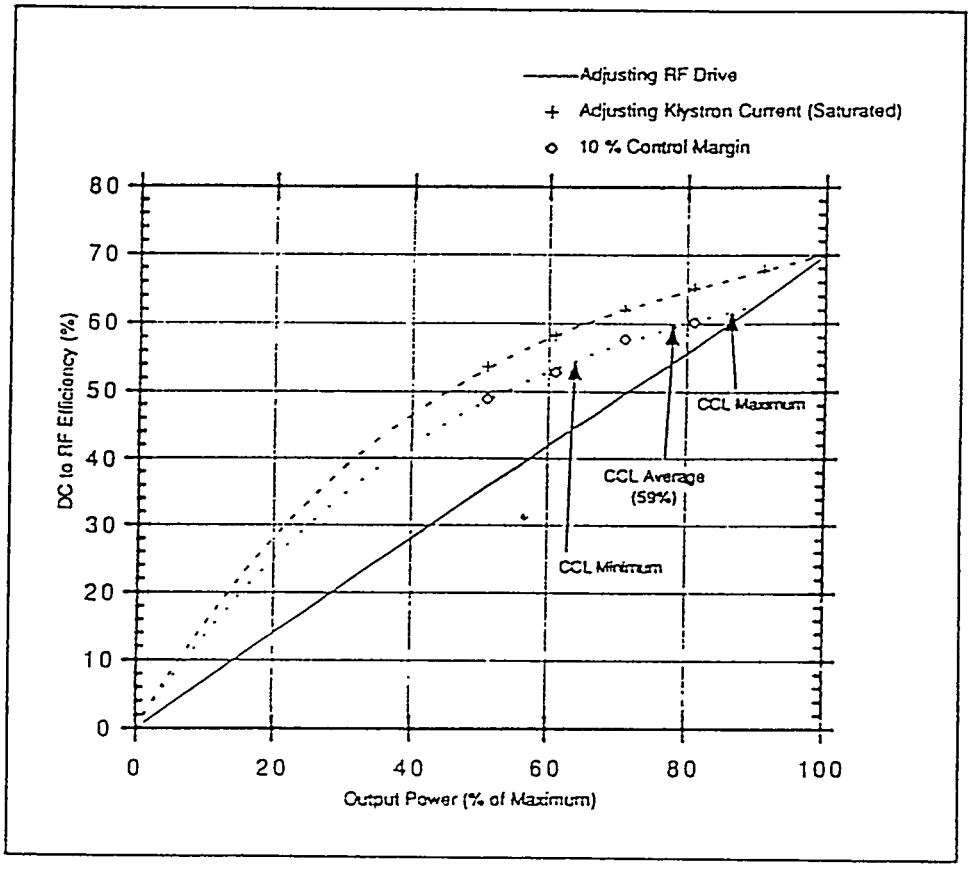


Fig. 8-7. CCL output efficiency using GTA klystron data normalized to CERN tube efficiency.

The third assumption is that a 10% control margin is sufficient for operation. This level was just adequate for the CRL proton cw RFQ accelerator. In most pulsed accelerators, at least 20% is needed to reduce the transient settling time. Because APT is a cw accelerator, there are no large transients that must be corrected. Continuous (cw) operation is inherently more stable, and smaller control margins are generally used (compared with pulsed). A small control margin does put added restrictions on other parts of the system: both the high voltage and accelerated current must be stable, and the cavity detuned to minimize reflected power.

The fourth assumption is that active resonance control of the accelerator cavities is done. Active resonance control maintains minimum reflected power during variations in water temperature, air temperature, and operating parameters.

8.2.3.3 Module Support Utilities

Cooling water and electrical power are required to support the RF modules. The RF modules require auxiliary electrical power for the klystron solenoid coils, the RF driver, the klystron controls, the mod anode power supply, the klystron filament, and the ion pump. The amount of electric power required for the pump motors for each cooling loop is approximately 550 kW. Other significant electrical requirements, per 40 klystron stations, are approximately 300 kW for the klystron solenoids and approximately 280 kW total for the klystron-filament power supply, mod-anode power supply, RF driver, and klystron and high-voltage protection-unit controls. This amounts to some 11.3 MW for RF system support electrical power for the whole accelerator.

Cooling water is required for the klystron collectors, RF loads, klystron output cavities, klystron oil tanks, klystron bodies, and solenoid coils. Such cooling is provided by water in a primary closed-loop cooling system. Ten such loops cool approximately 40 modules each. Each loop has its own electric-motor-driven pumps, valves, filters, flow and pressure monitoring diagnostics, and deionization equipment. On each primary loop, a 178 Million-Btu/hour heat exchanger passes the heat to a cooling-tower water loop.

8.2.3.4 Module Control

One major hurdle in controlling the RF field inside each accelerating cavity is the need to minimize high-frequency, repetitive transient errors that occur in the field. The APT LLRF control system is based on controlling the I&Q components of the RF field inside the accelerating cavity through feedback and feedforward, while an amplitude (A) and phase (ϕ) control system is the traditional approach to RF control. Figure 8-8 shows the relationship between the A&ϕ and the I&Q components of a vector.

One consideration that makes I&Q control more desirable over amplitude and phase control is the precision phase shifter required by an amplitude and phase system to set the cavity phase. With I&Q control, this phase shifter can be eliminated because any field vector can simply be selected with the I&Q amplitude-control setpoints. In addition,

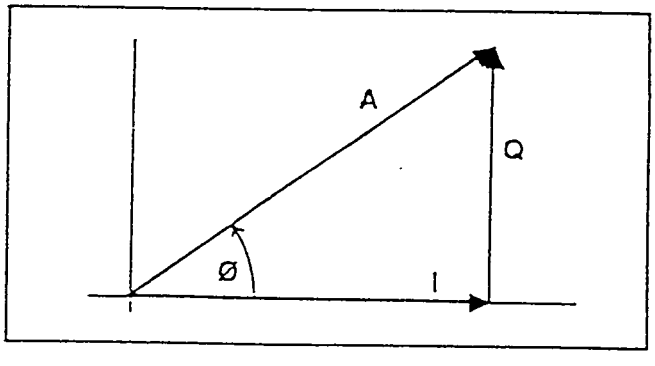


Fig. 8-8. Relationship of amplitude and phase to I&Q.

the signal processing that performs the modulation scheme in an I&Q system can be implemented with digital techniques or linear array products, thus driving the system to a more densely populated, smaller package.

Other considerations included the ease of implementing remotely operable RF control with automatic turn-on sequencing. The nonlinear and transcendental nature of the interactions between the cavity-field amplitude and phase responses due to the RF drive and beamloading does not lend itself to automatic control to achieve the desired performance (±0.5% amplitude and ±0.5° phase). For a heavily beamloaded machine, which requires a certain amount of detuning in order to operate, I&Q control enables easy decoupling of I&Q components. This is virtually impossible using amplitude and phase control. In addition, because of these complicated interactions, modeling the performance of an amplitude and phase control system at some point other than the resonant frequency of the cavity is not practical. To fully develop an operable and predictive RF control system, extensive modeling is performed initially. Models that neglect the cross coupling of the amplitude and phase responses that occur when the cavity is driven off resonance are limiting. An I&Q system, however, eliminates these restrictions.

Due to the physical properties of high-Q cavities, the high-power RF amplifiers, and the delay times associated with long cables between equipment, the potential closed-loop bandwidth of most feedback control systems is limited to a few hundred kHz. Any disturbances in the RF field that have spectral components outside of this bandwidth cannot be corrected by the feedback control system alone. Examples of such disturbances in APT are the beam turn-off transients, switching power-supply noise, and beam noise. Therefore, *adaptive feedforward* techniques are commonly used to predict system disturbances and correct them before the output parameters are modified. Feedforward functions can either be analytically derived in an open-loop manner or experimentally measured and adjusted in closed loop. For the RF control system, the system dynamics relating ripple and transient beam disturbances to the cavity RF field are complex and not well defined. Consequently, a closed-loop feedforward technique is preferable in which the correction function is continuously adjusted or adapted as the system operates.

8.2.4 High-Voltage Generation and Distribution Layout

Figures 8-9 to 8-13 show the high-voltage generation and distribution layout. The converter switchyards are located on grade near the BCDTL. One yard contains the two 250-MW converters, and the other contains the 15-MW converter. The short bus runs along the front end and is connected directly to the 15-MW converter. The long bus is located on the roof of the klystron gallery (see Fig. 8-13) for the BCDTL and CCL and can be connected to either the two 250-MW converters or the 15-MW converter. The site layout showing the converter switchyards is shown in Fig. 8-9. The converter switchyard itself is shown in Fig. 8-10.

8.2.5 Klystron Gallery Layout

Figure 8-11 is a plan view of the klystron gallery for the front end. It shows the klystrons for the RFQs, the DTLs, and the first two modules of the BCDTL. The RF feed points are shown along the beamline. The 350-MHz klystrons are mounted horizontally, and the 700-MHz klystrons vertically. All pieces of equipment were located in such a way as to allow enough space to move any piece of equipment, regardless of where it is located, into or out of the gallery.

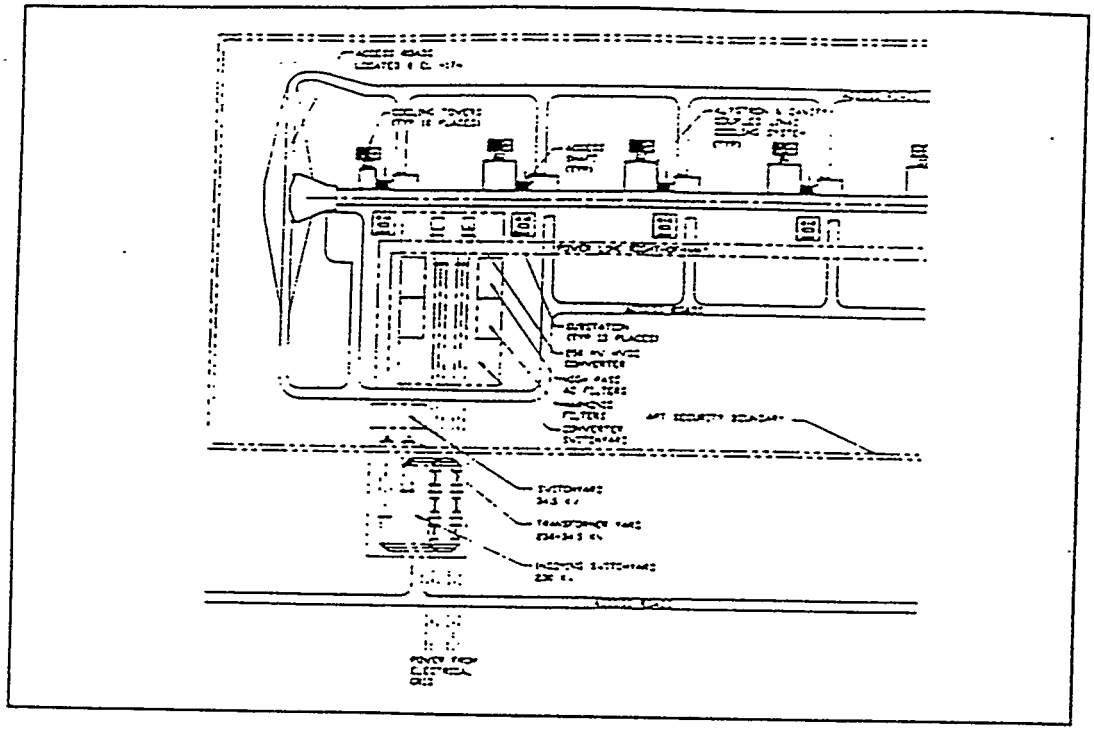


Fig. 8-9. Site layout showing switchyards.

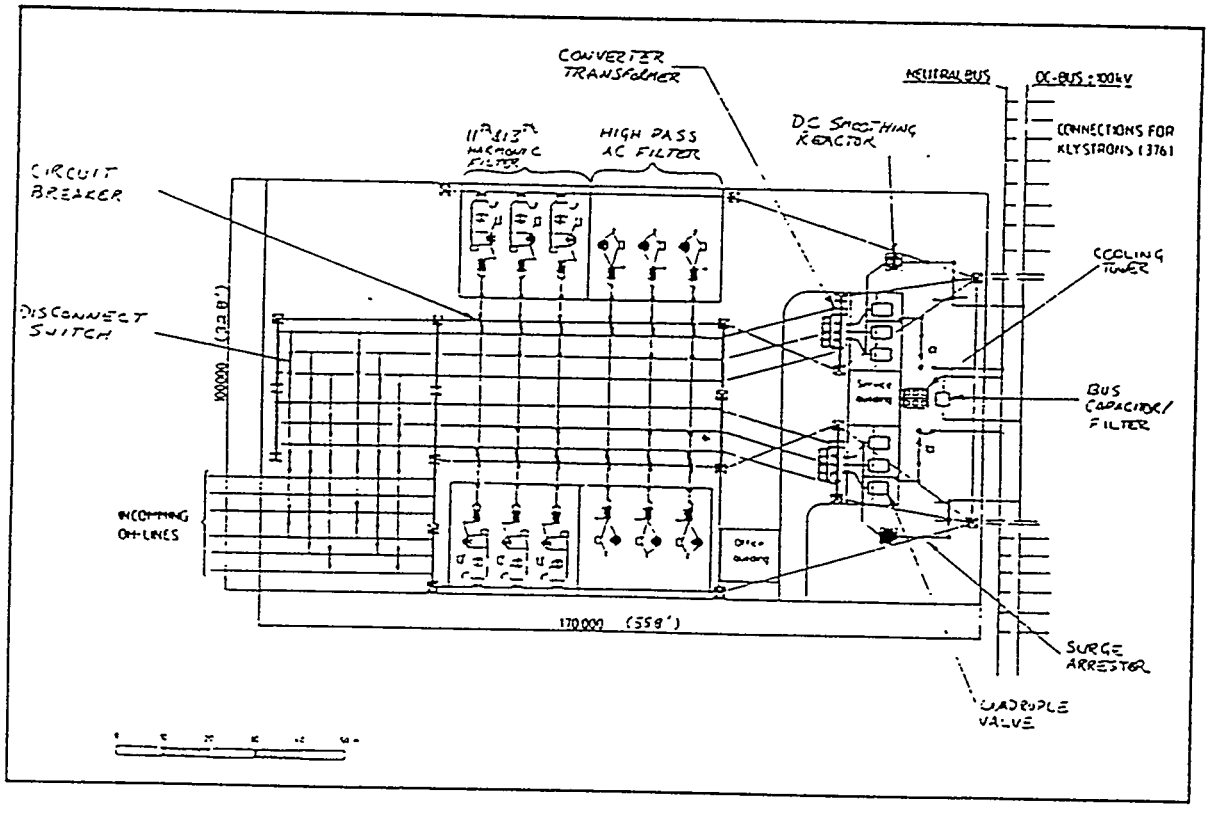


Fig. 8-10. Converter switchyard.

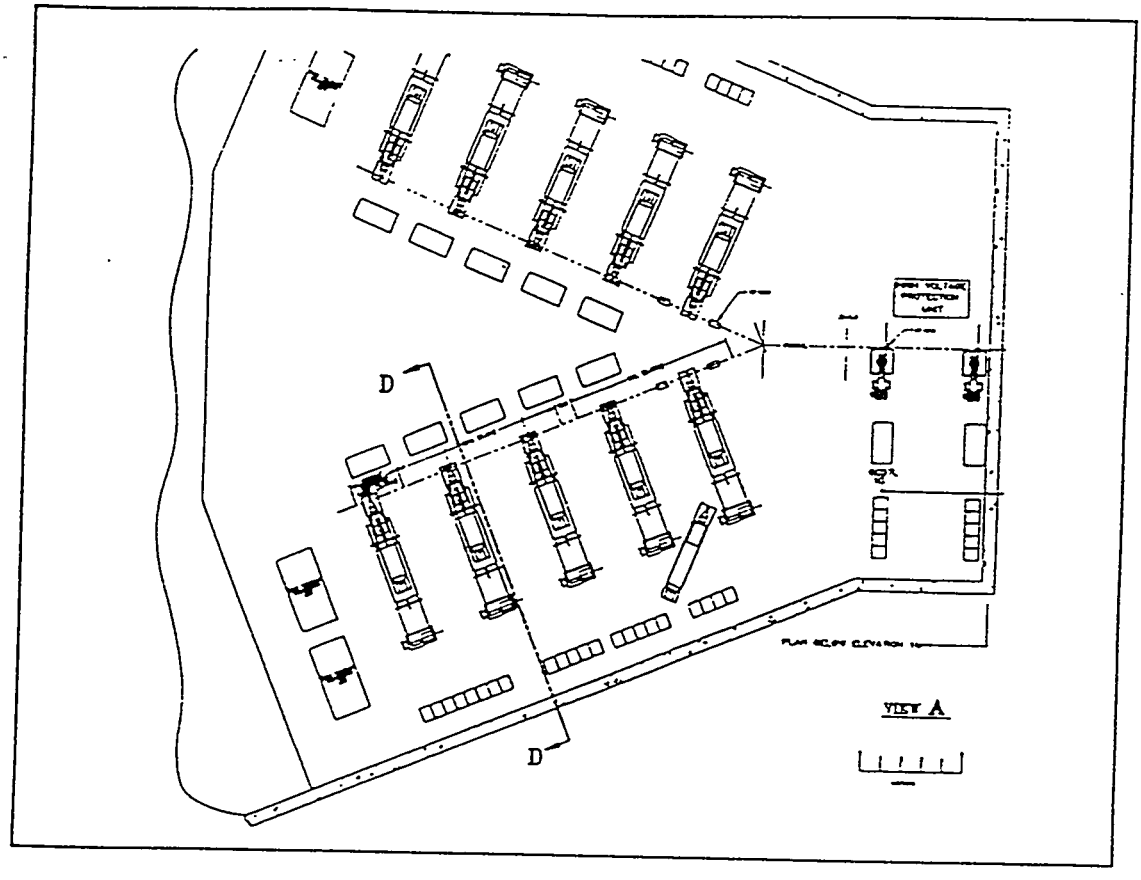


Fig. 8-11. Front-end klystron gallery.

An elevation view in the vicinity of a 350-MHz klystron is shown in Fig. 8-12, and one of the 700-MHz gallery is shown in Fig. 8-13. To minimize space requirements, the circulators were arranged immediately adjacent to the klystrons with their long axes parallel.

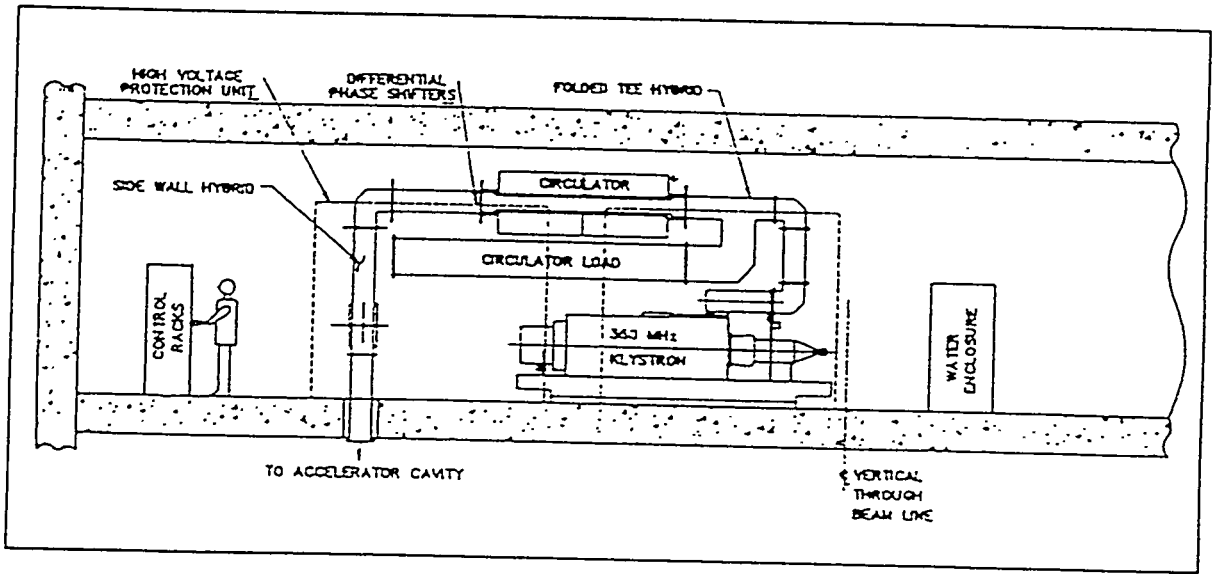


Fig. 8-12. 350-MHz klystron station.

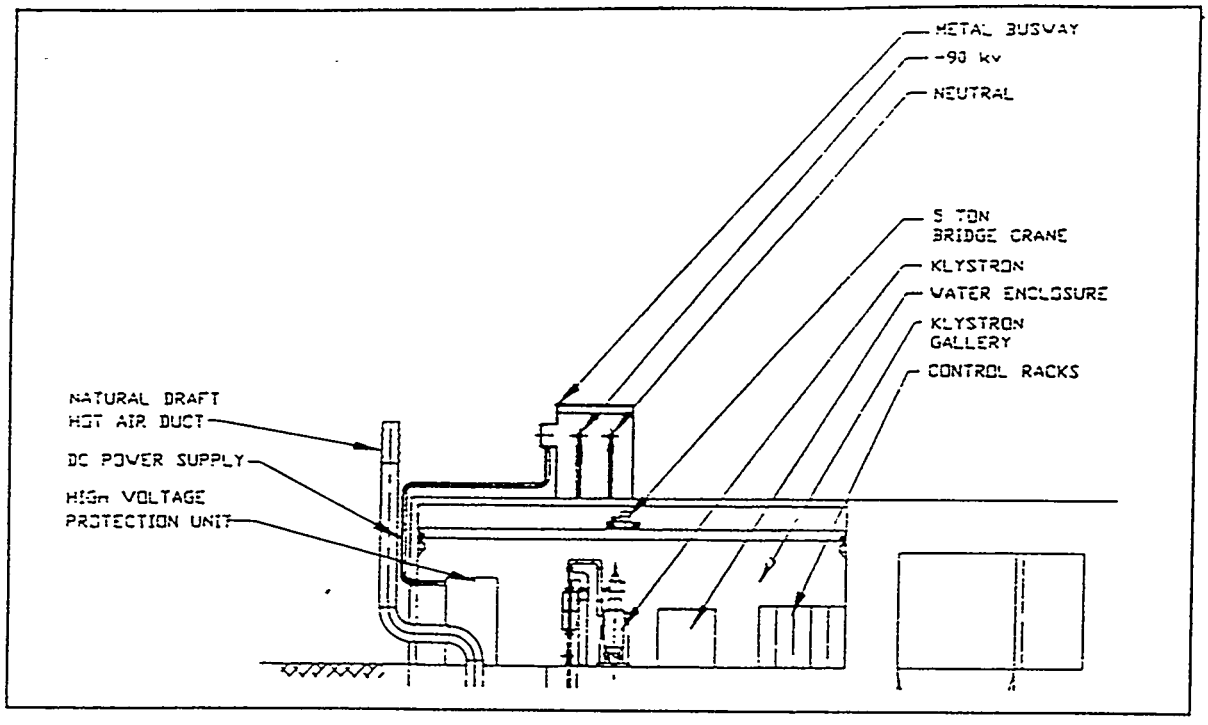


Fig. 8-13. 700-MHz klystron station.

The RF loads are water-cooled, matched terminations connected to one of the circulator ports. The RF loads are estimated to require approximately 15 ft of waveguide. Thus, the 350-MHz load is 15 ft long, and the 700-MHz load is comprised of two 7.5-ft-long sections fed in parallel from a "T" at the output of the circulator. With development, more compact loads and circulators could be available.

Water enclosures containing flow-control valves and gauges for the klystron and RF-load cooling water are also shown in the figures. The high-voltage protection units, as well as the relay racks, are shown for the klystron controls, protection-unit controls, central computer interface, accelerator-pump power supplies, and quadrupole-magnet power supplies. Also shown are the dc bus connections to the high-voltage protection units.

8.2.6 Waveguide Layout

The BCDTL and CCL waveguide layout can be seen in Fig. 8-14. In the front end, the waveguides pass from the output of the circulators through the floor of the klystron gallery to the RF feeds in the accelerator, located on the floor below. One RFQ is fed by two klystrons. The waveguide from each klystron is fitted with a "T" after passing through the floor. The "T" splits the RF power and feeds it to two groups of four drive points. Each DTL tank (three per leg) is powered by its own klystron. The waveguides will be cooled by free convection, dumping their heat to the front-end air conditioning.

The BCDTL and CCL waveguides pass through concrete passageways to the accelerator in the tunnel below. Each pair of waveguides, from adjacent klystrons, has its own passageway. The passageway is sealed at the penetration into the tunnel. The waveguides are surrounded by a thin-walled metal duct to allow free convective cooling. Air, warmed by

the waveguides, rises in the space between the guides and the duct. Cool air is drawn down the space between the duct and the concrete walls of the passageway to replace the rising air at the bottom of the passageway.

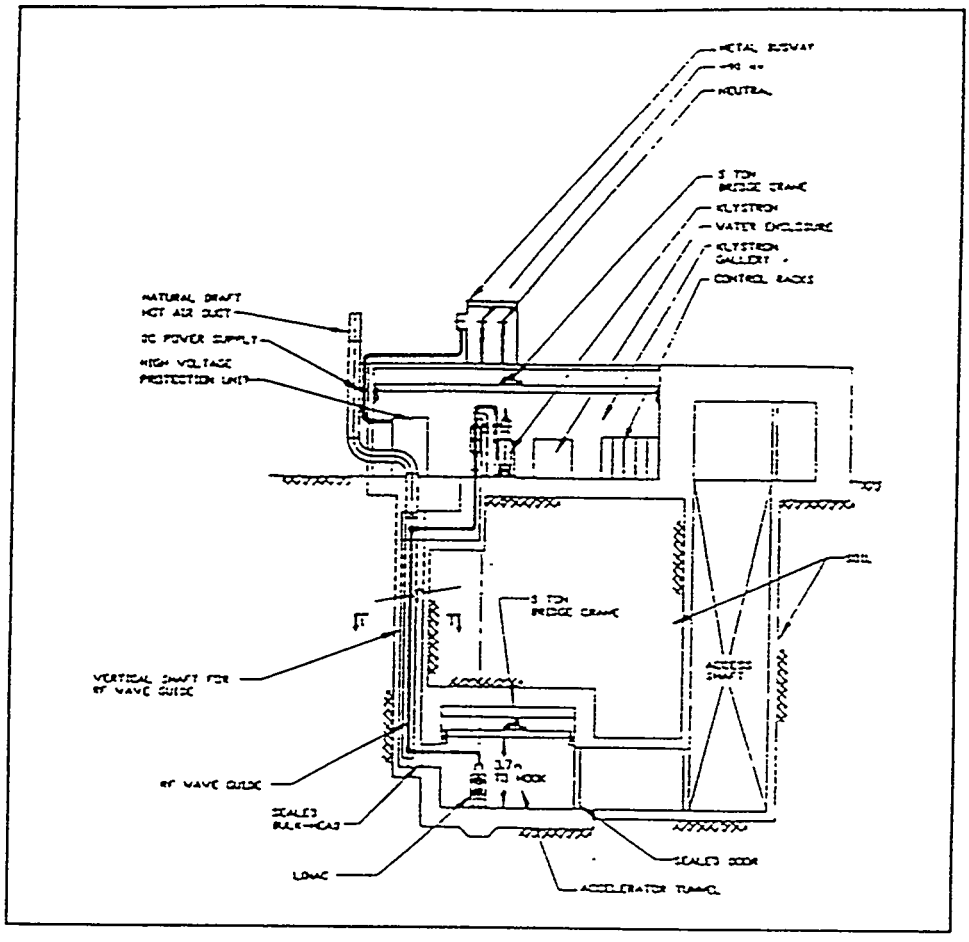


Fig. 8-14. BCDTL & CCL klystron gallery and tunnel.

8.2.7 Additional RF Generators

An option for the layout being considered is to provide a spare RF generator for a block of klystrons, say one spare for every seven klystrons. At LAMPF, the spare system is on the klystron floor, but is not plumbed in. To use the spare, the faulty unit must be disconnected and the spare put in its place. This change can be done reasonably quickly, but still requires a minimum of about 2 hours to complete the changeout. In addition, the spare unit sits unpowered until needed, so there is some risk that the klystron will need some conditioning before it can to be used.

Another option is to have the spare unit connected to power and water and to a load so that it can be running at some level and be a hot spare. As shown in Fig. 8-15, the waveguide runs include the waveguide switches to connect the unit to either a cavity or the dummy load. Figure 8-16 shows the spare klystron connected to a cavity and the failed klystron connected to the dummy load.

Note that the LLRF controls must be switched at the same time that the klystron is switched. Included in this scenario is the knowledge of the proper phasing. When the spare unit is engaged, the LLRF controls must rephase the feedback line to account for the difference in line lengths. This is something that can be measured during commissioning and maintenance periods, and the correction can be stored in the control system for use when needed.

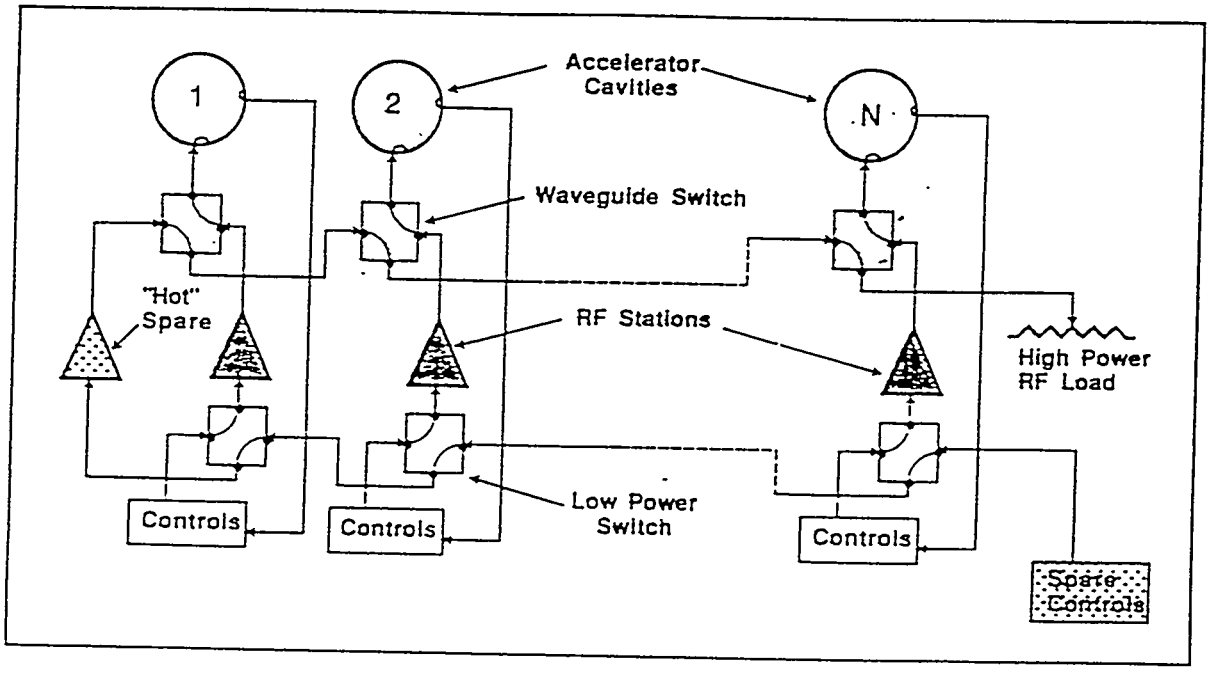


Fig. 8-15. APT multi-klystron unit with spare.

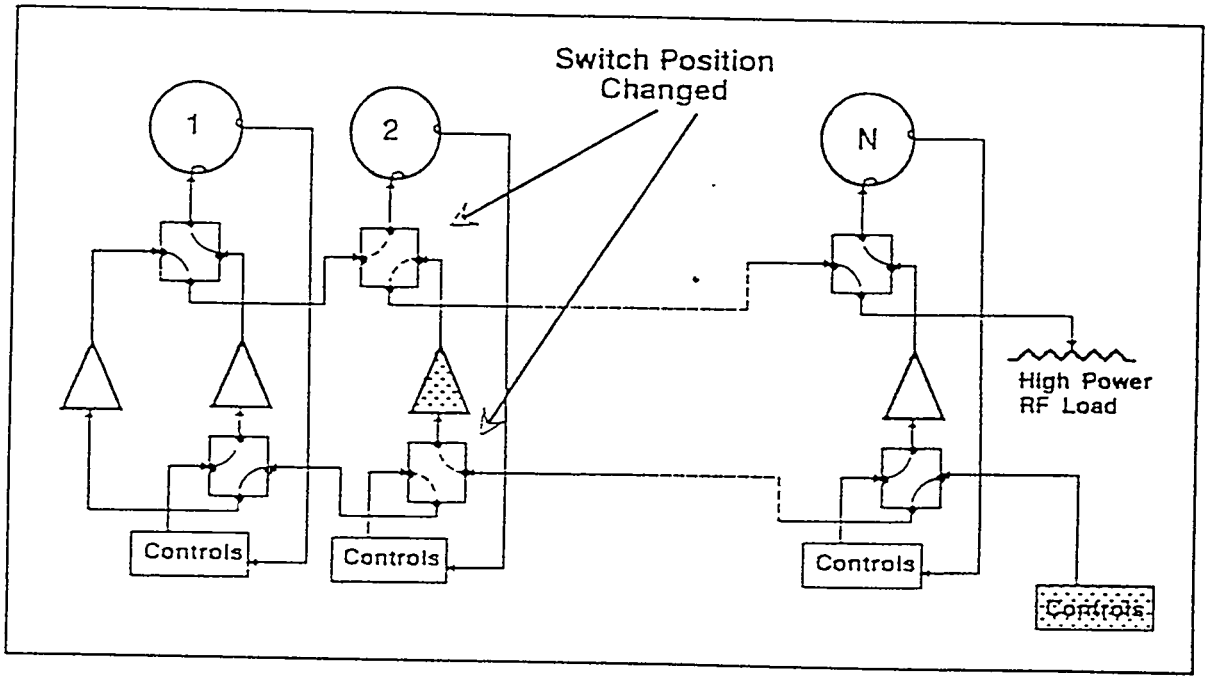


Fig. 8-16. APT multi-klystron unit with spare module in use.

8.3 RF SYSTEM CONTROLS

8.3.1 Control Logic

The system controls for the RF modules must monitor the status of the equipment and the interlocks. From the results of the these status indicators, the controls will either allow the next step to occur (such as enabling the RF) or actually begin the next step (such as turning on the klystron filaments). Generally, the system status and equipment controls have been implemented with programmable logic controllers. These units program in "ladder logic." They can monitor analog and digital inputs, and the outputs can be analog, digital, or switch opening or closing.

Figure 8-17 shows a sample of the logic for startup and shutdown that is based on the status of the system. Different levels of activities occur, depending on the status. For instance, if one klystron arcs, all of the actions described in the crowbar column occur. After the klystron is cleared, the actions reverse. If a high-voltage safety interlock is violated, all the activities in the safety column occur. Again, only after the violation is corrected can the activities be reversed.

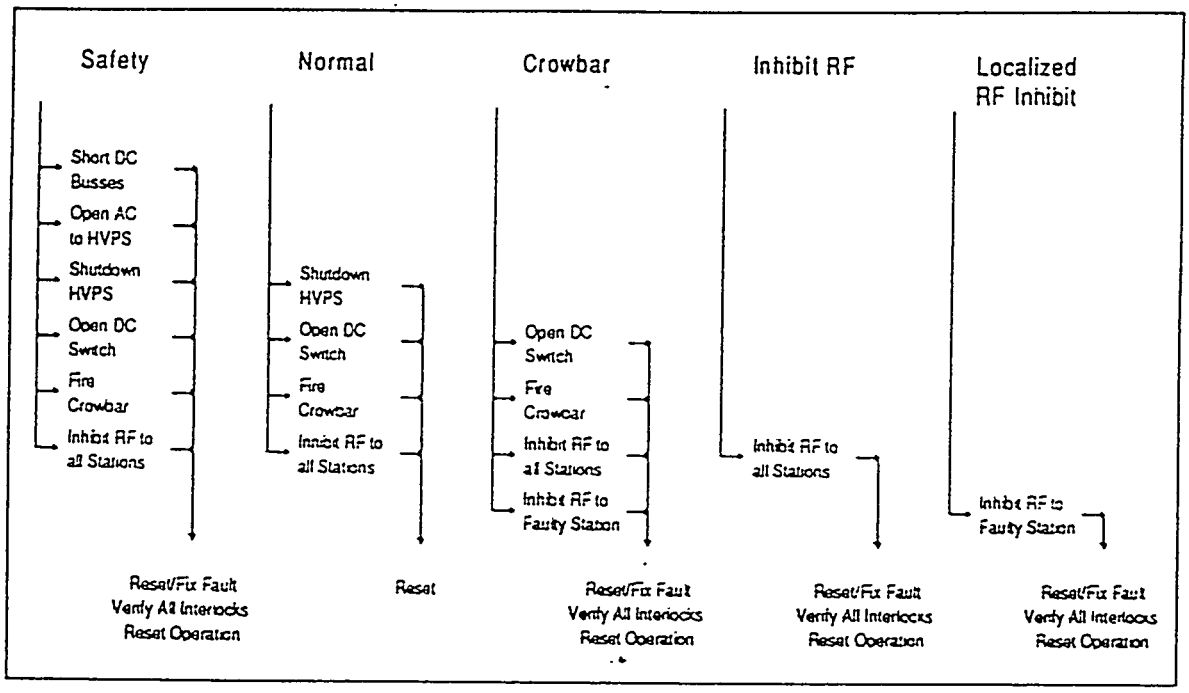


Fig. 8-17. Sample control system logic for startup and shutdown.

8.3.2 VXIbus Format

The LLRF control system is implemented in the VXIbus format. VXIbus (VMEbus eXtensions for Instrumentation) was established by a consortium of electronic test equipment manufacturers and users in 1989. The VXIbus is a complete modular standard that is designed to be independent of manufacturer and system hierarchy. Therefore, the user is not bound to a specific operating system or to a particular microprocessor. Because the VME code is an extension of the VMEbus, however, any existing developed VME code can be

used directly by the VXIbus system. The concept of shared resources dramatically shrinks component size and enables modules to be coupled close together, eliminating long cable connections and their associated propagation delays and timing uncertainties. In addition, the modularity provides good reconfiguration capability because modules are easily removed and installed. The standard VXIbus signal set is sufficient for complete operational control of the RF electronics on each LLRF control system module. A typical LLRF VXIbus module format is depicted in Fig. 8-18.

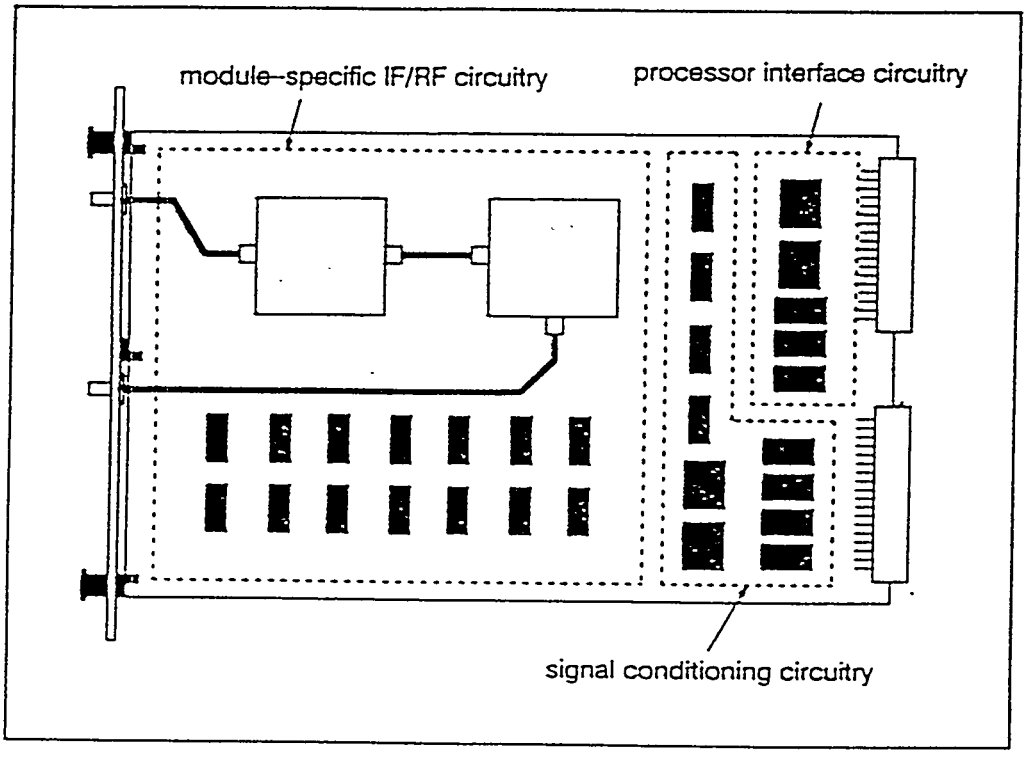


Fig. 8-18. Typical LLRF VXIbus module.

The functionality of the LLRF control system lends itself nicely to the VXIbus format. Figure 8-19, which is based on the various LLRF VXIbus modules, describes how the I&Q components of the cavity field are measured and regulated. It should be noted that the entire control system fits into a standard C-size VXI crate. Thus, it is feasible to fit four LLRF control systems into a standard laboratory 19-inch test-equipment rack.

8.3.3 Feedback/Feedforward

The basic feedback-control system works as follows: a sample of the RF field in the cavity is compared to the stable RF reference signal, downconverted to baseband (20 MHz), and then resolved into its I&Q components. The I&Q components are compared to user-defined setpoints, and I&Q error signals are generated. The I&Q errors undergo simultaneous proportional, integral, and differential (PID) control in parallel circuits. These modified components are the control outputs used to modulate the baseband signal. This modulated signal is up-converted to form the LLRF output signal that drives the high-power amplifier. Use of the feedback-control system has demonstrated less than ±0.5% amplitude and ±0.5° phase variation in the steady-state cavity field.

The feedforward function is incorporated into the control system by applying adaptive correction signals to the I&Q errors concurrently before the PID control circuitry. Each correction function is computed from the current error signal, along with an ensemble of past error functions. Adaptive feedforward techniques have demonstrated reduction in the beam turn-on transients in the cavity field.

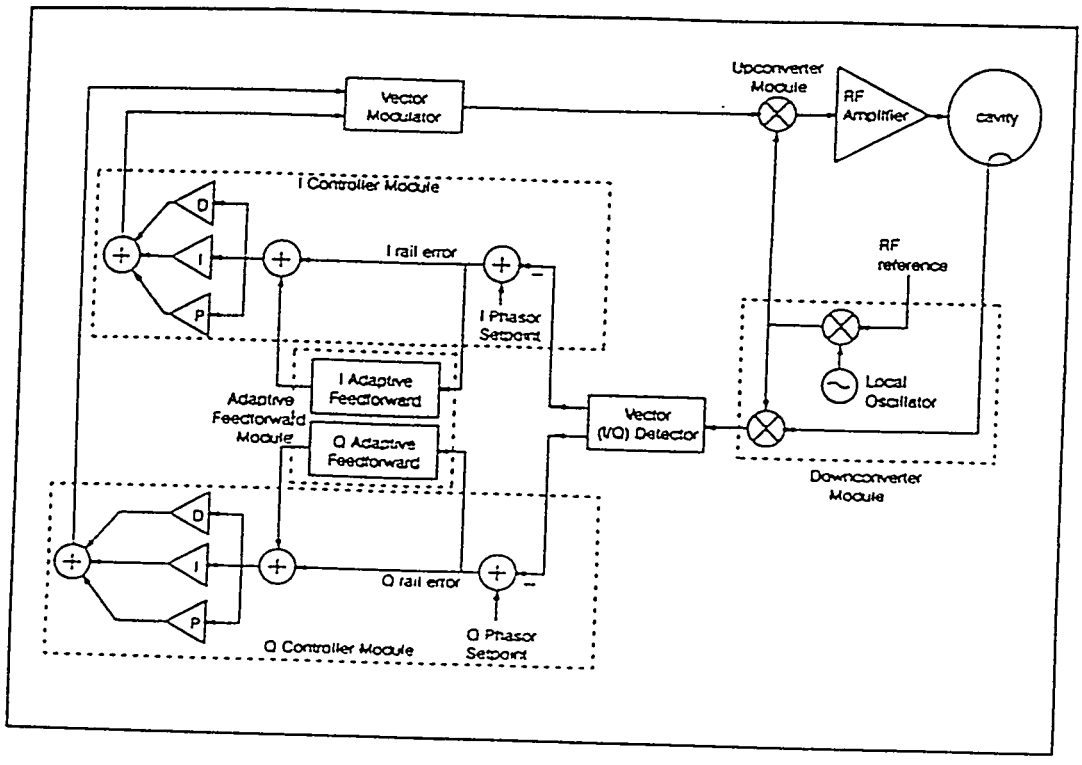


Fig. 8-19. Block diagram of LLRF control system (with power amplifier & cavity).

8.3.4 RF System Modeling

A comprehensive model for accelerator RF systems has been developed. This model allows closed- and open-loop analysis of the complete RF system, including the effect of transmission lines, amplifier saturation, beamloading, beam noise, and many other types of disturbances and nonlinearities. Some initial modeling of the APT 700-MHz system has taken place.

In almost any closed-loop system, there is a frequency range in which an input disturbance is amplified by the feedback disturbance rather than reduced. The goal is to design the system so that known disturbances are either very small in this band or occur at other frequencies. Some initial assumptions were made about the APT system, and the model was used to get an approximation of where this noise gain occurs. Figure 8-20 shows the model results. The gain occurs above about 60 kHz, which is not surprising for a system with one-way transmission-line lengths of 100 ft (as assumed for this exercise).

Another item that was modeled was the settling time for the system during beam startup. This was modeled for two situations (see Fig. 8-21). The first involves a klystron with a large amount of excess drive capability (more than 50% excess drive capability), meaning

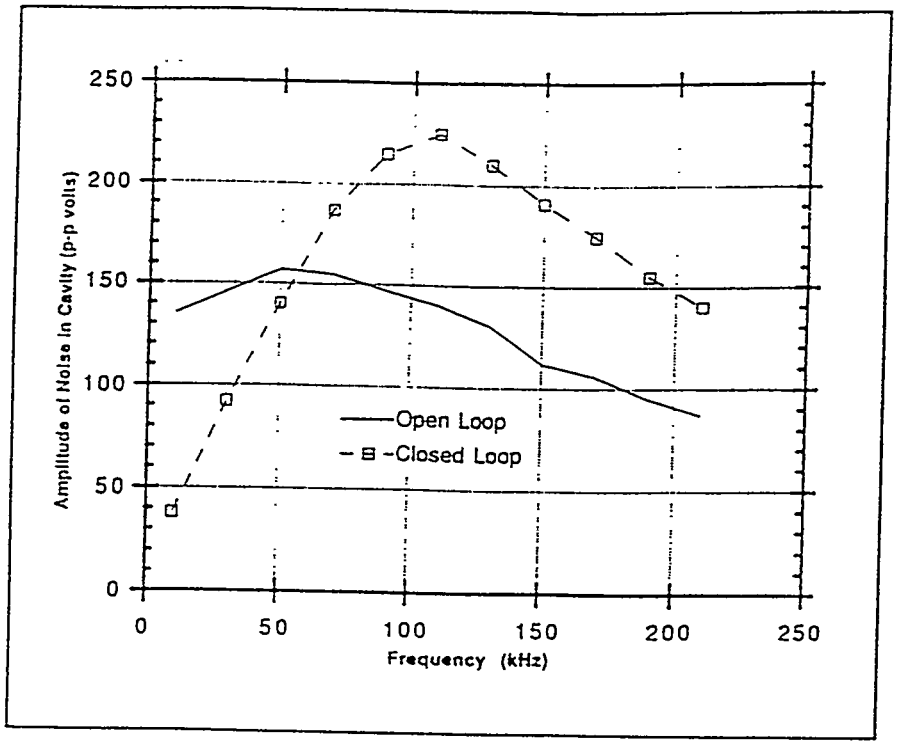


Fig. 8-20. Feedback control in APT: open vs. closed loop.

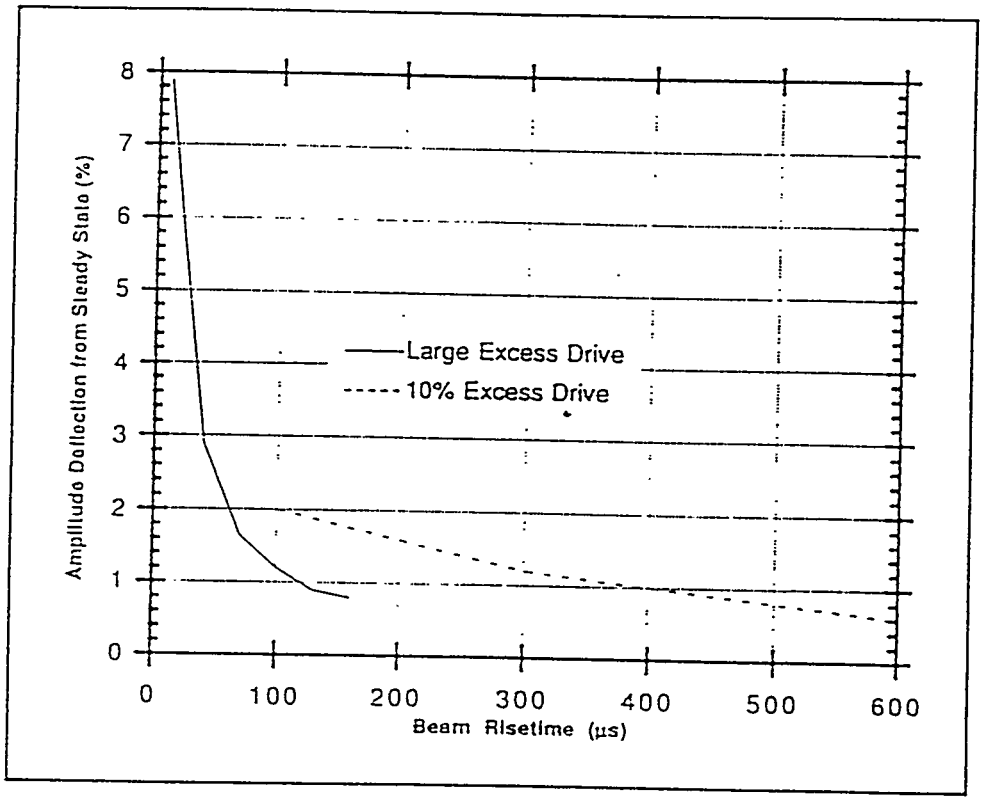


Fig. 8-21. Response of feedback system to beam rise-time.

that if 500 kW is needed in the steady-state case, the klystron is capable of putting out more than 750 kW. This situation implies that the klystron has a large amount of excess drive to apply to disturbance correction. The other case is a situation in which the klystron has only 10% excess drive capability. For both situations, the beam rise-time was varied, and the amount of variation in cavity field was viewed. The criterion we chose was that the cavity field could not vary by more than 1% during the beam turn-on (to minimize beamspill during turn-on). For the large excess-drive situation, the rise-time had to be greater than 120 μs to keep the cavity variation less than 1%. For the 10% excess drive case, the rise-time had to be greater than 400 μs. Feedforward was not used in either case. With feedforward, the situation in both cases would be improved.

8.4 OPERATION / MAINTENANCE / MANUFACTURE OF RF SYSTEMS

8.4.1 Operation

8.4.1.1 Initial Conditioning Operations

One problem with large accelerators is the initial operation difficulty. This problem is most severe with a new machine and usually occurs whenever a machine is operated after a long shutdown. We suspect problems arise mostly from absorbed layers of gas on the accelerating structures, although there may also be some need for polishing or dust removing on the surfaces. The gas is released because of the substantial RF fields, and plasmas and arcs will form during this outgassing process. After some time, the gas is desorbed, and normal operation is possible. The beam is *off* during the conditioning time, so the RF power requirements are low because no beamloading is taking place. The outgassing may be affected by two means: (1) we can heat the accelerator whenever it has been let up to the atmosphere, or (2) we can process the structures with RF power. We propose the latter choice for this structure because insulating the structure and installing heaters to raise the temperature to 400–450°C will not only make a significant impact on the capital costs of the accelerator but also complicate the maintenance procedures.

The initial RF-power conditioning can be accomplished with pulsed or cw RF. In our FMIT experience at Los Alamos, we usually combined the methods, and by starting at a low repetition rate and with narrow pulses, we increased the RF power to full cavity fields. Next, the duty factor was increased up to about 50%, and finally, the system was switched to cw at about 50% fields. The power then was increased until about 125% of full fields was achieved with no beam. The exact recipe for raising the power as a function of time is learned from experience with each new accelerating structure. The process is easy to automate because the input variables are the vacuum inside the accelerator, forward and reflected RF power, and the amount of x-rays being produced by the accelerator section. The conditioning philosophy is to have enough RF power in the accelerator to make enough sparking to raise the vacuum pressure by a factor of 2–5 while conditioning. The aim is to maximize the outgassing rate, subject to the very important practical consideration that the arcing must not be severe enough to damage the high-field surfaces. We were able to initially condition cw accelerator sections for the LANL-NBS Racetrack Microtron with this philosophy in approximately 4 hours per accelerating section. This maximum conditioning time is only required when the accelerator is up to atmospheric pressure, so we expect to do it only once on the whole machine, when it is first built. The maximum time is also required when a particular accelerating section is opened for repair or is replaced. This will be a very rare occurrence, and the vacuum valves between each accelerating tank will minimize the number of tanks that are exposed to the atmosphere.

The RF system will be operated continuously for a long period, such as an entire year, and only a few RF modules that need repairs will be shut down during the normal bimonthly maintenance periods. When the RF system is entirely shut down, generally for annual maintenance of the high-power ac or dc systems, a similar startup procedure will be followed, but the conditioning should require only a fraction of an hour per RF module because very little or none of the accelerator will lose vacuum. Because little outgassing will occur, the conditioning will be rapid, and all modules may be conditioned at the same time.

Conditioning the accelerator cavities with cw power is also possible. The same considerations apply; i.e., we want to outgas the surfaces as quickly as possible, but we do not want to damage these surfaces. Using cw power is simpler, but some conditioning problems, such as multipactoring, respond more rapidly to pulsed power. The specifications of the RF system must be written to permit pulsed operation, especially for the first time, when the cw conditioning has not been demonstrated. With the klystron RF system, we will specify the collectors to accept a certain large dc power, and low duty-factor power can then be produced by simply pulsing the RF drive at the milliwatt level and letting most of the dc beam power go into the collector. For example, if the collector can safely dissipate 1 MW cw, we can adjust the klystron beam parameters to produce a dc beam of 1 MW, and by pulsing the RF drive, we will obtain up to 700 kW of peak RF output power at any duty factor, as long as the klystron has an efficiency of 70% at this voltage and current. Because the accelerating modules are designed to use about 1 MW with full beamloading, the required power for conditioning is only about 200 kW because the accelerator is heavily beamloaded. The drive power may be pulsed by an RF electronic switch module, which is very inexpensive and has sub-microsecond response times. At low duty factor, or low average power, the accelerator sections will be too cold, and the RF systems will have to be operated from the local RF oscillator, which will track the accelerator section's resonance as it is warmed. The various RF systems and accelerator tanks will be delivered and installed over a few years on a project of this scale, and the conditioning will probably be performed during the last year (or longer) of installation. As each module is conditioned, the operating RF module will be fully manipulated and controlled by the central computer, and this will verify the computer-to-RF station communications, hardware, and software. The accelerator sections will be driven to at least 110%, and preferably 125% of the design fields, and they will be conditioned until the arc-down rate becomes sufficiently low. An arc-down rate of one per 8-hour shift per RF amplifier will probably be acceptable. The goal will be to have no more than one arc down, either in the RF generator or in the accelerating section, per 8-hour shift, while exciting the empty accelerator to 125% of the design fields.

8.4.1.2 RF System Startup

For the first startup of the accelerator, all accelerator cavities and RF generators will have been tested and installed, as outlined above. First, all cooling will be activated, and then all magnets will be activated. There will be so many cooling pumps and solenoids that a computer-controlled startup procedure will be preferable. This can be controlled by the main computer and need only take a few minutes. Next, the filaments in the injectors and RF systems will be activated, following the procedures recommended by the manufacturers. Once all filaments have been at full power for the time recommended by the klystron manufacturer (typically 20 minutes), the high voltages may be applied. First, all modulation-anode power supplies are set to the lowest value to minimize the klystron beam current. Then, the main power supplies may be turned on with a ramp, but the power increase must be within the allowable system limits, which might be 50 MW/min. In 2 minutes, the klystrons can be drawing 100 MW of beam power, which is sufficient to produce 50 MW of RF power. The accelerating cavities will not be at the correct frequency, so the individual local

oscillators on each RF system will be used to produce RF at the cavity's resonance frequency, and then the RF power is increased until a large fraction (say 125%) of the design fields are measured in the accelerators. While this procedure is happening, the vacuum and radiation levels, as well as the reflected power levels, are monitored, and a decision is made by the local computer every few seconds to either increase the power, hold it steady, decrease it, or even shut off the RF power to a particularly poor accelerating section. In a few minutes, all accelerator sections should be at full power. Any section that does not respond properly to the turn-on sequence requires manual intervention, and the module probably needs repair. As each section's temperature arrives within a degree or two of the design temperature, the local frequency source is replaced by the master frequency source. The klystron high voltage can be raised to the nominal operating value as the accelerating sections are being warmed up. When the phase and amplitude are locked at the proper values by the control system, an *RF module OK* signal is sent to the main computer. When the computer has received the *RF module OK* signals from all the modules, the proton beam may be turned on at an optimum rate to be determined. For now, we estimate that the beam turn-on process may require a minute or two. This will cause a transient in the cavity fields, but the control system will rapidly—within a small number of milliseconds—regain control of the amplitude and phase of the cavity fields. Because the accelerator sections already will have been conditioned, the entire procedure will be done with cw RF power.

8.4.1.3 Normal Operation

Once all the modules are up to full, nonbeamloaded RF power, the I&Q feedback system is turned on to establish the design values of cavity fields and phases. When all modules are within tolerance, typically ±0.5% in amplitude and ±0.5° in phase, the injector is allowed to turn on, which will probably be a ramped beam, going up to full current in minutes. Any deviation from full specifications triggers a fast-protect signal, and the injector may be stopped, depending on the severity of the fault. For the severe faults, such as the loss of a klystron due to arcing, the injector is stopped, and all other RF modules are reduced in power to supply only the copper (structure) power. As soon as the fault clears, normal operation is resumed, but if the outage lasts longer than ~1 minute, the accelerator tank connected to the faulted klystron may fall out of resonance, and the automatic heating by RF process must be repeated for that tank. A certain number of minor faults, such as the RF being out of tolerance for a few microseconds, are allowed, but recorded to guide future maintenance.

8.4.1.4 Effects on the Utility Grid

APT requires a large load, and the operation of the converters will have an impact on the utility power grid. The following major issues must be considered:

- overvoltages,
- voltage stability,
- resonances,
- overfrequency,
- recovery from disturbances and load ramping rate, and
- harmonic distortions and interferences.

Dropping one or both converters (load rejection) means losing a 250-MW or 500-MW load to the utility grid. The major concerns are the potential problems of overfrequency and

overvoltage on the utility system as a result of the load rejection. The frequency of load rejection is critical. Overfrequency can be a problem if the ac system supplying power to the converters is relatively small and isolated, i.e., with inadequate inertia. Transient overvoltages at the ac feedpoint will result from the generator's load rejection if the impedance of the connecting ac system, which is measured by the short-circuit capacity, is high relative to that required of the converter load.

A convenient means to characterize an ac/dc system is the SCPR, the short-circuit power ratio, defined as the ratio of the ac system short-circuit capacity to the dc power. The lower the SCPR, the greater will be the ac/dc interactions. The following SCPR values can be used to classify an ac/dc system:

- **High.** The SCPR ac/dc system is categorized by an SCPR value >3.
- **Low.** The SCPR ac/dc system is categorized by an SCPR value 2–3.
- **Very Low.** The SCPR ac/dc system is categorized by an SCPR <2.

The problems with low or very low SCPR are more acute when the converters are operating in the inverter mode. The converters for APT will operate in rectifier mode; however, the SCPR still is a good measure to evaluate the potential ac power grid site for APT.

On the basis of soil conditions, the APT project evaluated two potential ac sites. The power companies that will serve the two sites were surveyed—the Southwestern Public Service Co. for the site near Amarillo, Texas, and the Tennessee Valley Authority for the site near Oak Ridge, Tennessee. The responses received from the two utilities are shown in the Chap. 8 Appendix. The ac system strength at the two sites is very strong, and the SCPRs are significantly higher than 3, even with one of the ac lines feeding the ac station being out of service. The high SCPR for the two sites means the effect of the converter load on the ac system will be small and that no unusual or special (i.e., more costly) requirements will be imposed on the design and operation of the converters. The preliminary criteria on harmonic distortion and reactive power exchange mentioned by the two utilities surveyed can be met with standard design. The maximum load-ramping rate identified by the two utilities is not expected to pose operation restriction on the converters. The two utilities surveyed did not express concerns regarding the expected amount and frequency of load rejection. In view of this, it is concluded that both sites are technically feasible. No attempt was made to rank the two sites.

8.4.1.5 Loss-of-Beam Incidents

The beam may be lost or reduced through many mechanisms, and the exact list depends on the final design of the fault-protect logic, which has not yet been done. In this section, we consider some of the more common loss-of-beam incidents and the actions taken for recovery. The loss-of-beam mechanisms considered are: (1) a serious RF fault before the funnel or loss of an ion source; (2) beam interception and subsequent radiation production anywhere along the machine; (3) a signal from the target system that says the beam is out of tolerance or that the target is not ready; (4) RF out of tolerance anywhere in the machine; (5) a klystron arcdown after the funnel; (6) loss of a large RF power supply; (7) arcing in an accelerator cavity; (8) loss of accelerator vacuum; and (9) loss of a focus magnet or power supply. Each of these nine mechanisms are considered in detail below.

- **Loss of Ion Source or RF (before funnel).** The loss of an RF station before the funnel or the loss of one ion source will result in the loss of half the beam current

after the funnel. To maximize the system availability, it seems reasonable to operate the remainder of the system at the half-current level while the out-of-service funnel leg is brought back on-line. This ability to operate at half current is one main reason for using the funnel. During this time, the tritium-extraction rate is halved, but tritium is still being extracted. Preliminary beam-dynamics calculations have indicated that the half-current beam will be well focused in the accelerator, and the only adjustment the RF system will have to make is to reduce the output power of the remaining RF systems in the out-of-service leg to supply only the copper losses and to reduce by 50% the beamloading power for the RF systems after the funnel. The adjustments will be done in a few seconds, and the machine can then produce tritium at half the design rate. When the out-of-service leg of the funnel is repaired, that injector will be ramped on, and the beam current will increase to the design value. With feedforward and a warning that the beam current is about to ramp up, the cavity fields will remain locked at their proper values during the ramp. Indeed, the ramp time is chosen to make this happen, and we envision a ramp time of about one minute.

- Beamloss/Radiation Production. The entire beamline will have dc transducers to measure the current and radiation monitors along the entire beam path. The beam transducers will not be able to measure the normal beam losses, but they should be able to determine current changes to first order. The radiation-detector system will be more sensitive to beamloss. For small increases in radiation, the focus/steering systems will automatically adjust the appropriate magnets to reduce the radiation, but if a certain radiation (beamloss) threshold is exceeded, the whole beam must be shut off and the beam turned on with a ramp that is slow enough so the focus/steering magnets may be readjusted to the proper low levels of beamloss. The RF stations may all be left *on*, and all accelerator cavities will remain at their proper field and temperature levels.

- Beam Out of Tolerance/Target Not Ready. When the beam is out of tolerance at the target, or the target is not ready for beam, the beam must be shut off and not restarted until the target is ready. The RF systems are left on, and the cavity fields are maintained at the design levels. In the beam out-of-tolerance case, the ion sources can be immediately turned on again but slowly ramped up, and the HEBT magnets can be optimized to keep the beam within tolerance.

- RF Out of Tolerance. The RF fields in the accelerator will be within tolerances most of the time because the acceleration gradients are low. In most of the machine, the microdischarge rate will be low and acceptable, but a few cavities must run at fairly high gradients, such as the RFQ, and these cavities will microdischarge relatively frequently. As long as the vacuum in the accelerator is good, and the light from any window discharge goes out, the RF will automatically be reestablished as soon as possible after microdischarges. Once again, the rate of fault is important. If the fault rate is low enough, the RF is automatically reestablished, but if the fault rate is too high, more detailed diagnostics must be used to make other adjustments to reduce the fault rate. In the event that RF fields are out of tolerance by an amount that threatens to scrape the beam, the injectors must be shut off, and all RF systems will revert to the nonbeamloaded state. The beam is then ramped back on, and if the out-of-tolerance condition remains, the offending module must be repaired.

- Klystron Arc-down (after funnel). A klystron arc-down is expected to be a relatively frequent occurrence, especially when the klystrons are new and the final high-voltage conditioning of the klystrons is being done on the APT machine. As pointed out in the discussion on the dc power supply (Sec. 8.2), only two large power supplies power all the klystrons. The klystrons will be arranged in banks of eight that will share a common dc-disconnect switch and a crowbar. The disconnect switch is electronic, with a manual backup for maintenance and safety purposes. When a klystron arcs, its disconnect switch opens and its crowbar fires, and a signal is sent to shut down the injectors and to drop the RF power in all the other modules to maintain cavity-field level only. This protects the arcing klystron. The crow bar can fire in less than 10μ s, and the disconnect switch can be equally as fast. After a second or two, all electrical transients are over, and the klystron vacuum should recover. When the arcing klystron's diagnostics read normal, the crowbar is reset, and then the electronic disconnect switch is connected to the power supply again. The whole procedure should only take 10–30 seconds, but whether the temperatures of the accelerator tanks can be stabilized during this period is not clear. As the crowbar signal is detected, valves will start to close to drastically reduce the cooling of the affected modules. Under some conditions, however, the RF will be off for so long that the start sequence will have to be applied to the eight accelerator tanks. The local oscillators will drive the klystrons at the cold resonance frequency, and as the structures heat up, the frequency will follow the resonance until the resonance frequency matches the rest of the machine. Thus, in the worst-case scenario, each klystron arc can result in 2–3 minutes of lost beam time. A data-logging computer monitors each arc, and whenever a particular klystron arcs at too high a rate, it must be immediately replaced. Klystrons that arc at a high but acceptable rate are removed at the next maintenance period and high-voltage conditioned off-line.

- Loss of Large Power Supply. A large klystron power supply may fault, shutting down half the klystrons. As discussed in Chap. 10, three outages per year of the power supplies are anticipated, with a mean-time-to-repair estimate of 6 hours per outage. During this time, the other power supply may be shut down as well, and then the cold-start procedure must be applied to the entire accelerator.

- Arcing in Accelerator Cavities. Another problem that can occur in accelerators is an arc in an accelerator cavity. When this happens, the injectors are shut down, and the RF power in the arcing module is also shut down. All other RF sources go to their no-beam condition. As soon as the accelerator vacuum and light levels at the window are within tolerance, the RF is turned back on with a fast ramp to the no-beam level, and then the injectors are ramped on. When the arc rate becomes too high, the particular RF module must be reconditioned; however, because of the low gradients in the APT machin, this will be very rare.

- Loss of Vacuum. Loss-of-accelerator-vacuum incidents accounted for about 11% of the accelerator unscheduled downtime for LAMPF in the 5-year period summarized in Chap. 10, Table 10-1. In this case, the injectors and all power supplies are shut down, and the leaking accelerator module must be either repaired in place or replaced. Human inspection of the module is usually required, and enough time must elapse for any radioactive gasses to decay and/or be removed before human entry into the beam tunnel is allowed. In such a case, the mean time to repair may be long, e.g., 12 hours.

- Loss of Magnet Power. The focus and steering magnets along the accelerator and their power supply systems are other frequent failure mechanisms, as shown in Chap. 10, Table 10-1 (12% of the unscheduled down time for LAMPF). Because the magnets are on the beamline, time must elapse before they can be inspected by humans. Once the problem is found, the magnet is either repaired in place, or the magnet is removed and replaced. This process may take up to 12 hours. The power supplies are located in a more benign environment, and they can be replaced quickly. In either case, the beam must be shut off, and the RF systems either shut off (if tunnel entry is required) or turned down to the copper levels when a magnet power-supply problem arises.

Thus, many mechanisms exist for loss of beam current from failures on the accelerator, target, or the accelerator power systems. However, by careful, conservative designs, the failure rates can be low enough to meet the requirements for APT.

8.4.2 Maintenance

As stated before, a regular maintenance period is essential to meet the availability goals of the APT project. The intervals between the regularly scheduled maintenance period are driven by the requirements for the injectors and the RF system. At present, the injectors at LAMPF require scheduled maintenance every three weeks, but the klystrons, with their 20,000-hour MTBF, seem to require even more frequent maintenance. For this study, a single 8-hour shift every two weeks was chosen for the regularly scheduled maintenance. As the design progresses, this maintenance period will be further optimized. The intent is to shut down the injectors, but leave most of the other systems operational during the maintenance period. Any component that has been gradually moving towards its end-of-life condition will be replaced. The RF systems and power supplies must have many diagnostic devices that constantly monitor and report on the internal operation of the devices. These readings and their trends over time are the means by which incipient failures are identified and anticipated. Both the klystrons and their power supplies must be monitored so that 75%–80% of the failures may be anticipated. The anticipated failure idea has been studied most for the klystrons, and Table 8-5 shows some of the diagnostics that will be employed to predict problems before they occur. As an example, the gain of a klystron is not normally measured, but in the APT application, the feedback circuits can compensate for some loss of gain in the klystron. If the gain is decreasing over time because of gap erosion, however, the feedback circuit will lose its ability to compensate for beam-current fluctuations. In the past, accelerator operators simply lived with this gradual degradation in the secondary properties of the power amplifier, i.e., they saw a loss of bandwidth and an increase in noise level. Then, suddenly, the loop would not lock, and the amplifier would be replaced. By monitoring the gain, one can predict the time at which the feedback loop will cease to lock, and one can calculate the added noise and loss of bandwidth caused by the gain deterioration.

Another example of avoidable catastrophic failure is modulation-anode current failure. The modulation-anode current often increases over time, probably because of a film buildup of active cathode material on the anode. Modulation-anode driver systems must be designed with a current limit, usually only about 20 mA, because when new, the klystron will require less than 5 mA of modulating-anode current. If the current data is logged, the klystron failure can be predicted and the klystron replaced before an actual failure. Of course, there is a price for taking this extra data and analyzing it and making the decisions, but payoff is in much better availability. Modifications in the diagnostics listed in Table 8-5 will be based on future design efforts, and then again on actual experience with the cw RF systems.

Table 8-5. Klystron System Diagnostics

Cathode Current	Should be constant at constant voltage
Heater Voltage and Current	Monitor changes in resistance and power increase to maintain beam current
Ion Pump Current	Increase indicates a vacuum leak
Modulation Anode Current	Increase indicates either a change in surface properties of the anode or degradation of beam optics
Body Current	Increase indicates change in beam optics or failure in circulator
Solenoid Voltage and Current	Deviation from original values may imply the solenoid or power supply has changed, or the beam optics have changed
RF Drive Power (fwd and refl)	Any changes in gain are from tuning or geometry changes; can be retuned, but once the gain is too low, the klystron must be replaced
RF Output Power (fwd and refl)	Reduced forward power indicates klystron is failing, while increased reflected power indicates trouble in the waveguide system
Coolant Pressure Drop and Flow	Status of cooling channels and cooling system
Coolant Temperature Differential	Beam intercepted power
Beam and RF Arc Rates	Increasing trends are dangerous
Interlock Fault	Indicates problems with either protection rate circuits or the protection system

If the 20,000-hour MTBF estimate holds, there will be about 165 klystron failures occurring per year, or 13.8 per month in the steady state. Klystron repair contracts are usually written for three classes of repairs: (1) the easily repairable klystrons, which may cost 30%–40% of the new price; (2) the difficult repairs, which cost 60%–80% of the new price; or (3) irreparable damage, which costs slightly more to repair than the price of a new klystron because the klystron vendor must first determine that the klystron cannot be economically repaired. The facilities that build the original klystrons will be adequate to supply repairs and new production for the life of the project. The klystrons will operate for 8700 hours per year, and the manufacturers will be provided feedback about the failure modes, so weak links in the design will be eliminated over time. After a few years, the MTBF should grow, and it should eventually even double. Then of course, the failure rate would drop to half.

We estimate that 14 klystrons per month are likely to experience water leaks or other failure mechanisms that may be more economical to repair at the APT site. Thus, a testing and repair laboratory will be required to perform incoming tests, repairs, conditioning and analysis of faulted klystrons, and retesting of reconditioned klystrons (described in Sec. 3.8). One test stand for every 20–40 active klystrons is an estimate of the required number of test stands. It may be economical for the final conditioning and testing of all the klystrons to be done on the APT test stands because the capital investment is large for each test stand.

The maintainability of the converter station is increased by the introduction of redundancy to an economically reasonable level. The amount of time for maintenance, especially for work that requires system shutdown, is minimized by using exchange modules.

Total maintenance and repair for the required 210 high-voltage protection units would be approximately 90 hours per year. Such a small amount of time does not warrant a dedicated facility. Repair of high-voltage protection units can be performed in the same facility as that used for klystron maintenance and repair.

8.4.3 Manufacturing Issues

A production rate of 12 klystrons per month is required to provide an initial set of 396 klystrons (which includes some spares) in 33 months. At present, the largest klystron factory has produced a maximum of four 1-MW cw klystrons per month. This was done by making additions to an existing facility. The APT project would require three fairly substantial (but not huge) additions to existing klystron facilities. These additions must include both testing and manufacturing areas, and whether these facilities are best located near sites of existing klystron production or closer to the eventual APT site is not clear. Because the cost of each klystron is expected to be between $200–300K, the total cost will be approximately $100M, almost 20% of the entire worldwide microwave tube sales for a year. The factory additions are expected to cost a few tens of million dollars in total. Based on past experience with large accelerators, more than one klystron vendor is desirable.

The converters and the associated equipment in the ac and dc switchyards have been manufactured and used in numerous high-voltage dc systems. The ability to manufacture and supply the converter equipment is not expected to be of concern.

For the high-voltage protection units, manufacturing should take place at a minimum of two plants. A carefully planned assembly and test facility should be able to produce at least five units per month. Two facilities could supply all of the needed high-voltage protection units in less than two years.

SUPPORT SYSTEMS
CHAPTER 9

Page

9.1 ACCELERATOR CONTROL SYSTEM 1
9.1.1 Overview of Functional Requirements 1
9.1.1.1 Hardware Interfaces 1
9.1.1.2 Modes of Operation 2
9.1.2 Control System Architecture 3
9.1.2.1 Input-Output Controllers (IOCs) 3
9.1.2.2 Software Architecture 5
9.1.3 Performance 6
9.1.3.1 EPICS Performance 6
9.1.4 Availability 7
9.2 DIAGNOSTICS 7
9.2.1 Overview 7
9.2.1.1 Characterization Measurements 7
9.2.1.2 Operational Measurements 8
9.2.2 Measurement Systems Details 8
9.2.3 Transverse Measurements 10
9.2.3.1 Transverse Beam Centroids (Beam Position) 10
9.2.3.2 Transverse Beam Angular Trajectory 12
9.2.3.3 Transverse Beam Profiles and Divergence 12
9.2.3.4 Transverse Emittance 13
9.2.4 Beamloss, Halos, and Beam Current Measurements 14
9.2.4.1 Beamloss 14
9.2.4.2 Halo Monitor (Short-Term Interception) 14
9.2.4.3 Transient Beam Current 14
9.2.4.4 CW Average Beam Current 14
9.2.5 Energy, Phase, and Longitudinal Measurements 15
9.2.5.1 Energy 15
9.2.5.2 Output Phase 16
9.2.5.3 Phase Spread or Project Phase Distribution 16
9.2.5.4 Longitudinal Emittance and Energy Spread 16
9.3 MAJOR ACCELERATOR SUPPORT SYSTEMS 16
9.3.1 Magnet Power Supplies 16
9.3.2 Vacuum System 17
9.3.2.1 Ion Pumps (Large and Small) 18
9.3.2.2 Turbomolecular Pumps (Primary) 18
9.3.2.3 Auxiliary Roughdown Pumps (Cart Mounted) 18
9.3.3 Cooling System 19
9.3.4 Temperature/Resonance Control 20
9.3.4.2 CFC Temperature Control Sensitivity 22

9.3.5 Alignment 23
9.3.5.1 Alignment Monument System 23
9.3.5.2 Tunnel Coordinate System 24
9.3.5.3 Alignment Specifications 24
9.3.5.4 Alignment Procedure 25
9.4 INTERFACES 25
9.4.1 RF Power Interface 26
9.4.3 Vacuum Interface 27
9.4.4 Pneumatic Interface 27
9.4.5 Instrumentation Interface 27
9.4.6 Magnet Power Interface 28
9.4.7 Alignment/Installation Interfaces 28

LIST OF FIGURES

Page

Fig. 9-1. Low-energy structure probe design combined with profile measurements. 11
Fig. 9-2. Drift distances vs. beam energy for 0.005% accuracy and 0.1% resolution. 15
Fig. 9-3. Primary-cooling-loop temperature/resonance control system. 21
Fig. 9-4. Alignment monument system. 23
Fig. 9-5. Principal APT linac interfaces. 26

LIST OF TABLES

Page

Table 9-1. Allocation of IOCs to Accelerator Functions 4
Table 9-2. APT Diagnostic Hardware Requirements 9
Table 9-3. Diagnostic Requirements for Beam Parameter/Measurement Type 10
Table 9-4. Video Profile Signal-to-Noise Estimates Based on GTA, FMIT, and ATS* 12
Table 9-5. APT Accelerator Doublet Alignment Requirements 25

9.0 SUPPORT SYSTEMS

9.1 ACCELERATOR CONTROL SYSTEM

The control system for the accelerator is part of the plant-wide APT control system and shares the same software and hardware architecture. Approximately 450 IOCs (input/output controllers) will be located throughout the accelerator complex. These controllers will acquire data, automate most accelerator operations, and integrate the accelerator with the rest of the APT facility. Operation of the accelerator will be conducted from the central control room.

9.1.1 Overview of Functional Requirements

The accelerator control system provides the operational support for, and integration of, the various subsystems in the accelerator complex. Each subsystem—injector, linear accelerator, HEBT, RF power—and other support systems have unique requirements that must be met with a common architecture for control-system hardware and software. The control system will connect to the accelerator subsystems, to the protection systems (personnel protection, accelerator protection, SFAS, etc.), and to other support equipment. For effective control of the accelerator, the subsystems must be tightly integrated and automatically controlled. Operator consoles must provide information about the operation of the accelerator and allow changes to control parameters. Large amounts of data information also must be collected for immediate operator viewing and for archiving onto disk files for later analysis.

9.1.1.1 Hardware Interfaces

The hardware interfaces of the accelerator control system are described in the paragraphs that follow.

- Injector. In the injector, the control system will manage the microwave source, ECR gas flow, ECR solenoid electromagnets, extractor high voltage, extractor electromagnets, LEBT solenoid electromagnets, LEBT steering electromagnets, fast-kicker magnet, variable iris, insertable beam dump, cooling, vacuum, and diagnostics.

- RF. For the LLRF, the control system will perform phase and amplitude control of the cavity field through fast-feedback loops. It will adjust setpoints and monitor the operation of these loops. The LLRF will detect cavity resonance error, and the control system will use feedback to the cavity-cooling controller to reduce this error to an acceptable value. The control system will also adjust the LLRF local-oscillator frequency to track the cavity resonant frequency during cavity warmup. This will be done for all individual cavities. Other control functions include high-voltage control and protection, klystron power (mod anode, filament, and magnets), and cooling for the klystron, waveguide, and circulator load.

- High Voltage DC. The high voltage dc power for the klystrons will be controlled by hardware supplied by the high-voltage dc power-supply subcontractor. The high-voltage dc controls will be integrated with the accelerator control system through the standard accelerator control-system protocol.

- Accelerator Structures. In the accelerating structures, the control system will regulate each cavity resonant frequency using temperature control. The required frequency error band corresponds to about ±1.7C° temperature error. In addition, vacuum components, including pumps, valves, and gauges, will be monitored and controlled by the control system. In the transport sections, the control system will control current and cooling for the electromagnets. Most electromagnets will require adjustment during startup and operation.

- Cooling. Cooling is required for the injector, accelerator structures, beamstops, and electromagnets. The control system will control and monitor the primary, secondary, and tertiary loops (described in BOP topical report).

- Diagnostic Devices. Extensive data will be acquired and processed from beam diagnostic devices. Some diagnostics, such as flying-wire scanners, require active control during their use, and most will require automatic calibration and baseline reference measurements.

- Permit and Protection. The control system will implement a beam- or run-permit function, which prevents injection of the beam into the accelerator until specified conditions throughout the accelerator are met. Beam permit is described in Chap. 10. The control system will also monitor the hard-wired protection systems—the fast-protect, beam-trip, and personnel safety systems. Information on the status of these systems is vital to the operation of the APT facility, and this status will be displayed in the control room.

- Timing. During pulsed operation of the beam, the injector, RF system, and diagnostics are synchronized by a common, distributed timing system. This system will have a pulse delay and gating resolution of 10 ns and an accuracy of less than ±1 ns. The timing signals will be distributed on fiber optic cables.

- Target. Finally, the accelerator control system will receive permission from the T/B controls to switch the beam onto the target. Accelerator status, including beam energy and beam current will be transmitted to the T/B control system.

9.1.1.2 Modes of Operation

The accelerator control will support the following modes of operation: installation and checkout, accelerator commissioning (also recommissioning after extended shutdown), tuneup, standby (no beam on target), normal operation (beam on target), shutdown, and maintenance. These modes of operation are discussed in the paragraphs that follow.

- Installation and Checkout. Portable operator consoles, located near the subsystem equipment, will provide direct support during the equipment installation and checkout phase. The IOCs will operate primarily stand-alone during this phase and will exercise the basic functions of the equipment. In some cases, such as with RF power modules, the IOCs will be integrated into the equipment offsite before installation. This will allow full subsystem integration before installation and will eliminate the need for special test equipment.

- Commissioning. During commissioning, the beam parameters will be measured through diagnostics and adjustments made to system parameters. At times, mechanical adjustments to the accelerator will be required (e.g., aligning

magnets). During commissioning, a large amount of data is collected that must be conveniently available for analysis. RF conditioning of accelerator structures is one part of commissioning. The conditioning process, which can be time consuming when done manually, will be fully automated.

- **Tuneup.** Tuneup operations (see Sec. 10.3) will be automated to the extent made possible by existing technology. Such operations will require an accurate representation of the accelerator by an on-line model and comparing the accelerator operation to that predicted by the model. Wide deviations from the model will require operator intervention in the tuneup process. The automation algorithms must allow for such intervention.

- **Normal Operation.** During normal operation, the control system attempts to maintain optimum operation of the accelerator and watches for warnings, alarms, and impending failures. Beam current, energy, and target illumination must all be within specified ranges, and beamloss must be minimized.

- **Standby.** During standby, the beam is directed into the HEBT beamstop. The control system may operate the accelerator at reduced current. Otherwise, the processes are the same as those for normal operation.

- **Shutdown.** For shutdown, the control system will ensure an orderly shutdown of the RF power modules to prevent stress on equipment and the power grid.

- **Maintenance.** During maintenance operations, the control system will aid in identifying faulty components and in calibrating diagnostics and sensors. Operational data collected during each run will be stored in an on-line database and will be used to predict failures and enhance preventive maintenance. Maintenance and calibration records will also be stored in this database.

9.1.2 Control System Architecture

The control and data acquisition performance requirements and the relatively large geographic extent of the accelerator requires using high-performance IOCs distributed along the LINAC. These IOCs are interconnected via a LAN (local area network). Much of the processing is performed locally within the IOCs, but fast, efficient communication between IOCs is necessary to obtain integration and coordination of their functions. The IOCs will use microprocessors having high-processing capability, probably in excess of 100 MIPS. Based on the VMEbus and VXIbus standards, the IOCs will be highly modular, have excellent EMI protection, and provide high reliability. The LAN will use fiber-optic technology with a capability of at least 100 MBits/s.

9.1.2.1 Input-Output Controllers (IOCs)

Several criteria were considered in the assignment of functions to controllers:

- Integration of the IOCs into the controlled equipment simplifies checkout, troubleshooting, and maintenance;

- Assigning common functions to a single controller simplifies programming and minimizes communications between controllers; and

- Assigning functions on a geographic basis reduces the amount of cabling.

All the above criteria were considered in assigning IOCs, and the results are shown in Table 9-1. For RF controls, one IOC is integrated into each of the individual RF modules. In the case of accelerator cooling and magnet controls, the geographic assignment was more important. Vacuum controls will be put into separate IOCs because the vacuum systems usually operate unattended for long time periods. The cooling, vacuum, and magnet control functions have a large number of channels, but performance is not critical. These channels will be handled with industrial-grade, front-end-distributed I/O equipment connected to VMEbus controllers in the IOCs. Such equipment offers low cost for large numbers of channels and usually provides built-in isolation and signal conditioning. In Table 9-1, the numbers of required channels listed are preliminary and are based on preconceptual accelerator design information and experience with similar accelerator facilities. The known channels are documented in the Chap. 9 Appendix.

Table 9-1. Allocation of IOCs to Accelerator Functions

Accelerator Functions	No. of IOCs	No. of Channels	Location of IOCs
Injectors	2	100	Station 1 utility area
Control of cooling loops, cavity temperature, and electromagnets at RFQs, DTLs, Funnel, BCDTL & CCL	9*	6,000	TBD
Control of cooling loops and electromagnets at HEBT and main beamstop	2*	400	Station 10
Beam diagnostics (incl. fast protect for beamloss monitors)	20	1,500	Two at each utility station 1–10 (VXIbus)
Vacuum control for injectors, RFQs, DTLs, Funnel, BCDTL, CCL, & HEBT (incl. gate valve and cavity vacuum sensors)	10*	8,000	One at each utility station 1 - 10
RF power modules	381	20,000	Within RF power module (VXIbus)
Timing and gating	1	100	Near control room?
High voltage dc controls	2	TBD	Near high voltage dc stations
Beam permit master IOC	1*	50	Near control room?
Contingency	20	10,000	
Total	448	46,150	

*These IOCs may have redundant backup hardware and software to allow automatic functional switchover.

With respect to IOC hardware, it should be noted that most IOCs will be based on the VMEbus standard. A wide variety of VME I/O modules are available commercially. LLRF and diagnostics will be implemented with VXIbus modules. The VXIbus standard permits mixing of high-frequency signal processing with standard VMEbus functions within the same module. For slower I/O, an industrial I/O bus, such as Allen-Bradley, will be used. This will be interfaced to the IOC through a VME module.

The LAN will use the "hub" concept, which allows each IOC to be serviced by a separate fiber-optic cable. This arrangement isolates network traffic, isolates most network failures to a single node, and permits easier monitoring of network loading. A dual network will serve IOCs that require high availability or have high-performance demands on the network.

9.1.2.2 Software Architecture

The APT control system software will be based on the EPICS model. EPICS uses a high-performance runtime database that is distributed in the IOCs. A network-wide database-access standard is used throughout the EPICS components. Operator consoles run on graphical workstations using a window environment, which allows multiple displays on a workstation screen. Besides providing supervisory control, EPICS has tools for building a complete, automatic control system. A description of EPICS is contained in the Chap. 9 Appendix.

The accelerator will be operated from a central control room, and approximately six control consoles will be dedicated to accelerator operations as follows:

Console #1:	ACCELERATOR OVERVIEW, for operating mode, key beam parameters, high-level alarms, safety and protection systems monitoring, and target/blanket status
Console #2:	INJECTOR, for monitor and control of operating parameters
Console #3:	LINAC, for monitor and control of beam characteristics, beamspill monitors
Console #4:	HEBT, for monitor and control of beam characteristics
Console #5:	RF, for overview of all RF modules, with ability to call up details on any one module
Console #6:	BALANCE OF PLANT, for cooling systems, HVAC, etc.

Central services for the control network include network file system (NFS) services, database management system (DBMS) services, and central timing and gating. The NFS will hold files for loading into the IOCs and operator interface consoles. The DBMS will be used to hold operational, calibration, and maintenance data. This database will be used for on-line analysis from operator interface consoles, as well as off-line analysis. Timing and gating will be distributed to all IOCs. The IOCs will be synchronized to a common clock to within 1 ms. Master gating pulses in combination with delay generators at each IOC will allow hardware to be synchronized to within 10 ns.

The accelerator processes will be automated to the extent possible. The operators will guide the operation of the accelerator (supervisory control) and will be able to take over control from any automatic process. The control system will provide automatic fault detection, classification, and operator notification. Depending on the operating mode and the type of fault, the fault detection processes will shut down all or parts of the accelerator, give the operator recommended actions to perform, or continue operating the accelerator in an off-normal mode. EPICS supports automation by providing convenient access to I/O data and through such various EPICS modules as the alarm manager.

9.1.3 Performance

Modern networks and microprocessors have sufficient response time and bandwidth for use on the APT control system. Efficient use of the response time and bandwidth requires software that is optimized for this distributed control and data acquisition environment as discussed in the paragraphs that follow.

- **IOC Processing Speed.** As a general rule, a typical IOC must operate at no more than 50% of full capacity (worst case) when performing I/O, data acquisition, and local control. Under such conditions, I/O rates of 1000–4000 channels per second are achievable.

- **IOC to IOC Response.** Some control and fault detection processes will require access to data across the network. Guaranteed delivery times of 0.01–0.1 seconds will be typical.

- **Operator Interface Performance.** Requirements for update rate and control response on an operator interface display are rather subjective, depending on factors such as operator expectations (consistent response) and type of operation. Experience on typical accelerator control systems indicates that an update rate of 100–1000 channels per second and control response of 3–5 Hz are more than adequate on a single-operator console. An operator will tolerate an occasional slower update rate but will become frustrated with any appreciable slowdown in control response.

- **Data Acquisition.** Large amounts of data will be collected and stored in files for later analysis, particularly during the commissioning stages, beam tuneup, and fault conditions. Much of this data, such as transient waveforms and video images, will be multivalued. Peak data rates of 0.1–1.0 MBytes per second per IOC may be required.

9.1.3.1 EPICS Performance

Using current technology, EPICS has achieved the performance required for APT in all the above areas in systems with 20–40 IOCs, and 6–8 operator interface consoles using Ethernet-LAN technology (10 bits/s). This performance is achieved through the efficient use of the network resources and the asynchronous nature (e.g., no data polling) of the EPICS communications protocol. Additional performance to meet the APT requirements can be met by using dual, higher-performance networks (e.g., 100 Mbits/s each).

The dual-network approach will segregate the two classes of data. In the first class are data acquired for updating operator displays and for archiving to disk. Such data have high bandwidth requirements, but these data also have noncritical delivery times. The IOCs can act as data buffers during the short times when there are peak data rates. In the second class are data required for control and fault-detection processing. These data are generally low bandwidth, but have critical delivery times. Further performance improvements can be achieved by isolating segments of the networks with bridges.

9.1.4 Availability

Availability of the control system can best be met by minimizing the MTTR and providing redundancy. The modular nature of the IOC hardware will facilitate quick serviceability. Built-in self tests and diagnostics will help minimize the MTTR. Near identical IOCs—one a primary and one a backup—will perform the same operations, implementing redundancy. If the primary fails, the backup IOC will take over immediately.

The dual network gives the added benefit of redundant networks, albeit with reduced performance. If one network should fail, the control system could be operated in a degraded mode, with the remaining network handling all communications. Some reduction of allowable peak data acquisition rates would be required.

Most IOCs are not expected to operate through a power failure. However, a short-term, UPS for the IOCs would reduce the chance of short power line "glitches" from shutting the control system down. The UPS should also prevent EMI on the power lines from reaching the IOCs.

9.2 DIAGNOSTICS

9.2.1 Overview

The goal of APT diagnostics is to provide sufficient and necessary beam information to the accelerator commissioners and facility operators so that the machine may be operated under normal and expected off-normal conditions. The two types of beam diagnostics are *characterization* diagnostics and *operational* diagnostics. The characterization diagnostics more fully measure the six dimensions of beam phase space, but at the cost of intercepting the beam. The operational or permanent diagnostics provide a subset of beam information using noninterceptive or minimally interceptive techniques. The average cw beam-power density will vary from tens of kilowatts per square centimeter to over a million kilowatts per square centimeter. Operational diagnostics must be designed to operate throughout this range. The bulk of the diagnostic devices will be of the operational type.

9.2.1.1 Characterization Measurements

As previously indicated, characterization diagnostics measure the six dimensions of beam phase space, but intercept the beam. Characterization diagnostics are most useful in the low-energy portion of the accelerator, and mainly for commissioning efforts. With special care, however, some can also be used at the high-energy end of the accelerator. The characterization diagnostics will be located at key locations throughout the accelerator and at the end of each staged-commissioning experiment. For example, as each DTL is commissioned, a set of characterization beam diagnostics will be located at the end of the DTL so that the beam may be characterized and the operational beam diagnostics may be calibrated. Typical beamline devices used for characterization measurements include Faraday cups, harps, slits and collectors, and collimators. Faraday cups and segmented collimators will be used in the injector and LEBT areas to measure beam current and approximate beam position. The slit and collectors measure the transverse emittance (with pulsed beam), harps measure the expanded beam's profiles, and the beamstops (Faraday cups) will measure beam current.

The 20-MeV funnel area has a separate, permanently-installed offset beamline, the purpose of which is to characterize the beam entering the BCDTL. This beamline will have interceptive transverse emittance, energy, and phase-spread measurement devices, as well as many of the same nonintrusive diagnostics devices used to monitor the accelerator's operation during its normal operating mode

Installing an interim beamstop at or near the few-100-MeV point may be necessary so that tuning the amplitude and phase of the various cavities can be done without spilling beam on downstream components; we believe, however, that the straight beamline and full beam-power beamstop (at 1 GeV) will provide the necessary information for the BCDTL and CCL tuning. Most beam diagnostics of this tuning beamline will be operational, and only a few characterization diagnostics will be required.

9.2.1.2 Operational Measurements

Operational measurements are taken with permanent diagnostics that generally do not intercept the beam. Approximately 80% of the diagnostic devices are either microstrips (striplines) used to measure beam-centroid position, angle, phase, and energy, or ionization chambers (commonly known as beamloss monitors or BLMs) used to measure beamloss and beamspill. Another 10% of the operational diagnostics are video-profile monitors and the flying-wire-profile monitors, both of which are used for measuring transverse beam profiles and emittance. The video-profile monitor can also be used to measure beam position. The remaining devices are graphite jaws for measuring beam halos, beam transformers (toroids) for measuring pulsed and dc beam currents, and capacitive probes for measuring the bunched-beam phase spread.

Microstrips and BLMs will be located throughout the machine except in the injector, the LEBT, and the RFQ. For example, microstrips will be placed between the two magnets of every quadrupole doublet (of which there are over 400), and BLMs will be placed at every intertank spacer (again over 400). Beam toroids (40) will be located before and after every major section of the accelerator to measure and monitor beam transmission. Approximately 40 video-profile monitors will be used throughout the low-energy portion of the machine (to 100 MeV), followed by 45 flying-wire scanners in the high-energy end. Most beam-halo monitors (graphite jaws) will be used in the high-energy sections where beam-halo formation could lead to beamloss—a beam parameter that is to be minimized in this production facility.

All beam diagnostics, both characterization and operational, will be designed for high reliability. All permanent operational diagnostics will be designed to operate at full current. The goal at this stage in the design is to supply a quantity and type of beam measurement devices that will be sufficient to provide real-time beam control such that APT can operate either in a normal or off-normal mode. The ultimate quantities of diagnostics will result from cost-benefit systems analysis in follow-on studies.

9.2.2 Measurement Systems Details

The following beam-diagnostics list (Table 9-2) includes the baseline measurements for APT. This list assumes that there will be sufficient room in the intertank spaces for all the beam diagnostics; if such is not the case, however, compromises will be necessary. These recommendations are made as a function of type and location of measurement. Table 9-2 describes the quantity and type of each diagnostic beamline device required for APT and its

location. Table 9-3 summarizes the requirements for each of the measurement types described.

Table 9-2. APT Diagnostic Hardware Requirements

Accelerator Area	Beam Transformer	Pulsed Beam Transformer	Microstrips/ Striplines	Collimators	Slit and Collector	Harp	Beamstop
Injector/LEBTs	2	2	0	2	2	0	0
RFQs	0	2	0	0	2	0	0
Matching Sec.	0	2	6	0	0	0	0
DTLs	0	4	4	0	0	0	0
FUNNEL (Input Legs)	2	2	16	0	0	0	0
FUNNEL (Output Leg)	1	1	4	0	1	0	0
FUNNEL (Tuneup)	1	1	3	0	0	0	1
BCDTL	1	1	63	0	0	0	0
CCL	1	1	282	0	0	0	0
HEBT	5	5	57	4	0	3	1
Total	13	21	435	6	5	3	2

Accelerator Area	Video Profile Monitor	Flying-Wire Monitor	Beamloss Monitor	Beam-Halo Monitor	Phase Spread	Energy Spread	Faraday Cup
Injector/LEBTs	4	0	0	0	0	0	2
RFQs	0	0	0	0	0	0	0
Matching Sec.	6	0	0	0	2	0	0
DTLs	2	0	4	0	0	0	0
FUNNEL (Input Legs)	16	0	4	0	2	0	2
FUNNEL (Output Leg)	4	0	3	1	1	0	0
FUNNEL (Tuneup)	3	0	3	0	1	1	1
BCDTL	11	0	63	11	0	0	0
CCL	0	33	283	33	0	0	0
HEBT	0	33	55	3	3	2	0
Total	46	66	415	48	9	3	5

Table 9-3. Diagnostic Requirements for Beam Parameter/Measurement Type

Beam Parameter	Beam Device	Permanent Diagnostic?	Used for Real Time Control?	Requires Pulsed Beam?	Fast Protect Input?
Emit., Trans.	Slit and Collector	No	No	Yes	No
Profiles, Trans.	Flying Wire, Video	Yes, Yes	No, No	No, No	No
cw Beam Current	Multicore Toroid, Faraday Cup	Yes, No	Possible, No	No, Yes	Possible, No
Pulsed Beam Current	Single-Core Toroid, Faraday Cup	Yes, No	Possible, No	Yes, Yes	No
Phase Spread	Capacitive Probe	Yes	Possible	No	No
Energy Spread	Spectrometer, Profile/ Dispersive Area	No, Possible	No, No	Yes, No	No
Beam Position	Microstrips, Video	Yes	Yes, No	No	Possible, No
Trajectory Angle	Microstrips	Yes	Yes, No	No	No
Beam Energy	Microstrips	Yes	Yes	No	No
Beam Phase	Microstrips	Yes	Yes	No	No
Beam Loss	Ionization Chamber	Yes	Yes	No	Yes
Beam Halos	Graphite Jaws, Wire Scanners	Yes, No	No, No	No, Yes	No

Beam Parameter	Beam Device	Range	Accuracy	Resolution	Bandwidth
Emit., Trans.	Slit and Collector	±3 sigma, trans.	250μm x 2 mrad	100μm x 0.25mrad	few 0.1s Hz
Profiles, Trans.	Flying Wire, Video	±3 sigma, trans.	250μm	100μm	10 Hz
cw Beam Current	dc Transformer, Faraday Cup	<1–200 mA	< 1 mA	few 0.1s mA	few kHz
Pulsed Beam Current	Pulsed Transformer, Faraday Cup	<1–200 mA	few mA	< 1 mA	few MHz
Phase Spread	Capacitive Probe	5–40°	≥ ±10°	±1°	>50 kHz
Energy Spread	Spectrometer, Profile/ Dispersive Area	6 sigma, long.	few 0.1s% in ΔW/W	few 0.1s% in ΔW/W	few 0.1s Hz
Beam Position	Microstrips, Video	± 0.8 aperture	< few % of aperture	< 0.1s% of aperture	few MHz,10 Hz
Trajectory Angle	Microstrips	±few 10s mrads	±few mrads	±few 0.1s mrads	few MHz
Beam Energy	Microstrips	±20% nom. W	±few 0.1s% nominal W	± ≤0.01% nominal W	few MHz
Beam Phase	Microstrips	±170°	±5°	±0.1°	few MHz
Beam Loss	Ionization Chamber	10000:1 in loss	>10 few mA	20 pA or 20 pA/m	10 Hz
Beam Halos	Graphite Jaws, Wire Scanners	1 mA to 10s pA	>100 few pA	± few 10s of pA	>10 Hz

9.2.3 Transverse Measurements

9.2.3.1 Transverse Beam Centroids (Beam Position)

We suggest that beam position be measured once in every intertank spacer of the CCL and BCDTL. With a doublet installed in this space, the probes would be placed about every 70–80° in phase advance. This beam position information is the minimum necessary to resteer the beam if a misalignment should start a betatron-like oscillation.

The probe will be a four-quadrant probe that is either a microstrip (stripline) or a capacitive probe. The microstrips have a downstream termination on each lobe (the electrode inside the beampipe), whereas the capacitive probes have no terminations. We will need to use microstrips everywhere an output phase or a TOF energy measurement is performed. The maximum lobe lengths possible are 36 mm at 20 MeV and 100 mm at 1 GeV. The shortest lobe length possible is ~3 mm. The signal-to-noise (S:N) ratio expected for these measurements for the shortest lobe length (i.e., 3 mm long at a 45° subtended angle) at 200 mA of current is ~75–65 dB, and 35–25 dB at 2 mA of current, assuming a practical noise floor of –80 dBm. Typical resolutions for beam position measurements with respect to the beam lobe radius for 200 mA and 2 mA are 0.0065%–0.0200% and 0.65%–2.00%.

The baseline design for these probes is a microstrip or stripline probe whose lobe length is greater than 3 mm at a subtending angle of 45°. In some special cases, we may consider installing probe lobes inside magnets, but the disadvantages to this particular design include getting to the shorter lobes with high-frequency transmission lines, alignment errors, and characterization fixture design problems. The total z dimension to be used by the probe is approximately 1 inch (probe flanges only).

In the low-energy structures (matching section, DTL, and funnel), the probe design is likely to be combined with profile measurements, as shown in Fig. 9-1.

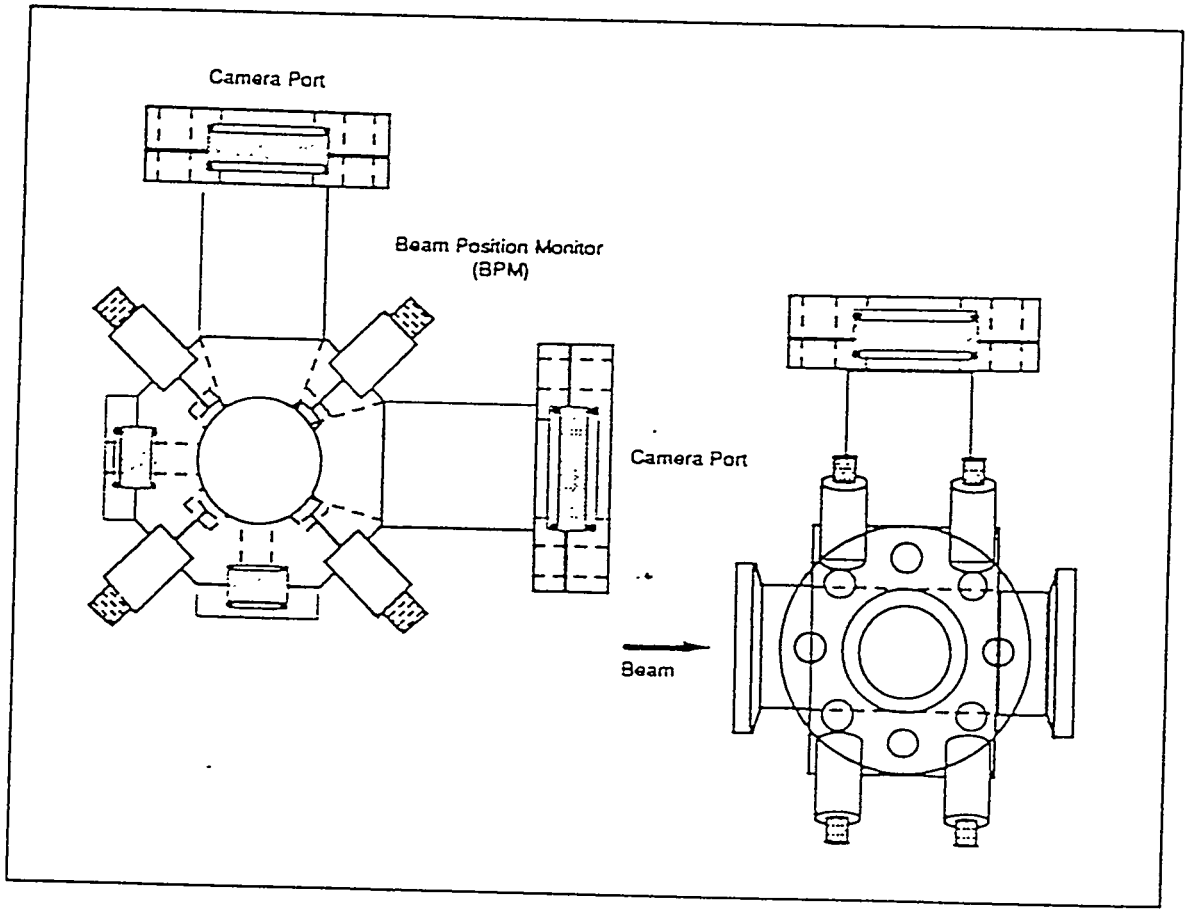


Fig. 9-1. Low-energy structure probe design combined with profile measurements.

9.2.3.2 Transverse Beam Angular Trajectory

In general, no direct measurements of trajectory angle will be done in APT. Multiple beam-position measurements within the beam transport coupled with various beam-transport codes will be sufficient to provide whatever beam angular trajectory information is needed.

9.2.3.3 Transverse Beam Profiles and Divergence

Beam profiles should be measured in the first five-to-seven intertank spacers after each reduction in intertank space length and in the first five-to-seven intertank spacers at the start of the BCDTL and the CCL. Beam profiles will also be measured in the RFQ-DTL matching section, the DTL, and the funnel areas. For energies above 80 MeV, a flying-wire or fiber measurement will acquire beam profiles. From 20–80 MeV, the energy deposited in a carbon fiber increases the fiber temperature above a practical limit (see below) and therefore requires another method. The intertank spaces where mismatches are most likely to occur are at the 20-, 40-, 60-, 80-, 100-, 400-, and 800-MeV energies. The main goal for these measurements would be to measure the cw beam emittance and Courant-Snyder (CS) parameters.

The signal-to-noise ratio using a video-profile monitor throughout the APT accelerator will be sufficient to acquire transverse beam profiles (see Table 9-4). Unfortunately, this measurement requires that the cameras and various light optics be within tens of centimeters of the beam tube. At the higher beam energies and with possible beamspill occurring, the electronics and optics could degrade because of exposure to radiation. Of course, shielding would improve the lifetime of these components. We tentatively suggest the APT baseline profile measurements for energies below the flying-wire cutoff energy (i.e., ~80 MeV) be done using the video-profile-monitor method. This measurement includes the beamline areas of the LEBT through most of the BCDTL. Because the APT beam is continuous, the fluorescent light may be accumulated throughout the standard-camera 16-ms integration time. The video-profile-measurement geometry may be approximately 2 cm long (without flanges) at the beampipe out to a 1-meter radius or incorporated with a beam-position measurement, as shown in Fig. 9-1. In addition, beyond an approximately 20-cm radius, the length grows to 10 cm. Typical resolution and accuracy for these profile measurements are 60 μm and 0.15 mm, respectively.

Table 9-4. Video Profile Signal-to-Noise Estimates Based on GTA, FMIT, and ATS*

Energy (MeV)	Gamma	Beta	Light Production Factor				Expected S:N**
			"1/Beta" Effect	Time Factor	Current Density	Total	
20	1.021	0.203	0.358	66.80	0.16	3.83	230
40	1.043	0.283	0.257	66.80	0.16	2.75	165
60	1.064	0.341	0.213	66.80	0.16	2.28	137
80	1.085	0.389	0.187	66.80	0.16	2.00	120
100	1.107	0.428	0.170	66.80	0.16	1.82	109
200	1.213	0.566	0.129	66.80	0.16	1.37	82
400	1.426	0.713	0.102	66.80	0.16	1.09	65
600	1.640	0.792	0.092	66.80	0.16	0.98	59
800	1.853	0.842	0.086	66.80	0.16	0.92	55
1000	2.066	0.875	0.083	66.80	0.16	0.89	53

*Expected gas pressure is 10^{-6} torr, and rms beam width is 2 mm.
**GTA IMS S:N=60; GTA rms width (mm)=0.8

The baseline design for profile measurements in the BCDTL and CCL will be the flying wire. The flying wire has a beamline space envelope of a 25-cm radius by 6.5-cm length (with a 20-cm length outside this radius). The expected resolution of the profile measurement is approximately 30 pC (or 3 μA) of beam charge (current) by 25 μm of relative wire position. The profile will either be measured by collecting the secondary electrons near the wire/beam interaction area or measuring the charge depletion (secondary electrons leaving the wire) on the moving wire. The wire position will be measured by recording and differentiating an attached tachometer signal.

A very specialized beam profile measurement is required just in front of the target and beamstop at the end of each of the HEBT beamlines. The profile measurements are necessary to verify the expected beam widths for a 50x100-cm rectangular distribution. The measurement will be done using a removable harp-style profile monitor that has wire spacing of 5% of the beam width (i.e., 2.5 x5 cm). Under cw beam conditions and using a specific set of heat transfer assumptions, a 0.50-mm carbon fiber will reach a steady-state temperature of 1284°C, which is well below the 1600°C temperature limit. The harp-profile device must be very robust and capable of withstanding large doses of neutron and gamma radiation from the interaction of the beam with the target area and window.

9.2.3.4 Transverse Emittance

The beam emittance and CS parameters will be measured using separate techniques for on-line or permanent diagnostics and off-line or characterization diagnostics. The permanent diagnostic technique relies on the ability to acquire several profiles of the beam in one axis along the transport of the beam and inferring the phase-space orientations and emittance from these multiple beam profiles or projections. This inference of the phase-space orientations is done by a procedure typically known as tomographic reconstruction and has been successfully demonstrated at several accelerator facilities. The advantage to this technique is that, depending on the profile acquisition method, the emittance and CS parameters can be acquired with little or no beam interception. The drawback to this technique is the difficulty in reconstructing beams that have unusual shapes in either real (x-y) space or in phase (x-x') space. Therefore, these measurements are best performed when it can be assumed that the beam is Gaussian-shaped in real space and ellipsoidal in phase space. Fortunately, it is our estimate that this assumption is adequate for the areas and beam energies in the facility where mismatches are likely to occur.

The characterization technique requires intercepting the beam. Therefore, the beam average-power density must be sufficiently low so that the measurement beamline components that come in contact with the beam are not damaged. In this case, a small area of the beam is allowed to pass through a few 100-μm-wide slits. This beamlet is then allowed to drift to a multichannel collector detector whose width and channel separation are defined so that angular distributions of a few tens of milliradians in angle can be resolved to within a few tenths of a milliradian. For each slit position, an angular or divergence distribution is acquired from the drifted beamlet intercepting the multichannel detector. Therefore, correlated x-x' phase space data are acquired. If it were possible to operate both x- and y-axis slits and collectors simultaneously, x-, y-, x'- and y'-correlated data could be acquired. Whether x- and y-axis data are acquired simultaneously or separately, this particular technique has the advantage of measuring odd beam shapes in both real and phase space. The disadvantage is that it totally destroys or intercepts the beam and usually takes longer to complete (i.e., much lower bandwidth of a few hundredths of a hertz). Also, it will not be operational under cw-beam conditions but under pulsed-beam conditions (<0.5 % duty factor) at full current.

9.2.4 Beamloss, Halos, and Beam Current Measurements

9.2.4.1 Beamloss

BLMs will be placed at every doublet slightly downstream from the second magnet. Placement of these devices are not difficult since they do not occupy any beamline space.

9.2.4.2 Halo Monitor (Short-Term Interception)

The halo monitor does not yet have a detailed design, but is likely to be a key measurement for APT. The existence of beam halo will be a sensitive measure of beam mismatch as the beam travels past the reduction in intertank spacer lengths. The measurement concept is to intercept a portion of the beam halo (i.e., past six rms-widths of the beam) for a short period of time (typically 1 ms) with a thin plate of graphite. A nearby BLM integrates the induced gamma radiation, which is proportional to the intercepted beam. These devices may resemble a flying-wire device and should be placed in the three subsequent intertank spaces past each possible mismatch area (i.e., reductions in intertank-spacer length).

9.2.4.3 Transient Beam Current

A transient beam current measurement will not be needed during normal operation of the accelerator. However, during startup and commissioning, conditions will occur when information of transient beam differences between accelerator cavities or major beamline components will be very useful (e.g., transient cavity beamloading). For this measurement, we recommend that a simple toroid core be provided. The positions of these toroids should be as follows: one in the area between the funnel and BCDTL, one between the BCDTL and CCL, and one after the CCL. Because these devices also have an *in situ* calibration winding, accuracy of <1% and resolutions <0.4% are typical.

Such devices consist of a single, tape-wound, highly permeable core with a single multiturn winding that acts as the secondary winding of a transformer, with the beam providing the primary winding. Typically, these cores and appropriate mechanical hardware are approximately 6 cm long and as much as 12.5 cm in outside radius. An electrical break in the beampipe will have to occur somewhere near the device so that the image current does not short out the beam current through a core.

9.2.4.4 CW Average Beam Current

The average beam current will not be measured in the DTL, funnel, BCDTL, or CCL because more sensitive measurements of beamloss will be made with BLMs, and there is little need for an absolute measurement. Therefore, measuring the cw beam current at the beginning of the BCDTL (i.e., in the funnel) and at the end of the CCL (i.e., in the HEBT) will be sufficient.

The average beam-current measurement will be done using a dc-current transducer, which is a multisaturable-core device that has several types of windings on the various cores (i.e., usually three or five cores). Two windings are *driver windings* that modulate the magnetic fields within the cores so that the cw beam field amplifies this field oscillation. The beam current is proportional to the amplitude of the field oscillation. A separate set of

windings senses the oscillating field that is fed into an amplifier similar to standard transient beam-current measurements. Such measurements are sensitive to shock, vibration, and temperature changes that show up as a drift in the field amplitudes within the core. These problems have been corrected with feedback windings. Overall accuracy, however, is typically 1%, and the resolution over short time periods (few seconds) is 0.5%.

In the *z* dimension (along the beamline), these devices take up more room than the transient beam-current measurements because more cores are needed. The baseline footprint for the actual beamline device is 12.5 cm outside radius and 10 cm in length. Again, an electrical break in the beampipe will have to occur somewhere near the device so that the image current does not short out the beam current through the cores.

9.2.5 Energy, Phase, and Longitudinal Measurements

9.2.5.1 Energy

The beam energy must be measured to set the amplitudes and input phases of the DTL, funnel, BCDTL, and CCL cavities properly. The longitudinal phase advance between tanks in the CCL is ~14°, and in the BCDTL, ~38°. Either phase scans or the ΔT method of determining the proper cavity settings are applicable because minimums and maximums in these scans are likely to occur (because the longitudinal phase advances are small).

The baseline method for measurement of the energy is the TOF technique developed on GTA. The TOF technique uses the four-lobe, summed signals from two microstrip probes with distance d_w between them. It calculates the time a particular bunch travels d_w by measuring the phase difference between the bunching frequency signals. Figure 9-2 shows typical required drift distances for the BCDTL and CCL beams for 0.005% Δw/w accuracy and 0.1% Δw/w resolution. From these plots we can see that TOF techniques will provide sufficient resolution (0.005% Δw/w) with approximately 12 meters of drift at 1 GeV and sufficient accuracy (0.1% Δw/w) with approximately 25 meters of drift.

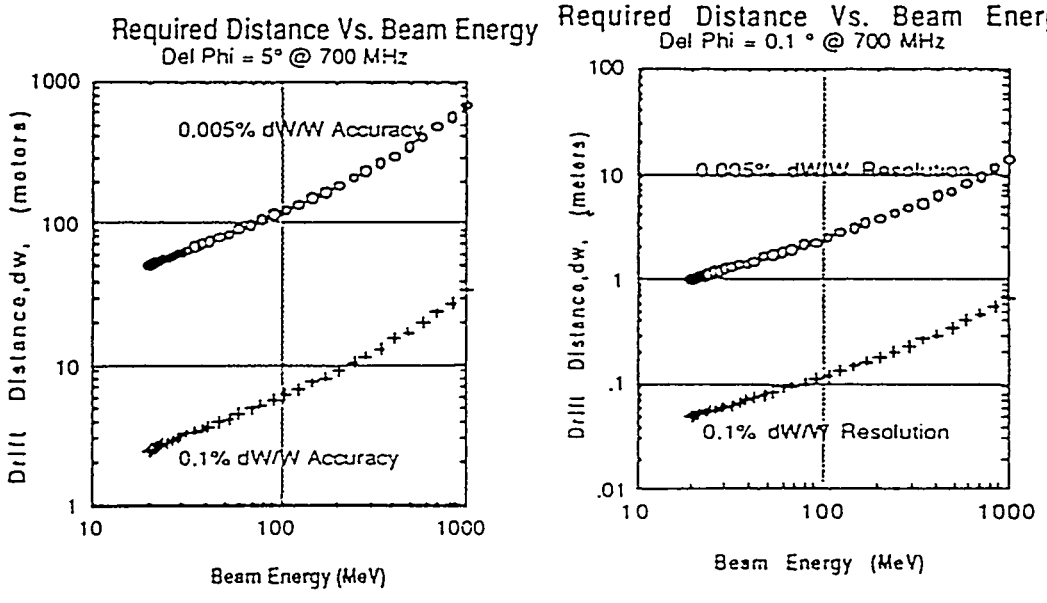


Fig. 9-2. Drift distances vs. beam energy for 0.005% accuracy and 0.1% resolution.

9.2.5.2 Output Phase

The beam output phase is the other beam parameter that is necessary to set the cavity amplitude and phase correctly. This measurement is the phase difference between the cavity accelerating field and the bunch. Physically, this measurement is performed by measuring the phase difference between a cavity field sample and a microstrip summed-lobe signal, compensating for the phase error because of energy differences. The Chap. 9 Appendix (Fig. 12.2.9-2) shows a typical phase scan for a simple single-cell cavity where both the output phase and the TOF/energy measurements are displayed.

9.2.5.3 Phase Spread or Project Phase Distribution

Typical rms-bunch lengths in the funnel, BCDTL, and CCL are 8° of the 700-MHz period, or 32 ps. This time is generally too short to do any time-domain acquisition of beam-induced signals. The baseline for these measurements is a technique developed on GTA for acquiring a relative-measured bunch length by measuring the ratio of the fundamental and higher harmonic of a beam-induced signal from a noninterceptive electromagnetic probe (i.e., a capacitive probe). We have implemented this particular measurement on GTA and calibrated it with LINDA. Its accuracy is <2° and its resolution is <1° over a 10-to-1 dynamic range in beam current.

9.2.5.4 Longitudinal Emittance and Energy Spread

The accelerator itself will require either an energy spread or a longitudinal emittance measurement. Energy spread and longitudinal emittance measurements are typically very difficult to perform in the range that this accelerator will be operating. The baseline concept for these measurements is to measure the beam's transverse width in a dispersive region of the beam transport. These dispersive regions are found in the area of the beam transport where the beam is bent. Larger bends produce greater dispersion (i.e., the effect in which a change in beam energy or energy spread produces a change in beam position and beam width). The primary location for these measurements is the two locations for offset beam-characterization beamlines. The design of these measurements has not been completed.

9.3 MAJOR ACCELERATOR SUPPORT SYSTEMS

The major accelerator support systems that have not already been mentioned include (1) the magnet power supplies, (2) the vacuum system, (3) the cooling systems, (4) the resonance control system, and (5) the alignment system. Some systems are large and costly, whereas others are less costly but have significant impact on the facility engineering design. Among the latter are the resonance control and alignment systems.

9.3.1 Magnet Power Supplies

The magnet power-supply system is a rather large support system for APT. For example, 403 quadrupole doublets are located in the BCDTL and CCL, and each doublet is supplied by an individual high-current, regulated power supply. The DTL operates groups of drift tube EMQs in series, but still requires 18 power supplies. In addition, 12 power supplies

are required in the 2 injector/LEBTs, 4 more in the matching sections, and 19 for both EMQs and dipoles in the funnel. The HEBT contains 39 quadrupole doublets, as well as 11 large dipoles operating on the 1-GeV beam. Therefore, another 50 power supplies of various capacities are needed in the HEBT. Besides the various quadrupole, dipole, and solenoid supplies, the APT accelerator point design is equipped with many small window-frame steering magnets that can be used to steer the beam in both x and y simultaneously. These window frame dipoles are driven by dual-output, bipolar supplies of modest power. Several hundred of these bipolar power supplies are included in the point design. Some of the quadrupole chains, such as those in the DTL, are equipped with shunts so that the individual quadrupoles can be independently adjusted by about 5% of their nominal current. This also occurs in the matching section quadrupole chains.

The power supplies, shunts, and controls are located in the klystron galleries above the shielding where continual occupancy is permitted. Between the magnets and the power supplies are the interconnecting bus-bar conductors. Providing for the voltage drops in these bus bars is necessary, as well as allowing for contact resistance (voltage drops) in sizing the power supplies. The bus bars are required to carry currents of several hundred amperes at modest voltages (up to 40 Vdc). Several options are available for this service, including welding cable, water-cooled conductors, and air-cooled rigid strapping. We have selected rigid strapping based on the experience of LAMPF where water-cooled conductors have proven to be unreliable over the years. Rigid conductors are also preferable for ease of support and packaging in the tight spaces of the waveguide raceways through which the conductors must pass. The straps are sized for free convection cooling in air, namely 155 amps/cm^2. The most typical is a 6.4x0.64-cm copper conductor. Other sizes, especially for the small EMQs and the large dipole magnets, will also be required. About 30 km of such conductor will be needed to supply the various magnets in APT. This estimate is based on the assumption that the power supplies are located an average distance of 25 meters from the magnets and that one pair of conductors is required per doublet or dipole. These straps contribute to voltage drops in supplying the magnets and also to thermal losses in the tunnel, klystron gallery, and in the waveguide raceways. The thermal dissipation in the bus-bar system contributes between 20–110 watts/meter, depending on the magnets being supplied. This represents only a small additional load on the facility air-cooling system but has been accommodated in the facility design.

Most magnet power supplies are driven by 480-Vac, three-phase power, with the exception of supplies for the small steering magnets and a few other special needs. Each power supply is conservatively sized for a power factor of 0.75. The total demand on the facility power grid will be about 10.2 MVA.

In conclusion, the number of magnet power supplies or shunts of various types and capacities needed for APT is measured in the hundreds. This is a fertile area in which careful scrutiny of the power supply market must be made. Because all this equipment is available from many sources around the world, considerable attention should be paid to specifications and parameter mixes to optimize the cost of this large and expensive support system.

9.3.2 Vacuum System

The vacuum system for the APT point design consists of four different types of pumps: (1) large ion pumps, (2) small appendage ion pumps, (3) turbomolecular (TM) pumps for primary pumping, and (4) auxiliary (mobile) roughdown pumps.

9.3.2.1 Ion Pumps (Large and Small)

The APT linac vacuum system is based almost exclusively on ion pumps. The DTLs, BCDTL, and CCL (which make up 97% of the machine) are pumped with 409 individual large ion pumps. In addition to carrying the main vacuum load of the accelerator tanks, ion pumps are also used as appendage aids at the locations of the various RF windows to assist in conditioning by monitoring activity at the window surfaces under high-power RF. In this capacity, another 372 smaller appendage ion pumps are required.

The reasons for choosing ion pumps for the bulk of the APT vacuum system are as follows:

- reliability;
- long operating life;
- no oils or volatile ices;
- no auxiliary compressors;
- no valve requirement;
- radiation resistance;
- vibration-free, nonmechanical operation;
- ease of maintenance and repair;
- no exhaust or effluent; and
- no external cooling requirement.

The price we must pay for these advantages is the high initial cost per l/s of pumping capacity, restriction to the 10^{-6} torr or better operating range, heavy weight (compared to TM or cryogenic pumps), and relatively large bulk per unit of pumping capacity.

The 20-l/s appendage pumps at the RF windows serve two purposes: (1) they provide a good vacuum at the vacuum surface of the window, and (2) they quickly indicate activity on the window surface that is due to multipactoring, glow discharge, or arcing. The latter indication is a useful function during conditioning of the modules when RF power can be regulated by observing the activity at the RF window.

9.3.2.2 Turbomolecular Pumps (Primary)

Four 2000-l/s TM pumps are located in the injectors, eight 1000-l/s TM pumps are located in the two RFQs, and several smaller TM pumps are connected to the matching sections and funnel. All TM pumps are used for primary pumping. In the injectors, the gas loads are quite high. The TM pumps are purchased as part of commercial pump packages that include the forepumps and all the necessary controls and instrumentation.

9.3.2.3 Auxiliary Roughdown Pumps (Cart Mounted)

In addition to the main pumping system, it is necessary to have a number of mobile, auxiliary roughdown units (~10) that can be quickly moved to various parts of the accelerator

when a module must be pumped down after repair. Such units consist of a 310-l/s oil-free forepump and a 330-l/s TM pump, along with associated control equipment mounted on a cart. The carts can be moved under the module and attached to the 4-inch manual gate valve that is provided at the roughdown nipple of each module. The valve is opened and the forepump begins roughdown. The TM pump is turned on shortly after this to aid in speeding the roughdown process. As the forepump loses speed below 10^{-2} torr, the TM pump carries the load with the forepump serving as a compression-ratio booster for the TM pump. The TM pump takes the system to 5×10^{-6} torr, where the ion pumps can be turned on. The roughdown valve is then closed and the roughing unit cart removed.

9.3.3 Cooling System

In the APT point design, about 54 MW of RF power is dissipated in the walls of the linac cavities. To control the stresses that result from the thermal distortions produced in these cavities, the ΔT of the cooling water has been limited to 10C°. This limitation on temperature rise results in large flow volumes of deionized and treated water being required. The water must be specially treated to avoid galvanic corrosion in the dissimilar metals that make up the various accelerator structures, and in some cases, the water must also cross electrical breaks. In these cases, deionization is important to reduce conductivity across the breaks. To meet these requirements, the cooling water for the APT linac must have the following minimum characteristics:

- deionized, low conductivity (1–5 MΩ-cm),
- acidity range = 6.5–7.5 pH,
- dissolved residues = <50 ppm,
- dissolved calcium and magnesium = <20 ppm, and
- filter screens = 50 μ or better.

It should be noted that the above specifications apply to the copper/stainless-steel sections of APT, namely the BCDTL and CCL. These sections make up the bulk of the cooling-water needs. There is an aluminum section of APT, however. This is the DTL (in which the six tanks and their girders are directly cooled by water) that will require somewhat different treatment. Galvanic potential differentials between aluminum, steels, and copper are quite high, and good water treatment is especially critical.

The quantity of water being circulated through the structures via the primary cooling loops is about 22,500 gpm, with another 2000 gpm circulating through the magnets. The structure coolant must be carefully temperature-controlled and must circulate at high flow rates, but relatively low pressure drops, through the primary heat exchanger loops. The temperature rise of the structure coolant is limited to 10C° with a pressure drop of about 40 psi. The magnet cooling permits a much higher temperature rise (40C°) and a pressure drop of up to 150 psi. The magnet coolant also passes through the primary heat-exchanger loops that must be sized to handle the sum of the thermal loads. The reason for providing these primary (localized) cooling loops is to keep any potentially radioactive water in the vicinity of the machine and not allow passage of this water into occupied areas of the facility. The secondary and tertiary heat-exchanger loops will transport the thermal energy up to the cooling towers. In addition to the ~54 MW of RF dissipation in the accelerator structures, another 416 MW is dissipated in the ac power system, the klystron collectors, and the targets or beam dump. About half of the coolant required to dissipate this power may be slightly

radioactive because of its association with neutron production in the machine, the beamlines, or the targets and beam dumps.

With this size thermal load on the cooling towers, operating the accelerator at as high an ambient temperature as possible is necessary to permit effective evaporative cooling under the hottest summertime conditions. The cooling system is designed around a circulating water supply temperature in the primary cooling loops of 36°C and a return temperature of 46°C, with a ΔT in all structures of 10C°.

9.3.4 Temperature/Resonance Control

The cooling of the accelerator structures is predicated on: (1) keeping the structures on frequency so as to limit VSWRs in the transmission lines; (2) allowing rapid (~1 minute) warmup of any cavity in case of a momentary klystron shutdown at that station; and (3) keeping the ΔT in the cavities below the maximum of 10C° to control thermal distortion, limit internal stresses in the structures and joints, and avoid any possibility of structural failure. This is accomplished by means of the resonance control system, which functions as part of the primary cooling loops for the accelerator, controlling the inlet temperature to the cavities. The cavities play the part of the heat sources in this control system, and the heat exchangers play the role of the heat sinks.

Two ways in which the modules can be cooled and controlled to remain on resonance are constant-flow cooling (CFC) and throttled- or variable-flow cooling (VFC). CFC is preferred over VFC and has the following characteristics:

- With CFC, flow through the cavities and the ΔT in the cells remain constant.
- With CFC, the internal stresses will be limited by controlling the ΔT in the cells.
- With CFC, $T_{(inlet)}$ is controlled by an external heater or bypass mixing.
- With CFC, $T_{(ambient)} = T_{(inlet)} + \Delta T/2$ will control the resonant frequency.

Although more complex and costly than VFC, CFC is safer than a VFC system because stresses are maintained within safe limits. The big disadvantage to the VFC system is that a large ΔT can lead to high internal stresses in the cells that add a high risk factor because of the potential for failure of brazed joints and permanent deformation. If the cavities were constructed of stronger material, or if the RF heating caused stress-free and uniform ambient-temperature changes, then variable-flow cooling would be a cheaper and less complex method than constant-flow cooling. Because of the distribution of skin currents in a typical accelerator cavity system, however, significant differential heating does occur, and a cooling system must be chosen that can limit the resulting differential stresses by limiting the ΔTs that cause them. This system is the CFC system that is described below.

9.3.4.1 CFC Primary Control Cooling Loop

A sketch illustrating the typical primary cooling loops for RF-structures resonance control is shown in Fig. 9-3. This sketch shows only one module; however, up to 40 such modules may be operated in parallel and serviced by a single, secondary HEX and cooling tower loop. The loop shown consists of the accelerator tank heat loads that might include several individual tanks in parallel, as in the BCDTL. The load consumes high flow rates of up to 160 gpm (BCDTL module #1). The pumps drive the heated water through a control valve (servo #1) and the HEX primary coil, with bypass flow regulated by another valve

(servo #2). The sum of the flow rates through both valves is constant (CFC). These valves are servo valves, actuated by a digital controller such as the Honeywell UDC 5000 shown. The controller receives its input signals from the RF six-port analyzer located in each RF-drive line. The six-port analyzer takes information from a directional coupler to generate a control signal based on RF phase as an indicator of the off-resonant state of the module. The signals are processed by the controller, which commands that the coolant be partially bypassed through the servo valve to control the temperature in the structure and thereby control the average resonant frequency of the module. The mixing section in the supply line assures that the heated-bypass flow and the cool-HEX flow are properly mixed before reaching the inlet to the module.

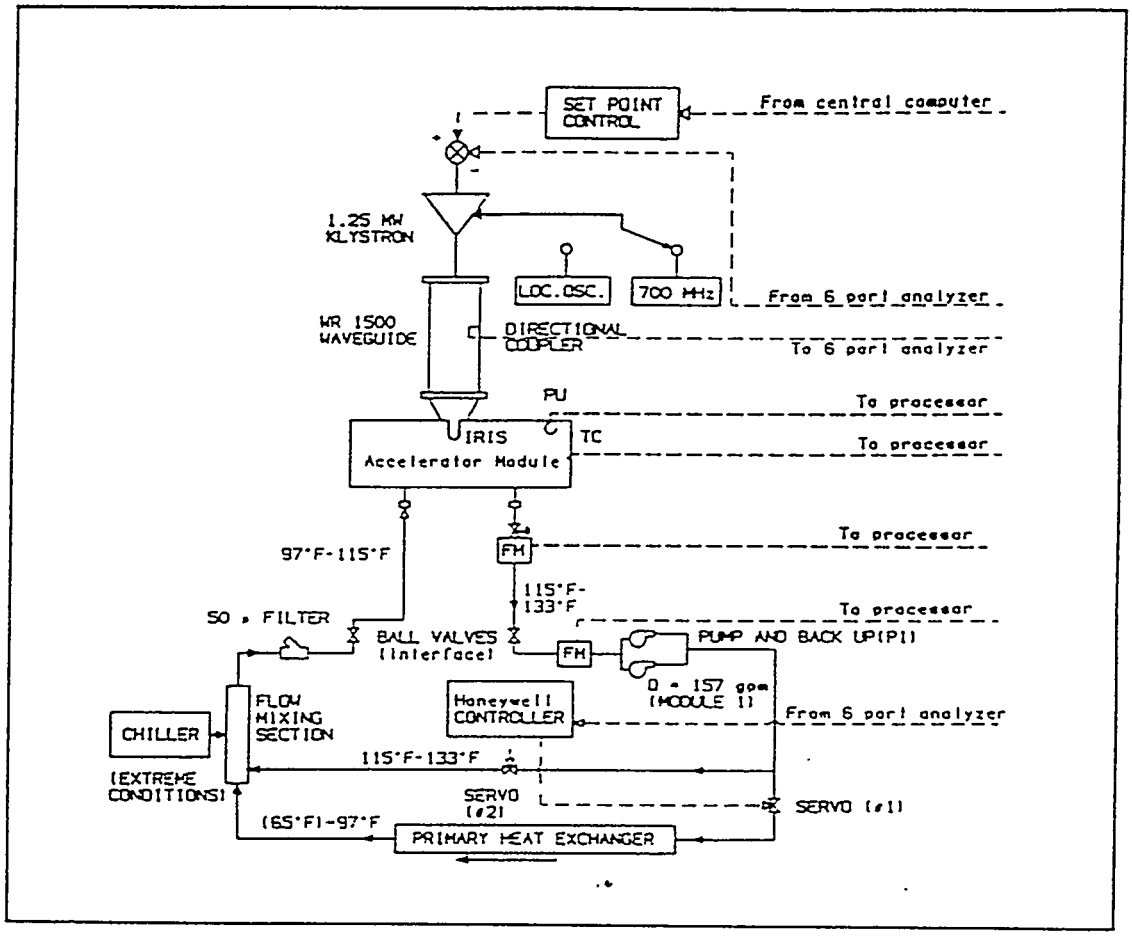


Fig. 9-3. Primary-cooling-loop temperature/resonance control system.

When the module is to be brought up from a cold start, the klystron is switched to the local oscillator. By cold start, we mean the structure temperature is 36°C, the ambient temperature of the circulating primary-loop coolant. At this point, the module frequency may be up to 200 kHz above resonance, that is, about 700.2 MHz instead of 700.0 MHz. However, the klystron can be easily driven this far off its nominal 700-MHz operating frequency without any retuning. So, the local oscillator sweeps the frequency of the klystron high and seeks the cavity resonance wherever it may lie. Each cavity will, of course, be different. Power is then delivered to the cavity. This very effectively heats the structures with

microwave power and rapidly brings the temperature of the copper up (and the frequency down). During this period, the controller is recirculating the cavity coolant, and little or no thermal energy is being removed in the HEX. The flow is remaining constant because of the servo control. The six-port analyzer monitors phase and adjusts the frequency of the local oscillator as the structure heats, converging on the nominal operating frequency of 700 MHz. When the structure nears the desired frequency, the water controller begins closing the bypass valve and opening the direct valve to the HEX simultaneously while maintaining the sum total flow constant. When the proper offset frequency condition has been achieved, the six-port analyzer holds the module at that offset. An offset frequency is necessary because the beam is not present during this procedure, and therefore, a large VSWR will prevail at the iris. Thus, the cavity will operate about 47 kHz off frequency because of iris-detuning effects without beam. When the beam is switched on, the cavity match becomes optimum, and the six-port analyzer transfers to the 700-MHz reference source.

9.3.4.2 CFC Temperature Control Sensitivity

The frequency of the cavity system is linear with the thermal expansion or contraction of the copper over the relatively narrow temperature control range of 10C°. This effect can be expressed as follows:

$$\Delta f/f_o = 1.66 \times 10^{-5} \times \Delta T\,(C) \ .$$

Therefore, for $f_o = 700$ MHz, $\Delta f = 11.6$ kHz/C°. The Q_o (unloaded Q) of the cavity will be in the range of 25,000–30,000, but when the large iris and transmission line loads down the cavity, the Q_{loaded} will be in the neighborhood of only 8000. Therefore, the bandwidth of the tank or module will be about 88 kHz. We can limit RF phase between incident and reflected signals in the transmission line to about 10° by controlling the resonance to about ±20 kHz. This implies control of the average structure temperature to about ±1.7C°. This is considered a reasonable control range.

While the structure is being held to a specific offset frequency by means of water temperature, as described above, the proper thermal distribution resulting from the internal field configuration within the cells will prevail. These distortions will cause internal stresses in the copper and the brazed joints. By holding the water ΔT to 10C°, we limit the maximum temperature excursions in the copper of the CCL to about 18C° (1000-MeV cell), and the Von Mises stresses to under 3800 psi.

LAMPF does not use the local oscillator approach, but preheats the cavities by means of pump-power dissipation and immersion heaters in a mix tank. This is a satisfactory approach for LAMPF because of the relatively low duty factor (10%). If an attempt were made to preheat the primary cooling loop with a heater in the mixing section for APT (not shown), the same offset frequency could be achieved; but if RF power were applied, the complex thermal distribution resulting from the actual field distributions under cw conditions would distort the cavities and produce a significant frequency error. For this reason, immersion heaters are not considered an option for the APT thermal control loops. There is more than enough thermal gain to be had for the control servos, derived from the local oscillator approach for driving the high-powered klystron starting at the "cool" frequency of the cavity.

In Fig. 9-3, we have shown a chiller connected to the flow mixing section labeled *extreme conditions*. This is a standby unit for an abnormal condition, should the control margin be inadequate to bring these cavities to resonance without adding some chilled water. The need for, the location of, and the capacity of these chillers cannot be specified without an exhaustive thermal analysis.

9.3.5 Alignment

The final major accelerator support system discussed in this section is the alignment system. The alignment system uses a facility-based target system where small optical targets, called horizontal and vertical alignment monuments, are surveyed into the walls and floor of the accelerator tunnel and made permanent fixtures for facilitating the alignment of any one module of the accelerator. The monuments are spaced no more than 10 meters apart, and can give precision readouts to ±0.05 mm when used with alignment scopes, optical levels, or plunging transits. The alignment in the tunnel is done in the tunnel coordinate system.

9.3.5.1 Alignment Monument System

A basic assumption in establishing a facility-based alignment-monument/target system is that the stability of the concrete and steel with which the facility is built is adequate. If the tunnel is somewhat flexible over a long span, this in itself does not make the alignment system unusable. Because we have established the targets only 10 meters apart, the only stipulation for the tunnel is that it be stiff and stable within a 10-meter span. It is expected that any flexing of the tunnel within a 10-meter span should be satisfactorily small, considering the high bending inertia of any conceivable structural-concrete design.

The targets themselves will be grouted into recesses in the floor and the walls of the tunnel. They will be covered with screwed-on protective plates and have tooling-ball sockets that are used to make offset measurements. In Fig. 9-4, we see such measurements being made to the module reference targets (which are also tooling balls). Tooling scales can be used to make these offset measurements. In vertical, for instance, a tooling scale can be hung from the vertical monument target, and a horizontal line of sight can be swept from the scale to the target ball on the module using wire-suspended self-leveling optical levels. In the horizontal, a plunging transit can be used to sweep a line of sight from the horizontal monument target to a horizontal tooling scale that touches a tooling ball on the module.

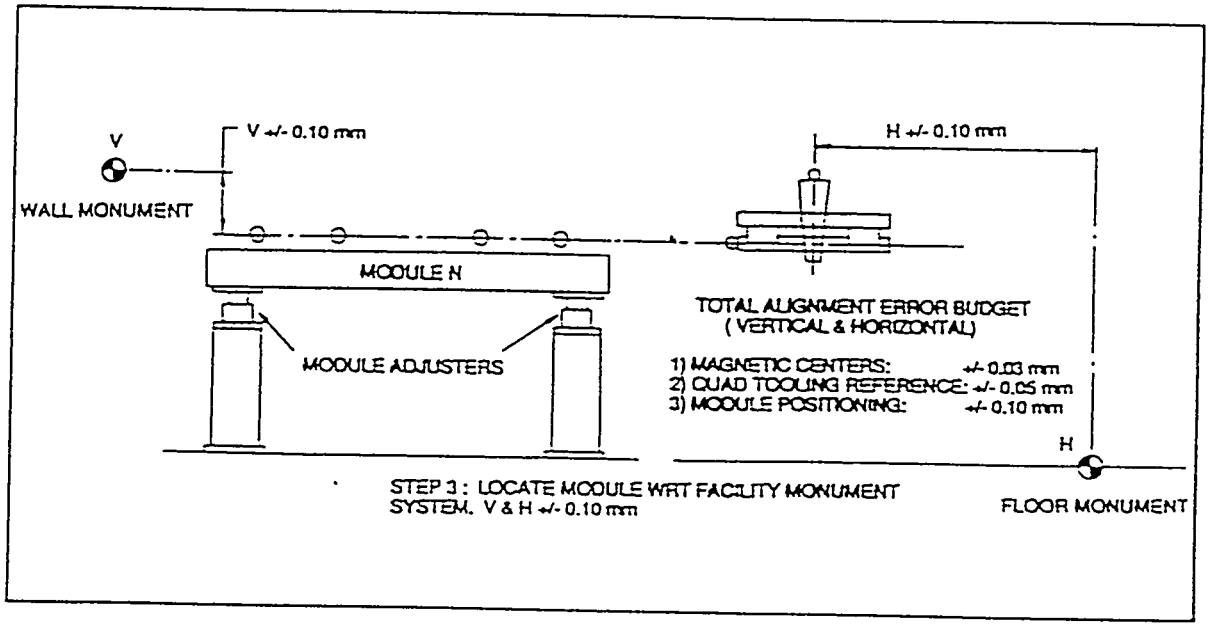


Fig. 9-4. Alignment monument system.

Other methods using laser-actuated or computerized, spatial-orientation optics can also be used with this monument system. By setting up the computerized optics and locating both the monument target and the module target in space, the relationship between them in the three spatial degrees of freedom can be ascertained.

The most critical part of the establishment of a tunnel-based alignment-monument system is the survey that locates the monument targets themselves. These surveys may have to be done several times and the results averaged to take into account the earth's curvature, thermal variations, and shifting mass balance as the facility is being built and covered with shielding. Once established, however, the monument system should be the one reference to which the machine can be installed and checked with confidence. If beam studies ultimately show that some element of the machine is losing beam or becoming activated because of what appears to be a misalignment error, but no error can be detected between the monument targets and the machine targets, it will be necessary to resurvey the monument system. However, with the close spacing of the monument targets specified (10 meters), it should be possible, with care, to use upstream or downstream targets beyond the affected zone to check any questionable results. Precision will not be as good as ±0.05 mm with line-of-sight distances beyond 6 meters, but even at 18 meters, good optics and carefully averaged surveys should still be able to measure alignment to a precision of about ±0.20 mm.

9.3.5.2 Tunnel Coordinate System

The accelerator interfaces are given as physical positions in tunnel coordinates relative to "butt-line zero" (BL0), defined as the upstream RF surface of the BCDTL (upstream end-wall internal surface at 20 MeV). The coordinate system is a left-handed system as follows, where the beam direction is left to right as seen from the aisle (maintenance/installation) side of the machine:

$+X$ = aisle side of machine, downstream to right;

$+Y$ = vertically upward; and

$+Z$ = downstream direction, to right from aisle side.

The emittance filter, funnel, RFQs, matching sections, LEBTs, and injectors are all positioned in $-Z$, $\pm X$ coordinates to accommodate the branch in the front end of APT that occurs at the funnel.

9.3.5.3 Alignment Specifications

Alignment of the APT linac is as critical, but no more so, than any other high-powered linac such as LAMPF. In fact, because APT carries particles of a single charge (whereas LAMPF accelerates opposed charges simultaneously), alignment precision in APT can be set to LAMPF standards with confidence. The fact that the beam current in APT is 200 times the average current in LAMPF is accommodated by the much larger aperture ratio that prevails in APT. The conclusion that LAMPF standards are applicable to APT is justified by error studies that have resulted in the alignment specifications shown in Table 9-5 for the six degrees of freedom of a given doublet taken as a fixed assembly of two quadrupole singlets on a stiff support. The same specifications are also applied to singlet quadrupoles where they exist in the matching sections, the DTLs, and the funnel.

Table 9-5. APT Accelerator Doublet Alignment Requirements

X	±0.13 mm
Y	±0.13 mm
Z	±0.50 mm
Roll	±0.25 deg
Pitch	±0.25 deg
Yaw	±1.00 deg

9.3.5.4 Alignment Procedure

The modular nature of the APT design allows many component parts of individual assembly units to be aligned off-line in the laboratory. The procedure for aligning individual quadrupoles in the laboratory using the taut-wire method is outlined in the Chap. 9 Appendix. The procedure for the alignment of individual components within a module, or module preassembly, is also discussed in the appendix. The unique part of the APT modular design is the capacity for complete alignment and checkout in the laboratory before installation of the module in the tunnel. See the Chap. 9 Appendix for a detailed outline of the alignment procedure.

9.4 INTERFACES

There are seven major interfaces to the accelerator, including the interfaces to the RF power system, the cooling system, the vacuum system, pneumatics, instrumentation, the ac power for the magnet supplies, and the alignment system. In brief, the interfaces can be defined as follows:

- **RF Power Interface:** RF window or WR1150 flanges on the BCDTL and CCL, and the coax or waveguide inputs on the DTL, funnel, and matching section cavities;
- **Cooling Interface:** disconnect valves on the various modules;
- **Vacuum Interface:** flanges on the modules that connect to the ion pumps, roughing vacuum pumps, and mobile roughing packages;
- **Pneumatic Interface:** the connectors to the pressurized air or nitrogen lines;
- **Instrumentation Interface:** connection points between the diagnostic packages and the cables that transmit their signals, and other electrical cables;
- **Magnet Power Interface:** the 480-V, three-phase power connection to the dc power supplies; and
- **Alignment Interface:** module adjusters mounted on pedestal supports in the tunnel and alignment tooling balls on the modules.

In addition, the accelerator interfaces are given as physical positions in tunnel coordinates relative to BL0, as explained previously. All interfaces are shown schematically in Fig. 9-5 and are described in detail below.

9.4.1 RF Power Interface

The location of the RF power interface is defined by the physical structure of the RF modules. For example, in the BCDTL there are four-, three-, and two-tank modules in which one bridge coupler is chosen as the one with the iris coupler. Which coupler in a given module is chosen is relatively unimportant (we chose the most central one, where possible). In addition, the position of the iris is defined by the powered cell that is most central in the bridge coupler. However, in the three-tank modules (of which there are a total of eight in the BCDTL), there is no central bridge coupler, only end bridge couplers; so in this case, we defined the upstream coupler as the one with the iris. In the CCL, on the other hand, each individual accelerator tank is driven with an iris in a centrally located accelerating cell, so the approximate center of each tank is considered to be the position of the RF power interface.

In summary, each RF power interface point is defined in tunnel coordinates by the physics of the design and the mechanical structure of the machine. The positions of the waveguide drops provided by the architectural engineer are of little concern to the module power demands. However, a wise choice of drop position and also of the number of waveguides per drop will affect the total power losses in the waveguides and the total length of waveguide that must be provided between the klystrons and the modules.

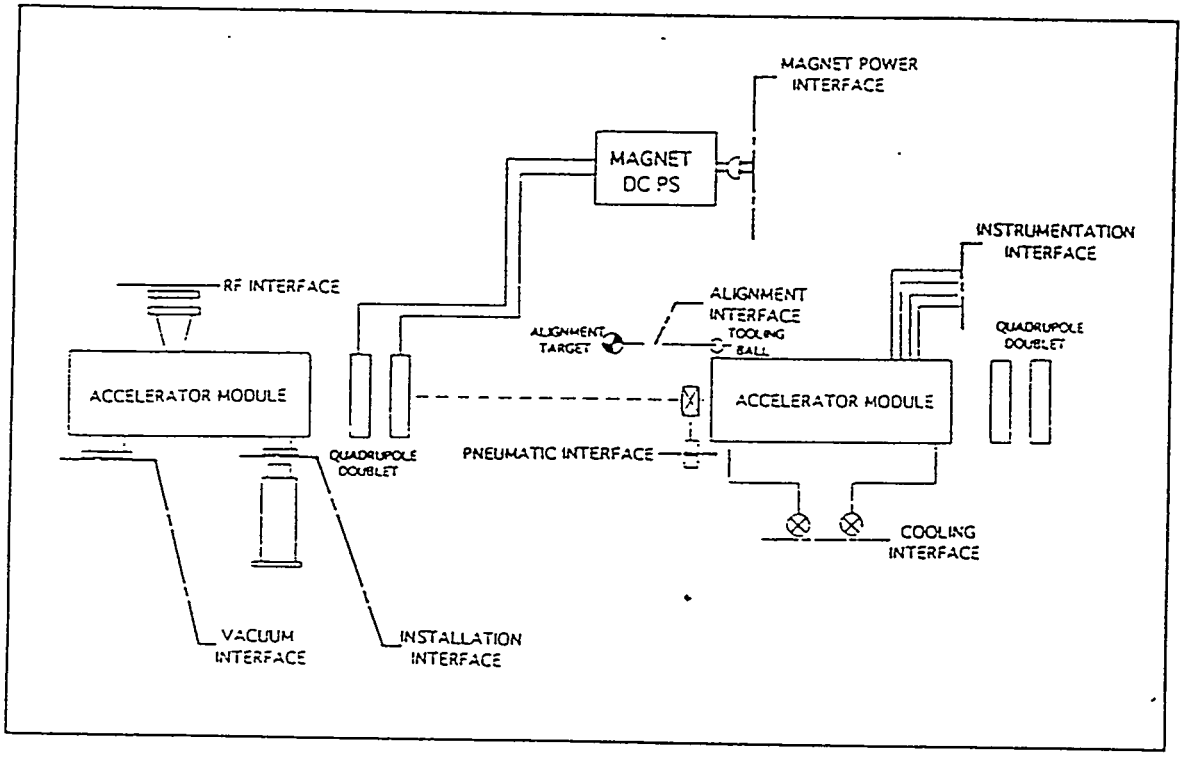


Fig. 9-5. Principal APT linac interfaces.

9.4.2 Cooling Interface

All assembly units are equipped with radiation-resistant ball valves that are closed during transportation, installation, and removal, and opened only during operation on-line or in the test lab. In general, two sets of such valves are located on each unit—one set for

cooling the RF tanks and one set for cooling the quadrupole doublets. For the RFQ, only structure cooling is required. All quadrupoles (and the dipoles located in the injectors and funnels), as well as the RF structures are cooled in parallel. The ball valves are the facility interfaces. Flex hoses are attached to the valves, which then connect the lines to the primary cooling loops. All the valves are physically located in tunnel coordinates relative to BL0.

Because of the possibility of radioactivity in the primary cooling water, the primary cooling loops and heat exchangers are local to the accelerator. To reduce transport lag and enhance control stability in the resonance control system, the servo valves that control structure temperature (and resonant frequency) should be located as close as is practical to the heat-dissipating loads. In the APT point design, the valves are assumed to be outside the modules, i.e., beyond the structure cooling ball valves.

9.4.3 Vacuum Interface

Each accelerator modular assembly unit has four hard-vacuum connections; one connection for the ion pump (or other pumping package in the case of the injectors and RFQs), one connection available for attachment of the mobile roughing-pump package when required, and two connections along the beamline itself, one downstream of the in-line valve. The connections of the beamtube itself are made during assembly of the linac and will rarely if ever require disconnecting. The ion pump is considered an integral part of the module assembly, but will require replacement for maintenance over periods of time measured in tens of thousands of hours. When an ion pump must be replaced, the roughing package will have to be brought in and attached. All other vacuum interfaces, such as vacuum gauges, high-voltage ion pump terminals, cables, etc., are defined as instrumentation interfaces. Again, as was the case with the RF connections, all of these interfaces are defined by the coordinate locations of the flange surfaces themselves.

9.4.4 Pneumatic Interface

There is one other hard-connected interface to the modules, namely the air supply to the electropneumatic-beamline valves. These valves are held open with air pressure, so a facility airline must be provided down the length of the tunnel to which the 380 beamline valves can be connected.

9.4.5 Instrumentation Interface

The APT linac is equipped with a substantial number of diagnostic and measurement devices, including the following items:

- beam diagnostic and measurement devices (Sec. 9.2);
- RF pickup loops;
- thermocouples;
- beamloss monitors (BLMs);
- vacuum-valve limit switches;
- flow meters or switches;
- directional couplers;

- arc detectors;
- vacuum gauges;
- thermocouple gauges;
- small appendage-pump readouts (RF windows); and
- ion-pump high-voltage cables.

All this equipment is interfaced, on a module-by-module basis, though connectors or hard-wired cables. It is possible to completely disconnect a modular assembly unit from the necessary signal, power, and instrumentation leads at the module itself. The conductors are delivered to the module using standard cable trays.

9.4.6 Magnet Power Interface

As discussed previously in the section on magnet power supplies, there are almost 1000 individual quadrupoles, dipoles, and solenoids found in the APT linac design, not counting the HEBT. Most quadrupoles are grouped in doublet pairs. Some quadrupoles, such as those in the DTL, are powered as strings of singlets in series. Each doublet and each series string of singlets requires a separate current-regulated, remote-controlled dc power supply. These power supplies are located above the earth-shielding overlay in the same gallery that houses the klystrons. The computed three-phase power demand of this array of power supplies is 10.2 MVA at a power factor of about 0.75. The interface with the facility is defined as the 480-V, three-phase ac input to the power supplies. Because the power supplies selected are air (fan) cooled, only the ac input is required at this interface; i.e., no water cooling is needed. The voltage, current, and power factor is defined for each power supply. The control input from the command and control system is ±10 V. The power supplies are internally regulated for ripple and drift. Specifications for the power supplies are given in Appendix 12.6.

9.4.7 Alignment/Installation Interfaces

The alignment and installation interfaces exist between the facility monument system and the module tooling balls and adjusters, both of which are mounted on the accelerator support pedestals. The position of the adjusters (and the pedestals) must be surveyed after the facility monument system has been installed. The alignment interface with the facility is not a physical connection of any kind. However, it is essential that the monument system be installed before the support pedestals are put in place. This interface is a schedule-driven interface during the finishing stages of construction, because it must be ready before installation of the machine can begin.

The module adjusters provide three-point supports that allow alignment of the modules in six degrees of freedom. This is not true in all cases; the RFQs and DTLs are overconstrained with four-point mounts. However, over the majority of the machine, three-point adjusters are used exclusively.

The alignment interface applies to the APT linac in the following manner (all of these steps are described in detail in the Chap. 9 Appendix):

(1) The pedestals are bolted and grouted to the facility floor with their mounting surfaces true and flat to ±13.0 mm in x, y, and z.

(2) The module adjusters are then bolted onto the tops of the pedestals and the screw adjusters set to ±6.5 mm in x, y, and z.

(3) The necessary surveys are done to assure this alignment precision using the nearest upstream and downstream floor and wall targets of the facility monument system.

(4) The same facility targets are also used after the module has been installed on the adjusters and all deflections are stabilized.

(5) The module adjusters are then manipulated to bring the appropriate tooling ball targets on the modules to within ±0.10 mm.

LINAC OPERATION AND SAFETY
CHAPTER 10

Page

10.1 AVAILABILITY AND RELIABILITY ANALYSIS 1
10.1.1 Availability Framework 1
10.1.2 Availability And Reliability in the RF System 3
10.1.2.1 Introduction 3
10.1.2.2 Availability Analysis of Klystrons 6
10.1.2.3 High-Voltage System Components 10
10.1.2.4 Availability Calculations 10
10.1.3 Injector Reliability 11
10.1.4 Supporting Subsystems Reliability 12
10.1.5 Summary 13
10.2 MAINTENANCE 13
10.2.1 Introduction 13
10.2.2 Major Maintenance Items Identified 14
10.2.3 Maintenance of Major Components/Modules 14
10.2.4 Routine On-line Maintenance 17
10.2.5 Remote Maintenance 18
10.2.5.1 Special Hardware Features 19
10.2.5.2 Tunnel Size 19
10.2.5.3 Radio-Controlled Bridge Crane 19
10.2.5.4 Servo-Manipulator System 19
10.3 STARTUP AND FAULT RECOVERY 21
10.3.1 Accelerator Startup 21
10.3.1.1 Optics Tuning Beam 21
10.3.1.2 RF Tuning Beam 22
10.3.1.3 Initiating Full Operation 22
10.3.2 Fault Recovery 22
10.4 PERSONNEL SAFETY, MACHINE, AND ENVIRONMENTAL PROTECTION 23
10.4.1 Introduction 23
10.4.1.1 Hazards of the APT Accelerator 23
10.4.1.2 Applicable DOE Regulations 24
10.4.1.3 Accelerator vs. Reactor Production of Tritium 25
10.4.2 Preliminary Hazard Analysis 26
10.4.2.1 DOE Hazard-Class-Determination Guidance 26
10.4.2.2 Categorization of Identified Hazards 27
10.4.2.3 Accelerator Safety Envelope 28
10.4.3 Designs for Personnel Safety and Machine and Environmental Protection 29

10.4.3.1 Design Philosophy 29
10.4.3.2 Passive Safety Designs 29
10.4.3.3 Active Safety Designs 30
10.4.3.4 Administrative Controls 31
10.4.4 Safety and Protection Systems Descriptions 32
10.4.4.1 Shielding and Tunnel 32
10.4.4.2 Fast-Protect System 33
10.4.4.3 Beam-Permit System 35
10.4.4.4 Personnel Safety System 36
10.4.4.5 HEBT/Target Interface 37
10.4.4.6 Activated Air Handling System 39
10.4.4.7 Activated Water Handling 41
10.4.5 Failure Mode and Effects Analysis (FMEA) 42
10.4.5.1 Overview 42
10.4.5.2 Summary 42

LIST OF FIGURES

Page
Fig. 10-1. Operating time, downtime, and availability for KEK TRISTAN injector. 3
Fig. 10-2. Fault rate/day/klystron for TRISTAN injector klystrons. 4
Fig. 10-3. H^+ beam availability vs. run cycle number for LAMPF. 4
Fig. 10-4. Hazard rates for LAMPF and PEP klystrons vs. klystron age. 7
Fig. 10-5. The probability of q failures during a 168-hour operating period for 376 klystrons with 20,000-hour MTBF. 9
Fig. 10-6. APT drift-tube linac with drift-tube girder removed. 15
Fig. 10-7. BCDTL assembly unit (module) with four tanks. 16
Fig. 10-8. BCDTL partitioned bridge coupler with common end cells. 16
Fig. 10-9. Typical intertank hardware (BCDTL or CCL). 17
Fig. 10-10. Tunnel equipped for remote handling. 20
Fig. 10-11. MANTIS—CERN's remote handling system. 20
Fig. 10-12. Tuning beams required for APT accelerator startup. 21
Fig. 10-13. Risk matrix from DOE 5480.25 guidance. 28
Fig. 10-14. Geometry for APT linac shielding calculations. 32
Fig. 10-15. Annual-dose vs. shield-thickness for beamloss (maximum normal continuous operation). 33
Fig. 10-16. Dose vs. shield-thickness for full beamspill (along 100-meter path for 1 hour, 200 mA at 1 GeV). 33
Fig. 10-17. Daisy-chain-type topology for the fast-protect system. 34

LIST OF TABLES

Page

Table 10-1. Failure Distribution for LAMPF for 5.7 years (2/79 to 10/84) 5
Table 10-2. Mean Time between Failures for Several Accelerator Klystrons 6
Table 10-3. Removal Causes for the LAMPF Klystrons and Modulators 8
Table 10-4. Failure Mechanisms for 110 SLAC Klystrons 8
Table 10-5. Unanticipated Outage Time Budget 11
Table 10-6. Preliminary Hazard Analysis for APT 28
Table 10-7. Isotopic Composition of APT Activated Air 40
Table 10-8. APT Activated Air Release Estimates 41
Table 10-9. Summary of APT Accelerator Failure Modes and Effects Analysis 43
Table 10-10. Description of Hazard Categories 43
Table 10-11. Description of Types of Events 43

10.0 LINAC OPERATION AND SAFETY

10.1 AVAILABILITY AND RELIABILITY ANALYSIS

The basic design goal for APT is to operate with complete safety and minimum environmental impact for a specified fraction of the year, subject to the constraints of minimum overall costs (capital plus operating) over a specified lifetime. A detailed analysis of the entire APT system has not yet been done. The preliminary work and existing experience, however, suggest that the availability goal can be met. APT has 325 days or 7800 hours/year of scheduled operating time. As stated in the injector subsystem description (Chap. 4), the scheduled maintenance scenario for the APT injector will be a single 8-hour shift every 2 weeks. In addition, we anticipate a 24-hour maintenance period every 8 weeks, and a 4-week maintenance shutdown each year. This defines an operation schedule that amounts to 89% of a calendar year.

The reliability requirements are specified in terms of system availability. System availability is defined as the probability that the system will be operational (meeting its requirements) when it is needed or scheduled. The APT system requirement is that it must be available for 75% of the total calendar time, including the effects of scheduled maintenance and unscheduled failures, diagnosis, and repairs. With these items included, the system must be available 84% of the scheduled time.

At the highest level of abstraction, a tritium production facility is composed of two subsystems—the accelerator, and the target. One can assume that the two subsystems fail independently, and then each subsystem must have an availability of 91.7%. The accelerator subsystem is broken down into three parts: (1) the accelerator and supporting subsystems, (2) the injector, and (3) the RF systems. With the failures being assumed to be mutually exclusive again, the availability of each subsystem must be 97.1%. Such good availability has been achieved at the KEK linac at Tsukuba, but the APT linac is larger and has more components. Thus, achieving the required APT availability is difficult, but certainly possible.

10.1.1 Availability Framework

Many factors influence the reliability of any system. The list includes the environment, operating stresses on the components, wearout mechanisms, redundancy, human error, maintenance, the component complexity, and the technology used. Each of these items is briefly discussed in this section to illustrate the trends in thinking on availability.

- **Environmental Stresses.** One benefit for most accelerator systems, including APT, is that they are often well shielded from environmental stresses. In the usual design, the accelerator is in a tunnel underground, and the electronics are in buildings above the accelerator. Both the tunnel and the buildings are shielded from the outside environment, and both have controlled temperature and humidity. External pollutants must be kept from sensitive systems. Dust and chemical contaminants must be filtered from the outside air, and even the electricity used by each component must be filtered to remove potentially damaging spikes and pulses. Components are only removed for replacement, modification, maintenance, or testing. These features minimize the environmental stresses and tend to maximize the component reliability. The tradeoff is in the cost of climate control because as the tolerances on temperature and humidity become greater, the climate control system becomes less costly, but the reliability

of the components is reduced. Even the water in the cooling systems must be carefully purified and monitored to assure that the equipment will not be damaged by corrosion.

- Component Operating Stresses. Similar compromises exist in the area of component stress levels. Initial component costs are minimized by purchasing components that operate near capacity, but the reliability of these components is enhanced by reducing the stress on the components. For example, voltage stresses reduce the maximum power output for cw klystrons to slightly above 1 MW, and for pulsed-modulating-anode klystrons to an output power at or below 6.5 MW. Mechanical stresses limit the wall thickness of pipes and vacuum systems. It must also be noted that the maximum allowable stresses often vary with temperature, pressure, and even the age of the component.

- Wearout. Every component has a life cycle; however, there should be as few wearout mechanisms in the system as possible to maximize the availability. An unavoidable wearout process occurs in the klystron cathode, as low-work-function material is evaporated from the hot cathode onto cooler surfaces. By careful design, cathodes have been made with lives of over 100,000 hours of operation for space-borne amplifiers, which is technology that must be used on this project.

- Redundancy. Redundancy can provide significant improvements in availability. The APT concept of two injectors and the funnel was made to provide some redundancy. The machine may operate at a reduced level on one injector whenever the other requires repair. Redundancy in the RF power amplifiers or power supplies is an expensive but necessary technique for adaptation in the RF systems. Redundancy will be used in all low-power diagnostics to reduce the frequency of poor or incorrect inferences about the state of the subsystems from faulty diagnostics. Redundancy will be used in the APT systems as long as the extra costs are justified by the increase that is gained in reliability. Standby water pumps may well be examples of redundancy for better reliability. However, it would be too expensive to have redundancy in the large cooling towers which would add little to the reliability of the overall system.

- Maintenance. Many accelerator support-system components, such as high voltage supplies and water pumps, will have scheduled maintenance requirements that must be rigorously followed to maximize reliability. In addition, some systems must be equipped with advanced diagnostics that warn of impending problems. The machine will be available for maintenance for a single 8-hour shift in each 2-week period. All systems that do not need repair will be left operating during these maintenance shifts. All advanced diagnostic readings will be reviewed before the maintenance shift to identify potential failures, and the appropriate actions will be taken. Each critical water pump should have a vibration sensor that is logged by the computer to identify a worn bearing or similar problem. Each klystron will have many of its secondary characteristics monitored, such as gain and temperature rise in the coolant circuits. When these parameters indicate a developing failure, the component will be replaced. Repaired components will be monitored to determine their quality and reliability.

- Human Error. Human error is a problem with any large-scale system that can be minimized by training responsible operators. A system of computer commands will operate and monitor remote valves and switches, and when the computers don't agree with an action, the operator will be warned to take corrective action.

- **Technology.** The technology used for such large projects must be proved by having operated under similar circumstances. Using proven technology will help ensure that a data base for the lifetime and reliability has already been established.

10.1.2 Availability And Reliability in the RF System

10.1.2.1 Introduction

The reliability of the RF system is a large component of the total reliability that may be estimated from operating experience at the various large accelerators. The most important point is that large accelerators have been operated with high availability. The best example of this is the electron injector for TRISTAN, in Tsukuba, Japan. It is a pulsed machine, and operates for an average of 5019 hours/year. In Fig. 10-1, the availability, unscheduled downtime, and operating hours are plotted for four fiscal years (1988–1991) from KEK's annual reports. The average downtime was 133.7 hours/year, and the average availability was 97.34% for the entire accelerator. This accelerator has 48 klystrons; and although it is a pulsed electron machine, its excellent availability demonstrates that the high availability needed for APT is possible.

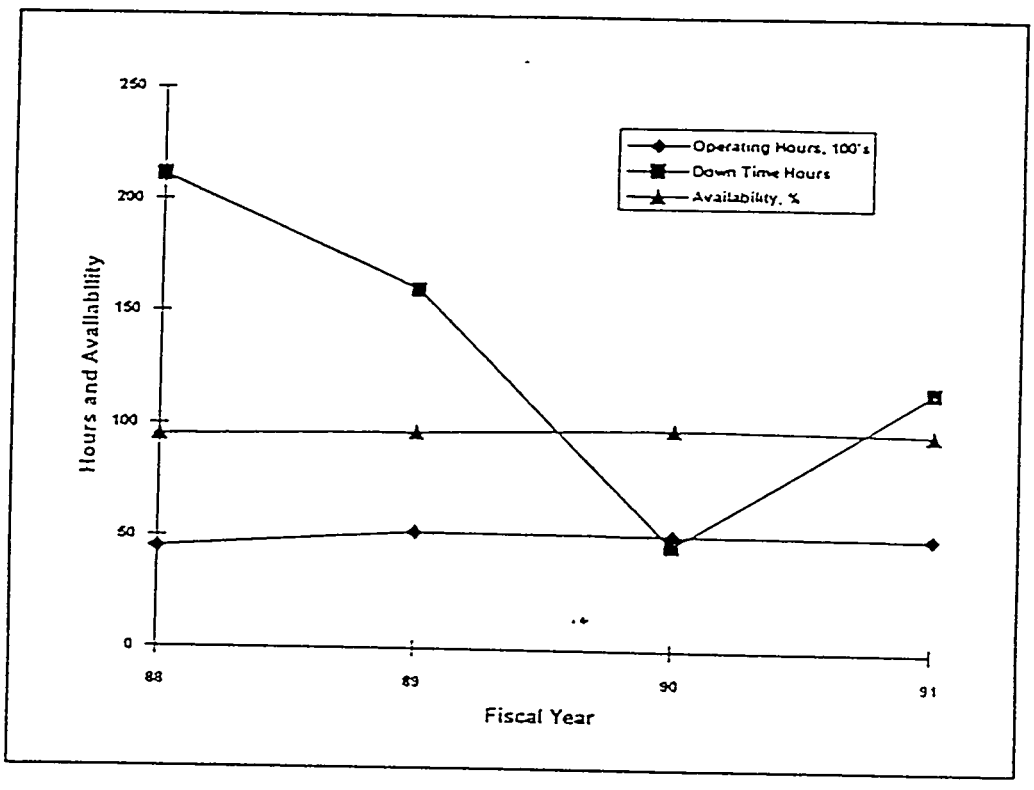


Fig. 10-1. Operating time, downtime, and availability for KEK TRISTAN injector.

The reliability of a machine usually increases with time. As defects in the original design are discovered and corrected, the performance improves. Figure 10-2 is a graph of the klystron fault rate, in faults per klystron per day, for nine fiscal years of an injector linac. A gradual downward trend is observed, showing that these faults are decreasing as the quality of the klystrons and their protective circuits has been improved.

In a well-designed circuit, klystrons will generally arc less and less as time passes because each arc should remove gas or sharp features from the high-voltage area. Thus, the trend shown in Fig. 10-2 applies to other klystrons as well. When an individual klystron begins to arc more frequently, it is a sign of trouble, and the individual klystron should be removed at the next maintenance period, repaired, and high-voltage reconditioned off-line.

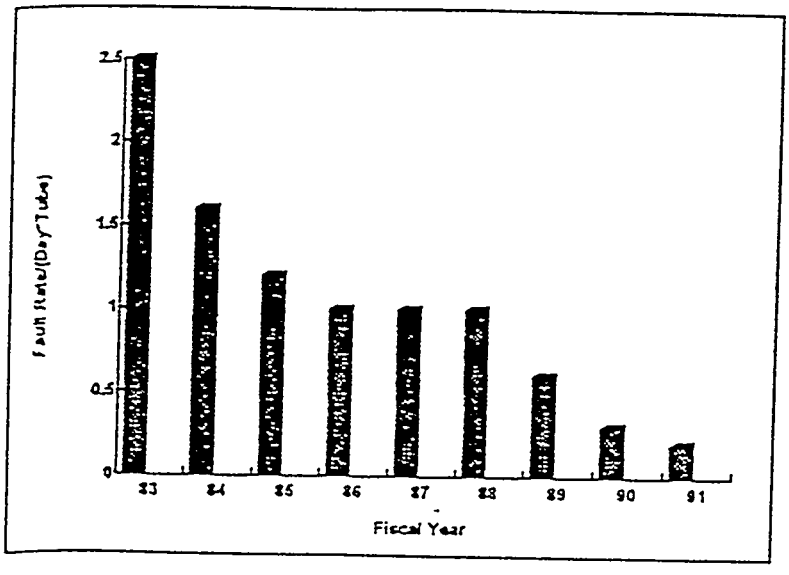


Fig. 10-2. Fault rate/day/klystron for TRISTAN injector klystrons.

The LAMPF accelerator in Los Alamos is one of the highest-power proton accelerators in the world and is therefore a model for the problems that may be expected to occur in the APT machine. Even though LAMPF is a pulsed linac, it is instructive to examine its failure records that encompass over 20 years of operating history. The machine first achieved its design energy of 800 MeV in 1972. Data for the 5.7 years of operation from February 1979 to October 1984 is summarized by the availability graph of the H^+ beam shown in Fig. 10-3.

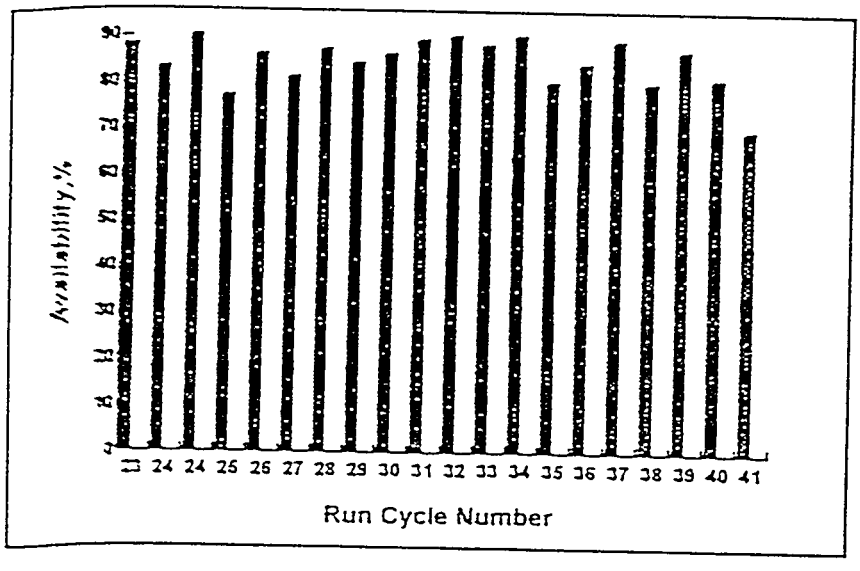


Fig. 10-3. H^+ beam availability vs. run cycle number for LAMPF.

As can be seen in Fig. 10-3, the average availability was 84.6% and the total operating time was 23,152 hours, or about 56.7% of the time. The highest availability for one week during this period was 96%, and the worst availability was during the last run period (also the longest), which lasted for 2356 hours. One shift per week was used as a maintenance period during the scheduled operation times. Table 10-1 shows the distribution of accelerator failures for these 5 years.

In Table 10-1, the total unscheduled downtime is only about 15% of the total scheduled operating time, partly because LAMPF is a multibeam machine with three separate injectors so if one injector is down, the other still operates. Moreover, some failures are counted twice: for example, a water leak into an RF system is both a water and an RF failure.

Table 10-1. Failure Distribution for LAMPF for 5.7 years (2/79 to 10/84)

Subsystem	Downtime (hours)	Unscheduled Downtime (%)
Injectors	1459	25.0
RF	1439	24.6
Magnets and Power Supplies	701	12.0
Vacuum	655	11.4
Utilities and Miscellaneous	581	9.9
Beamstop and Targets	428	7.3
Water and Cooling	231	4.0
Computer/Data Acquisition	187	3.2
Interlocks	149	2.6
Total Downtime	5840	

The downtime to repair the water system and the downtime to repair the RF system are both counted because different repair crews are involved in each process. The machine is not down for the sum of the repair times but for the longest repair time. The injector downtime may also be exaggerated: for example, when two injectors were scheduled to operate, the accelerator was shut down, even though it could have operated with just one of the injectors. The distribution of failures shown in Table 10-1, however, indicates the expectations for any large proton accelerator. Records show that the injectors and the RF systems are the two most fault-prone subsystems and together account for half the unscheduled downtime. Four 201-MHz and forty-four 805-MHz RF systems are located at LAMPF, but the 201-MHz systems accounted for 52.6% of the total RF downtime. Hence, the RF reliability would be almost doubled if the 201-MHz, gridded-tube systems were upgraded to be as reliable as the klystrons at 805 MHz. The LAMPF injectors operate at 750 kV. The more modern APT injectors will operate at only 50–100 kV, so they should be much more reliable. The cw duty factor of APT, compared to the 6%–12% duty factor of LAMPF, will make it a challenge to obtain high reliability.

The reliability data presented here were not carefully selected: although 15 more years of data are available, in recent years the availability has decreased because of serious quality problems in the 201-MHz gridded tubes, and funding limitations have led to a general lack of proper maintenance on the machine. The next two most common downtime failures are caused by the magnets and their power supplies and vacuum problems on the accelerator. For the few thousand hours that the power supplies and the magnets were tabulated

separately, 33% of the downtime came from the power supplies and 67% from the magnets themselves. The next most common cause of downtime was loss of the main power supply. Los Alamos (and LAMPF) is at the end of a long power grid, and power can be disrupted about 12 to 24 times per year, especially during the thunderstorm season in late summer, when LAMPF usually operates.

10.1.2.2 Availability Analysis of Klystrons

The klystron is often the most failure-prone portion of the RF system, especially in high-power systems. The MTBF of klystrons is best estimated by simply dividing the total operating hours of all the klystrons by the number of failures. This method is only correct when the hazard rate is constant. The hazard rate is the probability of failure per unit time. For electron tubes, the hazard rate generally starts fairly high, rapidly decreases as the infant mortality happens, and then remains constant until it again increases because of wearout. Accelerators are often shut down before the wearout period is observed, and the electron tube vendor usually increases the reliability (lowers the hazard rate) with each new order of tubes. Vendors also go out of business, change processes, and even change materials as the years pass, so a constant-hazard rate is usually the best approximation for a large set of electron tube data, especially when the data are taken over several years, with multiple tubes being replaced and taken out of service. For several pulsed and cw klystrons, Table 10-2 shows the MTBF, which is based on the constant-hazard approximation. The data in the table was obtained directly from operating personnel at the various facilities.

Table 10-2. Mean Time between Failures for Several Accelerator Klystrons

Accelerator		Total Hours	Total Failures	MTBF (hours)
TRISTAN Injector		1,691,200	107	15,800
LAMPF (failures)		2,880,000	18	160,000
LAMPF (removals)		2,880,000	140	20,571
PEP	(cw)	314,162	23	13,659
SLAC (5045)		8,727,686	229	38,112
CERN LEP	(cw)	272,000	6	45,333
TRISTAN Ring	(cw)	712,000	31	22,968

Two entries for the LAMPF klystrons are shown in Table 10-2. As explained below, the LAMPF klystron and its modulator are removed as a unit whenever either one has a problem. This is called a *removal* and is the third line in the table. In the removal process, the klystron and modulator are moved to a test building, and the cause for removal is determined and repaired. In 18 cases, the klystrons could not be quickly repaired and placed back into service, and these are the klystron failures on the second line of the table.

Exactly how the klystrons fail is also of interest, and the failure modes are different for each klystron type and application. The PEP, CERN, and TRISTAN klystrons are all cw klystrons, while the other examples in Table 10-2 are pulsed. The hour columns in Table 10-2 are high-voltage hours, except in the cases of TRISTAN and PEP, where only the filament hours have been published. As an example of the randomness of high-power klystron failures, consider the 1-MW cw 352-MHz klystrons at the CERN LEP. The six failures out of 16 klystrons (with high-voltage hours at failure in parentheses) were due to the following:

- low cathode emission (270 hours),
- water leak (2650 hours),
- vacuum leak (3655 hours),
- window failure (3800 hours),
- high modulating anode current (6140 hours), and
- heater feedthrough (15,950 hours).

Note that each failure is different, and no sign of wearout has yet been seen. Ten of the original 16 klystrons have operated for over 17,000 hours without problems. Even with this small number of failures, one can see that five of the six failures occurred at or before 6140 hours, yet most of the klystrons are now older than 17,000 hours. Such evidence of the infant mortality phenomena is always seen in high-power electron tubes.

Two more examples of infant mortality are shown in Fig. 10-4, which shows the observed hazard rate (observed failure probability per unit time as a function of age) for the PEP 500-kW cw klystrons and for the LAMPF-pulsed klystrons. In both cases, the hazard rate for the first 10,000 hours is greater than the average hazard rate. For the LAMPF case, 70 klystrons made up the sample population, but even after operating for 21 years, only 18 klystrons have failed. The real average life can only be determined when all the klystrons have failed, but this may take decades of operation. The removal data for the LAMPF klystrons is summarized in Table 10-3.

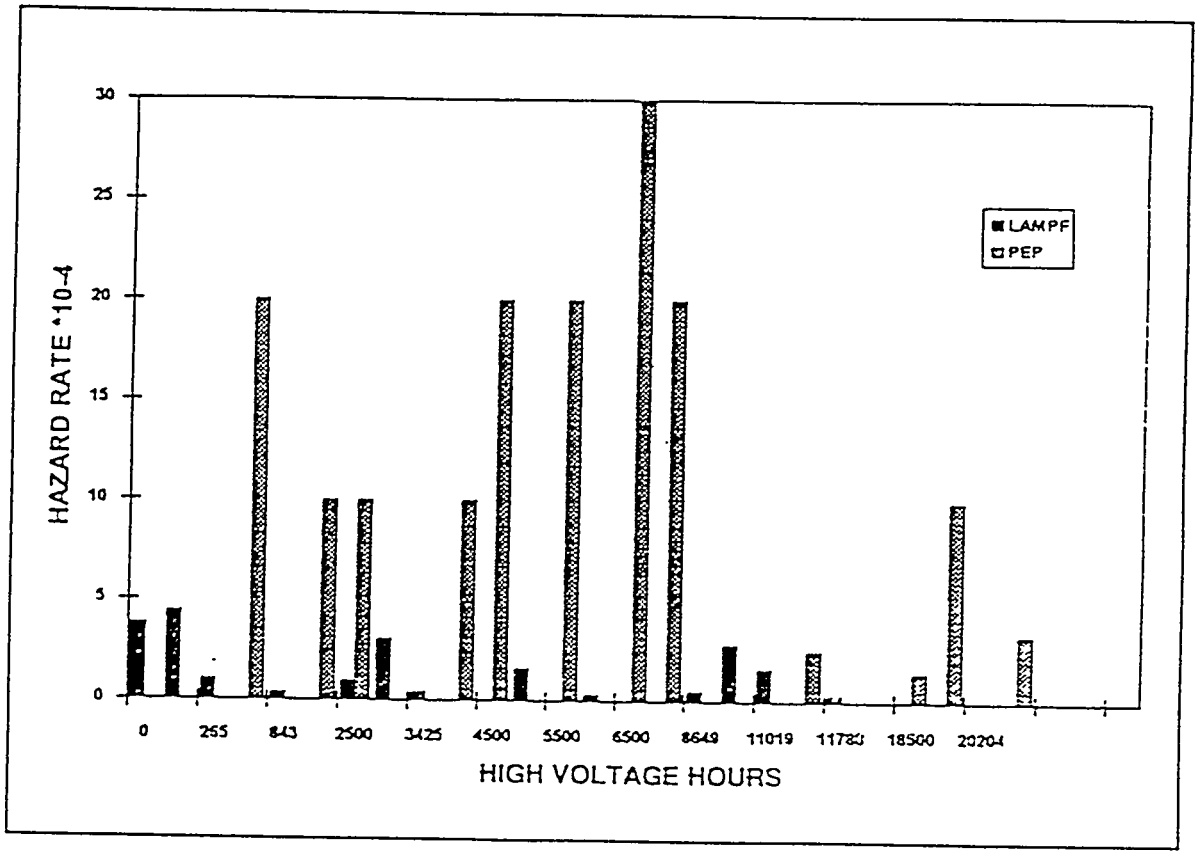


Fig. 10-4. Hazard rates for LAMPF and PEP klystrons vs. klystron age.

Table 10-3. Removal Causes for the LAMPF Klystrons and Modulators

Mechanism	Instances	Removals (/million hours)
System Problems	40	13.9
Water in Oil Tank	36	12.5
High-Voltage Arcing	29	10.1
Klystron Vacuum	17	5.9
Low Beam Current	10	3.5
Switch Tube Leakage	3	1.0
Human Error	3	1.0
Klystron Window	2	0.7

The klystrons at LAMPF are installed in large modulators, and both are removed as a unit whenever either has a problem. There have been 140 removals of the klystrons and their modulators. The leading cause of removal was system problems, which were usually found to be defective cables, connectors, or diagnostics that indicated something was wrong with the klystron/modulator. With redundancy in diagnostics, this type of removal would be eliminated. The total number of klystrons for the PEP case is about 20.

The SLAC SLC klystron (65 MW of pulsed, peak power) data represent 7 years of operation with 244 klystrons installed. A total of 229 klystrons have failed. There are 484 klystrons in this sample, but the average age of the failed klystrons is 12,091 hours, which is much smaller than the MTBF in Table 10-2. There are indications [10-1] that the infant mortality rate in the SLAC klystrons is now lower than it has been in the past because of more stringent manufacturing and testing. This reference also points out the correlation between long cathode life and low operating temperature of the cathode. When the emission current drops, one can restore the beam current by increasing the operating temperature of the cathode, but this accelerates the further droping off of the beam current. Conversely, reliable cathodes can be identified on new klystrons, and these cathodes run for very long times at low temperatures. Thus, cathode wearout failures can be anticipated by monitoring the power that goes into the heater circuit, and the klystron can be replaced before it fails. The failure mechanisms for 110 of the SLAC klystron failures are listed in Table 10-4. Due to the high peak powers, arcing in the high-voltage seals and window is the leading cause of failure, and this will not be nearly as important for the APT RF system because of the lower operating voltages.

Table 10-4. Failure Mechanisms for 110 SLAC Klystrons

Mechanism	Instances
High-Voltage Seal Puncture	37
RF Window	30
Low or Unstable RF	21
Klystron Vacuum	10
Gassy Cathode	7
Mechanical Failure	5

Informal discussions with klystron vendors indicate that a 20,000-hour life expectancy is a reasonable goal for the first set of klystrons for APT. After leading causes of failure are removed, doubling life expectancy by redesign is not unreasonable. Doubling the reliability requires at least five years of continuous operation to find the leading failure mechanisms.

The overall RF subsystem for APT contains 376 1-MW klystrons and RF systems. One may model the reliability of the RF system, but one has to know the reliability of each of the thousand or so components in the system. This is not possible because many components have not yet been designed or produced, so a more approximate approach is made to assigning MTBFs to the major subsystems. In the future, when more accurate reliability functions for the various subsystems are known, they can be incorporated into this framework. For the present design, constant-hazard rate and constant MTBFs are assumed. During a 1-week (168-hour) operating period, 63,168 socket hours are accumulated on the klystrons, and, because the MTBF is 20.000 hours, slightly more than three failures per week are expected. Because it will take about 3 hours to diagnose, to do the paperwork, and to change out a klystron, this situation is less than acceptable, with over 9 hours/week lost just to klystrons.

The mathematics of the availability calculation is straightforward. The constant hazard approximation means that the probability of no failures with n identical components in a time interval t is given by:

$$P_0(t) = \exp(-n\lambda t), \qquad \text{where } \lambda = 1/\text{MTBF}.$$

The probability of q failures with these same identical components is

$$P_q(t) = n\lambda t P_{q-1}(t)/q, \qquad \text{for } q>1.$$

By applying these formulae to the klystrons, with their 20,000-hour MTBF estimate, and a time interval of 168 hours (1 week), one calculates the following set of probabilities of the number of klystron failures in a week shown in Fig. 10-5.

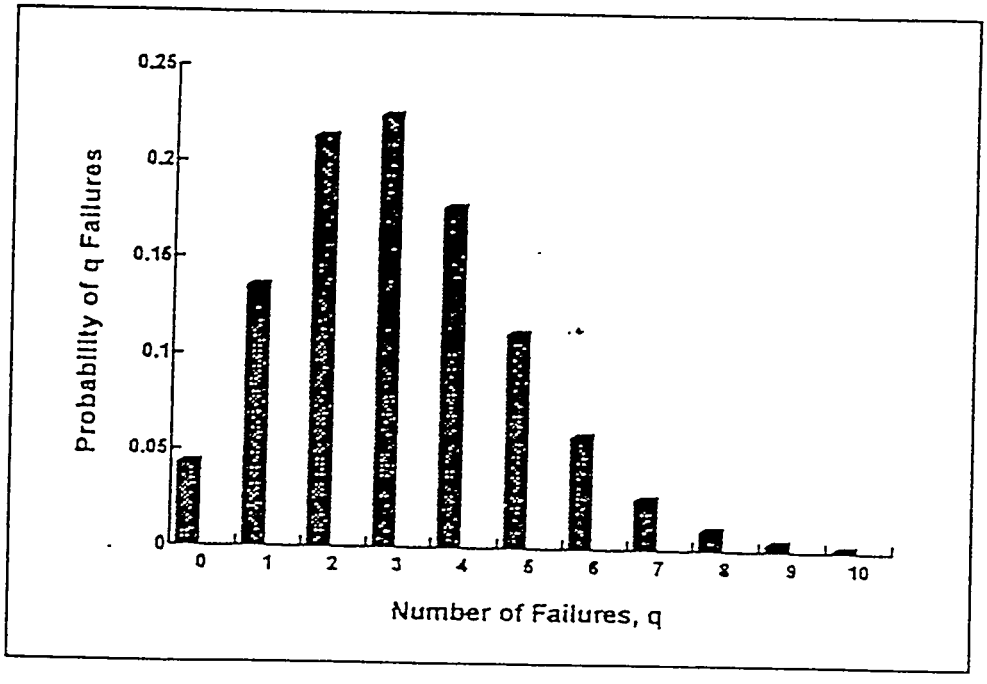


Fig. 10-5. The probability of q failures during a 168-hour operating period for 376 klystrons with 20,000-hour MTBF.

The expected number of failures in the interval t is then

$$E_{x(\text{fail})}(t) = n\lambda t \ .$$

Every component has a mean time to repair, MTTR, which is about 3 hours for the klystron. The expected time to repair in the interval t is then

$$E_{x(\text{mttr})}(t) = \text{MTTR} \cdot E_{x(\text{fail})}(t) \ ,$$

and this is how the 9 hours was calculated above. This 9 hours, however, is unacceptable. The solution is to anticipate most of the failures in the least reliable subsystems by placing good diagnostics in these subsystems. Of course, the individual subsystems must be designed to be as reliable as possible, subject to reasonable cost constraints. Let A denote the fraction of anticipated failures; then the expected downtime in an interval t is

$$E_{x(\text{mttrA})}(t) = \text{MTTR}(1 - A)E_{x(\text{fail})}(t),$$

and this time can be a small fraction of the time without anticipating failures. This formula is used below to calculate the availability of the RF system, but before applying it, the high-voltage system must be considered because some of the downtime obviously will come from the high-voltage system.

10.1.2.3 High-Voltage System Components

The high-voltage converter has a manufacturing basis in converters used to connect ac utility grids. Similar high-power units have been made, and they operate very reliably in the utility grid. Very high MTBFs have been established in these designs, and even higher reliability may be obtained at increased cost by overdimensioning all components to reduce the electrical and thermal stresses. Based on the usual utility-quality designs, we estimate that the MTBF is 0.05769 hours per week per converter. On a per hour basis, the MTBF is 2912 hours per converter. The MTTR is estimated at 6 hours. In addition to these unscheduled outages, a 24-hour scheduled repair time is also required once a year to perform preventative maintenance on the converters.

An industrial partner has estimated the failure rate for the high-voltage protection units at 9.7 failures per million hours by adding up the estimated failure rates of the major components in the high-voltage protection circuits. These circuits must also have a large complement of diagnostic equipment, so we will double the failure rate to 19.4 failures per million hours, or an MTBF of 51,500 hours. The MTTR is 5 hours, and the A (or anticipation factor) is assumed to be 80%. Although developing a high-voltage protection unit that performs as reliably as is required for this application will not be simple, several parts of the unit have already been designed and even tested for other programs.

10.1.2.4 Availability Calculations

With the failure rates and MTTRs discussed above and with the quantities of components as noted in Chap. 8, we arrive at the availability, as shown in Table 10-5. The total unanticipated downtime is only 5.55 hours/week, so the availability is 96.7%. Of

course, this just shows the feasibility of achieving these goals, and more work on design and prototype construction and life testing are required before the reliability goals can be unequivocally demonstrated.

Table 10-5. Unanticipated Outage Time Budget

Subsystem	MTBF (1000 h)	Installed (No.)	Failures (No./week)	Anti-cipated Failures (%)	Unanti-cipated Failures (No./week)	MTTR (hours)	Unanticipated Downtime per week (hours)
Klystron	20	376	3.1584	75	0.7896	3	2.369
Power Converter	2.9	2	0.1154	25	0.0865	6	0.519
HV Protection	51.5	210	0.6850	80	0.1370	5	0.685
Low-Level RF	100	376	0.6317	50	0.3158	2	0.632
RF Transport	150	376	0.4211	50	0.2106	4	0.842
Water Cooling	40	48	0.2016	50	0.1008	5	0.504
Total Unanticipated Downtime per Week							5.551

10.1.3 Injector Reliability

As introduced earlier (Sec. 10.1), the availability requirement for the APT injector is 97.1% to support the total system availability of 75%. In fact, the availability of an injector is a fairly complex analysis because ion sources have a tendency to operate at slightly off-normal conditions. We must define a specific set of operating standards at which the soft degradation of injector operation becomes an injector failure. The injector shall be designed with performance margins to permit such degradation. The performance proposed for APT is an improvement from the work done at CRL to date. The voltage will be increased from 50–75 keV, and the current will be increased from 80–130 mA.

Several prominent failure mechanisms in the injector subsystem include high-voltage breakdown, RF-window failure, and LEBT-magnet power-supply failure as the most important. The most likely injector failure is failure of the aluminum nitride RF window.

During a 2-month collaborative effort between Los Alamos and CRL in 1993, the cw ECR source had two window failures (cracking of the AlN microwave window) and no failures of any other type. These comments apply to full dc operation (100% duty factor) of the source, operating with a 5-mm-diameter aperture at extraction-current densities of 300–500 mA/cm^2 hydrogen ion beam. These current densities correspond to 60–95 mA of hydrogen-ion beam currents. In the present design, the extracted hydrogen-ion-current density cannot exceed 500 mA/cm^2 or a window failure may occur. Terry Taylor of CRL talks about 200–400 hours of source operation between AlN window failures, so this experience is consistent.

The failure mechanism is known. It is believed that cracking of the AlN microwave window occurs when electrons backstreaming from the extractor strike the window. A window has failed when the beam is run without the suppressor voltage on the extraction electrode. A single-window failure was observed when the extraction voltage was increased with the plasma generator on. This is perceived to be a beam mismatch problem that is taken care of by proper startup procedures. In the worst case, the window may be replaced during each 8-hour shutdown at the 2-week interval and not push the current state of the art. Once

window failures are eliminated as a reliability problem, either through reengineering or reliability-based maintenance, achieving 97.1% availability is well within reach.

Our position is that extensive ECR source lifetime/reliability tests remain to be done. Staffing limitations at CRL has prevented them from running 24-hours/day tests. We propose doing these lifetime tests on the Chalk River Injector Test Stand (CRITS) now being installed at Los Alamos. If there should be a microwave window problem, we propose to fix it by four different possibilities:

- Braze the AlN window to a cooled flange. Presently this joint is made with an O-ring, which does not give optimal heat transfer. A braze joint would remove the heat more effectively.

- Intercept the backstreaming electron beam by a piece of tungsten inserted in the plasma chamber. This sort of solution has been used in other cw ion sources, e.g., the Sandia monocusp source.

- Insert a dipole field to deflect the backstreaming electrons onto the plasma chamber wall.

- Fast shutdown of the high-voltage power supply. The ORAM tube is expected to have ~10 kHz bandwidth, so we may expect to shut the high voltage down in less than a millisecond.

10.1.4 Supporting Subsystems Reliability

As introduced earlier, the availability requirement for the APT-supporting subsystems is 97.1% to support the total system availability of 75% of the calendar year.

The five primary subsystems contributing to this next level in the availability calculation are the vacuum subsystem, temperature control subsystem, electromagnet subsystem, instrumentation and control subsystem (including beam diagnostics), and safety interlock subsystem (including the beam-permit, accelerator fast-protect, and the personnel safety system). Assuming independent failure modes again for these five subsystems derives a requirement of 99.4% for each subsystem.

Each system is highly complex, containing hundreds of pumps, valves, sensors, power supplies, magnets, motors, or switches. As the complexity, or number of active elements, increases by each order of magnitude, the failure rate must be reduced by an even larger factor. As an example of the factors involved, if one of these subsystems has 400 independent components and all are necessary for operating the accelerator within the required performance limits, each component is required to have an availability of 99.9985%.

The APT control system will comprise a network of 448 IOCs or stand-alone processors handling nearly 50,000 data channels. These may have redundant backup hardware and software to allow automatic functional switchover. The beam diagnostic subsystem includes 435 microstrip probes or stripline sensors, each with its own processing electronics. There are 415 beamloss monitors, each tied into both the instrumentation and control system and the accelerator safety systems. Over 500 electromagnet power supplies, located in the accelerator and HEBT, drive an even greater number of beamline electromagnets. There are 409 high-speed and 372 low-speed ion vacuum pumps. There are 372 separate cavity water-cooling systems for resonance control, each containing pumps, valves, servos, etc.

The number of components in the APT system is so large that at first glance it seems incredible that the system can meet even a modest availability goal. But there are larger systems, such as the electric power system and the telephone system, that meet higher availability goals. All the principles of Sec. 10.1.1 will be applied to achieve the required availability.

The general design rules are to use the best (most reliable) components, operate them below their ratings, and use redundancy where it is cost effective. With the recent worldwide focus on quality, reliable components are becoming less expensive and much more widely available. In other large accelerator systems (such as LAMPF), the availability is improved both by having a regularly scheduled maintenance period every week or two and by having diagnostic predictors of impending problems so that suspect subsystems can be replaced during the next scheduled maintenance period rather than after an actual failure. Thus, rather than operating the system until it fails, one may put extra diagnostics into the system, record the outputs, and then replace those subsystems before they fail. A small price in labor and capital is paid for this early replacement, but the payoff is the greatly reduced number of unanticipated failures.

10.1.5 Summary

A system availability is basically defined as the probability that the system will be operational (meeting its requirements) when it is needed (or scheduled). APT has 325 days or 7800 hours/year of scheduled operating time or 89% of the entire year. The APT system requirement is that it must be available for 75% of the total calendar time, so the system availability must be 84% of the scheduled time. Assuming for now that they are independent and equal, each of the major subsystems (injector, RF, and mechanical) will have to be 97.1% reliable.

A detailed analysis of the reliability and availability characteristics of the APT design is inappropriate for this preconceptual design stage. We can perform some of the basic analyses to show that reliability-centered maintenance will help us achieve our availability goals. We can find analogies in the existing technology that will provide some benchmarking. But at this level, we have had to rely on the concept of good design practices as our key to providing a system that is capable of the necessary availability. As the design matures over the next years, we must address the high-payoff reliability areas, as the injector team is doing, and use the accumulated data to develop a more quantitative evaluation of the reliability and availability situation.

10.2 MAINTENANCE

10.2.1 Introduction

There will be some unique maintenance required for the high-powered APT linac. The potential for activation and the high tunnel temperatures present special challenges for the design. Most problems, however, have been anticipated in the mechanical design of the linac. In addition to striving for high reliability and radiation resistance in the component parts, the machine has been modularized, or *packaged*, into sections that do not exceed five meters in length. The elements of the system that are expected to require periodic or frequent maintenance have been identified and have been made especially accessible. The interactive

tests that must be performed on the modules to assure proper operation on-line have also been identified. Finally, consideration for easy removal and replacement of modules, subsystems, and components has been addressed where practical.

Many of the features that are built into the design were done to facilitate safe and rapid handling of the majority of accelerator components. If remote handling is required, these same features will be invaluable for conducting safe and efficient remote operations. Even without radioactive components to handle, these features will be useful for speeding up hands-on maintenance of the machine under normal conditions when the ambient temperature in the accelerator tunnel will be around 36°C (97°F) immediately following a shutdown.

10.2.2 Major Maintenance Items Identified

The following items have been identified as requiring major and/or frequent maintenance:

- vacuum pumps,
- intertank and intermodule beamline hardware,
- RF structure cooling fittings and filters,
- magnet cooling fittings and filters,
- flow meters and klixons,
- RF windows,
- RF couplers,
- DTL drift tubes, and
- instrumentation.

Routine or scheduled maintenance will be required on items such as vacuum pumps, filters, and flow meters. Since there are ~800 ion pumps distributed along the linac, some ion pump replacement is expected to take place during every maintenance period. Some items listed above are physically bulky and heavy and will require the assistance of special trucks and grappling equipment or the overhead crane. Other items can be replaced or repaired on-line, given the working-time limitations imposed by the high ambient temperatures in the tunnel.

10.2.3 Maintenance of Major Components/Modules

Failures of such major components as drift tubes, accelerator tanks, or bridge couplers will be rare events, but must be anticipated. At LAMPF, there has been a need to replace all the drift tubes in the DTL because of melted RF bellows, one failed drift tube with an internal cooling leak, one bridge coupler in the CCL, and some quadrupole doublets in the CCL. Other than the drift tubes (which were underdesigned), the service record is excellent, considering the more than 20 years of operation. At LAMPF, all such failures must be dealt with on-line. With the APT design, however, failures of the above types can be dealt with by removing the assembly unit from the tunnel and conducting repairs in a laboratory work environment. In the DTL, for example, failure of a drift tube would be best dealt with by

removing the drift-tube girder from the tunnel altogether. An illustration showing a girder lifted out of a DTL tank can be seen in Fig. 10-6.

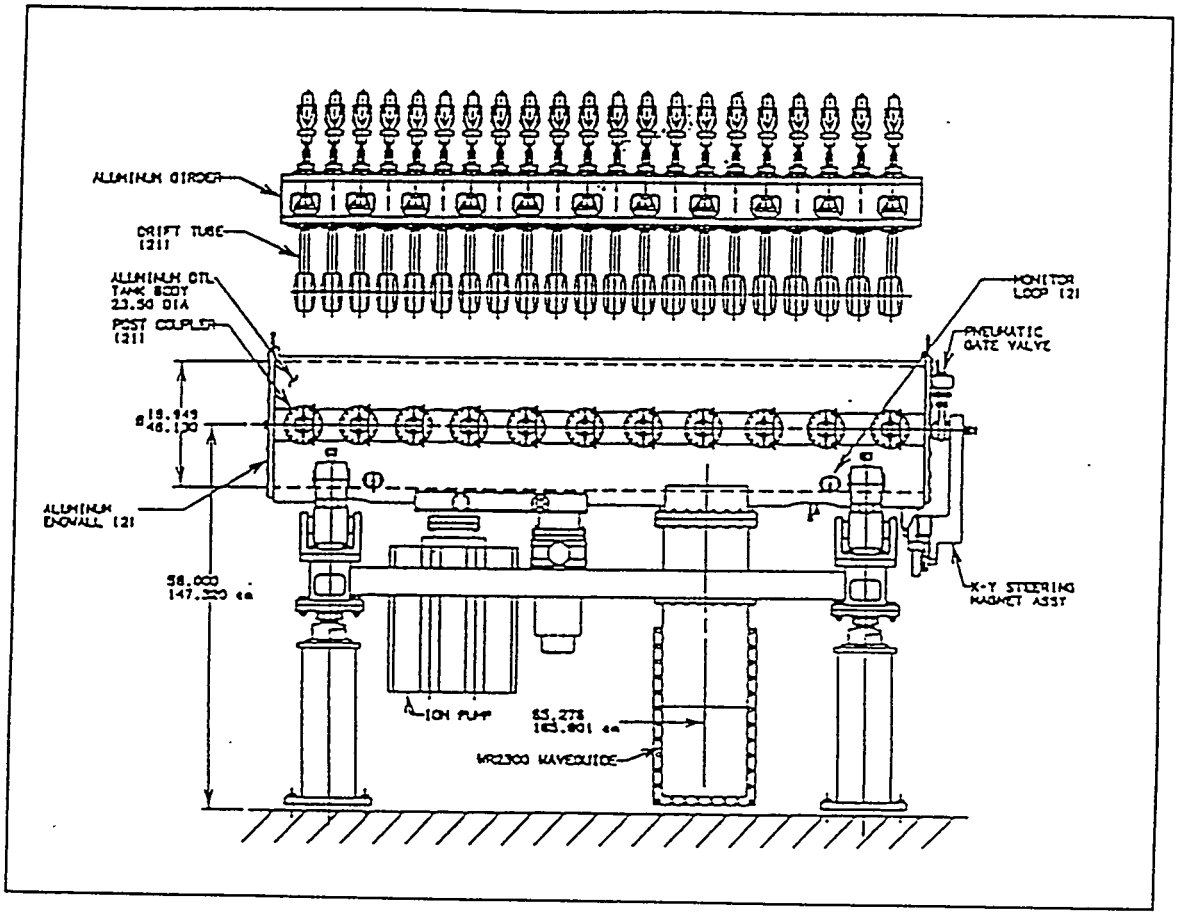


Fig. 10-6. APT drift-tube linac with drift-tube girder removed.

By transporting the girder *en masse* to the lab, it can be repaired more easily, and interactive tests can be better performed on the newly-repaired unit before returning it to service. The need for these interactive tests cannot be overemphasized. For instance, with the repair on the DTL girder, realignment of the drift tubes with the taut wire apparatus is an essential step, although a power supply and a coolant supply are required to operate the EMQs inside the drift tubes while in the lab. This is still preferable, because the taut wire alignment apparatus is delicate and bulky; it is much better to bring the girder to the apparatus rather than the other way around. During the repair process, the RF and vacuum seals on the girder itself could be inspected and replaced, while checks of the vacuum and cooling for the whole assembly could be done.

A similar procedure applies to the generic assembly units that make up the bulk of the APT linac. An illustration of a four-tank BCDTL module that is suspended from a crane is shown in Fig. 10-7. This represents either the initial installation of a BCDTL (or CCL) assembly unit into the tunnel, or the transport of a failed unit to the lab for repair. This sort of failure is serious and would entail a significant delay in operation of the facility; however, the probability of such a failure is extremely low.

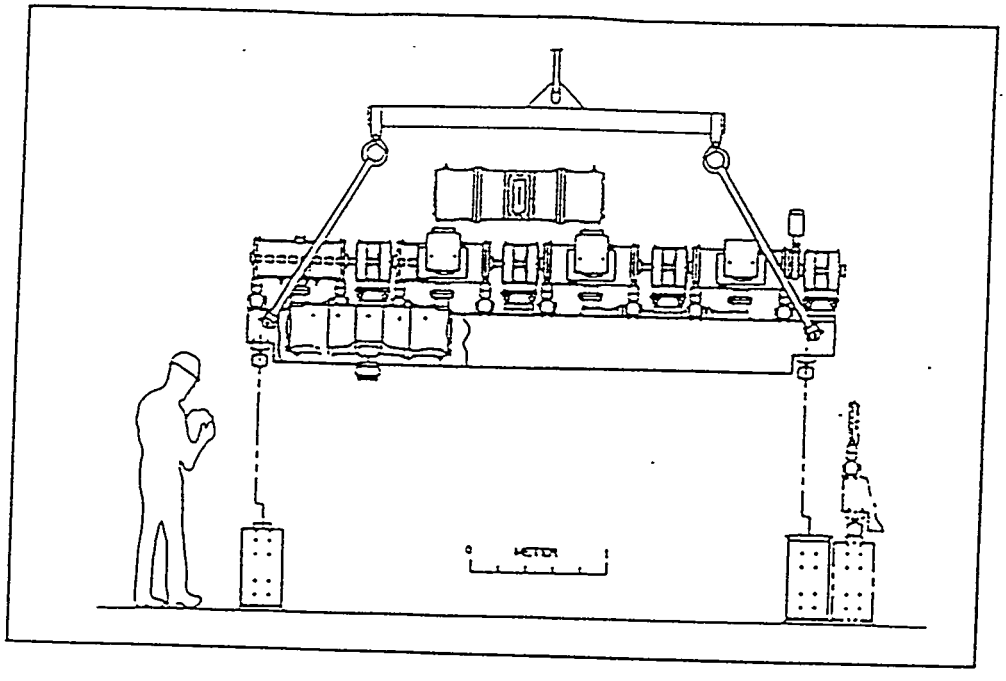


Fig. 10-7. BCDTL assembly unit (module) with four tanks.

Another example is a typical BCDTL bridge coupler, illustrated in Fig. 10-8. The bridge couplers are designed as three-piece assemblies, with end cavities identical (only minor differences in the coupling slots). Stocking spare end cavities is feasible, with sufficient extra stock in the slot area to be machined off for fine tuning to a specific module.

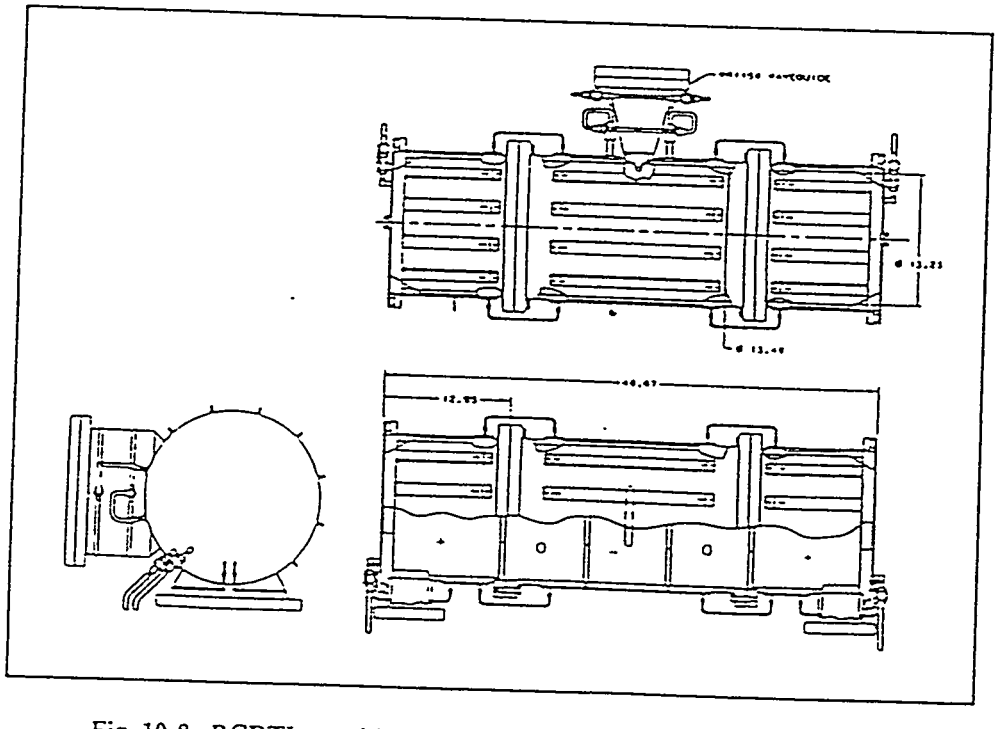


Fig. 10-8. BCDTL partitioned bridge coupler with common end cells.

If, however, the central barrel of the coupler fails or if the iris and waveguide transition fail, the entire barrel may have to be rebuilt. The end cavities can be salvaged and reused in the repaired unit. The bridge couplers are readily removed from the module by disconnecting the two coupling-cell vacuum joints so the entire bridge coupler can be easily transported to the lab for repairs. The interactive tests that assure RF tuning, vacuum, and cooling integrity can then be done in a lab environment. In the case of a failure of a major RF component, retuning the cavity with rebuilt parts will probably require bead pulls to verify the RF field distribution. In these cases, the entire assembly unit might be transported to the lab for this kind of testing.

10.2.4 Routine On-line Maintenance

The most likely components that might be handled on-line will be the vacuum pumps, the intertank and intermodule beamline components, water fittings, flow meters, filters, instrumentation, and the RF windows or couplers. For vacuum pumps (above 20 MeV), they are equipped with quick flanges that permit removal of the clamp with a single air-drive screw. The vacuum seal is all metal and easily replaceable when the pump is changed. The quick flanges are provided to speed the pump replacement because it is anticipated that several vacuum pumps may have to be changed out during any given maintenance period. The tunnel may be uncomfortably hot and the pumps are heavy and bulky.

Similarly, small quick flanges are used on the beamline sections between the tanks and between modules. Typical hardware installed in intertank gaps is shown in Fig. 10-9. It consists of a platform on which are mounted two sets of precision linear bearings, as was described for the BCDTL (Chap. 6). The quadrupoles are aligned in the lab relative to the centerlines of the linear shafts on which the linear bearings ride, as was described under Alignment (Chap. 9).

This typical intertank module contains the beamtube, diagnostic devices, bellows, and disconnect flanges. The in-line valve is considered an integral part of the tank or module to which it is attached. As a subassembly, the intertank module can be completely checked out and aligned in the lab before installation. It can also be repaired in this way. This technique is intended to facilitate maintenance and repair under potentially radioactive conditions and to generally facilitate the maintenance process.

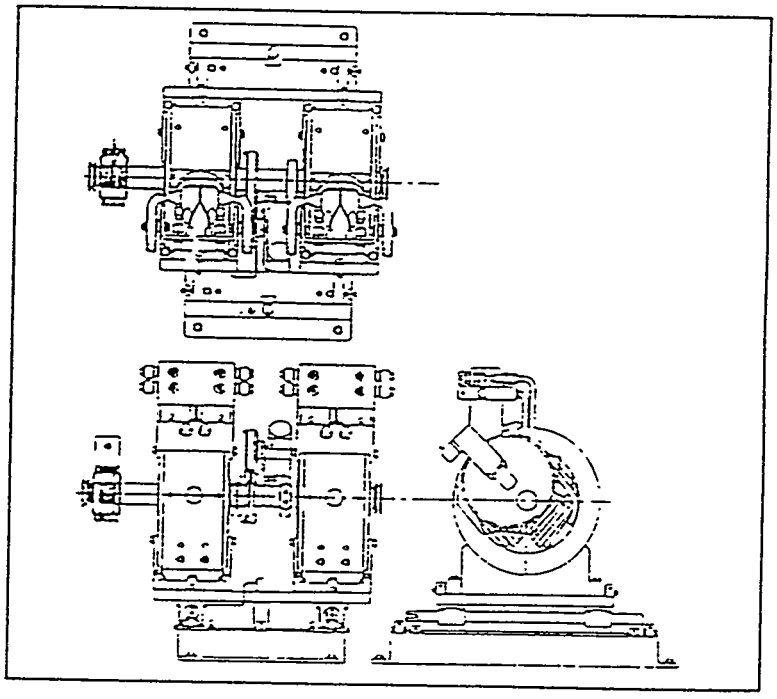


Fig. 10-9. Typical intertank hardware (BCDTL or CCL).

When doing on-line repairs of this intertank hardware, the small components can be removed and replaced. The quadrupole-doublet assemblies include a diagnostic device between the magnet pairs. At energies below 100 MeV, this device will be a stripline probe for beam-position monitoring, a beam-current monitor, and/or a video-profile monitor. Above 100 MeV, flying-wire diagnostic apparatus will be added at selected locations. Servicing the diagnostics requires separating the quadrupoles and replacing the beamtube section of the assembly. The beamtube sections are welded in place, so a sawing and welding operation will be necessary. In these cases, the entire quadrupole-doublet assembly is best repaired in the lab where all the essential subsystem checks and alignment can be done before returning the unit to service.

The quadrupoles are designed with split yokes that permit the field coils to be replaced while on-line. The failure of a field coil has happened a few times at LAMPF. In the APT design, the yoke can be taken apart by removing the connecting stripper bolts, leaving one half of the yoke securely attached to the platform so that alignment of the magnetic center is undisturbed. After replacing the failed field coil, the quad is reassembled, which should reestablish the alignment. If any question arises about the precision of the alignment after such a repair, perhaps caused by rough handling or slippage of the anchor bolts, the entire assembly can be taken to the lab and checked out with the taut-wire apparatus. The alignment precision of the reinstallation is assured by the linear rail system.

Small components, such as filters, flow meters, water valves, water fittings, and klixons (thermal switches for conductor-surface temperature-limit control), as well as instrumentation such as thermocouples, monitor loops, ion gauges, arc detectors, and so forth, will probably be repaired on-line. Most fittings will be sufficiently separated from the beam axis so that potential radiation levels at contact will be negligible or small. Because many fittings will be on the inboard side of the accelerator, access to that side is required. Because of the low beamline height, clearance under the machine is restricted, so a crossover ladderway is provided every 15 meters in the tunnel.

The RF windows in the BCDTL and the CCL are among the more difficult items to replace on-line because of the many bolts that are required to make up the RF and vacuum joints where the windows are connected. The windows are also located on the inboard side of the accelerator, at ~2 meters above the floor, so a portable platform is used to access them. To replace a window requires retracting an RF bellows on the air side for clearance and letting the module up to air (N_2). When the window is replaced, the appendage pump that maintains vacuum quality at the window will also be checked.

The large coupling loops in the DTL system are bulky and heavy. They are also critically matched to the resonant load of the DTL tanks. Failure of a window in these loops will be repaired by disassembling the power transmission coax from the loop, leaving the strap and vacuum coax in place. A new window is then inserted and all seals replaced. The air side of the coax is reinstalled.

Maintenance operations should be relatively routine on the low-energy portion of the machine (<20 MeV) because we do not expect to have any activation levels to contend with.

10.2.5 Remote Maintenance

In the event there are any activated components to handle in maintenance, it may be appropriate or necessary to make use of special tools such as air-drive hand tools. In cases of

high activation, it would be necessary to bring in remote handling equipment, as well as the air-drive tools. Maintenance with remote-handling equipment would be slow (by a factor of about 10) compared with hands-on maintenance and would have to be carefully planned in advance.

10.2.5.1 Special Hardware Features

Special hardware features have been included in the mechanical design to allow for the possibility of having to perform maintenance under nonideal conditions or even through remote operations. Some of these hardware features already mentioned include the quick flanges, the self-aligning linear rails, the easy removal or modularization of components, and rad-hard components.

10.2.5.2 Tunnel Size

One significant design consideration for maintenance under nonideal conditions is the size of the beamline tunnel itself. Even though any given machine design always strives for hands-on maintenance, we must allow for errors in design, future changes in personnel exposure limits, careless operation of the machine, malfunction of components or power supplies, failure of beamloss monitors, degradation of alignment precision, etc., and other performance characteristics, any one of which could lead to an increase in activation of the structures. For these reasons, we have sized the tunnel and provided enough room in the facility to allow for remote operations, such as a master-slave servo-manipulator system, in case radioactivity builds up in any part of the accelerator.

10.2.5.3 Radio-Controlled Bridge Crane

Another consideration is using radio-controlled bridge cranes to carry remotely operated surveillance booms. These booms would be useful during commissioning of the machine for special diagnostics and temporary monitoring equipment, and to detect water leaks, smoke, etc., without having to disable the shielding interlocks and send personnel into the tunnel.

10.2.5.4 Servo-Manipulator System

The final consideration is a high-performance, remote-maintenance, master-slave servo-manipulator system. Such a device is shown in Fig. 10-10. It is patterned after the system used at CERN and a similar machine that was developed for remote operations at LAMPF. The CERN system is called MANTIS, designed by Roger Horne, and is shown in Fig. 10-11. We designed APT to be serviceable with equipment such as MANTIS. Sufficient room is available in the tunnel for using air-driven tools, for the necessary shielding, and for remote handling equipment. Applications involving MANTIS require an unimpeded pathway alongside the machine. The manipulator is self propelled and can track a line on the floor to a specific location. If personnel must be in the vicinity to assist in operating MANTIS, shadow shielding might be required as shown in Fig. 10-10. The control of MANTIS is by means of a set of master arms that are manipulated by the operator to drive the slave arms. TV cameras and audio aids are used to enhance the effectiveness of the operations. The servoarms are equipped with cross-linked position feedback signals that provide force reflection so that the operator actually feels the forces being applied to the slave arms. The feedback gain can be adjusted to give the operator a mechanical advantage.

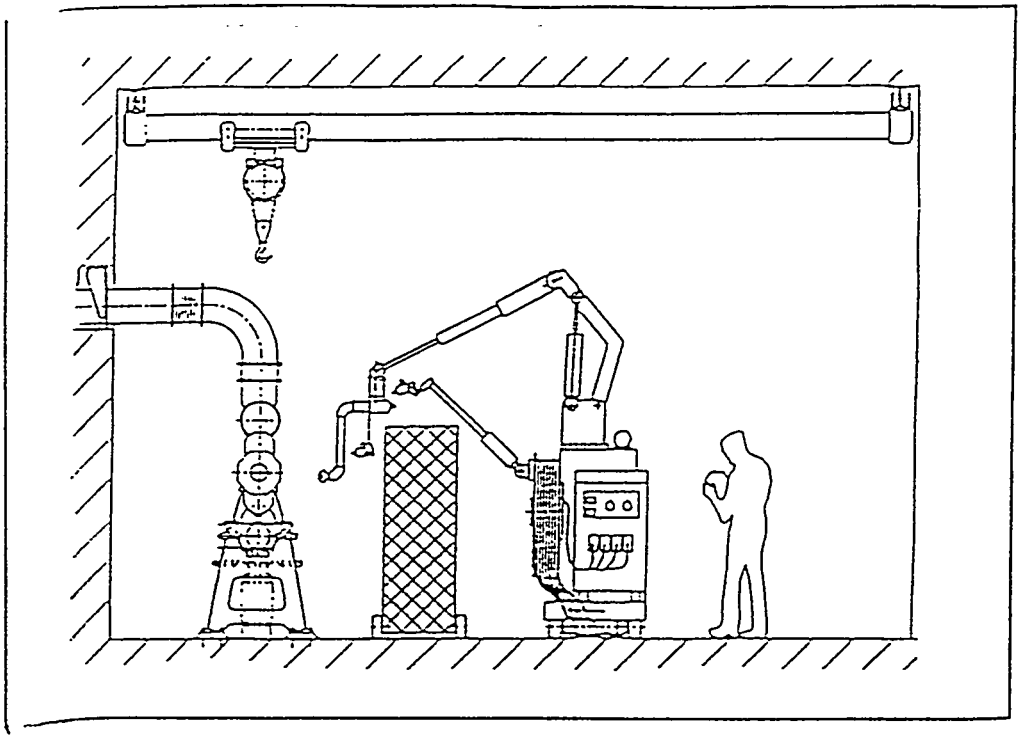


Fig. 10-10. Tunnel equipped for remote handling.

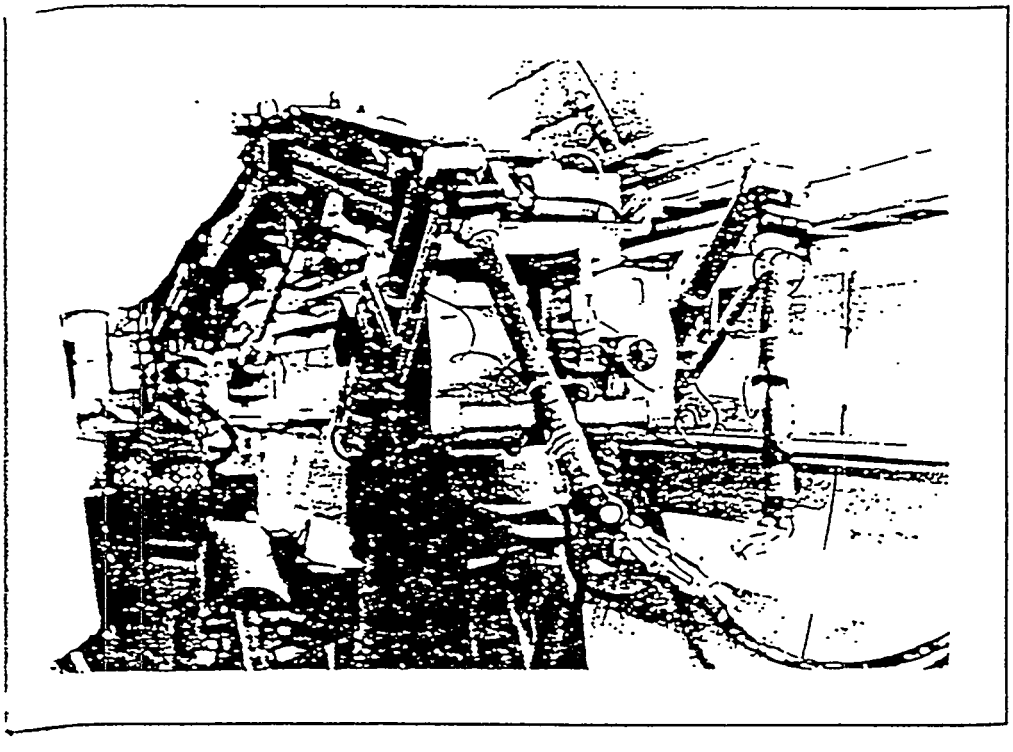


Fig. 10-11. MANTIS—CERN's remote handling system.

10.3 STARTUP AND FAULT RECOVERY

10.3.1 Accelerator Startup

The cold start of an accelerator consists of bringing the various operating systems up to prescribed setpoints and then using low-power beams to test sequentially the various accelerating modules in the machine. Several iterations may be required, and automated testing algorithms can be used if the hardware is sufficiently close to a proper operational state. Two beams that are anticipated to be required for the accelerator startup process include a beam for *tuning optics* and one for *tuning RF*. Both the optics-tuning beam and the RF-tuning beam will be a low duty-factor pulsed beam, and will probably be produced in the injector/LEBT with a fast kicker system or some form of an ion-source pulsing scheme, or both. The pulse structure required is shown in Fig. 10-12.

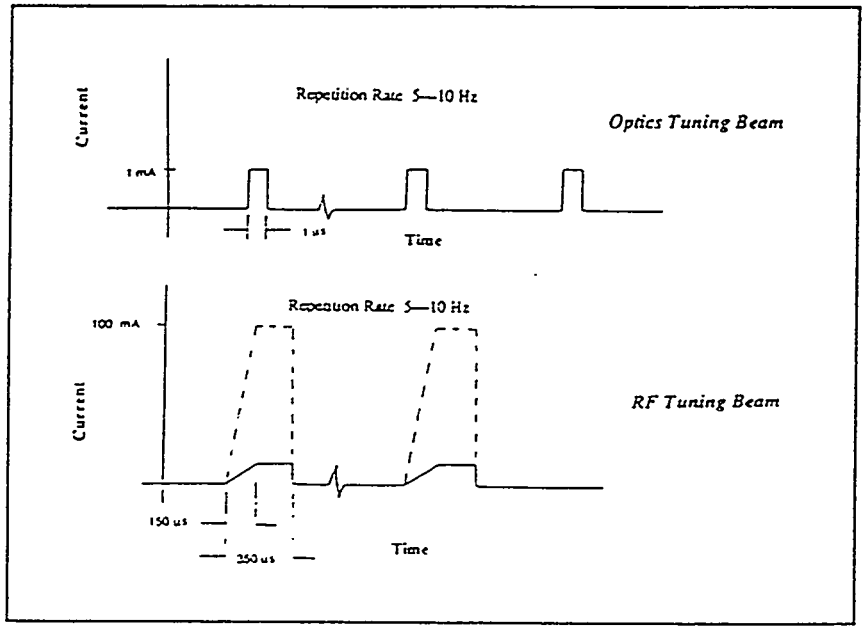


Fig. 10-12. Tuning beams required for APT accelerator startup.

10.3.1.1 Optics Tuning Beam

The beam for tuning beamline optics should be a very low-duty-factor, low-peak-current beam that will be threaded through the machine to establish centroid status and magnet settings. It is anticipated that the RF systems will have a limited control margin for transient loading, and that a limit of ~3 mA-μs (LAMPF limit on the 805-MHz cavities) will have to be met so that the short, transient energy droop in accelerating cavities will not exceed a prescribed error. For LAMPF, this limit is a 1% energy droop, and it is anticipated that a similar limit will be required for the APT accelerator. Thus, the optics beam will probably be limited to a few milliamperes with a few microseconds' duration. A beam current of 1 mA is expected to be easily observed in the beam diagnostic systems. A repetition rate of 5–10 Hz is sufficient for taking data, and entails a duty factor of less than 10^{-5}. Thus, at the exit of the accelerator, we will have no more than 200–300 W of beam power, which is sufficiently small to preclude damage to the structures. A tuneup beam dump will be needed, but

LAMPF experience shows that the entire optics-tuning beam can be lost in the machine during normal tuning periods. The beam tests will check the operating condition of steering and focusing elements, establish that their tune has been set to the previous tune, and that all accelerator systems are ready for the more detailed RF tuning.

10.3.1.2 RF Tuning Beam

The beam needed for RF tuning will be a low-duty-factor, high-current beam that will be used to set the amplitude and phase of all the RF systems in the accelerator. Again, the limited control margin on the RF systems require that the current risetime be limited for these higher current beams so that the energy droop can be controlled. Control-loop simulations that have been carried out with the CCL structures indicate that the risetime (from 10%–90% of the full RF amplitude) should be no shorter than 130–160 μs. An additional 100–200 μs (of flat pulse) is then needed to do the RF measurements. How much beam current will be needed to carry out these RF tuning exercises is not yet clear. Running each leg of the accelerator at full current would probably be useful to establish that the low-energy structures in each leg are operating properly at full current. Again, a repetition rate of 5–10 Hz is adequate. Thus, we will have a 0.3% duty factor (macroscopic) with a 100 mA-peak beam current giving an average current of 0.3 mA and an output beam power of 300 kW for this case. It will be most likely desirable to start RF tuning with much lower peak currents and then to increase the current after the entire accelerator is almost properly tuned. In any event, we will be dealing with tens to hundreds of kilowatts of final beam power, and we may need to consider using the expander and the full-power beam dump for this exercise.

10.3.1.3 Initiating Full Operation

For full-current operation, attention must be paid to control of the RF systems because of the beamloading effects. The CCL cavities will be 80% beam loaded. Thus, only 20% of the RF power delivered goes to cavity losses. The operating scenario envisioned for this turn-on mode is to detune the RF cavities approximately 47 kHz above frequency without beam, and to ramp up the RF power as the beam current is ramped up. This mode of operation will entail some 5%–10% reflected power when the beam is *off*, which will be handled by the RF systems. During the initial cold start of the accelerator, local oscillators will be used to provide RF heating of the cavities to bring them to operating temperature, at which point frequency control will be switched over to a master oscillator. During initial cold start, there will also be multipactoring problems to be addressed. Variable RF-pulse lengths (without beam) to the cavities from a few microseconds to a few milliseconds as well as low-power cw will be required. After all cavities are conditioned and up to operating temperature, operation with full beam current will be possible.

10.3.2 Fault Recovery

In addition to accelerator startup and tuning considerations, provision must also be made to bring the beam back up in the accelerator after a fault occurs. There will be a wide of range of fault conditions, and undoubtedly, different responses will be implemented depending on the exact nature of the fault. Opening an interlock chain, for example, will result in an immediate beam abort, while exceeding a lower threshold on a spill monitor could result in a warning message or an automated reduction in beam current. The hierarchy of responses will be developed with actual operation.

We envision that the response for turn-off and subsequent reestablishment of the beam will be as follows: we will use a fast kicker magnet in the low-energy beam transport line to turn off the beam within several microseconds, and then insert a variable iris into the beamline and use it to ramp up the beam current from some low value to full current. As this mechanical ramping is done, the RF amplitude will be ramped to keep the proper energy gain in the cavities. The use of a mechanical iris will preclude ion-source transients and will be slow enough so that accelerator timing can be done as the current is changed if, in fact, such tune shifts are needed. The iris will be designed to handle beam impingement for long periods of time, allowing operation at reduced currents for extended periods. Machine adjustments such as tuning out beamspill can be done with low-current cw beams.

10.4 PERSONNEL SAFETY, MACHINE, AND ENVIRONMENTAL PROTECTION

10.4.1 Introduction

APT is considered to be at a *preconceptual* design stage; therefore, much of this section on personnel safety and machine and environmental protection is highly preliminary. In this section, we describe what must be addressed with regard to the accelerator, such as the unique hazards, the applicable standards and regulations, and any future requirements that must be met, and briefly contrast accelerator safety with nuclear reactor safety. This is followed (in Sec. 10.4.2) by a preliminary hazard analysis, the required DOE hazard-class determination guidance, the classification of identified hazards, and a preliminary description of the accelerator safety envelope. In Section 10.4.3, we provide an overview of the safety philosophy, safety systems, and controls inherent in the design of the accelerator, while in Sec. 10.4.4, we describe each system and how each system address the identified hazards. An overview and summary of a preliminary Failure Mode and Effects Analysis Document is provided in Sec. 10.4.5.

10.4.1.1 Hazards of the APT Accelerator

This report describes the accelerator portion of the APT facility and therefore, is not subject to the more stringent nuclear facility requirements placed on the T/B portion of the facility. The hazard potential associated with the APT accelerator may seem unique in that the accelerator is unprecedented in its 200-MW power output. After careful design, however, the actual hazards are not really much different than those normally associated with RF accelerators. With existing RF accelerators, we have not only the normal industrial-type hazards but also those that can arise from high-voltage components and high-power RF systems, in addition to ionizing radiation or activation caused by beam impingement or beamspill on accelerator targets or components. Because the beam power and current are high compared with existing linear accelerators, a significant potential exists for damaging energy deposition in accelerating structures and beam transport lines if the beam is misdirected or misfocused for short periods (beamspill). A significant potential also exists for activating accelerator structures if even a small fraction of the beam is lost on a continuing basis. For this reason, special features have been included in the APT design that greatly reduce the potential for any beamspill or impingement on anything other than the target. Because of engineered safety, the accelerator can be classed as *low* hazard.

10.4.1.2 Applicable DOE Regulations

The APT accelerator facility must be designed in accordance with applicable DOE and federal requirements pertinent to the protection of the public, workers, and the environment. The following list, though not exhaustive, includes the primary ES&H requirements documents ordered in a general-to-specific fashion within the categories of general safety, radiation protection, environmental protection, fire protection, and general facility requirements. Some of these documents, especially DOE 5480.4, reference other mandatory standards that must also be applied to the design. A brief explanation of each document is given below.

- General Safety:
  - DOE 5480.4. *Environmental Protection, Safety and Health Protection Standards*. This document specifies requirements for the application of the mandatory ES&H standards applicable to all DOE and DOE contractor operations, provides a listing of reference ES&H standards, and identifies the sources of the mandatory and reference ES&H standards.
  - DOE 5481.1B. *Safety Analysis and Review System*. This document establishes uniform requirements for the preparation and review of safety analyses.
  - DOE 5480.25. *Safety of Accelerator Facilities*. This document establishes safety program requirements specific to accelerator facilities, and, along with its corresponding guidance document, includes requirements and guidelines for radiation safety, access control, life safety, hazard classification, safety analysis and review, and risk acceptance. The safety analysis requirements supplement those of DOE 5481.1B and provide an alternative to nuclear facility requirements.
- Radiation Protection:
  - DOE 5400.5. *Radiation Protection of the Public and the Environment*. This document establishes standards and requirements for operations of the DOE and DOE contractors with respect to protection of members of the public and the environment against undue risk from radiation.
  - DOE 5480.11. *Radiation Protection for Occupational Workers*. This document establishes DOE's radiation protection program requirements for protecting workers from ionizing radiation.
  - DOE/EH0256T. *DOE Radiological Control Manual*. This document establishes practices for radiological control activities at DOE and DOE-funded sites that manage radiation or radioactive materials.
- Environmental Protection:
  - 40 CFR 61. *National Emissions Standards for Hazardous Air Pollutants; Radionuclides*. This document is the final ruling on National Emissions Standards for Hazardous Air Pollutants under Section 112 of the Clean Air Act and establishes limits for emissions and provides air monitoring requirements.
  - DOE/EH 0173T. *Environmental Regulatory Guide for Radiological Effluent Monitoring and Environmental Surveillance*. This document establishes the elements of a radiological effluent monitoring and environmental surveillance program considered acceptable to the DOE.

- Fire Protection
  - DOE 5480.7. *Fire Protection.* This document establishes fire protection program requirements, including "improved risk" level of fire protection sufficient to attain DOE objectives.
  - NFPA 101. *Code for Safety to Life from Fire in Buildings and Structures.* This document (1) establishes minimum requirements that provide a reasonable degree of safety from fire in buildings and structures, and (2) endeavors to avoid requirements that might involve unreasonable hardships or unnecessary inconvenience or interference with the normal use and occupancy of a building but insists upon compliance with a minimum standard for fire safety consistent with the public interest.
- General Facility
  - DOE 6430.1A. *General Design Criteria.* This document provides criteria for the design of DOE facilities, and includes structural, electrical, mechanical, siting, materials, and radiation protection criteria.
  - UCRL 15910. *Design and Evaluation Guidelines for DOE Facilities Subjected to Natural Phenomena Hazards.* This document establishes guidelines for uniform design and evaluation of DOE sites and facilities throughout the United States for protection against earthquake, wind, and flood hazards.
  - DOE DGM. *DOE Design Criteria Manual for Weapons Complex Configuration.*

10.4.1.3 Accelerator vs. Reactor Production of Tritium

This report covers only the accelerator portion of the APT facility; Chap. 10 deals specifically with the operation and safety of the APT accelerator. When considering the operation and safety issues of APT, however, accelerator issues are better understood if we look at the operation and safety issues of the APT facility as a whole.

As reported previously, one key advantage of APT tritium production over reactor production (RPT) is the absence of fissionable materials and the much lower consequence of any accidental release of radioactive material. The anticipated worst-case dose release is negligible for the APT concept compared to the reactor or RPT process. In APT, tritium is produced under very low inventory conditions without any fissionable materials, and therefore, no high-level waste is produced. The ES&H impacts are *significantly reduced* compared to reactor systems. In addition, the amount of radioactive products from spallation in APT is at least an order of magnitude less than the amount of radioactive products produced in the reactor-fission process.

The APT process has not only low inventory conditions, no actinides, and a substantially lower waste stream, but also a significantly lower decay-heat level than that of a reactor, lower temperature and pressure conditions in the various APT cooling loops, lower thermal constraints, and, therefore, much lower accident consequences than that considered in reactor facilities.

The accelerator, which drives the spallation process with its beam of protons, is by itself, by and large, a device that *fails safe*. Before an *accident* could occur, almost any malfunction of the accelerator would shut down the machine and thereby discontinue the spallation

process. This is true even in the face of an otherwise deliberate attempt by an operator to keep the machine running. This can be compared to reactors that are designed to operate under conditions that are near criticality—a potentially serious *runaway* accident condition.

When considering the safety issues attributed solely to the accelerator, we include the effects of a worst-case *accelerator* accident, as used in the past, namely, a spill of the full beam lasting 1 hour. Even a deliberate attempt to initiate such an accident, however, would cause a fail-safe shutdown of the accelerator, probably within minutes because of a loss of vacuum in the beamline. Although the real safety issues for APT are concerned mainly with the target and accelerator/target interface (and are of far lesser significance or consequence than the safety issues related to reactor systems), the safety issues for the accelerator itself are identified in the preliminary hazard analysis below, followed by descriptions of the safety and protection systems that are designed to address these hazards.

10.4.2 Preliminary Hazard Analysis

The scope of this preliminary hazard analysis for the APT preconceptual design phase is limited to the identified hazards that are unique to accelerators, such as those that can arise from high-power RF systems, high-voltage components, radiation from normal operations, and radiation, activation and component damage that can occur because of beamspill, abnormal operations, or accident conditions. Items not covered in this preliminary analysis are such common industrial hazards as high pressure gases, forklift and crane operations, chemical hazards (such as solvents), and facility fire. In addition, such natural phenomena hazards as earthquake, lightning, flood and wind, or sabotage-type events, or incredible-type accidents (such as an airplane collision into the facility) are not included.

10.4.2.1 DOE Hazard-Class-Determination Guidance

In accordance with DOE 5480.25 Guidance, a summary description of the accelerator is given below, focusing on the hazardous features. The nature of these hazards is discussed along with an estimate of their impact on persons and the environment for the purpose of providing guidance to determine the hazard class of the accelerator.

- Summary Description. The APT accelerator consists of different kinds of accelerating structures that provide efficient energy gains to a beam of protons over different energy ranges. In the low-energy region of the accelerator, a continuous stream of protons is generated by an ion source and then injected at an energy of 75 keV into a RFQ, where it is formed into bunches at 350 MHz (frequency of RF power system for the low-energy structures) and accelerated to 7 MeV. The bunches are further accelerated to 20 MeV in a DTL and combined with a second (identical) bunch train in a device called a funnel. The combined proton beam is accelerated further to 100 MeV in a BCDTL and then to the full energy of 1 GeV in a series of CCL tanks. The latter two high-energy structures are powered by 700-MHz RF and constitute the bulk of the accelerator. The accelerator is designed for an average beam current of 200 mA, resulting in an average beam power exiting the accelerator of 200 MW. Monitoring and control of the APT accelerator would be similar to methods that are standard at all large accelerator facilities, i.e., through a central computer communicating with data-collection and manipulation nodes distributed throughout the system. Operations would be highly automated, with control being accomplished by four to six well-trained operators.

- Associated Hazards. Because the beam power and current are high compared with existing linear accelerators, there is a significant potential for *damaging energy deposition* in accelerating structures and beam transport lines if the beam is misdirected or misfocused for short periods of time (beamspill), and also, a significant potential for *activation* of accelerating structures and beamlines if even a small fraction of the beam is lost on a continuing basis.

- Engineered Safety. The first choice when designing for safety is to implement passive protection. Most of this discussion on engineered safety pertains to the active safety systems for APT. Distributed throughout the accelerator and beamlines are multiple, redundant sensors and diagnostics, all acting within very short time intervals (microseconds) to determine if the beam is out of acceptable limits in terms of position, angle, size, phase, energy, transmission, intensity distribution, local loss rate, etc. These detectors are integrated into several kinds of machine protection systems that prevent damage and activation buildup. Secondary information is provided on accelerator vacuum, coolant flow and temperature, integrated beamlosses along the linac, amplitude and phase of the RF power stations, energizing currents in the focusing magnets, etc., to confirm the correct operation of the beam manipulation elements of the accelerator and transport systems. Malfunctions or out-of-tolerance values for any of the devices automatically terminates or limits operation until the situation is corrected.

- Impact of Hazards. If the active engineered safety features should fail, beamloss could theoretically occur either for short periods of time because of misfocus (beamspill) or for longer periods with small lost fractions of beam causing component activation (beamloss). There is only the potential for minor onsite and negligible offsite impact to people or the environment as a result of the passive engineered safety features. Specifically, we would not expect there to be any permanent health effects to people or any damage to the environment. However, the hazard is of concern, because personnel exposure could exceed an exposure limit.

- Hazard Classification Recommendation. Based on the above rationale, and the following preliminary hazard analysis, we recommend that the accelerator facility be classified as *Low Hazard*.

10.4.2.2 Categorization of Identified Hazards

Using the DOE 5480.25 Guidance document, the identified hazards are categorized by consequence and probability as follows (each level is defined in the guidance document):

- Consequence: (1) high, (2) medium, (3) low, and (4) extremely low;
- Probability: (A) high, (B) medium, (C) low, and (D) extremely low.

A risk matrix made of these parameters is shown in Fig. 10-13. The shaded rectangles display the *risk levels* that, in general, are either acceptable or unacceptable. All hazards that we identified fall into the acceptable, negligible-risk level.

The hazards identified in the preliminary hazard analysis that can arise during normal operations (steady-state operations, startup, shutdown, fault recovery), maintenance operations, and abnormal or accident conditions (e.g., beamspill) are listed in Table 10-6.

Details regarding the needed safety provisions for each of the identified hazards are included in the Chap. 10 Appendix.

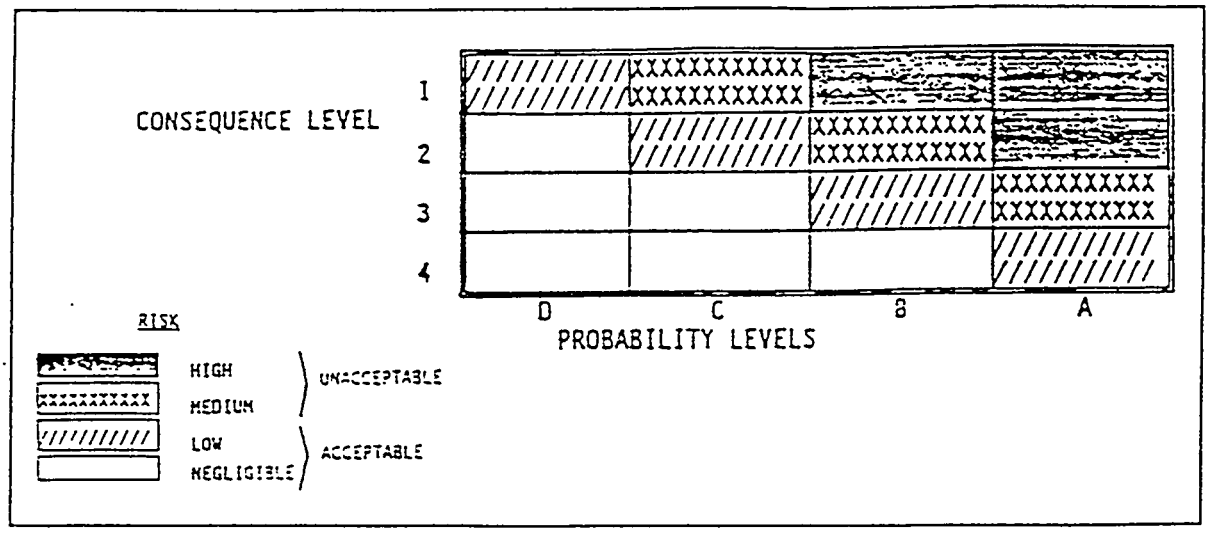


Fig. 10-13. Risk matrix from DOE 5480.25 guidance.

Table 10-6. Preliminary Hazard Analysis for APT

Mode	Hazard	Risk Level
Normal Operations	Injury from High-Voltage/Current (injector, klystrons)	2D
	Exposure to Nonionizing Radiation (injector)	3C
	Hydrogen Gas Handling (injector)	3C
	Exposure to Nonionizing Radiation (klystrons)	3C
	Oil Spill (klystrons)	4D
	Exposure to Ionizing Radiation (accelerator)	3D
	Exposure to Ionizing Radiation (klystrons)	4D
	Facility Contamination (cooling-water leak)	3D
Maintenance Operations	High-Voltage/Current Injury (injector, klystrons)	2D
	Exposure to Nonionizing Radiation (RF)	3C
	Exposure to Activated Components	4C
	Exposure to Activated Water	3D
	Exposure to Activated Air	3D
	Personnel Contamination	3D
Abnormal Operations	Exposure to Ionizing Radiation (injector extractor failure)	4C
	Personnel Injury (injector-cooling failure)	4D
	Exposure to Ionizing Radiation (beamspill)	3D
	Equipment Damage (DTL-CCL cooling failure)	4D
	Target Damage because of HEBT Failure (Loss of Uniform Beam Distribution or Loss of Defocus on Target)	2D

10.4.2.3 Accelerator Safety Envelope

The accelerator safety envelope is a set of both physical and administrative conditions that establishes the boundaries within which operational, developmental, and experimental

activities are constrained. The accelerator safety envelope is based on a comprehensive safety analysis and is subject to approval by DOE in accordance with DOE 5480.25.

The items that constitute the accelerator safety envelope will be easily verifiable by observation, but will be defined so that transient or unplanned events (such as a power outage) will not compromise safety or violate the envelope.

The specific items that define the accelerator safety envelope will be determined by the final design of the accelerator and the accelerator facility. Separate operational envelopes may be defined for different modes of operation, such as initial commissioning, full-power operation, normal maintenance, and test operations. Categories of items that will be considered for the accelerator safety envelope include the following:

- limits on operating variables (such as currents, voltages, energy potentials, beam power, pressures, temperatures, flow rates, etc.) needed to preserve physical barriers or prevent risk to personnel;
- status of active safety systems, such as the personnel safety system, fast-protect, beam-permit, and air and water handling systems;
- requirements related to calibration, testing, maintenance, and inspection of safety-related systems;
- shielding criteria and configuration;
- environmental protection requirements, such as the status of monitoring systems and limits on releases; and
- administrative controls, such as minimum staffing levels, qualification and training for operation, minimum operable equipment, critical documentation, currency of procedures, and immediate mitigative actions to be taken if the safety envelope is breached.

10.4.3 Designs for Personnel Safety and Machine and Environmental Protection

10.4.3.1 Design Philosophy

The design philosophy with regard to safety has been to design using the most conservative estimates, including redundant systems and defense-in-depth concepts where appropriate. The APT design uses very large margins for safety that, along with conservative estimates, results in orders-of-magnitude improvement over that which might be considered the minimum requirements.

10.4.3.2 Passive Safety Designs

The passive safety measures designed to be used on the APT accelerator consist of all the shielding and the fully sealed tunnel in which the accelerator will be housed. Not only will local shielding be placed around the high-energy portions of the beamline in the tunnel as needed, but also 12 meters of compacted earth-fill will be placed over and around the fully

sealed tunnel. Conservative estimates and preliminary calculations indicate that there will be several orders of magnitude of protection to the public from DOE radiation exposure limits at all locations. The passive safety designs alone fully protect the public from any excessive radiation exposure for all normal and abnormal conditions, including accident conditions.

10.4.3.3 Active Safety Designs

In addition to the passive safety designs mentioned above and the administrative control measures described below, the following five active safety systems are an integral part of the APT accelerator design:

Machine Protection:	(1) Fast-Protect System (2) Beam-Permit System
Personnel Protection:	(3) Personnel Safety System (PSS)
Environmental Protection:	(4) Activated-Air Handling System (5) Activated Cooling-Water System

A brief description of each active safety design is given below, with a detailed description provided in Sec. 10.4.4.

- Fast Protect. The fast-protect system is a hardwired, fast-response network of distributed monitoring devices that sense status inputs from accelerator diagnostics and interrupt the beam at the injector in the event of a failure mode, fault, beamspill, setpoint value gone out of bounds, accelerator parameter exceeding limits, etc. This system is intended to protect the accelerator from possible damage caused by faults. The sensor response time is estimated to be on the order of 1–5μs, with signal transmission to the injector <4μs and maximum transport time for beam in accelerator <7μs. This translates to a maximum of <16μs total response time from a sensed fault to a beam abort.

- Beam Permit. The beam-permit system will inhibit beam turn-on until certain relevant conditions are fully satisfied, including inputs or gauge readings to be compared to the operating setpoints for cooling water flows and pressures, RF system parameters, vacuum pressures, magnet currents, etc. The conditions also include inputs from various beam diagnostics to ensure that beam position, transmission, and profile measurements are within acceptable parameter ranges. An out-of-range parameter *drops* the beam permit.

- Personnel Safety System (PSS). The PSS is a combination of a radiation-monitoring system and an entry-interlock system. It is intended for personnel safety to keep personnel out of the accelerator tunnel whenever the possibility of measurable radiation exposure exists. Should radiation levels exceed a setpoint value, these systems will automatically place the accelerator in a standby mode.

- Activated-Air Handling. The air inside the accelerator tunnel may well become slightly activated during operation, and therefore, will be sealed off from the atmosphere and occupied areas and will remain stagnant during accelerator operation. The air-handling system will allow periodic purging of the tunnel air after checking that the air is below an allowable radioactive limit for release to the atmosphere.

- Activated Cooling Water. Although we do not anticipate activation products in any significant quantities in the accelerator cooling water, the primary coolant loops in the accelerator cavities and components will be treated as if the water were activated. Water treatment and filtration will be used to ensure cooling water that will be as clean as possible, and radioactive aqueous storage capability will be provided.

10.4.3.4 Administrative Controls

Administrative controls will be implemented throughout the facility and for all operations. The administrative controls will include such things as facility access, radiation safety, training and qualification, SOPs, written guidance for monitoring and for occurrence reporting, and internal safety reviews.

- Definitive Documentation. This documentation will be developed to describe the organization, the lines of authority, and individual responsibilities with respect to all administrative controls.

- Independent Internal Safety Reviews. These reviews will be conducted periodically in accordance with DOE requirements to give management reasonable assurance that ES&H issues are not being overlooked or ignored and are given appropriate priority.

- Operating Procedures. These procedures will be documented, reviewed, and approved on a periodic basis, including maintenance procedures and procedures applicable to abnormal operations or accident conditions.

- Access to the Accelerator Facility. Access will be controlled for all employees, as well as visitors or nonemployees. This will include posted signs, interlocked barriers, closed-circuit TV, and motion detectors for positive assurance.

- Training. Training in accordance with DOE 5480.24 will be required for all persons employed at the accelerator facility. Operations staff and maintenance crews will receive intensive and detailed training on the APT accelerator system and its components. A key element of the training will be the use of computer-based simulators that will represent the accelerator system and its components as completely as possible. These simulators will permit the operations and maintenance personnel to learn off-line how the accelerator works, to absorb tuning procedures and develop appropriate responses to a range of off-normal conditions, and to work out and optimize equipment maintenance procedures. No effort has been devoted up to this point to the specification or design of such simulation systems, other than to acknowledge the need and the general requirements. This work will be carried out at a later stage in the APT program.

  All employees will receive training in general safety, facility- and accelerator-specific safety, health physics and radiation safety, and task-specific training (e.g., SOPs). Some training will be required for site visitors and nonemployees (e.g., each person who visits the facility will wear a radiation-monitoring badge, and everyone will receive radiation training and site-specific training for possible hazards that pertain to the operations). All training will be used for qualification purposes and will be recorded. A retraining and recertification program will also be developed.

10.4.4 Safety and Protection Systems Descriptions

10.4.4.1 Shielding and Tunnel

- **Shielding Policy.** Shielding for APT is essential to personnel safety. The APT facility is designed to shield both employees and the public from the radiation generated by the accelerator during normal operations, maintenance, startup, shutdown, and any abnormal or accident conditions. The shielding provided by this design has been calculated to provide a margin of safety of at least two orders of magnitude. In addition, the LANL Accelerator Access-Control Systems Standard, LS107-01.1, is used as part of the APT shielding policy. The standard defines physical barriers, including shielding, as being substantial and capable of deterring entry. Moveable barriers, such as concrete plug or double-airlock doors, must be interlocked with the beam and radiation detectors to prevent exposure of personnel in excess of the most current DOE standard for ionizing and nonionizing radiation.

- **Requirements.** DOE Order 5480.5 establishes a limit for open areas (public access) of 20 mrem/year for normal operations and 10 mrem per beamspill accident (full beamspill for 1 hour). In closed or *controlled* areas, the radiation exposure limit is 200 mrem per year for authorized site workers during normal beam operations and 100 mrem per beamspill accident.

- **Design.** The accelerator will be housed in a concrete-lined tunnel with 12 meters of compacted earth around it. Figure 10-14 illustrates the geometry used for the APT linac shielding calculations.

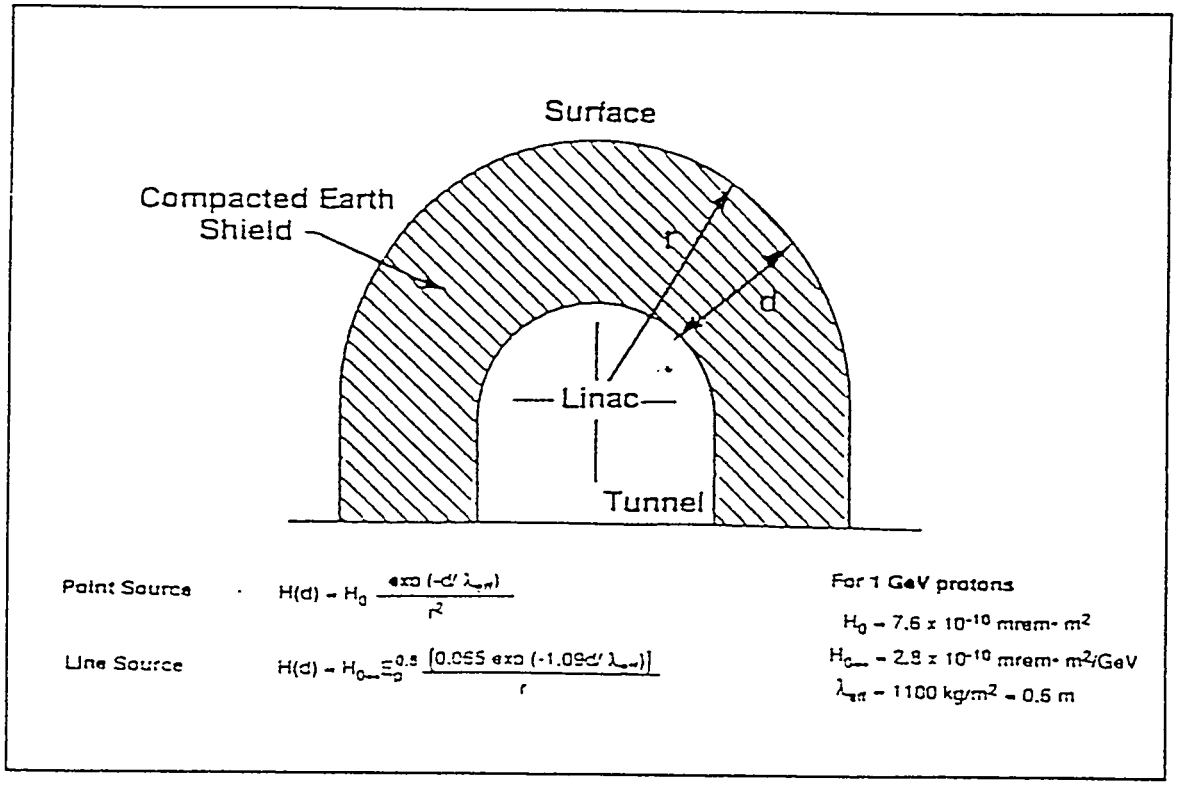


Fig. 10-14. Geometry for APT linac shielding calculations.

In Fig. 10-15, "Annual-dose vs. shield-thickness for beamloss (maximum normal continuous operation)," we note that for the APT design, the safety margin is equivalent to approximately four orders of magnitude; i.e., the design using 12 meters of earth shield thickness results in an annual surface dose of 1×10^{-3} mrem/year compared to the allowable dose of 2×10^{1} mrem/year for normal continuous operation. Fig. 10-16 shows the calculated dose for a one-time beamspill accident to be 2×10^{-1} mrem, two orders of magnitude less than the DOE limit of 10 mrem per beamspill accident.

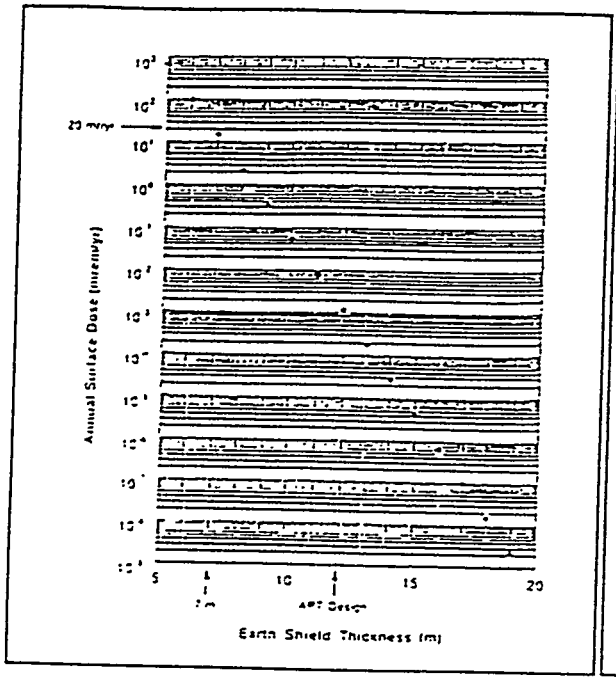


Fig. 10-15. Annual-dose vs. shield-thickness for beamloss (maximum normal continuous operation).

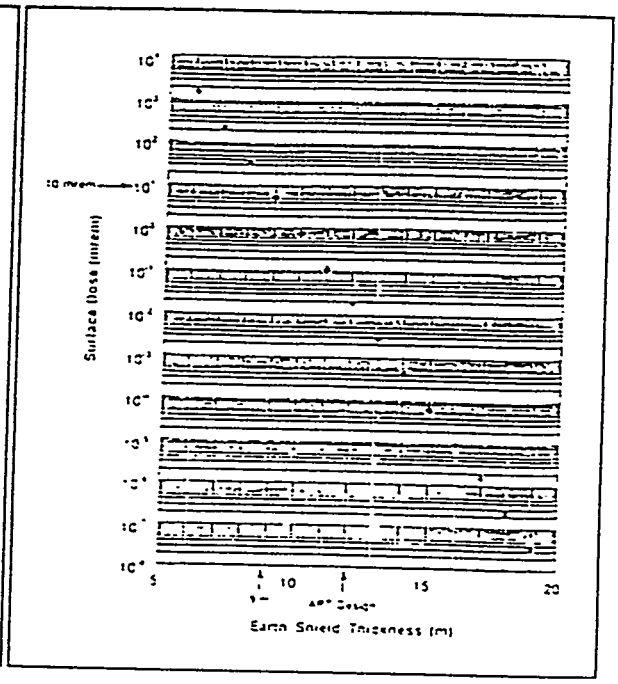


Fig. 10-16. Dose vs. shield-thickness for full beamspill (along 100-meter path for 1 hour, 200 mA at 1 GeV).

The components that make up the accelerator access control system are identified by two classes: (1) warning barriers, and (2) physical barriers. The *warning barriers* are used for demarcation of areas with a radiation hazard. According to LS 107-01, warning barriers are required where the dose equivalent is >5 mrem/hour ; but <100 mrem/hour . Demarcation of areas with radiation hazards is done with posting pursuant to the DOE Radiological Control Manual. The *physical barriers* include the 6-ft, chain-link fence that surrounds the facility, the concrete tunnel housing the accelerator that is covered with 12 meters of compacted earth, interlocked moveable-concrete barriers, and personnel doors that provide access to the tunnel. All radiation monitors are integrated with the moveable shielding and personnel access-door interlocks to prevent accidental entry into the tunnel and to ensure the structural integrity of the shielding system. Most critical is that the beam is shut off by the personnel safety system interlocks.

10.4.4.2 Fast-Protect System

- **Description.** The fast-protect system is a distributed network of monitoring devices that sense status inputs from accelerator diagnostics and interrupt the

beam at the injector in the event of a failure, a fault, beamspill, or some out-of-bounds parameter. The proposed system implementation is based on a similar system used on the GTA accelerator. This system consists of three module types, the master module, the slave module, and the interlock module. The master module sources a 10-MHz optical carrier, which is propagated by the slaves. The slave module monitors diagnostic inputs and interrupts the carrier in the event of a failure. The last slave in the chain outputs discrete fault signals that are used by the interlock module and other safety hardware. The interlock module accepts discrete fault signals from the fast-protect and other systems, interrupting the injector enable-control signal if any system faults. These modules can be connected in several topologies to achieve the desired operating characteristics.

A simple daisy-chain topology is shown in Fig. 10-17. Tree-like topologies are also possible using the status output of a chain of slaves to drive a diagnostic-monitor input of a slave module in the main fast-protect chain. This flexibility allows the system to be easily configured for a large facility and satisfy a wide range of speed requirements.

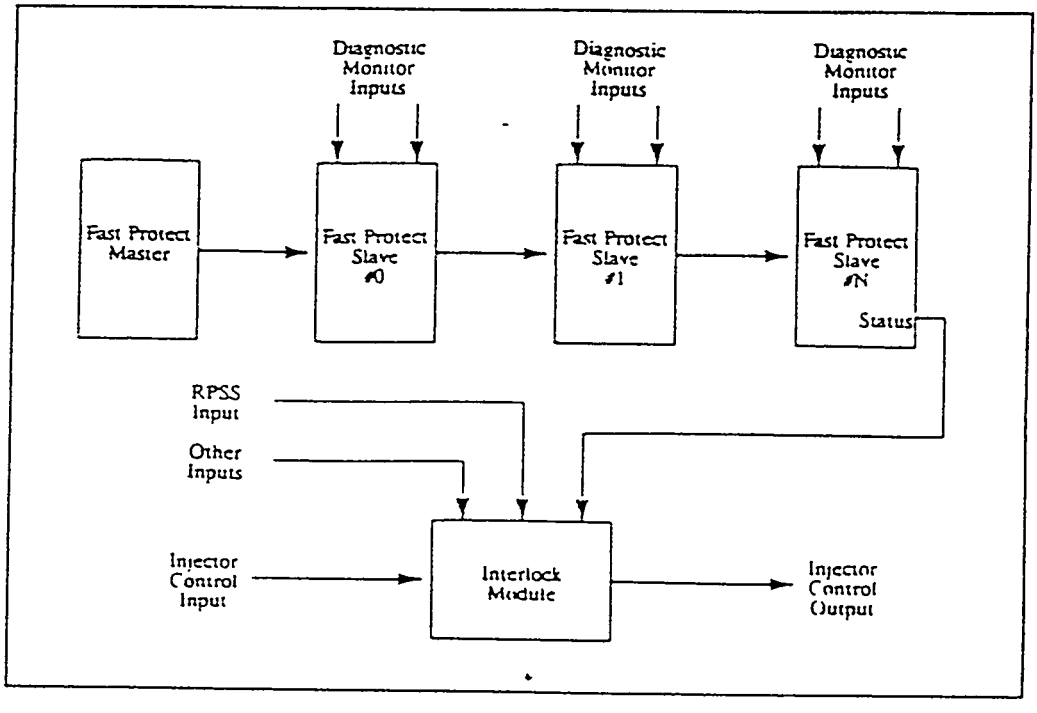


Fig. 10-17. Daisy-chain-type topology for the fast-protect system.

- Operation. In normal operation, the master module sources a 10-MHz carrier (fiber-optics link) that is propagated through a chain of slaves. The last slave module outputs a system-status discrete, which is monitored by the interlock module. In the event of a fault, the carrier is interrupted and the beam shut off. The slave module, which detects the fault, latches the diagnostic-monitor inputs at fault determination for readback by the control system. The system automatically resets when the fault condition is removed.

  This operation can lead to *chattering* of the beam at the natural frequency of a diagnostic sensor or the fast-protect daisy chain, whichever is slower. To avoid

this behavior, the interlock module will be designed to have a minimum time off, so it controls the chattering rate. If the chattering continues for more than a set period of time, the interlock module will lock the beam *off* and require an operator reset. The actual chattering rate and duration limits will be defined by the requirements of the target window.

Each master and slave device will have a control-system interface, allowing operators to view detailed system status. The slaves will *latch* (i.e., record) first fault information for diagnostic purposes. The master devices will allow the operators to turn the carrier *on* and *off*, and will be capable of generating invalid carriers for system test.

- **Reliability and Redundancy.** The fast-protect system will be designed to be as reliable as possible, using redundant or fail-safe logic in all critical elements of the system. The design philosophy is to ensure that the failure of any single component will not jeopardize system operation, and will be detectable by automatic or periodic testing. Module types are intentionally designed to be single purpose, reducing the chance of human error, and to provide the minimum of setup options. The system configuration will be done manually but will be readable by the control system, allowing automatic verification. In a manner similar to that of the GTA system, redundant logic will be implemented using different I&C technologies, which exhibit different failure modes when exposed to voltage, temperature, and radiation extremes. This design methodology results in a device that is much more likely to degrade gracefully when exposed to environmental stress.

The implementation of fast-protect system will include two redundant systems, each of which is also dual redundant in critical logic. Either system will provide adequate protection for APT operation, which will allow maintenance to be performed during normal operation.

10.4.4.3 Beam-Permit System

- **Purpose and Function.** The purpose of the beam-permit system is to prevent inadvertent operation of the accelerator with beam in a way that could cause equipment damage. The beam-permit system prevents operation outside of a safe operating envelope by preventing the acceleration of the proton beam if certain conditions are not met. This envelope is dependent on the mode of operation of the accelerator (e.g., operational mode, maintenance mode, etc.), the condition of each of the support systems, and the state of health of the beam-permit system itself.

  Although beam permit is not responsible for personnel safety, it monitors the status of the personnel safety systems to prevent the unnecessary activation of their safety features. The beam permit is more than just hardware interlocks; it is a *watchdog* over many of the accelerator conditions. Some of the many conditions that the beam-permit system must checkout and verify are as follows:

  - the proper vacuum level and temperatures of all accelerator tanks and beampipes;
  - the setting of bending magnets to switch the beam to the proper target or beam dump;

- a clear beam path, ensuring that invasive devices such as diagnostics and in-line beamstops are retracted;
- a readiness status from the T/B or beam dump;
- a complete check of the personnel safety system, ensuring there are no unsafe conditions for the particular mode of operation;
- a readiness status from the RF power system;
- a readiness status from the cooling and HVAC systems; and
- hardware interlocks confirming safe operating conditions.

The status of the beam-permit system is displayed to the operators. The status includes the current operational mode of the accelerator and a summary of conditions, if any, that would prevent turning on the beam. An operator override capability may be necessary, but this capability will require close control and validation.

- **Interfaces.** Beam-permit functions are distributed throughout the accelerator IOCs. Most of its inputs are derived from instrumentation (values within setpoint limits) and the correct state of control programs. It also has self-checking features, such as a computer-to-computer *heartbeat* to detect remote software or hardware problems and watchdog-timer hardware to monitor critical computer processes. Because the beam permit uses the same interfaces and data paths as the rest of the control system software, the integrity of the control system is continually monitored. One IOC will be dedicated to coordinating the accelerator-wide beam-permit functions. The output of this IOC will be a beam-enable signal to the injector.

10.4.4.4 Personnel Safety System

The primary risk of the APT accelerator is radiation exposure to personnel. The heart of the radiation-protection safety system is a radiation-monitoring and entry-interlock system designed to keep personnel out of the beam tunnel whenever there is a possibility of measurable radiation exposure. But nevertheless, this system must still permit accelerator operators and maintenance personnel access to the equipment when conditions are safe. It is a combination of a radiation-interlock system and a barrier-interlock system.

- **Description.** The PSS is basically a radiation-monitoring system that is interlocked with the double-airlocked doors, the moveable shielding, and the accelerator beam-permit safety system. In addition, it consists of warning beacons, solid fences, rope barriers, and administrative controls. The radiation-interlock system continuously monitors radiation and displays the information on station. The accelerator will automatically be placed in a special operating or standby mode to ensure that personnel are safe from prompt radiation at all times when radiation levels exceed a preset level and/or a tunnel entryway is breached. Areas where personnel may be subjected to potential radiation exposure are designated and posted in accordance with the DOE Radiological Control Manual. All personnel must be on a dosimetry program and receive appropriate radiation training.

  Of course, the possibility always exists that an employee will be overlooked during an area sweep and tunnel closeout before accelerator operation; or there is

the possibility of failure of the PSS combined with employee ignorance or error that could result in a worker being behind the shielding when the accelerator is operating. To minimize the probability of this risk, announcements will be made to clear the tunnel before each operation. The announcement would be followed with a sweep of the area to ensure that no one is left in the tunnel. As an additional safeguard, the PSS will be tested periodically to ensure proper operation.

- Interfaces. The PSS is an independent system integrated with the beam-permit system (described earlier) that receives inputs directly from the radiation monitors that are located in each zone throughout the accelerator tunnel. When an unsafe condition is detected by a radiation monitor, an input signal is sent from the monitor to the beam-permit system, which activates a beacon to warn personnel of the hazard and to inform them of the zone within the tunnel and the accelerator structure where the source of radiation is located. If a predetermined upper radiation limit is exceeded, the input can also be set to disable the beam. Before the beam permit *personnel-protection-OK* output can be satisfied and beam operations resumed, three conditions that reset corresponding series-wired relays must be met: (1) exclusion area barrier continuity, (2) radiation monitors *on*, and (3) all monitors indicate less than 5 mrem/hour, the limit for occupational radiation workers (Los Alamos requirement).

10.4.4.5 HEBT/Target Interface

The HEBT transports an very high-current, high-power beam from the linac to the target window with minimal loss through a transport line, an achromatic bend, and a beam expander. In the beam expander, the beam phase space is *folded* to produce an expanded and uniformly distributed beam in transverse (x-y) space to meet the requirements of the target. The loss of uniform beam-energy density (*loss-of-defocus*) on the target window, or the loss of beam (either partial or total) anywhere in the HEBT are the two potential hazards of concern. Potential causes for either of these events include the loss of one or more of the beamline elements, severe position jitter of the beam ($>0.25\sigma$), or significantly off-momentum beam particles or beam bunches (>1%). A multilayered interlock and diagnostic system is included in the preconceptual design to defend against these potential causes that could lead to the potentially hazardous events in the HEBT.

- Magnet Power Supplies. The most serious potential event would be a significant increase of the beam-energy density at the Inconel-718 superalloy target window, which has the potential to cause damage to or failure of the window. The first line of defense is the magnet-interlock system. Every magnet power supply is electrically connected in series such that if any unit fails, an electrical signal shuts down the beam in <20 μs. The total stored-beam energy that could be transmitted to the target after an interlock beamtrip is extremely small and can not cause damage to the target window, even with a completely focused beam.

- HEBT Diagnostics. Beam-profile monitors (multiwire harp or video-profile devices) and beam-position monitors interspersed throughout the HEBT will provide beamsize, intensity distribution, and centroid information. This information will be used as the second line of defense for early detection of nonuniform beam-intensity distributions that would require interruption of the beam. The data from these diagnostic devices is continuously monitored and

compared with values stored in computer databases that represent the safe operating range for each parameter. Deviation from the safe operating range will cause a computer shutdown of the beam.

- Magnet Current Setpoints. Software limits on magnet currents will provide the third layer of defense against target window damage. All electromagnets in the HEBT are designed to operate at a given current, determined during the commissioning and tuneup phase of the facility operation. Ion optical calculations and empirical experiments will be used to determine the safe operating range for the current of each electromagnet and these values will be entered into a computer database. The current readback for each electromagnet will be continuously monitored during accelerator operation and deviation from the safe operating range will cause a computer shutdown of the beam.

- Window Sensor. The fourth and final layer in the defense against target window damage is a beam power *fuse*. This device is simply a continuous ribbon wound back and forth across the target window. The ribbon material and thickness is chosen to cause it to break if the beam power density at any point exceeds a given threshold that is above the *nominal* value but below the point at which target window damage commences. Once the ribbon is broken, the electrical circuit of which it is a part is opened causing a fast-protect shutdown of the accelerator.

- Target Diagnostics. Diagnostics within the target, such as target-rod thermal profiles, will also provide information regarding the beam intensity distribution. Thermal distributions of massive systems, such as the target assembly, react relatively slowly to changes in the beam-intensity distribution; thus, this is not envisioned to be tied into the accelerator fast-protect hardware. Rather, it will be a long-term diagnostic used primarily for beam tuning if necessary.

- Beamloss and Beamloss Monitors (BLMs). Substantial beamloss along the HEBT beamline, though not as serious as an overfocus event at the target, has the potential to damage the beamline and beamline components. The first line of defense for this event is identical to that used for target protection: every magnet power supply is electrically connected in series such that if any unit fails, an electrical signal shuts down the beam in <20 μs. This is particularly important for the dipole magnets that bend the beam. BLMs are placed throughout the HEBT beamline region. These devices detect radiation (particularly x- and γ-rays) resulting from beam impingement on beampipe or beamline components. Detection of beamloss is an extremely fast process (~1 μs), and any signals above a hardware threshold would trigger a fast-protect shutdown of the accelerator beam. Diagnostic devices that monitor the beam position and intensity distribution, as noted above, would also be used to prevent excessive beamloss in the HEBT.

- Off-Momentum Beamstops. Off-momentum components in the beam that exceed the acceptance of the HEBT (~1% δp/p) will be lost, typically, in the first bending magnet of the achromatic bend. This first dipole magnet of the achromatic bend is designed with off-momentum beamstops sufficiently thick to intercept these beam bunches without damage to beamline components. The quantity of off-momentum beam impinging on these beamstops will be monitored with both beamloss monitors and current monitors (reading the current deposited directly into the beamstops). Safe operating limits on these monitors will also enable a fast-protect accelerator beam shutdown should the beamloss fall outside the bounds of safe operation.

- Permanent Magnet Elements. Loss of one or more of the beam-expander nonlinear-magnetic elements is not addressed because the baseline design calls for these units to be permanent-magnet devices. These devices cannot lose magnetism suddenly under any conceivable accident scenario. Although permanent-magnet materials may degrade over time because of radiation, the degradation would be extremely slow, allowing the elements to be replaced when sufficient degradation has occurred. Although the baseline design for the HEBT calls only for permanent magnets for the nonlinear expander elements, studies continue to examine more widespread use of permanent-magnets in the HEBT to reduce the risk of an overfocus or *loss-of-defocus* event.

We believe that each of these layers of protection will prevent any possibility of damaging, either permanently or temporarily, the target window or the HEBT/target interface area. In the unlikely event that all these redundant, multilayered lines-of-defense fail, and the target window is indeed damaged, vacuum sensors in the HEBT will detect any breech of vacuum, trip the beam through the fast-protect system, and close the fast-acting valves that are included in the HEBT design.

10.4.4.6 Activated Air Handling System

- Hazard. Air in the APT accelerator and beam transport tunnels will likely become activated during accelerator operation by the small fraction of beam that is continuously lost during normal operations or by larger amounts of beam lost during a short-duration abnormal condition. The air is activated directly by protons that penetrate through the accelerator structures and into the surrounding air, and indirectly by neutrons produced by collisions between these protons and the accelerating structures, beampipes, and magnet poles. The radioactive isotopes created by these interactions decay by gamma or beta emission with relatively short half-lives, ranging from a few seconds to a few hours. While beam is *on*, the air inside the APT accelerator tunnel is held stagnant (no exchange with outside air), and the tunnel is sealed to prevent leakage of activated air to the atmosphere. The tunnel seal is not absolutely airtight, but penetrations and doors will be sufficiently well-gasketed that the total leakage rate is held below approximately 1.0 liter per second per meter of tunnel length, on average. The concentration of activated air in the tunnel decreases rapidly after beam shutdown, and acceptable dose levels for service entry or for release of the tunnel air to the atmosphere are achieved by simply waiting for times ranging from a few minutes to a few hours.

  The potential hazard of the activated air is exposure to gamma and beta radiation from the decaying isotopes. If significant quantities of activated air were to leak inadvertently from the tunnel because of greatly degraded seal performance, or were to be released prematurely from the vent stack before the level of radiation has decayed sufficiently, such air could cause plant operating personnel or nearby off-site individuals to receive radiation doses above acceptable limits.

- Description. Activated air resulting from accelerator operations will be monitored, managed, and disposed of in accordance with DOE regulations. After beam shutdown, the procedure to be followed will be to permit the activated air to decay to an acceptable level and then purge it from the tunnel via the ventilation vent stack to the atmosphere. This is accomplished by an operator selecting the tunnel ventilation system exhaust mode and turning on the appropriate blowers.

Fresh air is brought in from the outside to purge the residually radioactive air from the tunnel into the exhaust ducts of the system, where it passes through a system of prefilters and HEPA filters before being exhausted up the stack. The waiting time for decay of the activated air in the tunnel will be determined by DOE-mandated exposure limits (<10 mrem per year) for maximally exposed individuals in uncontrolled areas adjacent to the APT site.

- **Air Release Situations.** Three operational situations have been considered which bound the estimation of activated air release from the accelerator and beam transport tunnels. The annual dose obtained from such releases would be determined by several key factors representing these situations as outlined below.

  - **Situation 1. Air leakage from tunnel during normal beam operations.**
    - equilibrium concentration of activity in the accelerator tunnel,
    - air leakage rate at or near surface level from accelerator tunnel, and
    - yearly average wind distributions from tunnel to offsite populated areas.

  - **Situation 2. Air exhaust from tunnel before maintenance operations.**
    - air activity concentration in tunnel before exhaust through stack,
    - flow delay time from tunnel to stack exhaust,
    - tunnel air volume and time to exhaust it through the stack, and
    - yearly average wind distribution from tunnel to offsite populated areas.

  - **Situation 3. Air leakage from tunnel during beamloss accident.**
    - maximum credible beamloss and maximum credible duration of loss,
    - average concentration of activity in tunnel during accident, and
    - other factors similar to Situation 1.

- **Activated Air Estimates.** Activated air production and release estimates for the APT accelerator in normal operation have been facilitated by calibration data from operations of the LAMPF linac and the Proton Storage Ring (PSR) at LAMPF [10-2]. Both LAMPF and PSR operate with protons at an energy of 800 MeV. The PSR tunnel has transverse dimensions that are similar to those for APT, and the air is also static during operation. Based on the LAMPF/PSR data, allowing for energy scaling and appropriate averaging, we can estimate the equilibrium isotope distribution in the APT tunnel, the resulting activity distribution, and the annual release of activity attributable to each isotope at the surface of the tunnel earth shield. The results are shown in Table 10-7.

Table 10-7. Isotopic Composition of APT Activated Air

Isotope	Equilibrium Distribution (%)	Activity Distribution (%)	Annual Release (Ci)
^{10}C	0.0	0.7	0.7
^{11}C	51.8	48.3	42.0
^{13}N	9.8	18.9	16.4
^{16}N	0.0	0.2	0.2
^{14}O	0.1	1.1	1.0
^{15}O	2.7	24.4	21.2
^{41}Ar	35.5	6.2	5.4

Using the LAMPF calibration of dose at the site boundary for fixed activity releases of each of the above isotopes, and taking a factor of 2.5 penalty for ground-level air release (compared to release from the LAMPF stack), the offsite dose-level estimates for Situations 1, 2, and 3 have been calculated and are summarized in Table 10-8. For normal operations and maintenance, the resultant offsite dose to the public is much less than 0.1% of the exposure limit; and for the accident condition, it is close to 0.1% of the limit. The DOE public radiation exposure limit for uncontrolled areas adjacent to a site is 10 mrem/year.

Table 10-8. APT Activated Air Release Estimates

Scenario	Resulting Public Offsite Dose
Normal operations with maximum tolerable beamloss (20 nA/m)	0.039 mrem/year
Tunnel exhaust before maintenance operations (once per beam-on day)	0.015 mrem/year
Maximum credible beamloss accident (200-mA spill at 1 GeV for 1 hour)	0.120 mrem

- Additional Situations. In addition to the above scenarios, workers may need to enter the tunnel several times a year to perform short-duration service on the linac without exhausting the activated air. Such entries would be made through double (airlock) doors with the small enclosed volume of activated tunnel air exhausted through the stack before the outer door is opened. The annual dose at the site boundary from these releases is estimated to be negligible compared to the situations described above because of the very small air volumes involved (<100 m^3/year).

- Components. Although the activated air handling system may be operated manually, an interlock with the personnel safety system will prevent the exhaust blowers from running when the air within the tunnel is above a preset allowable radioactive limit for release to the atmosphere. The major components that make up the system are the control system, a welded air-duct system complete with remote-controlled air dams, a blower, prefilters, HEPA filters, and a 25-meter high vent stack equipped with a sample port.

10.4.4.7 Activated Water Handling

The primary coolant loop is a closed-loop system that removes heat from the accelerator. The system circulates water through the accelerator cavities, components, intermediate-tuning beamstops, vacuum pumps, and diagnostics to remove heat. Through beamloss, the coolant can become activated by protons. The primary hazard is the potential of exposing personnel to radiation or to activation products should there be a leak in the primary coolant loop.

Available data from LAMPF accelerator operations indicates that almost no activation products are present in the accelerator cooling water when sampled 2–3 days after a shutdown, and less than 1 μCi/l of activity from tritium. Most significant in the LAMPF accelerator cooling water assay is the absence of ^{7}Be which has a half-life of about 53 days

and appears as an activation product in target cooling water in quantities that are more than 30 times any other radionuclide. Extrapolating to the higher-current, higher-energy APT parameters and estimating what the activity would be 2 hours after shutdown, there is no need to be concerned regarding personnel exposure.

With deionized water and filtration systems for treating the primary coolant, we do not anticipate activation products in any significant quantities in the accelerator cooling water. In spite of the data, and as a extra measure of safety, the APT accelerator primary coolant loop has been designed and will be treated as though it were activated. Spill containment will be addressed for any potential leaks or spills either from water piping or holding tanks.

Although the primary cooling loop should be leak free and trouble free, there will be times when the integrity of the system will have to be breached for maintenance purposes. On such occasions, the subject lines and/or cooling channels will be purged with dry nitrogen to displace the water from the lines and force it into the cooling system expansion tank. The nitrogen used to displace the water will be exhausted up the vent stack. Should some water still remain in a low point within a section of line, this water will be drained and captured in a holding container and either returned to the cooling system or will be transferred to the radioactive aqueous storage.

10.4.5 Failure Mode and Effects Analysis (FMEA)

10.4.5.1 Overview

An FMEA is a systematic way of analyzing single-point failure modes for each discrete accelerator module and safety system. Because the APT accelerator is a preconceptual design, we used the GTA at Los Alamos as an example for many accelerator systems. Only out-of-the-ordinary failure modes were examined and included in the FMEA document. Typical industrial failures were examined but are not included. The process used in this analysis is to systematically identify failure modes of the accelerator and the hazardous effects that can result from such failures. The accelerator facility was addressed as a unit and then broken into discrete modules for the analysis. Specific failures, hazards, and risks were first identified and then analyzed so as to provide an understanding of the risks involved in operating the APT accelerator with a known failure.

Each failure was assigned a hazard classification that is based upon the D. E. Lucas "A Practical Approach to Hazard Classification, Rev. 1" (March 1991). The hazard classifications by D. E. Lucas have been incorporated into DOE Order 5480.25. To determine the hazard class for each discrete module, a systematic study was performed on each accelerator module to identify the hazards of accelerator operation. We identified the consequence from the hazards expected in each broad category. These hazards included electrical, mechanical, chemical, and ionizing radiation. Each hazard, as it was identified, was evaluated for its safety and health implications on a worst-case basis and was then given an appropriate hazard-level classification. A safety analysis was then performed on those cases where the hazard had not already been previously analyzed and documented. We then examined ways to eliminate, control, or mitigate the identified hazards.

10.4.5.2 Summary

As mentioned, the FMEA document for APT and all the tables were prepared using the GTA at Los Alamos as an example. When a preliminary design for APT is completed, the

FMEA will be updated. The FMEA document for APT is included in Appendix 12.3 of this report.

In summary, no hazards were identified in the FMEA in the *catastrophic* category. There were, however, 19 *critical*, 18 *marginal*, and 92 *negligible* hazardous effects identified. Tables 10-9 to 10-11 summarize the accelerator failure modes and describe the hazard categories used and the designators for the types of events.

Table 10-9. Summary of APT Accelerator Failure Modes and Effects Analysis

Designator	Total	Hazard Category	Type of Event
IIc	3	Critical	Personnel exposure to hazardous materials
IId	16	Critical	Personnel exposure to other than hazardous materials
IIIc	10	Marginal	Personnel exposure to hazardous materials
IIId	4	Marginal	Personnel exposure to other than hazardous materials
IIIe	3	Marginal	Loss of operational capability
IIIf	1	Marginal	Loss of systems capability
IVc	15	Negligible	Personnel exposure to other than hazardous materials
IVe	41	Negligible	Loss of operational capability
IVf	36	Negligible	Loss of systems capability

Table 10-10. Description of Hazard Categories

Designator	Hazard Category	Consequences to Public, Workers, or Environment
I	Catastrophic	May cause deaths, loss of the facility operation, or severe impact on the environment
II	Critical (Major)	May cause severe injury,* severe occupational illness, major damage to a facility/operation, or major impact on the environment
III	Marginal (Minor)	May cause minor injury, minor occupational illness, or minor impact on the environment**
IV	Negligible (Trivial)	Will not result in a significant injury, occupational illness, or significant impact on the environment

*Or death to a worker.
**Or moderate damage/impact to a facility/operation.

Table 10-11. Description of Types of Events

Designator	Type of Event
a	Hazardous materials release to the environment
b	Hazardous materials release within the building
c	Personnel exposure to hazardous materials
d	Personnel exposure to other than hazardous materials
e	Loss of operational capability
f	Loss of systems capability

CHAPTER 10 REFERENCES

10-1. R.F. Koontz, T.G. Lee, C. Pearson, A.E. Vlieks, "Recent Performance, Lifetime, and Failure Modes of the 5045 Klystron Population at SLAC", Proceedings of the 1992 Linear Accelerator Conference, Ottawa, ON, pp. 740-742 (1992).

10-2. G. Lawrence, "Estimate of Activated Air Release from APT Accelerator Tunnel," Los Alamos National Laboratory Technical Note, 93-2-GL-1, Rev. 4 (1993).